ISBN : 978-84-931247-6-5

SECOND INTERNATIONAL CONFERENCE ON
ADVANCES IN MATERIALS SCIENCE
22-23 December 2017

राजे रामराव महाविद्यालय, जत

ADVANCES IN MATERIALS SCIENCE

(A SPECIAL ISSUE FOR ICAMS - 2017)

DR. V. S. DHEKALE
EDITOR IN CHIEF

DR. SHRIKANT R. KOKARE
EDITOR

DR. SANJAY S. LATTHE
ASSOCIATE EDITOR

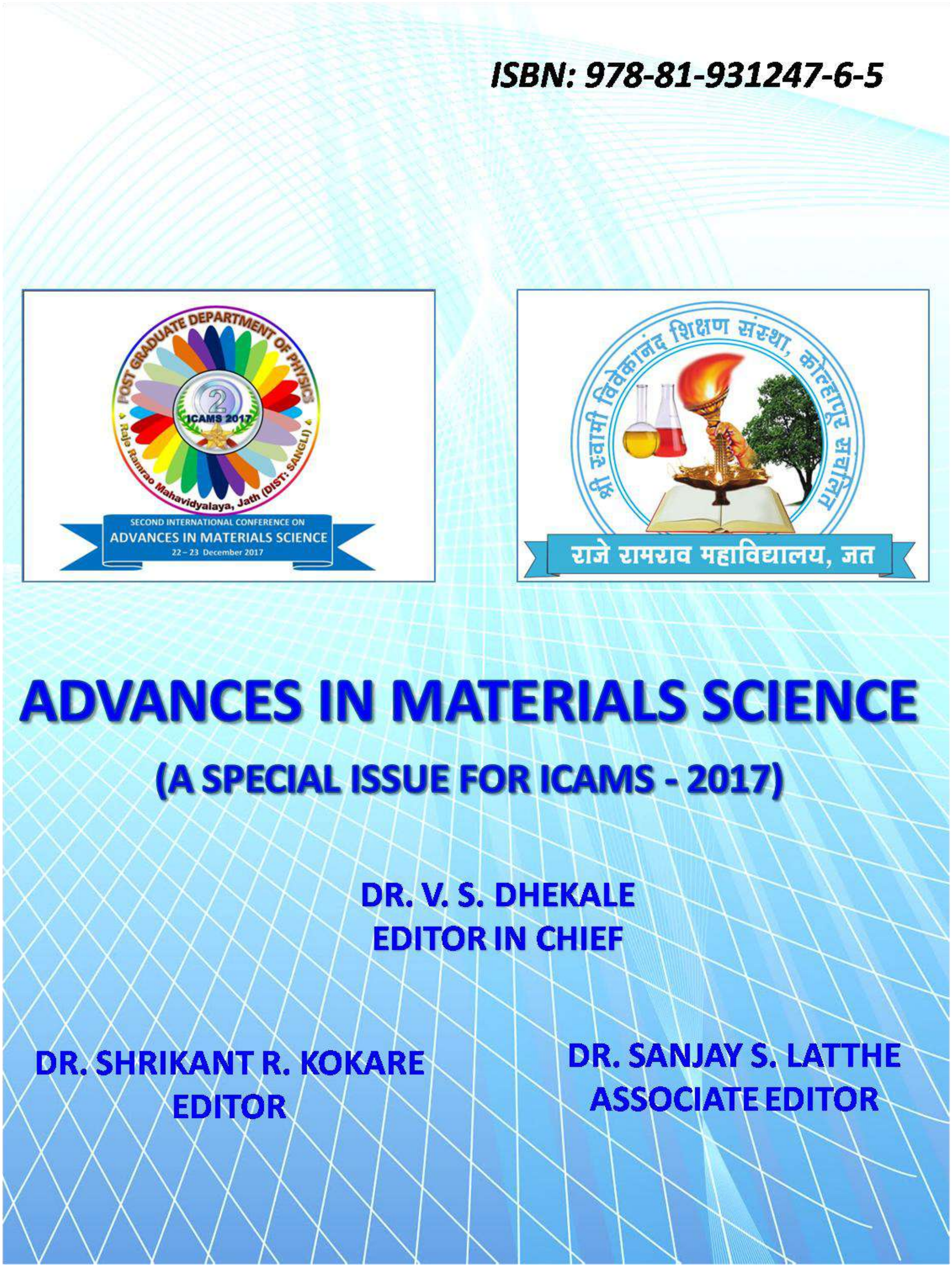

ISBN: 978-81-931247-6-5

ADVANCES IN MATERIALS SCIENCE

(A SPECIAL ISSUE FOR ICAMS - 2017)

DR. V. S. DHEKALE
EDITOR IN CHIEF

DR. SHRIKANT R. KOKARE
EDITOR

DR. SANJAY S. LATTHE
ASSOCIATE EDITOR

ISBN: 978-81-931247-6-5

Published by:

Bhumi Publishing,
Nigave Khalasa, Kolhapur 416207, Maharashtra, India
Website: www.bhumipublishing.com
E-mail: bhumipublishing@gmail.com

Available online at:

www.bhumipublishing.com/books/ Advances in Materials Science

PREFACE

Materials are a very important part of human life due to the fact that they are used on a daily basis. Every part of our body is a material. Bones, muscles, fingernails, hairs and skin are some of the examples. New materials are created all the time making new and fascinating things.

The properties of a material are important because it show you what it can and cannot be used for. There are two types of materials such as naturally found materials and manmade materials. From the beginning of time, human has used materials to survive. Before going to details of these materials, we have to look for a quick history of materials

Ancient cultures began their existence by making use of the stone, soil, plants and bones found in the environments. For nearly 2.3 million years, human lived using only these naturally occurring materials in a period known as the Stone Age. Normally this period counts from 15000 BCE to 7000 BCE.

Later human leaned how to convert copper and tin ore into metallic bronze and Stone Age became the Bronze Age. Around 3000 BCE, a technique of producing metal from mineral-rich ores was developed and then Bronze Age started. The technique uses heat and chemical reactions to produce metal from the more complex mixture of minerals found in ore.

The discovery of a method for producing iron and steel from ore was developed around 1200 BCE and the Iron Age began. Making iron is a more complicated process than that for copper and bronze. Agriculture development in the progress of human history has been practical since at least 1000 BCE. The wheel was developed around 4000 BCE and the first writing systems developed about 500 years later. The earliest method for producing glass from the melting of sand and other quartz based minerals was developed around 2500 BCE. Around 500 CE the Middle Ages began with the introduction of paper to Europe, which was first development in China around 200 CE.

By the 1500s human entered in the Modern Age, when trade and technology reached new level of complexity. The Industrial revolution began around 1760 and developed the steam power, factory manufacturing and the use of iron and cement as structural materials.

The Polymer Age is also called the age of plastics. Thousands of polymers exist in nature. The natural polymer in the environment is cellulose, the major structural material of trees and other plants. The proteins that make up our body are also polymers which include deoxyribonucleic acid (DNA). In 1861 the British chemist Thomas Graham had noted that when he dissolved organic compounds in solutions, some of them would leave sticky residues when passed through fine filter paper.

Many other 19th century scientists modified colloids and natural polymers to form new materials. In 1870 the American inventor John Wesley Hyatt produced an astonishing new product called celluloid. Celluloid is a plastic made from natural cellulose and it could be used for everything from movie film to cricket balls. In 1907 American chemist Leo H. Baekeland took two ordinary *chemicals phenol and formaldehyde, mixed them in a sealed vessel and subjected them to neat and pressure.*

Now a days people are not only using the materials for their modest living purpose but they are becoming the part and parcel of human body. Stent used for Blood flow, rods used to connect or replace the bone, thin membrane used as lenses in the eye etc are not the materials only but they becomes part of human body. Advances in the materials science made this possible and it has not been stopped. Overnight people around the globe are engaged in making the advances in materials science. A day is not fat away that we may have all disposable kitchenware, foldable aeroplane, Hydrogen as an efficient and pollution free fuel. We may have non-terable and wash – free cloths too.

More recent milestones include the development of synthetic plastics in 1907 and the identification of the first synthetic nanomaterials, the carbon fullerene in 1985. As these new materials have been developed, they have made new products and technologies such as computers, space crafts and robotics.

*A lot can happen in future and it is only due to the advances in Materials Science. In the History of Human development, man has managed materials for their development. Now man can't be lived with materials and a day will come in future on which materials can manage the man also. In this connection its great pleasure to publish our book entitled "**Advances in Materials Science**". This book is the compilation of esteemed articles of experts in the various fields of basic and applied science of materials providing a sufficient depth of the subject. We hope that the students, teachers, researchers, scientists and policy makers in India and abroad will find this book much more useful.*

We feel fortunate enough for having a strong support from Principal, Abhaykumar Salunkhe, Chairman, Principal Shubhangi Gavade, Secretary, Principal Dr. R. V. Shejwal, Joint Secretary (Finance) Hon. P. S. Chavan, Joint Secretary (Administration) of Shri Swami Vivekannand Shikshan Sanstha, Kolhapur for their moral support and guidance. We are also thankful to Dr. V. S. Dhekale, Principal, Raje Ramrao Mahavidyalya, Jath and Dr. S. Y. Hongekar, Principal, Vivekanand College, Kolhapur. Both of them gave us full liberty to carry out the things smoothly. We are also thankful our publisher Bhumi Publishing, Nigave Khalasa, Kolhapur for taking pains in bringing out the book.

Dr. Shrikant R. Kokare, Editor
Head and Assistant Professor
Post-Graduate Department of Physics,
Raje Ramrao Mahavidyalaya, Jath (Sangli)
Email: kshirikant@yahoo.com
Mobile: +91-9421219424

Dr. Sanjay S. Latthe, Associate Editor
Assistant Professor
Post-Graduate Department of Physics,
Raje Ramrao Mahavidyalaya, Jath (Sangli)
Email: latthes@gmail.com
Mobile: +91-7030310947

INDEX

ATTEMPT TO ENHANCE THE PHOTOCATALYTIC PERFORMANCE ON MESOPOROUS TiO_2 THIN FILM

Norihiro Suzuki[1], Akihiro Okazaki[2], Haruo Kuriyama[2], Izumi Serizawa[2],
Chiaki Terashima[1], Kazuya Nakata[1,3], Ken-Ichi Katsumata[1] and Akira Fujishima[1]
[1]Photocatalysis International Research Center, Tokyo University of Science
[2]RC Manufacturing Co. Ltd.
[3]Graduate School of Science and Technology, Tokyo University of Science

Mesoporous ceramics with pore of 2 – 50 nm in diameter are interesting materials due to its unique features such as large pore volume, large surface area, and uniform pore size. Mesoporous ceramics can be synthesized easily by the surfactant-assisted sol-gel method (soft-template method), in which the self-assembly of the amphiphilic surfactant micelles is used as a template. By combining the organic-template and inorganic sol, the organic/inorganic hybrid is created. Finally, calcination was conducted to remove the organic template and crystallize the inorganic framework (Fig. 1).

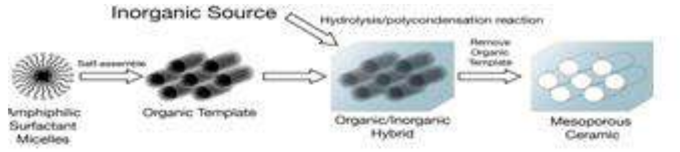

Fig.1: Fabrication process of mesoporous ceramics by surfactant-assisted sol-gel method

Due to their large surface area, mesoporous ceramics would be superior photocatalyst. Indeed, in my previous studies, mesoporous n-type semiconductor ceramics (i.e. titania and niobia) showed good photocatalitic activity when both large surface area and high crystallinity in the framework was achieved [1,2]. In addition, by introducing inert mesoporous silica with high surface area, photocatalitic activity became stronger than original nonporous titania [3].

However, in the single component materials, recombination of photo-carriers often occurs. This carrier recombination reduces the number of holes/electrons reach to the active sites, leading the lowering photocatalytic properties. Thus, suppressing photo-carriers recombination is also important to enhance photocatalytic performance.

To suppress the carrier recombination, p-n heterojunction has been used. At the hetero-interface, an energy gradient is created to match the energy level of both bulk, and this gradient is useful to promote photo-generated charge separation. In this study, we fabricated mesoporous titania thin film (n-type semiconductor) on the p-type semiconductor substrate (boron-doped diamond, hereafter denoted as BDD), aiming to enhancing the photocatalytic activity.

Precursor solution was prepared by following previous studies[4] and as-prepared film was made on BDD substrate by spin coating. To increase the film thickness, thermal treatment and spin coating was repeated 5 times. Finally, calcination was conducted at 400 ºC for 1h to obtain a porous thin film.

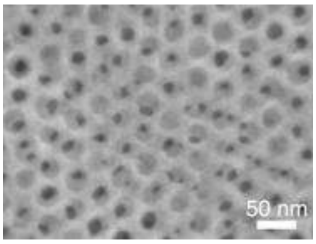

Fig.2 Top-view SEM image of mesoporous titania thin film fabricated on BDD

The morphology of synthesized thin film was examined with SEM image. As shown in Fig. 2, very well ordered structure with hexagonally packed mesopores was obtained. The XRD pattern revealed that the framework was crystallized to anatase phase (Fig. 3).

The photocatalytic activity was examined from the decomposition of methylene blue (Fig. 4). Although titania amount was trace (1.5 cm × 1.5 cm × 1 - 2 µm in thickness), phtocatalytic activity well appeared.

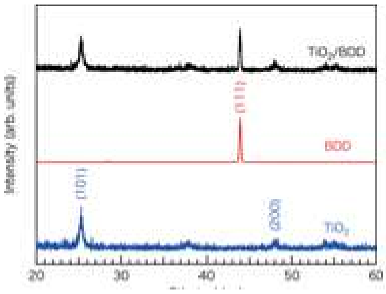

Fig.3 XRD spectrum of synthesized mesoporous titania thin film

Compared to the porous titania on glass substrate, sample on BDD showed superior photocatalytic activity, suggesting the photo-carrier separation at p/n hetero-interface.

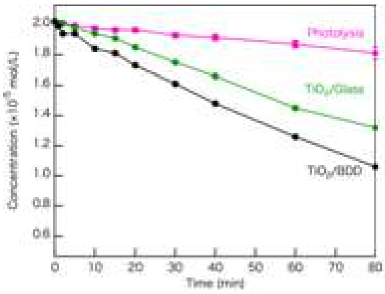

Fig.4 Result of decomposition of methylene blue

In my presentation, I would like to explain why photocatalytic performance enhances in mesoporous TiO_2/BDD composite in detail. In addition, I would like to talk about a microwave heating, which is an alternative way to crystallize the titania framework.

REFERENCES:

1. H. Oveisi, N. Suzuki et. al., J. Sol-Gel Sci. Tech., 56, 212 (2010).
2. N. Suzuki et. al., J. Ceram. Soc. Jpn., 119, 405 (2011).
3. N. Suzuki et. al., Bull. Chem. Soc. Jpn., 84, 812 (2011).
4. (a) X. Jiang, N. Suzuki et al., Eur. J. Inorg. Chem., 2013, 3286 (2013).
5. N. Suzuki et al., Chem. Lett., 44, 656 (2015).

NANOSTRUCTURED MATERIALS AND ITS POTENTIAL APPLICATIONS

Kalagadda Venkateswara Rao* and Solleti Goutham

Center for Nanoscience and Technology, IST

JNT University Hyderabad, Kukatpally, Hyderabad, Telangana -500085, India

Nanotechnology is that as a particle gets smaller their surface area to volume ratio increasing dramatically. A particle having with a more surface area has a great number of reaction sites than bulk materials and thus results in higher chemical reactivity. Presently increasing the civilization a healthy and fresh environment is needed for the society, this creates the serious essential of environment monitoring, detection of pollutant gases is required thus this kind gas sensor to be developed by using nanotechnology. The present work deals with the synthesis of nano materials that is metal oxide nano particle for various applications such as solar energy, sensors. The obtained nano materials improves the overall sensing behavior as well increases the efficiency of solar cell.Nanotechnology is opening new and exhilarating opportunities for exploring Solar cell applications of the newly prepared nano structured materials. During the last decade, transition metal oxides have been actively investigated as hole- and electron-selective materials in organic electronics due to their low-cost processing. In this study, transition metal oxides (FLG/SnO_2, FLG/ZnO) for use in solar cell applications.

Moisture sensors are used in various areas based on their different operating conditions. Humidity sensing studies have advanced and widely employed in industrial and household applications. The majority of humidity applications was chosen with relative humidity measurements because it is very comforting to use and cost-effective. Ceramic humidity sensors exhibit chemical resistance. However, the semiconductor nano structured materials like ZrO_2, CeO_2, TiO_2 metal oxides and its composites ZrO_2/TiO_2, CeO_2/TiO_2 and ZrO_2/CeO_2 have been charming attention due to their physical stability, chemical stability, wide band gap and mechanical strength. The morphology of the nano structured materials also plays an important role to measure the humidity sensitivity. The obtained nano materials improves the overall sensing behavior as well increases the solar cell efficiency.

RECENT ADVANCES IN FERROELECTRICS/FERRITES – AN OVERVIEW

V. M. Jali

Department of Physics, Gulbarga University, Kalaburagi – 585 106

E-mail: vmjali@gmail.com

The present invited talk is dedicated to late Prof. P B Joshi of Solapur University, Solapur. An overview of the recent advances made in the field of ‘Ferroelectrics’ and ‘Ferrites’ will be presented.

Ferroelectric and ferrite materials find innumerable applications. Ferroics are the newly added class of materials which exploit the combined effects of applied electric and magnetic fields. The contributions made by us, in collaboration with Materials Research Centre, Indian Institute of Science, Bengaluru will be highlighted. Radiation plays an important role in controlling, modifying the properties of these materials. The effects of irradiation, such as electrons, Gamma, Swift heavy ions on the ferroelectric, dielectric, piezoelectric properties will be explained. Similarly, this talk would focus on our recent contributions to the field of ‘Ferrites’

Various applications of ferroelectrics and ferrites will be explained. The radiation resistant ferroelectrics identified by our group will be mentioned. Our recent contribution in ‘ferroelectric polymers’ will also be presented.

DEVELOPMENT OF EXOTIC NANOMATERIALS FOR VARIOUS APPLICATIONS

Pramod S. Patil
Dean, Science & Technology,
Former Coordinator, Energy Technology,
Founder Coordinator, School of Nanoscience and Technology,
Thin Film Materials Laboratory,
Department of Physics, Shivaji University, Kolhapur-416 004 (M.S.), India.
Email: psp_phy@unishivaji.ac.in

ABSTRACT:

Nanoscience and nanotechnology has been evolving at an unprecedented rate during the last few decades, because of its potential in transforming existing technologies. The wide varieties of nanomaterials have been discovered with unique properties that facilitate designing and developments of novel technologies. The nanomaterials will change the way we produce electricity, the way we store electricity, the way we travel, the way we sense and actuate. It will soon change everyday aspects of our everyday life. Nanomaterials are useful in various applications ranging from military to medicine and agriculture to textiles. The success of the nanotechnology by and large depends on quality of the nanomaterials.

Several products based on the carbon nanotube (CNT) and graphene are already in the market. Various forms of nanomaterials like nanotubes, nanofibres, nanorods, nanoflowers, nanostars, nanoprisms, nanospheres, nanoplates etc. of oxides, nitrides, sulphides and metals have been synthesized during last few decades. The very high surface area to volume ratio of these materials is the key to the success.

In this talk, various chemical techniques, their optimization and fine tunning to obtain TiO_2 nanotubes, nanoflowers, nanorods , ZnO nanorods, nanoflowers, nanowires will be discussed with a view to obtain efficient DSSC and perovskite solar cells. The materials like WO_3 nanosheets, In_2O_3 hollow nanoparticles using kirkendall effect, ZnO obelisk, SnO_2 nanofern, and In_2O_3 nanocubes for sensing of toxic gases will also be discussed. The materials like MnO_2 nanopetals, polyaniline nanofibres-Ag nanostick nanocomposites and their application in supercapacitors will be highlighted. The smart window technology with WO_3 nanogranules, WO_3 reticulated morphology, NiO nanoflakes, MoO_3 micro-nanorods will also be explained in brief.

HYBRID FLEXIBLE AMMONIA GAS SENSORS

V. B. Patil

Department of Physics (Materials Science)

*Functional Materials Research Laboratory, School of Physical Sciences,

Solapur University, Solapur -413255, (MS), India

E-mail: drvbpatil@gmail.com

Flexible gas sensors have a broad range of application areas e.g. fertilizer and chemical industries. With increasing market demand, improvement to the gas sensing performance in terms of selectivity, sensitivity, stability, and operation at room temperature challenges to researchers involved, having led to a host of attempts have been made to rationalize miniaturized design of a sensor . The most crucial criteria for the fabrication of a good sensor is that it must operate at room temperature and have ability to detect gas below a threshold considered to be acceptable by relevant institutions such as Environmental Protection Agency (EPA). According to EPA criteria, NH_3 is hazardous above 25 ppm. 90% of all NH_3 emissions are generated from livestock waste management and fertilizer production. As a result sensing hazardous NH_3 at low ppm require low cost, highly sensitive, and room temperature operating gas sensor systems.

Therefore, the development of simple and low-cost ammonia base hybrid gas sensors for health and safety precautions are necessary.

A novel flexible, ultra-sensitive, selective, and room temperature operable polyaniline based hybrid (PAni/α-Fe_2O_3 PAni/WO_3) ammonia (NH_3) gas sensors were developed onto a flexible polyethylene terephthalate (PET) substrate by in situ polymerization process. The observations were recorded to 100 ppm fixed level for various gases including NO_2, CH_3OH, C_2H_5OH, NH_3, and H_2S through monitoring the change in resistance of the developed sensor. The flexible (PAni/α-Fe_2O_3 PAni/WO_3) hybrid sensor demonstrated better selectivity towards NH_3. The synergistic response of the flexible hybrid sensors were remarkable than that of the PAni and α-Fe_2O_3 and WO_3 alone; indicating the effective improvement in the performance of PAni flexible sensor on nanocomposite process.

TOF-SIMS: ADVANCED MATERIALS CHARACTERIZATION TOOL

Anil Vithal Ghule*[,1,2,3,4]
Tel: 231-2609165 Mobile:09145772101; 09730283381
*Department of Chemistry, Shivaji University, Vidyanagar, Kolhapur 416004
[1]Department of Nanotechnology,
Dr. Babasaheb Ambedkar Marathwada University,Aurangabad, Maharashtra, India
[2]Inorganic Nano-Materials Laboratory, Department of Chemistry,
Hanyang University, Seoul, Republic of Korea 133-791
[3]Nevada Nanotechnology Centre, University of Nevada (Las Vegas) Las Vegas 89119, USA
[4]Green Chemistry and Mass Spectrometry Laboratory, Department of Chemistry,
National Tsing Hua University, Hsinchu, Taiwan 30013
E-mail: anighule@gmail.com; avg_chem@unishivaji.ac.in

With the growing knowledge and progress in nanotechnology, interest has been developed to integrate nanosciences into present and new emerging technology. It is also important to have efficient tools to cope up with the growing needs of characterization of complex systems involving nano-materials. Thus, scientists are in search of alternative tools or methods for their characterization of nano-materials. TOF-SIMS with its unique capability of providing information on atomic or molecular level, while dealing with organic, inorganic, and organic-inorganic hybrid samples is justifying its role in nanotechnology.

This presentation is focused on demonstrating the utility of TOF-SIMS in nano-material analysis. Method development and analysis of wide variety of samples like semiconductor nanomaterials, OLED, functionalized carbon nanotubes, quantum dots immobilized self-assembled monolayer systems, nanomaterial coated paper, cotton, and wool fibers, distribution of metal ions in biological samples etc would be discussed in detail. Depth profile and 3D imaging capabilities of TOF-SIMS are also explored to understand the distribution of the metal ions and nanoparticles in the samples. We have tried to address through our work some of the potential applications of TOF-SIMS in materials characterization in the field of nanotechnology, physics, and chemistry towards its specific applications.

CHARGE ORDERED STATES IN OXIDE MAGNETIC SYSTEMS

S. I. Patil[1], Balu Thombare[1], Pravin Dusane[1], Shankar Kekade[1],
Ashwini Salunkhe[1], R. J. Choudhary[2], D.M.Phase[2] and R.S.Devan[3]
[1]Department of Physics, S.P.Pune University, Pune 411007, India
[2]UGC-DAE Consortium for Scientific Research, Khandwa Road, Indore 452001, India
[3]Indian Institute of Technology Indore, Khandwa Road, Simrol Indore 453552, India

Doped rare earth manganites with general formula $AxA'_{1-x}BO_3$ (A= La, Nd, Pr etc. A'= Ca or Sr) shows diverse magneto-electronic phases like, Paramagnetic Insulator (PMI), Ferromagnetic Metal (FMM) , Anti-Ferromagnetic Metal (AFM) etc. due to coupling between lattice, charge, spin and orbital degrees of freedom. Magneto-electronic properties of these materials are dictated by various parameters like average A-site cation radii, size mismatch of the cations, oxygen stoichiometry, Mn^{3+}/Mn^{4+} etc. In this context wide bandwidth manganites like $LaCaMnO_3$ (LCMO) and $LaSrMnO_3$ (PCMO) have been studied extensively. The effective bandwidth plays majour role in the transport and magnetic properties of manganite systems. During the presentation, charge ordered phenomena will be discussed in detail for different systems. Majour focus will be on the intermediate bandwidth manganites like $Nd_{1-x}Sr_xMnO_3$ (NSMO), though it exhibits the most complex phase diagram. Strontium doping improves the chemical stability and enhances electrical conductivity of Neodymium manganite due to Mn^{4+} cation formation.

ADVANCED LITHOGRAPHY: A NOVEL PLATFORM FOR FABRICATION OF MICRO/NANO DEVICES AND SYSTEMS

Suresh Gosavi

Centre of Advanced Studies in Material Science and Solid State Physics,
Department of Physics, Savitribai Phule Pune University (Formerly University of Pune),
Pune- 411007, INDIA
E-mail: swg@physics.unipune.ac.in

"Microfbrication" has given world a whole together new vision to look at the world of miniaturization, in the area of semiconductor science and technology. In the recent years Microfluidics devices have emerged as novel analytical tools in many areas of science. Their inherent qualities including low power requirements, low sample consumption, rapid and parallel analysis, all with automation provide unique opportunities to create novel and more powerful devices with many applications also referred as micro Total Analysis System (μ-TAS).

Importantly, the performance of these devices are mainly depends on the geometry, surface quality and chemical functionality of surface. In recent years variety of polymers are widely used for microfluidics, replacing Silicon for nano electromechanical structures because of its low-cost fabrication processes such as replica moulding and templating as well as its properties such as transparency in visible range, chemical stability, gas permeability and flexibility.

The ability to micropattern the material is of great importance. There are many well established methods for microfabrication mainly categorized as replica moulding and direct micromachining techniques. However each of them has limitations in terms of quality and ace of fabrication. Replica moulding techniques provide good quality (in terms of surface roughness and feature dimensions) microfabrication but the process is slow responding to the geometry and design changes of the microstructures hence limit the fast prototyping. Direct machining techniques offer fast prototyping but in most of the cases such as direct UV lithography, laser lithography, e-beam lithography and X-ray lithography shows the morphological changes (inducing surface roughness and debris contamination) with chemical modifications which limit its application in μ-TAS. This suggests the need for micromachining process refinement which includes detailed analysis of lithography resist development and processing parameters optimization.

The work presented here briefly includes resist development, prototyping in devices design and fabrication of functionalised micro-nano structures. Doping of photosensitizers in polymers was initiated for its application in resist development for laser lithography, e-beam lithography and X-ray lithography. Lithography process was optimized by tuning the resist composition, lithographic parameters and physico-chemical properties of fabricated microstructures. All lithography techniques except e- beam lithography produce microstructure with straight sidewall, whereas the e-beam lithography produces the microstructures with curved sidewalls, which are eventually be useful as Micro Lens Array (MLA).

Our group is also active in device designing, prototype fabrication and its application for nanoparticles synthesis for its application in targeted drug delivery. One of the device prototypes was also developed for artificial human-skin growth. Wherein the device was designed in such a way that the membrane on which cells to be grown has to be maintain at air-liquid and liquid-liquid interface with controlled flow of media (nutrients) should be provided to that membrane for artificial skin growth.

The most fascinating part of the microfabrication techniques is its application for “spoofing of the biometric authentication systems (AADHAAR)”. Towards this objective, we aim, at first coming up with authentic ways to spoof the server by fabricating artificial fingerprints and iris with inherent photo-modulation and dynamic pupil functionality. By this an interesting problem of server sensitivity to spoof attacks gets posed, which we typically propose to solve by introducing wavelets based techniques to resolve the captures iris responses to infra red wavelengths by resolving the parts in time as well as frequency. The project thus aims at producing deployable solution to “strengthen AADHAAR live iris and fingerprint database” by making it error resilient against spoof attacks of sophisticated nature, which is of “national importance”.

Fabrication of functionalized microstructure is also one of the most important ongoing researches in the lithography field. Our group is involved in the fabrication of micro/nano patterns of Au-PMMA and Au-SU8 using e-beam lithography techniques.

MAGNETISM AND MAGNETIC PROPERTIES OF MATERIALS: A CASE STUDY

Y. D. Kolekar

Department of Physics, Savitribai Phule Pune University, Pune-411 007, MH, India

Magnetism and magnetic materials have a long and well-known history from ancient times to the present. Devices and technologies based on magnetism, from loadstone (magnetite, Fe_3O_4), in the ancient, to the spin-valve Giant Magneto-resistance (GMR) read-heads in our computers now, to the new memories e.g., Spin-transfer torque magnetic random-access memory (STT-RAM or STT-MRAM) in the future, may be the longest running technology in human endeavor. A fundamental understanding of magnetism requires quantum mechanics that has been superior in the 20th century. In this lecture, I will try to explain the origin of atomic magnetic moments, their mutual interaction that leads to magnetism, the generation of magnetic field, and the development of magnetic materials for technological applications. The lecture is proposed to provide an overview of the main phenomena that determine the magnetism of matter and the properties of magnetic materials. The main interactions involved are qualitatively described and the models at the basis of interpretation of the magnetic properties of materials are presented.

THE NORMAL APPROACH TO HANDLE VERTICAL HANDOFF AVALANCHE EFFECT AND 2PC PROTOCOL IN A WIRELESS NETWORK

D. K. Gautam and G. U. Mali

Department of Electronics Engineering and Technology

North Maharashtra University, Jalgaon, Maharashtra, India

In the previous generation, i.e. 1G to 3G, have limitation like limited data rate, upload data rate, download data rate, more hand off latency, less bandwidth and more network cost, etc. All these limited and insufficient features which will not support today's requirement because of high demand for speed, multimedia support, high capacity, other resources and IP based services. The main object of 4G is takeover existing technology with a single universal technology based on IP. They have a potential to provide flash high data rates over a wide area, global roaming facility, multimedia support and better system with reduced cost.

Nowadays, many of the digital electronic gadgets are being developed to boost the smaller networks like in office, universities and companies etc. So vertical handoff is of highest priority now. A no. of vertical handoff systems or methods done vertical handoff efficiently without sacrificing the quality, but In most of the vertical hand off the system the load is put on the mobile nodes to look over the data flow mechanism. This may add some contribution to increase the delay in the delivery of the data in the established network.

Also, due to the network nature is dynamic like DSR and AODV routing protocols are failing to perform well. By studying details merits, demerits and scope of all the techniques and proper analysis we found that address configuration, locking mechanism, Quality of service (QOS), power consumption (battery depletion), security and higher buffer space requirement is still challenging problem of designing a perfect and suitable protocol for better communication.

So for successful implementation of 4G and for future generation, Vertical handoff with best routing protocol is an essential tool for wireless network. So when a node moves from one networks to another network it establishing first contact with new one and maintains contact with old one while braking is called vertical handoff.

The main challenge is to implement proper hand off system with minimum No. of hand offs, low processing time and nearly zero data loss. If handoff processing time is more, it leads disconnection which affects the service quality. Therefore a proposed an idea for better and reliable communication is a pool tile based vertical handoff with avalanche effect mechanism (PTVHO) along with 2pc protocol implementation.

The pool manger for vertical handoff designed based on the tile (i.e. Time) which is catalyzed by fuzzy logic and simultaneously analyzes two phase commit protocol running in two different phases and measures the effects successfully.

INVESTIGATION OF THE OPTICAL POTENTIALS ON THE ^{40}Ca(α,t)^{41} Sc REACTION AT 40 MeV

K. Mazumder[1], A. Somadder[2], E. Hoque[2], Y. Haque[2], S. K. Das[2] and H. M. Sen Gupta[3]

[1]Department of Physics, Chandina Redwan Ahmed College, Comilla 3500, Bangladesh

[2]Department of Physics, Shahjalal University of Science and Technology,
Sylhet 3114, Bangladesh

[3]Department of Physics, University of Dhaka, Dhaka 1000, Bangladesh

ABSTRACT:

The ^{40}Ca(α,t)^{41}Sc reaction has been studied at 40 MeV incident energy. The angular distributions of the 8 states of the reaction are analyzed by using the full finite-range (FFR) distorted wave Born approximations (DWBA) for both the bound and unbound states of the ^{41}Sc nucleus by using the normal optical, Michel and molecular potentials. The spectroscopic factors that have been extracted for the three optical potentials are compared with the previous zero range (ZR) calculation of the ^{40}Ca(α,t)^{41}Sc reaction for the normal optical potential. The χ^2 values of all the potentials for different l transfers are calculated to estimate the quality of fits. The molecular potential fits the data more satisfactorily almost all the levels than the other two forms of optical potentials.

DEVELOPMENT OF FUNCTIONALIZATION PROCESS ON THE SEMICONDUCTOR SUBSTRATE FOR THREE-DIMENSIONAL STRUCTURE SEMICONDUCTOR

Hiroshi Ikari[1], Chiaki Terashima[2], Norihiro Suzuki[2], Kazuya Nakata[1,2], Ken-ichi Katsumata[2], Takeshi Kondo[1,2], Makoto Yuasa[1,2] and Akira Fujishima[2]

[1]Department of Science and Technology, Tokyo University of Science,

[2]Photocatalysis International Research Center, Tokyo University of Science

INTRODUCTION:

High density integration and multifunctional are required for semiconductor integrated circuits used in smart phones and PCs. The limits of miniaturization of currently used two-dimensional(2D)structure semiconductors are becoming visible. Therefore, the development of three-dimensional(3D) structure semiconductors is proceeding for further functionalenhancement. There are some methods of manufacturing 3D structure semiconductors. As a main method,micropores are formed by etching in laminated Sisubstrates.And then a metalsolution(cometo be a through electrode)is poured into the micropores.However, in this method, the metal solution is clogged at the entrance of the micropore and cannot flow into the micropore. This is because the micropore diameter is small and the polarity (amphiphile) between the substrate and the metal solution is greatly different.To overcomethat problem, a methodthatembedsin several µm holeby changingthe composition of the metalsolution is studied1). However,it will be necessary to embed in even finer poresin the future.Therefore, by implanting not only the plating process but also the substrate side treatment, it is possible to embed in a microscopic hole oftens nm by increasing the wettabilitybetween the substrate and the metalsolution.Thus, this research focuses on the development of a surface reforming process for Si substrates.

EXPERIMENT:

To investigate the fundamental physical properties and behaviors of the silicon substrate,2D smooth substrate was subjected to a hydrophilic treatment and analyzed. The silicon substrate was immersed in the following three mixed solutions. These solutions are used to hydrophilic treatment2) for semiconductors.

STEP1: H_2O : H_2O_2 : NH_4OH (v : v : v) = 1 : 1 : 5 for 10 min at 70℃

STEP2: H_2O: H_2O_2 : HCl (v : v : v) = 1 : 1 : 5 for 10 min at 70℃

STEP3: HNO_3 (65%) at room temperature for 10 min

Also, with a view to industrialization, we aimed at a more convenient process. The hydrophilic treatment was carried out as follows.

(1)Process to perform three steps in order(STEP 1 → STEP 2 → STEP 3)

(2)Process to perform each step independently (STEP 1 or STEP 2 or STEP 3 at 70 ℃)

(3) Process to perform each step independently at room temperature (STEP1 or STEP 2 or STEP 3 at r.t.)

Contact angle meter was used for evaluation of hydrophilicity.

RESULTS AND DISCUSSION:

Fig. 1 shows the contact angle measurement results of (1).

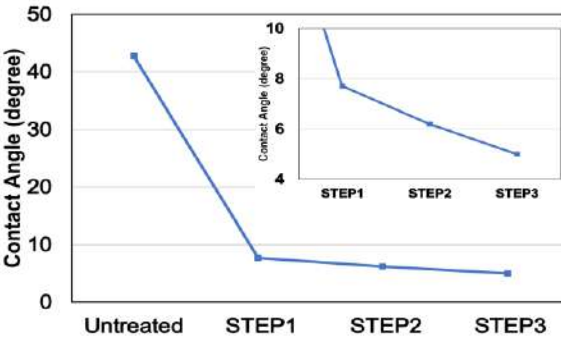

Fig. 1:
Contact angle measurement results of process to perform three steps in order

Fig. 2 shows the contact angle measurement results of (2) and (3). From Fig. 1, it can be confirmed that the contact angle (CA) was decreased by the treatment, and the final CA was 5 ~ 7 °. From Fig. 2, it was revealed that among the three steps, STEP 1 and STEP 3 greatly contributed to hydrophilization regardless of the treatment temperature.

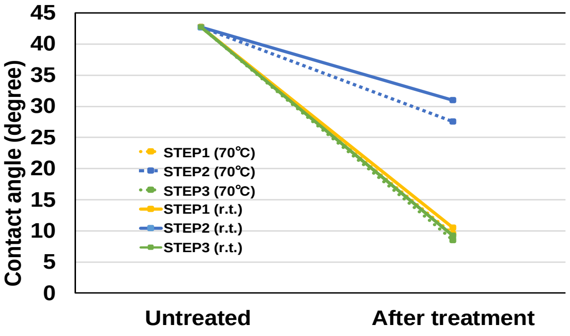

Fig. 2:
Contact angle measurement results of process to perform each step independently (70°C or r.t.)

And, it was found that the same effect can be expected even at room temperature. Therefore, it is considered that the process using HNO_3 (STEP 3) at room temperature is appropriate for more conveniently.

However, since the CA of HNO_3 to the silicon substrate is 35~40°, it is considered that it does not penetrate the actual micropores. Therefore, as a preliminary step of the treatment using

HNO_3, hydrophilicity was imparted by modifying amphiphilic sodium dodecyl sulfate (SDS) on the silicon surface. Since the CA of SDS to the silicon substrate is 7 ~ 10 °, it is thought that it penetrates the actual micropores. For the modification, 8 mmol / L SDS solution was used. Fig. 3 shows the CA measurement results of the silicon substrate after treatment with the SDS solution at each pH.

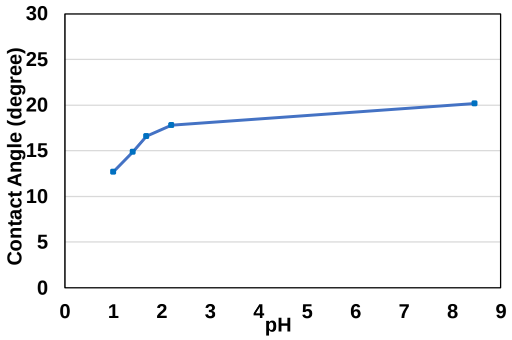

Fig.3:

Contact angle measurement results of process to perform SDS solution at each pH

From Fig. 3, it was confirmed that the lower the pH, the lower the CA and the higher the hydrophilicity. This is because as the pH decreases, the adsorption amount of the surfactant to the substrate increases. And, the hydrophilic group facing outwards is hydrolyzed in water to change to a hydrophilic -OH group$^{3)}$.

Fig. 4 shows the result of CA measurement of the optimized process. The process is immersed in an 8 mmol / L SDS solution adjusted to pH 1 and then hydrophilized with HNO_3. As a result, the final CA was 5 ~ 7 °, and it is the same degree of hydrophilicity as the process in Fig. 1.

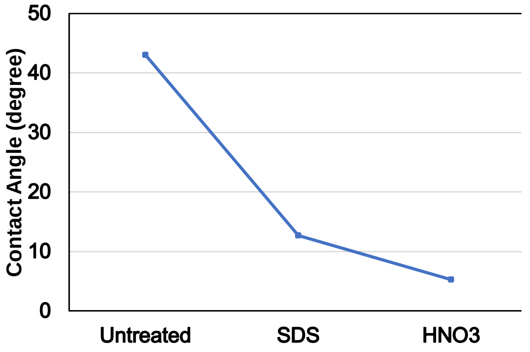

Fig.4:

Contact angle measurement results of optimized process

Based on the above, we have developed a more simplified hydrophilic treatment method for smooth 2D silicon substrate for semiconductor.This method has the same effect as the conventional method. By using amphiphilic SDS as a pretreatment step, application to 3D silicon substrate having micropores can be expected. After this, it is necessary to investigate the change of the surface state before and after treatmentby measuring the change of the amount of functional group with XPS.

REFERENCES:

1. R Abbaspour, D K Brown, M S Bakir,J. Micromech. Microeng. 27, 1 (2017).
2. Zhongpeng Zhu, Ye Tian, Yupeng Chen, Zhen Gu, Shutao Wang, Lei Jiang, Angrew. Chem. Int. Ed. 56, 1 (2017).
3. J. Penfold, E. Staples, I. Tucker, Langmuir. 18, 2967 (2002).

EFFICIENT NITROGEN FIXATION BY USING PULSED SOLUTION PLASMA AND PHOTOCATALYST

J. Ishii[1,2], K. Honda[1,2], C. Terashima[2], K. Nakata[1,2],
N. Suzuki[2], K. Katsumata[2], T. Kondo[1,2], M. Yuasa[1] and A. Fujishima[1,2]
[1]Graduate School of Science and Technology, Tokyo University of Science, Chiba, Japan
[2]Photocatalysis International Research Center, Tokyo University of Science, Chiba, Japan

INTRODUCTION:

Nitrogen fixation is a very important process because nitrogen compounds (such as ammonia and nitric acid (NO_3^-)) are essential for plant growth. However, current industrial processes depend on fossil fuel. Therefore, the load on the environment is large. In the last decade, a unique method of nitrogen fixation called as "pulsed solution plasma" has been studied [1]. This method could synthesize NO_3^- ion from only air and water. However, this method provides a low conversion efficiency of NO_3^- because of a small reaction field and larger generation of NO_x. To expand application fields, it is necessary to develop a more efficient method. Photocatalyst is well-known to convert NO_x to NO_3^- by using UV, which is also contained in plasma. Thus, this study focuses on improving efficiency of NO_3^- generation by combining pulsed solution plasma and photocatalysis. Experimental method and results are given below.

At first, effect of a reaction interface area was considered in order to achieve larger reaction field. Fig. 1 shows a schematic of pulsed solution plasma system. 100ppm K_3PO_4 was used as a solvent. Inserted air is decomposed at the apex of tungsten electrode by bipolar pulsed plasma.

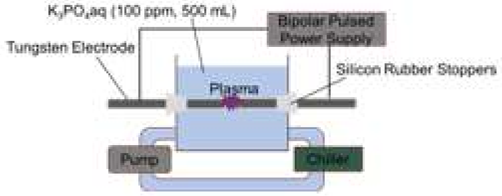

Fig.1: The schematic of pulsed solution plasma

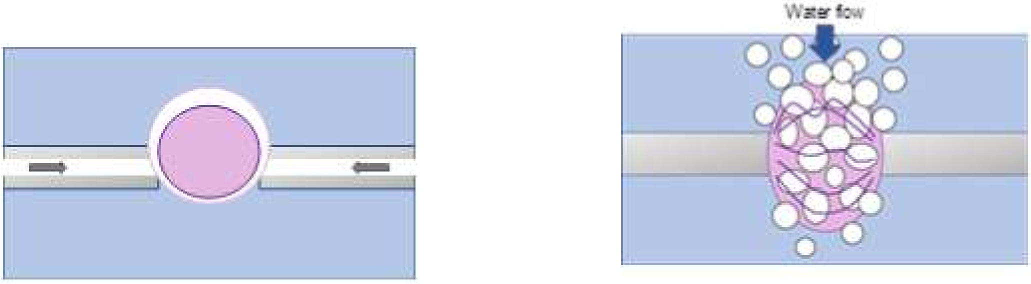

(a) conventional method **(b) new method**

Fig.2: Differences of bubble generation and plasma condition

In a conventional method (hereafter, described as method (a)), bubble is inserted to system from hollow electrodes (Air flow rate: 200 mL/min) as shown in Fig. 2 (a). In contrast, to expand reaction interface area, the new equipment was assembled as shown in Fig. 2 (b). In the new equipment, a large number of fine bubbles come to be generated by water flow from the top of electrodes (hereafter, described as method (b)). Frequency, pulse width, and voltage of power source was set to 100 kHz, 0.18 µsec, and 4 kV respectively. Nitrite ions were detected by ion chromatography.

Fig. 3 represents the result of NO_3^- synthesis by using method (a) or method (b).Concentration of NO_3^- increased with reaction time. To enhance the NO_3^- production, we increased the air flow rate from hollow electrodes in method (a), though NO_3^- generation was independent on the air flow rate.

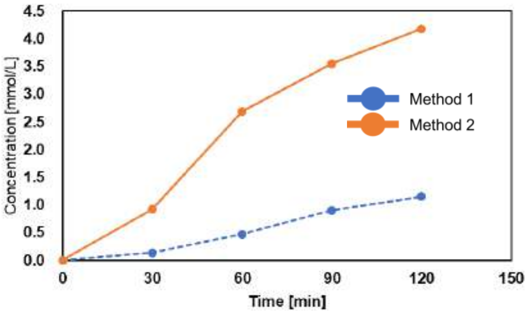

Fig.3: The result of NO_3^- ion synthesis

On the other hand, by taking in fine air bubbles by water flow from the top, method (b) synthesized NO_3^- around 4 times amount compared with method (a). It can be considered that the reaction efficiency improved due to increasing the gas-liquid interface from a number of finer bubbles.

Next, we examined whether TiO_2 can produce NO_3^- by its photocatalytic reaction. A schematic of simulation apparatus of photocatalytic reaction is shown in Fig. 4. The experimental apparatus containing TiO_2 (ST-01: Ishihara-Sangyo) was filled with 0.01 mM $NaNO_2$ (Fig. 4). Then UV light (330 nm) was irradiated to the system for 1 h. The intensity of UV light was 3 mW/cm^2. Air was bubbled as oxygen donor.

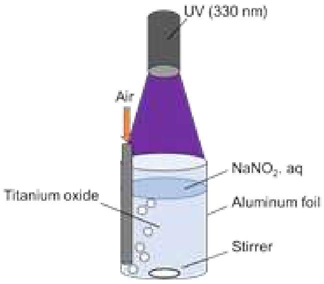

Fig.4: The simulation apparatus of photocatalytic reaction

Fig. 5 shows the result of photocatalytic oxidation of NO_2^-. This TiO_2 was found to oxidize $NO_x$to NO_3^- in presence UV light. After 1 h of UV light illumination, 0.04 mM NO_3^- was produced. Thus, it can be expected that NO_3^- generation rate improve by combing this photocatalysis and UV light of plasma. In the current presentation, results of combing photocatalysis and UV light of plasma will be discussed in detail.

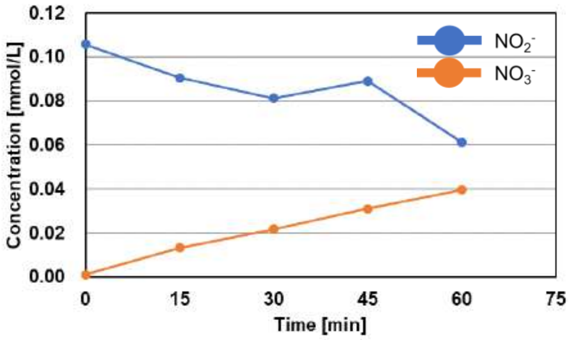

Fig. 5: The resultof photocatalytic oxidation of NO_2

REFERENCES:

1. K. Honda, Master thesis of Graduate School of Science and Technology, Tokyo University of Science, (unpublished, 2017).
2. Shifu Chen, Gengyu Cao, Desalination, 194, 127-134 (2006).

DEVELOPMENT OF FLOW-TYPE POLYSACCHARIDE SENSOR CAPABLE OF SCREEN PRINTING USING PAPER SUBSTRATE

***K. Katagishi[1], C. Terashima[2], N.Suzuki[2], I. Shitanda[1,2], K. Nakata[1,2], K. Katsumata[2], Y. Hoshi[1], M. Itagaki[1,2] and A. Fujishima[2]**

[1]Tokyo University of Science (2641, Yamazaki, Noda, Chiba, 278-8510, Japan)

[2]Research Institute for Science and Technology, Tokyo Univ. Sci.

[*] Corresponding author E-mail:7216621@ed.tus.ac.jp

Screen printing has been widely applied for the fabrication of electrochemical devices because a wide variety of inks can be used to generate precise patterns with high reproducibility. And it is possible to print on objects of various shapes, and the cost is low. In this study, we adopted a paper substrate. The paper-based electrochemical devices are easy to use, require small volumes of reagents and sample, provide rapid analysis, and are readily disposable. In addition, since the main component of the paper is cellulose fiber, it is possible to infiltrate the liquid into the hydrophilic fiber without requiring an active pump or an external supply source1). TiO2, which is a photocatalyst, shows extremely strong oxidizing power by irradiation with ultraviolet light. If TiO2 ink can be prepared and screen printed on a paper substrate, the reaction system which has proceeded with a complicated reaction can proceed with a simple system and can be quantitatively determined at low cost. In this study, a reaction part on which a TiO2 ink was printed was placed upstream, and a three electrode chip was placed downstream. We have developed a device that detects the substance at photoreacted upstream on the electrode part.

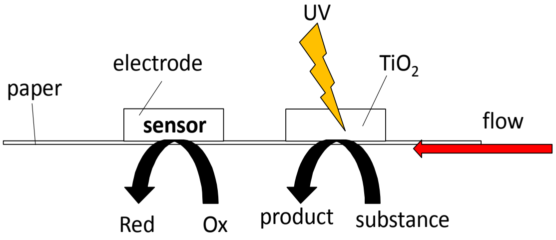

Fig. 1: Design of the cell

The design of the cell in this study is shown in Fig.1. TiO2 ink was prepared by adding 10 wt% of titanium dioxide nanoparticles (P-25, Nippon Aerosil Co.,Ltd.) using EC vehicle (200FTR, Nissin Kasei Co., Ltd.) or polyvinylidene fluoride (PVdF) as a binder and stirring for 30 minutes. This ink was printed on a filter paper using a screen printing machine (LS-150TV, New Long Industrial Co., Ltd.) and dried at 120 ºC for 15 minutes. In order to evaluate the printability of the prepared TiO2 ink, rheometer (MCRxx2, Anton Paar) was used. And in order to confirm the photocatalytic activity, a methylene blue solution was used. The lower part of the paper substrate was immersed in the solution, and then solution flows to the TiO2. Ultraviolet light of 50 mW/cm2 (MAX303, Asahi Spectroscopical Co., Ltd.) was used as a light source. Carbon ink was printed on the working electrode and counter electrode, and Ag/AgCl ink was printed for the reference electrode.

TiO2 ink using EC vehicle and PVdF as a binder was prepared. As a result of screen printing using these inks, it was confirmed that the ink using EC vehicle was printable. From the results of rheometer, it is considered that viscosity is higher and decreased by increasing shear rate when EC vehicle is used. The prepared TiO2 ink was printed using a screen printing machine, and a decomposition experiment of methylene blue was carried out by a flow type. From the results of the experiments, by irradiating the TiO2 layer with ultraviolet light, the methylene blue solution became transparent showing the decomposition. Therefore, it was confirmed that prepared TiO2 ink produced has oxidizing power and photocatalytic activity by irradiation with ultraviolet light even when it was used in flow system. Next, cyclic voltammetry was measured in 5 mM K4[Fe(CN6)] solution using three electrodes chip. As a result, the redox peak of [Fe(CN6)]4- / [Fe(CN6)]3- appeared and it was confirmed that it functions as an electrode.

Next, sucrose was allowed to flow from downstream to ascertain the response of the sensor Sucrose was changed to glucose in the TiO_2 layer, and the response of glucose was measured. (Fig. 2). In order to measure glucose, tetrathiafulvalene (TTF) was cast as a working electrode and dried under reduced pressure for 15 minutes. Then, glucose oxidase (GOD) was cast and dried under reduced pressure for 15 minutes. Measurement of the glucose solution from the sucrose solution was carried out by irradiating UV (50 mW / cm^2) onto the TiO_2 layer for 300 seconds, then applying cyclic voltammetry (Scanning speed : 50 mV/s, Applied potential : □ 0.3- +0.5 V vs. Ag/AgCl, Electrolyte : Phosphate buffer solution and sucrose (50 mM)). As a result, the anode peak current derived from glucose increased with light irradiation (Fig. 3).

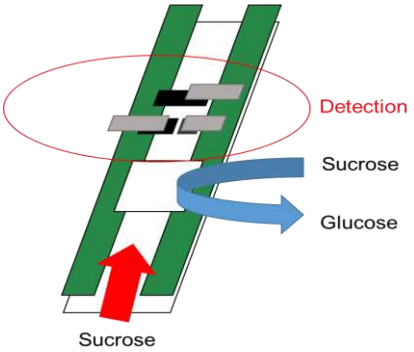

Fig. 2: Device structure

As a result, sucrose was decomposed into glucose in the TiO_2 layer, and succeeded in measuring glucose changed in the electrode layer.

By using this TiO_2 ink and three electrodes chip, it becomes possible to create a flow type sensor.

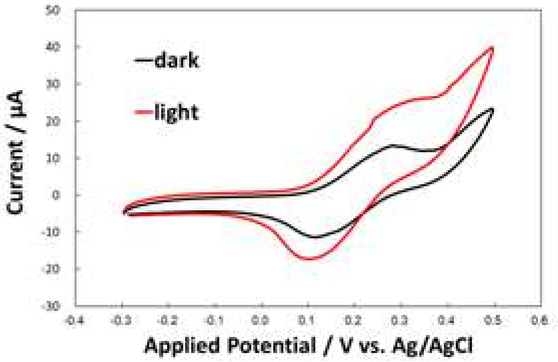

Fig. 3: Cyclic voltammogram in 50 mM sucrose solution (under dark and UV irradiation)

REFERENCES:

1. Martinez, A.W.; Phillips, S.T.; Whitesides, G.M. Carrilho, *Anal. Chem.* 82, 3–10 (2010).

RAPID SYNTHESIS OF DIAMOND ELECTRODE USING IN-LIQUID MICROWAVE PLASMA CVD PROCESS

Kazuya Miyasaka[1], Yusei Sakurai[1], Yohei Harada[1,2], Chiaki Terashima[3], Hiroshi Uetsuka[2,3], Norihiro Suzuki[3], Kazuya Nakata[1,3], Ken-ichi Katsumata[3], Takeshi Kondo[1,3], Makoto Yuasa[1,3], Akira Fujishima[3]

[1]Department of Science and Technology, Tokyo University of Science,

[2]Asahi Diamond Industrial Co., Ltd.,

[3]Photocatalysis International Research Center, Tokyo University of Science

INTRODUCTION:

Boron doped diamond (BDD) is useful for sensing and electrolysis applications because of its wide potential window1). Chemical vapor deposition method is used for synthesis BDD. However, this method has low growth rate. In-liquid microwave plasma CVD (IL-MPCVD) is possible to synthesize diamond rapidly. Therefore, this research focuses on high speed synthesis of BDD using microwave assisted in-liquid plasma method. Electrochemical properties of BDD films were then investigated.

EXPERIMENTAL:

Fig. 1 shows the schematic image of IL-MPCVD machine. A solution was prepared by adding boron oxide (1%, B/C) to a mixture of methanol and other solvnt (ethanol, methyl acetate, tetrahydrofuran (THF) or acetone).

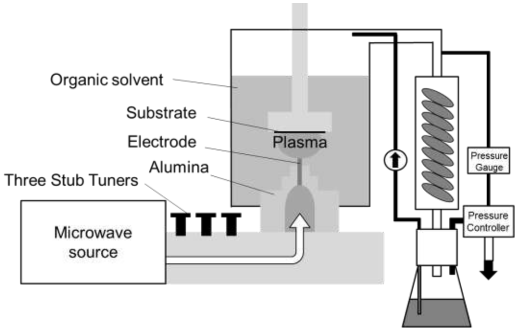

Fig. 1: IL-MPCVD machine

2.45 GHz microwave (440 W) was irradiated from the generator, and conducted into the reactor via a waveguide. The mixture was adjusted so that the ratio of C: H: O is 17.2: 66.7: 16.1. Monocrystalline silicon was used as a substrate. The distance between the tip of the electrode and the substrate was set to 1.0 mm. The diamond was synthesized for 5 minutes under 60 kPa.

RESULT AND DISCUSSION:

Fig. 2 shows Raman spectra of BDD films synthesized in different solvents. From the Raman spectra, it was revealed that boron was doped in the diamond, because a peak attributed to the optical phonon at near 1280 cm^{-1} and a peak derived from the B-B bond of boron at near 500 cm^{-1} were also confirmed. From this, BDD was obtained in all conditions using IL-MPCVD method.

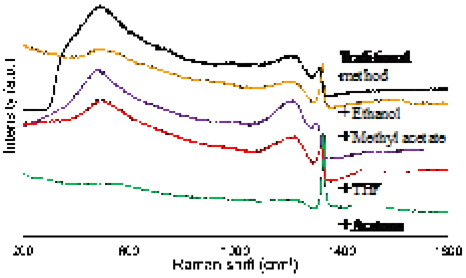

Fig. 2: Raman spectra of BDD films synthesized in different solvents

The boron concentration was calculated from the peak position at around 500 cm^{-1}. When methyl acetate was added to the mixture, the boron doping amount was estimated to be as high as 9×10^{20} cm^{-3}. Next, the growth rate was calculated from the film thickness measurement. When acetone was added to the mixture, we succeeded in high speed synthesis with growth rate of 196 μm/h. But boron doping is thought to be fewer as revealed by the peak intensity at near 500 cm^{-1}. Therefore, boron could be doped at a high concentration when the growth rate was slow.

Finally, the electrochemical properties of the synthesized BDD film were investigated using cyclic voltammetry (CV). Fig. 3 shows the results of CV in 0.1 M H_2SO_4. As results of analysis, synthesized BDD using this method showed a wide potential window, which is a characteristic of diamond electrode. From these results, we reveal that the microwave assisted in-liquid plasma method is useful method for making diamond electrode. It was found that the film growth rate and the doping amount depend on the solvent. Therefore, it is considered that BDD with the necessary concentration can be produced by selecting an appropriate solvent.

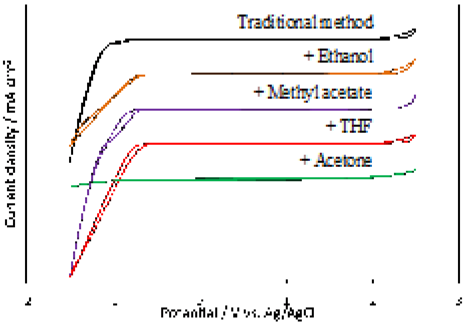

Fig. 3: Cyclic voltammetry of BDD films synthesized in different solvents

REFERENCES:

1. K. Nakata, et al., Angew Chem. Int. Ed., 126, 890-893(2014).
2. S. Nomura, J. Plasma Fusion Res., 89, 4, 199-206 (2013).

APPROACH TO SYNTHESIS OF THE LARGE-SCALE DIAMOND FILM USING IN-LIQUID MICROWAVE PLASMA CVD PROCESS

Y. Sakurai[1], Y. Harada[1, 2], K. Miyasaka[1], C. Terashima[1], H. Uetsuka[1, 2], N. Suzuki[1], K. Nakata[1], K. Katsumata[1], T. Kondo[1], M. Yuasa[1], A. Fujishima[1]

[1]Tokyo University of Science, Japan,

[2]Asahi Diamond Industrial Co., Ltd., Japan

*Corresponding author E-mail: 7216636@ed.tus.ac.jp

INTRODUCTION:

Diamond (including boron-doped diamond) is a versatile material as cutting tools and electrodes. Thus, development of effective growth method is needed. In the last decade, a unique method of diamond growth from organic solvents called as “in-liquid microwave plasma CVD (IL-MPCVD)” has been studied [1]. The growth rate of diamond by IL-MPCVD exceeds 100 μm/h, however, growth area is limited by size of electrode (3-5 mm in diameter). To expand application fields, it is essential to develop a method for uniform and large-scale diamond film.

EXPERIMENTAL:

Fig. 1 shows a schematic of IL-MPCVD system. Organic solvents are vaporized and decomposed at the apex of electrode by microwave plasma. Diamond films were deposited on substrate from mixture of MeOH and EtOH with or without tetrahydrofuran (THF) at 60 kPa with microwave power of 440 W. In addition, the system has an XY substrate stage moving horizontally. The distance between Si substrate and the electrode was set to 1.0 mm.

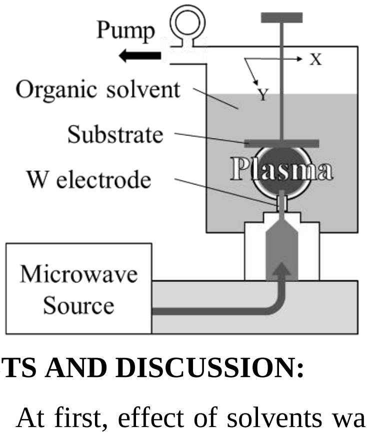

Fig. 1: A schematic of IL-MPCVD system

RESULTS AND DISCUSSION:

At first, effect of solvents was considered in order to achieve uniform diamond film. Fig. 2 represents summary of Raman measurements. Diamond film with THF tend to show higher crystallinity with a small disperse. On the other hand, quality of diamond film without THF is scattered and sometimes no diamond was grown. From the below figure, it was revealed that adding

THF caused to decrease sp^2 component. Thus, uniformity of diamond film was improved when THF was added.

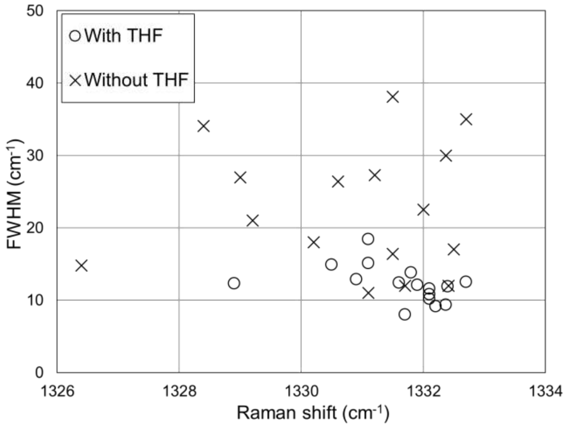

Fig. 2: Summary of Raman measurements

Fig. 3 shows photographs of diamond film grown with or without the stage movement from MeOH and EtOH with THF. A large diamond growth area of 6 x 6 mm^2 was achieved along the stage moving at 0.5 mm/min. As shown in the SEM images taken at certain positions on the large diamond film (Fig. 4), diamond grain size depends on its location. However, (111)-oriented grains appeared similarly, indicating that growth condition was rather uniform.

From these results, it was revealed that the diamond film can be expanded to any size theoretically. Thus, IL-MPCVD process is expected as a versatile method of diamond synthesis.In the current presentation, effect of solvents and uniformity of large-scale diamond film will be discussed in detail.

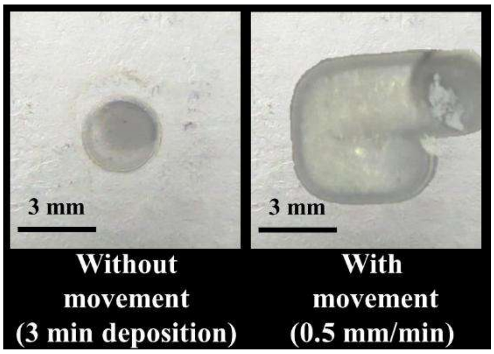

Fig. 3: Photographs of diamond film

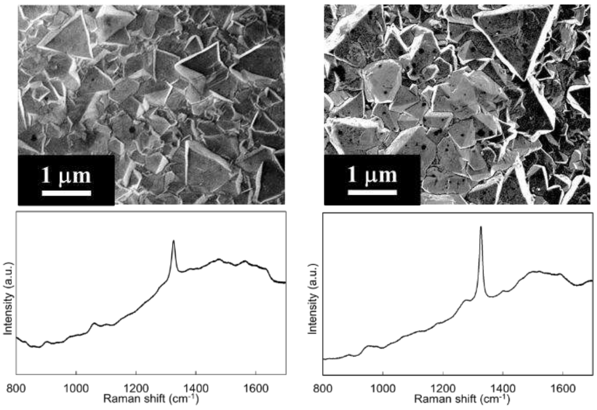

Fig. 4: SEM image of the large diamond film

REFERENCE:

1. Y. Harada et al., Diamond Relat. Mater.63, 12 (2016).

DEVELOPMENT OF LIQUID FERTILIZER WITH ANTI-ALGAL EFFECT FOR PLANT GROWTH BY SOLUTION PLASMA TREATMENT

S. Suzuki[1,2], K. Honda[1,2] , C. Terashima[2], K. Nakata[1,2], N. Suzuki[2], K. Katsumata[2], T. Kondo[1,2], M. Yuasa[1] and A. Fujishima[1,2]

[1]Graduate School of Science and Technology, Tokyo University of Science, Chiba, Japan

[2]Photocatalysis International Research Center, Tokyo University of Science, Chiba, Japan

INTRODUCTION:

Many thunders were believed to bring a good harvest. Thunderdischarges in air, and dissociating nitrogen in air forms nitrogen compound, which is a nutrient source of plants. We thought to imitate such a natural system by solution plasma. And anti-algal effect can be expected by using plasma treated water with sterilization effect. In this study, we make development of liquid fertilizer with anti-algal effect for plant growth by solution plasma treatment.

EXPERIMENT:

The solution plasma equipment is shown in Fig. 1.Solution used in this study was K_3PO_4 aq. (100 ppm,350 mL). Solution plasma treatmentwas conducted in N_2 gas atmosphere. In this study, N_2 gas was introduced by using W tube electrode from both sides (100 mL/min).Plasma was generated by pulse discharge (100 kHz, 0.18μs, 4kV). It was confirmed that the nitrogen fixing amount in this plasma treated K_3PO_4 aq. increased with treatment time.

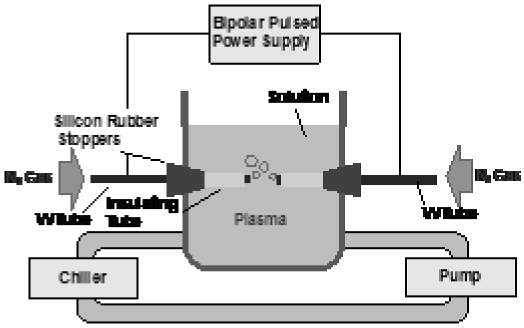

Fig. 1: Solution Plasma Equipment

Then, we conducted anti-algal experiment. Hoagland-Solution(5 mL) and sample (0.5 mL) were fractionated in test tube. Culture medium, initial K_3PO_4 aq., or 30, 60, 90, 120 minutes treated K_3PO_4 aq. was used as sample.*Chlorella vulgaris* (80 × 10^4 cells/mL) were introduced to the sample tubeand cultured under LED (10000 lx, 25 ℃). In addition, we cultivated basil using plasma treated K_3PO_4 aq.

RESULT AND DISCUSSION:

The result of anti-algal experiment is shown in fig. 2. It is found that only 120 min treated K_3PO_4 aq. have anti-algal effect. And plasma treated K_3PO_4 aq. left for 2 weekhas the same effect.

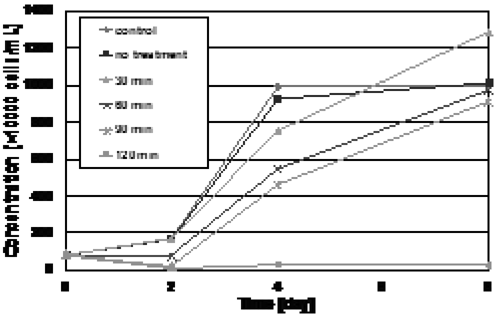

Fig. 2: Anti-Algal experiment

We also cultivated basil with Hoagland-Solution and 120 min treated K_3PO_4 aq. The result of cultivating basil is shown in fig. 3. Hoagland-Solution grows alga, but plasma treated K_3PO_4 aq. does not grow. We succeeded in makingliquid fertilizer with anti-algal effect for plant growth by solution plasma treatment.

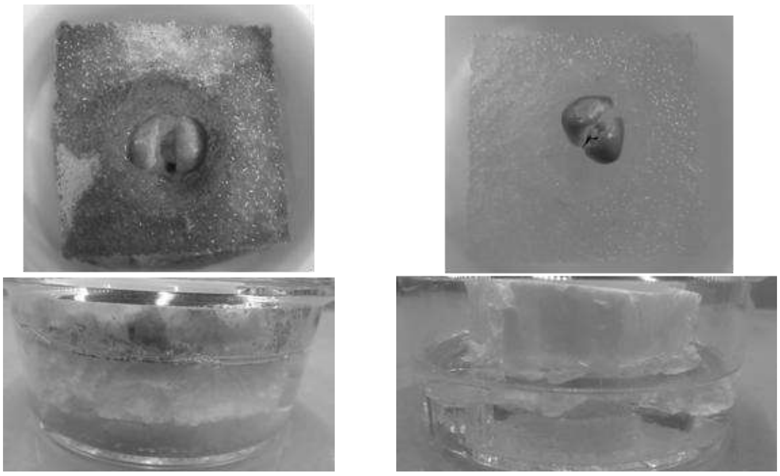

(a) Hoagland-Solution (b) 120 min treated K_3PO_4 aq.

Fig. 3: Cultivating basil

REDUCTION OF CARBON DIOXIDE USING HYBRID SYSTEM OF Ag-MODIFIED DIAMOND PHOTOELECTRODE AND TiO_2 PHOTOELECTRODE

*** Y. Hirano[1], N. Roy[2], Y. Nakabayashi[2], C. Terashima[2], N. Suzuki[2], K. Nakata[1,2], K. Katsumata[2], T. Kondo[1,2], M. Yuasa[1,2] and A. Fujishima[2]**

[1] Graduate School of Science and Technology, Tokyo University of Science, Noda, Chiba, Japan

[2] Photocatalysis International Research Center, Tokyo University of Science, Noda, Chiba, Japan

*Corresponding author E-mail: 7216661@ed.tus.ac.jp

KEYWORDS: CO_2 Reduction, Photoelectrochemistry, Boron-doped Diamond, Semiconductor

Recently, it is important to reduce atmospheric CO_2 concentration because of global warming. CO_2 is a very stable molecule which has high-energy barrier of −1.9 V vs. SHE for one electron reduction[1)]. To reduce CO_2, there are various attempts under aqueous conditions but selective reduction with high efficiency is difficult.

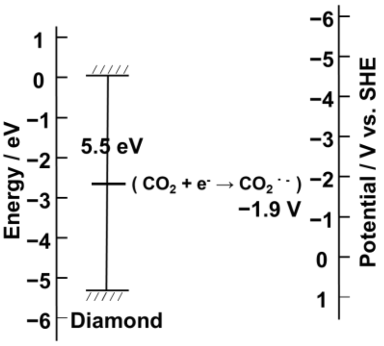

Fig.1: Band Diagram of Diamond

Diamond is one of the materials with very high conduction band position as shown in Fig.1. Light with high energy excites electrons to the conduction band and these excited electrons have high energy for selective photoreduction. Therefore, diamond is a suitable material for photocatalytic or photoelectrochemical CO_2 reduction. In this study, semiconductive lightly boron-doped diamond (BDD) is found to have an effect on CO_2 reduction with Ag, which is known as electrocatalyst for CO_2 reduction[2)], as a cocatalyst using an excimer lamp of 222 nm[3)].

BDD was synthesized by microwave plasma chemical vapor deposition method with boron source and carbon source in the ratio of 0.1 to100. Ag modified BDD (Ag-BDD) was fabricated by electrodeposition method in 0.1 M $AgNO_3$ aq. at −0.5 V for 1 min. FESEM was used to investigate the deposition of Ag.

A two-compartment cell was used with 25 mM Na_2SO_4 aq. as supporting electrolyte for both the working electrode and the counter electrode compartments, respectively. Both compartments were firstly purged with N_2 to remove the impurity gaseous species dissolved in the electrolyte and then purged with CO_2 for 30 min. Cyclic voltammetry was used to fix the bias potential. At −1.6 V vs.

Ag/AgCl, current density in CO_2 saturated condition was found to increase compared to N_2 saturated condition. It was considered that CO_2 reduced at −1.6 V vs. Ag/AgCl. Then, light of 222 nm was irradiated and bias potential of −1.6 V vs. Ag/AgCl was applied to BDD or Ag-BDD for 3 hours. In these conditions, CO and H_2 were observed as the primary gaseous product. Amount of them was analyzed using gas chromatography. When BDD was used as a working electrode, H_2 was produced mainly and amount of CO was small. However, Ag-BDD produced CO mainly and its amount was higher than that of produced from BDD.

To investigate whether this CO was produced from CO_2 reduction or other sources, isotopically labeled $^{13}CO_2$ was used and analyzed using gas chromatography mass spectroscopy. It reveals that 86–96% of CO produced by Ag-BDD was ^{13}CO, which was produced from photoelectorochemical reduction of CO_2 but not from other sources. It was confirmed that Ag-BDD was effective for photoelectrochemical reduction of CO_2.

To reduce CO_2 at smaller cell voltage, Pt counter electrode was changed to TiO_2 photoelectrode. The TiO_2 photoelectrode can absorb irradiated solar light and cause the oxidation of water to oxygen gas at lower applied bias potential rather than Pt[3]. Therefore, it is expected that CO_2 can be reduced at small cell voltage with light source by using hybrid system of Ag-BDD photoelectrode and TiO_2 photoelectrode (Fig.2).

TiO_2 photoelectrode was fabricated by heating a plate of titanium in a fire of gas. Raman spectra confirmed that the TiO_2 photoelectrode consisted of rutile.

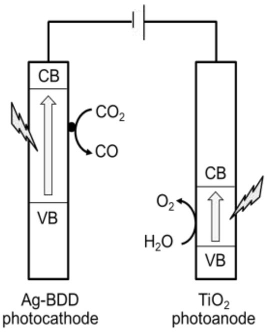

Fig. 2: Hybrid system of Ag-BDD and TiO_2

Cyclic voltammetry was used to check the cell voltage of Ag-BDD and TiO_2 photoelectrode. By using TiO_2 photoelectrode irradiated solar light as counter electrode, the cell voltage was decreased compared to Pt counter electrode as shown in Fig. 3. In the case of Pt counter electrode, CO_2 reduction was occurred at nearly −2.5 V. On the other hand, using TiO_2 photoelectrode as counter electrode can reduce CO_2 at nearly −1.0 V. These results were obtained in the condition that CO_2 saturated Na_2SO_4 aq. (pH 4.5) was used as supporting electrolyte for both of the reduction side and the oxidation side. Then, the supporting electrolyte of the oxidation side was changed to NaOH aq. (pH 13.0) from Na_2SO_4 aq. In this condition, cell voltage for CO_2 reduction was further decreased (−0.1 V) by chemical bias (Fig. 4) and CO was produced from CO_2 reduction.

By using hybrid system of Ag-BDD and TiO_2, the reduction of CO_2 proceeded at small cell voltage with light irradiation.

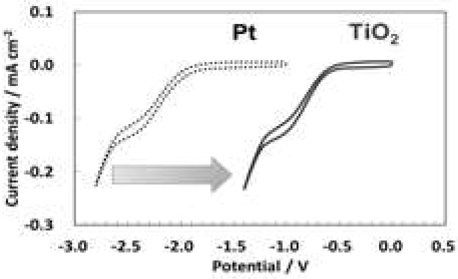

Fig. 3: Influence of counter electrode (W.E. Ag-BDD, C.E. Pt or TiO_2)

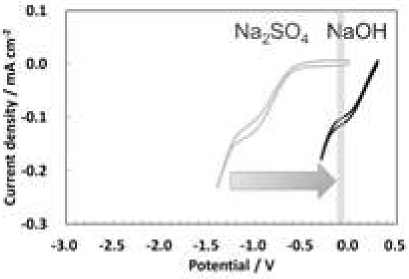

Fig. 4: Influence of electrolyte pH of the oxidation side (Na_2SO_4 or NaOH)

REFERENCES:

1. Linghong Zhang et al., Angew. Chem. Int. Ed., 53, 9746–9750 (2014).
2. Kousuke Iizuka et al., J. Am. Chem. Soc., 133, 20863–20868 (2011).
3. Nitish Roy et al., Scientific Reports, 6, 38010 (2016).
4. Akira Fujishima et al., Bulletin Chem. Soc. Japan, 44, 1148–1150 (1971).

FABRICATION OF TiO_2 FILM BY USING OF ATMOSPHERIC PRESSURE PLASMA JET AND PLASMA POLYMERIZATION

Rena Tabei[1,2], Chiaki Terashima[2], NorihiroSuzuki[2], Kazuya Nakata[1,2],
Ken-ichiKatsumata[2], Koji Arimitsu[1,2], Takeshi Kondo[1,2],
Makoto Yuasa[1,2] and Akira Fujishima[2]
[1]Graduate School of Science and Technology, Tokyo University of Science, Japan
[2]Photocatalysis International Research Center, Tokyo University of Science, Japan

TiO_2 shows photocatalytic properties such as strong oxidizing power and super-hydrophilicity under ultraviolet light, thus it has self-cleaning properties. There are many methods of synthesizing TiO_2 films, for example, thermal spraying, dip coating and spray coating. However, heat resistance is needed for the substrate in thermal spraying. The film synthesized by dip coating or spray coating is easy to peel off. Therefore, it is requested that the method which is unnecessary high-temperature processing and enables the film to have high durability. Generation of atmospheric pressure plasma jet (APPJ) using dielectric barrier discharges was reported by Engmann in 2005[1]. APPJ is non-thermal equilibrium plasma under normal pressure, thus plasma temperature is low, whereas electron temperature is thousands of degrees. In this study, TiO_2 precursor was synthesized and delivered to APPJ to synthesize TiO_2 film under normal pressure and temperature. Moreover, surface modified TiO_2 and siloxane resins were prepared and combined for organic-inorganic hybrid material to immobilize TiO_2.

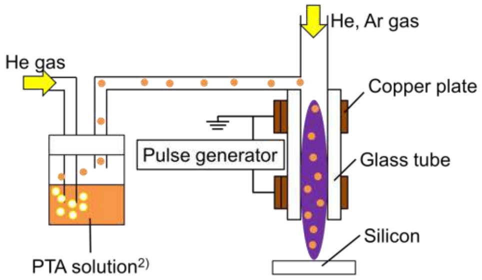

Fig. 1: Experimental set up

Peroxotitanic acid (PTA) solution was prepared and used as the precursor that was described in detail elsewhere[2]. APPJ generator consisted of Pyrex tube and two tubular copper electrodes on it. He and Ar gases were flowed through the tube, and plasma was produced by applying voltage from bipolar pulsed power supply. Gaseous PTA was delivered to the plasma by bubbling He gas. Si substrate was placed at the end of the plasma where the film was synthesized (Fig. 1).

The film synthesized by APPJ in 5 min was white and circular (3 mm diameter). Film quality became better when He and Ar mixed gas was used than only He gas was used. The crystallinity of the film was analyzed by XRD and a peak assignable to the plane of TiO_2(B) was observed(Fig. 2).

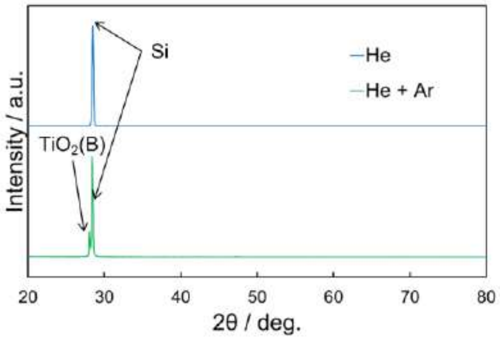

Fig. 2: XRD pattern

Photocatalytic activity of water oxidation for the synthesized film was analyzed by linear sweep voltammetry. The current density increased a little when the film was irradiated simulated solar light. However, photocatalytic activity was not enough, thus,this process needs improvement.In addition,the development of coating process using these materials is a further task in order to synthesize TiO_2 film on fiber materials such as paper and clothes. For this purpose, we applied the surface modified TiO_2 and siloxane resins, which are described in detail elsewhere[3], to the APPJ process.Radical polymerization isoccurred by radical and base with photobase generator and UV irradiation. It was reported OH radical was generated by mist plasma[4]. Thus, in this research, we used mist plasma instead of photobase generator for radical polymerization.

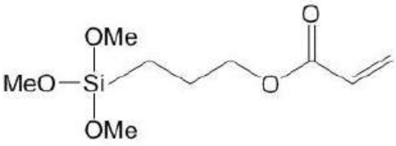

Fig. 3: Silane coupling agent

Siloxane resins were prepared by the sol-gel method with silane coupling agent (Fig. 3). Surface modified TiO_2 was also prepared by the sol-gel method with silane coupling agent. Siloxane resins and surface modified TiO_2 were dissolved and dispersed tetrahydrofuran by ultrasonic irradiation. Si substrate was coated with prepared solution by spin coating. And then, the Si substrate was placed at the end of the mist plasma (Fig.4).

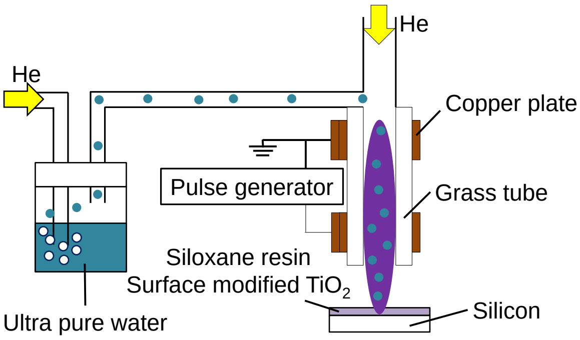

Fig. 4: Experimental set up (mist plasma)

As shown in Fig5, the peak area of C=C group was decreased, it can be considered plasma polymerization was occurred by mist plasma irradiation.

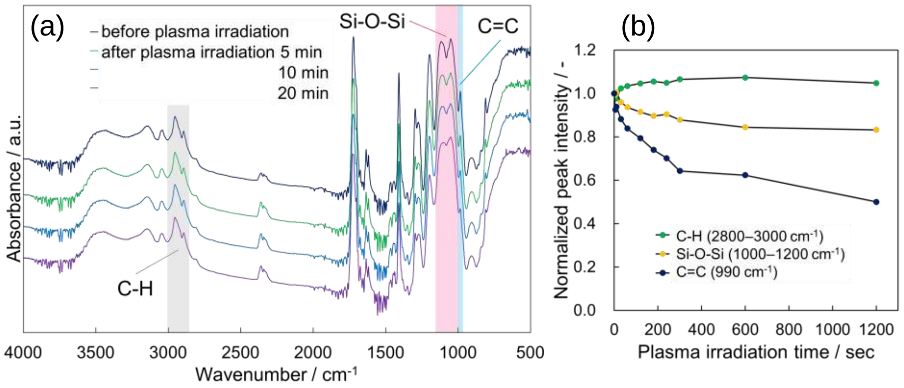

Fig. 5(a) FT-IR spectral, (b) peak area changes during mist plasma irradiation

REFERENCES:

1. M. Teschkeet al., IEEE T. Plasma Sci., 33–2, 310–311 (2005).
2. H. Ichinose et al., J. Ceram. Soc. Jpn., 104–8, 715–718 (1996).
3. K. Arimitsu, Photocatalysis, 50, 44–47 (2016).
4. N. Takamuraet al, J. Inst. Electrodtat. Jpn. 38-1, 22–27 (2014).

ELECTROCHEMICAL CORROSION PERFORMANCE OF POLYPYRROLE ASSISTED ANODIC FILMS ON AA2024 ALLOYS IN 3.5% NaCl SOLUTION

A. Madhan Kumar

Centre of Research Excellence in Corrosion, Research Institute, King Fahd University of Petroleum and Minerals, Dhahran, Saudi Arabia

ABSTRACT:

Polypyrrole assisted anodic Al_2O_3 films were electrochemically synthesized on AA2024 alloy substrates from an aqueous solution of oxalic acid. The surface morphology and structural characterizations were performed using the scanning electron microscopy (SEM), and Attenuated total reflectance- Infrared (ATR-IR) spectroscopy. Water contact angle measurements was also done to check the hydrophilic character of the synthesized anodic films. Further, electrochemical corrosion testing was done using potentiodynamic polarization and electrochemical impedance spectroscopy in 3.5% NaCl solution. Based on the electrochemical results, it could be concluded that the polypyrrole assisted anodic films exhibited better corrosion protection performance than pure anodic films due to its compact nature and doping-dedoping chemistry of conducting polymer chains.

INTRODUCTION:

Owing to its advanced strength/weight ratio and noble mechanical properties, AA2024 alloy is extensively employed in the aerospace industry. For the past few decades, anodically formed Al_2O_3 films on AA2024 alloy have attained significant attention as efficient materials in an abundant range of applications owing to the potentials in varying their dielectric, conducting, mechanical and anti-corrosion features by optimizing the series of synthetic parameters, using simplistic and ecologically friendly strategy and low cost equipment [1-3]. Most of the Al alloys used in practice are anodically oxidized (anodized) for protection against corrosion and wear. The protective properties of the films change with thickness and structure, providing better resistance to corrosion than that of bare aluminum.

In general, the anodic film consisted of a compact inner layer and a porous outer layer which could be normally sealed to enhance the corrosion resistance. Dichromate and nickel acetate sealing are deliberated the most operative sealing approaches for corrosion inhibition [4]. In order to limit the use of toxic Cr (IV), a number of sealants have been proposed for sealing applications and new sealing processes are emerging. In spite of these efforts to improve the performance, more convenient and effective processes are still needed. A strategy to offer chromate-free corrosion protection system is the utilization of conducting polymers that could be directly electrodeposited on Al substrates by anodic oxidation [5, 6]. Hence, in the present work, polypyrrole assisted anodic Al_2O_3 films were electrochemically deposited on AA2024 alloys and their corrosion performance was also investigated using electrochemical experiments in 3.5% NaCl solution.

EXPERIMENTAL:

AA2024 substrates with dimension of 5. 0 × 2. 5 × 0.2 cm^2 were purchased from the Q-Lab Corporation, USA. These substrates were mechanically grounded using 320–2000 grit standard abrasive papers, washed with deionized (DI) water, followed by ultrasonic cleaning in acetone for 5 min and dried in air. Anodisation was performed at a constant voltage of 8 V in 0.5 M oxalic acid solution containing 0.1 M pyrrole monomer. The cell was maintained under a nitrogen atmosphere with continuous stirring during anodizing.

The morphology and composition of the coatings were examined by scanning electron microscopy with energy dispersive X-ray analysis (SEM/EDX), using JEOL, JSM-6360 fitted with INCA 300 spectrometer. The structure of the anodized films was characterized by an IR spectrometer (PerkinElmer, with universal ATR attachment, range 400–4000 cm−1). Contact angles of the substrates were measured by contact angle goniometry at 25 °C using an Attension optical goniometer interfaced with image-capture software by introducing a 2 µL liquid drop.

Electrochemical corrosion measurement was conducted using a Gamry Instrument potentiostat/galvanostat/ZRA (Reference 3000). A graphite rod and a silver/silver chloride (Ag/AgCl) electrode were served as counter and reference electrodes, respectively. The base substrates with exposed area of 1.766 cm^2 served as the working electrode. EIS were recorded at OCP in a frequency ranging of 100 kHz to 10 mHz with amplitude signal of 10 mV. Potenitiodynamic polarization tests were carried out through varying the electrode potential range of ± 250 mV from the OCP at a scan rate of 1 mV s^{-1}.

RESULTS AND DISCUSSION:

ATR-IR curves for the pure anodic films and anodic films with polypyrrole additions is shown in Figure 1. In the case of anodized films, the peaks in the range of 400–600 cm^{-1} are associated with the asymmetric and symmetric vibrations of Al-O which indicated the passivated layer of Al_2O_3 on AA2024 alloy substrates [7]. Further, the presence of fundamental peaks at 980, 1190, 1360, 1439, 1698, 3200–3600 cm^{-1} in anodized layer with PPy confirmed the existence of polypyrrole moieties in the anodic Al_2O_3 films [8]. From the comparison of the two spectrums, it’s clear that the presence of polypyrrole moieties have influenced the structural configuration of anodic Al_2O_3 films.

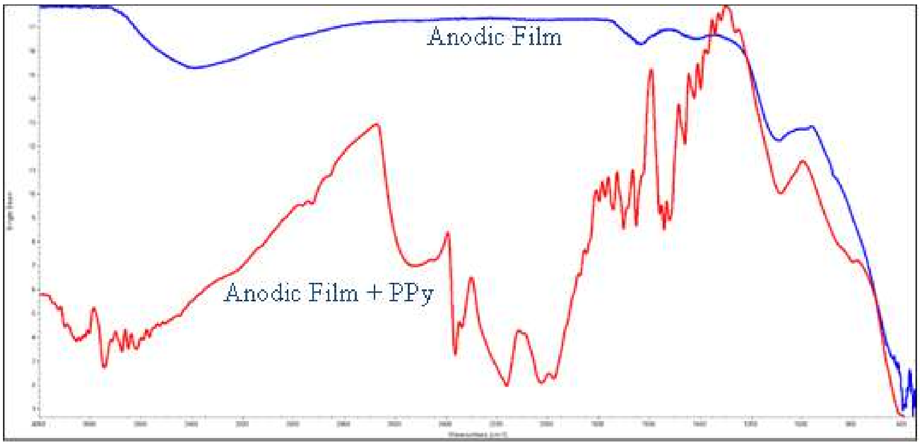

Fig. 1: ATR-IR spectra of Anodic films with and without polypyrrole

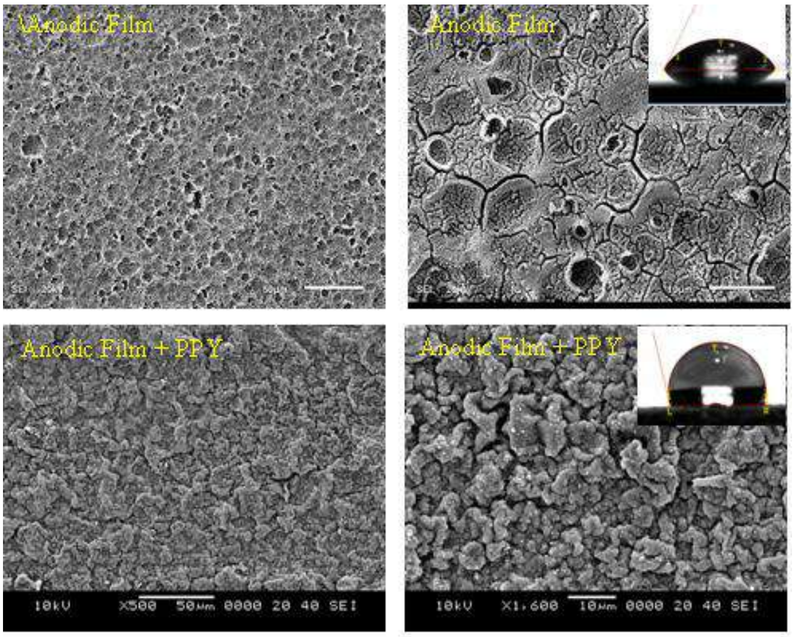

Fig. 2: SEM images of Anodic films with and without polypyrrole

SEM images of anodized Al_2O_3 films on AA2024 alloy substrates is displayed in Figure 2. From the observation of pure anodized Al_2O_3 films, it's clearly understood that the anodized films have the compact structure with open pores which are uniformly distributed over their surface [9]. On the other hand, anodic films with PPy displayed the typical cauliflower morphology of PPy coatings [10], further confirmed the influenced surface morphology of anodized Al_2O_3 films due to the inclusion of polypyrrole moieties in anodisation medium.

Water contact angle value (Fig.2 inset) of anodized Al_2O_3 films was found to be about 65° whereas, the anodized films with PPy additions exhibited the water contact angle value of 102° which indicated that the hydrophocitic behavior of anodized layer was enhanced with the addition of polypyrrole moieties on the anodized layer.

Figure 3 represents the obtained potentiodynamic polarization curves for anodic films with and without polypyrrole addition. From the observation of the curves, it's obviously indicated that the addition of polypyrrole into the anodized layer can increase the corrosion protection performance of anodized films by showing the lower i_{corr} value with nobler shift in E_{corr} value. In general, lower the value of i_{corr} higher the corrosion protection performance of the coatings [11]. This behavior may be due to the compact nature of anodized films with the addition of polypyrrole moieties which cover most of the pores present on the surface of anodized layer as shown in SEM images.

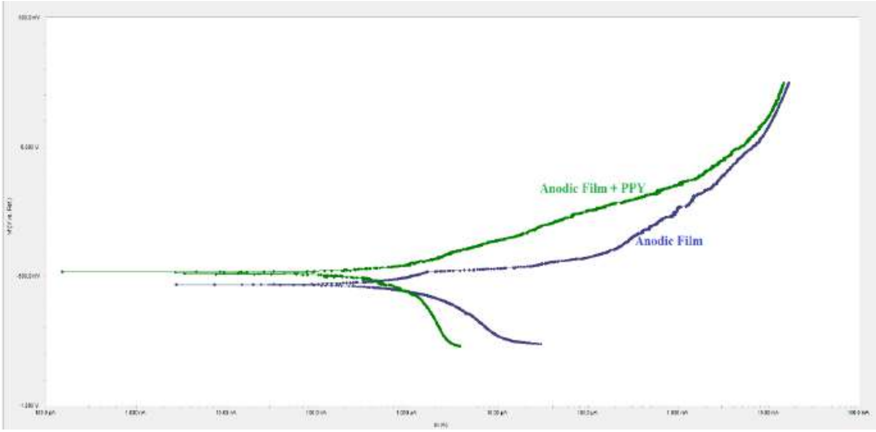

Fig. 3: Potentiodynamic polarization curves of Anodic films with and without PPy

Nyquist plot of anodized films with and without PPy additions are shown in Figure 4. Both the anodic films exhibited the two time constant behavior, one in middle frequency region and other one obtained at low frequency region. In general, the diameter of the capacitive arc in Nyquist plot used to calculate the overall corrosion resistance of the materials [12]. Normally, the higher the diameter present the better corrosion resistance. In the present study, anodic films with the PPy inclusion presented the larger diameter capacitive arc than the pure anodic films which further confirmed the enhanced corrosion resistant behavior of the anodic films. This behavior possibly due to the addition of polypyrrole moieties on the anodized films which alters the surface microstructure with hydrophobic nature of the films resulted in the improved corrosion protection performance.

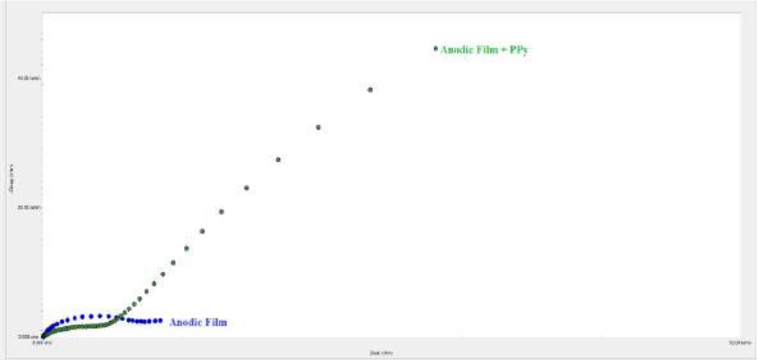

Fig. 4: Nyquist plot of Anodic films with and without PPy

CONCLUSIONS:

Anodized film with the addition of polypyrrole moieties was successfully prepared on AA2024 alloy substrates. The structural characterization by IR spectral analysis confirmed the presence of PPy moieties on anodized layer of Al_2O_3 films. SEM observation indicated the effective influence on the surface morphology of anodized layer caused by the addition of PPy. Hydrophobic behavior was increased by the addition of PPy on the anodized Al_2O_3 films which can further influence the corrosion resistant behavior. Electrochemical studies confirmed the improved corrosion protection performance in 3.5% NaCl solution by representing the lower i_{corr} values and higher R_{ct} values. Based on the obtained results, it was concluded that the addition of polpyrrole on the anodized layer of Al_2O_3 films increase the corrosion resistance performance on AA2024 alloys.

REFERENCES:

1. Woo Lee, Kathrin Schwirn, Martin Steinhart, Eckhard Pippel, Roland Scholz and Ulrich Go Sele, Nature Nanotechnol. 3, 235-239(2008).
2. Bertrand Priet, Grégory Odemer, Christine Blanc, Kévin Giffar, Laurent Arurault, Surf. Coat. Technol. 307, 206–219 (2016).
3. S. Kozhukharov, Ch. Girginov, I. Avramov, M. Machkova, Mater. Chem. Phy.180, 301e, 313(2016).
4. Naiping Hu, Xuecheng Dong, Xueying He, James F. Browning, Dale W. Schaefer, Corr. Sci. 97, 17–24 (2015).
5. O. Zubillaga, F.J. Cano, I. Azkarate, I.S. Molchan, G.E. Thompson, A.M. Cabral, P.J. Morais, Surf. Coat. Technol. 202, 5936–5942 (2008).
6. O. Zubillaga, F.J. Cano, I. Azkarate, I.S. Molchan, G.E. Thompson, P. Skeldon, Sur. Coat. Technol., 203, 1494–1501 (2009).
7. O. Zubillaga, F.J. Cano, I. Azkarate, I.S. Molchan, G.E. Thompson, P. Skeldon, Thin Solid Films, 517, 6742–6746 (2009).
8. A. Madhan Kumar, P. Sudhagar, Akira Fujishima, Zuhair M. Gasem, Polymer, 55, 5417e5424 (2014).
9. Majid Shahzada, Michel Chaussumier, Rémy Chieragatti, Catherine Mabru, Farhad Rezai-Aria, Surf. Coat. Technol., 206, 2733–2739 (2012).
10. A. Madhan Kumar, S.Nagarajan, Suresh Ramakrishna, P.Sudhagar, Yong Soo Kang, Hyongbum Kim, Zuhair M. Gasem, N. Rajendran, Mater. Sci. Eng. C 43, 76–85 (2014).
11. Y. Sasikumar, A. Madhan Kumar, Zuhair M.Gasem and Eno E.Enbenso, Appli. Surf. Sci.. 330, 207–215 (2015).
12. Popat G. Pawar, Ruimin Xing, Rahul C. Kambale, A. Madhan Kumar, Shanhu Liu, Sanjay S. Latthe, Prog. Org. Coat., 105, 235–244 (2017).

SYNTHESIS AND TEXTURAL CHARACTERISTICS OF ALUMINA-ZIRCONIA COMPOSITE AEROGELS VIA AMBIENT PRESSURE DRYING

Uzma K.H. Bangi[1*], Shivani S. Pandit[1], Dhanashri B. Bagal[1] and Hyung-Ho Park[2]

[1]School of Physical Sciences, Solapur University, Solapur - Pune National Highway,
Kegaon, Solapur - 413 255, Maharashtra, India

[2]Department of Materials Science and Engineering, Yonsei University,
Seoul 120-749, Republic of Korea

*Corresponding author, E-mail: uzma.phys@gmail.com, Tel.: +91 217 2744771*154

ABSTRACT:

The experimental results in this work reports the synthesis and textural characteristics of alumina-zirconia composite aerogels via ambient pressure drying. The composite aerogels were prepared via sol-gel process using a surfactant (Brij-76) as organic additives and the influence of addition of Brij-76 prior- and post-sol formation have been studied. The textural characteristics of composite aerogels were analyzed using N_2 adsorption-desorption, field emission scanning electron microscopy (FESEM) and X-ray diffraction techniques. The composite aerogels prepared using Brij-76 post- sol formation have surface area (127 m^2/g) larger than other aerogels.

Keywords: Brij-76; Sol-gel; Ambient pressure drying; Alumina-Zirconia, Composite aerogels

INTRODUCTION:

"Aerogels, the lightest and transparent nanostructured porous materials, are obtained from a gel by the replacement of liquid with air". They are extremely low dense (0.004 - 0.500 g/cc) materials with an open cross-linked network having particle size of <10 nm and pore size of <50 nm. They possess a wide variety of outstanding properties such as high porosity (80-99.8%) and surface area (500-1200 m^2/g) etc. Exhibiting such exceptional properties, aerogels are applicable in various fields such as catalysis, sensors, oil spill cleanup, biomedical and space technology etc. Amongst these, catalysis is a potential application of aerogels. To obtain the aerogels, the first key step is a sol–gel process to prepare gel pursued by drying of the gel via either supercritical drying (SCD) or ambient pressure drying (APD) or freeze drying (FD). Conventionally, aerogels are synthesized via expensive and energy intensive SCD method which restricts the commercialization of the aerogels. But, the recent developments have shown great potential of the APD as an alternative and very simple method for the synthesis of the aerogels. It is observed that alumina and zirconia are the most common support materials in heterogeneous catalysis [1]. Zirconia is found to be more stable than alumina; however, the use of zirconia is limited due to the tetragonal and cubic phases transformation into monoclinic phase below 1443 K. Because monoclinic phase possess weak pore structure and low surface area [2, 3]. Therefore, to overcome this limitation of zirconia, in nineties many attempts have been made by doping it with alumina [4, 5]. Recently, more work is needed to perform to synthesize composite aerogels via ambient pressure drying. Therefore, in the present work attempts have been made to synthesize alumina-zirconia composite aerogels employing surfactant.

EXPERIMENTAL:

For the synthesis alumina- zirconia composite aerogels, zirconium n-propoxide (ZrPr, 70% in n-PrOH, Sigma-Aldrich) and aluminium sec-butoxide (AlBu, Sigma-Aldrich) were used as precursors, n-propanol (n-PrOH, Duksan) as a solvent, acetic acid glacial (CH_3COOH, Sigma-Aldrich) as a stabilizer (inhibitor), Brij-76 (M.W. 711 g) as organic additive, hexane as a aprotic solvent and hexamethyldisilazane (HMDZ-10%) as a silylating agent and D. I. water for hydrolysis purpose. The experimental procedure for the synthesis of zirconia-alumina composite aerogels via ambient pressure drying is presented in fig. 1. During the synthesis, precursors:solvent molar ratio was kept constant at 1:4, AlBu:ZrPr :: 1:3 and Precursor:AcAc:H_2O :: 1:0.5:0.5 respectively. The influence of addition of Brij-76 prior- and post-sol formation on the textural properties of composite aerogels was studied.

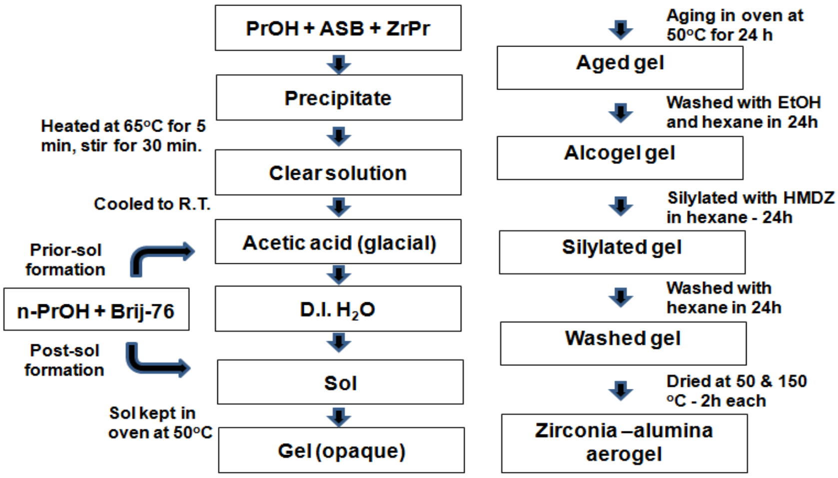

Fig. 1: Schematic presentation for the synthesis of Alumina-Zirconia composite aerogels via ambient pressure drying

The surface area and pore size distribution of the zirconia powder were determined using N_2 adsorption desorption analysis (TriStar 3000 V6.05 A). The morphological investigation of the powder samples was carried out by field emission scanning electron microscopy (FESEM, JEOLJSM-600F). An X-ray diffractometer (XRD, Model Rigaku Ultim) was used to analyze the amorphous or crystalline phase of the composite aerogels.

RESULTS AND DISCUSSION:

The N_2 adsorption-desorption isotherms and pore size distribution of alumina-zirconia composite aerogels synthesized employing Brij-76 prior- and post-sol formation are shown in fig. 2 (a) & (b). From fig. 2 (a) it is observed that both the samples manifested type-IV isotherm with type H3 desorption hysteresis indicating different pore sizes. Also, a broad pore size distribution from micro to mesopore range with a sharp peak centered at around 40Å is observed for both the samples (fig. 2 (b)). Surface area of sample synthesized using Brij-76 post-sol formation is larger (127 m^2/g) than other sample (50 m^2/g) with pore volume of 0.18 and 0.13 cc/g respectively. This is due to, using Brij-76 prior-sol formation may lead to a complicated sol-gel reaction causing an untailored structure which shrunk during drying. In case of sample synthesized using Brij-76 post-sol formation, well tailored three dimensional network formation occurs which sustain during drying.

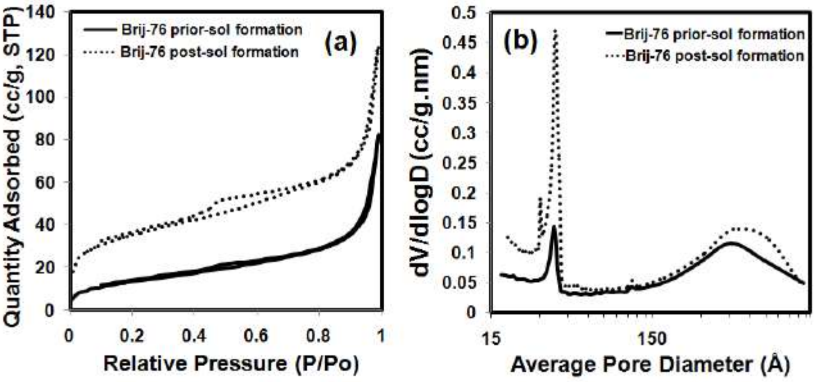

Fig. 2. (a) N_2 adsorption-desorption isotherms and (b) pore size distributions of alumia-zirconia composite aerogels synthesized using Brij-76

Fig. 3 shows the FESEM images of alumina-zirconia composite aerogels synthesized using Brij-76 prior-sol formation (a) and post-sol formation (b). As seen from the image (a) of fig. 3, the particles are agglomerated forming bundles, while in images (b) the particles are connected with each other forming a network. XRD diffractograms of alumina-zirconia composite aerogels synthesized using Brij-76 are shown in fig. 4. As seen from fig. 4, broad peaks are observed for both the samples exhibiting the amorphous nature.

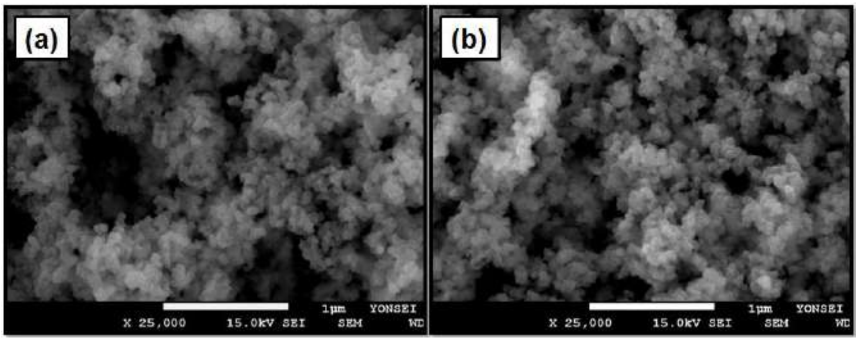

Fig. 3: FESEM images of alumia-zirconia composite aerogels synthesized using Brij-76 prior-sol formation (a) and post-sol formation (b)

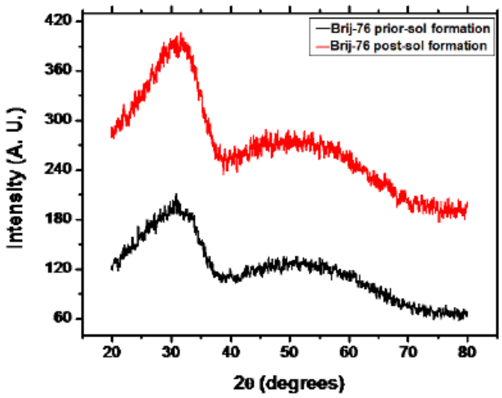

Fig. 4: XRD diffractograms of alumia-zirconia composite aerogels synthesized using Brij-76

CONCLUSIONS:

The successful synthesis of alumina-zirconia composite aerogels via ambient pressure drying was carried out. Employing Brij-76 post-sol formation led to high surface area (~ 127 m^2/g) composite aerogels.

ACKNOWLEDGMENTS:

This study was financially supported by the Department of Science and Technology – Science & Engineering Research Board (DST-SERB), New Delhi, through a major research project on “aerogels” (no. SB/FTP/PS-030/2014). One of the authors, Uzma K. H. Bangi, is very grateful to the DST-SERB for Young Scientist Fellowship under fast-track scheme.

REFERENCES:

1. G.G.E. Gardes, G.M. Pajonk, S.J. Teichner, Bull. Soc. Chim.Fr. 1321 (1976).
2. D. A. Ward, E. I. Ko, Chem. Mater. 5, 956 (1993).
3. T. Klimova, M. L. Rojas, P. Castillo et. al. Micro. Meso. Mater. 20, 293 (1998).
4. E. Zhao, S. E. Hardcastle et. al. Micro. Meso. Mater. 31, 9 (1999).
5. J. Klein, W. F. Maier, Chem. Mater. 11, 2584 (1999).

SYNTHESIS OF NANOSTRUCTURED CdO-ZnO NANOCOMPOSITE THIN FILMS BY SILAR METHOD

A.K. Sharma[a], S. S. Potdar[a,b*], M. A. Yewale[a],
D. B. Kamble[a], U. M. Patil[c] and M. V. Rokade[d]
[a]Earth and Space Science Laboratory, Department of Physics,
Shivaji University, Kolhapur- 416004, India
[b]Department of Physics, Shree Datta Polytechnic College,
Shirol, Tal- Shirol, Dist- Kolhapur 415120 , India
[c] Centre for interdisciplinary research studies, D.Y.Patil University, Kolhapur,416006, India.
[d]Semiconductor Laboratory, Centre for Materials for Electronics Technology (C-MET),
IDA Phase-III, Cherlapally, HCl (PO), Hyderabad 500 051, India

ABSTRACT:

The facile SILAR method has been used to synthesize CdO-ZnO nanocomposite thin films. In preparation of composite thin films, 0.1M Cd $(NO_3)_2$ and 0.1M Zn $(NO_3)_2$ were used as a sources of Cadmium and Zinc ions, respectively. The supersaturated solutions of Cd and Zn ions complexing with aqueous ammonia were used as cationic bath and 0.075M NaOH solution bath as anionic bath. Moreover, both baths was used for rapid adsorption and reaction to form composite thin films on glass substrates. The XRD patterns of composite samples exhibits distinct peaks of ZnO and CdO, which clearly indicates formation of CdO-ZnO nanocomposites in thin film form. The cauliflower like ZnO and hexagonal petals like CdO morphology were observed by FE-SEM studies, whereas nanocomposite shows interlocked sheets like morphology. EDAX mapping study confirms that the obtained nanocomposites are actually composed of CdO and ZnO, and oxygen vacancies exist in the lattice of CdO-ZnO composites.

Key words: SILAR method, XRD, SEM, EDAX mapping, etc

INTRODUCTION:

Currently, great deal of research is concentrated towards the development of gas sensors for monitoring and detection of toxic gases. Numerous metal oxides have been investigated for gas sensor application. Among all metal oxides, Zinc oxide has proven its diverse usage in different fields due to its fascinating properties, such as, wide direct band gap (~3.3eV)[1] and excitation binding energy (60meV) [2]. Also, Cadmium oxide (CdO), with low resistivity and high transmittance in visible region is advantageous in several applications [3-4]. Different metal oxide materials appear advantageous in some of these properties, but very few of them are favorable in all requirements. To overcome with these drawbacks, fabrication of nanocomposite can be the effective approach for high performance gas sensors. So, several nanocomposites such as ZnO-CuO [5], CdO-ZnO [6], ZnO-SiO_2[7] were prepared and studied for various applications like gas sensors, light emitting diode and supercapacitor application. Among the facile chemical deposition methods, Successive ionic layer adsorption and reaction method (SILAR) is advantageous in terms of simple, inexpensive, facile and rapid deposition technique. On the basis of above considerations, in present work we have synthesized CdO-ZnO nanocomposite by facile SILAR method. The influence of composition variation of CdO and ZnO on structural, morphological and optical properties of CdO-ZnO thin films are investigated by means of XRD, SEM, EDAX, etc., analysis.

EXPERIMENTAL:

The CdO-ZnO nanocomposite was synthesized by SILAR method. Initially, glass substrates thoroughly by the procedure described elsewhere [8]. Afterward, 0.1M Zinc nitrate [$Zn(NO_3)_2$] and 0.1M Cadmium nitrate [$Cd(NO_3)_2$] solutions were used as cationic source of Zinc and Cadmium ions, respectively. These salts were supersaturated by using liquor ammonia as complexing agent in precursor solutions. The NaOH (0.075M) solution was used as anionic bath for rapid reaction with adsorbed cations. To remove loosely held molecules present on the substrate of newly adsorbed layer of ions, distilled water bath was used as rinsing bath. Furthermore, successive dipping of cleaned glass substrates in cationic and anionic bath separated by rinsing bath were carried out for deposition of thin films. Similarly, by changing the dipping sequence of CdO and ZnO three samples were synthesized with stoichiometry as 1:1, 1:2 and 1:3, respectively. In this method, the material deposition rate was very slow at initial stage, after 20 cycle increases rapidly up to 80 cycles. All five samples were synthesized and named as pure CdO (SC), pure ZnO (SZ) and CdO-ZnO nanocomposite S1, S2 and S3 in the stoichiometric dipping of 1:1, 1:2 and 1:3 cycles, respectively. As-deposited samples were finally annealed at temperature 450°C for 2 hrs.

RESULT AND DISCUSSION:

Thin film formation and structural studies (XRD):

The structural changes and identification of phases of the thin films obtained by SILAR method are investigated with the help of X-ray diffraction (XRD). The **Fig.1** reveals that, all the samples are polycrystalline in nature.

The XRD pattern obtained for the CdO-ZnO composite structure showed peaks from (111), (200), (220) and (311) planes corresponding to cubic CdO [marked as “@” (JCPDS no. 05-0640)]. Also, the peaks from planes (101), (102), (002) and (110) of ZnO were observed with little less intensity (marked as “#”).

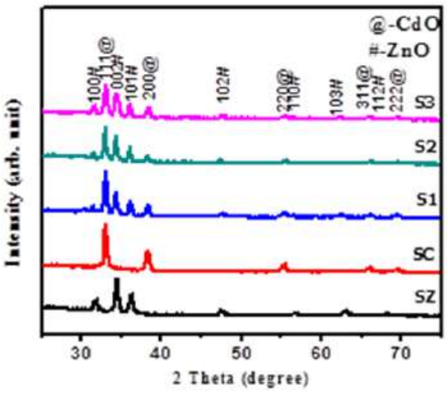

Fig. 1: XRD patterns of annealed CdO (SC), ZnO (SZ) and CdO-ZnO (S1, S2, S3) sample

Scanning Electron Microscopy (SEM) and EDAX mapping:

The surface morphological study of annealed samples were investigated by Scanning Electron Microscopy (SEM) and shown in **Fig.2 (a to e)** at different magnifications. The SEM micrographs of pure CdO are well-developed hexagonal petals with average thickness of 320-360 nm. However, bare ZnO thin films exhibits cauliflower like morphology.

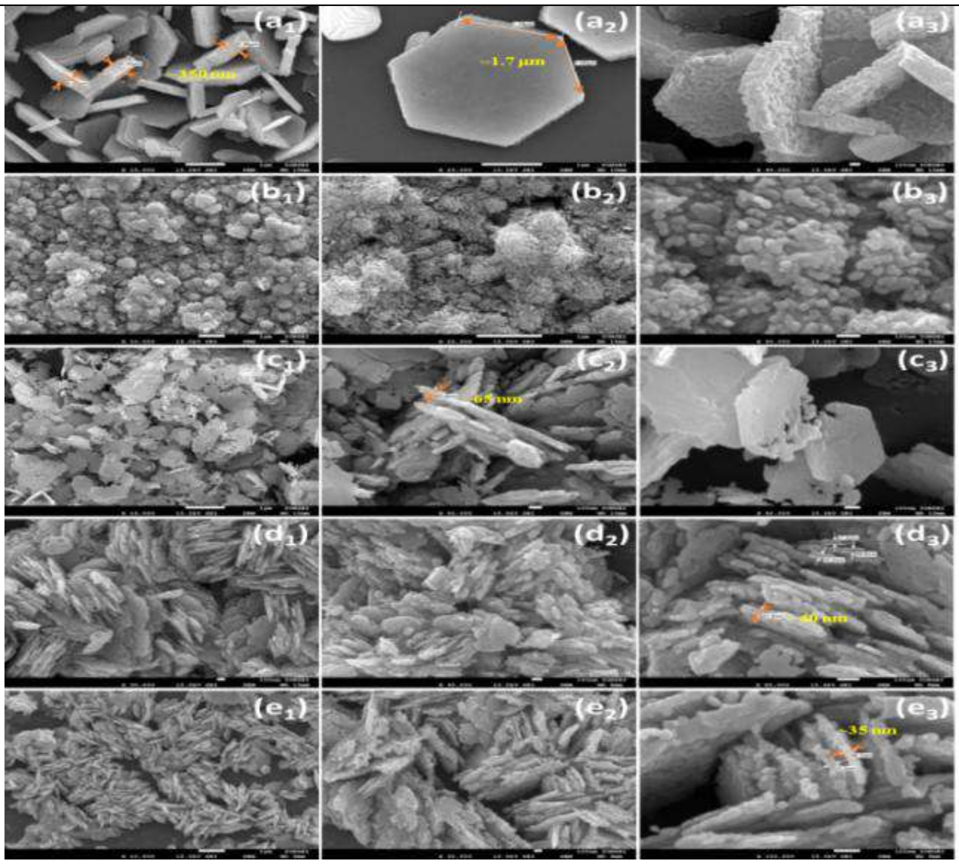

Fig. 2: Scanning electron micrographs of $a_{1\text{-}3}$) SC $b_{1\text{-}3}$) SZ $c_{1\text{-}3}$) S1 $d_{1\text{-}3}$) S2 $e_{1\text{-}3}$) S3

The SEM images of CdO-ZnO compositions as 1:1, 1:2 and 1:3 (Cd:Zn) shown in Fig.2(c-$e_{1\text{-}3}$) reveals a similar hexagonal petals-like structure. Interestingly, the size and width of hexagonal petals of CdO is reduced from 300nm and found to be in the range of ~65 nm for CdO-ZnO with composition 1:1 (fig. 2 c_{1-3}). The size of the petals of CdO-ZnO with composition 1:2 was further reduced and found to be ~40 nm (shown in Figure 2 d_{1-3}). Furthermore, petals were found with a small size about ~35 nm, as shown in Figure 2 $e_{1-3}$for the 1:3 compositions. The SEM analysis reveals hexagonal petals of CdO reduce in size from ~350 to ~35 nm with increases in ZnO content.

The EDS line scan of sample SC along line is shown in Fig. 3 (A) indicating that, the synthesized sample is highly Cd-rich. Elemental mapping of sample S3 shown in Fig. 3 (B) reveals that Cd, Zn, and O are the main elements present in the sample. The Cd deposited to large extent in the central part of the substrate while Zn deposited around the Cd.

.

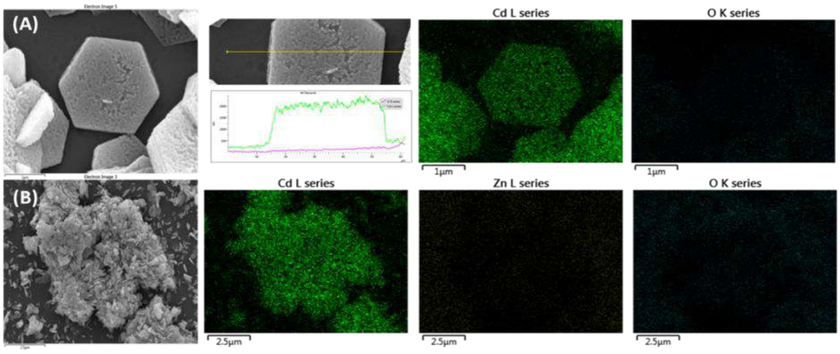

Fig. 3 A) Elemental mapping of CdO (SC) Sample and B) CdO-ZnO Sample.

CONCLUSION:

The CdO, ZnO and CdO-ZnO nanocomposite thin films have been successfully synthesized by SILAR method. The XRD, SEM, and EDAX mapping depicts that, formation of polycrystalline, cauliflower like morphology for ZnO while hexagonal petals like morphology for CdO. However, nanocomposite of CdO-ZnO shows interlocked petal like sheets with average size about ~65-35 nm.

REFERENCES:

1. M. H. Huang, S. Mao, H. Feick, H. Yan, Y.Wu, H. Kind, E.Weber, R. Russo, P. Yang, Science, 292, 1897 (2001).
2. A. I. Inamdar, S. H. Mujawar, and P. S. Patil, Int.J.Electrochem .Sci.,2, 797 (2007).
3. M. Ocampo, A. M. Fernandez, P. J. Sebastian, J. Semicond. Sci. Technol., 8, 750 (1993).
4. A. C. Nwanya, P. R. Deshmukh, R. U. Osuji, M. Maaza, C. D. Lokhande, and F. I. Ezema, Sens.Actuat. B Chem., 206, 671 (2015).
5. M. Bahu, K. Kumar, T. Bahu, E. Devices, 14, 1137 (2012).
6. H. Karami, Int.J.Electrochem. Sci., 5, 720 (2010).
7. J. Zhai, X. Tao, Y. Pu, X. F. Zeng, J. F. Chen, Appl. Surf. Sci., 257(2), 393 (2010).
8. A. K. Sharma, S. S. Potdar, K. S. Pakhare, B. M. Sargar, M. V. Rokade, N. L. Tarwal, J. Mater Sci: Mater. Electron, 28, 3752 (2017).

SUPERHYDROPHOBIC COATING USING ORGANICALLY MODIFIED TiO_2 NANOPARTICLES

Ashvini M. Kokare, Rajaram S. Sutar, Dipali M. Chougule and Sanjay S. Latthe*
Self-cleaning Research Laboratory, Department of Physics,
Raje Ramrao College, Jath - 416 404, Maharashtra, India
*Corresponding author E-mail: latthes@gmail.com

ABSTRACT:

The water drops on Lotus leaf (contact angle higher than 150° and sliding angle less than 10°) roll off and pick up dust particles when surface is tilted confirming self-cleaning property. Durable superhydrophobic coatings are very essential for potential application in many fields. We achieved superhydrophobic coating on glass substrates using organically modified TiO_2 nanoparticles. The superhydrophobic coating was prepared from simple and low cost dip coating technique by using surface modified TiO_2 nanoparticles dispersion. The concentration of TiO_2 was varied. The five layer deposited coatings showed the water contact angle higher than 166° and sliding angle less than 7°. The rough morphology was observed which is suitable for superhydrophobic coating and stable against water drop impact test.

INTRODUCTION:

The surfaces having contact angle higher than 150° and sliding angle less than 10° are generally called as superhydrophobic surfaces. On superhydrophobic surfaces water drop easily roll off by picking up the dirt particles showing self-cleaning property [1-3]. In nature self-cleaning property was observed on lotus leaves due to the combination of rough surface structure and low surface free energy [4]. Hence the leaves of lotus always remain clean and it is famously called as lotus effect [5]. In nature these type of behavior occur in other plant leaves and wings of insects also [6]. Superhydrophobic surfaces play a role in technical applications from self-cleaning window glasses to paints and textiles [7-11]. For the preparation of artificial superhydrophobic coatings, many methods have been used like electrochemical deposition, phase separation, plasma etching and polymerization, lithography, sol-gel, layer by layer (LBL) and colloidal assembly [12-15]. In this paper, we have prepared superhydrophobic coating from ODS and different concentration of TiO_2 and by simple dip coating method. The prepared coating shows contact angle higher than 150° and sliding angle less than 10° due to rough surface morphology.

EXPERIMENTAL DETAILS:

Material:

Octadecyltrichlorosilane (ODS) (>90% Purity) and titanium nanoparticles (mixture of rutile and anatase nanopowder < 100 nm) were obtained from Sigma Aldrich, USA. The ethanol (99.9%) was purchased from Changshu Hongsheng Fine Chemical Co., Ltd, China. The glass plates were bought from Blue star (5 mm x 25 mm), Polar Industrial Corporation, Mumbai.

Methods:

The glass plates were cleaned by distilled water and dried at room temperature. Firstly 5 mg, 10 mg and 15 mg of TiO_2 nanoparticles were dispersed in 40 ml ethanol under ultrasonication for 30 min. In this dispersion, 0.4 ml concentration of ODS was added separately. This solution was stirred continuously by using magnetic stirrer. The cleaned glass plate was immersed in the coating solution and immediately taken out under constant stirring. The coating was dried in oven at 50 °C for half hour. The coating was prepared by 5 deposition layers and dried for evaporate the solvent. For the preparation of superhydrophobic coating, different concentrations of TiO_2 was used 5 mg, 10 mg and 15 mg (all five times deposition) were named OT-1, OT-2 and OT-3, respectively.

Characterizations:

The water contact angle and sliding angle were measured using Contact Angle Meter (Halmarc Co. Ltd.). The durability of the prepared coating has confirmed by water impact test and adhesive tape test.

RESULT AND DISCUSSION:

Measurement of water contact angle:

The water contact angle on the OT-1, OT-2 and OT-3 coatings with their respective snapshots are shown in **Fig. 1**. The OT-1coating showed contact angle around 143° due to smooth morphology and lack of surface roughness. The low surface energy is not the only criterion to achieve superhydrophobicity, whereas the surface roughness is needed in combination [16]. The TiO_2 concentration of 5 mg/ml is very small to achieve superhydrophobicity for any numbers of deposition layers.

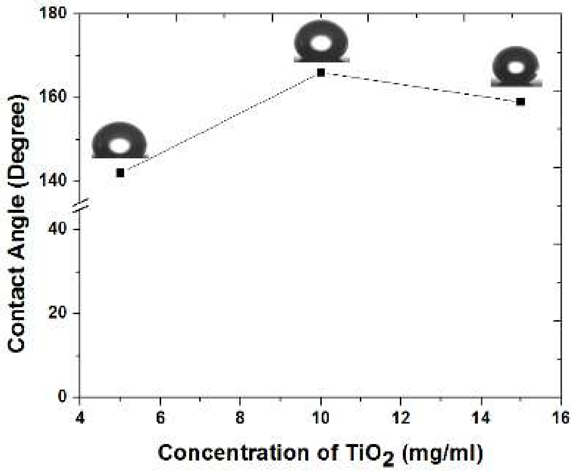

Fig. 1: Water contact angle on the coatings prepared with different concentrations of TiO_2 nanoparticles

The OT-2 coatings showed increase in contact angle of 166° and sliding angle of 7°. The rough surface morphology was observed which eventually increased the surface roughness of the coating. The contact angle of 159° was observed on OT-3 coatings due to loosely adhered particles on the coating due to high concentration of TiO_2 nanoparticles. Generally, pristine TiO_2 coatings show hydrophilic wetting behavior with water contact angle less than 90°. Though the deposition layers were increased, the contact angle remains in hydrophilic state. However, after ODS modification, the hydrophilic TiO_2 nanoparticles turns into hydrophobic TiO_2 nanoparticles and subsequently with increase in deposition layers, the water contact angle increased considerably in the superhydrophobic state with self-cleaning properties.

Water drop impact test:

The mechanical durability of the prepared coating was checked by water drop impact test by impacting water drops from the height on coating surface. The water drop impact test set up is shown in **Fig. 2**. The water drop impact height (needle to coating) was varied from 1.5, 5 and 10 cm for OT-2 and OT-3 coatings. The OT-2 coating showed loss in superhydrophobicity for the water drop impact test from the height of 1.5, 5, and 10 cm for the time of 180, 74, and 45 min, respectively. For less height, the wettability was lost after longer time whereas for high height, the wettability was lost after short time. The OT-3 coating showed loss in superhydrophobicity for the water drop impact test from the height of 1.5, 5, and 10 cm for the time of 58, 40, and 30 min, respectively. From this observation, it is confirmed that the OT-3 coating lost the superhydrophobicity rapidly in comparison with OT-2 coating. Thus OT-2 coating are durable than OT-3 coating. Water drop does not stay on surfaces it simply jumps due to rough surface and low surface free energy [17].

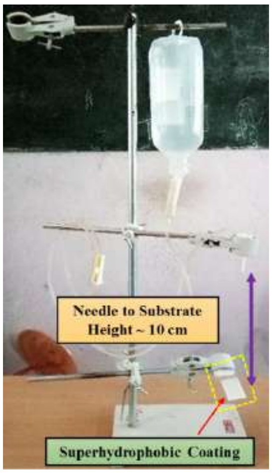

Fig. 2: Set up of water drop impact test

Adhesive Tape Test:

Mechanical durability of coated surface has also confirmed by the adhesive tape test. The adhesive tape was placed firmly on the OT-1, OT-2 and OT-3 coatings and taken out slowly as shown in **Fig. 3**. After peeling off, the TiO_2 powder was appeared on the adhesive tape, confirming damage to the coating. The adhesive tape partially detached the loosely bounded coating and eventually the superhydrophobicity of the coatings was lost. The adhesive tape test has confirmed the weak adhesion of coating on the glass substrate. Such mechanically weak superhydrophobic coating can limit its use in industrial applications.

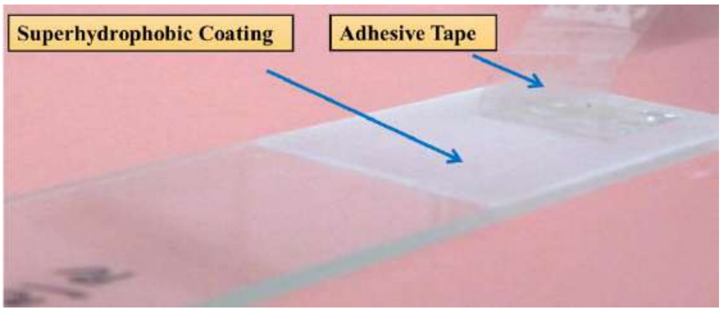

Fig.3: **Adhesive tape test on the superhydrophobic coating**

CONCLUSION:

The ODS modified TiO_2 nanoparticles were used to prepare superhydrophobic coating by simple dip coating method. The effect of ODS and TiO_2 suspension and number of deposition layers on wettability of prepared coating was studied. The prepared superhydrophobic coating showed contact angle higher than 150° and sliding angle less than 10°. The effort has to be made to improve the durability of the superhydrophobic coating.

ACKNOWLEDGMENTS:

One of the authors S. S. Latthe is grateful to Department of Science and Technology (DST), Govt. of India, for financial assistance under the DST-INSPIRE Faculty Scheme (DST/INSPIRE/04/2015/000281).

REFERENCES

1. Dhere, S.L., et al., 72(1): p. 45-49 (2011).
2. Gurav, A.B., S.S. Latthe, and R.S. Vhatkar, Surface Innovations, 1(3): p. 157-161 (2013).
3. Kim, D.-Y., et al., J. Mate. Chem. A, 3(7): p. 3975-3983 (2015).
4. Barthlott, W. and C. Neinhuis, Planta, 202(1): p. 1-8 (1997).
5. Barthlott, W., et al., Nano-Micro Letters, 9(2): p. 23 (2017).
6. Qu, M., et al., Langmuir, 24(8): p. 4185-4189 (2008).
7. Latthe, S.S. and A.V. Rao, 207(Supplement C): p. 489-492 (2012).
8. Latthe, S., et al., Coatings, 4(3): p. 497 (2014).
9. Liu, S., et al., RSC Advances, 5(84): p. 68293-68298 (2015).
10. Park, J.-J., et al., ACS Applied Materials & Interfaces, 5(13): p. 6155-6160 (2013).
11. Madhan Kumar, A., et al., Polymer, 77(Supplement C): p. 79-86 (2015).
12. Latthe, S.S., et al., J. Porous Materials, 17(5): p. 565-571 (2010).
13. Yoon, H., et al., J. Materials Chemistry A, 3(21): p. 11403-11410 (2015).
14. Xing, R., et al., J. Mol. Liquids, 247(Supplement C): p. 366-373 (2017).
15. Xu, X.H., et al., Colloids and Surfaces A: Physico. and Eng. Aspects, 377(1): p. 70-75 (2011).
16. Yu, Q., et al., Colloids and Surfaces A: Physico. and Eng. Aspects, 427: p. 1-6 (2013).
17. Yildirim, A., et al., ACS applied materials & interfaces, 5(3): p. 853-860 (2013).

HIGH CONCENTRATED III-V MULTI JUNCTION SOLAR CELLS

Kaveri S. Ghiwari and Alfaz M. Bagawan

Department of Physics, R. L. Science Institute, Belagavi, Karnataka, India

ABSTRACT:

Concerns about the changing environment and fossil fuel depletion have promoted much controversy and scrutiny. With looming energy crisis across the globe, achieving high efficiency and low cost solar cells have long been the key objective for photo voltaic researches. III – V Compound semiconductor based MJ solar cell have been dominant choice for space power due to their superior performance compared to any other existing solar cell techniques. This Article is III – V Compound multijunction (MJ) Tandem solar cells are an alternative to flat plate module to produce cost competitive electricity. HCPV have the potential for achieving high conversion efficiency of over 50%. The photovoltaic device is today well established in space applications and recently has entered the Terrestrial market.

Keywords: Solar Cell, Concentrator, III-V Multi junction Semiconductor Materials.

INTRODUCTION:

It has been proven that the only realistic path to practical ultra-high efficiency solar cells is the monolithic multi-junction approach, i.e., to stack p-n junctions made of different semiconductor materials on top of each other. Each sub p-n junction, i.e., sub solar cell, converts a specific part of the sun's spectrum. In this way, the energy of the sunlight photons is converted with low thermalization losses. However, large-area multi-junction solar cells are still far too expensive if applied in standard PV modules. A viable solution to solve the cost issue is to use tiny solar cells in combination with optical concentrating technology, in particular, high concentrating photovoltaics (HCPV), in which the light is concentrated over the solar cells more than 500 times.

The combination of ultra-high efficient solar cells and optical concentration lead to low cost on system level and eventually to low levelized cost of electricity, today, well below 8 €cent/kWh and, in the near future, below 5 €cent/kWh. A wide variety of approaches exists for III-V multi-junction solar cells and HCPV systems. This article is intended to provide an overview about the different routes being followed. However, current multi-junction solar cells are far too expensive if applied in standard PV modules. A viable solution to the cost issue is to use optical concentrating technology, in particular, high concentrating photovoltaics (HCPV), in which the light is concentrated on the solar cells at more than 500 times. Hence, the required active area of the solar cell devices is also more than 500 times lower than the area of the cheaper lenses or mirrors

What are Multi junction Solar cells?

Multi junction (MJ) solar cells are solar cells with multiple p – n junctions made of different semiconductor materials. Each material's p-n junction will produce electric current in response to different wavelengths of light. The use of multiple semiconducting materials allows the absorbance of a broader range of wavelengths, improving the cell's sunlight to electricity energy conversion efficiency.

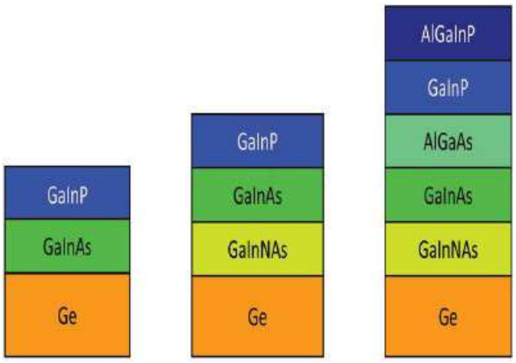

Fig 1.different multi-junction solar cells made of III-V semiconductor materials. The subcells are interconnected with tunnel diodes

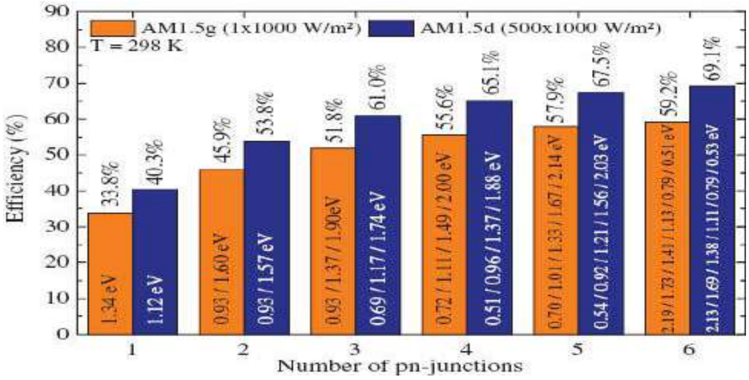

Fig. 2: Dependence of the theoretical efficiency limits on the number of p-njunctions (sub cells) for the reference spectrum AM1.5d under 500 times concentration (500×1000 W/m^2, 25°C) and the reference spectrum AM1.5g (1000 W/m^2, 25°C).

The calculation was carried out by Fraunhofer ISE with the program etaOpt [2] according to Shockley and Queissers' detailed balance approach. The structure of MJ solar cell. The six important different types of layers: p-n junctions, BSF layers, window layers, tunnel junctions, anti reflective coating and metal coating.

Process to Design High efficiency III – V Multi junction solar cell:

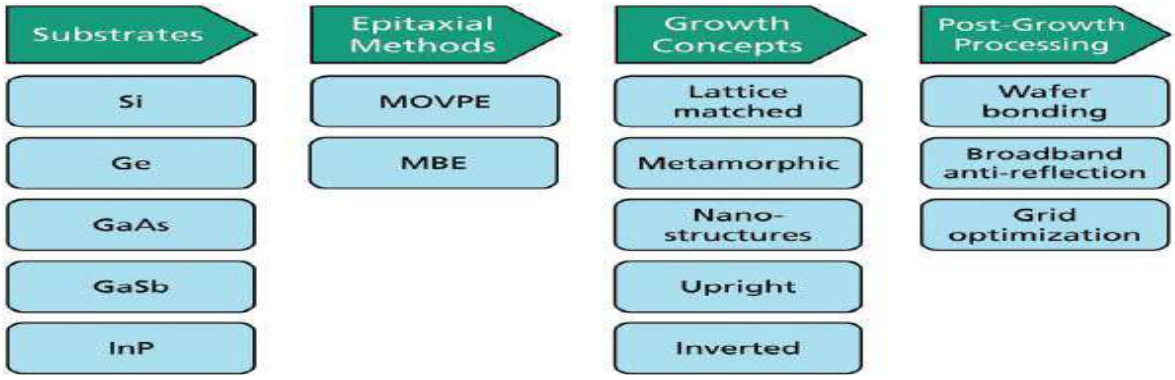

Fig. 3: Technological tools and processes that are used to design new high-efficiency III-V multi-junction solar cell

SIGNIFICANCE:

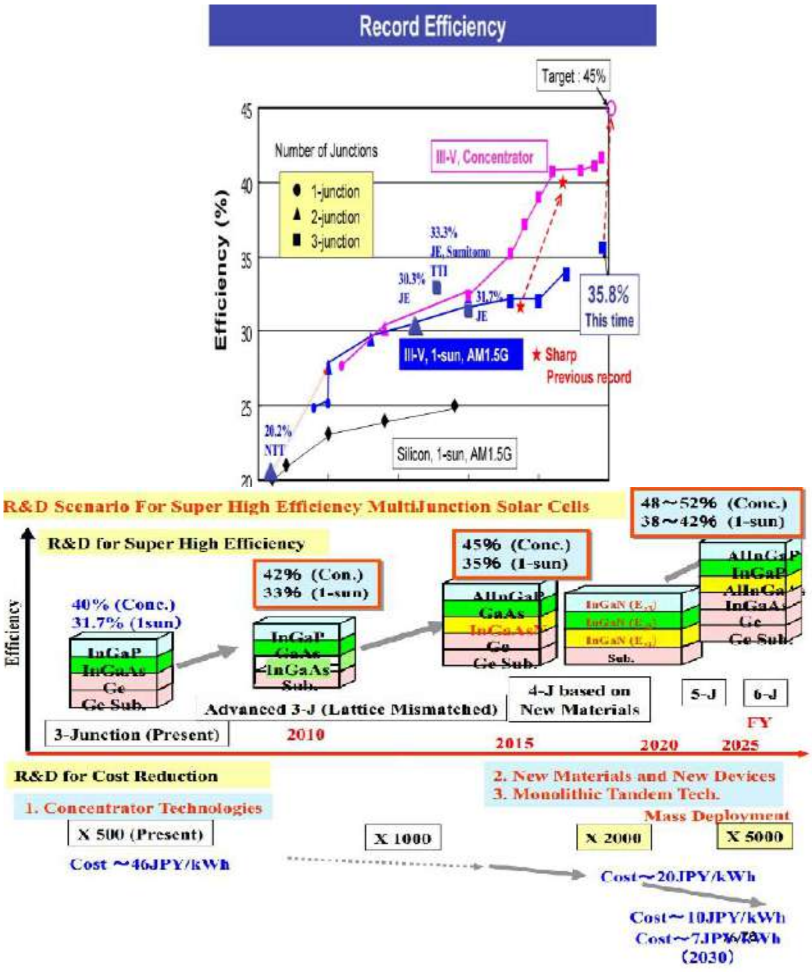

Moreover, by using a high concentration factor, two further advantages are obtained: (i) due to lower entropy losses, the solar cell efficiency value increases; (ii) by strongly reducing the area of the

Semiconductor material needed for converting the solar light, an effective answer to the problem of scarcity or limited amounts of materials in nature is found, thereby, offering a practical path to reduce the environmental impact of PV technology. In terrestrial concentrating the blue light by the atmosphere reduces the photon flux above 1.87eV. MJ cells offer higher radiation resistance, higher efficiency and a lower temperature coefficient.

HOW DOES THE MULTI JUNCTION SOLAR CELL MARKET LOOK TODAY?

When all is said in done, III – V Multijunction advancements can be seen as partitioned into four principle classes: wafer-based PV (likewise called first era PVs) and thin-film cell PVs. Conventional crystalline silicon (c-Si) cells (both single crystalline silicon and multi-crystalline silicon) and gallium arsenide (GaAs) cells have a place with the wafer-based PVs, with c-Si cells ruling the current PV showcase (around 90% piece of the pie) and GAs displaying the most elevated effectiveness. Thin-film cells regularly ingest light more productively than silicon, permitting the utilization of to a great degree thin movies. Cadmium telluride (CdTe) innovation has been effectively popularized, with over 20% cell proficiency and 17.5% module effectiveness record and such cells presently hold around 5% of the aggregate market. Other business thin-film advances incorporate hydrogenated formless silicon (a-Si: H) and copper indium gallium (di)selenide (CIGS) cells, taking around 2% piece of the pie every today. Copper zinc tin sulfide innovation has been under R&D for a considerable length of time and will most likely require some time until real commercialization.

REASON FOR HOLDING MULTI JUNCTION PVS BACK?

Starting at 2010, the cost of MJ sun powered cells was too high to permit use outside of specific applications. The high cost is predominantly because of the mind boggling structure and high cost of materials. All things considered, with light concentrators under enlightenment of no less than 400 suns. The cells have a poor match because of a more noteworthy photon transition of photons above1.87eV versus those in the vicinity of 1.87eV and 1.42 eV. This outcomes in too minimal current in the GaAs intersection, and hampers the general effectiveness.

Regardless of its extraordinary potential, this innovation is still in the beginning periods of commercialization contrasted and other develop sun oriented advances as there are various concerns remaining. Imperfections that reason states close to the center of the hole is most serious issue. This has a tendency to be crystallographic abandons (disengagements, surfaces, grain(boundaries) and high cost.

What Next?

To achieve PV system with high efficiency of 50% by 2050. Sharp Aim for the future is to apply this latest development to efficiently generate electricity using small area solar cells and make them for terrestrial use. To introduce new concepts as a challenge of Quantum structure, Optimize Eg using conventional materials and controlling them by quantum structures. To reduce the cost and increase availability by using efficient concentrator.

CONCLUSION:

With efficiencies up to 46.5% (324xAM1.5d), III-V-based multi-junction solar cells have achieved the highest conversion efficiency of sunlight into electricity and outperform all other materials. By implementing these devices into concentrating photovoltaic modules and systems, high efficiencies and low levelized cost of electricity can be achieved in areas with a high share of direct sunlight. The key driver for low cost is the efficiency. A continuous increase has been achieved, and projections indicate that there is still a large room for improved practical performances. It is also noteworthy that a comparably large gap of more than $10\%_{abs.}$ exists between cell and module efficiencies, which indicate significant losses in the module that must be reduced. New designs as well as new tools and fabrication processes must be developed to fulfil the efficiency projections. Several of these have been outlined in this paper.

REFERENCES:

1. https://en.m.wikipeadia.org/wiki/Multi-junction_solar_cell
2. http://www.energy.gov/eere/solar/multijunction/research
3. Mantu K. Hudait, Kathleen Meehan " Design of III-V Multijunction Solar cells" Virginia Polytechnique Institute.
4. Eduardo F. Fernandez , Antonio J. Garcia – Loureiro and Greg P."Multijunction Concentrator Solar Cells: Analysis And Fundamentals. Spinger International publishing Switzerland 2015.

SYNTHESIS AND STRUCTURAL PROPERTIES OF COPPER – ZINC - NICKEL SPINEL FERRITE

B. L. Shinde[1], S. M. Patil[2], K. S. Lohar[3]*

[1]Department of Chemistry, Waghire College, Saswad, Dist: Pune, 412301 (M.S.) India
[2]Department of Chemistry, Karmaveer Hire College, Gargoti, Dist: Kolhapur, 416209 (M.S.)
[3]Department of Chemistry, Shrikrishna Mahavidyalaya, Gunjoti, 413606, Dist: Osmanabad
*Corresponding author E-mail: kslohar@rediffmail.com

ABSTRACT:

$Cu_{0.2}Zn_{0.6}Ni_{0.2}Fe_2O_4$ nanoparticles synthesized by the wet chemical co-precipitation method. TG and DTA of precursor carried to find sintering temperature. The XRD pattern confirmed the formation of single phase cubic spinel structure of ferrites without additional peaks corresponding to any other phases. Infrared spectra were recorded at room temperature in the wave number range of 200–800 cm^{-1}, indicate two major absorption bands. The low frequency band ν_2 observed at 433 cm^{-1} is assigned octahedral site and high frequency band ν_1 observed at 561 cm^{-1} assigned tetrahedral site. Surface Morphology of sintered sample was studied by SEM and TEM.

Key Words: Spinel Ferrite, XRD, Morphology.

INTRODUCTION:

Ferrites are magnetic materials containing iron oxide as a major constituent in it. Materials containing magnetic nanoparticles, isolated in nonmagnetic matrices at the distances longer than their diameters, are most interesting for magnetic investigations. Unique physical properties of ferrite nanoparticles are under intensive research. A special place belongs to the magnetic properties in which the difference between a massive (bulk) material and a nanomaterial is especially pronounced. Today ferrites are used in a wide range of applications, and have contributed materially to the advances in electronics [1-3] In the area of new materials, ferrites with permeabilities up to 30,000 and power ferrites for frequencies up to 10 MHz have been made available commercially [4]. Even though, improvements and innovations continue to take place; many new applications, theories and preparation technologies are currently under development in field of ferrites. Spinel ferrites containing transition metal ions can act as efficient catalysts in a number of heterogeneous chemical processes such as CO oxidation [5], catalytic combustion of hydrocarbons [6] or selective oxidation and reduction of several organic molecules [7]. For these applications of metal oxides as heterogeneous catalysts, high surface area and accessible porosity arc relevant properties.

EXPERIMENTAL AND CHARACTERIZATION:

$Cu_{0.2}Zn_{0.6}Ni_{0.2}Fe_2O_4$ synthesized by the wet chemical co-precipitation method by using AR grade corresponding metal sulphates and 2M NaOH solution as precipitant, in oxygen atmosphere at 60 ^{O}C. The precursor precipitate was filtered, washed with deionized water and dried in inert atmosphere. TG and DTA of precursor was carried on SDT Q600 V20.9 Build 20 instrument. The crystal structure was studied by Phillips X-ray diffractometer (Model 3710). The IR spectra were recorded on a Perkin-Elmer infrared spectrometer in the range 200-800 cm^{-1}. Morphology and structure of the powder sample was studied on JEOL-JSM-5600 N Scanning Electron Microscope (SEM) and on Philips (model CM 200) Transmission Electron Microscope (TEM).

RESULTS AND DISCUSSION:

The TGA curve of precursor is given in Figure 1.

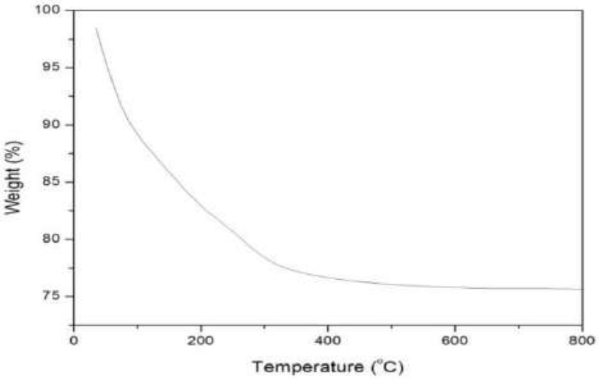

Fig. 1: TGA plot of precursor

The weight loss observed up to 500 °C temperature. No weight loss observed above 600 °C. The precursor of the sample was sintered at 600 °C for 4 hour to obtain the final product.

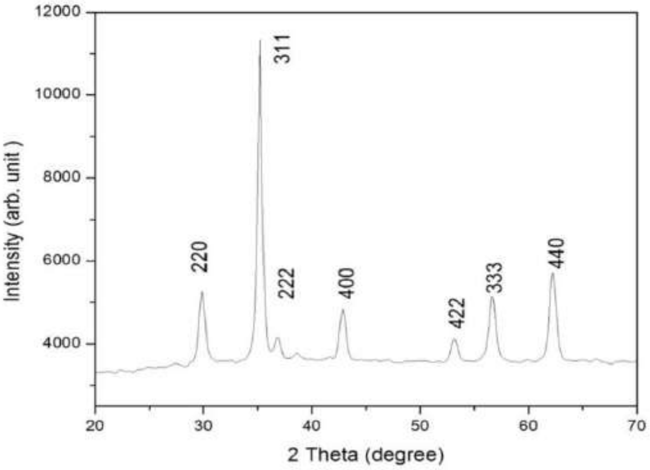

Fig. 2: XRD pattern of sintered sample

XRD pattern of the sintered sample is shown in Figures 2. The XRD patterns confirmed the formation of single phase cubic spinel structure of ferrites without additional peaks corresponding to any other phases.

The infrared spectra show two major absorption band ν_1 and ν_2 shown in Figure 3.

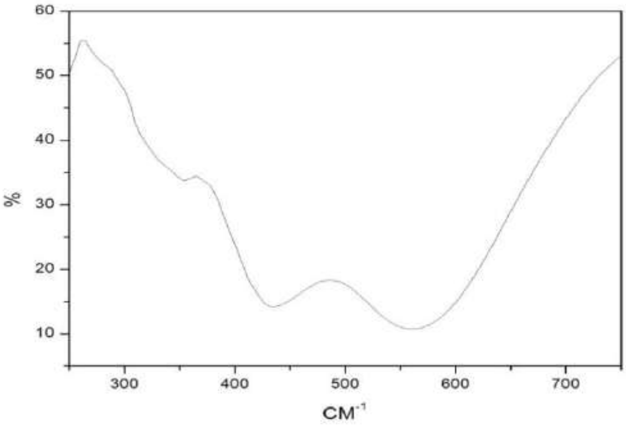

Fig. 3: IR spectra of sintered sample

The low frequency band ν_2 observed at 433cm^{-1} is assigned octahedral site and high frequency band ν_1 observed at 561 cm^{-1} assigned tetrahedral site. These bands are characteristics features of spinel structure.

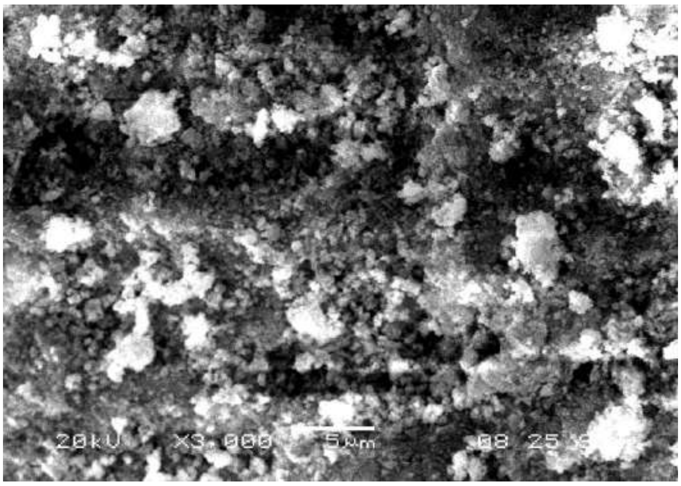

Fig. 4: SEM image of sintered sample

Scanning electron micrograph (SEM) of the surface of the sample is shown in Figure 4. It is observed from the SEM images that the prepared samples are amorphous and porous in nature.

TEM image of the sample is presented in Figure 5. The particles were well distributed and slightly agglomerated. The agglomeration is the indication of high reactivity of the prepared sample with the heat treatment and it may also be come from the magnetostatic interaction between particles.

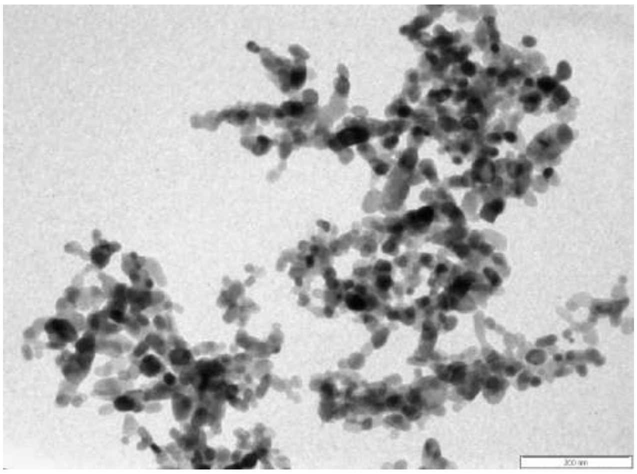

Fig. 5: TEM image of sintered sample

CONCLUSION:

$Cu_{0.2}Zn_{0.6}Ni_{0.2}Fe_2O_4$ nanoparticles synthesized by the wet chemical co-precipitation method. The precursor was sintered at 500 °C for 4 hour to obtain the final product. The XRD patterns confirmed the formation of single phase cubic spinel structure of ferrites. The low frequency band ν_2 observed at $433 cm^{-1}$ is assigned octahedral site and high frequency band ν_1 observed at $561\ cm^{-1}$ assigned tetrahedral site. SEM and TEM images indicate that the prepared sample is amorphous and porous in nature.

REFERENCES:

1. Gusev, A. I., & Rempel, A. A., Fizmatlit, (2001).
2. Cornell, R. M., & Schwertmann, U., John Wiley & Sons. (2003)
3. Krishnaveni, T., Kanth, B. R., Raju, V. S. R., & Murthy, S. R. J. alloys and compounds, 414(1), 282-286 (2006).
4. Cornell, R. M., & Schwertmann, U., John Wiley & Sons (2003).
5. Ghose, J., & Murthy, K. S. R. C. J. Catalysis, 162(2), 359-360 (1996).
6. Guilhaume, N., & Primet, M., J. Chem. Soc., Faraday Trans., 90(11), 1541-1545 (1994).
7. Słoczyński, J., Ziółkowski, J., Grzybowska, B., Grabowski, R., Jachewicz, D., Wcisło, K., & Gengembre, L., J. Catalysis, 187(2), 410-418 (1999).

STUDY OF STRUCTURAL PROPERTY AND RESISTIVITY OF LANTHANUM STRONTIUM COBALTITE THIN FILMS AS CATHODE FOR SOFC

B. S. Kamble*[1], R. M. More[1], V. J. Fulari[2] and R. K. Nimat[3]
[1]Department of Physics, D. B. J. College, Chiplun-415605, India
[2]Department of Physics, Shivaji University, Kolhapur-416004, India
[3]Department of Physics, Balasaheb Desai College, Patan-415206, India
*Corresponding Author E-mail: kamblebabaso@yahoo.com

ABSTRACT:

Different types of ceramic materials are currently being studied as possible cathodes in solid oxide fuel cell (SOFC), due to reduce operating temperatures. Strontium doped lanthanum cobaltite ($La_{1-x}Sr_xCoO_{3-\delta}$-LSC) was used as cathode for solid oxide fuel cell (SOFC). LSC thin films with 0.1, 0.2 and 0.3 mol % strontium were synthesized by spray pyrolysis technique. These thin films were sintered at 1000°C has been characterized by X-ray diffraction to determine the crystalline perovskite phase. D. C. resistivity was measured with variation of temperature and it decreases as temperature increases.

Keywords: Spray Pyrolysis, Resistivity, Dielectric constant, Cathode, LSC, SOFC.

INTRODUCTION:

Recently, solid oxide fuel cell (SOFC) studies on cathode development have focused on lanthanum strontium cobaltite (LSC). Lanthanum strontium cobaltite has been studied widely as a promising candidate for cathode materials for SOFC [1-4]. It is applied to high temperature ionic devices such as SOFCs, oxygen monitors and gas-separation membranes for its high electronic conductivity. Strontium doped lanthanum cobaltite show mixed ionic-electronic conduction and high catalytic activities for oxygen reduction. Undoped and doped lanthanum cobaltite has been focused due to potential applications as catalysts for hydrocarbons oxidation [5].

EXPERIMENTAL:

The Lanthanum Strontium Cobaltite ($La_{1-x}Sr_xCoO_{3-\delta}$) thin films were deposited on alumina substrate by using chemical spray pyrolysis (SP) technique. The basic principle used in chemical SP technique is that, a smallest droplet of the precursor solution sprayed from nozzle, reaches to the hot substrate leads to the pyrolytic decomposition of the solution which forms the adherent thin films in the presence of air as neutral gas [6]. The details of the preparation procedure of $La_{1-x}Sr_xCoO_{3-\delta}$

(LSC) thin film are given in the schematic diagram shown in fig.1. Lanthanum nitrate, strontium nitrate and cobalt nitrate were used as precursors of La, Sr and Co components. This precursor solution is used to deposit LSC thin films on alumina substrate at deposition temperature of 225 °C, this further leads to pyrolytic decomposition of these metallic salts and formation of lanthanum strontium cobaltite thin film [7]. The precursor thin films were sintered at 1000°C in the muffle furnace for 2 hours. The crystal structures of the sintered LSC thin films were studied by X-ray diffraction (Brucker X-Ray Powder diffractometer) with Cu Kα radiation (λ= 1.5418A.U.) and resistivity of samples was measured using two probe method and Dielectric constant was measured using LCR meter.

RESULTS AND DISCUSSION:

XRD studies:

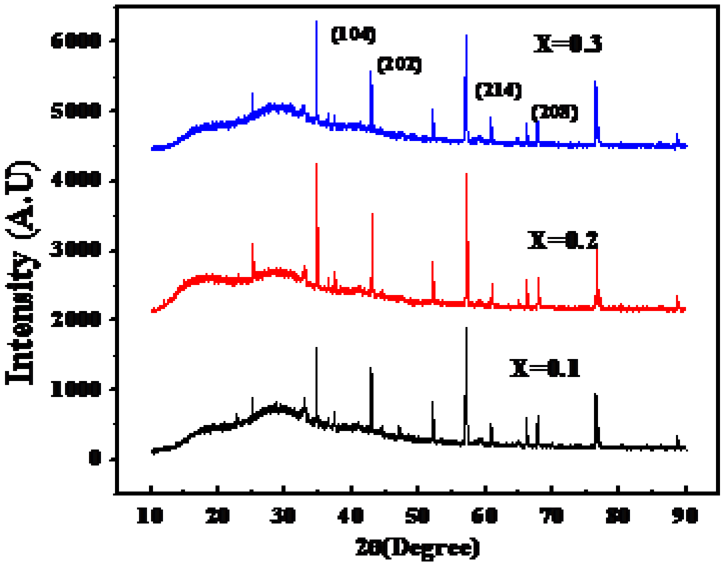

Fig. 1: The XRD of LSC sintered at 1000°C

XRD pattern of lanthanum strontium cobaltite thin films are shown in fig.1. The strongest reflections of the XRD patterns that matched with JCPDS file 48-0121 were indicate the formation of perovskite phase [8], therefore thin films clearly presented a well crystallized perovskite phase. XRD peaks were noticeably broadened. The planes observed are (104), (202), (214), (208), in XRD confirms crystallized rhombohedral structure with space group $R\bar{3}C$.

Resistivity measurements:

By using two probe method resistivity of the thin film samples of $L_{1-x}Sr_xCoO_{3-\delta}$ heat treated at 1000°C for two hours were carried out. The temperature dependence of resistivity is measured using standard two probe technique with a nano ammeter (2182A-Roorky), current source (6221-

Equiptronics). For taking the measurement, the sample is mounted on heating plate then two probes are electrically connected to the sample by highly conducting silver paste.

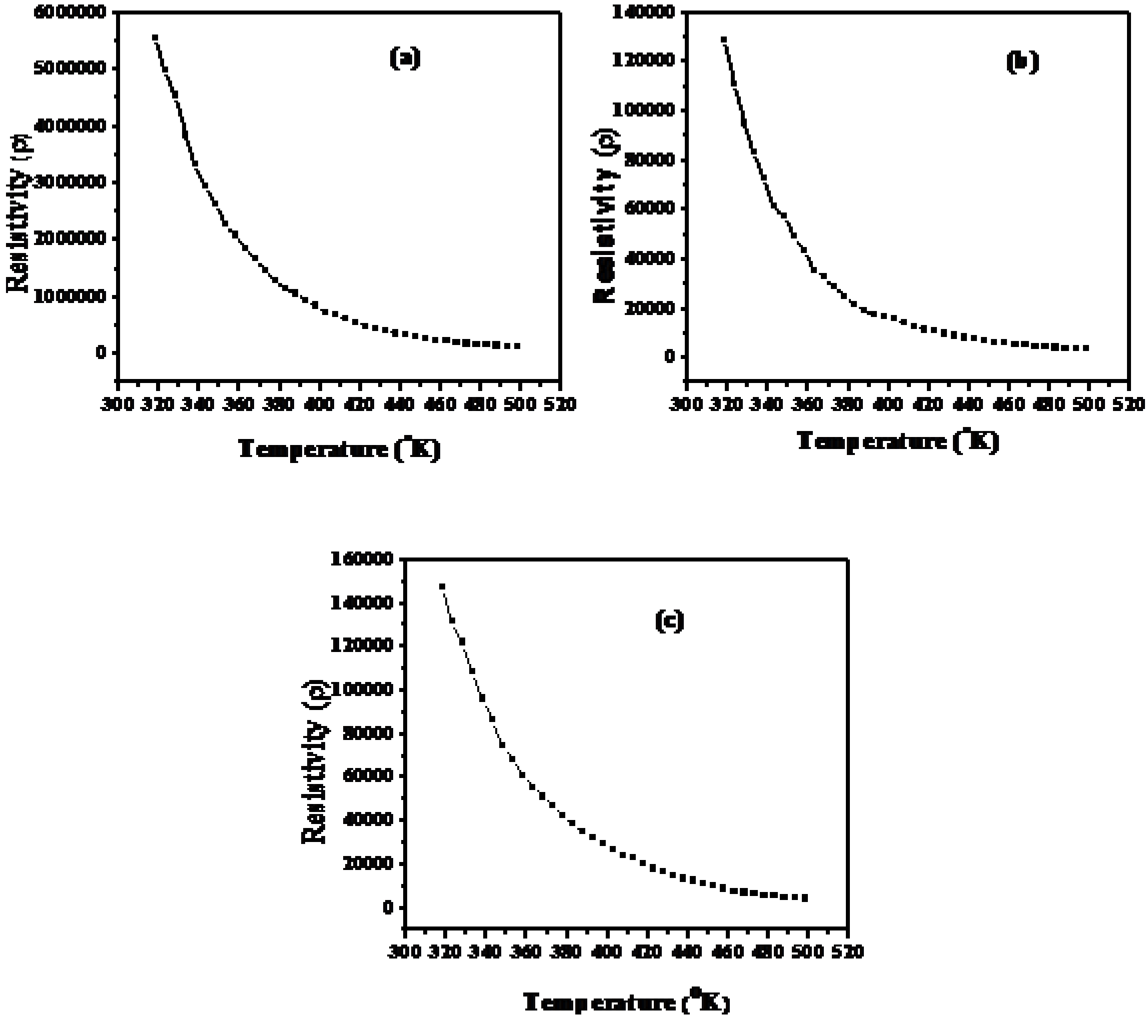

Fig. 2: Resistivity of LSC films (a) X = 0.1, (b) X = 0.2 , (c) X = 0.3

As temperature increases resistivity increases and further increase in temperature causes decrease in resistivity. It is found that all the samples show semiconducting behavior. The decrease in resistivity with increase in temperature is due to increase in thermally activated drift mobility charge carriers according to hopping conduction mechanism [9].

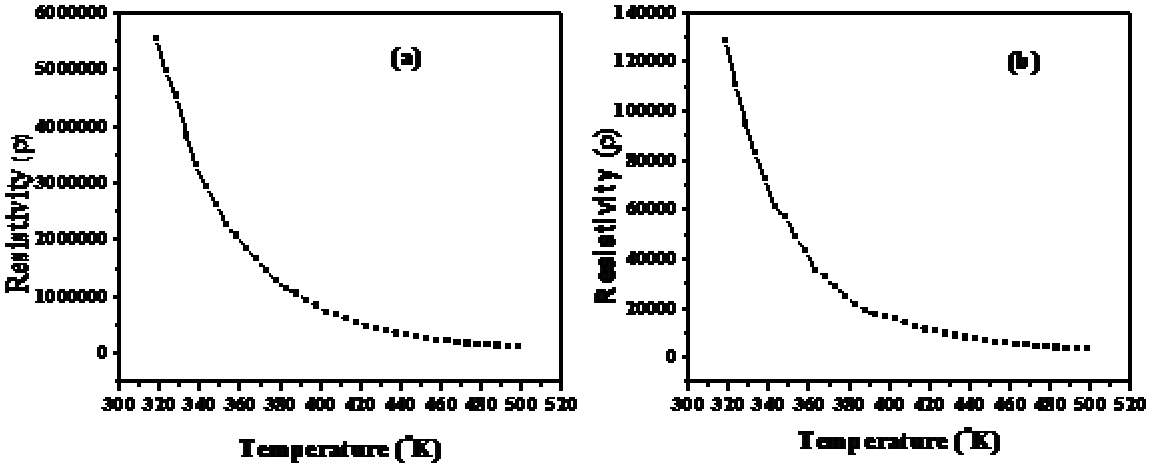

CONCLUSION:

Lanthanum Strontium Cobaltite ($La_{1-x}Sr_xCoO_{3-\delta}$) thin films as cathode for solid oxide fuel cell were synthesized by spray pyrolysis technique successfully. The phase formation takes place after sintering at 1000°C, which was identified by XRD. The crystal structure is found to be rhombohedral with $R\overline{3C}$ space group. The resistivity study shows as temperature increases resistivity decreases and it is semiconducting behavior which is usable as cathode for SOFC.

REFERENCES:

1. S. B. Alder, Chem. Rev. 104, 4791 (2004).
2. R. M. Ormerod, Chem. Soc. Rev. 32, 17 (2003).
3. W. G. Wang, Y. – L L. Liu, R. Barford, S. B. Schouhaard, P. Gordes, S. Ramousse, P. V. Hendriksen, M. Mogesen, Electrochem. Solid – State Litt. 8 (12), A619 (2005).
4. W. Winkler, J. koppen, J. Power Sources 61, 201 (1996).
5. D. Berger, N. V. Landschoot, C. Ionica, F. Papa, V. Fruth, J., Optoelect. Adv. Mat. Vol. 5, 719 (2003).
6. R. Chiba, R. A. Vargas,Macro Andreoli, E. S. Miyamaru Seo. Materials Science Forum Vols. 591-593, pp 459-464 (2008).
7. A. Alberto, M. Cardoso de et al.Material Research, 14(1):91-96 (2011).
8. Abdullah Abdul Samat, Mohd Azlan Mohd Ishak, N. Osman, jurnal Intelek
9. S. M. Khetre, H. V. Jadhav, P. N. Jagdale, S. R. Kulal, S. R. Bamane, Adv. In Mat. Sci. Research 503 (2011).

RECENT ADVANCES IN CARBON SOOT COATED SUPERHYDROPHOBIC MATERIALS FOR OIL-WATER SEPARATION (SHORT REVIEW)

Balaji T. Khogare[1, 2], **Rajaram S. Sutar**[1], **Krishna K. Rangar**[2] **and Sanjay S. Latthe**[1*]
[1]Self-cleaning Research Laboratory, Department of Physics,
Raje Ramrao Mahavidyalaya, Jath, Dist- Sangli (MS) India.
[2]Department of Chemistry, Raje Ramrao Mahavidyalaya, Jath Dist- Sangli (MS) India
*Corresponding authors E-mail: khogare1988@gmail.com latthes@gmail.com

ABSTRACT:

There is need to develop clean up technology for oil-water separation because the spilled oil affects the ecological and environmental system. Superhydrophobic materials have outstanding water repulsion and oil absorption capabilities, high selectivity, chemical inertness and excellent recyclability, due to this they shows potential application in the field of oil spill cleanup. In this paper, recent applications of carbon soot coated superhydrophobic materials for oil-water separation is discussed.

INTRODUCTION:

During the past few years, due to accidents during transportation, extraction and storage of oil there have been many oil spill. On December 2014, around 3000 barrels of oil spilled into the waters of the world famous Sundarbans nature reserve in Bangladesh after a collision between a tanker and another vessel. The oil spill blackened the shoreline, threatening trees, killing large numbers of sea birds, small fishes, dolphins and mammals because of its poisonous chemical constituents. In July 2015, on the beach of Kinmen County of Fujian province, a large black viscous oil patch was found with a total length of approximately one kilometer. After primary investigation, it was concluded that the oil leaked from a ship and was immediately cleaned-up to protect the environmental and ecological system. Oil spill can cause environmental impacts such as physical damage to wildlife and their habitats, chemical toxicity and ecological changes [1]. There is need to solve this problem. Carbon soot coated superhydrophobic materials are the best solution for this problem. The superhydrophobic surfaces on which water achieves contact angle higher than 150° and sliding angle less than 5° are attracting minds of researchers due to their self-cleaning abilities [2-12].

Straw soot sponge for highly efficient oil/water separation:

A piece of commercial polyurethane foam was cleaned and dried in an oven at 70 ^{0}C for 30 min. The grown straw soot on the glass slide was collected by shaving soot from the glass using a spatula. The superhydrophobic foam was prepared by a dip-coating method in a colloidal suspension of soot in ethanolic medium. The magnetic hydrophobic sponge was obtained by immersing the hydrophobic sponge in 20 ml of absolute ethanol containing magnetic nanoparticles (**Fig. 1**). The prepared sponge showed excellent superhydrophobicity with water contact angle as high as 154°. Experiments showed that the amount of the absorbed oil was about 30 times of sponges own weight, it has our 30 times recyclability and the advantage of magnetic separation [13].

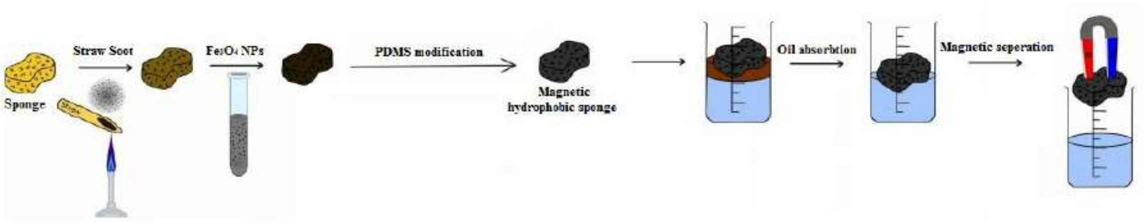

Fig.1: Schematic illustration of preparation modified polyurethane sponge and oil separation process. Images reprinted from [13], with permission from Elsevier, Copyright 2017

Carbon Soot Sponge for Oil Cleanup:

The growth of carbon soot was performed using a combustion flame process in open air using ethylene (C_2H_4) and oxygen (O_2) as precursors with a flow ratio of 5:3. The carbon soot was collected by placing a silicon wafer on top of the flame. The carbon soot-sponge was prepared by dip-coating. First, 25 mg of as-grown carbon soot was dispersed in 20 mL of dichloroethane solution, followed by a 60 min sonication. Then, melamine sponge, which was cleaned by acetone and dried in an oven (80 °C), was immersed in the carbon soot dispersion. The carbon soot-coated sponge was again dried in the oven at 80 °C for 2 h (**Fig. 2**). The carbon soot-sponge demonstrates high absorption capacities (up to 80 times its own weight) for a broad spectrum of oils and organic solvents with a recyclability of more than 10 times. These research results show evidence that the carbon soot-sponge is promising in environmental remediation for large scale, low cost removal of oils from water [14].

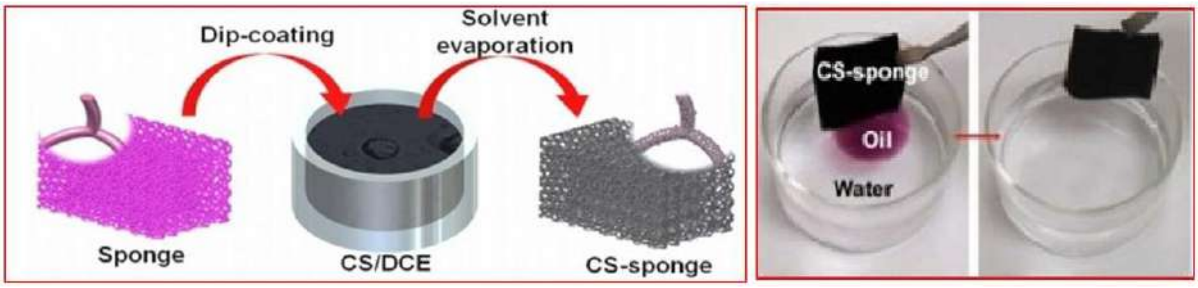

Fig.2: **Schematic showing the carbon soot-sponge preparation by dip-coating and carbon soot-sponge before & after oil absorption. Images reprinted from [14], with permission from American Chemical Society, Copyright 2014.**

Separation of oil and water with special wettability mesh membranes

A stainless steel meshes (350 mesh, 316L) were place above the wick and soot was collected on the surface. And 10 nm carbon nanoparticles were coated onto the stainless steel meshes. Then we used a chemical vapor deposition method to form a more stable layer of SiO_2/carbon on the stainless steel meshes. Finally, the SiO_2/carbon stainless steel mesh were modified with PFOTS and PDDA–

PFO respectively to form the superhydrophobic/superoleophilic and oleophobic/superhydrophilic mesh membrane (**Fig. 3**). Separation experiments show that these superhydrophobic/superoleophilic or oleophobic/superhydrophilic mesh membranes can be used to selectively separate oil/water with a high flux of more than 930 L m^{-2} h^{-1} and a collecting efficiency of over 97%. Furthermore, the repetitions of the separation experiments demonstrate that these superhydrophobic/superoleophilic or oleophobic/superhydrophilic mesh membranes are durable, stable and reusable, making them encouraging candidates for practical oil-polluted water treatment [15].

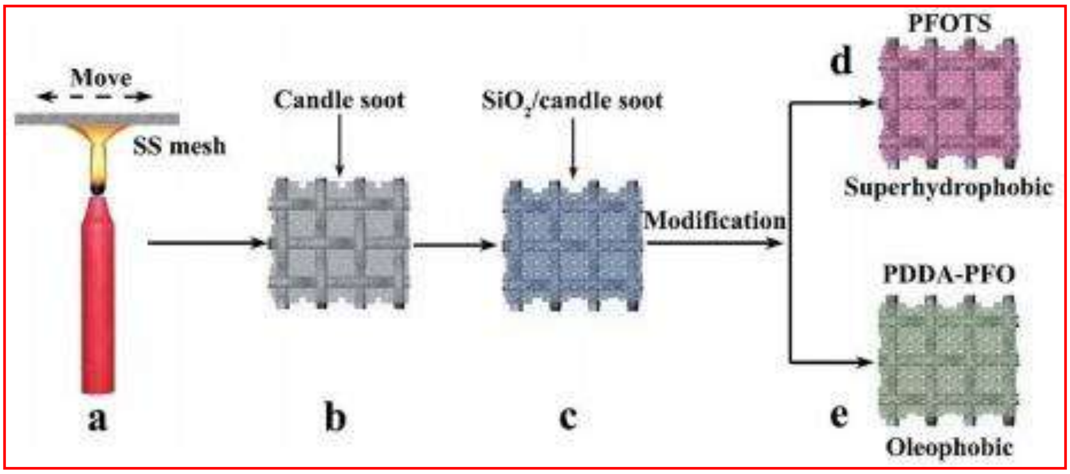

Fig.3: **Process of Superhydrophobic and oleophobic mesh membranes preparation: (a) coating stainless steel mesh with carbon nanoparticles (candle soot), (b) carbon nanoparticles coated stainless steel mesh, (c) SiO_2/carbon stainless steel mesh, (d) PFOTS modified SiO_2/carbon stainless steel mesh, (e) PDDA-PFO modified SiO_2/carbon stainless steel mesh. Images reprinted from [15], with permission from Royal Society of Chemistry, Copyright 2017**

Superhydrophobic mesh:

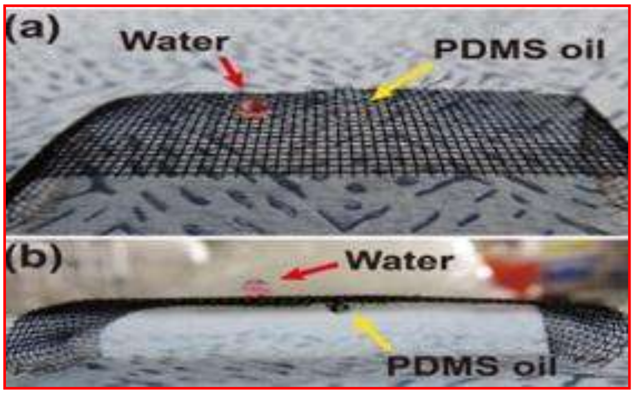

Fig.4: **A superhydrophobic mesh prepared with a PFCS coating. (a) While the water drop remains on the mesh, the PDMS oil drop passes through the mesh and (b) dangles from the mesh. Images reprinted from [16], with permission from Elsevier, Copyright 2014**

Mesh prepared with a PFCS coating can be used to separate oil. After cutting a piece of iron mesh and coating the mesh with paraffin wax, a metal sheet was patched onto the back of the mesh to induce incomplete combustion. After coating the mesh with soot from a candle flame a superhydrophobic mesh was created. Because the superhydrophobic coating is oleophilic, a water drop cannot penetrate through the mesh, but polydimethylsiloxane (PDMS) oil can, as shown in **Fig. 4** shows a side-view of the drops. While the water drop remains on the mesh, the PDMS oil drop with a low surface tension passes through the mesh and dangles from the mesh. The mixture of water and PDMS oil was easily separated with the mesh. This mesh can be effective in oil collection systems and functional filtration systems [16].

CONCLUSION:

Carbon soot coated sponge and mesh for use in oil-water separation has been developed in this study. The carbon soot synthesis and carbon soot coated sponge and mesh preparation procedures are simple, cost-effective and scalable. The absorption/separation investigation demonstrates that the carbon soot sponge and mesh is highly efficient and stable in absorbing a wide range of oils and organic solvents.

ACKNOWLEDGEMENT:

The authors would like to thank Principal, Raje Ramrao Mahavidyalaya, Jath Dist- Sangli, for providing the basic infrastructure facilities.

REFERENCES:

1. Yong, S., et al., 43(16): p. 1741-1794 (2013).
2. Latthe, S., et al., Coatings, 4(3): p. 497 (2014).
3. Liu, S., et al., RSC Advances, 5(84): p. 68293-68298 (2015).
4. Latthe, S.S., et al., 17(5): p. 565-571 (2010).
5. Dhere, S.L., et al., J. Phy. and Chem.of Solids, 72(1): p. 45-49 (2011).
6. Xing, R., et al., J. Mol. Liquids, 247(Supplement C): p. 366-373 (2017).
7. Kim, D.-Y., et al., J. Materials Chem. A, 3(7): p. 3975-3983 (2015).
8. Park, J.-J., et al., ACS Applied Materials & Interfaces, 5(13): p. 6155-6160 (2013).
9. Gurav, A.B., S.S. Latthe, and R.S. Vhatkar, Surface Innovations, 1(3): p. 157-161 (2013).
10. Latthe, S.S. and A.V. Rao, Surface & Coat. Tech., 207(Supplement C): p. 489-492 (2012).
11. Madhan Kumar, A., et al., Polymer, 77(Supplement C): p. 79-86 (2015).
12. Yoon, H., et al., J. Materials Chem. A, 3(21): p. 11403-11410 (2015).
13. Beshkar, F., H. Khojasteh, and M. Salavati-Niasari, J. Coll. Interface Sci., 497: p. 57-65 (2017).
14. Gao, Y., et al., ACS applied materials & interfaces, 6(8): p. 5924-5929 (2014).
15. Liu, D., et al., RSC Advances, 7(21): p. 12908-12915 (2017).
16. Seo, K. and M. Kim, Carbon, 68: p. 583-596 (2014).

CHEMICAL SYNTHESIS AND CHARACTERIZATION Cu-DOPED SnO_2 NANOPARTICLES

Bharat Govind Pawar

Department of Chemistry, Sangola College Sangola,
Kadlas Road Sangola, MS, India – 413307

ABSTRACT:

Nanosized Cu-doped SnO_2 particles were synthesized by chemical route. The typical procedure involves mixing of Tin chloride with nitric acid. Then P^H was made alkaline by adding dilute ammonia, Then whole mixture is kept for refluxing for removing excess of ammonia. Products formed were dried in oven then in muffle furnace and then characterized with scanning electron microscopy, X-ray powder diffraction, FTIR, This nanoparticles have possible application in the field of nanotechnology.

Keywords: Chemical Synthesis, SnO_2, Nanoparticles.

INTRODUCTION:

SnO_2 semiconducting transparent thin films have various appealing features for technical applications in solar energy conversion, flat panel displays, electrochromic\ devices, invisible security circuits, LEDs, etc. Hence large area SnO_2 films on cheap and easily available substrates are of considerable interest for the formation of most of the photonic structures. There are various methods such as chemical vapour deposition, sol gel, spray pyrolysis, electron beam evaporation, vepour deposition, pulsed laser deposition, molecular beam epitaxy, thermal evaporation, reactive evaporation and magnetron sputtering, etc. for the preparation of pure or doped thin films [1-2]. Copper is very good electrical and thermal conducting material so it doped with metal oxides, composites for improve the electrical and thermal conducting property of that materials.

EXPERIMENTAL PROCEDURE:

Synthesis of doped SnO_2 nanoparticles prepared as modification of reported earlier wet chemical method [3] a typical process consist of 1.5 g tin chloride dihydrate 0 .400 g copper chloride and 5 g citric acid in 8 M HNO_3 in a conical flask until a clear solution was obtained. Aqueous ammonia was added dropsies into the solution with stirring, until a pH of 9 was reached. Thus prepared solution was found to be transparent and stable with no precipitation or turbidity. The obtained sol was refluxed at 373 K for 2 h upon which it slowly turned into a turbid colloidal solution. After 5-6 h, the gel was separated via decantation, washed several times with double distilled water and ethanol to remove impurities. Finally sintered at 600 °C in muffle furnace. For further characterization.

Fig.1. Experimental set of preparation Cu-doped SnO_2

RESULT AND DISCUSSION:

Figure 2 shows the XRD spectrum with intense and distinct peaks of pure and cu-doped SnO_2 nanoparticles.. Observed reflection peaks were coppered with JCPDS (41-1445), and confirmed the presence of pure crystalline SnO_2. No peaks corresponding to tin metal or any other phase as impurity peaks were identified. The obtained peaks were with characteristic diffraction peaks of SnO_2 corresponding to (110), (101), (200), (111), (211), (220), (002), (310), (112), (301), (202), and (321) reflection planes. Crystalline size "D" was obtained by the measurement of the broadening of diffraction lines and applying the Debye- Scherrer formula. The crystalline size calculated from (110) peak was 25 nm while as doping nanoparticles grain size was 18 nm. The reduction in peak intensity and increase in width broadening support lowering in crystallite size and thus confirms the role of Cu as grain growth inhibitors.

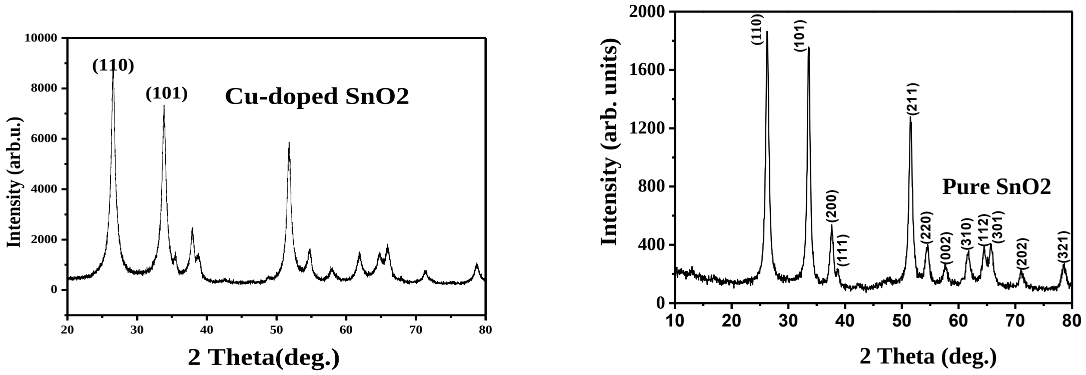

Fig. 2: shows the XRD spectrum SnO_2 and Cu-doped SnO_2

Further evidence is found in the X-ray diffraction patterns shown in Fig. 2. From this figure it is observed that the reflection peaks in the doped films shifted from their standard positions in the presence of the dopant. The deviation in the lattice parameters is mainly due to occupying of doping atoms into the interstitial positions of the lattice. However, the peak position shifts to higher angle with doping of Cu content, revealing the changes in lattice parameter values. [4]. It indicates that crystallite size increased with the increasing in the Cu doping. The lattice parameter decreases with the increasing the dopant concentration of Cu and crystallite sizes also increases.

FTIR spectrums of pure and Cu-doped SnO_2 nanoparticles are shown in Fig. 3. It indicates that there are three peaks at around 671 cm-1, 1628 cm1, 3460 cm-1for pure SnO2 nanoparticle. The peak at 625 $cm^{-}1$ can be assigned to the stretching vibration of the O–Sn–O bond formed by oxolation reactions. A weak bond at 1617 $cm^{-}1$ is attributed to the deformation mode of OH groups. The peak at 3112 cm-1 corresponds to the OH vibrational mode [5]. It has also been attributed that, the increase in Cu content causes the small shift in wavenumber to lower region.

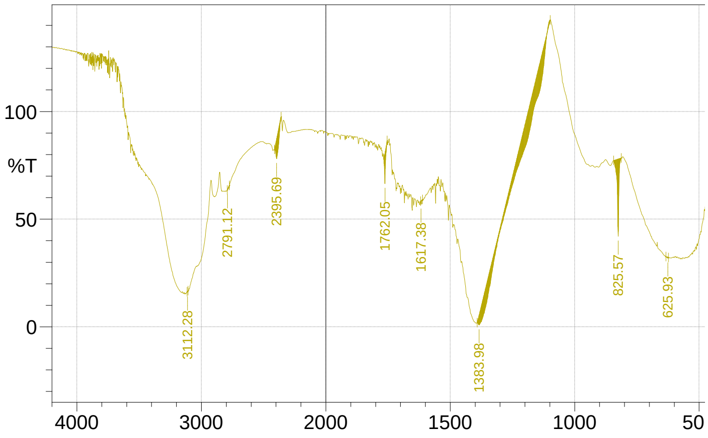

Fig. 3: FTIR spectrums of Cu-doped SnO_2

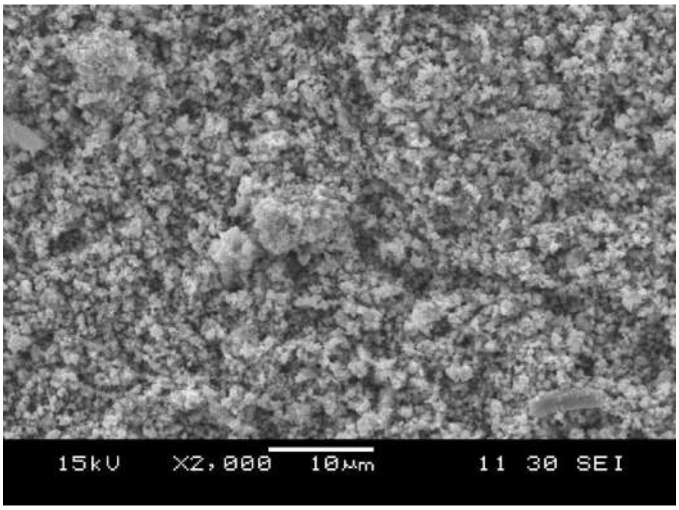

Fig. 4: SEM image of cu-doped SnO_2 nanoparticles

Fig. 4 Shows the SEM images of cu-doped SnO_2 nanoparticles. The microstructure reveals formation of the agglomerated grains with remarkable porosity which is useful for gas sensing application. Due to the Cu maximum porosity as compared to the other samples and it provides maximum surface area for adsorption of oxygen and test gases.

CONCLUSIONS:

The pure and Cu doped tin oxide nanoparticles are prepared by chemical method. The incorporation of Cu, is found to introduce significant structural and morphological changes in SnO_2. The substitution of Sn ions by Cu ions modifies the surface of base material by providing larger surface area and reactivity for adsorption of oxygen. The simultaneous doping of Cu in SnO_2 showed profound effect on the gas sensing properties hence it can be used as promising candidate for the fabrication of high-performance gas sensor.

REFERENCES:

1. R. S Pusu, G. I Rusua, J. Optoelect. Adv.Mater.7, No.2, 823 – 828 (2005).
2. M. R. Islam and , J. Podder, Cryst. Res. Technol. Vol. 44, No. 3, 286 – 292 (2009).
3. B. G. Pawar, D. V. Pinjari, S. S. Kolekar, A. B. Pandit, and S. H. Han ISRN Chemical Engineering (2012)
4. A. S, Rashmi, and K. Jain, Material Chem. Phy., 105, No.2-3, 385-390 (2007).
5. F. Gu, S. Wang, C. Song, M. Lü, Y. Qi, G. Jun, Dong Xu, D Yuan, Chem. Phy. Lett. 372, 451-458 (2003).

MORPHOLOGY AND DIELECTRIC STUDIES OF PIEZOELECTRIC POLYMER BASED NANOCOMPOSITES

C. V. Chanmal[1]*, R. N. Mulik[1], S. G. Pawar[1] and J. P. Jog[2]
[1]Department of Physics, D. B. F. Dayanand College of Arts & Science, Solapur
[2]Polymer Science and Engineering Division, NCL-Pune
*Corresponding author E-mail:cvchanmal@gmail.com

INTRODUCTION:

Piezoelectric PVDF based nanocomposites with Si_3N_4 nanoparticles were prepared by simple melt compounding technique and characterized by morphology and dielectric studies. The morphology study shows uniform distribution of Si_3N_4 nanoparticles into polymer matrix. The dielectric permittivity increases monotonically with the increasing content of Si_3N_4 content. The dielectric permittivity increases significantly with addition of Si_3N_4. For 7wt% loading, permittivity reaches as high as 2000 at 10^{-02} Hz. The dielectric permittivity loss curve show two relaxations corresponding to the glass transition temperature and crystalline relaxation. However, crystalline relaxation in PVDF/Si_3N_4 nanocomposites is significantly suppressed due to high values of permittivity in the low frequency region. The dielectric mechanism shows a broad relaxation at low frequency region which is attributed to the Mawell-Wagner-Sillars (MWS) type of relaxation. However the MWS type relaxation is found to significantly enhanced in PVDF/Si_3N_4 nanocomposites. This indicates presence of strong interaction between PVDF and Si_3N_4. Heterogenity introduced due to addition of nanofillers has increased the space charge density in polymer based nanocomposites.

EXPERIMENTAL:

The polymer PVDF and Si_3N_4 nanparticles were used as received. The nanocomposites were prepared by melt mixing method at temperature of 200 °C, 5 min residence time and 60 RPM. The nanocomposites were characterized for morphology and dielectric studies.

RESULTS AND DISCUSSION:

The morphology of nanocomposites was studied using scanning electron microscopy (SEM). Figure 1 shows SEM micrographs of PVDF/Si_3N_4 nanocomposites. The SEM study shows the uniform dispersion of nanofillers into polymer matrix. The morphology study shows the network like assembly of nanoparticles in the PVDF matrix. The uniform dispersion of nanoparticles is very important in achieving desired properties of nanocomposites.

The dielectric properties of nanocomposites were studied as a function of frequency. The permittivity data for nanocomposites is shown in figure 2. The permittivity study shows increase in permittivity with the increasing content of Si_3N_4 nanoparticles. The permittivity approximately increases upto 2000 with 7 wt % loading of nanoparticles. The tan shows that dielectric losses are also less than 0.03. Thus significantly improved dielectric permittivity was obtained at relatively low dielectric losses.

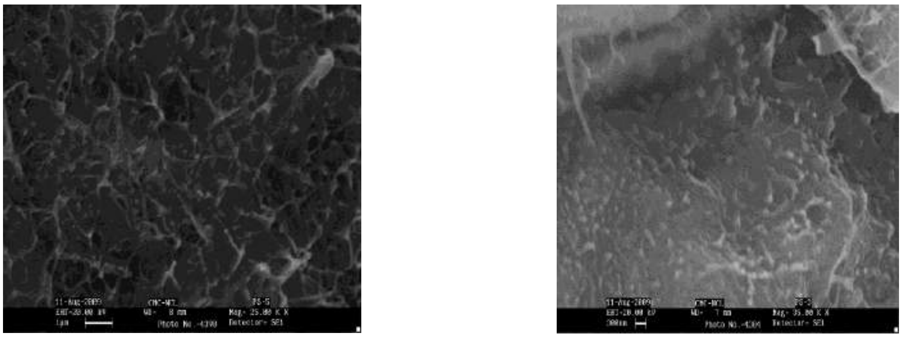

PVDF/Si_3N_4-5%

PVDF/Si_3N_4-7%

Fig. 1: SEM micrographs of PVDF/Si_3N_4 nanocomposites with different filler loading

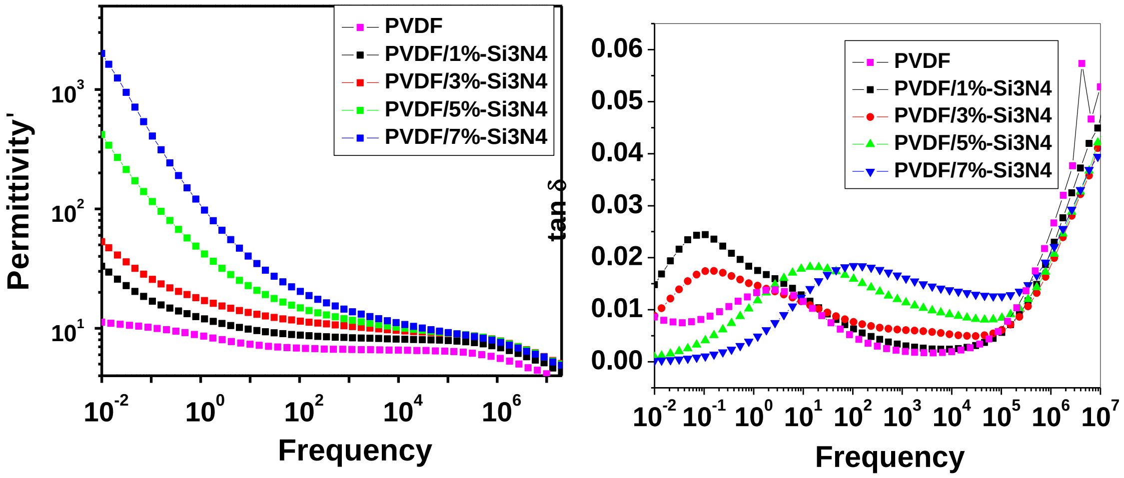

Fig. 2: Permittivity and tan δ for PVDF/Si_3N_4 nanocomposites as a function of frequency

CONCLUSIONS:

The PVDF/Si_3N_4 nanocomposites were prepared by simple melt mixing method. The morphology study shows uniform dispersion of nanoparticles in polymer matrix. The dielectric permittivity study shows tremendous increase in permittivity at relatively low dielectric losses. Thus, the nanocomposites can be useful in application of electromagnetic shielding material where high dielectric constant materials with low losses are necessary.

REFERENCES:

1. Jin-Kai Yuan, Zhi-Min Dang, Sheng-Hong Yao, Jun-Wei Zha, Tao Zhou, Sheng-Tao Lib and Jinbo Bai, J. Mater. Chem., 20, 2441–2447 (2010).
2. Yang Shen, Yuanhua Lin, and Ce-Wen Nan, Adv. Funct. Mater. 17, 2405–2410 (2007).
3. J.I. Hong, P. Winberg, L.S. Schadler, and R.W. Siegel, Mater.Lett., 59, 473–476 (2005).
4. Baojin Chu, Minren Lin, Bret Neese, and Qiming Zhang, J. Appl. Phy., 105, 014103 (2009).
5. G. A. Kontos, A. L. Soulintzis, P. K. Karahaliou, G. C. Psarras, S. N. Georga1, C. A. Krontiras, M. N. Pisanias, Express Polymer Lett., 1, No.12,781–789 (2007).

SYNTHESIS OF CO DOPED ZnO NANOPARTICLES BY SOL GEL METHOD AND THEIR CHARACTERIZATIONS FOR SOLAR CELL APPLICATION

D. A. Kumbhar[1, 2], A. M. Nalawade[2], S. S. Kumbhar[3], R. A. Nalawade[2], G. D. Salunke[1]

[1]Department of Chemistry, R. R. College, Jath, Maharashtra, 416404, India

[2]Department of Chemistry, L. B. S. College, Satara, Maharashtra, 415002, India

[3]Department of Physics, R. C. S. College, Kolhapur, Maharashtra, 416004, India

ABSTRACT:

Co doped ZnO Nanoparticles has been synthesized by the sol-gel method using Zinc acetate and Co acetate as a precursors. The effect of Co doping on the structural and morphological propertiese of ZnO is studied. The X-ray diffraction (XRD) analysis reveals that the samples are polycrystalline and with hexagonal wurtzite crystal structure. The SEM images of ZnO nanoparticles show that the grain size decreased after Co doping. UV-Spectrophotometer measures the absorbance and the band gaps calculated by taucs plots. It is 3.19 eV for pure ZnO and it was decreased to 2.76 eV after Co doping which is applicable to use in solar cell application

Keywords: Co doped ZnO nanoparticles, XRD, SEM, UV-Visible.

INTRODUCTION:

Solar energy provides renewable and cheap energy source for people. Water, bio-energy, wind energy and fossil fuels are the type of primary energy resources. However, the use of fossil fuels has contributed to the recent increase in the greenhouse gas effect and CO_2 emissions, as well as global warming. Solar energy is the most abundant renewable energy source, which provides very high temperature heat. This heat energy useful for electricity to drive a generator or a machine. Solar power can also be directly converted into electricity unit by a photovoltaic (PV) effect. One example of these third-generation technologies is dye-sensitized solar cell (DSSC), which provides a low cost method to convert sunlight to electricity. It is also known as a photoelectrochemical cell [1-3]. Recently nanoscale materials are of great interest for research point of view because nanomaterials are very sensitive and functionally well-organized because of smaller grain size, quantum confinement effect and high surface to volume ratio as compared to the bulk materials. In the range of nanoscale the optical and electrical properties change due to the change of band gap and make the materials suitable for new applications and devices. Zinc oxide (ZnO) is a wide band gap hexagonal n-type semiconductor material. Zinc oxide is a transparent electro conductive and piezoelectric material [4]. Zinc Oxide is an excellent Ultraviolet absorber and antibacterial agent.

A direct band gap of 3.37 eV and exciton binding energy 60 eV allows for effeient UV stimulated emission at room temperature. ZnO has been used in solar cells, transparent electrodes, and blue/ UV light emitting devices. This nanomaterial is a promising candidates for nano-electronic and photonics [5-6]. Transition metal (TM)-doped ZnO nanoparticles are promising candidates for a variety of potential applications due to the charge and the spin of electrons that lead to a new magnetic, optical and transport properties of these materials. Numerous studies of these materials grown by several methods have exhibited room temperature ferromagnetic (RTFM) [7]. Dye-sensitized solar cells (DSSCs) have attracted much attention for inexpensive production and relatively high energy conversion efficiency. Up to now, ruthenium photoactive dye and porous film of TiO_2 nanoparticles (NP, 0D) have been mostly used as sensitizer and semiconductor, in DSSCs with the highest efficiency of 11% and ZnO is good alternative for TiO_2 but less efficiency [8-11]. The purpose of present study is to investigate the effect of Co doping on to the morphological, structural and optical properties of ZnO nanoparticles and to tune the band gap and improve the material performance for its Solar cell application.

EXPERIMENTAL:

Synthesis of ZnO nanoparticles:

Zinc oxide nanoparticles were prepared by sol-gel method. For this 0.2 M zinc acetate dehydrate solution, prepared in distilled water. The ammonium hydroxide added drop wise to this prepared solution till pH becomes 8 with continuous stirring and formation of sol take place. This sol of zinc hydroxide is dried at 80 ^{0}C for 6 h to get gel. The obtained gel is calcinated at 400^{0}C for 3 h in a muffle furnace which forms pure Zinc oxide nanoparticles. Same procedure followed for doped ZnO synthesis using dopant Co acetate of 3 mol% which is added with zinc acetate precursor to form doped ZnO nanoparticles.

Finally, the sample was obtained after cooling down at room temperature in air. The XRD patterns were recorded on Bruker D2 PHASER XRD. SEM and EDAX image was obtained on JEOL JSM-6360. TEM image was obtained on JEOL JEM 2100. DRS-UV visible obtained by Labindia UV-3092.

RESULTS AND DISCUSSIONS:

Structural properties (XRD):

Fig. 1 shows the X-ray diffraction patterns of Co doped ZnO obtained with Cu-Kα (1.54056 Å) radiation. It has been observed that all of peaks of XRD pattern belong to the hexagonal lattice of ZnO with three most preferred orientations namely (100), (002) and (101). Most importantly, all of the XRD peaks were attributed to ZnO and no other undesired peaks were observed due to secondary phases or impurity phases within the detection limit of the X-ray diffractometer. From fig. it is seen that the all samples are polycrystalline in nature with no impurity peak present. The peaks obtained are indexed by using JCPDS card no. 36-1451. The average crystallite size ‘D’ of the samples was calculated using the Debye-Scherer formula

$$D = \frac{0.9\lambda}{\beta \cos\theta} \qquad (1)$$

where ‘λ’ is the wavelength of X-ray (1.5406 Å), ‘β’ the full-width at half-maximum in radian, and ‘θ’ the angle of diffraction. It is seen that crystallite size (D) varies in between 40 and 45 nm.

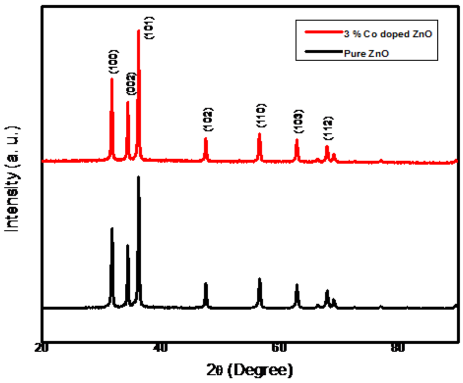

Fig. 1: XRD pattern of prepared samples

Morphological Properties (SEM):

Fig.2 shows the SEM images of pure ZnO nanoparticles and Co doped ZnO nanoparticles. It also shows show that the grain size decreased after 3% Co is doped. The morphology show the formation of cube likes structure of the grains.

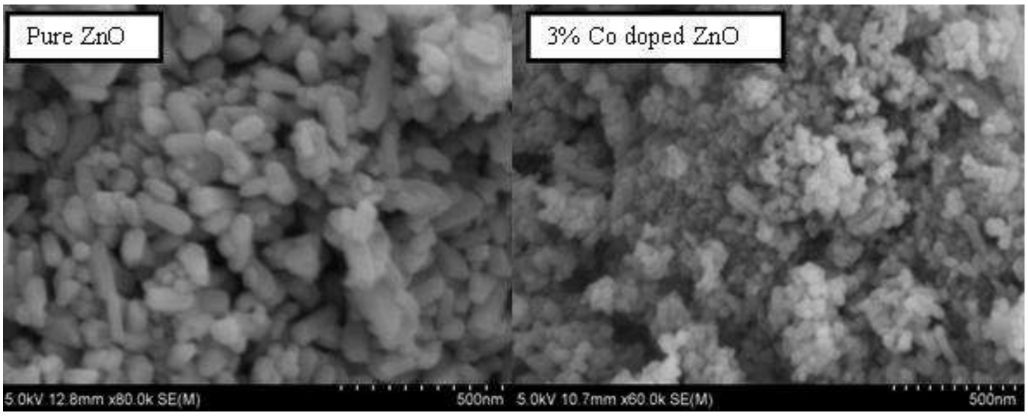

Fig. 2: SEM images of Pure and 3% Co doped ZnO samples

UV-Visible:

Fig.3 shows UV-Visible reflectance spectra of the 3% Co doped ZnO nanoparticles. Spectra reveals characteristic absorption peak of ZnO. The change in absorption peak due to Co doping indicates a change in the band structure. A red shift is observed in the band gap energy for the cobalt doped samples compared to the undoped ZnO. Doping metal ions with their electron density in ZnO leads to change in the conduction band level of the nanoparticles and give modification to the particular band gap. These shifts towards the higher energy wavelength of UV- light suggest the band gap narrowing in the doped compounds which is confirmed via tauc plot analysis of spectroscopic data, Fig.4. The tauc plots are drawn using Tauc equation $(\alpha h\nu)^2 = A\,(h\nu - Eg)$, where, ν is the frequency of light, A is a constant, h is the planck's constant, and Eg is energy band gap of the material. The band gap calculated for the Pure ZnO and 3% Co doped ZnO is 3.12, 2.76 respectively. So, it is observed that the band gap decreased by Co dopant ion.

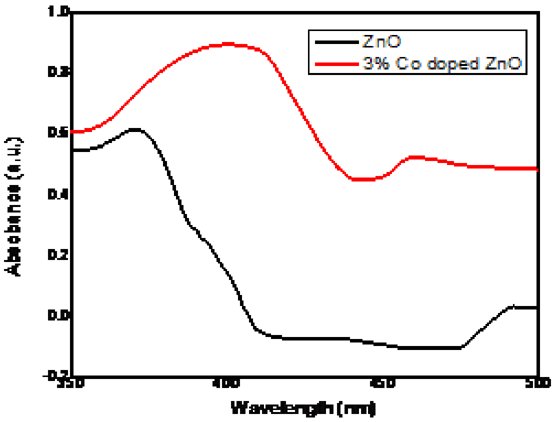

Fig. 3: UV-Vis absorption spectra of Pure and 3% Co doped ZnO NPs

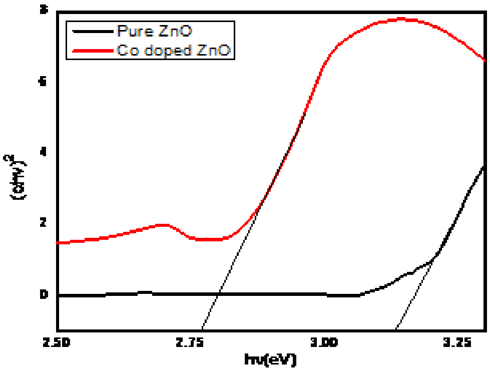

Fig. 4: Tauc's plots for band gap evaluation

CONCLUSION:

Sol-gel synthesis route has been successfully used to synthesize Co-doped ZnO nanoparticles. The XRD pattern reveals the formation of hexagonal wurtzite structure with average crystalline size of 40 to 45nm. SEM images reveal the nanoparticles are in Cubic shape with the particles are uniformly dispersed. The UV-DRS spectra reveal that significant decreases in optical band gap from pure ZnO to Co doped ZnO (3.12eV to 2.76eV). Thus the cobalt doping can be used as a method to control the optical and structural properties of ZnO nanoparticles and it is very useful in the fabrication of new solar cell devices.

ACKNOWLEDGMENTS:

The authors would like to thank the Shivaji University of Kolhapur, Maharashtra for providing Characterizations i.e. XRD, SEM and DRS UV-visible.

REFERENCES:

1. Omar, H. Abdullah, Renewable and Sustainable Energy Reviews, 31, 149-157 (2014).
2. L. Chaar, L. Iamont, N. Zein, Review of photovoltaic technologies, Renewable Sustainable Energy Rev, 15, 2165-75 (2011).
3. J. Lee, M. Rahman, S. Sarker, N. Nath, A. Ahammad, J. Lee, Advances in composite materials for medicine and nanotechnology, 182-210 (2011).
4. M. Hassan, W. Khan, A. Azam, A. Naqvi, Journal of Luminescence, 145,160–166 (2014).
5. V. Karpina, Res. Tech., 39, 980, 2004, Efros A L,and Rosen M, Annu. Rev. Mater. Sel., 36,475 (2003).
6. G. Varughese, K. Usha , A. Kumar, International Journal of Latest Research in Science and Technology, 3, 133-136 (2014).
7. N. Djaja, D. Montja, R. Saleh, Advances in Materials Physics and Chemistry, 3, 33-41 (2013).
8. R. Pawar, J. Shaikh, P. Shinde, P. Patil, Materials Letters, 65, 2235–2237 (2011).
9. Pal and P. Giri, Journal of applied physics, 108, 322-324 (2010).
10. M. Nair, M. Nirmala, K. Rekha, A. Anukaliani, Materials Letters, 65, 1797–1800 (2011).
11. A. Jacob, L. Balakrishnan, K. Shambavid and Z. Alex, The Royal Society of Chemistry, 7, 39657–39665 (2017).

SYNTHESIS AND CHARACTERIZATION OF Fe_3O_4 NANOPARTICLES

***E. K. Kore[1], J. G. Dhumal[2], S. S. Bandagar[2] and G. S. Shahane[2]**

[1]Dept of Physics, DBF Dayanand College of Arts & Science, Solapur, Maharashtra, India

[2]Dept of Electronics, DBF Dayanand College of Arts & Science, Solapur, Maharashtra, India

*Corresponding author E-mail: eknathkore011@gmail.com

ABSTRACT:

In the present work nanoparticles of magnetite (Fe_3O_4) are synthesized via facile wet chemical co-precipitation route using aqueous ferrous and ferric chloride solutions. The method provides; fine, high purity, stoichiometric particles of magnetite with narrow size distribution by accurately regulating process conditions such as precursor concentration, stirring rate, reaction temperature, solution pH, etc. During the growth of nanoparticles oleic acid was used as capping agent to avoid agglomeration. The powder samples are characterized by X-ray diffraction (XRD), Transmission Electron Microscope (TEM), Fourier Transform Infrared (FTIR) and Vibrating Sample Magnometer (VSM). The XRD pattern confirms the formation of single crystalline phase of Fe_3O_4 nanoparticles. The crystallite size calculated from XRD is about 10 nm with narrow size distribution makes these particles; apt to use for ferrofluid. The value of lattice parameter determined from XRD is 8.4080 Å. The strain in the sample and crystallite size is determined from Williamson-Hall plot. The material has little strain. The crystallite size determined from Williamson-Hall plot is in good agreement with that determined from XRD. Morphological characterization is done by TEM. The crystallite size determined from TEM is 10-15 nm. The magnetic characterization of sample was carried out using VSM. The VSM of the sample shows that the particles are superparamagnetic in nature with saturation magnetization, 63 emu/gm. The nanometer size of these particles makes them suitable for ferrofluid and hyperthermia treatment.

Keywords: co-precipitation, Fe_3O_4, magnetic nanoparticles, superparamagnetic, VSM.

INTRODUCTION:

Magnetic nanoparticles are widely synthesized for their various biological applications, magnetic storage and catalysis [1]. Metal oxides have important applications such as magnetic storage media, solar energy transformation, electronics and biological applications such as imaging and delivery [2]. Iron oxide powder at nanometer scale is utilized at length because of development in preparation technology. Monodispersed magnetite nanoparticles have given a new impetus in the applications where magnetic nanoparticles are extensively used in ferrofluid, biological imaging and therapies [3].

Magnetite is a common magnetic iron oxide that has a cubic inverse spinel structure with oxygen forming FCC closed packing and Fe cations occupying interstitial tetrahedral and octahedral sites [4]. The electrons can hop between Fe^{2+} and Fe^{3+} ions in the octahedral sites at room temperature rendering magnetite an important class of half-metallic material [5].

Various chemical synthesis routes have been employed to produce magnetite nanoparticles such as co-precipitation of aqueous ferrous (Fe^{2+}) and ferric (Fe^{3+}) salt solution by the addition of base [6], chemical combustion [7], hydrothermal [8] and by biogenic synthesis [9]. Chemical co-precipitation is an attractive method of producing nanoferrites as it gives high purity samples with advantage of increased homogeneity. Co-precipitation method is relatively simple, low cost, low temperature alternative to other methods and particle size can be tuned by accurately controlling preparative parameters.

EXPERIMENTAL DETAILS:

Magnetite (Fe_3O_4) nanoparticles were synthesized by co-precipitation method. Aqueous equimolar solutions of AR grade ferrous chloride ($FeCl_2$) and ferric chloride ($FeCl_3$) were mixed with their stiochiometric ratio and homogenized with constant stirring at room temperature. The pH of the solution was adjusted by adding sodium hydroxide (NaOH) solution. The particles may aggregate during their growth; hence, a monounsaturated omega-9 fatty acid (oleic acid) was added into the solution as capping agent to avoid agglomeration of particles. The solution was heated to about 60 ℃ with vigorous stirring. The salts and unmagnetic parts were removed by decantation and washing the precipitate several times by double distilled water (DDW) till the pH becomes 7. The wet magnetic particles thus obtained were dried in oven at 80 ℃ and crushed to fine powder.

Ferrite nanoparticles by co-precipitation route are formed in two steps: co-precipitation and ferritization [10]. In the first step is conversion of metal salts into hydroxides known as co-precipitation. And the second step is transformation of hydroxides into nanoferrites called as ferritization. The overall chemical reaction can be summarized as [11]:

$$FeCl_2 + 2FeCl_3 + 8OH^- \rightarrow Fe(OH)_2 + 2Fe(OH)_3 \downarrow$$

$$Fe(OH)_2 + 2Fe(OH)_3 \rightarrow Fe_3O_4 + 4H_2O$$

The prepared powder samples were directly used for structural, morphological and magnetic characterization. The X-ray diffraction patterns of the samples were recorded on Rigaku make powder X-ray diffractometer (Model XRG 2KW) at a scanning rate of 0.02 $°/s$ in the 2θ range from 20 to 80 degrees at 40 kV, 30 mA using CuKα radiation ($\lambda = 1.54059\,Å$). FTIR transmission spectrum was recorded on Perkin Elmer Spectrum 65 Spectrometer from 4000 to 400 cm^{-1}. The magnetization measurements were carried out using VSM (Lake Shore Model 7307).

RESULT AND DISCUSSION:

XRD:

The XRD can be used to characterize the crystallinity of nanoparticles and it gives average diameter of all the nanoparticles.

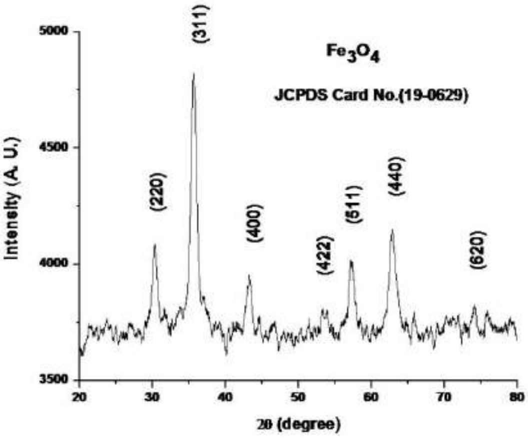

Fig. 1 XRD of Fe$_3$O$_4$

The X-ray diffraction pattern of as-synthesized sample is shown in Fig. 1. The diffraction pattern gives clear evidence of formation of ferrite phase. The perceptible peaks can be indexed to (220), (311), (400), (422), (511), (440) and (620). The crystallite size (D) was calculated from X-ray line broadening of the (311) diffraction peak using Debye Scherrer formula Eqn. (1).

$$D = \frac{0.9\lambda}{\beta \cos\theta} \qquad (1)$$

Where β is the full-width at half maximum of the strongest intensity diffraction peak (311) λ is the wavelength of radiation and θ is the angle of the strongest characteristic peak. The crystallite size calculated is about10 nm. The dislocation density (δ) is calculated from crystallite size by using Eqn. (2).

$$\delta = \frac{1}{D^2} \qquad (2)$$

Further from the calculated d -spacing value, the lattice parameter (a) can be determined using Eqn. (3).

$$a = d\sqrt{h^2 + k^2 + l^2} \qquad (3)$$

Where h, k, l are miller indices of the set of planes. The calculated value of lattice parameter is 8.4080 Å is slightly greater than its standard value 0.8396 nm which is indication of strain developed in sample. The strain in the synthesized material is calculated by Williamson-Hall method; in which a graph between $\beta \cos\theta$ and $4\sin\theta$ is plotted. The nature of graph is a straight line of the form $y = mx + c$ given by Eqn. (4) and the slope of which gives strain while the intercept; $\frac{\lambda}{D}$ from which crystallite size D can be calculated.

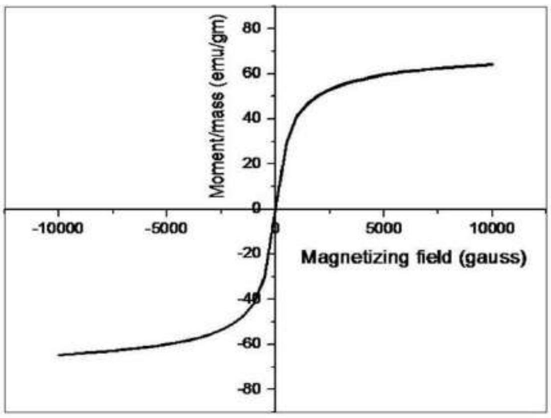

Fig. 3 VSM of Fe_3O_4

$$\beta \cos\theta = 4\varepsilon \sin\theta + \frac{\lambda}{D} \qquad (4)$$

In which β is full-width at half maximum (FWHM) measured in radians, ε is the strain induced in the sample and θ is the Bragg's angle [12].The induced strain and crystallite size calculated from this plot are 0.0029 and about 11nm respectively. The strain in the sample is quiet low. The micro strain arises due to the lattice misfit and varies on the deposition conditions.

TEM:

The morphological investigations of the sample are carried out using TEM. Fig. 2 shows a TEM image of as synthesized Fe_3O_4 sample.

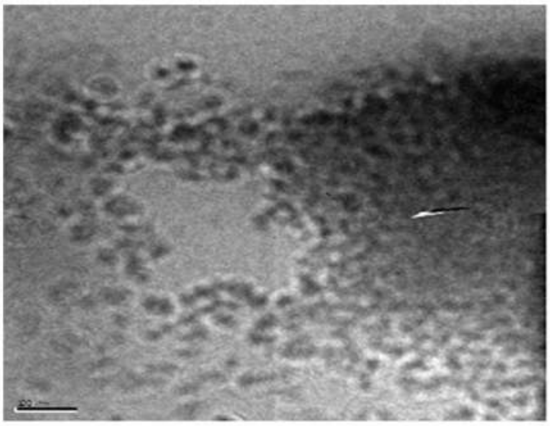

Fig. 2 TEM Image of Fe_3O_4

From the micrograph the size and shape of the nanoparticles are investigated. The sample shows roughly spherical particles with narrow size distribution. The average size of particles estimated is of the order of 10-15 nm which is in good agreement with the value determined using XRD.

VSM:

The magnetic characterization of Fe_3O_4 particles were carried out using VSM. The VSM of the sample is shown in Fig.3.The particles show zero remanence and coercivity at room temperature and no hysteresis loss. The behavior is called superparamagnetic. The saturation magnetization is quiet high of 63 emu/gm. The nanometer size of particles together with superparamagnetic nature makes them suitable for ferrofluid and hyperthermia treatment. Such particles when used to prepare ferrofluid the individual particles align in the field direction and loose the magnetism when field is removed and act as Newtonian fluid.

FTIR:

In order to confirm the formation of the spinel phase the FTIR spectra of the synthesized sample were obtained. The FTIR spectrum of the Fe_3O_4 is shown in Fig.4.

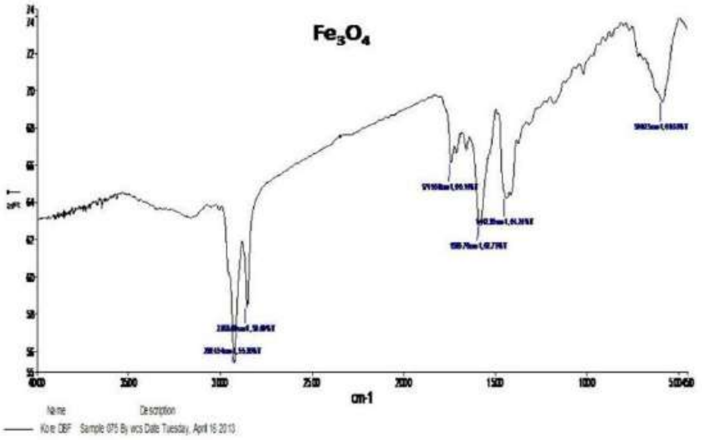

Fig. 4 FTIR spectra of Fe_3O_4

FTIR analysis also supports the formation of spinel Fe_3O_4 nanoferrite. The characteristic peaks at about 550 cm^{-1} corresponds to intrinsic stretching vibrations of the metal ions at the tetrahedral and octahedral sites. The peak at 1384 cm^{-1} is assigned to the C═C vibrations in oleic acid. The strong peak at 1636 cm^{-1} can be assigned to stretching vibrations of $-CH_2$. These characteristic peaks confirm the formation Fe_3O_4 and oleic acid coating to the nanoparticles.

CONCLUSION:

Facile wet chemical co-precipitation method is used for synthesis of Fe_3O_4 nanoparticles. We have reported a simple, economical, low cost and less time consuming approach to synthesize iron oxide nanoparticles. The X-ray diffraction pattern confirms the formation of single crystal Fe_3O_4 nanoparticles. The lattice parameter and crystallite size are 8.4080 Å and 10.4 nm respectively. Use of oleic acid as surfactant puts good control over growth of crystallite size to get almost uniform size of particles suitable for ferrofluid application. The use of oleic acid gave lack of aggregates in the sample. The particle size determined by Williamson-Hall plot is closer to the value determined from XRD. Further the particle size determined from TEM is also close to that obtained from XRD and Williamson-Hall method. The magnetic measurement by VSM shows superparamagnetic nature of particles. The remanence and coercivity are precisely zero. And the saturation magnetization obtained from VSM is 63 emu/gm which is quite large and it makes these nanoparticles apt to use for ferrofluid and hyperthermia treatment.

ACKNOWLEDGEMENT:

One of the authors (EKK) is thankful to the UGC (WRO), Pune, for financial assistance under Minor Research Project (File No. 47- 455/12(WRO)).

REFERENCES:

1. Sadeghpour, S., Amirjani, A., Hafeji, M., Zamanian, A. Ceram Int 40, 16107-16114 (2014).
2. Ashoori, R. C. Nature, 379, 413 (1996).
3. Kim, D. K., Zhang, Y., Kehr, J., Klason, T., Bjelke, B., Muhammed, M. J. Magn Magn, Mater 225, 256 (2001).
4. Cornell, R. M., Schwertmann, U., VCH: New York (1996).
5. Verwey, E. J. W. Nature, 144, 327 (1939).
6. Shahane G.S., Zipare K.V. and Pant R. P., Magnetohydro., 49 (3-4) 317-321 (2013).
7. Y.T. Prabhu, K. Venkateswara Rao, etal., Int Nano Lett (2015).
8. Prashan Acharya, Rucha Desai, V K Aswal and R V Upadyay, Pramana J. of Phy. Vol. 71, 5 pp. 1069-1074.
9. M. Senthil, C. Ramesh, Digest J. Nanomat. Biostru., Vol. 7 No. 3, 1655-1660 (2012).
10. G.S. Shahane, Ashok Kumar, M. Arora, R. P. Pant, and K. Lal, J. Magn. Magn. Mater, 322, 1015-1019 (2010).
11. S. Wu, A. Sun, F.Zhai, J. Wang, W. Xu, Q. Zhang, A. A. Volinsky, Mat. Lett, 65, 1882 (2011).
12. A. Shankar, S. Kumar, S. Thakur, R. Porwal and R. P. Pant, Adv. Mat. Lett. 3(5), 415 (2012).

FLUORESCENCE QUENCHING STUDIES OF TYROSINE WITH RIBOFLAVIN

Sunanda T. Mahanwar, Shilpa S. Patil, Ravi. D Waghmare,
Prashant V. Anbhule and Govind B. Kolekar*
Fluorescence Spectroscopy Research Laboratory, Department of Chemistry,
Shivaji University Kolhapur (MS), India-416004

ABSTRACT:

Interaction between Tyrosine and Riboflavin was studied by spectroscopic method under physiological conditions. Fluorescence intensity of Tyrosine decreases with increasing concentration of riboflavin. Stern-volmer quenching constants are positively related with temperature reveals dynamic type of fluorescence quenching.

Keywords: Tyrosine, riboflavin, Stern-volmer relation, Fluorescence quenching.

INTRODUCTION:

Fluorescence of the aromatic amino acids like phenylalanine, tyrosine, tryptophan and their residues merged into a protein or peptide, is studied widely due to their use as internal probes in conformational analysis. L-Tyrosine (Tyr) is one of the 22 amino acids which is used by cells to synthesize proteins and plays an important role in biological systems. Phenolic OH group of hydrophobic Tyr acts as H- bond donor or acceptor and forms network of H-bond which plays vital role in protein structure and function [1]. The photo physical properties of buried tyrosine residues in proteins are different than those of tyrosine that has been exposed to the solvent [2].These properties of tyrosine and its derivatives are multifarious and were broadly investigated [3-5].

Riboflavin (7,8-dimethyl-10-ribitylisoalloxazine) also termed as vitamin B_2 is water soluble vitamin, important biological molecule which is essential in the human diet required for growth and development of cell. It supports energy production, metabolic pathways and biosynthesis of many compounds via its coenzyme forms, Flavin adenine dinucleotide (FAD) and Flavin mononucleotide (FMN) [6]. In the present investigation interaction between these two biologically important molecules has been explored by spectroscopic technique to study the quenching mechanism.

EXPERIMENTAL

Materials:

L-Tyrosine (Tyr) was bought from Himedia laboratories, Mumbai. Riboflavin (RBF) from (Loba Chemie). Di Potassium hydrogen phosphate, Potassium dihydrogen phosphate were obtained from Spectrochem. Ltd. Mumbai, India. These chemicals were used as received.

Equipment:

The absorption spectra of Tyr and RBF were recorded on a UV-Visible-NIR spectrophotometer [Specord 210 plus analytic jena]. Fluorescence Spectra were scanned on Jasco Spectrofluorimeter (FP 8300) equipped xenon lamp source and 1 cm quartz cuvette.

General procedure:

Definite volume of Tyr (6x10^{-4} mol dm^{-3}) was kept constant while the RBF (1x10^{-4} mol dm^{-3}) was varied from 0.0 to 1.6 cm^{3}. 1 cm^{3} of 0.1 mol dm^{-3} of phosphate buffer was added to each solution to maintain physiological pH (7.4). Further all the solutions were diluted to 10 cm^{3} by using double distilled water. Absorption spectra and Fluorescence spectra of each solution was recorded.

RESULTS AND DISCUSSION:

Absorption Spectroscopy:

Figure 1 displays the absorption spectra of individual Tyr and RBF while Figure 2 shows absorption spectra of their mixtures.

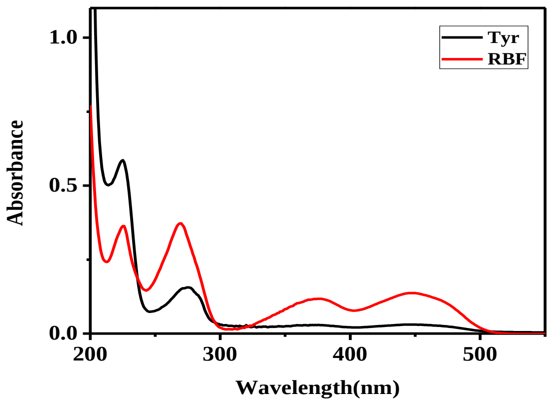

Fig. 1: UV-Vis Spectra of Tyr-RBF

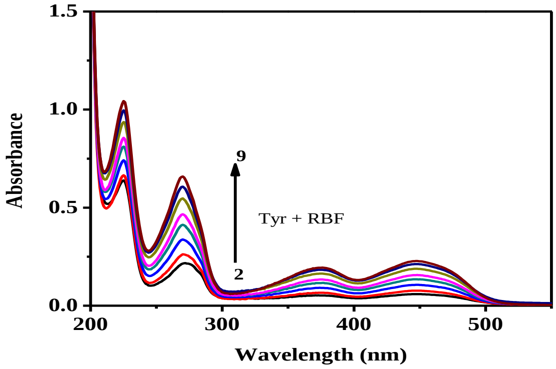

Fig. 2: UV-Vis Spectra of Tyr –RBF mixtures

From these figures it is clear that there is no change in the spectral characteristics of Tyr and RBF, which means that these two types of molecules retain their identity in the mixtures suggesting no ground state complex formation and hence rules out the possibility of static quenching. Therefore, it is concluded that the observed quenching is due to diffusion, that is, dynamic quenching occurs in the present system [7-8].

Fluorescence quenching of Tyr by RBF:

Various molecular interactions decreases the fluorescence intensity of sample. Figure 3 displays the fluorescence spectra of Tyr in presence of different concentrations of RBF.

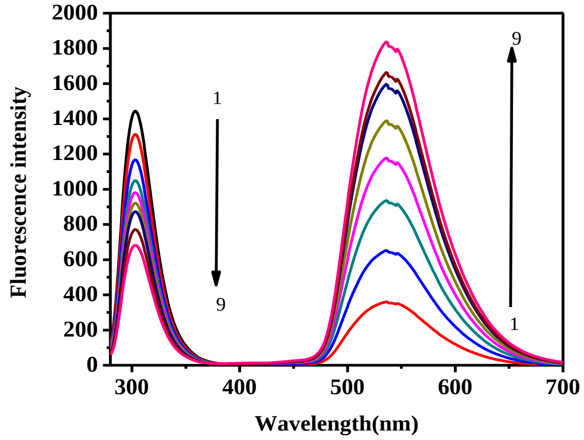

Fig. 3: Fluorescence spectra of Tyr in presence of different concentration of RBF

From the spectra it is observed that fluorescence emission spectra of Tyr is sharp with maximum at 303 nm and its fluorescence intensity drops regularly with the progressive addition of RBF followed by the increase in fluorescence intensity of RBF. This indicates that the interaction between Tyr and RBF takes place [11]

Temperature dependence of quenching was performed to analyze the quenching mechanism by using Stern-volmer equation.

$$\frac{F_0}{F} = 1 + K_{sv}\,[Q] \qquad [1]$$

The graph of F_0/F against [RBF] were plotted from the fluorescence data measured at 303,313 and 319 K and displayed in Fig. 4.

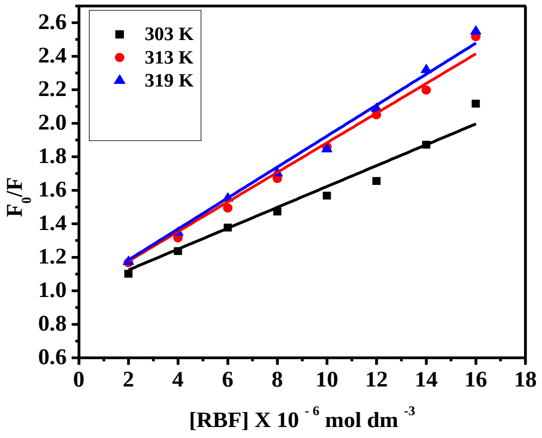

Fig. 4: Stern-Volmer plots of Tyr-RBF at different temperatures

Good linear relationship indicates only one type of quenching mechanism and values of slope increases with temperature suggesting the possible quenching mechanism is dynamic quenching.

CONCLUSIONS:

In the present investigation we studied the interaction between Tyr and RBF by absorption and fluorescence spectroscopy. Stern-Volmer quenching constant K_{sv} is positively related with temperature indicating the probable quenching mechanism is dynamic quenching which is also supported by absorption spectroscopy.

ACKNOWLEDGMENTS:

The author (Sunanda T. Mahanwar) gratefully acknowledges UGC, New Delhi for receiving a fellow- ship from UGC, New Delhi [University Grant Commission, the XII th plan (Faculty Development Programme)].

REFERENCES:

1. Liao F, Yuan H, Du KJ, You Y, Gao SQ, Wen GB, Lin YW and Tan X .Mol. BioSyst. 12, 3139—3145 (2016).
2. Giancotti V, Quadrifoglio F, Cowgill R. W.,Crane-Robinson C. Biochim. Biophys. Acta 1 624, 60-65 (1980).
3. Seidel C, Orth A, Greulich KO (1993) Electronic effect on the fluorescence of tyrosine in small peptides Photochem, Photobiol 58, 178-184, (1993).
4. Pal H, Palit DK, Mukherjee T, Mittal P. J. Photochem. Photobiol. A52, 391 (1990).
5. Rehhms AR, Callis PR . Chem. Phys. Lett. 208, 276-382 (1993).
6. Wang F, Huang W, Dai Z. Journal of Molecular Structure 875, 509–514 (2008).
7. Hongwei Z, Min G, Zhaoxia Z, Wenfeng W, Guozhong, W. Spectrochim. Acta, Part A, Mol. Biomol. Spectrosc. 65, 811–817 (2006).
8. Chakraborty, B., Basu, S. J. Lumin. 129, 34–39 (2009).
9. Xing-Jia Guo, Xiu-Dan Sun , Shu-Kun Xu . J. Mol. Stru., 931, 55–59 (2009).

DESIGN OF EMBEDDED SYSTEM FOR WATER QUALITY MONITORING USING WSN

P.M.Gavhane[1*], B.N. Jamadar[2], A.S.Relekar3, S.M.Jogade[4], D. S. Sutrave[4]
[1]Department of Computer Science, Sangameshwar College, Solapur, India
[2]Department of Physics, Walchand College of Engineering, Sangali, India
[3]Department of Electronics, Shankarrao Mohite Mahavidyalaya, Akluj, India
[4]Department of Electronics, D.B.F. Dayanand College of Arts and Science, Solapur, India
*Corresponding author E-mail: prasannagavhane13@yahoo.co.in, dssutrave@dayanand.net

ABSTRACT:

Water contamination is one of the key dangers for the green globalization. The requirement for viable and proficient observing, assessment and control of water contamination has turned out to be all the more requesting in this period of urbanization, populace development and environmental change and fluctuation. To keep the water contamination, first we need to identify the poison. In prior days, the water contamination was identified by synthetic test or research facility test by utilizing this framework the testing gear will be in stationary and tests will be given to testing hardware. Keeping in mind the end goal to expand the inescapability, testing gear can be set in the stream water and recognition of contamination can be made remotely. In this paper, a Wireless Sensor Network (WSN) framework model produced for water quality checking, which will identify the contamination introduce in the water and give a ready back rub to the specialist. The pH and turbidity sensor will be kept in the waterway water surface and the information caught by the sensor will be given to microcontroller and after that the information are transmitted remotely utilizing Zigbee module to the base station. The improvement of graphical UI (GUI) for checking purposes at the base observing station is another primary segment talked about in this paper. The GUI ought to have the capacity to show the parameters being observed constantly progressively. The trial comes about demonstrated that the framework has extraordinary prospect and can be utilized to work in certifiable condition for ideal control and security of water assets by furnishing key elements with pertinent and convenient data to encourage brisk move making.

Keywords: Water pollution, Wireless Sensor Network (WSN), PIC microcontroller, Zigbee module, Graphical User Interface.

INTRODUCTION:

Water is a basic constrained asset for industry, horticulture and home utilize and furthermore for animals presence on earth including individuals. The genuine significance of drinking water doesn't understand by bunches of individuals on earth. The issue is unobtrusively related wasteful utilize, poor water distribution, and absence of sufficient utilize. Along these lines water checking and productive utilize are potential imperative for home and office water administration framework. On earth each living thing need water to survive. Each Human body is comprised of more than 70 percent water.

We utilize water for drinking, work plants, and develop crops for nourishment. Each part of our lives has crucial significance of water. Checking the water quality will shield our water sources from contamination. For Better administration of their territory and harvests, ranchers can utilize these data. Our national governments, state governments and neighborhood bodies utilize data checking to control contamination levels.

The drinking water ought to be free from any synthetic materials that can hurt the wellbeing. Water for mechanical utilizations ought to have low certain inorganic chemicals. What's more, water quality observing can help water contamination discovery.

In this paper, a WSN water quality observing framework is displayed. The framework comprises of a PIC microcontroller, an arrangement of water quality sensors and a system association module. It gauges water quality parameters including pH and turbidity esteems continuously. In this paper this sensor esteems are gathered by the microcontroller hub which will additionally transmit the sensor esteems to the base station through the remote correspondence module, for example, zigbee .

EXPERIMENTAL SETUP:

The experimental setup consists of sensor node and base station.

Fig. 1: Experimental Setup

PROPOSED SYSTEM:

In the present work, the proposed arrange arrangement of remote sensor model was produced. The primary purpose behind growing such a framework is to assess the water quality for deciding if it achieves the criteria for drinking and urbanization. The WSN framework proposed here comprises of three noteworthy building squares to be specific sensor hubs, and application software(GUI), Zigbee transceiver [1].

SENSOR NODE:

For creating WSN framework model the WSN sensor hub is primary building piece. Remote sensor hub is outfitted with sensor, for example, pH sensor, turbidity sensor and microcontroller units, control supply and Zigbee handset. The contribution from water asset is being detected by the sensors which are then changed over into electrical flag and further experiences the flag molding circuit.

At that point this flag is passed to a microcontroller that procedures it to the esteem justifiable by human.

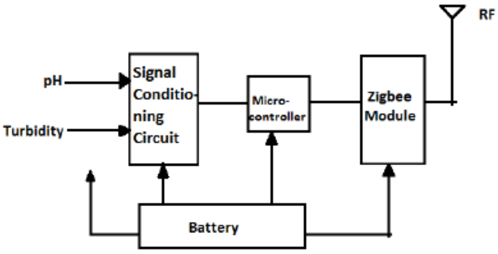

Fig. 2: Sensor node [1]

pH:

The framework utilizes pH sensor from equiptronics .It quantifies pH extend from 0 to 14 and works in temperature scope of 00c to 800c. The pH sensor size of acidic arrangement has a low pH esteem, for example, 0, 1 or 2 and high pH esteem, for example, 12, 13 or 14. A nonpartisan arrangement, for example, water has a pH of around 7 [2].

Turbidity:

Turbidity is the measure of relative lucidity of a fluid. It is an optical normal for water and is a statement of the measure of light that is scattered by material in the water when a light is radiated through the water test. The higher the force of scattered light, higher the turbidity [2].

Wireless detecting hub:

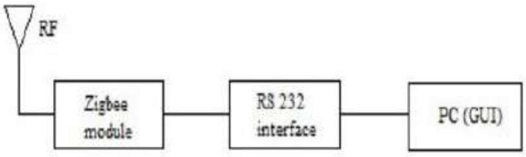

Fig: 3 Base stations Node [1]

In the remote detecting hub, diverse sensor hub consolidates with the zigbee module .It comprise of the zigbee transmitter which deals with the recurrence of 2.4GHz , which is institutionalized by IEEE 802.15.4 and can surrender the range to 1.6Kms. Serial information from the transmitter line is given to the zigbee transmitter which is designed to keep up the baud rate of 9600 bauds [3].

Base Station Node:

The base station comprises of Zigbee module modified at a recipient. It gets the information sent from the sensor hubs The Base station module is typically mains controlled. Information got from the gadget is sent to the PC utilizing the RS-232 convention and information got is shown utilizing the constructed GUI on the base observing station [4].

SOFTWARE DEVELOPMENT:

The GUI stage was effectively created utilizing the MATLAB programming that could connect with the equipment (facilitator) at the base station.

Once the battery is controlled, sensor hub turns on the pH and turbidity sensors submerged in water and begin detecting the particular information. Diverse push catches are accommodated perusing the pH and turbidity esteems. Once the client clicks run catch on board the zigbee handset on the recipient side sends a flag to the zigbee transmitter on the transmitter side requesting the comparing information esteems to be sent. The comparing diagrams are naturally plotted by utilizing the information got on the recipient side. Once the qualities are plotted, it is innately spared and put away in PC as a database record

SIMULATION AND RESULTS:

The graphical UI utilizing MATLAB, shown in figure 4. Water parameters are gathered from the hubs as appeared in figure 2. Gathered information is sent to the server PC with GUI appeared in figure 4. From earlier testing, an edge esteem (scope of qualities) is characterized for the checking of pH and turbidity Depending on whether the normal of the qualities got is not exactly or more prominent than the characterized edge, we become more acquainted with whether the water is acidic or fundamental and is the water unadulterated or sullied and consequently on the off chance that it is appropriate or not for the particular reason.

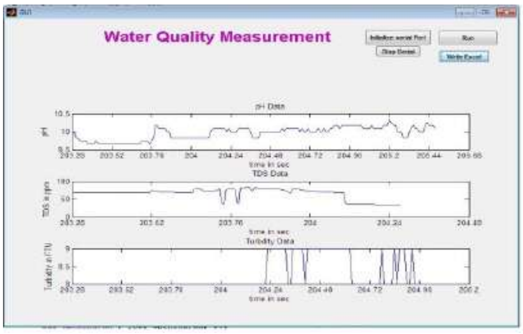

Fig. 4: Photograph of GUI Matlab Pattern

CONCLUSION:

In this paper, water quality observing framework in light of remote sensor organize is exhibited . The framework is constituted by a base station and a few sensor hubs . In the hub side, water quality information is gathered by various sensors, for example, pH and turbidity . This information, after voltage change by interface circuit, is sent to zigbee for remote transmitting . This paper additionally displays itemized equipment outline of a few modules in the sensor hub, together with general programming stream diagrams of the affirmation recipient and information sender utilized as a part of transmission. The information handset is incorporated in zigbee and is programmable. At long last, the model framework with sensor hub and base station is actualized. Continuous water quality information can be seen from a GUI window in PC. The framework has favorable circumstances, for example, low carbon emanation, low power utilization, more adaptable to send and so on.

REFERENCES:

1. Shruti Sridharan, Int. J. Adv. Res. Electro. & Comm. Eng., 3, 4, (2014).
2. T. Deepiga, A. Sivasankari, Int. Res. J. Eng. And Tech. Vol.2, 4 (2015).
3. K. Karuppasamy, B Abinaya, R Sudha, J P Arun Prasath Int. Res. J. Eng. And Tech., Vol.3:3 (2016).
4. P. Aswale, S. Patil, D. Ahire, S. Shelke, M. Sonawane, Int. J. Adv. Res. Electro. & Comm. Eng., Vol 4:4 (2015).

RUTHENIUM OXIDE THIN FILM: ELECTROCHEMICAL PROPERTIES

S. D. Gothe[1], P. S. Joshi[2], S.S.Gaikwad[3], S.G.Madale[3] and D. S. Sutrave[3]
[1]Sangameshwar College, Solapur Maharashtra 413003
[2]Walchand Institute of Technology, Solapur, Maharashtra 413003
[3]D.B.F Dayanand College of Arts and Science, Solapur, Maharashtra 413003
*****Corresponding Author's E-Mail: dssutrave@dayanand.net Tel.: **+91-9422026583**

ABSTRACT:

There is a growing necessity of transition metal oxide thin film for many important technological applications such as smart windows gas sensors, solar cells, super capacitors etc. Among the other transition metal oxides, ruthenium oxide is a potential material as it exhibits interesting structural, optical, chemical, electrical properties. In this investigation ruthenium oxide thin films have been synthesized using spin coating technique. Here ruthenium oxide thin films have been deposited on stainless steel substrate by sol-gel spin coating method. The properties of deposited samples were studied by cyclic voltammetry study and chronopotentiometry were carried out with 0.1M KOH electrolyte. The C-V plot showed the rectangular shape and maximum specific capacitance 1010 $F.g^{-1}$at a scan rate of 10 $mVSec^{-1}$ was observed. The Specific Power, Specific Energy and Columbic Efficiency of the RuO_2 thin film electrode were 28.706 $kWhkg-^{1}$, 7.9101 $KW.kg^{-1}$ and 99.30% respectively.

Keywords: Supercapacitor, Ruthenium oxide, CV, Galvanostatic Charge-Discharge, Sol-gel Spin-coating,

INTRODUCTION:

Ruthenium oxide is superior due to the unique combination of characteristics, such as metallic conductivity, high chemical and thermal stability, catalytic activities, electrochemical redox properties, highly reactive with reducing agents due to its oxidizing properties and field emitting behaviour etc.[1]. It has been widely used in supercapacitor because of its good catalytic properties [2]. Ruthenium oxide thin films have been prepared using various techniques, including organometallic chemical vapour deposition [3], sol gel, electro deposition [4]. Here, attempts are made to deposit RuO_2 thin films using sol-gel spin coating deposition technique. The cyclic voltammetry study and chronopotentiometry was carried out with 0.1M KOH electrolyte to study the supercapacitor properties.

Experimental Deposition of RuO_2 Thin Films:

RuO_2 thin films have been synthesized by a sol-gel spin coating technique using ruthenium trichloride as a source of Ruthenium oxide [5]. In a typical experiment, 0.01 M solution of ruthenium trichloride was mixed with ethyl alcohol to obtain homogeneous solution a magnetic stirrer was used. After aging for 24 hours a gel was formed and then deposited on steel substrate by spin coating unit. The sample was then rotated about 3000 rpm and films were annealed at a temperature of 900°C for 3 minutes. The deposition was repeated for number of time to increase the thickness of the film [6].

RESULTS AND DISCUSSIONS

Cyclic Voltammetry Analysis:

The electrochemical behaviour of RuO_2 thin films was analysed by cyclic voltammetry technique in 0.1 M KOH electrolyte. Cyclic voltammetry (CV) technique was used to investigate the supercapacitive properties of the RuO_2, The CV curves of the RuO_2 are shown in Fig1. The CV curves of RuO_2 were obtained in the potential window of 0 to +1 V vs SCE as the area under the CV curves was observed maximum in this potential window for the RuO_2 electrode materials. The CV curves were carried out at 10 mV.s^{-1} to 100 mV.s^{-1} scan rate. The CV curve of RuO_2 shows pseudocapacitive behaviour in the potential window -1.5 to +1 V vs SCE [7,8]. The appearance of single pair of redox peaks indicates that the RuO_2 gives rise to pseudocapacitance of the electrode. At lowest scan rate 10 mV.s^{-1}, maximum specific capacitance is found to be 1010 Fg^{-1} and at 100 mVs^{-1} the specific capacitance is 600 Fg^{-1} The decreasing trend of the capacitance suggests that part of the surface of the electrode material are inaccessible at high charging–discharging rates. Hence, the specific capacitance obtained at the slow scan rates is believed to be closest to that of full utilization of the electrode material. The capacitive behaviour of the oxide is enhanced by rectangular shape of the plot. [9]

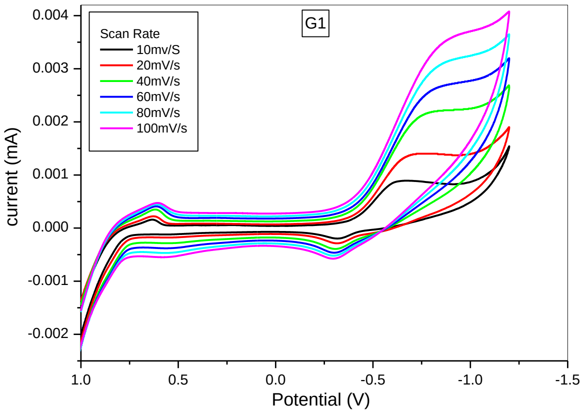

Fig. 1: CV of RuO_2 with different scan rate

Fig2. shows the variation of interfacial capacitance with scan rate of the RuO_2 thin films. It is observed that as scan rate increases the interfacial capacitance decreases. Similar inclinations were reported in the literature [10].

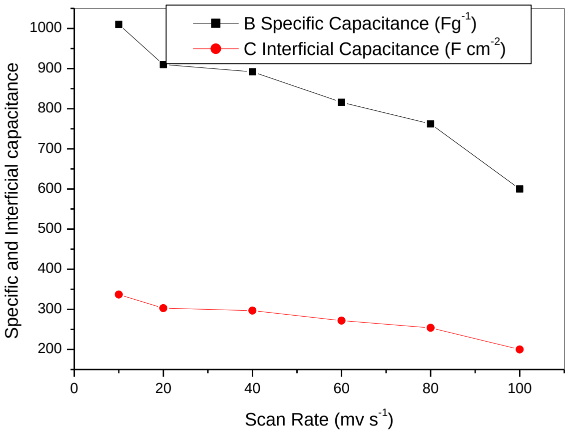

Fig. 2: Variation of specific and interficial capacitance with scan rate.

Galvanostatic Charge –Discharge Analysis:

The charge–discharge behaviour of the RuO_2 thin films was examined by chronopotentiometry in the potential range of - 0.7 to + 0.7 V vs. SCE at 2 mA.cm^{-2} current density. The charge-discharge curves of RuO_2 thin films are shown in Fig 3. The charge-discharge curve of RuO_2 showed the approximately linear charge and discharge time. The supercapacitor parameters such as specific power (SP), specific energy (SE) and columbic efficiency (η) are calculated are shown in Table1.[10]

Table 1: Supercapacitive parameters of RuO_2 thin film electrodes:

Parameters/ Material → ↓	**RuO_2**
Specific Power (S.P.) kWhkg^{-1}	28.71
Specific Energy (S.E.) KW.kg^{-1}	07.91
Columbic Efficiency (η) %	99.30

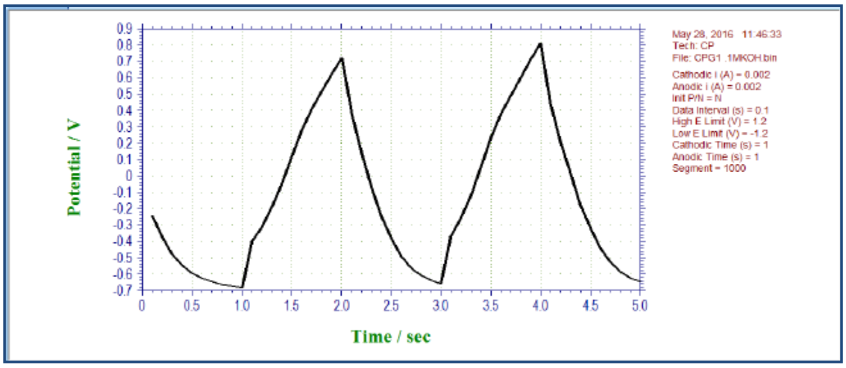

Fig.3: Galvanostatic charge-discharge curves of RuO_2

Stability Study RuO_2 thin films:

The stability and reversibility of an electrode material are important for its use in an electrochemical supercapacitor. Stability of RuO_2 composite electrode was tested by cyclic voltammetry. Figure 4 shows the CV curves of RuO_2 electrode at the scan rate of 10 mV.s^{-1} within the voltage range - 1.2 to + 1.0 V vs. SCE for 1st and 1000th number of cycle. The current under curve is decreased by 11 % up to 1000 cycles. We found that our system can withstand about 1000th cycles without a significant decrease in the supercapacity, illustrating the fairly stable (89%) nature of RuO_2 electrode in energy storage application. The specific and interfacial capacitance values are decreased by small amount with the number of cycles due to the loss of active material [11].

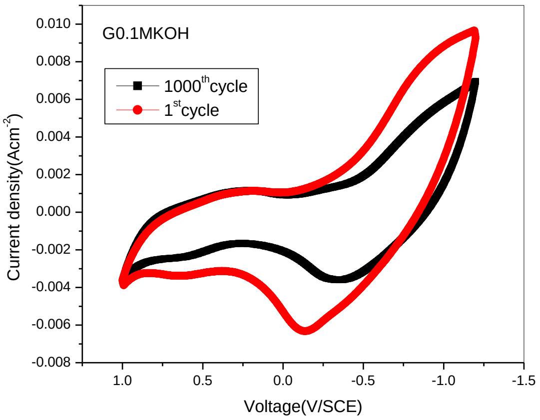

Fig. 4: The CV curves of RuO_2 thin film electrode at 1st and 1,000th cycles.

Figure 4 shows stability study of RuO_2 thin films. Figure shows the 79% stability of RuO_2 over the 1000th cycles. It is observed that the material showed the excellent stability over the 1000th cycles.

CONCLUSIONS:

In conclusion, RuO_2 thin films were deposited on stainless steel substrate by sol-gel spin coating method. The suitable annealing temperature was 900°C.The C-V plot showed the rectangular shape and maximum specific capacitance 1010 $F.g^{-1}$at a scan rate of 10 $mVSec^{-1}$. The Specific Power, Specific Energy and Columbic Efficiency of the RuO_2 thin film electrode were calculated based on the charge/discharge curves are 28.71 $kWhkg^{-1}$, 7.91 $KW.kg^{-1}$ and 99.30% respectively. A stability of RuO_2 is 79 %. The specific and interfacial capacitance values are decreased in small amount with the number of cycles due to the loss of active material.

REFERENCES:

1. Gujar T.P., Kim W.Y., Puspitasari I., Jung K.D., Joo O.S, Int. J. Electrochem. Sci., 2, 666 (2007).
2. Zheng J.P., Cygan P.J., Jow T. R, J. Electrochem. Soc., 142, 2699 (1995).
3. Huang Y.S. and Liao P.C., Solar Energy Mater. Sol. Cells, 55, 179 (1998).
4. Park B.O, Lokhande C.D, Park H.S, Jung K.D. and Joo O.S, J. Power Sources, 134, 148 (2004).
5. D. S. Sutrave, P. S. Joshi, S. D. Gothe, S.M. Jogade, Int. J. Chem. Tech. Res., 6-3, 1991-1993 (2014).
6. Joshi P. S. and Sutrave D. S., Elixir Thin Film Tech., 97, 42049-42052 (2016).
7. Burke A, J. Power Sources, 91, 37 (2000).
8. Frackowiak A, Lota G., and Pernak, J., Appl. Phys. Lett., 86, 164104 (2005).
9. Conway B.E., Kluwer Academic Publishers/Plenum Press, New York, (1999).
10. Park B.O., Lokhande C.D., Park H.S., Jung K.D., Joo, O.S., J. Materials Sci., 39, 4313 (2004).
11. Joshi P.S. and Sutrave D.S., Int. J. Res. In Appl. Sci. & Eng. Tech. Vol. 4 Issue VIII (2016).

SYNTHESIS AND PHOTOLUMINISCENCE PROPERTIES of Er^{3+} –Yb^{3+} CO-DOPED $LiMgBO_3$ PHOSPHOR

S. P. Hargunani[1*], R. P. Sonekar[1], S. K.Omanwar[2]
[*1]Department of Physics, G. S. College, Khamgaon, Dist: Buldhana (M.S.), INDIA
[2]Department of Physics, SGB Amravati University, Amravati - 444602(M.S.), INDIA
*Corresponding Author email: sphargunani.SH@gmail.com

ABSTRACT:

Lithium strontium borate phosphor ($LiMgBO_3$) doped with rare earth elements ${}_{0.02}Er^{3+}$ and ${}_{0.08}Yb^{3+}$ has been synthesized by solution combustion technique. For the first time Upconversion phenomenon was investigated in the samples at fixed concentration of rare earth dopants Er^{3+} and Yb^{3+}. Study shows that the synthesized materials emits in visible region after excitation in Infrared region. $LiMgBO_3$:${}_{0.02}Er^{3+}$,${}_{0.08}Yb^{3+}$ shows the absorption in infrared region ie 820 nm to 1080 nm and at 545nm ,656nm respectively. At the excitation of 980 nm it shows the emission peakings at 590 nm and 596 nm. Upconversion mechanism was investigated in detail and attributed to the efficient resonant energy transfer from Yb^{3+} to Er^{3+} ions in this host material. Our results suggest a potential borate phosphor for Natrium Yellow and Amber upconversion phosphor.

Keywords: Borate phosphor; Upconversion; Luminescence.

INTRODUCTION:

Upconversion phenomenon is now becomes an interesting topic of research due to wide range of applications ie from medical [1]to solar energy sector. Spectral mismatch losses in solar cell were reduced by upconversion materials [2]. Upconversion materials absorb near infrared light and re-emit in red, green, and blue. This three colors can combine to create a white-light source [3].

Recently, phosphors based on borates have attracted much attention due to their high stability, low synthetic temperatures, and high ultraviolet and optical damage threshold [4, 5, 6]. Borate crystals are intrinsically luminescent and show thermo luminescence and other interesting optical properties [7, 8]. Chr. Wyss et al used Yb^{3+} as co-dopant (sensitizer) in Er^{3+} doped (activator) laser hosts. According to them Er^{3+} has narrow absorption band from 970 to 1010 nm wavelength and Yb^{3+} has a broad absorption band from 900 nm to 1025 nm wavelength and a higher absorption cross-section [9]. Subrata Das, et al reported strong green upconversion emission from Er^{3+}–Yb^{3+} co-doped $KCaBO_3$ phosphor. It gives intense green emission ($^2H_{11/2}$,$^4S_{3/2}$ to $^4I_{15/2}$) through cooperative upconverted emission on 980 nm excitation [10].

The rare-earth ions Er^{3+} and Yb^{3+} are up-conversion activator and sensitizer ions, which emit green to red light effectively in different host lattices. Er^{3+} has a simple energy-level structure that consists of $^4I_{15/2}$, $^4I_{11/2}$, $^4I_{13/2}$, $^4F_{9/2}$, $^4S_{3/2}$,$^2H_{11/2}$, and $^4F_{7/2}$ states [Figure (1)].Usually, the $^2H_{11/2}$, $^4S_{3/2}$ to $^4I_{15/2}$ and $^4F_{9/2}$to $^4I_{15/2}$ transitions lead to green and red emissions, respectively, in Er^{3+}-activated phosphors. The luminescent properties of materials activated by Er^{3+} ions can be enhanced by the addition of Yb^{3+} ions via resonant energy transfer from Yb^{3+} to Er^{3+} through the absorption of a 980 nm photon [11].

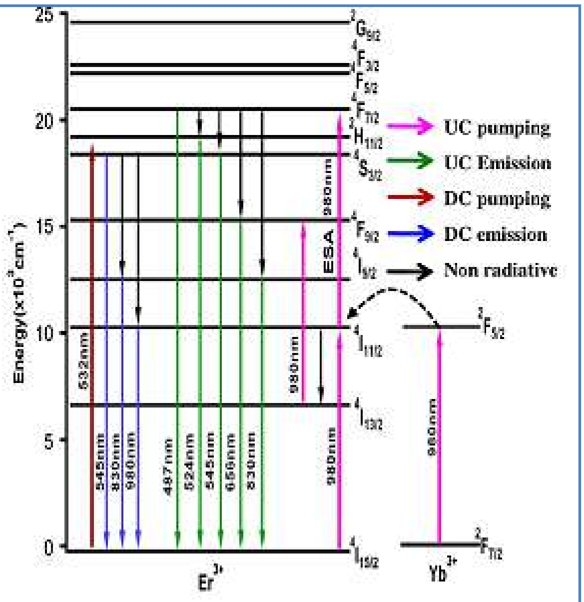

Figure (1):- Energy levels of Er^{3+} and Yb^{3+} ions showing different electronic transitions. [source:- Subrata Das, A. Amarnath Reddy, G. Vijaya Prakash,'' Strong green upconversion emission from Er3+–Yb3+ co-doped KCaBO3 phosphor'', Chemical Physics Letters 504 (2011) 206–210]

In this work upconversion emission properties of $LiMgBO_3$ co-doped with Er^{3+} and Yb^{3+} ions was investigated. We report the synthesis of single monoclinic phase doped $LiMgBO_3{:}_{0.02}Er^{3+}{,}_{0.08}Yb^{3+}$. It gives Natrium Yellow and Amber emission ($^4F_{9/2}$,$^4S_{3/2}$ → $^4I_{15/2}$ in the Er^{3+}) through cooperative upconverted emission on 980 nm excitation.

EXPERIMENTAL:

Sample preparation:

The powder sample of $LiMgBO_3{:}_{0.02}Er^{3+}{,}_{0.08}Yb^{3+}$ was prepared by using solution combustion synthesis [12, 13]. Several borate host materials were successfully synthesized using this method [14]. The stoichiometric amounts of high purity starting materials $LiNO_3$; H_3BO_3; NH_2CONH_2; NH_4NO_3; $Mg(NO_3)_2$ and Er_2O_3;Yb_2O_3 was used for phosphors preparation. The stoichiometric amounts of the ingredients was mixed in an agate mortar with adding little amount of double distilled water. The materials then transferred into china basin. It was heated on heating menthol at about 70°C so as to obtained clear solution. The solution was then introduced into a pre-heated muffle furnace maintained at temperature 550 °C for combustion. The solution boils and ignites to burn with flame which gave a voluminous, foamy powder. Following the combustion, the resulting foamy samples were crushed to obtain fine powder and then heated at temperature 750°C for 2 hr and suddenly cooled to room temperature.

Material characterizations:

The phase and surface morphology of as prepared phosphors were characterized by powder X-ray diffraction pattern using Rigaku Miniflex II X-ray Diffractometer with Cu Kα radiation (λ=1.54059 Å) with scan speed 2°/min and field emission - scanning electron microscopy (FE-SEM) (Hitachi, Model-S4800 type II). The PL measurements at room temperature were performed on Hitachi F-7000 Spectroflurometer with spectral resolution of 2.5 nm.

RESULTS AND DISCUSSION:

X-ray Diffraction Pattern:

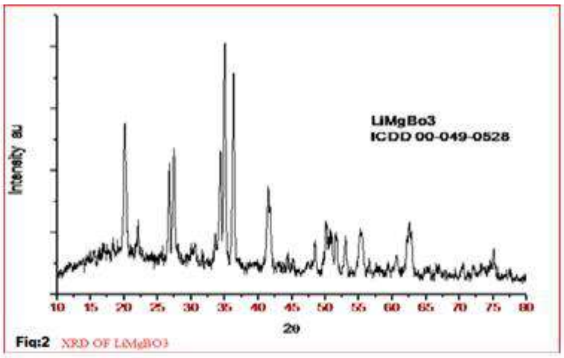

Fig:2 XRD OF LiMgBO3

Fig.2 shows the powder X-ray diffraction (XRD) patterns of $LiMgBO_3{:}_{0.02}Er^{3+},_{0.08}Yb^{3+}$, and it was found to be in good agreement with the reported standard data in ICDD file no. 00-049-0528. The result clearly implies that the obtained samples are single phase and the doping of Er^{3+} and Yb^{3+} does not cause any significant change to the detection limit of the technique in the host structure.

Absorption analysis of $LiMgBO_3{:}_{0.02}Er^{3+},_{0.08}Yb^{3+}$ phosphor:

To decide excitation wavelength of sample for study of UC we did the absorption study of sample using Shimadzu UV-VIS-NIR Spectrophotometer in the range 400 nm to 1200 nm. Figure(3) shows absorption spectra of $LiMgBO_3{:}_{0.02}Er^{3+},_{0.08}Yb^{3+}$.

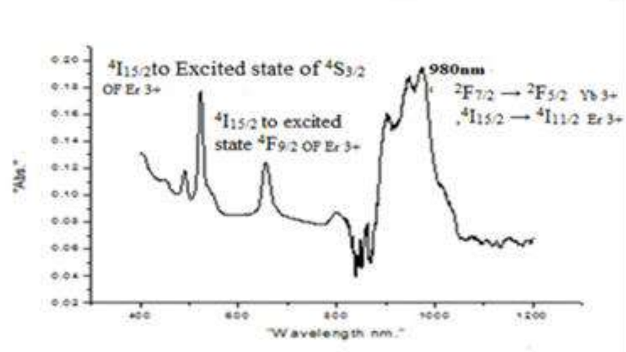

Figure 3: Absorption spectra of $LiMgBO_{3}{:}_{0.02}Er^{3+},_{0.08}Yb^{3+}$

It shows the wide absorption band from 820 nm to 1080 nm and maximum intensity at 980 nm (Resonant transition from $^4I_{15/2}$ to $^4I_{11/2}$ in Er^{3+} and $^2F_{7/2}$ to $^2F_{11/2}$ in Yb^{3+}). It also shows absorption peaks at 545 nm (from $^4I_{15/2}$ to $^4S_{3/2}$ transition in Er^{3+}) and 656 nm ($^4I_{15/2}$ to $^4F_{9/2}$

transition in Er^{3+}). Due to both activator and sensitizer ions host material shows wide absorption from visible to IR.

Photoluminescence analysis of $LiMgBO_3$:$_{0.02}Er^{3+}$,$_{0.08}Yb^{3+}$ phosphor:

Photoluminescence characteristics of $LiMgBO_3$:$_{0.02}Er^{3+}$,$_{0.08}Yb^{3+}$ is shown in **figure(4).**

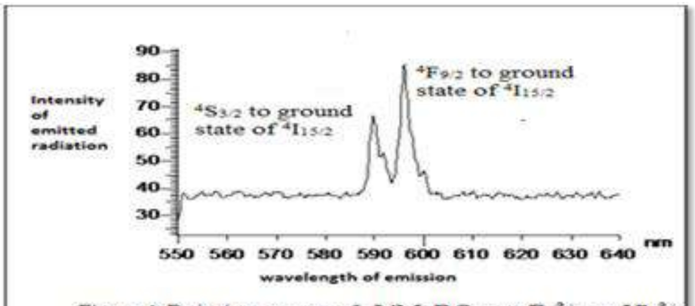

Figure 4: Emission spectra of $LiMgBO_3$:$_{0.02}Er^{3+}$,$_{0.08}Yb^{3+}$

It shows two upconversion emission peaks at 590 nm and 596 nm when excited in infrared region. It is due to mixed transitions from $^4F_{9/2}$ and $^4S_{3/2}$ to $^4I_{15/2}$ in the Er^{3+}.

CIE chromaticity coordinates for $LiMgBO_3$:$_{0.02}Er^{3+}$,$_{0.08}Yb^{3+}$ phosphor (λ_{ex} = 980 nm):

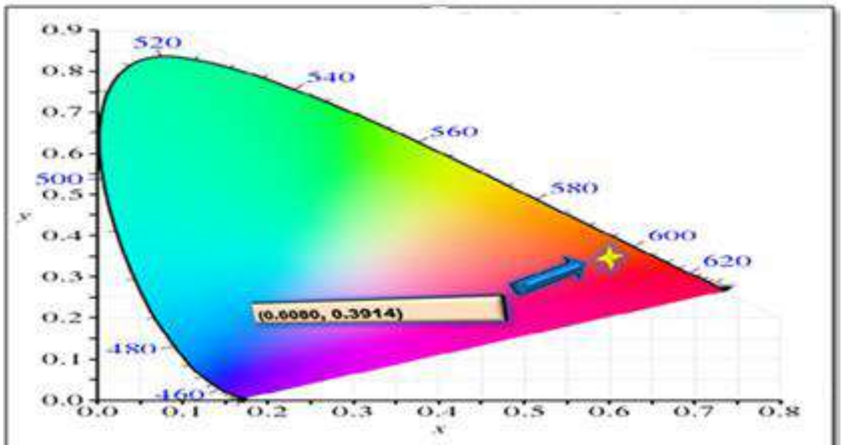

Fig.5. Presentation of the CIE chromaticity coordinates for $LiMgBO_3$:$_{0.02}Er^{3+}$,$_{0.08}Yb^{3+}$ phosphor (λ_{ex} = 980 nm).

CIE chromaticity coordinates for $LiMgBO_3$:$_{0.02}Er^{3+}$,$_{0.08}Yb^{3+}$ phosphor at λ_{ex} = 980 nm for emission wavelength 596nm are shown in the figure (5). It shows the colour of emitted light was orange.

CONCLUSIONS:

Single phase monoclinic $LiMgBO_3$:$_{0.02}Er^{3+}$ phosphors doped with $_{0.08}Yb^{3+}$ concentration has been synthesized by solution combustion technique and upconversion from near-infrared to visible was reported for the first time. Their absorption spectra were recorded which shows the broad absorption range of material. Absorption band is broad in infrared region. Absorption intensity is maximum at 980 nm. The upconversion spectra of as synthesized phosphor showed Natrium Yellow and Amber (590nm and 596nm) emission of Er^{3+}, due to the mixed transitions from $^4F_{9/2}$ and $^4S_{3/2}$ to $^4I_{15/2}$ in the Er^{3+}. The intense upconversion emission from these mixed borate phosphor could be found very useful in different emerging fields.

ACKNOWLEDGEMENT:

S. P. Hargunani is thankful to the Chairman of FIST-DST project SGB Amravati University Amravati, for providing XRD facility to this work and also to Dr.Vivek Gupta, Professor and Head Physics Dept. Jammu University for providing Absorption spectra of sample.

REFERENCES:

1. Dev K. Chatterjee, Muthu Kumara Gnanasammandhan, Yong Zhang,” Small Upconverting Fluorescent Nanoparticles for Biomedical Applications”.
2. P. Ramasamy, P. Manivasakan and J. W. Kim, RSC Adv., 66 (2014).
3. Janet Milliez, Alexandra Rapaport, Michael Bass, Arlete Cassanho, and Hans P. Jenssen, J. Display Technology.
4. G. Bertrand-Chadeyron, R. Mahiou, M. El-Ghozzi, A. Arbus, D. Zambon, and J. C. Cousseins, J. Luminescence, vol. 72–74, pp. 564–566 (1997).
5. P.A. Nagpure, S.K. Omanwar, J. Rare Earths, Vol. 30, No. 9, P. 856 (2012).
6. N.S. Bajaj, S.K. Omanwar, J. Rare Earths, Vol. 30, No. 10, P. 1005 (2012).
7. H. Huppertz and G. Heymann, Solid State Sciences, vol. 5, no. 2, pp.281–289 (2003).
8. Xuebin Qiao a , Yu Cheng b , Lin Qin b,c , Chuanxiang Qin b , Peiqing Cai c , Sun Il Kim, Hyo Jin Seo, J. Alloy and Comp. 617, 946–951 (2014).
9. Chr. Wyss, W. Liithy. H.P. Weber, P. Rogin, J. Hulliger, Optics Comm.I-M) 31-35, (19Y7).
10. Subrata Das, A. Amarnath Reddy, G. Vijaya Prakash, Chem. Phy. Letters 504, 206–210 (2011).
11. Sangmoon Park, So-Hye Cho, J. Alloy and Comp., 584, 524–529 (2014).
12. N.S. Bajaj, S.K. Omanwar, J. Rare Earths, Vol. 30, No. 10, P. 1005 (2012).
13. P.A. Nagpure, S.K. Omanwar, J. Rare Earths, Vol. 30, No. 9, P. 856 (2012).
14. R. S. Palaspagar, A. B. Gawande, R. P. Sonekar, S. K. Omanwar, J. Lumin. 154, 58 (2014).

EFFECT OF ANNEALING TEMPERATURE ON OPTOSTRUCTURAL AND OPTOELECTRONIC STUDIES OF NANOCRYSTALLINE ZnO THIN FILMS

Dadaso B. Shinde[1], Sandip K. Jagadale[2], Popatrao N. Bhosale[3], Raghunath K. Mane*[4]
[1]SPK Mahavidyalaya, Sawantwadi, Sindhudurg, India, e-mail: **dbshinde22@gmail.com**,
[2]S.B. Patil College of Engineering, Indapur, Dist. Pune (MS) India
*[4]Smt.K.R.P. Kanya Mahavidyalaya, Islampur-415 409, Tal.Walwa, Dist. Sangli, (MS) India
E-mail: **rmane.1970@gmail.com**
[3]Materials Research Laboratory, Department of Chemistry, Shivaji University, Kolhapur-416004, E-mail: **p_n_bhosale@rediffmail.com**

ABSTRACT

Zinc oxide nanorods were successfully deposited on the glass and FTO coated glass substrate in aqueous medium using zinc acetate, ethylene diamine, hexamethylene tetra-amine chemical reagents using simple chemical reflux method. In order to study the effect of annealing temperature on optostructural and optoelectronic studies of the ZnO samples, the annealing temperature range of 300°C–400°C was selected. The structural, optical, morphological, and electrochemical properties are investigated. Optical spectra showed strong light absorption in UV region. The XRD spectra and TEM examination demonstrated pure wurtzite phase hexagonal ZnO nanorods. The SEM images confirm uniform, compact and well aligned nanorods were grown on the overall substrate surfaces of both samples. The ZnO nanomaterials showed photoconversion efficiency (ŋ) 1.29 eV and 1.84 eV.

Keywords: Single crystalline, Nanocomposite architecture, Photoconversion efficiency.

INTRODUCTION:

Zinc oxide (ZnO) is an important semiconducting material used for variety of technological applications due to its wide band gap (3.37 eV) and high excitonic energy (60 MeV), environmental friendly and low cost material [1-2]. To date ZnO has variety of applications such as solar cells, nanolasers, transparent conductors, photocatalysts, optics, optoelectronics, biological sciences, energy storage, gas sensors and biosensors, photodegradation of organic pollutants, hydrogen generation, self cleaning coatings, supercapacitors, electronic components, chemical catalysis, paintings, medicines, bactericides etc [3-4].

METHOD AND MATERIALS:

For the deposition of ZnO thin films zinc acetate dihydrate ($Zn(CH_3COO)_2 \cdot 2H_2O$), diethanolamine (DEA) ($HN(CH_2CH_2OH)_2$, ethanol and hexamethylenetetraamine (HMTA)

($(CH_2)_6N_4$); these analytical reagent (AR) grade chemicals were used without further purification. The solutions were prepared in double distilled water. The glass substrates were ultrasonically cleaned using detergent, acetone and double distilled water.

Thin film synthesis:

For deposition of seed layer Zinc acetate dihydrate ($Zn(CH_3COO)_2 \cdot 2H_2O$), complexed with diethanolamine (DEA) in ethanol solvent. The ultrasonically cleaned glass substrates were dipped in seed solution for 10 sec. then slowly removed and overnight dried at room temperature . The seeded films were annealed at 300 ° C for 10 minute and used for deposition. In a typical synthesis, zinc acetate dihydrate and HMTA solutions were prepared in double distilled water. These two solutions were mixed and stirred for 10 minutes. The seeded substrates were dipped in the solution and refluxed to deposit ZnO thin films. Finally, the substrates were washed with double distilled water, dried at room temperature and used for annealing treatment at temperature 300°C and 400°C for two samples Z_1 and Z_2 samples respectively..

RESULTS AND DISCUSSION:

1) Optical absorbance study

The possible reaction and growth mechanism is as discussed (7-8). UV-Vis-NIR absorption spectra of the deposited ZnO films were recorded in the range of 300-800 nm is shown in Fig. 1 (a). Using the absorption edge value, band gap was calculated according to the Tauc relation, i.e. $(\alpha h\nu)^2$ vs. hν [5-6]. The plot of $(\alpha h\nu)^2$ vs. hν gives straight line at higher energies indicating direct type of transition. The band gap of thin films were found 3.12 and 3.18 eV respectively.

2) Structural study

The XRD patterns of the deposited ZnO thin films were shown in Fig. 2. All the obtained peaks well matches with the hexagonal wurtzite crystal structure of ZnO (JCPDS 80-0078). No other impurity peaks were observed in XRD pattern indicating ZnO nanorods having pure hexagonal wurtzite crystal structure. Applying the Debye Scherrer's formula to the prominent diffraction peak (002) of spectrum, which is unique for cubic crystal structure of ZnO and the crystallite size is found 30 nm [7-8].

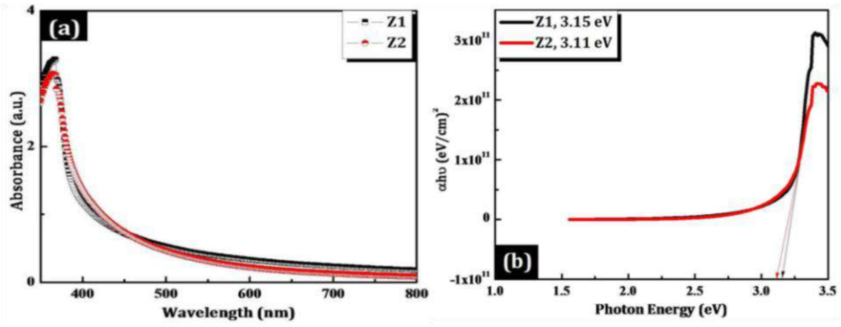

Fig. 1: (a) The plot of wavelength vs absorbance, (b) shows $(\alpha h\nu)^2$ vs. hν of the ZnO thin film

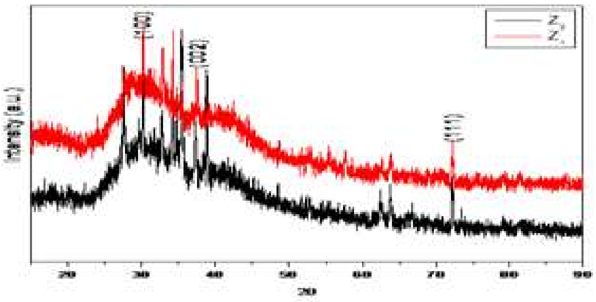

Fig. 2. XRD pattern of as deposited ZnO thin films

3) SEM analysis

The SEM images of the deposited ZnO thin films were shown in Fig.3. SEM images clearly shows the formation of uniform ZnO nanorods on the overall substrate surface. Average length and diameter of ZnO nanorods is found to be 50 nm and 10 nm respectively. The uniformly arranged ZnO nanorods can provide the faster conduction pathway (less grain boundaries, which associate with traps and barriers) for charge transport and the electron transfer time from the point of carrier generation to the collection electrode is significantly reduced [9]

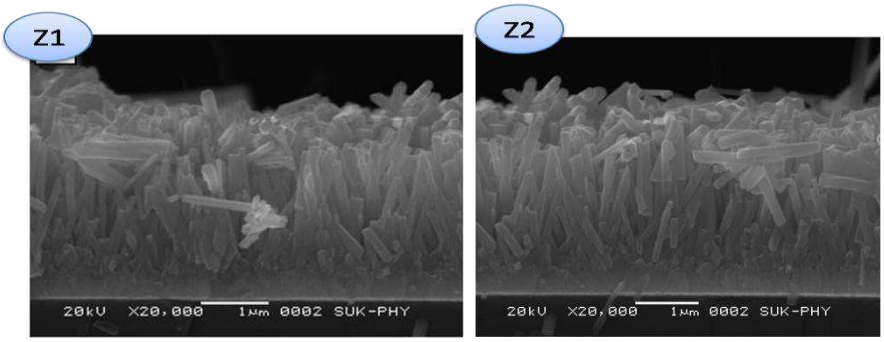

Fig. 3: **SEM cross section views of sample Z_1 and Z_2 respectively**

4) Photoelectrochemical property

The metal oxide semiconductors can absorb large amount of light radiation to form photogenerated electron–hole pair. The photogenerated electrons can transport directly through crystallites and compact layers to the conducting substrates with minimum loss. This photogenerated electrons travel through the external load and completes the circuit by entering back through the counter electrode [10-11]. The J-V characteristic curve of ZnO nanorod thin films under UV illumination in light and dark is shown in Fig. 4 (a and b). The PEC solar cell device fabrication and PEC output parameters are as follows,

Glass-FTO/ZnO/0.1 M Na_2SO_4/Graphite

Sample code	V_{oc} (mV)	V_{max} (mV)	J_{sc} (mA/cm^2)	J_{max} (mA/cm^2)	FF	η %
Z_1	716	338	0.319	0.191	0.283	1.29
Z_2	720	325	0.279	0.169	0.274	1.84

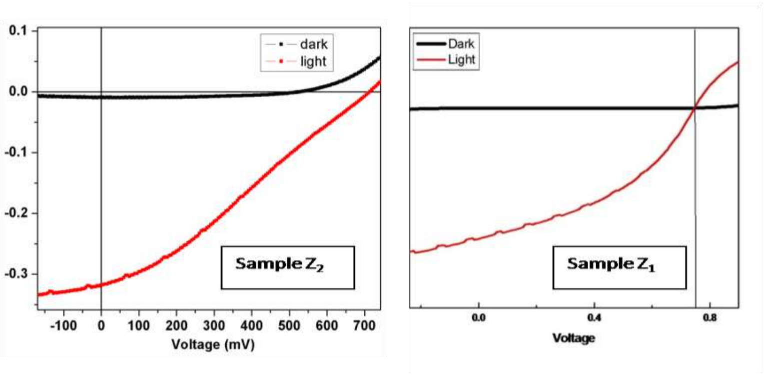

Fig. 4: J-V characteristic curve of ZnO nanorods thin films sample Z_1 and Z_2

CONCLUSIONS:

The well aligned, uniform and compact hexagonal wurtzite ZnO nanorods can be deposited on overall substrate surface. The absorption spectrum showed the strong absorption in UV region and the band gap of deposited ZnO thin films were found 3.15 eV and 3.11 eV. The SEM study showed the uniform, compact arranged and well aligned nanorods on overall substrate surface. PEC study showed that with increasing annealing temperature the efficiency increases from 1.29 to 1.84%. The low PEC efficiency for sample Z_1 is due to irregular arrangement of nanorods at low temperature annealing, while as the annealing temperature increases PEC efficiency increases to 1.84 % due to regular arrangement of nanorods.

REFERENCES:

1. S. Agilan, D. Mangalaraj, S. Narayandas, G. M. Rao, Physica B. 365, 93 (2005).
2. M. Altosaar, M. Danilson, M. Kauk, J. Krustok, E. Mellikov, J. Raudoja, K. Timmo, T.Varema, Sol. Energy Mater.Sol. Cells. 87, 25-32 (2005).
3. A. Bouraiou, M. Aida, E. Tomasella, N. Attaf, J. Mater. Sci. 44, 1241-1244 (2009).
4. S. Karan, B. Mallik, Nanotechnology 19, 495202, pp10 (2008).
5. S. Peulon, D. Lincot, Adv. Mater. 8, 166-170 (1996).
6. X. Zhao, T. Xu, W. Yao, Y. Zhu. J.Thin Solid Films, 517, 5813-5818 (2009).
7. D. B. Shinde**,** S. K. Jagadale, R. K. Mane, R. M. Mane, V. B. Ghanwat, K.V.Khot, S. S. Mali, C. K.Hong and P. N. Bhosale.J.Nanomed. and Nanotech (2015).
8. P. Christian, P. O'Brien, J. Mater. Chem. 15, 3021-3025 (2005).
9. L. Schneemeyer, M. Wrighton J. Am. Chem. Soc. 102, 6964-6971 (1980).
10. B. D Ajalkar, R. K. Mane, B. Sarwade and P. N. Bhosale,J. Solar En. Mat.,81,101.
11. R. K. Mane, B.Ajalkar, P. N. Bhosale, J.Mate.Chem.Phys. 82, 534-53 (2003).

POTENTIOSTATICALLY ELECTROPLATED MnO_2 ELECTRODE AND THEIR SUPERCAPACITIVE PERFORMANCE

I. A. Dhole*[1, 2], S. G. Pawar[1], C. S. Pawar[2], Y. H. Navale[1], Y. M. Jadhav[1], V. G. Mule[1] and V. B. Patil[1*]

[1]Functional Materials Research Laboratory, School of Physical Sciences,
Solapur University, Solapur – 413 255, (M.S.), India
[2] Materials Research Laboratory, Shankarrao Mohite Mahavidyalaya, Akluj-413101 (M.S.)
*Corresponding athor E-mail: iadhole@gmail.com

ABSTRACT:

MnO_2 thin films have been successfully prepared by controlled potentiostatic electrodeposition route. The structural, morphological and wettability properties are studied by means of X-ray diffraction (XRD), scanning electron microscopy (SEM) and contact angle study. From the XRD pattern it is clear that the MnO_2 films are amorphous in nature. The Scanning electron micrograph shows that MnO_2 film consists of nanoplatelets, well covered to the substrate exterior. MnO_2 films shows hydrophilic behavior as water contact angle is 71^o. Supercapacitive properties of MnO_2 electrode are examined using cyclic voltammogram, charge-discharge technique and stability study. The cyclic voltammogram study of the MnO_2 films in 1 M KOH shows maximum specific capacitance of 605.3 Fg^{-1} at scan rate of 5 mVs^{-1}. The charge-discharge technique was employed to estimate the values of specific energy, power and coulombic efficiency as 17.13 $Whkg^{-1}$, 15.55 $kWkg^{-1}$ and 95.10 %, respectively. The electrode reveals a cyclic stability of 93.3 % over 1500 cycles. This kind of electrode could be effectively utilized for the supercapacitor fabrication, especially for microelectronics.

Keywords: Manganese oxide; XRD; SEM; CV; CD

INTRODUCTION:

Supercapacitors have been examined commonly as the next cohort of energy storage. They play more and more major roles in power source relevance's such as in short term power sources for mobile electronic apparatus and supplementary power sources for hybrid electric automobiles [1,2]. Because of the potential relevances and outstanding electrochemical properties, the manganese oxide (MnO_2) is predicted in research in different forms as electrochromic film, fuel cell electrode, electrochemical capacitors and battery, etc. [3,4].

EXPERIMENTAL:

0.1 M manganese sulfate was used as precursor to form MnO_2. Potentiostatic electrodeposition was carried out using three-electrode electrochemical arrangement containing platinum wire as counter electrode, stainless steel as working electrode, and standard calomel electrode (SCE) as reference electrode. Potentiostatic electrodeposition method gives, homogeneous and well-adherent film, which when annealed at 500 °C for 1 hr produced the required MnO_2 product.

RESULTS AND DISCUSSION:

Structural, morphological and surface wettability test:

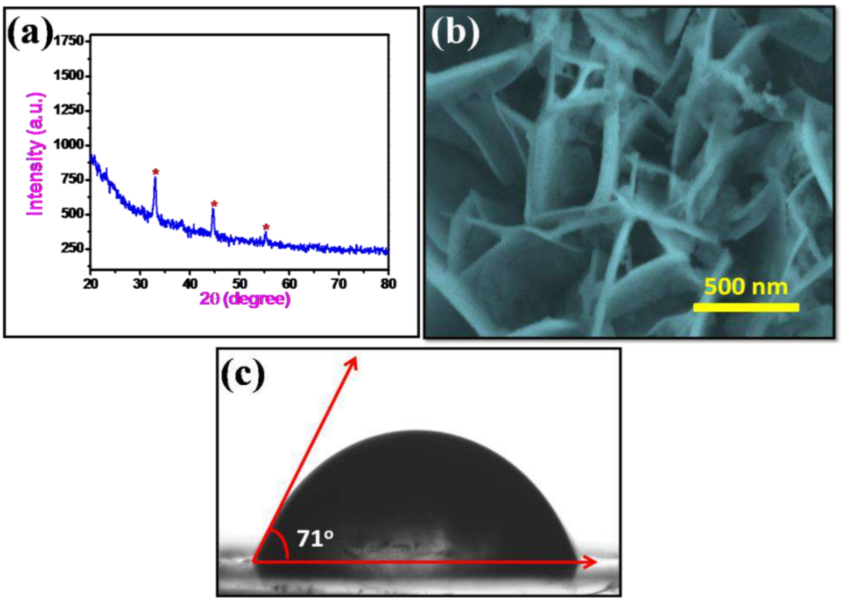

Fig.1: (a) XRD of MnO_2 thin film (b) SEM micrograph of MnO_2 thin film (c) Contact angle of MnO_2 thin film

Fig. 1(a) shows the XRD pattern of MnO_2 thin film on SS substrates. No discrete diffraction peak other than SS substrate is viewed in XRD pattern, which perhaps means that the film consisted of MnO_2 colloidal particles in amorphous segment. The peaks attained due to SS substrate are indicated by the asterisk symbol. Amorphous phase of the oxide material is viable for supercapacitor application due to effortless diffusion of ions during the bulk of the active material [5]. Fig. 1 (b) shows the SEM image of MnO_2 thin film with total substrate surface was covered uniformly. This type of morphology is electrochemically favorable, since they exhibit high surface area for electrochemical application [6,7]. From Fig. 1 (c) we observed that, the MnO_2 thin film is hydrophilic as water contact angle is less than 90^o means high wettability. The water contact angle is found to be 71^o for MnO_2 thin film. This may perhaps because of the strong cohesive force among the water droplet and material present in the MnO_2. Due to which the water is pull towards somewhat repelled by the MnO_2 thin film. This specific possession is helpful for making close contact of aqueous electrolyte with electrode surface in supercapacitor appliance [8-11].

Cyclic voltammogram, charge- discharge and stability study:

Fig. 2 (a) shows the cyclic voltammogram curves of the MnO_2 samples measured in a 1 M KOH solution, with different scan rates ranging from 5 to100 mVs^{-1}, where the current has been converted to the specific capacitance per unit mass of MnO_2. It can be concluded that the specific capacitance of MnO_2 rises with the increasing amount of electrodeposition charges and then decreases at the same scan rate [12].

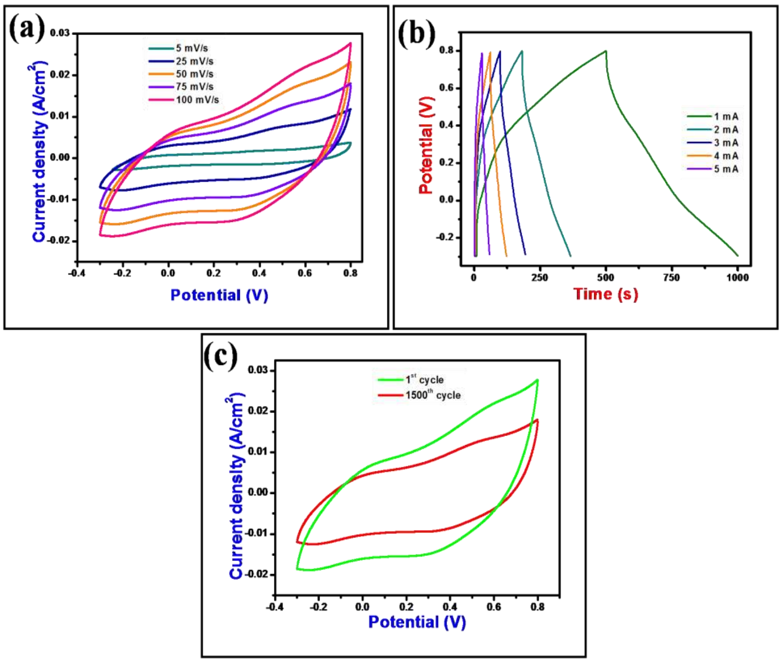

Fig.2. (a) Cyclic voltammogram of MnO_2 electrode (b) Charge-discharge study of MnO_2 electrode (c) Stability study of MnO_2 electrode

The maximum of specific capacitance determined by CV at the scan rate of 5 mVs^{-1} is 605.3 Fg^{-1}. Charge-discharge plot assessed at 1 to 5 mA is shown in Fig. 2. (b). At the opening of the charge and the discharge, a spiky alter in voltage is because of the equivalent series resistance (ESR) of the electrochemical cell [13,14]. The stability of MnO_2 electrode in 1M KOH was tested by CV. Fig. 2 (c) shows the CV curves for 1st and 1500th number cycle. The decrement in specific capacitance occurs with the 1500th cycles caused by the loss of active material through the dissolution and/or detachment, during charging/discharging cycles in the electrolyte. We found that our method can endure about 1500 cycles without a considerable reduce in the capacity judged against MnO_2 electrode, illustrating the steady character of MnO_2 electrode in energy storage relevance [15].

CONCLUSION:

In this paper, nanoplatelet structure of MnO_2 was synthesized by a potentiostatic electrodeposition method. The XRD pattern of MnO_2 shows amorphous in nature. The SEM reveals that MnO_2 film consists of nanoplatelets, well covered to the substrate exterior. MnO_2 films shows hydrophilic behavior as water contact angle is 71°. The cyclic voltammogram study of the MnO_2 films in 1 M KOH shows maximum specific capacitance of 605.3 Fg^{-1} at scan rate of 5 mVs^{-1}. The charge-discharge technique was employed to estimate the values of specific energy, power and coulombic efficiency as 17.13 Whkg^{-1}, 15.55 kWkg^{-1} and 95.10 %, respectively. The electrode reveals a cyclic stability of 93.3 % over 1500 cycles, indicating the prepared MnO_2 film structure is a very promising electrode material for high-performance supercapacitors.

ACKNOWLEDGEMENT:

Prof. V.B. Patil is thankful to the CSIR (India), for financial support through Scheme No. 03 (1319)/14/EMR-II. Authors also would like to thank DAE-BRNS for the financial support through Scheme No. 34/14/21/2015-BRNS and RUSA Maharashtra for the financial support through Scheme No. RUSA/R&I/2016/267.

REFERENCES:

1. Simon, P. & Gogotsi, Y., Nat. mater., 7, 845–854 (2008).
2. I.A.Dhole,S. T. Navale,Y. H. Navale,Y. M. Jadhav , C. S. Pawar, S.S.Suryavanshi, V. B. Patil, J. Mater Sci: Mater Electron, 28, 10819-10829 (2017).
3. P. D. More,P. R. Jadhav, A. A. Ghanwat, I. A. Dhole,Y. H. Navale,V. B. Patil, DOI: 10.1007/s10854-017-7725-5.
4. Wu, Z. S. et al. ACS Nano., 4, 5835–5842 (2010).
5. Yang, P. et al. Nano Lett., 14, 731− 736(2014).
6. Fan, Z. et al. Adv. Funct. Mater., 21, 2366–2375(2011).
7. S.M.Ingole, Y.H. Navale, D.K. Bandgar, I.A. Dhole, M.A. Chougule, P.S. Kulkarni and V.B. Patil, DOI 10.1007/978-3-319-53556-2_51.
8. Qu, Q. et al. J. Phys. Chem. C, 113, 14020–14027(2009).
9. Cheng, S. et al. Nano Energy, 9, 161–167 (2014).
10. Dubal, D. P., Kim, W. B. & Lokhande, C. D., J. Alloy. Compd., 509, 10050–10054 (2011).
11. Yang, P. et al. Nano Lett., 14, 731-736 (2014).
12. Gund, G. S., Dubal, D. P., Patil, B. H., Shinde, S. S. & Lokhande, C. D. Electrochim. Acta, 92, 205– 215 (2013).
13. I.A.Dhole,Y.H. Navale, S.M. Ingole, R.N. Mulik, Y.M. Jadhav, C.S. Pawar and V.B. Patil, DOI 10.1007/978-3-319-53556-2_52.
14. Wu, Z. S. et al. ACS Nano, 4, 5835–5842 (2010).
15. S.M.Ingole, S. T. Navale , Y. H. Navale, I. A. Dhole, R. S. Mane, F. J. Stadler, V. B. Patil, J. Solid State Electrochem., 21, 1817-1826 (2017).

SUPERCAPACITOR BASED ON GRAPHENE OXIDE AND ETHYL CELLULOSE

Jasmin S. Shaikh[1], T. S. Bhat, Jyoti V. Patil, S. A. Beknalkar, M. S. Khandeker[2], S. I. Patil[3] and Pramod S. Patil[1*]

[1]Thin Film Materials Laboratory, Department of Physics,
Shivaji University, Kolhapur, India-416004

[2]Department of Physics, M.U. College, Udgir, Dist - Latur 413517

[3]Department of Physics, Pune University, Pune

* Corresponding author. Tel.: +91-231-2609230; E-mail: psp_phy@unishivaji.ac.in (P.S. Patil)

ABSTRACT:

We report the synthesis of graphene oxide (GO) by modified Hummer's method for supercapacitor application. For supercapacitor fabrication; mostly fluorinated binders have used as binder for electrode preparation which have cost expensive as well as toxic. In order to achieve cost effective and eco-friendly electrode preparation for supercapacitor, we presented GO as active electrode material and ethyl cellulose used as binder. X-ray photoelectron spectroscopy (XPS) was used for phase identification and to study the chemical properties of GO. To understand the functional group attached, structural properties and defects were studied using FT-Raman analysis. Surface morphology of the GO sample was examined by scanning electron microscopy. The GO was then coated on nickel foil and used to measure the specific capacitance (C_{sp}) in the 3 M KOH. Cyclic voltammetry is employed to estimate specific capacitance, stability and rate capability of the same. Sample shows accepted level of capacitance (274 F/g), high rate capability and high stability up to 1000th cycle. In summary, this is successful step towards development of eco-friendly supercapacitor by using eco-friendly and cost effective ethyl cellulose binder.

Key words: Supercapacitor, graphene oxide and ethyl cellulose.

INTRODUCTION

There is lot of array of carbon materials that can be used for energy storage. Currently, activated carbon, carbon aerogels, carbon nanotubes, template carbons, graphene, etc., is one of the most frequently used electrode materials for supercapacitor [1-3]. However, if one is concerned about the energy/weight ratio, eco-friendless and cost of the material, the choice of materials shrinks [1-5]. Graphene oxide (GO), a single sheet of graphite oxide, is an intermediate during graphene synthesis by the method of oxidation–exfoliation–reduction of graphite powder. Modified Hummers method is usually used for the synthesis of GO, due to its low cost, facile preparation processes and large productivity. GO can be regarded as functionalized graphene, bearing oxygen functional group on its basal planes and edges. Due to these oxygen functional groups, GO is hydrophilic in nature and water molecule can readily intercalate into the interlayer galleries. This behavior is beneficial for easy intercalation and de-intercalation of ions for charge storage in supercapacitor. Also presence of oxygen, nitrogen, or phosphorus functional group can considerably enhance the total capacitance through additional faradic reactions called pseudo-capacitance effects. In recent years considerably work focused on the development of electrode materials and electrolytes for the development of supercapacitor. However, only few studies focused on the binder for the supercapacitor fabrication, and they might strongly affect the performance of the supercapacitor. Mostly, fluorinated thermoplastics binders, such as polytetrafluoroethylene (PTFE) and polyvinylidenedifluoride (PVdF), have been widely used as binder. These binders have cost expensive as well as they required cost expensive solvent.

In this manuscript we report the GO as the electrode and ethyl cellulose as binder for cost effective and environmental friendly supercapacitor. Graphene oxide was prepared by simple cost effective modified Hummer’s method. The electrochemical performance of the electrode has been carried out in aqueous KOH electrolyte for to get information about the specific capacitance, rate capability and stability of electrode.

EXPERIMENTAL DETAILS:

Graphene oxide has been synthesized by simple and cost effective modified Hummer’s method. The electrodes for supercapacitor have been prepared on nickel foil current collector based on GO active materials. The electrode slurries have been prepared with 93 % active material and 7 % ethyl cellulose dispersed in tetrahydrofuran solvent. The homogeneous slurry has been coated on nickel substrates and dried at 40 °C in oven for 30 min. The mass of active material was 8 mg. Supercapactior have been fabricated based on GO, ethyl cellulose and deposited on nickel as working electrode; graphite and SCE as counter and reference electrodes, respectively in an aqueous 3 M KOH electrolyte.

RESULTS AND DISCUSSION:

To understand the structural properties and defects of the surface of the carbon materials, which were directly related to presence of functional group are studied by using FT-Raman analysis. Figure 1 shows the Raman spectrum of GO sample. In spectrum the band at 1591 cm^{-1} is assigned to the G band associated with the vibration of sp^2 carbon atoms in a graphitic 2D hexagonal lattice. The band at 1355 is D band and it related to the vibrations of sp^3 carbon atoms defects and disorder [31]. The intensity of G band is higher than the D band confirm that the successfully formation of graphene oxide take place.

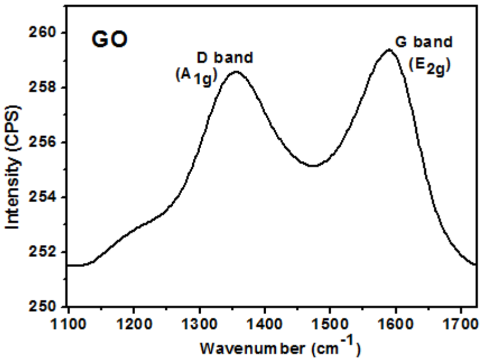

CV is employed to deduce $C_{sp}$of GO sample in 3M KOH electrolyte in distilled water electrolyte. Figure 2 shows the CV of the GO sample was swept between +0.3 to – 0.3 vs. SCE at 5 mV/ s. The CV curve of GO showed a box-like shape with presence of two pair of redox peak. The cathodic peak of first pair is observed at +0.22 V and respective anodic peak observed at -0.19 V. The cathodic and anodic peak of second redox pair is observed at -0.1 V and -0.02 V respectively. The presence of dominant redox peaks in CV indicates the existence of oxygenated groups on the surface of the GO. This oxygenated group comes from well oxidation during GO formation and ethyl cellulose which provides more oxygenated group to GO from like functionalization of carbon materials. These oxygenated groups of GO leads to remarkable pseudocapacitance [5]. Also, presence of prominent redox peaks in CV reveled that ethyl cellulose effectively act as spacer and inhibit the restacking of GO sheets and therefore facilitate the diffusion of electrolyte. Since, GO sheets are well known to agglomerate due to strong Vander walls force of attraction between the layered sheets. The stacking of layers in GO resulting a smaller surface area for ions exchange and electric double layer. The capacitance of carbon-based electrochemical supercapacitors depends on two kinds of accumulated energy: the electrostaticattraction in EDLCs and pseudocapacitance [5].

The stability of an electrode material is important for its use in an electrochemical supercapacitor. Figure 2 shows CV upon 1000 cycle of GO sample in the voltage range of +0.3 to -0.3 V vs. SCE at 20 mV/s. Inset shows the variation C_{sp} as a function of CV cycles. It is revealed that the GO sample electrode is highly stable upon 1000 cycles.

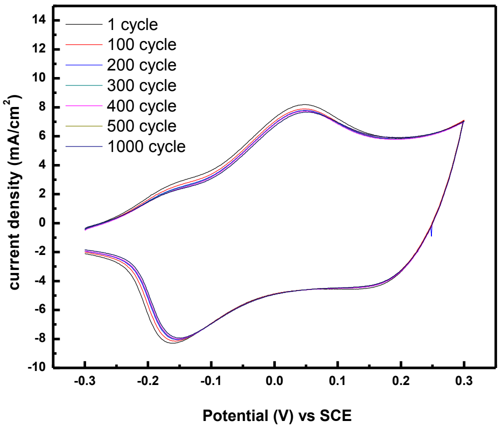

CONCLUSIONS:

We prepared GO by simple and cost effective Modified Hummer's method. Prepared GO used as active electrode material for supercapacitor application. And ethyl cellulose used as binder for cost effectiveness and its eco-friendly nature. Sample shows accepted level of capacitance (274 F/g), high rate capability and high stability up to 1000th cycle. Here, ethyl cellulose and conducting agent effectively act as spacer and inhibit the restacking of GO sheets and therefore facilitate the diffusion of electrolyte. Also, they provide more oxygenated groups for redox reaction and may increase conductivity by π-π bonding. From this study we conclude that GO as active material and ethyl cellulose as binder are useful to developing green chemistry approach for better supercapacitor.

REFERENCES:

1. Lei Z, Shi F, Lu L, ACS Appl. Mater. Interfaces 4: 1058 (2012).
2. Simon P, Gogotsi Y, Nat. Mater. 7: 845 (2008).
3. Xue T, Xu C, Zhao D, Li X, Li H, J. Power Sources 164: 953 (2007).
4. Conway B. E, J. Electrochem. Soc. 138: 1539 (1991).
5. Sarangapani S, Tilak B.V, Chen C. P, J. Electrochem. Soc. 143: 3791 (1996).

IMPEDANCE STUDIES OF MAGNESIUM – DYSPROSIUM FERRITES

J. S. Ghodake*, A. A. Pawar, S. S. Patil and R. N. Kumbhar

Department of Physics, Padmabhushan Dr. Vasantraodada Patil Mahavidyalaya,
Tasgaon, Dist: Sangli, 416 312, Maharashtra, India
*Corresponding author E-mail: jeevan.ghodake@rediffmail.com Tel:91-02346-250665

ABSTRACT:

Magnesium – Dysprosium ferrites were successfully prepared by a chemical combustion route. The synthesized powder was sintered at 950^0C for 1hr. The conduction mechanisms of Magnesium – Dysprosium ferrites were studied by using Hioki LCR - Q meter over the frequency range 42 Hz to 5 MHz. The real part of impedance (Z') of prepared samples decreases with increasing frequency which may be attributed to the space charge polarization effect in the material. The complex impedance plots obtained from the impedance data as a function of frequency for studied samples suggests that the conduction mechanism in ferrites is due to the grain boundary contribution.

Keywords: Impedance, Combustion route, ferrite.

INTRODUCTION:

Ferrites have versatile magnetic and electric properties that vary with substitutions of ions. Rare earth ions substituted into the spinel structure which can modify electrical and magnetic properties of ferrites [1]. Magnesium ferrites are widely used as catalysts have many applications in sensors and magnetic technologies [2]. Rare earth elements have high resistivity and good electrical insulators. N. Rezlescu et al [3] have studied effects of iron substitutions by rare earth ions on electrical and magnetic properties of zinc nickel ferrite. They have found that substitution of small amount of rare earth ions instead of iron produces modification of magnetic and electrical properties.

Impedance spectroscopy is a powerful tool for investing electrical behavior of spinel ferrites. Impedance studies are important way to analyze resistance in materials and find out relaxation behavior of materials. In present work we have study the impedance of Dysprosium substituted Magnesium ferrite synthesized by combustion method and measure the real and imaginary part of impedance with frequency.

EXPERIMENTAL:

Magnesium – Dysprosium ferrites having composition $MgDy_{0.03}Fe_{1.97}O_4$ were prepared by chemical auto-combustion route, in which metal nitrates are used as an oxidizing agent and fuel glycine as a reducing agent. The as synthesized powder was presintered in air at 600^0C for 1hr [4]. The presintered powder was mixed with small amount of polyvinyl alcohol and uniaxially pressed at 6 tones/inch to form pellet shaped sample with diameter 1cm and thickness 15mm and finally sintered at 950^0C for 1hr.

Pellets of samples were used for measurement of impedance using Hioki (3532-50) LCR-Q meter at room temperature. The real (Z') and imaginary (Z") parts of impedance of $MgDy_{0.03}Fe_{1.97}O_4$ were determined by using the relations described elsewhere [5].

RESULTS AND DISCUSSION:

Real and imaginary part of impedance studies of Magnesium – Dysprosium ferrite were performed at room temperature by using Hioki LCR - Q meter in the frequency range 42 Hz to 5 MHz. From impedance analysis of spinel ferrites we are understand electrical properties and gives the data for real part of impedance (Z') and imaginary (Z") parts of impedance [5]. Complex impedance plane plots are called as Nyquist diagram which represents a combination of grain and grain boundary resistances. The variation of real part of impedance (Z') and imaginary part of impedance (Z") with frequency at room temperature is as shown in figure 1 and 2.

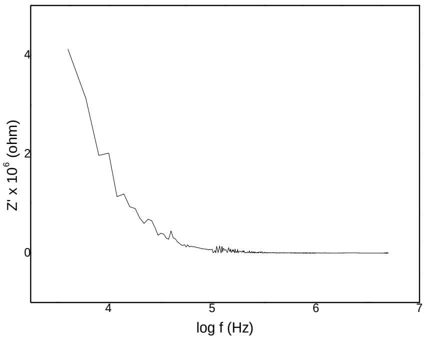

Fig. 1: Frequency variation of Real part impedance (Z’) at room temperature

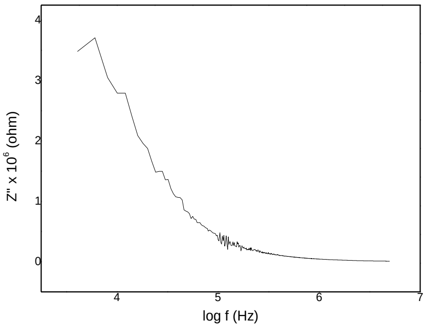

Fig. 2 Frequency variation of Imaginary of part of impedance (Z") at room temperature

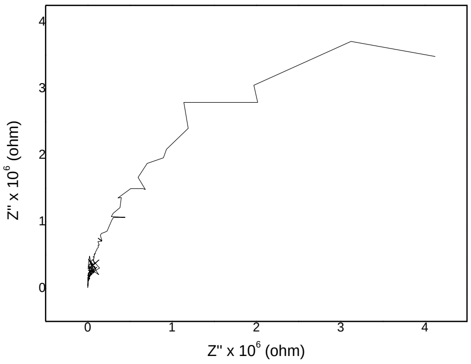

Fig. 3: Complex impedance planes at room temperature

From figure 1, it is seen that the values of real part of impedance (Z') are decreases with increase in the frequency up to 100 kHz, thereafter it becomes constant with increase in frequency. The real part of impedance (Z') are decreases with frequency due to the space charge polarization effect in the material. These results are in good agreement with reported results for different spinel ferrite materials [6, 7]. From figure 2, it is observed that the value of imaginary part of impedance (Z”) becomes maximum, which indicates existence of relaxation effects and changes resistance of the materials. Fig. 3 shows complex impedance plane at room temperature performed using Hioki LCR - Q meter over the frequency range 42 Hz to 5 MHz. From this plots we have distinguish the grain resistance and grain boundary resistances. It is seen that there is one semi circle in the low frequency region, shows predominance of grain boundary resistance. Similar results observed in Gd doped in cobalt ferrites [5].

CONCLUSION:

Magnesium – Dysprosium ferrites were successfully prepared by a chemical combustion route. The real (Z’) and imaginary (Z") parts of impedance were studied by using LCR-Q meter. The real part of impedance (Z') of prepared samples decreases with increasing frequency which may be attributed to the space charge polarization effect in the material. Complex impedance plots obtained from the impedance data as a function of frequency for studied samples suggests that grain boundary are offering more resistance and hence the conduction mechanism is due to the grain boundary contribution.

REFERENCES:

1. Smitha Thankachan, Binu P. Jacob, Sheena Xavier, and E. M. Mohammad, Phys. Scr. 87, 7pp (2013).
2. K. K. Bamzai, Gurbinder Kour, Balwindar Kaur, Manju Arora, Manju Arora, R. P. Pant, J. Magnetism and Magnetic Mat., 345, 255- 260 (2013).
3. N. Rezlescu, E. Rezlescu, C. Pasnicu and M. L. Craus, J. Phy.: Conde. Matt. Vol.6, 29.
4. R. C. Kambale, P. A. Shaikh, C. H. Bhosale, K. Y. Rajpure, and Y. D. Kolekar, Smart Mater. Struct. 18, 115028(2009).
5. 6th Vacuum and Surface Sciences Conference of Asia and Australia, J. Phy.: Conf. Series 439, 012015 (2013).
6. B. Ramesh, S. Ramesh, R. Vijay Kumar, M. Lakshmipathi Rao, J. Alloys Comp. 513, 289 (2012).
7. Khalid Mujasam Batoo, Physica B, 406, 382 (2011).

BIOSYNTHESIS OF BIOLOGICALLY ACTIVE SILVER AND GOLD NANOPARTICLES BY KOKUM FRUITS

Kiran D. Pawar

School of Nanoscience and Biotechnology, Shivaji University, Kolhapur

Keywords: *Garcinia indica* Choisy, AgNPs, AuNPs, antimicrobial activity, antioxidant activity, photoluminescence, photo-catalysis.

There is a growing need to develop reliable, nontoxic and eco-friendly methods for the synthesis of nanoparticles. Various biological agents and their products such as plants, plant extracts, fungi and bacteria can be used as the for biogenic synthesis of nanoparticles. Among these biological entities and their products, plants and their extracts are being explored on large scale. Extracts of plants and their fruits that contain natural antioxidants such as flavonoids, alkaloids, coumarins, and phenolics which can be good sources of reducing and capping agents and used for biogenic synthesis of metal nanoparticles. *Garcinia indica* Choisy is one of medicinally important phytochemically rich tree species whose fruit extract contains significant amount of HCA and other secondary metabolites like xanthones, benzophenones, flavonoids, biflavonoids and triterpenoids. Kokum fruit extract could be a good source of biomolecules that can be used for biogenic synthesis of nanoparticles.

The present study demonstrates the biosynthesis, characterization and applications of silver (AgNPs) and gold nanoparticles (AuNPs) from Kokum fruit extract. For the synthesis, the optimization of various parameters for biogenic synthesis using Kokum fruit extract was carried out and characterized by UV-visible absorption spectroscopy, Fourier transform infra-red (FT-IR) spectroscopy, field emission scanning electron microscope (FE-SEM) imaging, energy dispersive X-ray(EDS) spectrometer, X-ray powder diffractometer (XRD), high resolution transmission electron microscope (HR-TEM) imaging and the selected area electron diffraction (SAED) pattern. For optimization, the effects of various parameters such as concentration of precursor, ratio of precursor to extract, pH, incubation temperature and time were varied and studied for their effect on synthesis. 1.5 mM AgNO3, 1:1 ratio of $AgNO_3$ to extract, pH 10, incubation of reaction mixtures at 37^0C for 24 hrs were the optimum parameter for biogenic synthesis of AgNPs. For AuNPs, the parameters such as 0.6 mM $HAuCl_{4,}$ 1:3 ratio of $HAuCl_4$ to extract, pH 4 and incubation at 80^0 C for 15 min were found optimum.

Synthesis of nanoparticles was confirmed by characterization techniques. AgNPs show the characteristic SPR peak in the visible range at 420 nm, mainly due to surface Plasmon resonance by the collective oscillations of conduction electrons whereas AuNPs show SPR peak in the range of 520-550nm. The XRD pattern analysis confirmed the crystalline nature with cubic face centred (FCC) structure of AgNPs and AuNPs by Bragg's reflections at 2θ values. It represented (111), (200), (220), (311) and (222) planes for AgNPs and [111], [200], [220], [311] and [222] planes for AuNPs. EDS confirmed elemental compositions of AgNPs and AuNPs. AgNPs were mostly spherical and few hexagonal in shape with size ranging between 5-30 nm. AuNPs were found crystalline, spherical in shape with size between 20-30 nm. Photoluminescence investigation showed broad excitation band with excitation maximum at 311 nm and emission band with an emission maximum at 455 nm. Noteworthy, the fluorescence emitted by AuNPs was found to be excitation dependent. Without any surface modification and functionalization, as prepared AuNPs showed excitation wavelength dependent plasmonic emissions demonstrating the good photoluminescent property that can be used for applications such as biological sensing, biolabeling, and bioimaging.

Feasibility and suitability of AgNPs and AuNPs were checked for different application. The Antimicrobial activity of biogenic AgNPs was tested and antioxidant activities of biogenic AgNPs and AuNPs were evaluated. The biogenic AgNPs alone and in combination with Tetracycline showed antibacterial activity against the four of seven tested bacteria. In addition, biogenic AgNPs also demonstrated good antioxidant activities such as DPPH, hydrogen peroxide, nitric oxide (NO) radical scavenging and reducing power activities. Methylene violet dye degradation ability of AuNPs have been studied by observing change in absorbance at specific wavelength in presence of gold nanoparticle with varying parameters. The investigation of catalytic activity demonstrated that AuNPs possess good photocatalytic activity and could be used for rapid photocatalytic degradation of methylene violet (MV) dye. In addition, AuNPs showed good dose dependent DPPH radical scavenging activity.

SENSITIVE DETECTION OF AMMONIA GAS BY USING NANOFIBROUS PANI THIN FILMS

N. S. Harale[1,2], A. B. Nagare[3], N. L. Tarwal[1], V. K. Rao[4] and P. S. Patil[1*]

[1]Thin Film Materials Laboratory, Department of Physics,
Shivaji University, Kolhapur-416 004, M.S., India
[2]School of Nanoscience and Technology, Shivaji University, Kolhapur-416 004, M.S., India
[3]Thin Film Nanomaterials Laboratory, Department of Physics,
Shivaji University, Kolhapur, MS 416-004, India
[4]Defence Research & Development Establishment, Jhansi Road, Gwalior-474002, M. P., India
*Corresponding authorE-mail: psp_phy@unishivaji.ac.in

ABSTRACT:

In present investigation we have synthesized nanofibers of Polyaniline (PANI) by in situ oxidative polymerization of aniline monomer and thin film coated by drop casting method on glass substrates. The deposited thin films were characterized for their structural, morphological and compositional studies using X-ray diffraction (XRD), Scanning electron microscopy (SEM) and Fourier transform Raman spectroscopic (FT-Raman) spectroscopic studies. PANI nanofibers exhibit amorphous nature as confirmed from XRD studies. Based on SEM analysis, the spongy and porous nanofibrous nature of PANI with average diameter of 45 nm was confirmed. The gas sensing properties of PANI thin film based gas sensor were studied at room temperature. The PANI thin film gas sensor showed highest sensitivity of 12.6% at room temperature. The gas sensing results suggested that nanofibrous PANI thin film sensor exhibited selective and good response toward ammonia gas.

Keywords: porous; nanofibers; PANI; gas sensor.

INTRODUCTION

In recent years, the drastic industrial growth resulted deteriorating the natural atmospheric environment. The atmospheric pollution is one of the most sensational and global issues. To prevent environmental disasters, it is essential that such pollutants to be monitored and controlled. A large variety of gases in the atmospheric environment, such as NOx, COx, SO_2, H_2S, NH_3, volatile organic compound (VOCs) and so on, need to be detected. In recent years, toxic or bad-smelling gases frequently encountered in living circumstances such as H_2S and NH_3 as well as hazardous gases used for industrial processes such as AsH_3 and PH_3 have long been the targets of gas sensors [1, 2]. Therefore, gas detection instruments are increasingly needed for industrial health and safety, environmental monitoring and process control [1, 3]. The present gas sensor technology is based on semiconductor metal oxides. However, the problems with these semiconductor metal oxides are their low sensitivity, selectivity and higher operating temperatures. As an alternative to semiconductor metal oxides, conducting polymers have attracted much attention in gas sensor technology due to their facile synthesis, flexibility in operation, short response-recovery times and room temperature operation [4]. Recently, nanostructured Polyaniline (PANI) is one of the considerable candidates for the development of highly sensitive and selective gas sensor for the detection of toxic gases. The properties like environmental stability, facile synthesis, tunable conductivity and reversible doping/dedoping chemistry make it suitable for gas sensing application [5, 6]. So, we are much interested to study their gas sensing features such as lower detection limit, short response time and improvement in recovery of sensors.

In this present investigation, we report on the sensitive detection of ammonia gas by using branched spongy nanofibrous PANI thin films. The gas sensing properties of the PANI thin film sensor were investigated at room temperature for different concentrations of ammonia gas.

EXPERIMENTAL:

The formation of PANI (emeraldine salt) was carried out by employing simple chemical oxidation polymerization method. Aniline monomer and other reagents were purchased from SD Fine Chemicals, Mumbai, India (AR grade). The reaction was carried out in a beaker and the bath temperature was mentioned at 0-5 ^{o}C. The solution bath was prepared using acidic solution of 0.1 M aniline and 0.1M ammonium persulphate (APS). The reaction mixture was kept for overnight at the room temperature with continuous stirring. The obtained product was washed and dried. PANI thin films were deposited using drop casting method and employed for further characterizations.

RESULTS AND DISCUSSION

Fig. 1(a) shows the XRD pattern of PANI films recorded over the 2θ values in the range of 10° to 80°. The XRD pattern displays broad diffraction hump concentrated around 2θ = 25 °, similar observed by other groups [7]. The XRD result confirm the amorphous nature of PANI thin film. The chemical structure of PANI was examined by FT-IR spectroscopy. Fig. 1(b) shows the FT-IR spectrum of PANI indicating characteristics peaks corresponding to quinoid and benzene ring are observed at 1558 and 1471 cm^{-1}, respectively [8]. The FT-IR spectrum confirms the presence of doped polyaniline structure. The surface morphological features of PANI thin film was examined by SEM technique.

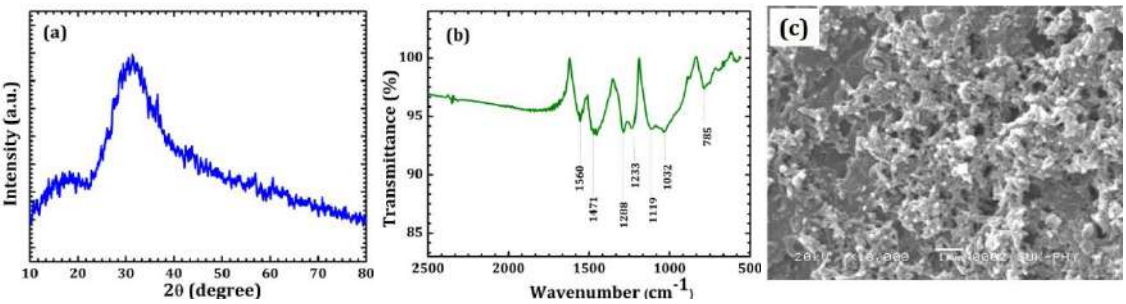

Fig. 1: (a) XRD pattern, (b) FT-IR spectrum and (c) SEM image of the PANI thin film

Fig. 1(c) displays SEM image of PANI thin film showing porous and spongy network composed of numerous nanofibers. The average diameter about 45 nm and the lengths are in several hundred nanometers, maintaining higher aspect ratio. Such a porous and nanofibrous structure provides a large surface area which is much beneficial for the gas sensing application.

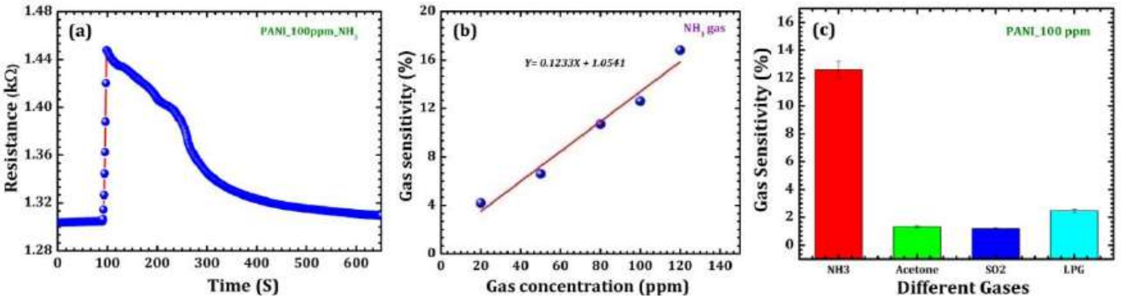

Fig. 2: (a) Gas sensing transient curve at 100 ppm of NH_3, (b) Relation between sensor response and NH3 gas concentrations and (c) Selectivity histogram of PANI sensor towards 100 ppm of different gases

Gas-sensing performance of PANI thin film sensor was measured in an indigenous computer-controlled static gas sensing characterization unit at room temperature. The dynamic gas response of PANI sensor to 100 ppm NH_3 gas operating at room temperature shown in Fig. 2(a) and it was found to 12.6%. The real-time gas response-recovery studies of PANI sensor were carried out upon exposure to different concentrations (20 to 100 ppm) of NH_3 gas. It is observed that the gas response increased with increase in concentration of NH_3 gas due to higher gas adsorption takes place for higher gas concentration [9-10]. The relationship between the gas sensitivity and the gas concentration is shown in Fig. 2(b). The linear regression equation is $Y=0.1233X+1.0541$ where, Y is the gas sensitivity and X is the concentration of NH_3 gas. Fig. 2(c) shows bar diagram of gas sensitivity to different reducing and oxidizing gases at a fixed concentration of 100 ppm for NH_3, C_3H_6O, SO_2 and LPG. PANI thin film sensor offers maximum response to NH_3 gas as compared to other tested gases. This may be due to different binding energies for different gases to occur chemisorption at the interface of PANI sensor [11].

CONCLUSIONS:

The nanofibrous PANI thin film sensor was successfully fabricated and tested for gas sensing application. The gas sensing measurement showed the PANI gas sensor works efficiently as a NH_3 gas sensor with sensitivity 12.60 % at 100 ppm concentration and it is highly selective towards NH_3 gas among other interfering gases. Although sensor response is lower as compared with reported, present sensor is highly selective towards NH_3 gas and attempt will be made to further increase its sensitivity.

ACKNOWLEDGEMENT:

The authors are grateful to the DRDO, New Delhi, for the financial support through project-DRDO/ERIP/ER/0803719/M/01/1343.

REFERENCES:

1. A.J. Heeger, Chem. Soc. Rev., 39, 2354-2371 (2010).
2. K. Okamoto, C.K. Luscombe, Polym. Chem., 2, 2424-2434 (2011).
3. S. Cui, J. Wang, X. Wang, RSC Adv., 5, 58211-58219 (2015).
4. H. Bai, G. Shi, Sensors 7, 267-307 (2007).
5. X. Zhang, Z. Qin, X. Liu, B. Liang, N. Liu, Z. Zhou, M. Zhu, J. Mater. Chem. A, 1, 10327–10333 (2013).
6. D.K. Bandgar, S.T. Navale, S.A. Vanalkar, J.H. Kim, N.S. Harale, P.S. Patil, V.B. Patil, Synth. Met., 195, 350–358 (2014).
7. D. Geethalakshmi, N. Muthukumarasamy, R. Balasundaraprabhu; Optik, 125, 1307–1310 (2014).
8. D.S. Patil, J.S. Shaikh, D.S. Dalavi, S.S. Kalagi, P.S. Patil, Mater. Chem. Phys., 128, 449–455 (2011).
9. D.S. Dalavi, N.S. Harale, I.S. Mulla, V.K. Rao, V.B. Patil, I.Y. Kim, J.H. Kim and P. S .Patil, Mater. Lett., 146, 103–107 (2015).
10. N.S. Harale, A.S. Kamble, N.L. Tarwal, I.S. Mulla, V.K. Rao, J.H. Kim, P.S. Patil, Ceram. Int., 42, 12807-12814 (2016).
11. S.T. Navale, G.D. Khuspe, M.A. Chougule, V.B. Patil, Ceram. Int., 40, 8013–8020 (2014).

MANGROVES AS POTENTIAL SOURCE OF NANOPARTICLE SYNTHESIS

Narendra A. Kulkarni

Department of Botany, P. D. V. P.Mahavidyalaya, Tasgaon, Sangli 416 312 (MS) India

ABSTRACT:

Nanoscience is a recent branch of science which is improving day by day in making an impact on all facets of life. Marine ecosystem has variety of living resources which comprises prokaryotes like organisms to eukaryotic organisms like higher plants and animals. In the higher plants growing in marine environment, mangroves dominates all other vegetation's and also support them in one or the other reason. Mangroves are a special group of plants adopted to grow in high salinity waters. The adaptations are exhibited in many forms of the life cycle as flowering and fruiting pattern, rooting behavior, anatomical characters, physiological characters to normalize the biological clock. Mangroves show the typical salt glands in various parts of the plant body. These glands secrets additional salt in the plant body. At the same time mangroves show a very special physiological process called ultra-microfiltration. This has been already proved by pulse chase study and autoradiography.(1) This has also manifested the presence salt tolerant genes in mangroves. The present review dealt with the applications of mangroves in nanotechnology. In this paper attempt is made on what the mangroves are involved in and what type of nanoparticles are synthesized including size and medicinal applications. This attempt may help for exploring the use of mangroves of Maharashtra in nanotechnology.

INTRODUCTION:

In the recent years biologically synthesized nanoparticles are of considerable interest in the area of biology and medicine due to their unique particle size and shapes along with their physical, chemical and biological properties.(2) Marine plants are rich source of bioactive compounds with remarkable impact in the field of pharmaceutical, industrial and biotechnological product development. In recent years the researches have focused on the synthesis of nanoparticles from marine resources which are biocompatible and biodegradable with the particle size ranging from 1 to 100 nm.(3) Table – 1.comprises the average size of nanoparticles derived from various plant groups.Table – 2. Comprises the existing knowledge on potential applications and current information about research on nanoparticles derives from the mangroves.

Table 1: Average size of AgNP nanoparticles from various plant groups

Sr.No.	Name of plant group	AgNP size range (nm)
1.	Algae	1-42
2.	Bryophytes	20-65
3.	Pteridophytes	20-45
4.	Gymnosperms	1-5
5.	Angiosperms	1-145
6.	Fungi	2-100
7.	Bacteria	1-78
8.	Biopolymers	2-60

Table 2: Reviews the existing knowledge on potential applications and current information about research on nanoparticles derived from mangroves

Sr.No.	Name of the mangrove	Size of AgNP (nm)	Property
1.	*Avicennia marina* var. *acutissima* Staff and Moldenk.	71-110	Antibacterial, Larvicidal (10)(11)
2.	*Avicennia officinalis* L.	71-110	Antibacterial, Larvicidal
3.	*Avicennia alba* L.	71-110	Antibacterial, Larvicidal(8)
4.	*Avicennia marina* (dwarf) Forsk.	60-95	Antibacterial, Larvicidal
5.	*Avicennia officinalis* (dwarf)	71-110	Antibacterial, Larvicidal
6.	*Aegiceras corniculatum* (L.) Blanco	55-125	Antibacterial, Larvicidal
7.	*Acanthus ilicifolius* Linn.	40-65	Antibacterial, Larvicidal
8.	*Bruguiera cylindrica* (L.) Blume	15-45	Antibacterial
9.	*Bruguiera gymnorrhiza* (L.) Lamk.	15-45	Antibacterial
10.	*Ceriops tagal* (Perr.) Robin	25-75	Antibacterial
11.	*Cynometra iripa* L.	45-110	Antibacterial
12.	*Excoecaria agallocha* Linn.	35-70	Antibacterial(9)
13.	*Kandelia candel* (L) Druce.	50-95	Antibacterial
14.	*Lumnitzera racemosa* Wild.	30-85	Antibacterial
15.	*Rhizophora mucronata* Lamk.	4-26	Antibacterial, Larvicidal(5)
16.	*Rhizophora apiculata* Blume.	60-95	Antibacterial, Larvicidal
17.	*Sonneratia alba* J. Sm.	60-110	Antibacterial, Larvicidal
18.	*Sonneratia apetala*Buch. Ham.	20-40	Antibacterial, Larvicidal
19.	*Sonneratia caseolaris* (L.) Engl.	55-95 (18.3)	Antibacterial, Larvicidal(12)
20.	*Xylocarpus granatum* Koen.	5-20	Antibacterial, Larvicidal
21	*Heritiera fomes* Lamk.	45-95	Antibacterial, Larvicidal

COMMAN METHODOLOGIES USED FOR AgNP BIOSYNTHESIS: (13)

1. Green synthesis
2. Biological Reducing agent
3. Separation of AgNPs.
4. Monitoring of AgNPs.
5. Mechanism of AgNPs synthesis
6. Factors affecting AgNPs synthesis
7. Analysis of SEM and TEM data

APPLICATIONS OF AgNPs:

1. Anti-microbial
2. Anti-bacterial
3. Anti-fungal
4. Anti-parasitic
5. Anti-fouling action
6. Therapeutic agents
7. Nano carriers
8. Radiation therapy
9. As catalyst

MANGROVE FLORA BASED NANOPARTICLES:

Plants have been proved as the source of nanoparticles synthesis with broad variability of metabolites and their efficacy. The main phytochemicals responsible for their activity have been identified as terpenoids, flavones, ketones, aldehydes, amides and carboxylic acids.

Mangroves are growing in an extremely different environment from other terrestrial plants. Hence they are producing number of bioactive compounds like polyphenols, flavonoids, alkaloids and tannins. These bioactive compounds are synthesized as a counteraction to survive in high salt contents. The biosynthesis of nanoparticles from mangroves *and* associate plants is very limited. Twenty six coastal plants are recorded as good source for nanoparticles.(4) AgNPs are recorded from *Rhizophora mucronata* Lamk. Which are effective for the fish pathogens.(5) Anti cancer activity of AgNPs have been reported from *Sueada monoica*.(6)Insecticidal activity from AgNPs has been seen in *Hibiscus tiliaceous*.(7) Antibacterial activity of AgNPs from *Avicennia alba* Blume. are recorded.(8) Green synthesis of AgNPs has been recorded in *Excoecaria agallocha* Linn.(9) Antibacterial and Larvicidal activity has been recorded in *Avicennia marina* var. *acutissima* Staff and Moldenk.(10)(11) AgNPs of 18.3 nm size has been observed in *Sonneratia caseolaris* (L.) Engl.(12) The present attempt is to understand the potential of mangrove species from the coast of Maharashtra as the source of nanoparticles.

CONCLUSION:

The syntheses of nanoparticles from marine organisms have a lot of potential. But still it has to explore cautiously. The coastal vascular plants have some obstacles of tannins and higher salt contents. Mangrove may provide safe, stable and environment friendly particles. The marine environment has captured attention of the material scholars. They are sure that these potentials can be explored for the beneficial aspects of human life. Still other mangrove species can be explored for new dimensions.

REFERENCES

1. Joshi G.V., Shubhangi Sontakke, Leela Bhosale and A.P.Waghmode, Physiol. & manag. of mangroves. Dr.W.Junk Publisher, (1984).
2. Ko SH, Park I, Pan H, Grigoropoulos CP, Pisano AP, Luscombe CK, Frechet JMJ, Nano. Let.7:1869-1877 (2007).
3. Asmathunisha N, Kathireson K., Colloids & Surfaces B: Biointerfaces, 103:283-287 (2013).
4. Asmathunisha N. M. Phil thesis, CAS in Marine Biology, India. 98 pp (2010).
5. Umayaparvati S, Arumugam M, Meenakshi S, Balasubramanian T. Int.J.Sci.Nat. 4(1): 199-203 (2013).
6. Satyavani K, Gurudeeban S, Ramanathan T, Balasubranian MT. J.Med.Biotech.4(1):35-39 (2012).
7. Usha Rani, P., Prasanna Laxmi, K., Vadlapudi, V. and Sreedhar, B. J. Biopest 9(2): 167-179 (2016)..
8. Nagababu P, Umamaheshwara Rao V. Asian J. Pharma. & Clin. Res., Vol 9, 1 (2016).
9. Sangeetha arun, Saraswati U and Singarvelu. Int. J. Pharma. Sci. Inven. 3(10), pp 54-57 (2014).
10. Gnanadesigan M, Anand M, Ravikumar S, Maruthupandi M, SyedAli M, Vijaykumar V, A.K.Kumarguru. J. Biosci. 2(2), pp 143-147 (2012).
11. Balkrishnan S, M Srinivasan and J Mohanraj. J. Biosci. 40(3), pp 991-996 (2016).
12. Bakshi M, Ghosh S and P Chaudhari. BioNanoSci., 5(3), pp 162-170 (2015).
13. Sista Kameshwara Srikar, Deen Dayal Giri, Dan Bahadur Pal, Pradeep Kumar Mishra, SiddhNath Upadhyay. Green and Sust. Chem., 06,34-56 (2016).

NOVEL BIS-FERROCENYL NHC COMPLEXES OF NOBEL METALS: A SUCCESSFUL APPROACH TO MULTI-TARGETING ANTI-BREAST CANCER AGENTS

Prakash Bansode, Altafhusen Naikwade, Shivanand Gajare and Gajanan Rashinkar*
Department of Chemistry, Shivaji University, Kolhapur, 416004, M.S., India
*Corresponding autjor E-mail: gsr_chem@unishivaji.ac.in

Breast cancer is a most commonly diagnosed type of cancer among women [1]. Although current breast cancer therapies including hormone modulators and targeted antibodies have been developed, the mortality rate from breast cancer incidences has still not improved over the past few decades[2]. Majority of breast cancers are invasive and recurrence is rate is high. The search for new effective therapy protocols for breast cancers is complex by its heterogeneous pathologies and biomolecular profiles [3]. It is well estabished that breast cancers are associated with overexpression multiple hormone receptors such as estrogen receptors (ER), progesterone receptors (PR), and human epidermal growth receptor 2 (HER2) [4]. Hormonal therapies and/or molecular targeted therapies are applied as an effective treatment option for triple negative breast cancer (TNBT) [5]. However, problems are linked with the treatment of breast cancer with heterogeneous triple-negative type lacking ER, PR, and HER2 expression, which accounts for 15-20% of breast cancers and usually has poor prognosis, and the discovery of an effective anti-breast cancer agent that targets triple-negative breast cancer (TNBC) in multitargeted approach has been a challenge in oncology [6, 7].

Ferrocene is an orange crystalline, diamagnetic solid. It is non-toxic and referred as ‘Safe’ metallocene. It has high stability in the presence of air and water, it is highly soluble in organic solvents. It undergoes Friedel-Crafts acylation, alkylation, Vilsmeier formylation etc. So ferrocene is widely regarded as a substitute for the aromatic benzene ring [6].

Inclusion of ferrocene improves the biological activity of compound:

Chloroquine to Ferrochloroquine:

Chloroquine is active against malaria parasite in blood but does not destroy *Plasmodium flaciparum* parasite that may remain in liver. The insertion of ferrocene group into the side chain of chloroquine forms a compound Ferrochloroquine. Ferrochloroquine is active against both chloroquine-sensitive and chloroquine-resistant *Plasmodium flaciparum.*

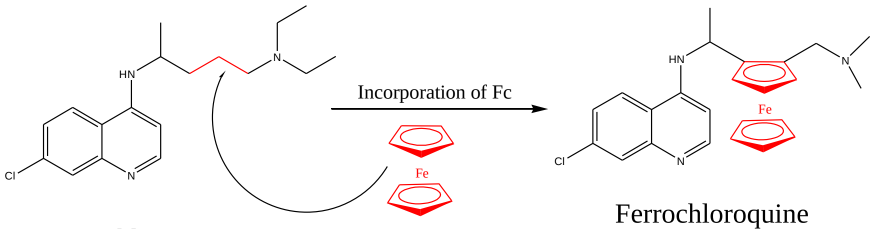

Chloroquine

Ferrochloroquine

Tamoxifen to Ferrocifen:

The replacement of phenyl ring by ferrocene in tamoxifen, forms ferrocifen, ferrocifen has excellent anti-breast cancer activity than tamoxifen.

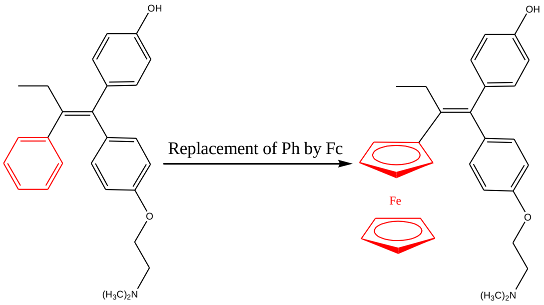

Tamoxifen

Ferrocifen

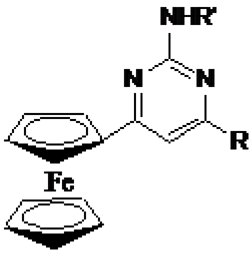

C. Feher, *J. Organomet. Chem*, *2009*, 694, 4036

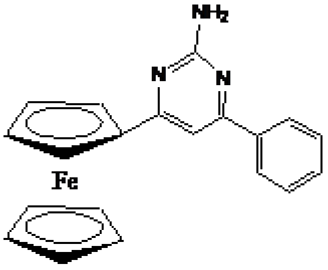

G. S. Rashinkar, *Ind. J. Chem*, 2009, 48B, 606

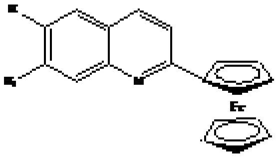

A. Patti, *J. Organometallic. Chem*, 2012, 716, 216

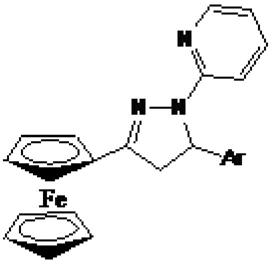

V. Kudar, *J. Organomet. Chem*, 2005, 690, 4018

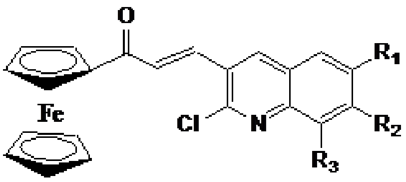

M. Gormen, Middle Eeast Technical University, 2005

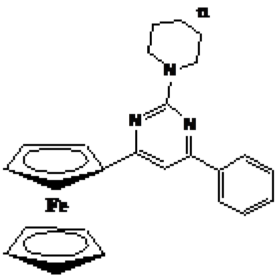

H. Parveen, *Eur. J. Med. Chem*, 2010, 45, 3497

REFERENCES:

1. American Cancer Society. Cancer Facts & Figures 2017. Atlanta: American Cancer Society; (2017).
2. Benson J., Jatoi I., Keisch M., Esteva F., Makris A., Jordan V. Lancet, 373, 1463–1479 (2009).
3. Biot G., Glorian L., Maciejewski A., Brocard J., J. Med. Chem., 40, 3715 (1997).
4. Liu; W., Gust; R. Chem. Soc. Rev., 42, 755–773 (2013).
5. Sambrook, J., Fritsch, E.F. and Maniatis, T. Molecular cloning, A laboratory Manual. 2ndEdn. Cold Spring Harbor Laboratory, Cold Spring Harbor, New York (1989).
6. Bansode P., Jadhav J., Kurane R., Choudhari P., Bhatia M., Khanapure S., Salunkhe R., Rashinkar G. RSC Adv., 6, 90597-90606 (2016).
7. Anantacharya R, Manjulatha K, Satyanarayan ND, Santoshkumar S, Kaviraj MY. Cogent Chem, 2, 1172542 (2016).

STRUCTURAL AND MORPHOLOGICAL STUDY OF $BaNd_{1.98}La_{0.02}Ti_3O_{10}$ AND $BaNd_{1.96}La_{0.04}Ti_3O_{10}$ CERAMICS

P. B. Abhange[1], N. T. Padal[2], S. Chandralingam[3] and S. R. Kokare[4*]
[1]Department of Physics, G. M. Vedak College of Science,
Tal. Dist. – Raigad, MS, 402111, India
[2]Department of Physics, Willingdon College, Sangli
[3]Jawaharlal Nehru Technological University, Hyderabad, Telangana- 500085, India
[4]Department of Physics, Raje Ramrao Mahavidyalaya, Jath, Dist- Sangli, MS 401404
*Corresponding author E-mail: kshirikant@yahoo.com

ABSTRACT:

The high dielectric constant, low dielectric loss, high quality factor and small temperature coefficient ofresonant frequency are important characteristics ofmicrowave dielectric materials. Due to thehazardous nature of lead based ceramics many researchers have paid great attention to synthesize lead-free perovskite ceramic. Here wehave synthesized the material$BaNd_{2-x}La_xTi_3O_{10}$(for x = 0.02 and 0.04) by solid statereaction method which is low cost and easy. The X- RayDiffraction (XRD) data confirms its orthorhombic crystalstructure and Scanning Electron Microscopy (SEM) picturegives the average grain size less than 2 µm. The dielectric measurement gives temperature independency in the range from roomtemperature to 523 K.

Keywords: Barium Neodymium Titanate, Microwave Ceramic, ferroelectric materials, DielectricConstant.

INTRODUCTION:

The microwave applications related to radio, high-speed microelectronics, radar and telecommunications are todays increasing market demand of microwave devices. The microwave dielectric ceramics have become very important materials due to their growing potentialin applications to mobile communication system [1-3]. The high dielectric constant, low dielectric loss, highquality factor and small temperature coefficient of resonant frequency are the most desirable characteristics of the microwave dielectric materials [4].The ferroelectric materials having high dielectric constant and low dielectric loss plays animportant role in devices like high-speed random access memories (FRAMs) anddynamic random access memories (DRAMs). The earlier researchers have reported that the compounds in Ba-Nd-Ti-O systems possess excellent dielectric properties and temperature stability; therefore they can be used in microwave devices [5-7].Also the recent trends in technological developmentof microwave integrated circuits (MICs) are attracting the material scientiststo synthesize a newer material having high power, small size, light weight, and low costfor passive as well as active devices for microwave applications.[8-10]. In last decade there are large number of research publications on thehot topic of environment friendly lead free materials. The European Union(EU) in2003 included lead (Pb) in its legislature to be a hazardoussubstance. Similar activities and regulations are carried bymany countries in the world. The literature survey madeby Chinese scientist Yong-Xiang Li [11] indicates that thelead free material synthesis is the need of present for betterfuture. At the 9th international meeting on ferroelectricity,the demand of eco materials or environment friendlymaterials are pointed out that ferroelectric material shouldcomprise non-hazardous substance [11]. Since then manygroup has paid great attention to the research on non-leadbased perovskite ceramic.

EXPERIMENTAL:

To synthesize the required material we have chosen the solid-state reaction method which is low cost and easy. Parent materials were $BaCO_3$, Nd_2O_5,TiO_2 and La_2O_3 (more than 99.9 % pure) in the powder form. These powders wereweighed and mixed in stoichiometric proportion with anacetone to grind for 2 hours with agate mortar.After grinding the powder were presinteredat 1050 ^{0}C for five hours. After presintering the material was again grinded in an agate mortar for 1 hour and used for pelletization. Polyvinyl acetate (PVA) was used as anorganic binder. Five ton/cm^2 pressure is applied whilepelletization. The pellets were sintered in an aluminium crucible at 1150 ^{0}C for seven hours. Sintered samples areallowed to anneal at the rate of 20C/min up to 400^{0}C.Further the samples are brought to room temperature bynatural rate of cooling.The synthesized material was studied for their structuralcharacterization through powder x-ray diffraction pattern.Miniflex-2 Goniometer was used to scan the sample fromangle (2θ) 20 to 80 with step of 0.02 and CuKα as sourceof x-rays. Further the morphological studies were madeusing Scanning Electron Microscopy (SEM). The samplesare exposed by the SEM with x500, x5000, x10000 andx20000 with 20 KV as an excitation voltage.Density of the synthesized material was obtained byhydrostatic weighing method and it is observed that thematerials synthesized werehaving more than 98% denseas compared to its theoretical density. The dielectricmeasurements were carried out using a PrecessionalImpedance Analyzer (Wayne-Kerr 6500B) in thetemperature range from roomtemperature to 523 K. Thetemperature variation is made by laboratory designedvertical tubular furnace. The complex impedance variationand its temperature dependence are also studied with thesame setup.

RESULTS AND DISCUSSION:

XRD:

Figures 1 and 2 shows the XRD patterns of $BaNd_{2-x}La_xTi_3O_{10}$ for x=0.02 x=0.04.These XRD patternsarecompared with the standard JCPD data (JCPDF No. 35-0331). The comparison showsthat the patterns are in good agreement with the reported data. The nature of synthesizedbulk powders of lanthanum-doped barium neodymium titanate is orthorhombic.The XRD patterns do not contain any additional peaks and it is due to the very small doping of lanthanum.

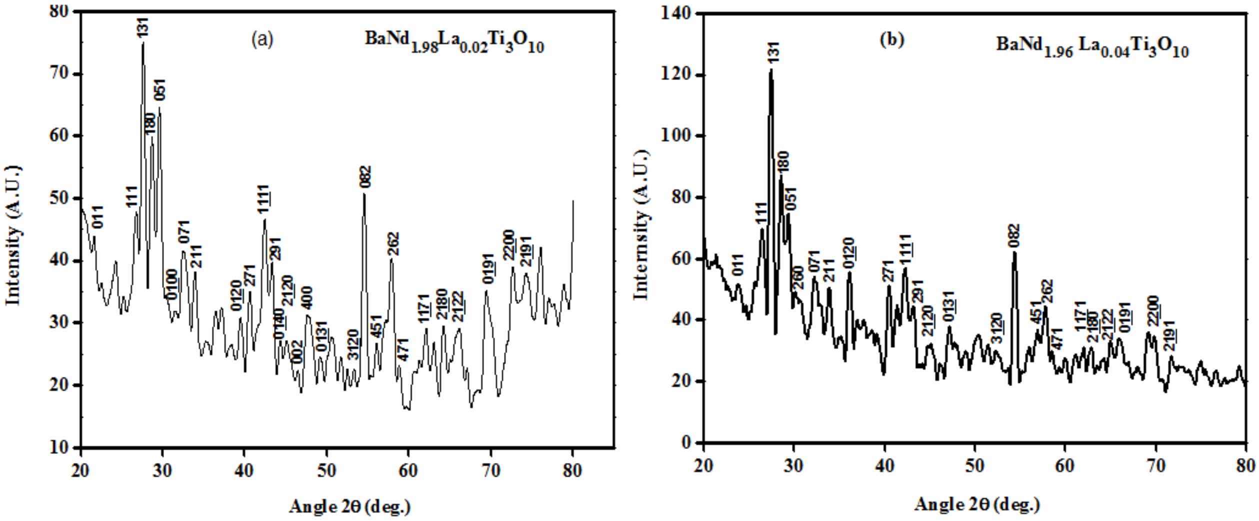

Fig. 1: XRD patterns of (a) $BaNd_{1.98}$ $La_{0.02}Ti_3O_{10}$ and (b)$BaNd_{1.96}$ $La_{0.04}Ti_3O_{10}$

SEM:

The surface morphology of synthesized material can be studied the scanning electron microscopy (SEM).TheSEM images confirms that the material synthesized is dense. Also the SEM micrographs confirms that thematerial synthesized is of single phase with grain size varying from4-5 µm to 400 nm.Figure 2 gives the SEMmicrographs of $BaNd_{1.98}La_{0.02}Ti_3O_{10}$ and$BaNd_{1.96}La_{0.04}Ti_3O_{10}$.

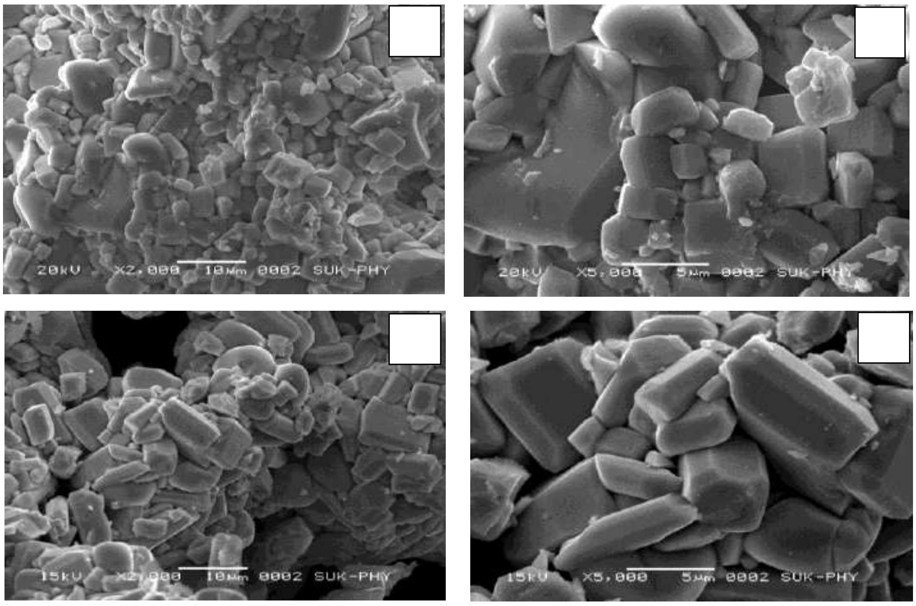

Fig. 2: SEM pictures of (a and b) $BaNd_{1.98}$ $La_{0.02}$ Ti_3O_{10}(c and d) $BaNd_{1.96}$ $La_{0.04}$ Ti_3O_{10}

Dielectric constant:

Figure 3 shows temperature dependence ofdielectric constant of the synthesized samples. From figures it was found that there is no direct effect of temperature variation on the dielectric constant of all thesamples[1]. However beyond 450 K temperaturethe dielectric constant slightly increases. Thetemperature variation was made from room temperature to523 K.From figures it is observed that the room temperaturedielectric constant is more than 100. From the earlierreport it is observed that the dielectric constant is less than 100. This increase in dielectric constant is observed due to the increase in level of substitution, since for x=0.02 the value of dielectric constant is nearly 125 and it is nearly 500 for x=0.04. This value of doping concentrationand the dielectric constant suggest that one may tailor thedoping concentration still further to achieve the largerdielectric constant by keeping the low dielectric loss. This is an optimistic result towards its microwave dielectric constants. The values ofloss factor are also promising andit remains below unity. The variation of loss factor withtemperature gives goodcoordination with thedielectricconstant. Fig.3 shows the loss factor variation withtemperature.

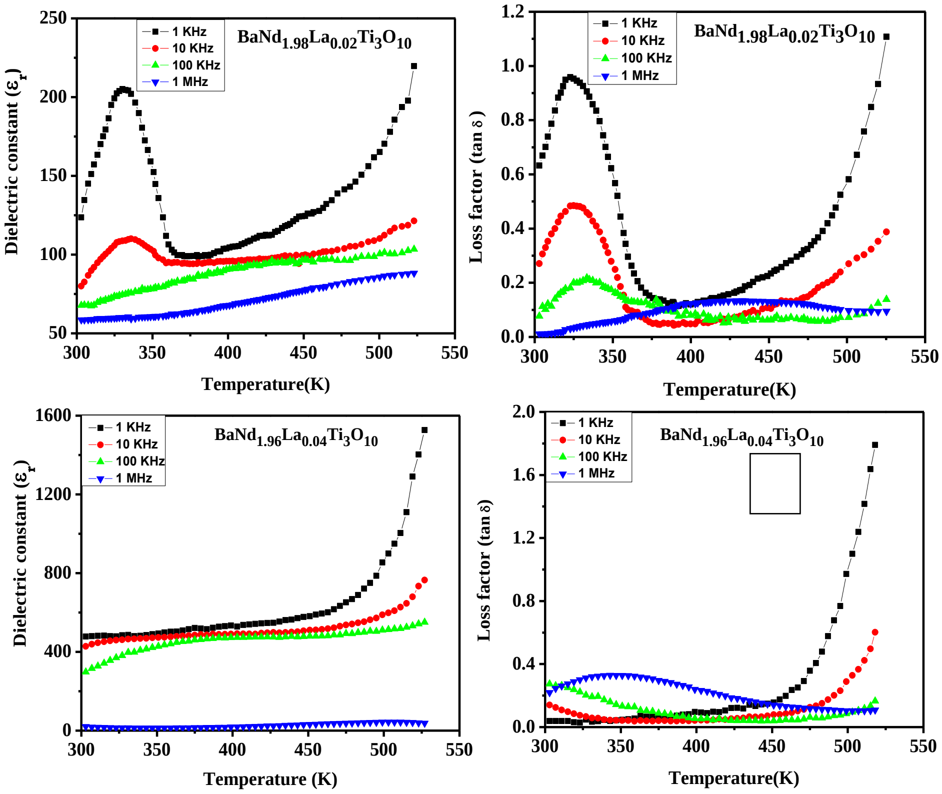

Fig. 3: Variation of Dielectric constant (□ r) and Loss factor(tan□) with Temperature for (a, b) $BaNd_{1.98}La_{0.02}Ti_3O_{10}$ and (c, d) $BaNd_{1.96}La_{0.04}Ti_3O_{10}$

CONCLUSION:

The lanthanum doped $BaNd_2Ti_3O_{10}$ materials were preparedby solid state reaction method, pressing and sinteringat 1150°C. The XRD patterns confirm that the material formed is oforthorhombic in nature. Also the XRD patterns contains no additional peaks, it is due to thevery small doping concentration of lanthanum. The SEM images confirm that the materialformed is dense. Also SEM confirms the single phase material synthesis with average grainsize less than 2 μm.The increase in dielectric constant increase in doping concentration withsmall dielectric loss is indication that material can beuseful for microwave dielectricresonators. However, toget any final conclusion one may need to study the dielectricresponse at microwave frequencies with fine tuning ofsubstitution.

REFERENCES:

1. C. -H. Lu and Y. -H. Haung, Mate. Sci. and Eng., B 98, pp. 33-37 (2003).
2. K. Wakino, T. Nishikawa, Y. Ishikawa, H. Tamura, Brit. Ceram.Trans. J. vol.89, pp.39-43 (1990).
3. X. M. Chen and J. S. Yang, J. Eur. Ceram. Soc. Vol.19, pp.139-142 (1999).
4. E. A. Nenasheva and N. F. Kartenko, J. Eur. Ceram. Soc., vol. 21, pp.2697-2701 (2001).
5. J. H. Choi J. H. Kim, B. T. Lee, Y. M. Kim, J. H. Moon, Mater. Lett., vol. 44, pp. 29-34 (2000).
6. X. M. Chen, Y. Suzuki, N. Sato, Mater. Lett., vol.16, pp.75-78 (1993).
7. D. Kolar, S. Gaberscek, B. Voavsek, J. Solid State Chem. vol.38, pp. 158-164 (1981).
8. R. Ratheesh, H. Sreemoolanadhan, M. T. Sebastian, P. Mohanan. Ferroelectrics, 211, 1-8 (1998).
9. D. Kolar, S. Gaberscek, B. Volavset, H. S. Parker, R. S. Roth., J. Solid State Chem, 38, 158-164 (1981).
10. J. M. Durand, J. P. Boilot. J. Mater. Sci. Lett, 6, 134-136 (1987).
11. Y.-Q. Lu and Y.-X.Li, J. Adv. Dielectrics, vol.3, p.269 (2011).

STRUCTURAL AND OPTICAL STUDY OF CHEMICALLY DEPOSITED CUPROUS OXIDE (Cu_2O) THIN FILMS

Pavan K. Pagare and A. P. Torane*

Solid State Physics Laboratory, Department of Physics,

Yashavantrao Chavan Institute of Science, Satara, 415001, Maharashtra, India

Corresponding author E-mails: appasahebtorane@yahoo.in, pavanpagare25@gmail.com

ABSTRACT:

Cu_2O thin films have been deposited onto fluorine doped tin oxide (FTO) substrates using chemical bath deposition method. The structural, vibrational and optical properties of the deposited thin films have been studied by using X-ray diffraction (XRD), UV-Visible, and Raman spectroscopy techniques. The maximum intensive peak of Cu_2O thin film is observed at (111) hkl plane. The optimized band gap of Cu_2O thin film is found to be 2.36 eV. The Raman spectroscopic result shows maximum intensive peak at 110 cm^{-1} with other peaks of Cu_2O. Above all properties shows that pure Cu_2O phase is formed using chemical bath deposition (CBD) method.

Keywords: Chemical bath deposition; Cu_2O; Band gap; Raman spectroscopy; Thin Films.

INTRODUCTION:

Copper is an important material due to its good electrical conductivity, high catalytic activity, and low growth temperature. Cu_2O is a first known semiconducting material having direct band gap of 2.17 eV [1]. Cu_2O is well known material for low cost, earth abundant, promising visible light absorption and non-toxic [2].Cu_2O thin films having large number of applications such as photocatalyst [3], solar cell [4], glucose sensor [5], solar water splitting [6], gas sensor [7], chemiluminescence [8], transistors [9] and lithium ion batteries [10].

Nowadays chemical bath deposition method is more useful for the deposition of thin films. While there are numerous methods are available for deposition of Cu_2O thin films. The deposition of Cu_2O is carried out using other techniques such as electrodeposition, radio frequency magnetron sputtering, solvothermal, sol gel method [11-14] and etc. The deposition of Cu_2O as p-type and n-type semiconductor is also promising by varying bath pH [15]. The formation of single phase Cu_2O with different morphology is very difficult task. The change in bath pH, chemical concentration and bath temperature of Cu_2O gives morphologies like cuboctahedra, cubes, complete octahedra, tip-truncated octahedra, truncated octahedra, nanowires, nanotubes, tip-truncated cubes [16, 17].

In this study, we report deposition of Cu_2O thin films onto FTO substrates using chemical bath deposition method. The variation in concentration, pH, and temperature of bath, we obtained optimized Cu_2O thin films. The reported results display that the pure Cu_2O phase is formed in absence of other mixed phases of copper. The optimized band gap detects that it is promising material for photovoltaic applications.

EXPERIMENTAL:

Preparation of Cu_2O thin films:

Cuprous oxide (Cu_2O) thin films were prepared onto FTO substrates via chemical bath deposition method. Firstly FTO substrates were washed with laboline and double distilled water. The solution containing all analytical reagent chemicals such as 1.5 M $CuSO_4$ and 0.5 M $C_3H_6O_3$. A 5M NH_4OH was used for balancing the pH. The 50 ml solution was stirred for 3h and heated upto 40^oC. The deposited Cu_2O thin films were washed with double distilled water and dried by hair dryer. After deposition the thin films were annealed in air atmosphere at 450 ^oC for 5h.

Characterizations:

The crystal structure of Cu_2O thin films was studied by X-ray diffraction (XRD) technique with model Bruker D8 Advance with Cu Kα radiation ($\lambda=1.54A^o$) in the range (2θ) of 30° - 80°. The chemical composition inside the morphology were analyzed using energy dispersive X-ray spectroscopy (EDAX) of model JEOL JSM-6360 having operating bias voltage 20kV. The optical measurements were carried out using UV-Visible spectrophotometer SYSTRONICS 119.The Raman spectra was studied by micro-Raman Renishaw spectrometer of wavelength 532 nm.

RESULTS AND DISCUSSION:

XRD measurement:

The phenomenon of X-ray diffraction is administered by the Bragg's diffraction law,

$$2d\sin\theta=n\lambda \tag{1}$$

Where λ is the wavelength of the monochromatic X-ray,'d' is lattice spacing, 'n' is order of diffraction and θ is diffraction angle.

The XRD pattern of Cu_2O thin films is as shown in Fig. 1. The XRD results of Cu_2O thin films shows polycrystalline in nature. The peaks of FTO onto Cu_2O thin films marked by dollars. The bath temperature was kept constant at 40 ^oC. The 2□ values of deposited Cu_2O thin films are in good agreement with standard values of JCPDS card no. 03-0892.

The XRD results shows the hkl plane (111) is more intensive having $2\theta = 36.56^o$. The other weaker peaks of Cu_2O thin films observed are at $2\theta = 42.21^o$, 61.40^o, and 74.05^o show (200), (220), and (311) hkl planes respectively [18].

The crystallite size (D) for the more intensive peaks (111) of Cu_2O thin films are valued by full width at half maximum (FWHM) using Debye- Scherrer's formula:

$$D=0.9\lambda/\beta\cos\theta \qquad (2)$$

Where θ is the Bragg's angle, D is crystallite size, λ is wavelength of X-ray used, β is full width at half maximum of the peak in radian and 0.9 is a constant. The crystallite size 25.30 nm is observed for (111) plane.

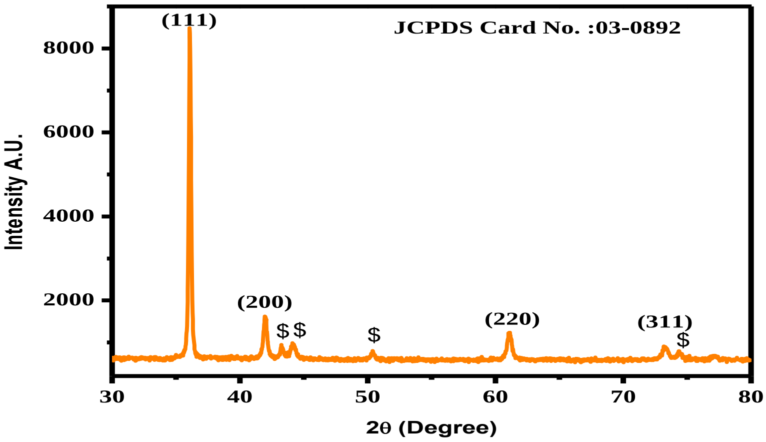

Fig.1: XRD pattern of Cu_2O thin films

Chemical composition study:

The chemical composition of Cu_2O thin films was measured by energy dispersive X-ray spectroscopy (EDAX) method. The EDAX pattern of Cu_2O thin films is as shown in Fig. 2. The results display that the occurrence of Sn in EDAX is accredited due to Cu_2O deposited onto SnO_2 substrates and it also marks more atomic weight percent of oxygen (O) in associated to Cu. The EDAX patterns display no other impurity peaks, which confirm the purity of Cu_2O material.

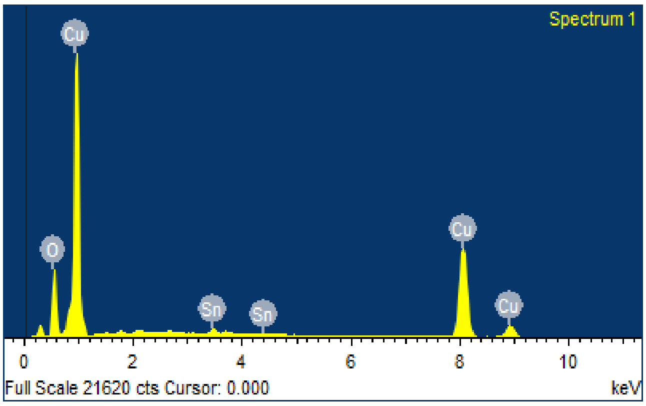

Fig. 2: EDAX spectra of Cu_2O thin films

Optical measurements:

The optical band gap (Eg) of Cu_2O thin films using absorption spectra is determined by the equation.

$$(\alpha h\nu) = A\,(Eg - h\nu)^n \qquad (3)$$

Where Eg band gap, hν incident photon energy, A constant, □ coefficient of absorption and n determines the electronic transition causing absorption. Tauc plot detects the value of band gap of Cu_2O thin films in Fig.3. The optical band gap of optimized Cu_2O thin films is found to be 2.36 eV. The reported band gap value is related to our previous reports on Cu_2O thin films prepared by electrodeposition method [19].

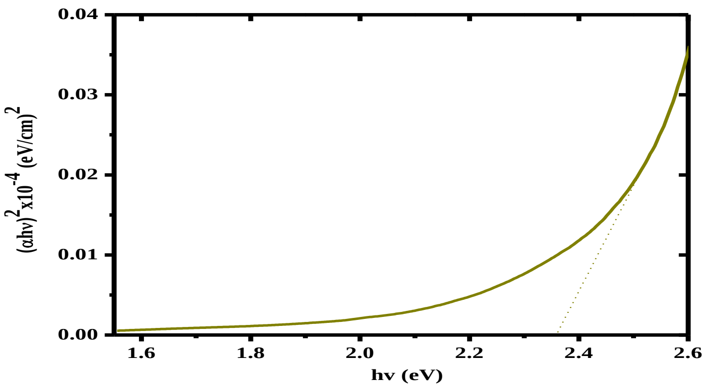

Fig. 3: Tauc plot of Cu_2O thin films

Raman spectra of thin films:

The Raman spectroscopy in the range of 100 to 700 cm^{-1} is as shown in Fig. 4. It specifies that pure Cu_2O phase is formed. The strongest peak is detected at 110 cm^{-1}, extra peaks of Cu_2O are displayed at 148, 201, 220, 525, and 635 cm^{-1}. The peaks at 148, 220, and 635 cm^{-1} are matching to second order overtone □$_{□□□}^{□□□}$□ □ 2□$_{□□}$□ □ and □$_{□□□}^{□□□}$□ vibrations of the Cu_2O thin films respectively [19, 20].

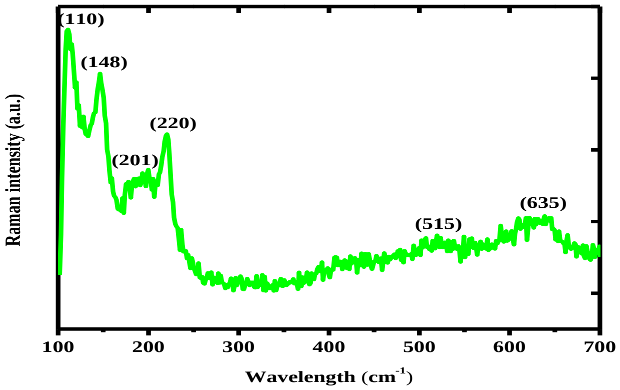

Fig. 4: Raman spectra of Cu_2O thin films

CONCLUSIONS:

In summary, we successfully synthesis Cu_2O thin films using chemical bath deposition method. The crystallite size of Cu_2O thin films is found to be 25.30 nm for (111) plane. The EDAX pattern confirms the chemical composition of Cu_2O material. The band gap 2.36 eV is observed for the Cu_2O thin films. The Raman spectroscopy shows single phase Cu_2O thin films, in absence of other impurities like Cu, CuO, and $Cu\,(OH)_2$. Above all properties indicates that Cu_2O is the best candidate for photovoltaic applications.

REFERENCES:

1. Mei L-P, Feng J-J, Wu L, Chen J-R, Shen L, Xie Y, Wang A-J, Microchim Acta, 183:2039 (2016).
2. Kim J, Kim HS, Choi J H, Jeon H, Yoon Y, Liu J, Park J-G, Braun P V, Chem Mater, 26:7051 (2014).
3. Luo Y, Huang Q, Li B, Dong L, Fan M, Zhang F, Applied Surface Science 357:1072 (2015).
4. Vequizo J J M, Zhang C, Ichimura M, Thin Solid Films 597:83 (2015).
5. Mei L-P, Song P, Feng J-J, Shen J-H, Wang W, Wang A-J, Weng X, Microchim Acta, 182:1701 (2015).
6. Ma Q-B, Hofmann J P, Litke A, Hensen E J M, Sol Energy Mater Sol Cells 141:178 (2015).
7. Hsu C-L, Tsai J-Y, Hsueh T-J, Sensors and Actuators B 224:95 (2016).
8. Kaviyarasan K, Anandan S, Mangalaraja RV, Sivasankar T, Ashokkumar M, Ultrasonics Sonochemistry 29:388 (2016).
9. Al-Jawhari H A, Mater Sci Semiconductor Processing 40:241 (2015).
10. Valvo M, Rehnlund D, Lafont U, Hahlin M, Edstr¨oma K, Nyholm L, J Mater Chem, A 2:9574 (2014).
11. Pagare P K, Torane A P, J Mater Sci: Mater Electron 28**:**1386 (2017).
12. Poulopoulos P, Baskoutas S, Pappas S D, Garoufalis C S, Droulias S A, Zamani A, Kapaklis, V, J Phys Chem C 115:14839 (2011).
13. Luo X-L, Wang M-J, Yun L, Yang J, Chen Y-S, J Phys Chem Solids 90:1 (2016).
14. Yu W L, Lin Y Z, Zhu X W, Hu Z G, Han M J, Cai S S, Chen L L, Shao H H, J Appl Phys 117: 045701 (2015).
15. Liau L C-K, Lin Y-C, Peng Y-J, J Phys Chem C 117:26426 (2013).
16. Susman M D, Feldman Y, Vaskevich A, Rubinstein I, ACS Nano 8:162 (2014).
17. Choi K-S, Dalton Trans 40:5432 (2008).
18. JCPDS card no. 03-0892.
19. Pagare P K, Torane A P, Microchim Acta 183:2983 (2016).
20. Pagare P K, Torane A P, Mater. Res. Express 4:105011 (2017).

CHEMICAL SYNTHESIS AND CHARACTERIZATION OF La^{3+} SUBSTITUTED Mg-Zn FERRITE

R. A. Bugad[1], R. G. Khanapure[1], B. B. Navale[2] and B. R. Karche[3]
[1]Sangola College, Sangola, Dist: Solapur (M.S.) 413307, India
[2]Vidnayan Mahavidhayalay, Sangola, Dist: Solapur (M.S.) 413307, India
[3]Materials and Thin Films Laboratory, Department of Physics,
Shankarrao Mohite Mahavidyalaya, Akluj, Dist: Solapur (M.S) 413101, India

ABSTRACT:

Nanoparticles of Lanthanum substituted Magnesium Zinc ferrites with general formula $Mg_{0.6}Zn_{0.4}La_{2y}Fe_{2-2y}O_4$ (where y = 0.0, 0.05, 0.1, 0.15, 0.20 and 0.25) have been synthesized using co-precipitation method. The prepared sample was characterized by different physical and chemical characterization techniques for their structural and micro-structural properties. The X-ray diffraction (XRD) analysis was carried out to confirm the single-phase cubic spinel structure of La^{3+} substituted magnesium zinc ferrites. As composition y varies from 0.00 to 0.25 then lattice constant decreases from 8.4514 A^o to 8.4488 A^o. The surface morphology of L-MZF shows that the interlocked nanoparticles with average grain size varying from 300 nm to 40 nm. Also, energy dispersive analysis by X-ray (EDAX) shows the presence of all the metals in the exact composition as that of precursors used for preparation of samples.

INTRODUCTION:

Magnetic properties of nanoparticles find wide technological applications such as high density recording, magnetic refrigeration, Spintronics and drug delivery etc. [1-2]. Ferrites have wide application in cores of audio frequency and high frequency transformer coils, magneto optical displays, electromagnetic wave absorption [3]. Ferrites containing Mg and Zn have higher resistivity and it makes more effective in higher frequency [4]. Lanthanum doped Mg-Zn ferrites are found to exhibit large relaxation which made them useful for microwave application [5]. It is found that magnesium – Zinc ferrite with x= 0.3 were significantly obtained magnetic properties. The $Mg_{0.7}Zn_{0.3}Fe_2O_4$ is one of a ferrites material, displaying increasing magnetic properties [6].The addition of rare earth metal ions like La^{3+} introduces changes in the structure and texture. [7]. Ishtiaq Ahmad reported that lanthanum substituted magnesium zinc ferrite finds a wide number of applications in gas sensors [8].

EXPERIMENTAL:

Synthesis of La3+ substituted Mg-Zn ferrite:

The $Mg_{0.6}Zn_{0.4}La_{2y}Fe_{2-2y}O_4$ **(**where y=0.0, 0.05, 0.10, 0.15, 0.20 & 0.25) were prepared by the oxalate co-precipitation method. The high purity starting materials $MgSO_4.7H_2O$, $ZnSO_4.7H_2O$, $LaSO_4.7H_2O$ and $Fe_2SO_4.7H_2O$ were used for preparation of samples. All chemicals are in AR grade. These chemicals were weighted in desired stoichiometric proportion and dissolved in distilled water. The pH of the solution was maintained at 4.8 by drop wise addition of concentrated H_2SO_4. The resulting solution was heated at 80 ^{0}C for 1 h in order to complete the ionization of metal sulfates [9].

RESULTS AND DISCUSSIONS:

XRD studies:

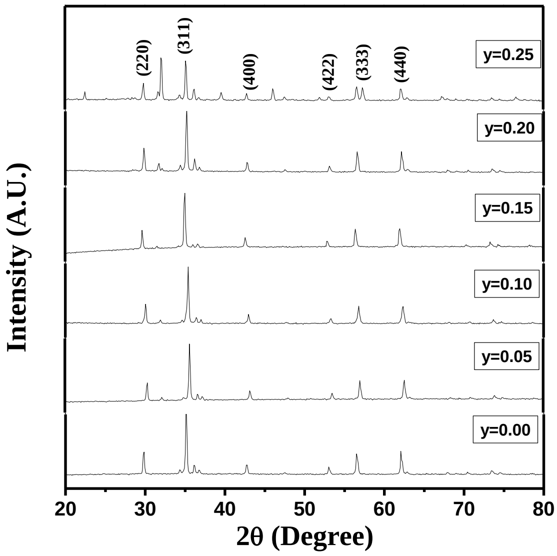

Fig.1: XRD patterns of $Mg_{0.6}Zn_{0.4}La_{2y}Fe_{2-2y}O_4$ Ferrite System

Fig.1 shows the XRD patterns of composition $Mg_{0.6}Zn_{0.4}La_{2y}Fe_{2-2y}O_4$ (where y = 0.0, 0.05, 0.1, 0.15, 0.20 and 0.25). The analysis of XRD patterns reveals that all the samples have single phase spinel cubic structure. The interplaner spacing was calculated using the relation [1];

$$d_{cal} = \frac{n\lambda}{2.\sin\theta} \qquad \text{----- (1)}$$

Surface morphological studies :

The measurement of grain size is counted by counting the number of grain boundaries intersected by a known measured length from the magnification. By drawing random such line and repeating same procedure average grain size is calculated.

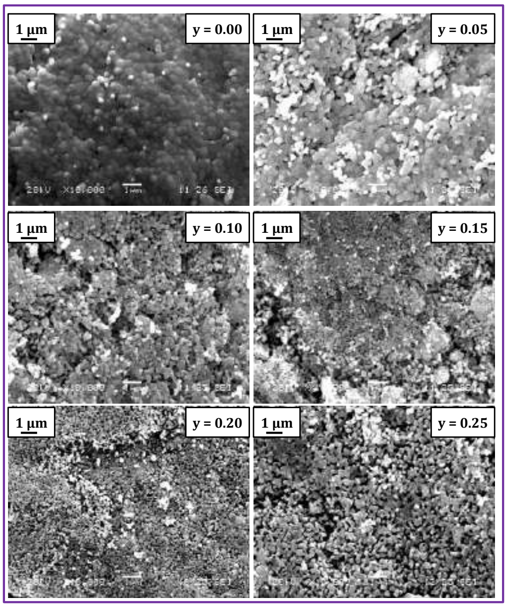

Fig. 2: SEM of $Mg_{0.6}Zn_{0.4}La_{2y}Fe_{2-2y}O_4$ Ferrite System

EDAX studies:

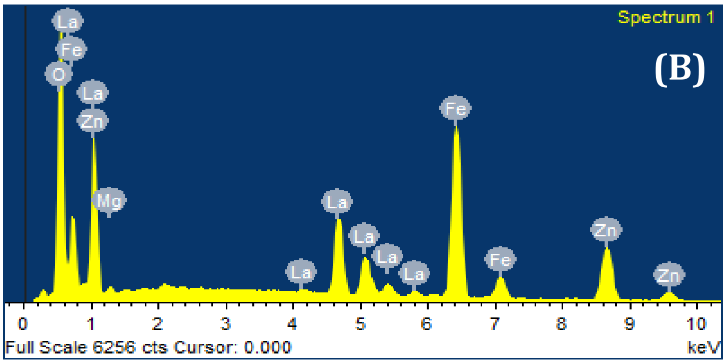

Fig. 3: EDAX patterns of $Mg_{0.6}Zn_{0.4}La_{2y}Fe_{2-2y}O_4$ System

Two representative EDX spectra are shown in Figs. 3. Fig. 3 indicates La substituted Mg-Zn ferrite. EDX has been performed in order to study the compositional analysis of La substituted Mg-Zn ferrite. EDX analysis exhibits the elemental percentage of each element expected to be present in the La substituted Mg-Zn ferrite sample. The heights of the peaks in the EDX graphs represent the proportion of each element in the finally sintered La substituted Mg-Zn ferrite. A change has been observed in the size and height of the peaks of all the La-substituted samples. With the increase of La concentration, the graph exhibits an increase in the height of the La peaks. In the present study, the Lanthanum is substituted for iron. Hence, the amount of iron decreases and this decrease in iron is observed in the peak height of Fe as shown in Fig. 3. The observed percentage of metals of each composition is consistent with the stoichiometry of the prepared samples.

Table1: Different parameters estimated for $Mg_{0.6}Zn_{0.4}La_{2y}Fe_{2-2y}O_4$ from XRD technique

La^{3+} content y	Crystalline size (D) nm	Lattice constant In A.U.	Ionic Bond length in A.U. (A-O)	Ionic Bond length in A.U. (B-O)	Ionic Radii A.U. Tetrahedral (R_A)	Ionic radii A.U. Octahedral (R_B)
0.00	48	8.4514	1.9176	2.0621	0.6576	0.8021
0.05	48	8.4509	1.9175	2.0620	0.6575	0.8020
0.10	45	8.4506	1.9174	2.0619	0.6574	0.8019
0.15	41	8.4501	1.9173	2.0618	0.6573	0.8018
0.20	42	8.4497	1.9172	2.0617	0.6572	0.8017
0.25	41	8.4488	1.9170	2.0615	0.6570	0.8015

Table2: Different parameters estimated for $Mg_{0.6}Zn_{0.4}La_{2y}Fe_{2-2y}O_4$ from XRD technique

La^{3+} content y	physical density D_p gm/cc	X-ray density D_x gm/cc	Porosity (P)%	Grain size
0.00	4.0189	4.7641	15.64	300
0.05	4.2333	4.9455	14.40	210
0.10	4.4152	5.1288	13.91	142
0.15	4.6223	5.310	12.95	118
0.20	4.8122	5.4961	12.44	95
0.25	4.9891	5.6809	12.18	130

CONCLUSION:

Lanthanum substituted magnesium zinc ferrite is cubic spinel ferrite. Nanocrystaline Lanthanum substituted magnesium zinc ferrite have been prepared by oxalate co-precipitation method at a pre-sintering temperature of 700^0C for 5h and final sintering temperature of 900^0C for 12h . The crystalline size and Lattice constant exhibit decreases as a function La+ concentration. . The linear variation of X-Ray density with La+ content suggest the occupancy of La+ on tetrahedral (A) sites. Crystallites size of all samples is found in the range of 48 nm to 41 nm. The effect of lanthanum substitution was observed on X-ray density, ionic radius and bond length. Bond length and ionic radii were decreases with La^{3+} content. X-ray density of samples goes on increasing with La^{3+} content and found in the range 4.76 gm/cc to 5.68 gm/cc. The microstructure of ferrite prepared by co-precipitation method consists of grain size in the range 300 to 95. The structure is compact with small amount of pores on the scale of crystallites.

REFERENCES:

1. P. C. Rajesh Varma et.al, J. Alloys.comp. 453, 29 (2008).
2. Mytil Kahn and John Zhang (2001).
3. S.N. Dolia, Solid State Phenomena, 171, 79-91 (2011).
4. Skolyszewska, B., Physica C, 387: 290-294 (2003).
5. R.U. Mullai, P. Priyadharsini Pradeep, G.Chandrasekaran, Inter. J. Recent Trends Sci. & Tech. Vol. 5, 78-85 (2012).
6. Aurawan Rittidech and Panuthat Khotsongkram. American J. Appl. Sci.3(3); (2006), 1760-1762.
7. Ishtiaq Ahmad, Muhammad Tahir Farid, Robina Kousar and Shahida. B. Niazi. World Appl. Sci. J. 22(6): 796-801 (2013).
8. Liu, Y.L., Z.M.Liu, Y.Yang, H.F. Yang, G.L. Shen and R.Q. Yu, Sensor and Actuators B; Chem. 107, 600-604 (2005).
9. A. B. Gadkari, T. J. Shinde, P. N. Vasambekar, J. Mater Sci: Mater Electron 21, 96-103 (2010).

A FACILE FABRICATION OF DURABLE PS-SiO_2 COMPOSITE SUPERHYDROPHOBIC COATINGS

Rajaram S. Sutar [1], A. K. Bhosale [1]* and Sanjay S. Latthe [1]*

[1] Self-cleaning Research Laboratory, Department of Physics,
Raje Ramrao College, Jath 416 404, Maharashtra, India
*Corresponding authors E-mail: latthes@gmail.com, akbhosale1@gmail.com

ABSTRACT:

The superhydrophobic surfaces are known for high water contact angle (>150°) and low sliding angle (<10°). The hydrophobic silica nanoparticles suspension was deposited on clean glass plate by dip-coating method. This silica nanoparticle deposited glass plate again coated by layer of polystyrene (PS) to form durable superhydrophobic surface. A superhydrophobic coating with a water contact angle (WCA) 168° was achieved. A sliding angle (SA) of less than 3° can help for the self-cleaning properties of the superhydrophobic surface which mimics lotus effect. The mechanical durability of the prepared superhydrophobic coatings was confirmed by water drop impact test and stability was confirmed by adhesive tape test. A dip-coating technique is suitable to fabricate superhydrophobic, self-cleaning and adherent coating which can be applicable for windows glass, solar cell module, vehicle glass, metals, fabrics and many.

INTRODUCTION:

The surface structure of lotus leaf has two levels of roughness (on the micro and nano scale) that enable the rolling water droplet effect, it is characteristic of a well-designed superhydrophobic surface. Self-cleaning Lotus leaf is a well-known superhydrophobic surface in nature which is composed of micro and nanometer-scaled patches coated with a few nanometer thick hydrophobic wax layers [1, 2]. A surface with micro- or nano sized roughness was developed by lithography technique or by deposition of a micro or nano-materials, molecules with a low surface energy were deposited for water-repelling properties [3]. Shuaixia et al have reported solution casting method to deposit amorphous polystyrene (PS) under ambient atmosphere and the resultant coating showed unitary micro-scale structure and showed excellent superhydrophobicity [4]. Cheng-Wei Tu and his research group have sprayed a PS solution onto a large area of any type of substrates and formed superhydrophobic film that consists of a mixture of micro-bead and nano-fiber structures with water contact angle 155° [5]. Bravo and co-researcher demonstrated the transparent superhydrophobic coating by layer-by-layer method using various sizes of SiO_2 nanoparticles. Thickness and roughness was increased with increasing layers and transparency decreased. The nanoporous nature of the silica nanoparticle layer gives rise to antireflection properties [6].

Lebo et al have reported the roughness of surface was increased by using silica nanoparticles via dip-coating, which enable for water repellency. They also showed small decrease in water contact angle after water drop impact and scotch tape test [7]. Chen et al have adjusted the wettability of the surface by controlling the content of SiO_2 nanoparticles in water-repellent SiO_2/polymer composite coating [8]. Herein we report a simple method to prepare a superhydrophobic coating by silica nanoparticle deposition on glass substrate and applying a layer of PS by dip coating method with varying concentration of silica nanoparticles. Water droplets easily roll-off the surface at around 3° tilting indicating good water repellency. Superhydrophobic coating can be prepared by using cheapest polymer and simple dip coating method in low cost on large area. It is applicable for windows glass, solar cell panel, vehicle glass, metals, and apparels and so on [9-19].

EXPERIMENTAL SECTION:

Material and Chemicals:

Glass slides (75 mm long X 25 mm wide) were purchased from Polar Industrial Corporation Mumbai (India). Silica nanoparticles (RX-300-5, Hydrophobic fumed silica treated with HMDS) was purchased from NIPPON AEROSIL Co. Ltd., JAPAN. Hexane was purchased from Spectrochem Pvt. Ltd. Mumbai (India). Polystyrene (average Mw ~ 192,000) was obtained from Sigma-Aldrich Co. (USA). Toluene (99.5%) was purchased from Loba Chemie Pvt. Ltd. Mumbai (India).

Preparation of Silica Nanoparticles (SNPs) coated glass substrate:

Silica nanoparticles were dispersed in hexane with different concentrations (2, 4 and 6 mg/ml) and solution was ultrasonicated for 10 minute before coating. The cleaned glass substrate was coated using this prepared solution by dip coating method and then dried at room temperature.

Preparation of Superhydrophobic Coating:

A 4 mg/ml solution of polystyrene (PS) in toluene was prepared and it was ultrasonicated for 30 minutes. Silica nanoparticles coated glass substrate was dipped into this polymer solution for 4 minute and taken out. This PS layer coated silica nanoparticle coating was dried at temperature 100°C for 1 h. The PS modified coatings with silica nanoparticle concentrations of 2, 4 and 6 mg/ml were labeled as S1, S2 and S3 respectively.

Characterizations:

Water contact angle (WCA) and sliding angle was measured by contact angle meter (HO-IAD-CAM-01, Holmarch Opto-Mechatronics Pvt. Ltd.). Durability was investigated by water drop impact test. An adhesive tape test was performed by applying the tape on the coating and taking out gently. WCA was measured after water drop test and adhesive tape test.

RESULTS AND DISCUSSION:

Measurement of water contact angle and sliding angle:

At first, the coatings were prepared from different concentrations of the SNPs namely from 2, 4 and 6 mg/ml and dried at room temperature for 10 min. The coatings prepared with 2 to 6 mg/ml showed very less water contact angle (70° to 100°). At the same time, the coating was easily wiped out by gentle finger touch, which confirms weak mechanical stability. To improve the mechanical stability of the prepared coating, we deposited a layer of polymer (PS) on coating. The polystyrene solutions in toluene were prepared with concentrations of 4 mg/ml and the prepared SNPs coatings were dipped in these solutions for 4 minute.

As shown in **Fig.1**, after deposition of PS layer on 2 mg/ml SNPs coated coating (S1) showed water contact angle of nearly 137°. A superhydrophobicity was achieved for the 4 mg/ml SNPs deposited coating (S2) dipped in PS solution for 4 min. This is optimum SiO_2 concentration to achieve the water contact angle 168° and sliding angle nearly 3°. However for the higher concentrations (6 mg/ml) of SNPs coating (S3), the WCA was decreased (158°) due to decrease in surface roughness. For higher concentration of SNPs, the roughness achieved by SNPs was ruined by the PS and the coating is smooth in nature which is not a good for superhydrophobicity. So it was possible to achieve critical surface roughness where the 4 mg/ml SNPs coating modified with 4 mg/ml PS solution with dipping time ~ 4 min showed superhydrophobicity.

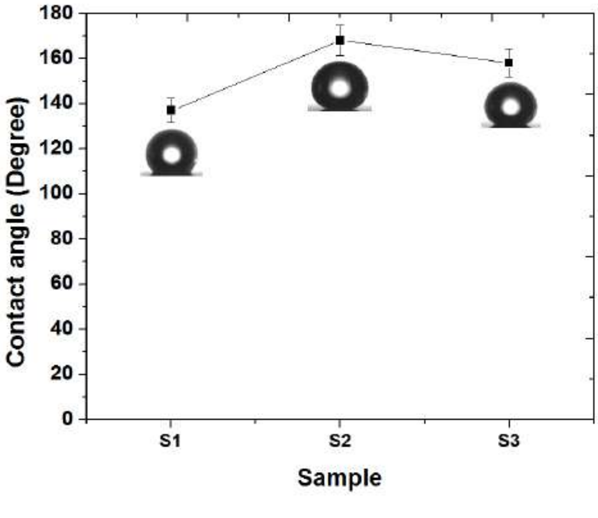

Fig.1: **Water contact angle on coating with different concentration of SNPs.**
(S1 = 2 mg/ml, S2 = 4 mg/ml, S3 = 6 mg/ml)

Adhesive Tape test:

In adhesive tape test, the tape was applied on prepared superhydrophobic coating to make good contact and gently detached from superhydrophobic coating (**Fig.2a**). The wettability of superhydrophobic surface was examined by measuring water contact angle before and after adhesive tape test. The coating prepared with SNPs concentration of 4 mg/ml (S2) showed strong adhesion between coating and glass substrate, which was confirmed by small reduced water contact angle (164°) as shown in **Fig.2b**. It indicates that prepared coating is mechanically stable. In other cases, S1 and S3 samples showed drastic decrease in water contact angle after adhesive tape test. The S1 sample showed decrease in WCA from 137° to 48°, whereas the S3 sample showed drastic decrease in WCA from 158° to 27°, confirming very poor mechanical stability.

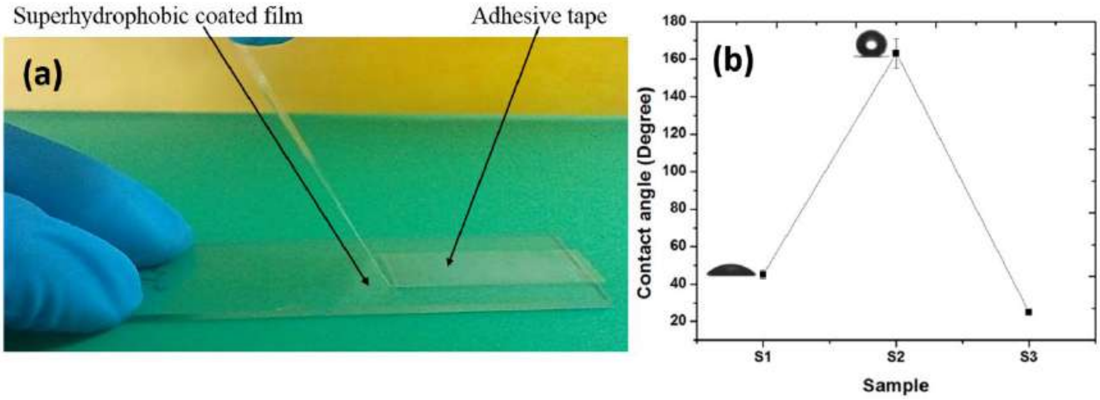

Fig.2: **(a) Detaching the adhesive tape from superhydrophobic coating. (b) Water contact angle on surface with different concentration of SNPs after adhesive tape test**

Water dripping test:

Water droplets were dropped on superhydrophobic coating from the height of 20 cm and measured the water contact angle after every one hour of water drop impact.

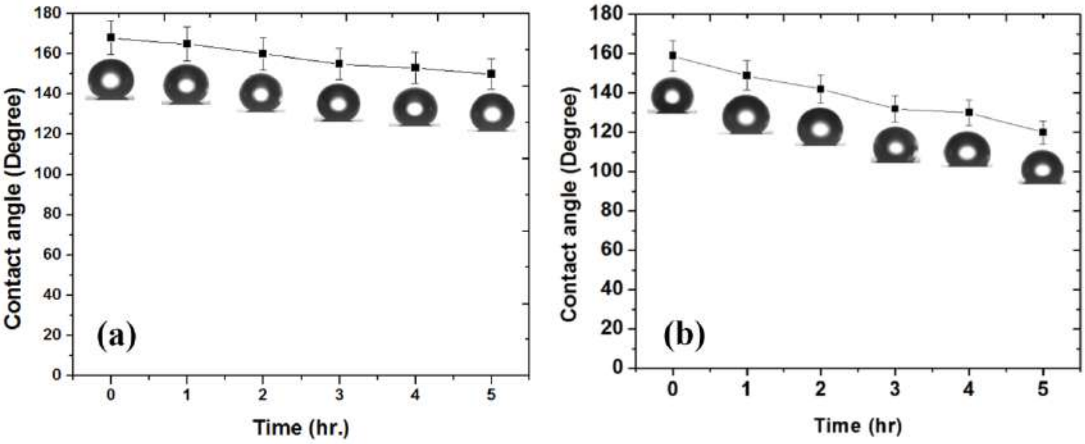

Fig.3: **(a) Effect of water drop impact test on S2 sample and (b) Effect of water drop impact test on S3 sample**

As shown in **Fig. 3a**, after 5 hour water drop impact test on S2 sample, the small decrease in water contact angle (154°) indicate that prepared superhydrophobic coating are durable against water drop impact. The binding between glass surface and SiO_2 nanoparticle was very strong, as the polymer (polystyrene) act as a binder. In case of S3 sample, the significantly reduced water contact angle shows less durability of the coating (**Fig.3b**).

CONCLUSION:

We have prepared durable and stable PS-SiO_2 superhydrophobic coating by dip coating technique. These coatings showed WCA greater than 168° and sliding angle less than 3°. This method is simple, low cost and not needed costly equipment's. We have achieved the superhydrophobicity at the concentration of silica nanoparticles (4 mg/ml) with dipping time (4 min) in 4 mg/ml concentration of PS. This technique has high potential to applicable for windows glass, solar cell panel, vehicle and so on.

ACKNOWLEDGMENT:

This work is financially supported by DST-INSPIRE Faculty Scheme, Department of Science and Technology (DST), Government of India. [DST/INSPIRE/04/2015/000281].

REFERENCES:

1. Xu, Q.F., J.N. Wang, and K.D. Sanderson, ACS Nano, 4(4): p. 2201-2209 (2010).
2. Li, X.-M. D. Reinhoudt and M. Crego-Calama, Chem. Soc. Rev., 36(8): p.1350-1368 (2007).
3. Kong, J.-H., et al., Nanoscale, 6(3): p. 1453-1461 (2014).
4. Tan, S., et al., J. Colloid and interface sci., 322(1): p. 1-5 (2008).
5. Tu, C.W., et al., Macromolecular Rapid Comm., 28(23): p. 2262-2266 (2007).
6. Bravo, J., et al., Langmuir, 23(13): p. 7293-7298 (2007).
7. Xu, L., et al., ACS applied materials & interfaces, 4(2): p. 1118-1125 (2012).
8. Chen, H., et al., Applied Surface Science, 261: p. 628-632 (2012).
9. Dhere, S.L., et al., J. Phy. and Chem. of Solids, 72(1): p. 45-49 (2011).
10. Gurav, A.B., S.S. Latthe, and R.S. Vhatkar, Surface Inno., 1(3): p. 157-161 (2013).
11. Kim, D.-Y., et al., J. Mat. Chem. A, 3(7): p. 3975-3983 (2015).
12. Latthe, S., et al., Coatings, 4(3): p. 497 (2014).
13. Latthe, S.S., et al., J. Porous Materials, 17(5): p. 565-571 (2010).
14. Latthe, S.S. and A.V. Rao, Surface & Coatings Tech. 207(Supplement C): p. 489-492 (2012).
15. Liu, S., et al., RSC Advances, 5(84): p. 68293-68298 (2015).
16. Madhan Kumar, A., et al., Polymer, 77(Supplement C): p. 79-86 (2015).
17. Park, J.-J., et al., ACS Applied Materials & Interfaces, 5(13): p. 6155-6160 (2013).
18. Xing, R., et al., J. Molecular Liquids, 247(Supplement C): p. 366-373 (2017).
19. Yoon, H., et al., J. Materials Chemistry A, 3(21): p. 11403-11410 (2015).

PREPARATION OF $NiCo_2O_4$ NANOFLAKES FOR SUPERCAPACITOR APPLICATION

R. B. Waghmode and A. P. Torane

Solid State Physics Laboratory, Department of Physics,

Yashwantrao Chavan Institute of Science, Satara, MS, India

Author E-mail: appasahebtorane@yahoo.in, ratnamalawaghmode@gmail.com

ABSTRACT:

In present study, $NiCo_2O_4$ nanoflakes have been synthesised using a chemical bath deposition (CBD) method and used for supercapacitor application. The prepared thin films are characterized for their structural and morphological studies, respectively. The $NiCo_2O_4$ nanoflakes exhibit maximum specific capacitance of 734 F/g at scan rate of 5mV/s. The specific capacitive retention 93. 2% is obtained after 1000 cycles. From this study it can be concluded that the low cost and environmental friendly CBD method could be used to deposit efficient $NiCo_2O_4$ nanoflakes for supercapacitor application.

Keywords: Nickel cobalt oxide; thin film; $NiCo_2O_4$ nanoflakes;XRD; chemical bath deposition; supercapacitor

INTRODUCTION:

In recent years, in order to solve global energy demand; researchers developed cost-effective, eco-friendly fresh and reproducible energy devices. [1, 2]. Based on the electrode materials and energy storage mechanism, supercapacitors can be divided into two categories: electrochemical double layer capacitors (EDLCs) and another pseudocapacitors [3–6]. Among the various psedocapacitive electrode materials RuO_2 shows high specific capacitance; however, its high cost limit practical application of RuO_2 [7]. Recently ternary nickel cobalt oxide ($NiCo_2O_4$) has caught much research attention because it offers many advantages such as comparative capacitance, low cost and environmental friendliness. Up to now different nanostructures of $NiCo_2O_4$ have been synthesized with different morphologies like; nanowires[8], nanotubes[9], nanosheets[10] and microspheres[11].

In this work, $NiCo_2O_4$ nanoflakes thin films were successfully synthesized by using a CBD method. The structural, morphological and electrical properties of $NiCo_2O_4$ nanoflakes thin film have been investigated.

EXPERIMENTAL DETAILS:

$NiCo_2O_4$ thin films were synthesized by a simple, cost effective, chemical bath deposition (CBD) method. Analytical grade nickel chloride ($NiCl_2\cdot 6H_2O$), cobalt chloride ($CoCl_2\cdot 6H_2O$), and hexamethylenetetramine (HMTA, $C_6H_{12}N_4$) were purchased from Loba chemicals ltd and used without further purification. The deposition of $NiCo_2O_4$ thin films, the reaction bath was prepared in 50 ml beaker, to which 0.2 M $NiCl_2·6H_2O$ and 0.4 M $CoCl_2·6H_2O$ were taken. Further, 0.05 M HMTA was added and stirred for 15 min to obtain a clear pink solution. The mirror polished steel substrates were mounted vertically in reaction bath. Then, the temperature of reaction bath was maintained at 80°C for 5 h. After deposition, the thin films were rinsed 2 to 3 times in double distilled water. Finally, as deposited thin films were annealed to 300°C in air for 3 h to convert hydroxide form in to pure oxide form.

Characterizations:

The crystal structure of the deposited thin film was studied by X-ray diffraction (XRD) technique (Bruker D-8 diffractometer) using Cu Kα (λ= 1.5418 A^o) radiation in 20° to 80° 2θ range. The surface morphology and chemical composition of thin film were studied by using scanning electron microscope (SEM) of model (JEOL model 6360). The Raman spectra were examined by using micro- Raman Renishaw spectrometer of wavelength 532 nm. The electrochemical measurements were carried out on Autolab PGSTAT101 electrochemical work station using three electrode cell configurations. For measurement platinum was used as a counter electrode, Ag/AgCl as a reference electrode and $NiCo_2O_4$ thin film as a working electrode. Electrochemical impedance spectroscopy (EIS) measurements were carried out in a frequency range from 0.1 Hz to 100 kHz with an amplitude 5 mV at open circuit potential.

RESULTS AND DISCUSSION:

Structural analysis:

The structural analysis of deposited thin films was carried out by using XRD pattern. Fig. 1. shows the XRD pattern of $NiCo_2O_4$ nanoflakes after annealing at 300 °C for 3 h on stainless steel substrate. The diffraction peaks are in good agreement with those of the standard data card (JCPDS Card no. 73-1702) of the $NiCo_2O_4$ having cubic spinel crystal structure. No any characteristic impurity peak was observed, indicates the high purity of $NiCo_2O_4$ nanoflakes. The * marked peaks are of stainless steel substrates. The crystallite size was determined by using Scherer's formula shown in equation (5) for high intense peak (311),

$$D = \frac{K\lambda}{\beta \cos\theta} \tag{1}$$

where 'D' is crystallite size, 'K' is constant (0.9), 'λ' is wavelength of monochromatic X-ray (1.5418 Å), 'β' is full width at half maxima of the peak and 'θ' is diffraction angle. The crystallite size for (311) plane was found 26 nm.

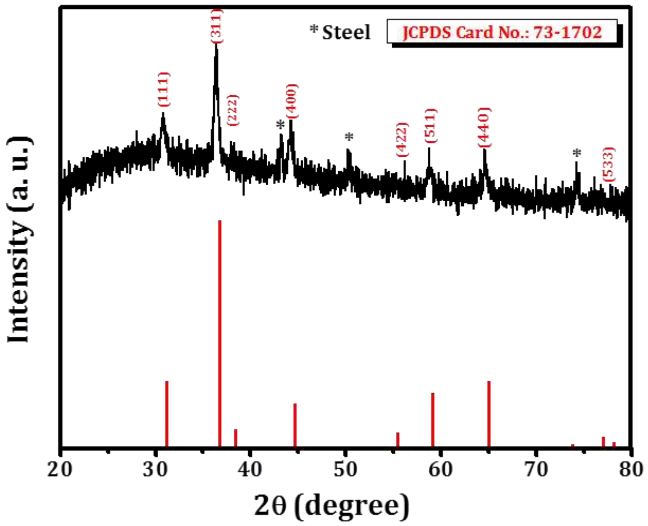

Fig.1: XRD pattern of $NiCo_2O_4$ nanoflakes thin film

Raman Spectroscopy:

In order to obtain the chemical composition and structure of annealed $NiCo_2O_4$ thin film, Raman analysis was performed. The Raman spectra recorded over 100-1000 cm^{-1} for the $NiCo_2O_4$ nanoflakes thin films is shown in Fig.2.The well-defined peaks at 186, 465.5, 507.2 and 654.2 cm^{-1} corresponds to F_{2g}, E_g, F_{2g} and A_{1g} vibrational modes of spinel of $NiCo_2O_4$, respectively. These results are well consistent with those the reported values in previous reports [12].

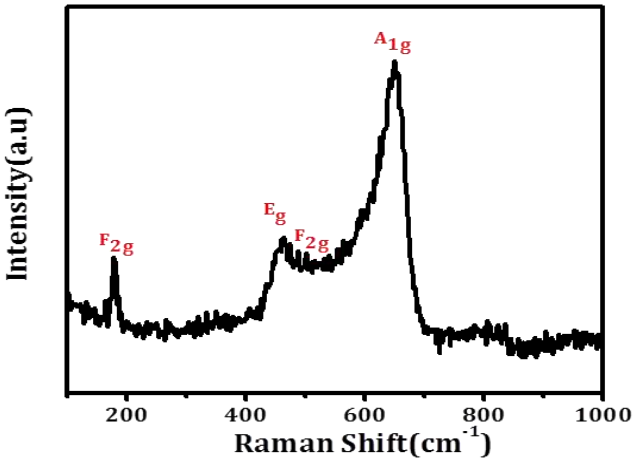

Fig.2 Raman spectra of $NiCo_2O_4$ nanoflakes thin film

Surface morphological studies:

Fig.3.shows the SEM images of $NiCo_2O_4$ nanostructure thin film on to a stainless steel substrate at different magnifications. The SEM images show formation of nanoflakes structure of $NiCo_2O_4$. Due to presence of higher surface area, it is possible for electrolyte ions to diffuse in the

nanoflakes to give maximum active contact with the material which will improve the supercapacitive performance. It can be seen that the film consists of a porous structure with nanoflakes provides easy access for ions to access the electrode|electrolyte interface, which is a very important factor for the faradic surface reaction.

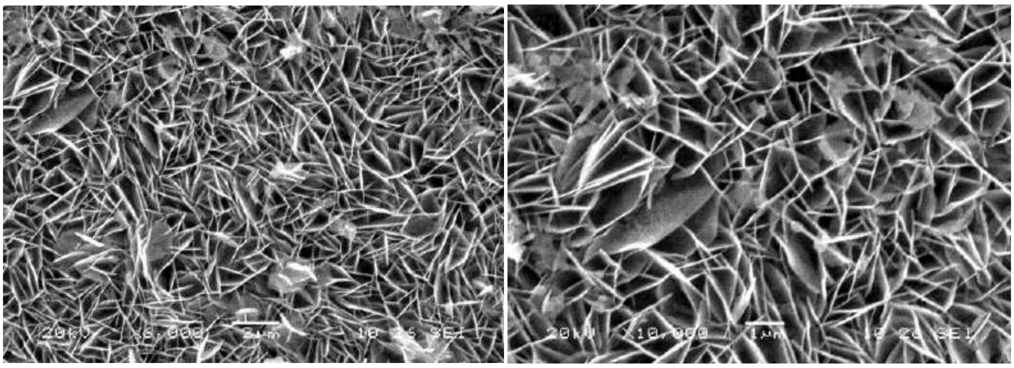

Fig. 3: SEM of $NiCo_2O_4$ nanoflakes thin film

Supercapacitive properties:

Cyclic voltammetry of $NiCo_2O_4$ thin tilms:

The specific capacitance is determined by cyclic voltammetry (CV) measurements of the NiCo2O4 nanoflakes in aqueous KOH electrolyte. Fig.4 shows the CV curves of the electrode with different scan rates ranging from 5 to 100 mV s^{-1} in the potential window of -0.2 to 0.6 V.

The specific capacitance of the sample is 634.2, 556.4, 488.1, 410.5, 338.6 and 263.7 F/g at scan rates of 5, 10, 25, 50, 75 and 100 mV/s respectively.

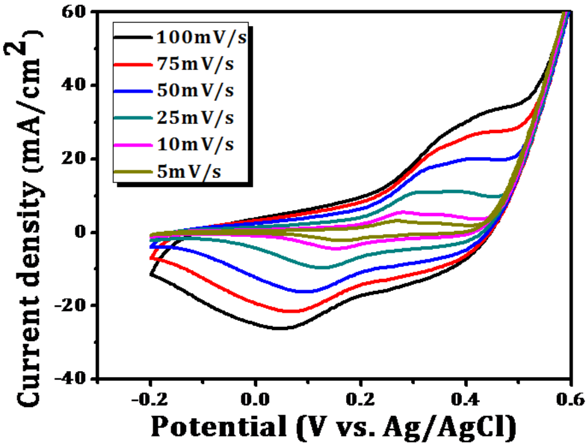

Fig. 4: CV curve pattern of $NiCo_2O_4$ nanoflakes thin film

Galvanostatic charge discharge measurements:

Fig.5.shows the galvanometric charge discharge behavior of electrode within the potential range of -0.2 to 0.4 V vs Ag/AgCl electrode at various current densities from 1 to 9 mA/cm^2. The

nearly triangular shape of the charge discharge curves for the $NiCo_2O_4$ nanoflakes sample shows the good pseudocapacitive behavior of the electrode material.

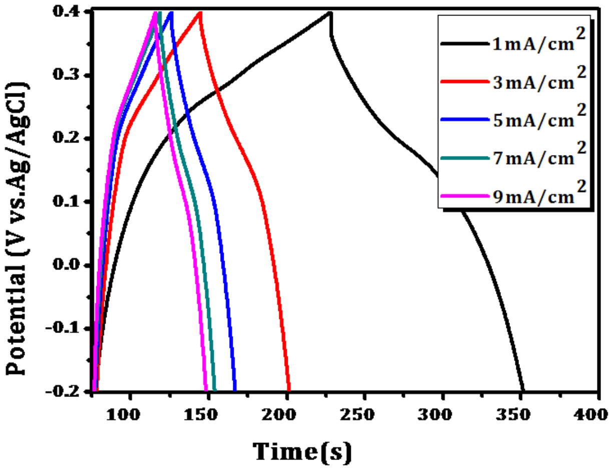

Fig. 5: Charge-discharge measurement of $NiCo_2O_4$ nanoflakes thin film

Stability Study

To evaluate the cyclic performance and electrochemical stability of the electrode, the material is performed at constant scan rate of 100 mV/s as shown in Fig. 6. It shows the initial (1st cycle) and final (1000th cycle) CV curves. From figure it is observed that the capacitance retention is 93.2 % after 1000 cycles. The $NiCo_2O_4$ nanoflakes show excellent cycling stability.

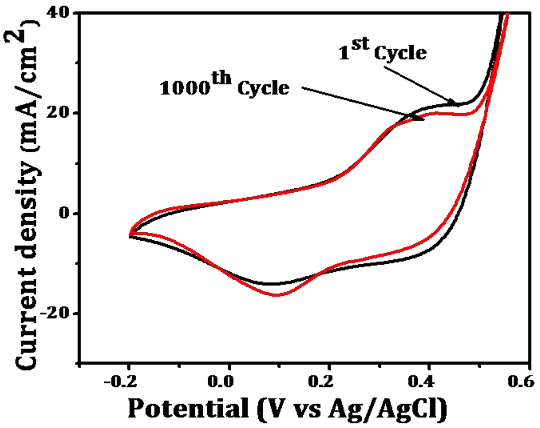

Fig. 6: Stability study of $NiCo_2O_4$ nanoflakes thin film

Electrochemical impedance spectroscopy measurements:

Fig. 7.shows the Nyquist plot of NiCo2O4 nanoflakes electrode tested in aqueous 2M KOH The value of R_{ct} can be calculated from the diameter of semicircle arc. The value of R_s for the $NiCo_2O_4$ nanoflakes is 0.99 Ω and the value of R_{ct} is 3.01 Ω.

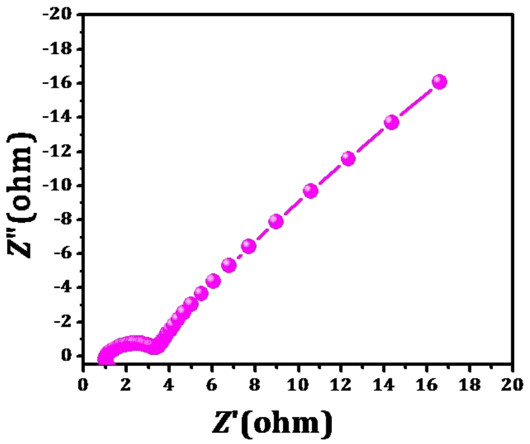

Fig. 7: Nyquist plot of $NiCo_2O_4$ nanoflakes thin film

CONCLUSIONS:

In summary $NiCo_2O_4$ nanoflakes thin films are directly deposited onto the stainless steel substrate surface by using simple CBD method. The XRD study confirms the formation of polycrystalline cubic spinel crystal structure. The SEM study shows formation of $NiCo_2O_4$ nanoflakes uniformly dispersed on to stainless steel substrate. The $NiCo_2O_4$ nanoflakes exhibited high Cs of 634 F/g at 5mV/s and excellent cycle life up to 1000 cycles. This manuscript represents the excellent electrochemical performance of $NiCo_2O_4$ nanoflakes synthesized by facile synthesis method at relatively low cost and $NiCo_2O_4$ nanoflakes believed to be a promising electrode material for supercapacitor application.

REFERENCES:

1. Kuang M, Zhang W, Guo X L, et al., Ceram. Int. 40:10005–10011 (2014).
2. Patil S J, Lokhande V C, Chodankar N R, Lokhande C D, J Colloid Interface Sci. doi: 10.1016/j.jcis.2016.02.003 (2016).
3. Jiang L, Zou R, Li W, et al., J Mater Chem A 1:478–481 (2013).
4. Jin Y, Chen H, Chen M, et al. ACS Appl Mater Interfaces 5:3408–3416 (2013).
5. Bhattacharjya D, Kim M S, Bae T S, Yu J S, J Power Sources 244:799–805 (2013).
6. Jiang H, Li C, Sun T, Ma J, Chem Commun 48:2606–2608 (2012).
7. Wu Z S, Wang D W, Ren W, et al., Adv Funct Mater 20:3595–3602 (2010).
8. Wei T Y, Chen C H, Chien H C, et al., Adv Mater 22:347–351 (2010).
9. Wang H, Gao Q, Jiang L, Supercapacitors, 2454–2459 (2011).
10 Li L, Peng S, Cheah. Small Y, et al., Chem - A Eur J 19:5892–5898 (2013).
11. Zhang G, Lou X W, Adv Mater 25:976–979 (2013).
12. Liu Z, Xiao K, *et al*, RSC Advances 3:4372–4380 (2013).

EFFECT OF SOME INORGANIC ACID DOPANTS ON ELECTRICAL CONDUCTIVITY OF POLYANILINE

Raviraj S. Kamble*and Tanaji S. Patil

Bhogawati Mahavidyalaya, Kurukali, Tal. Karveer, Dist. Kolhapur

* Corresponding author E-mail: ravikam11@gmail.com

ABSTRACT:

Polyaniline material were prepared and doped with different acids like H_2SO_4 andHClat room temperature. The prepared samples were characterized with IR, XRD, SEM etc. Their electrical conductivities were tested with four probe set up. It was found that H_2SO_4 acid doped polyaniline (PAni-H_2SO_4)exhibited good electrical conductivity as compared to HCl doped polyaniline (PAni-HCl).The electrical conductivity of the PAni-H_2SO_4 was 2.12 S cm^{-1}, while that of the PAni-HCl was 0.143 S cm^{-1} confirming the results of FT-IR,

INTRODUCTION:

With the discovery in 1960 of intrinsically conducting polymers (ICPs), a new arena in research was initiated. ICPs like polypyrrole, polythiophene, polyacetylenes, and Polyaniline has been studied and researched extensively [1,2]. ICPs are organic polymers that conduct electricity. The intrinsically conducting polymers (ICPs), more commonly known as “synthetic metals”, refer to the large class of organic polymers which possess not only the mechanical properties and processability of conventional polymers, but also unique electrical, electronic, magnetic, and optical properties of metals, which conventional polymers do not have [3-5]. However, the main difficulty related with the effective utilization of all ICPs is inherent in their lower level of conductivity compared to metal, and their infusibility and poor solubility in all available solvents. However, the solubility of some ICPs can be improved through doping with a suitable dopant or modifying the starting monomer.

Among all conducting polymer, Polyaniline (PANI) is one of the most promising conducting polymers due to its ease of preparation, good environmental stability, betterelectronic properties, low cost, low density and its applications in electrochromic display, electro catalysis, rechargeable batteries, sensors and biosensors. Polyaniline was originally recognized in 1835 as “aniline black”, a term used for any product acquired by the oxidation of aniline. The processability and conductivity of PANI are also fairly good. Therefore there is ample scope for modifying the conductivity and processabilty of PANI [6-8]. The significance of PANI can be understood from some of the following applications attributed to PANI materials. PANI being electrically conducting in nature can be used for conductive adhesive, conductive ink, conductive paint and electrostatic discharge materials [9].

Properties of PANI are dependent on polymerization conditions (pH, temperature and time), concentration of monomer, dopant type and mainly monomer to oxidant molar ratio.The conductivity of polyaniline is induced by doping. Doping with suitable dopant plays key role in conductivity mechanism by structural modification in backbone of polyaniline polymer. Doping an insulating or a semi-conducting polymer results in a significant increase in its electrical conductivity which can go up to the metallic regime. Electrical conductivity usually increases with the doping level due to increase in charge carriers concentration [10-12]. A large number of synthesis routes and types of dopants have been identified for producing polyaniline, its derivatives and composites. Doping with different inorganic and organic acids is popular in case of polyaniline.

In the present study, the effect of different doping agents mainly acids, and their counter ions on the electrical conductivity of polyaniline has been studied along with characterization of synthesized polyaniline samples. Keeping in mind the useful properties of inorganic acids such as handling ease, solubility, we have chosen inorganic acids as a dopant for PANI

EXPERIMENTAL:

Preparation of Polyaniline using different doping agent as acid:

Polyaniline material was prepared by using different dopants. 0.2 M Aniline was prepared from Aniline (Merck). 0.25 M Ammonium persulfate (APS) was prepared from Ammonium persulfate (Merck). The solutions were prepared from different acids having different concentrations. The aniline: APS ratio was kept 1:1.25. First 0.2 M aniline solution in beaker was kept on the magnetic stirrer surrounded by ice pieces for cooling for about 10 min, After that 0.25 M APS solution was added to 0.2 M aniline solution drop wise under constant stirring very carefully. The reaction was carried out at low temperature in ice bath becausepolymerization reaction is exothermic reaction. It was stirred for 24 h on the magnetic stirrer. The dark green coloured polyaniline precipitate was filtered and washed with acid of corresponding strength. It was washed thoroughly with double distilled water several times followed by acetone to remove impurities like oligomers. It was washed until the filtrate became colourless. The precipitate of polyaniline was dried in oven at 6o ^{0}C for 16 h. Polyaniline were prepared in different acids as follows:

Table 1: Different doping acids and their concentrations

Sr. No.	Doping Acid	Concentration (N)	PAni doped with acid
1	HCl	1	(SR-12)
2	H_2SO_4	1	(RP-12)

RESULT AND DISCUSSION:

XRD of polyaniline samples are shown in the Fig. 1. The diffraction patterns show amorphous components. The crystallinity indicates the higher molecular alignment. The sample SR-12exhibited Bragg's peaks for 2θ ≈18.8◦.The sample RP-12exhibited amorphous in nature.Samples showed either partial, low crystallinity or amorphous nature. The polyaniline is basically not perfect crystalline in nature. It is evident from XRD spectra of polyaniline samples. However the alignment of PANI fibres gave the partial crystallinity. The effect of dopant ions also plays an important role in crystallinity.

Fig. 2 showsIR spectra of Polyaniline samples SP-12 and RP-12. IR spectra is in good agreement with the previously reported results. From IR spectra certain peaks which are associated with different bonds of polyaniline structure could be easily recognized thereby confirming the formation of polyaniline material. The nature of IR spectra is different for different samples where type of acid used for the synthesis is also different. The values of IRabsorption frequencies for different samples could be correlated with each other. The appearance of band at around 1560 and 1480 cm^{-1}mode in spectra is consistent with quinoid and benzenoid ring stretching vibration respectively. The IR band at 2000 cm^{-1} or higher than 2000 $cm^{-1}$is due to the absorption of free charge-carriers in the protonated polymer. It is characteristic of a conducting form of PANI. A Peak at around 1600 $cm^{–1}$ in the spectra is characteristic of C=C ring vibrations in the polymer chains. It suggests that symmetry has been broken by conformational changes induced by protonation.

The peak at around 830 cm^{-1} is assigned to an out of plane C-H bending of 1,4disubstitutedbenzenoid rings. The band characteristic of the conducting protonated form is observed at 1248 $cm^{–1}$ in the spectra. a strong and broad band centered at 1148 $cm^{–1}$, which has been assigned to the vibration mode of the –NH+= structure, and is associated with the vibrations of the charged polymer units. The peak at around 1300 cm^{-1} can be attributed to C-N stretching of secondary aromatic amine. The peak at around 1248 cm^{-1} can be assigned to C-N+ (polaron) stretching. . Band at 3380 cm^{-1} is assignedto N-H stretching vibrations. Presence of these characteristics bands confirms the presence of conducting ES phase in the polymer.

SEM images of the PANI samples are shown in Fig. 3. The formation of PANI nano fibres was confirmed by these images. The nano fibers of 500 nm range could be observed in sample RP-12. So far the chemical oxidative method does not yield the nanofibres of PANI. But by employing the suitable conditions, we have successfully synthesized nanosized PANI material. Some choral like morphology of polyaniline material was observed in sample SR-12. The structural part and arrangement of polyaniline fibers could be of great importance in its applications.

The electrical conductivity of PANI samples were measured by four probe method. The conductivity was calculated by following equation in S/cm.

$$\sigma = \frac{I}{V \, . \, 2\pi S}$$

The influence of doping on the electrical conductivity is clearly evident and traced. The extent of conjugation, the length of polymer chain, the alignment of fibers and formation of polarons and bipolarons play vital role in the electrical conductivity of polyaniline samples. The increase of conductivity with increased doping concentration is a well-known phenomenon, The conductive inhomogeneous polymer phase can be created by varying oxidant species, oxidant to monomer molar ratio, dopant species and processing conditions (temperature, pH, mixing mechanism).These structural changes lead to such morphology of chains which have charge transitions and hence there will be improved ion transfer (delocalization and hopping-jumping-leaping).

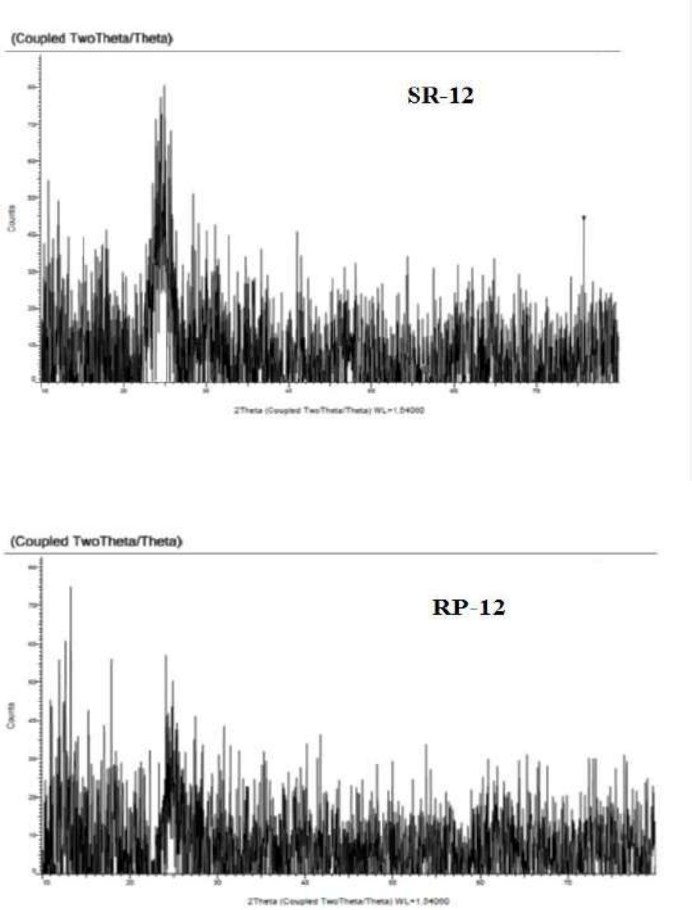

Fig. 1: XRD spectra of polyaniline samples i) SR-12 ii)RP-12

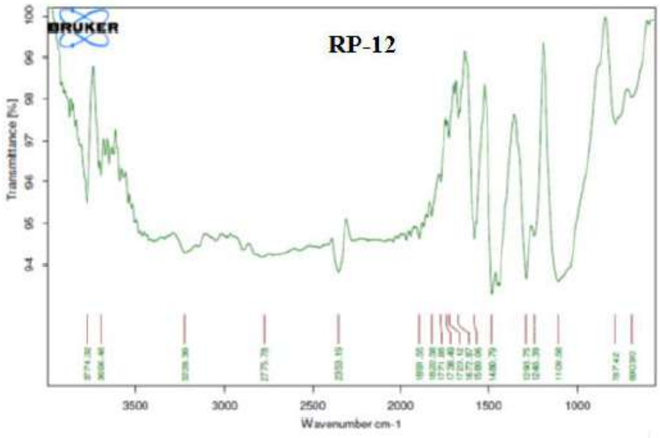

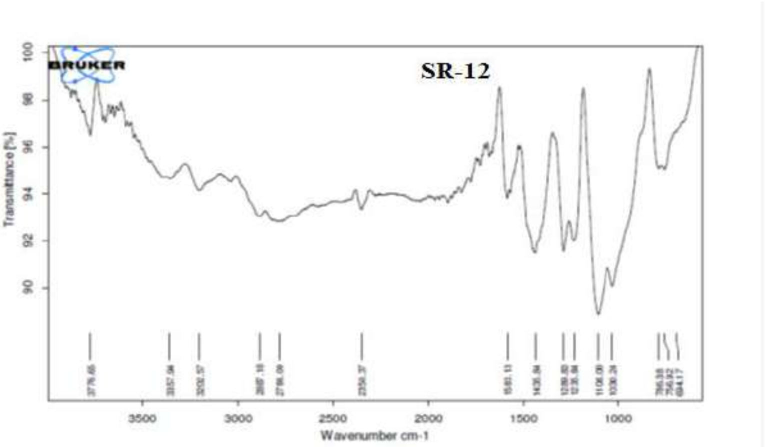

Fig. 2 : FT-IR spectra of Polyaniline samples i) RP-12 ii) SR-12

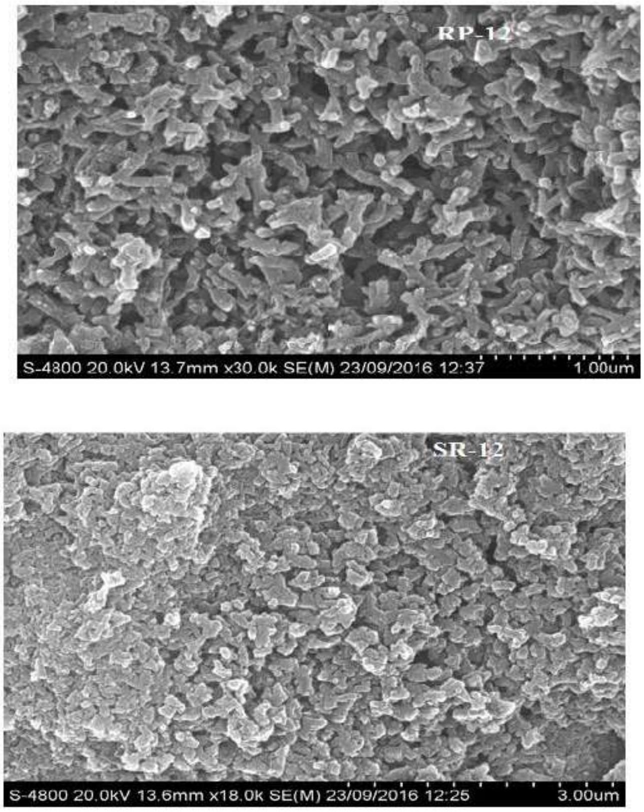

Fig. 3: SEM images of polyaniline samples i) RP-12 ii)SR-12

The dopant ion or counter ion used, their concentration has to be considered when it come to electrical conductivity. It was found that H_2SO_4 acid doped polyaniline (PAni-H_2SO_4)exhibited good electrical conductivity as compared to HCl doped polyaniline (PAni-HCl) The electrical conductivity of the PAni-H_2SO_4 was 2.12 Scm-1, while that of the PAni-HCl was 0.143S cm-1 confirming the results of FT-IR, The formation of emeraldine salt and hence polaron and bipolaron increased with change in acid dopant ion. The order of conductivity for different acids was found as below:

H2SO4>HCl

CONCLUSION:

Polyaniline materials were synthesized by chemical oxidative method using different acid dopant ions keeping monomer and oxidant ratio constant. The yield of emeraldine salt were found to be good but varied for different acids. The prepared polyaniline samples were characterized for XRD, SEM and FT-IR. The characterization confirmed the formation of polyaniline material where SEM images of some samples indicated formation of nanosized polyaniline material. The electrical conductivity of PANI samples was measured by four probe technique. The effect of acid dopant ions and crystallinity play important role in case of electrical conductivity.

REFERENCES:

1. MaddisonD.S and Unsworth J, Synth. Met., 22, 257 (1988).
2. ReghuMenon et al, Synth. Met.,69, 329 (1978).
3. Fernando G. Souza Jr, Ricardo C. Michel, Bluma G. Soares; Polymer Testing, 24,998–1004 (2005).
4. Li, Y. Q., Yang, T. Y., Yu, T., Zheng, L. X., Liao, K., J. Mater. Chem., vol. 21, pp. 10844–10851 (2011).
5. Song, S. H., Adv. Mater., Vol. 25, pp. 732–737 (2013).
6. Li C, Bai H, Shi GQ. ChemSoc Rev 38: 2397–409 (2009).
7. Zhang D H, Wang YY. Mat SciEng B-Solid;134: 9–19 (2006).
8. Jang J. AdvPolymSci;199: 189–259 (2006).
9. DuvailJL, Retho P, Fernandez V, Louarn G, Molinie P, Chauvet O. J PhysChem B;108: 18552–6 (2004).
10. MativetskyJM, DatarsWR. Physica B; 324: 191–204 (2002).
11. Faez, R., I.M. Martin, M.A. De Paoli, M.C.Rezedene, Synth.Met, 119, 435 (2001).
12. R.Surville, M.Josefowicz, L. T., Yu, J. Perichon and R.Buvet, Electrochim. Acta.13, 1451 (1968).

INVESTIGATIONS ON FERROELECTRIC PROPERTIES OF BCZT CERAMICS

S. D. Chavan[1] and D. J. Salunkhe[2*]

[1]Department of Physics, D. B. F. Dayanand College of Arts and Science, Solapur, 413002

[2]Laxmibai Bahurao Patil Mahila Mahavidyalaya, Solapur, 413002, India

*Corresponding author E-mail: salunkhedj@rediffmail.com

ABSTRACT:

The paper reports synthesis, characterization and ferroelectric properties of $(Ba_{(1-x)}Ca_{(x)})(Zr_{(y)}Ti_{(1-y)})O_3$ (BCZT) ceramics with x = 0.05, 0.075 and y = 0.075, 0.10. The BCZT ceramics are synthesized via ceramic route of synthesis. The crystal structure show tetragonal crystal structure. The particle size is found out to be 46 nm for BCZT1, 56 nm for BCZT2 and 55 nm for BCZT3 ceramics. The elemental analysis of these ceramics shows that the atomic weight % of (Ba,Ca):(Ti,Zr) ≈1.0. The investigations on ferroelectric properties show that all BCZT ceramics possess useful values of maximum polarization (P_{max}) and remnant polarization (Pr). The present observations suggest that all BCTZ ceramics are useful lead free ferroelectric ceramics.

Key words: BCZT, Ceramic route, Ferroelectric properties, Remnant Polarization.

INTRODUCTION:

Ferroelectric materials with perovskite structures are useful for microelectronic devices. The most widely used ferroelectric material is $BaTiO_3$ (BT). The structure of unit cell is temperature dependent. There are three phase transitions in order of decreasing temperature (120^oC, 5^oC, -90^oC) [1]. The substitution of Sr, Pb ,Ca and Zr into BT shows interesting ferroelectric properties. Zhuang et al. reported that addition of even a small quantity of Ca ions at Ti-sites leads to a diffused phase transition curve and lowers the phase transition temperatures [2]. Tiwari et al. reported that calcium doping increases the phase transition temperatures of BCT ceramics and Ba^{2+} substitution by Ca^{2+} leads to diffused transition curve. Earlier it was believed that Ca substitution decreases the Curie temperature [3]. Recently, it has been reported that Ca doping can also increase the Curie temperature depending on the powder preparation method & the site occupancy of calcium [4]. The paper report synthesis, characterization and ferroelectric properties of a ceramics having a general formula $[Ba_{(1-x)}Ca_{(x)}][(Zr_{(y)}Ti_{(1-y)}]O_3$ (BCZT) for x= 0.05, 0.075 & y = 0.075, 0.10.

EXPERIMENTAL:

The BCZT solid solutions have been synthesized via ceramic route of synthesis using the AR grade precursors $BaCO_3$, $SrCO_3$, ZrO_2 and TiO_2. The stoichiometric amounts of the precursors were well mixed together and ground for 2 hours in an agate mortar with pestle. The calcination was carried out at 1150^{0}C.The calcined powder was mixed with a polyvinyl acetate (PVA) binder solution and compacted into disk shaped samples. The final sintering process was carried out at 1200^{0}C for 24 h in two steps. The Bruker D8 advance X-ray diffractometer was used for the determination of X-ray diffractograms. The HP4284A LCR-Q meter was used for the measurements of dielectric constant (ε), loss tangent tanδ. P-E hysteresis loops were determined using P-E loop tracer, Marine India Pvt. Limited.

RESULT AND DISCUSSION:

Structural Analysis:

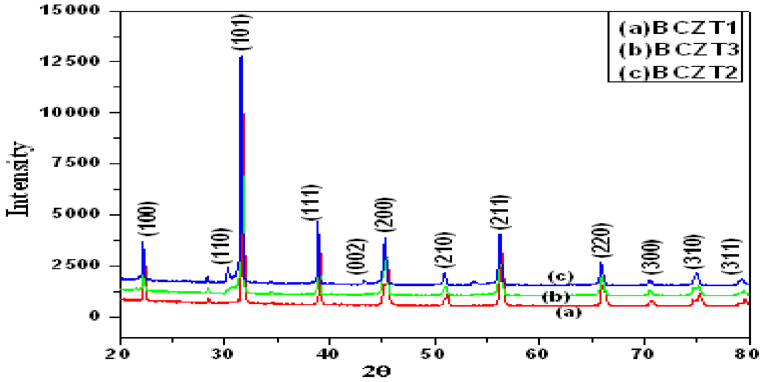

Fig.1: XRD patterns of BCZT ceramics

Figure 1 show XRD patterns of $(Ba_{0.95}Ca_{0.05})(Ti_{0.90}Zr_{0.10})O_3$(BCZT1), $(Ba_{0.95}Ca_{0.05})(Ti_{0.925}Zr_{0.075})O_3$(BCZT2) and $(Ba_{0.925}Ca_{0.075})(Ti_{0.925}Zr_{0.075})O_3$(BCZT3) ceramics respectively. The presence of sharp and well defined diffraction peaks indicate that this composition has a degree of crystallinity at a long range. The result suggest that Ca^{2+} and Zr^{4+} have been successfully incorporated into $BaTiO_3$ lattice to form inhomogeneous solid solution, It is seen that the composition under investigations are polycrystalline in nature and all the peaks in the spectra could be accurately indexed using standard JCPDS data. Further, no peak corresponding to any impurity phase is observed in the XRD patterns. The particle size is found out to be 46nm for BCZT1, 56nm for BCZT2 and 55nm for BCZT3 ceramics.

Ferroelectric Properties:

The Polarization P versus Electric field E loop i.e hysteresis loop is the most important measurement on ferroelectric materials for characterizing its electrical behavior. An ideal P-E loop is symmetrical in nature with positive and negative values of coercive field (Ec) and also positive and negative values of remnant polarization (Pr) are equal. The values of coercive field (Ec), remnant polarization (Pr) and the shape of P-E loop may be affected by many factors such as thickness of the sample, mechanical stress, preparation condition, thermal treatment and charged defects.

The ferroelectric hysteresis loop of BCZT1, BCZT2 and BCZT3 ceramics are obtained by using P-E loop tracer, Dept. of Physics, University of Pune, Pune. The measurements are carried out at different applied field. The thickness of BCZT1 samples was 1.22 mm, 1.35 mm of BCZT2 and 1.34 mm of BCZT3 sample. The area of all samples was nearly 120 mm^2. Room temperature P-E loop recorded at a frequency of 50 Hz for BCZT1, BCZT2 and BCZT3 ceramics. Figure 2 shows P-E combine loops for BCZT1, BCZT2, and BCZT3 ceramics. Table 1 shows the values of maximum polarization (P_{max}), remnant polarization (Pr), a coercive field (E_C) and Pr/P_{max} for BCZT1, BCZT2 and BCZT3 ceramics.

It is observed that, all P-E loops for BCZT1, BCZT2 and BCZT3 ceramics are symmetrical in nature with positive and negative values of coercive field (Ec) and also positive and negative values of remnant polarization (Pr) are equal. All P-E loops for BCZT1, BCZT2 and BCZT3 ceramics are slim hysteresis loops, which is one of the characteristic of relaxor ferroelectric. A low coercive field implies that the all studied BCZT ceramics are “soft” with respect to the electric field. In studied ceramics, it can be observed that all ceramics are typically soft, with a very low coercive field Ec and a relatively high remnant polarization Pr. These results are in good agreement with reported result. It is observe that the P–E hysteresis loops are slim, which are characteristic of relaxor ferroelectric. The area within loop is proportional to the loss tangent. Due to slim P–E hysteresis loops all ceramics possesses low loss tangent. Also all BCZT ceramics possesses a relaxor contribution, may be partial in case of BCZT2 and BCZT3 also possesses low loss tangent.

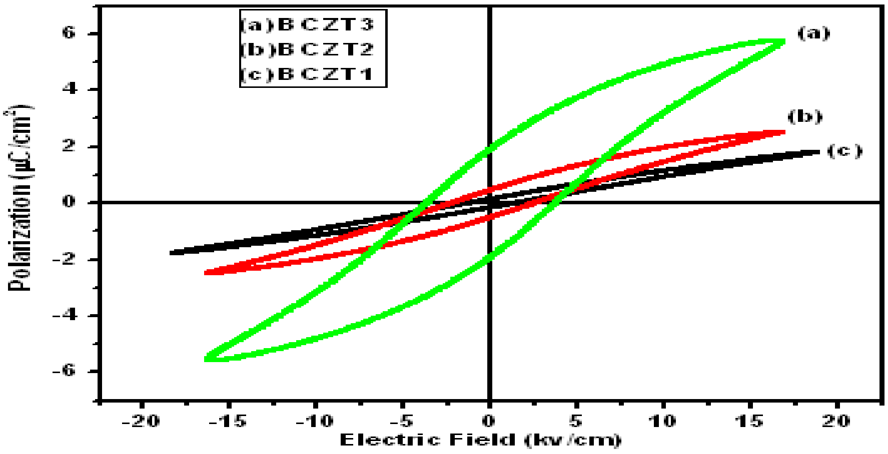

Fig. 2: P-E Hysteresis loops of BCZT Ceramics

Table 1: P_{max}, P_r, E_{C} and P_r/P_{max} for BCZT1, BCZT2 and BCZT3 ceramics

Ceramics	P_{max} µc/cm^2	P_r µc/cm^2	E_c KV/cm	P_r/P_{max}
BCZT1	1.792	0.143	1.289	0.080
BCZT2	3.187	0.583	2.410	0.182
BCZT3	5.715	1.930	3.580	0.337

CONCLUSION:

The ferroelectric ceramics BCZT are successfully synthesized using ceramic route of synthesis. The room temperature XRD pattern suggests that all BCZT ceramics are polycrystalline in nature. The particle size is found out to be 46 nm for BCZT1, 56 nm for BCZT2 and 55 nm for BCZT3 ceramics. All BCZT ceramics possess useful values of maximum polarization (P_{max}), remnant polarization (Pr) and coercive field (Ec). Thus all BCTZ ceramics could be useful lead free ferroelectric ceramics.

REFERENCES:

1. E.Wainer and A.N.Soloman, Titanium Alloy. Mfg.Co.Ele. Report 8 (1943).
2. Z.Q .Zhuang, M.P.Harner,D.M.Smyth., Mat.Res.Bull 22, 1329 (1987).
3. A.J. Moulson, J.M. Herbert, Electro-ceramic materials: Properties and Applications, Chapman and Hall, London, (1990).
4. V.S. Tiwari, D. Pandey, P. Groves, J. Phys. D, 22 837 (1989).

STRUCTURAL, RAMAN AND WETTABILITY PROPERTIES OF NANOCRYSTALLINE ZnO THIN FILM DEPOSITED BY SILAR METHOD

S. G. Deshmukh[1]*, A. M. More[2] and S. S. Latthe[3]

[1]Department of Engineering Physics, SKN Sinhgad College of Engineering,
Korti, Pandharpur-413304, Maharashtra, India
[2]Department of Physics, K. N. Bhise Arts, Commerce College,
Kurduwadi, 413208, Maharashtra, India
[3]Self-cleaning Research Laboratory, Department of Physics,
Raje Ramrao Mahavidyalaya, Jath, 416404, Maharashtra, India
*Corresponding author E-mail: samseeraj2009@gmail.com

ABSTRACT:

We regulate the deposition of nanocrystalline zinc oxide (ZnO) thin film using successive ionic layer adsorption and reaction (SILAR) method. The structural and wettability properties of ZnO thin film were examined using X-ray diffraction (XRD), Raman spectroscopy and contact angle measurement. The XRD shows the deposited ZnO thin film has a hexagonal structure with strong c-axis orientation. The crystallite size for ZnO thin film was found to be 31.35 nm along (002) plane. The ZnO thin film exhibits two Raman peaks at 561 and 1094 cm^{-1} assigned to E_1 (LO) and $2E_1$(LO) phonon mode of pure ZnO. The wettability study shows deposited ZnO thin film is hydrophobic in nature as water contact is greater than 90^0.

Keywords: ZnO, XRD, Raman and wettability

INTRODUCTION:

Zinc oxide (ZnO) is an II-VI compound with a direct band gap of 3.37 eV and a great excitons binding energy about 60 meV [1]. ZnO has attracted attention due to its non-toxicity, chemical stability, good electrical and optical properties. ZnO with a hexagonal crystal structure has wide applications in piezoelectric devices, photodiodes, Photocatalysis, transistors etc. [2]. Many methods have been employed for the synthesis of ZnO such as, hydrothermal method [1], pulsed laser deposition (PLD) [3], chemical vapor deposition [4], thermal evaporation [5], sol-gel [6], chemical bath deposition [7], successive ionic layer adsorption and reaction method (SILAR) [8] etc. In view of the less production cost, more convenient control over the synthesis process, and the high quality of prepared film, the deposition of ZnO thin film by SILAR method is stressed. SILAR method involves multiple successive dipping of the substrate in an anionic and cationic precursor and the substrate rinsing procedures in between. SILAR method has been widely applied to the synthesis of ZnS, Zn(O,S), ZnO, CdS etc.

In the present work, the synthesis of ZnO thin films by SILAR method on a glass substrate and its structural, Raman and wettability properties was reported.

EXPERIMENTAL:

All the chemicals used for the synthesis of ZnO were analytical grade. The synthesis of ZnO thin films was grown on the glass substrate as reported earlier [8]. The 50 number of SILAR cycles produces a uniform, white and well-adherent ZnO thin film. This sample is coded as S1 for further characterizations.

The thickness of S1 was measured by a weight-difference method in which area, mass and density of the material were considered. For the study of structural property of S1, X-ray diffraction (XRD) pattern was obtained from Bruker axe D8 Advance diffractometer with CuK_{α} (λ = 0.15406 nm) target. The Raman spectra of S1 was recorded in the spectral range of 400-4500 cm^{-1} using a Raman spectrometer (Bruker RFS 27, Stand-alone Model) equipped with Nd:YAG laser source. The wettability of S1 was studied by water contact angle measurement (Rame Hart Inc.).

RESULTS AND DISCUSSION:

Film thickness:

The thickness of S1 was measured by using a weight-difference method. i.e. the relation $t = m/(\rho \times A)$, where 'm' is the mass of the ZnO deposited on the substrate in 'g', ρ is the density and 'A' is the surface area of the film in cm^2. For bulk ZnO, ρ =5670 kg/m^3 [9]. The thickness of S1 was found to be 561 nm.

Structural studies:

Fig. 1 shows the XRD pattern of ZnO sample S1. The XRD profile of the S1 ZnO thin film shows diffraction peaks at angles 31.89^0, 34.45^0, 36.37^0, 47.68^0, 56.75^0, 62.98^0 and 68.13^0 of (100), (002), (101), (102), (110), (103) and (112) planes of hexagonal structure of ZnO. These observed peaks are in good agreement with the JCPDF card number 79-0205 with lattice constant a=3.241 Å and c=5.187 Å. The S1 is preferentially oriented with the c-axis perpendicular to the plane of the glass substrate resulting in relatively high intensity for (002) reflection. The crystallite size was determined by using the Debye-Scherrer's formula, $D = 0.9\lambda/\beta.\cos\theta$. [10], in which D is the crystallite size, λ is the X-ray wavelength used (λ=0.15406 nm), β is the FWHM in radian and θ is Bragg's angle. The crystallite size was found to be 16.42, 31.35 and 22.55 nm for (100), (002) and (101) peak respectively. For the more information on the amount of defects in the film, the dislocation density (δ) and micro strain (ε) was calculated by using formula,$\delta=1/D^2$ [11], where D is the crystallite size and $\varepsilon = \beta\cos\theta/4$ [12] respectively. The structural parameters such as observed 'd' values, FWHM (β), crystallite size (D), dislocation density (δ) and micro strain (ε) for the S1 ZnO thin film was summarized in Table 1.

Raman Spectroscopy:

Raman spectra can be used to study the crystal quality, disorders of materials and structural defects. Figure 2 shows the Raman spectra of S1 ZnO thin film. For S1, two peaks at 561 and 1094 cm^{-1} was detected. Compared with the Raman spectra of ZnO crystal, the observed peaks are assigned to E_1 (LO) and $2E_1$(LO) phonon mode of pure ZnO [13,14]. Thus, from Raman study the formation of ZnO phase with hexagonal crystal symmetry is confirmed.

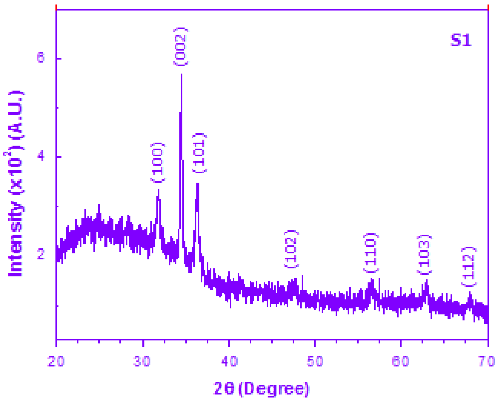

Fig. 1: X-ray diffraction profile of S1 ZnO thin film

Table 1: Summery of standard and observed ‘d’ values, FWHM (β), crystallite size (D), dislocation density (δ) and micro strain (ε) of S1 thin film for (100), (002) and (101)

Parameter → Planes ↓	Standard ‘d’ (A^0)	Observe d ‘d’ (A^0)	FWHM (β)	D (nm)	δ in (nm)$^{-2}$ (x10^{-3})	ε (x10^{-3})
(100)	2.8073	2.8047	0.5033	16.42	3.708	2.111
(002)	2.5938	2.6020	0.2654	31.35	1.017	1.106
(101)	2.469	2.4693	0.3709	22.55	1.966	1.537

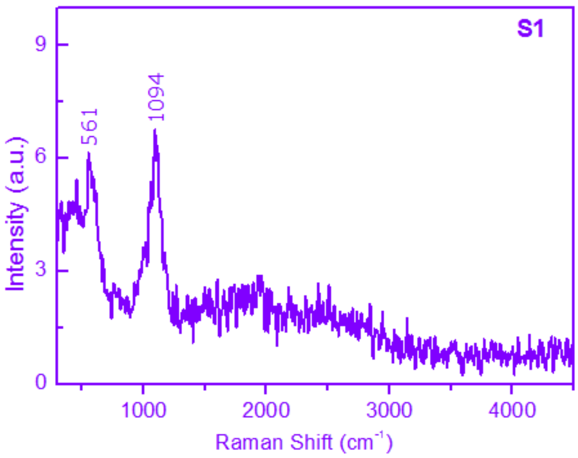

Fig. 2: Raman spectra of S1 ZnO thin film

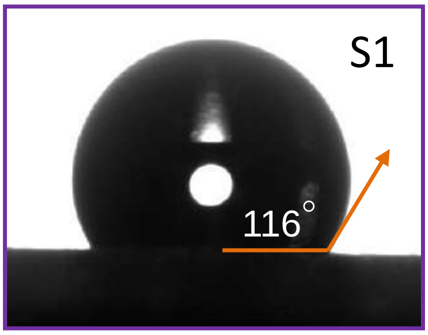

Fig. 3: Water contact angle image of S1

Wettability Study:

Wettability involves the interaction between a solid and liquid in contact, characterized by a value of the contact angle, microscopic parameter. If the wettability is good, contact angle will be small and the surface is hydrophilic. On the other hand, if the wettability is poor, contact angle will be large and the surface is hydrophobic. Figure 3 shows the image of water contact angle measurement for S1 of ZnO thin film at room temperature. The water contact angle was found to be 116^0, confirming the surface is hydrophobic in nature. For practical applications, both highly hydrophobic and highly hydrophilic materials are practically desirable [15].

CONCLUSION:

In summary, we successfully deposited nanocrystalline ZnO thin film using successive ionic layer adsorption and reaction (SILAR) technique. The XRD shows the formation of a nanocrystalline ZnO thin film with the crystallite size of 31.35 nm having hexagonal phase. The deposited nanocrystalline ZnO thin film reveals strong c-axis orientation. The ZnO thin film exhibits two Raman peaks at 561 and 1094 cm^{-1} assigned to E_1 (LO) and $2E_1$(LO) phonon mode of pure ZnO. The wettability study shows deposited ZnO thin film is hydrophobic in nature as water contact is greater than 90°.

REFERENCES:

1. Zhiwei Dong, Bing Han, Shixiong Qian, Deying Chen, J. Nanomaterials, Art. ID 251276 1-5 (2011).
2. Tengfa Long, Shu Yin, Kouta Takabatake, etc. Nanoscale Res. Lett. 4, 247-253 (2009).
3. T. K. Subramanyam, B. Srinivasulu Naidu, S. Uthanna, Cryst. Res. Technol. 35, 1193-1202 (2000).
4. Ning Zhang, Ran Yi, Rongrong Shi, Guanhua Gao, Gen Chen, Xiaohe Liu, Materials Lett. 63, 496-499 (2009).
5. Umar, A., S. H. Kim, J. H. Kim, Y. B. Hahn, Mater. Lett. 62, 167-171 (2008).
6. J. N. Hasnidawani, H. N. Azlina, H. Norita, N. N. Bonnia, S. Ratim, E. S. Ali, Procedia Chemistry 19, 211-216 (2016).
7. Bingqiang Cao, Weiping Cai, J. Phys Chem C 112, 680-685 (2008).
8. S. G. Deshmukh, A. M. More, Proceeding Int. Conf. Adv. Mater. Sci. Vol. I , 46-48 (2016) .
9. Rakhshni, A. E., A. Bumajdad, J. Kokaj, Appl. Phys. A, 89, 923-928 (2007).
10. S.C. Shei, P. Y. Lee, J. Alloys Compd. 546, 165-170 (2013).
11. M. Ali Yildirim, Aytune Ates, Optics communications 283, 1370-1377 (2010).
12. Mohammad M. Ali, Journal of Basrah Researches (Sciences) 37, 3 A, 49-56 (2011).
13. Yanhong Tong, Lin Dong, Yichun Liu, Dongxu Zhao, Jiying Zhang, et al, Materials Letters 61, 3578-3581 (2007).
14. Ni Xu, Yong Cui, Zhigao Hu, Wenlei Yu, Jian Sun, Ning Xu,Optics Express 20, 14857 (2012).
15. S. G. Deshmukh, A. K. Panchal. V. Kheraj, J. Mater. Sci.: Material Electron. 28, 11926 (2017).

SYNTHESIS, STRUCTURAL AND PROPERTIES OF (BSPT) COMPOSITIONS

S. N. Tambe, S. R. Kulal, S. R. Kokare and D. J. Salunkhe*
Department of Physics, Nano- Composite Laboratory,
Karmaveer Bhaurao Patil Mahavidyalaya, Pandharpur, 413 304, India
*Corresponding author E-mail: salunkhedj@rediffmail.com

ABSTRACT:

The ferroelectric composition $Ba_{(0.8-x)}Sr_xPb_{0.2}TiO_3$ (BSPTx) with x = 0.2 to 0.4 are synthesized using ceramic route of synthesis. From XRD, it is observed that with increase in x the c/a ratio decreases. From the observations of variation of dielectric constant (ε) with temperature, it is revealed that for x =0.3 and 0.2, the BSPTx shows a relaxor behavior. The present observations suggests that, the BSPTx could be a useful ferroelectric system.

Keywords: X-ray diffraction, EDAX, Dielectric Properties, diffused phase transition.

INTRODUCTION:

$Ba_{(1-x)}Sr_xTiO_3$(BSTx) is a well known ferroelectric material, which has a large number of applications for the devices like DRAM, FERAM, tunable filters, tunable resonators etc. . It is observed that, the dielectric properties of BST are dependent on the percentage of Sr i.e. x. Here BST0.3 is known to possess a very large value of dielectric constant ε at T_c nearly equal to 35°C [1-3]. In addition to the compositions above $(BaSrPb)TiO_3$ (BSPT) systems have also attracted enormous interest in past a few years [4,5]. Here it is observed that the properties of BSPT are critically dependent on the percentage of Pb, Ba and Sr. Here BSPT compositions have shown a large value of dielectric constant ε. The substitution of lead causes an increase in the curie temperature Tc of $BaTiO_3$(BT) or $SrTiO_3$ (ST) compositions. It is reported that the substitution of Pb at 20% in $BaTiO_3$(BT) increases the curie temperature of BT by nearly 75°C [6].

EXPERIMENTAL:

Synthesis of BSPTx Compositions:

All the compositions in the series $Ba_{0.8-x}Sr_xPb_{0.2}TiO_3$ (BSPT) with x = 0.2, 0.25, 0.3, 0.35 and 0.4 were synthesized by using conventional ceramic synthesis route. Here $BaCO_3$, $SrCO_3$, Pb_3O_4 and TiO_2 of AR grade are used as starting materials. All these starting materials carbonates/oxides were mixed together in the required stoichiometric ratio and were ground thoroughly and manually for 3 to 4 hours. After grinding thoroughly, powders were calcinated at 1000 °C for 12 hours. The corresponding powders were then pelletized with diameter 1.2 cm and final sintering was carried out at 1180°C for 12 hours [3]. In the present case, the silver paint was employed as an electrode for characterization, where it is observed that by using silver paint to form the electrodes, the electrode effect could be minimized [7].

RESULTS AND DISCUSSIONS:

XRD and EDAX Spectra of BSPTx Compositions:

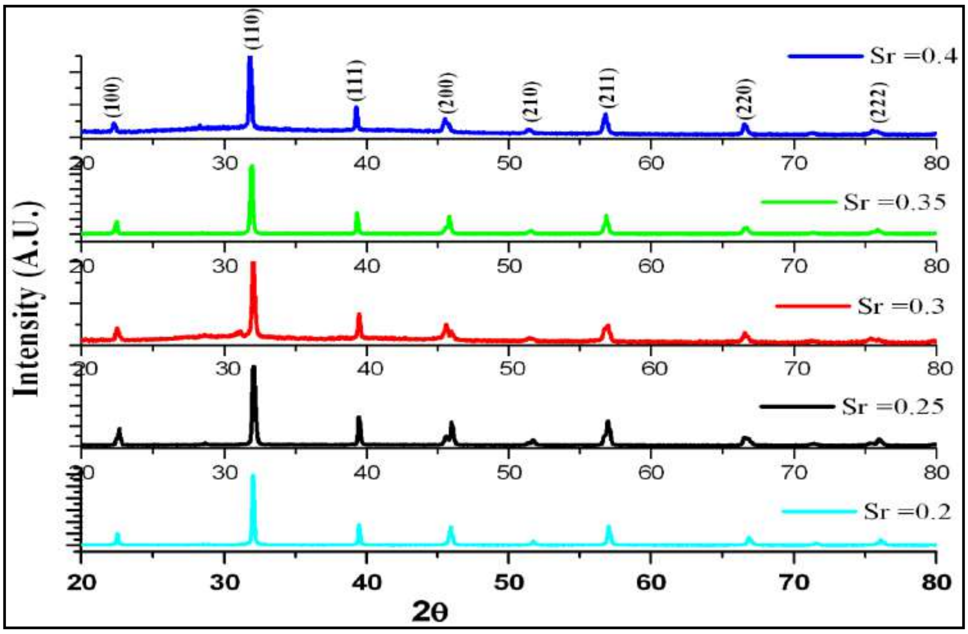

Fig . 1: Show the X Ray Diffractograms of (BSPTx) compositions with x = 0.2, 0.25, 0.3, 0.35 and 0.4

Figure 1 show the X-ray diffractograms of the BSPTx for x = 0.2, 0.25, 0.3, 0.35 and 0.4. It could be seen from figure 1 that the XRD spectra are typical of the ABO_3 system and all the peaks could be indexed according to the standard JCPDs (card no.440093). It is also seen that no peak corresponding to any impurity is recorded in figure 1. Therefore it is seen that, the BSPTx is formed as a single phase tetragonal composition.

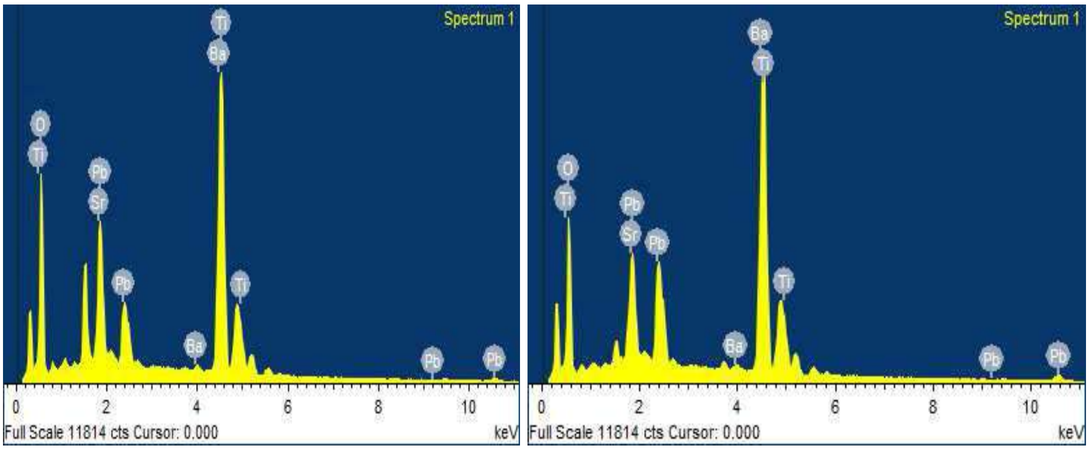

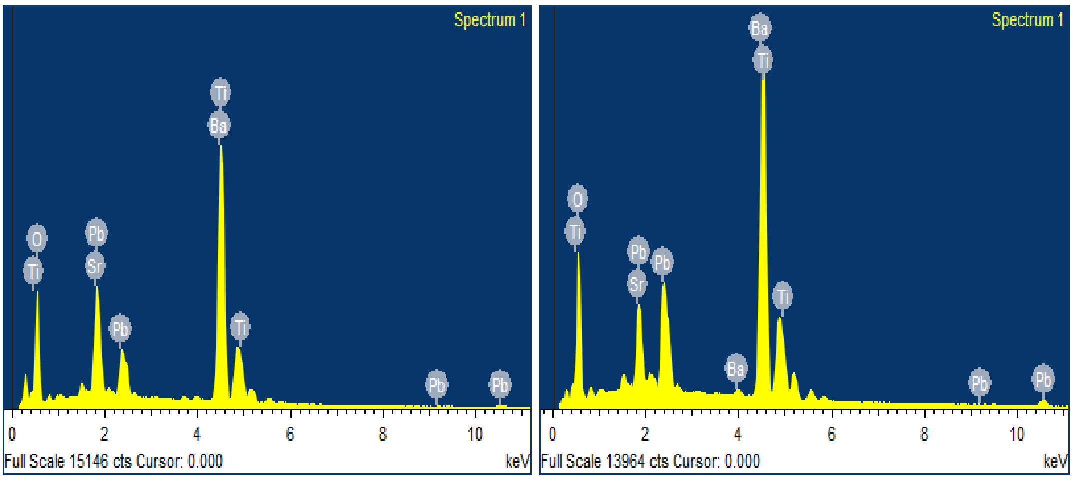

Fig. 2 Show the Energy dispersive x-Ray analysis (EDAX) for BSPTx for x = 0.2, 0.25, 0.3, 0.35 and 0.4 compositions

Table 1: Data on Energy dispersive x-Ray analysis (EDAX) for BSPTx for x = 0.2, 0.25, 0.3, 0.35 and 0.4 compositions

Element	Atomic % (Observed)				
	X = 0.2	X = 0.25	X = 0.3	X = 0.35	X = 0.4
O	83.97	81.08	79.99	78.94	79.77
Ti	7.18	9.03	9.95	9.93	9.61
Sr	2.94	2.19	3.39	2.11	4.33
Ba	4.87	5.82	5.50	6.95	4.70
Pb	1.03	1.88	1.17	2.07	1.59
Total	99.99	100	100	100	100

Composition and stoichiometry of the material was studied by using energy dispersive x-ray (EDAX) analysis. Figure 2 shows Energy dispersive x-ray (EDAX) spectra for $Ba_{0.8-x}Sr_xPb_{0.2}TiO_3$(BSPTx) for x = 0.2, 0.25, 0.3, 0.35 and 0.4 compositions. The EDAX spectrums indicated the presence of major elements Ba, Sr Pb, Ti and O in the sample. Table 1 shows atomic percentage of the element of Ba, Sr, Pb, Ti and O and confirms the formation of BSPTx for x = 0.2, 0.25, 0.3, 0.35 and 0.4 compositions . From table 1 it is clear that the observed atomic percentage of all compositions are equal.

Dielectric Properties of $Ba_{0.8-x}Sr_xPb_{0.2}TiO_3$ (BSPTx) Compositions:

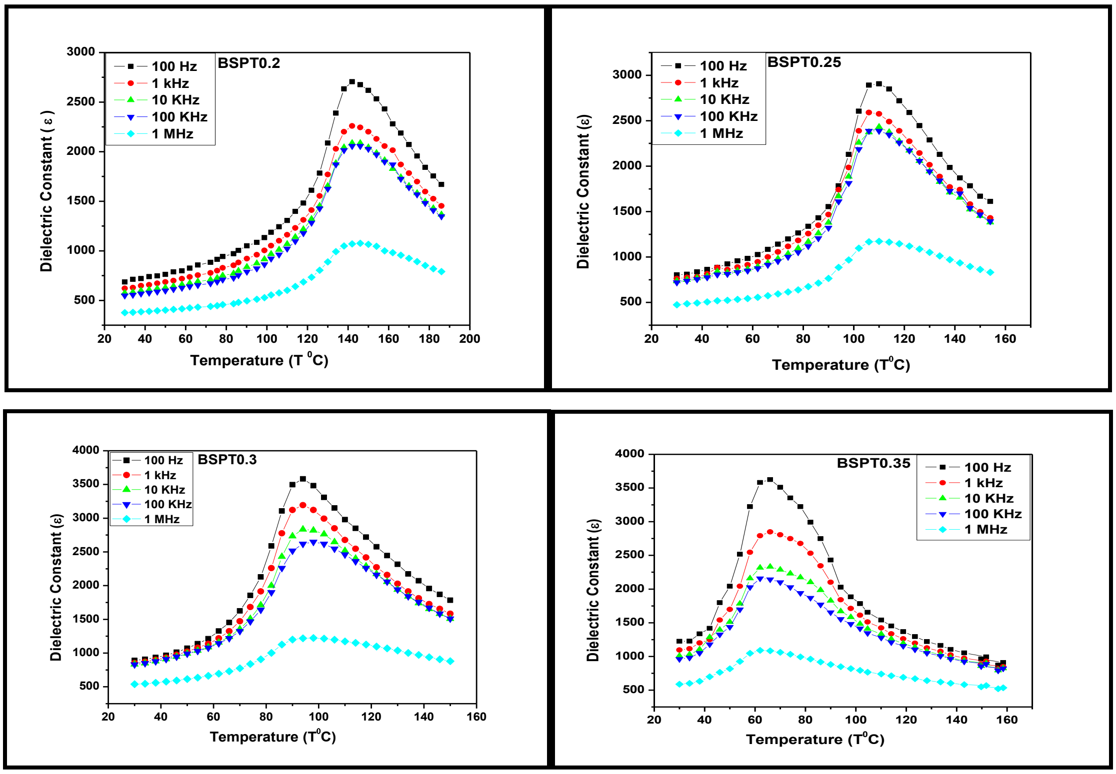

Fig. 3: Show the Variation of Dielectric constant (ε) as a function of Temperature for BSPT0.2 - BSPT0.35

Table 2: Values of ε_{RT}, $\varepsilon_{TC,}$ and T_C for $Ba_{0.8-x}Sr_xPb_{0.2}TiO_3$ at f =100Hz, 1kHz, 10kHz, 100kHz and 1MHz

x	Dielectric constant (ε_{RT}) for different Frequencies					T_C in ^oC	Dielectric constant (ε_{TC}) for different Frequencies				
	100Hz	1KHz	10KHz	100KHz	1MHz		100Hz	1KHz	10KHz	100KHz	1MHz
0.2	1007	912	843	806	553	142	3976	3320	3066	3024	1582
0.25	1335	1265	1220	1196	788	106	4824	4299	4036	3964	1946
0.3	1202	1149	1124	1120	726	95	4836	4311	3826	3573	1650
0.35	1532	1370	1260	1199	735	66	4532	3560	2913	2697	1363
0.4	700	673	657	646	481	46	1293	1237	1202	1188	776

The figures 3 show the variation of dielectric constant with temperature for conventional sintered samples. Using HP4284A LCR-Q meter, the dielectric constant of the $Ba_{0.8-x}Sr_xPb_{0.2}TiO_3$ (BSPTx) for x = 0.2, 0.25, 0.3, 0.35 and 0.4. are measured in the temperature range 28^0C to 190^0C and in the frequency range 100 Hz to 1 MHz. Table 2 Values of ε_{RT}, $\varepsilon_{TC,}$ and T_C for $Ba_{0.8-x}Sr_xPb_{0.2}TiO_3$ at f =100Hz to 1MHz.

Here the dielectric constant ε is determined relative to the dielectric constant of the free space. It is observed that the ε passes through a peak at the Curie temperature T_C. Additionally it could be seen that the T_C shifts slightly towards higher temperature as the frequency increases from 100 Hz to 1 MHz and it appears that the transition is a diffused phase transition (DPT). These features indicate that the BSPT0.3 and BSPT0.2 are diffused phase transition (DPT) materials having a signature of relaxor behavior. Further, for other compositions of $Ba_{0.8-x}Sr_xPb_{0.2}TiO_3$ for x = 0.25, 0.35 and 0.4 BSPTx for x = 0.4, 0.35 and 0.25 there is variation of ε as a function of temperature which also shows the transitions to be a diffused phase transition (DPT).

CONCLUSION:

The present observations show that the BSPTx compositions exhibit a tetragonal crystal structure. However, certain distortions are seen in the crystal structure mainly because of evaporation of PbO during sintering. It is observed that the dielectric constant passes through a peak at the Curie temperature. Additionally it could be seen that the T_C shifts slightly towards higher temperature as the frequency increases from 100 Hz to 1 MHz and it appears that the transition is a diffused phase transition (DPT). These features indicate that the BSPT0.3 and BSPT0.2 are diffused phase transition (DPT) materials having a signature of relaxor behavior.

REFERENCES:

1. A Iansculescu, D Berger, L Mitoseriu, L P Curecheriu, N Dragan, D Crisan, et al. Ferroelectrics 369 (1) 22 (2008).
2. Lavinia Petronela Curecheriu, Liliana Mitoseriu, Aldelina Ianculescu J. of Alloys and Comp., 482, 1-4 (2009).
3. M M Sutar, A N Tarale, S R Jigajeni, S B Kulkarni and P B Joshi, Appl. Nanosci., 2 311 (2012).
4. Xiaohua Sun, Huiming Huang, Shengxiang Wang , Meiya Li, Xing-zhong Zhao., Thin Solid Films, 516, 1308–1312 (2008).
5. Wei Liu, Xiaohua Sun, Hongwei Han, Meiya Li, and Xing-Zhong Zhao, Applied Physics Letters 89, 163122 (2006).
6. S M Salunkhe, S R Jigajeni, M M Sutar, A N Tarale, P B Joshi, J. of Phy. & Chem. of Solids 74, 388 (2013).
7. S R Jigajeni, A N Tarale, D J Salunkhe, P B Joshi, S B Kulkarni, Cera. Int. 39, 2331 (2013).

INFLUENCE OF AIR ANNEALING ON OPTOSTRUCTURAL PROPERTIES OF CdZn $(S_{0.5}Se_{0.5})_2$ THIN FILMS DEPOSITED BY SIMPLE AQUEOUS ROUTE

Sandip K. Jagadale[1], Dadaso B. Shinde[2],
Popatrao N. Bhosale[3] and Raghunath K. Mane*[4]
[1]S.B. Patil College of Engineering, Indapur Pune
[2]SPK Mahavidyalaya, Sawantwadi, Sindhudurg, India
*[4]Smt. K. R. P. Kanya Mahavidyalaya, Islampur-415 409, Tal.Walwa, Dist. Sangli,
E-mail: rmane.1970@gmail.com
[3]Materials Research Laboratory, Department of Chemistry,
Shivaji University, Kolhapur- 416004
*Corresponding author E-mail: p_n_bhosale@rediffmail.com

ABSTRACT

In the present study, we have successfully deposited $CdZn(S_{0.5}Se_{0.5})_2$ thin films by using simple aqueous arrested precipitation technique (APT). Preparative conditions were optimized during initial stage of experimentation to obtain good quality $CdZn(S_{0.5}Se_{0.5})_2$ thin film. Thus obtained thin film are air annealed at 100° C for 1hr. Further Optical, structural, morphological and compositional properties of annealed thin film were investigated. The optical band gap value of thin film was found to be 1.84 eV. X-ray diffraction (XRD) study reveals the formation of nanocrystalline $CdZn(S_{0.5}Se_{0.5})_2$ thin film with hexagonal crystal structure. The SEM micrograph shows the formation dense layer covered by uniform distribution of spherical grains. Energy dispersive X-ray (EDS) analysis confirm the presence of Cd, Zn, S and Se elements in the synthesized and annealed thin film..

Keywords:-Arrested Precipitation Technique, Thin Films, Surface Morphology, X-ray diffraction.

INTRODUCTION:

Mixed transition metal chalcogenide semiconducting thin films have been widely investigated in the last few decades due to their potential applications in devices [1-4]. At present, solar energy is the most prominent and clean energy source hence thin film solar cells are the most promising device in the solar cell development and research. A variety of techniques presently used for the synthesis of IIB-VIA semiconductor thin films [5-6]. Among all these techniques, arrested precipitation technique is most simple method and has many advantages over the routine chemical deposition methods [7-8]. However none of the single technique has been entirely satisfactory when considered from production perspective. Therefore, studies of annealing effect on the surface and optostructural properties play important role in enhancing device efficiency. In the present communication we describe the effect of annealing on quaternary $CdZn(S_{0.5}Se_{0.5})_2$ thin film films grown on glass substrates by APT.

Structural, morphological, optical and compositional properties of annealed films were studied and reported.

MATERIALS AND METHODS:

All the chemicals used for film deposition are of AR grade and used directly without further purification. The Cadmium sulfate hydrate ($CdSO_4.3H_2O$) (99 % Mereck) , zinc sulfate hydrate ($ZnSO_4.7H_2O$) (99% Mereck), thiourea (NH_2-CS-NH_2) (99 % Mereck), and sodium selenosulfite (Na_2SeSO_3) were used as precursors for Cd^{2+}, Zn^{2+}, S^{2-}, Se^{2-} ions. Ammonia is used to maintain bath on alkaline side and triethanolamine was used as complexing agent. The recipe is as: 0.05M 10 ml Cd-TEA complex, 0.2M 10 ml Zn-TEA complex, 0.1M 10 ml thiourea and 10 ml 0.1M sodium selenosulphite solution was taken in 100 ml beaker. Commercial glass slides were used as substrate and vertically mounted on a substrate holder. The thin film deposition parameters such as pH, deposition time, temperature of deposition bath and speed of substrate rotation were optimized10.8 ± 0.2, 2.5 h, 55 ± 2°C, 45± 5 rpm respectively. After deposition samples washed with distilled water and dried in dessicator. Further as deposited thin film annealed in air at 100°C for 1h. APT is based on Ostwald ripening law [9]. The possible growth mechanism for formation of $CdZn(S_{0.5}Se_{0.5})_2$ thin film is given below.

In alkaline medium Cd-TEA and Zn-TEA complex slowly releases Cd^{2+} and Zn^{2+} ions at pH 10.8±0.2

$$(NH_4)_4[Cd\ 2N(CH_2\text{-}CH_2\text{-}O)_3] + 6\ H_2O \longrightarrow Cd^{2+} + 4NH_4OH + 2OH^- + 2TEA \tag{1}$$

$$(NH_4)_4[Zn\ 2N(CH_2\text{-}CH_2\text{-}O)_3] + 6\ H_2O \longrightarrow Zn^{2+} + 4NH_4OH + 2OH^- + 2TEA \tag{2}$$

At the same time, Na_2SeSO_3 and thiourea dissociates in alkaline medium to produce Se^{2-} and S^{2-} ions respectively

$$Na_2SeSO_3 + OH^- \longrightarrow Na_2SO_4 + HSe^- \tag{3}$$

$$HSe^- + OH^- \longrightarrow Se^{2-} + H_2O \tag{4}$$

$$(NH_2)_2C{=}S + OH^- \longrightarrow (NH_2)_2C{=}O + HS^- + H_2O \tag{5}$$

$$HS^- + OH^- \longrightarrow S^{2-} + H_2O \tag{6}$$

$$Cd^{2+} + Zn^{2+} + Se^{2-} + S^{2-} \longrightarrow CdZn(S_{0.5}Se_{0.5})_2 \tag{7}$$

XRD analysis was used to find structure of the thin film [Brukers AXS Analytical Instruments Pvt. Ltd. Germany : D2 PHASER] with Cu $K\alpha$ target for the 10^o to 100^o 2θ range. The film thickness was determined by surface profilometer (AMBIOS XP-1). EDAX attached to scanning electron microscope (SEM) model JEOL-JSM- 6360A employed for elemental analysis of deposited thin film. The optical transmittance was measured using UV-Visible NIR- spectrophotometer Hitachi model 330, Japan in the wavelength range 300-1100nm.

RESULTS AND DISCUSSION:

Optical study:

The optical absorption was measured at room temperature for the CdZn($S_{0.5}Se_{0.5}$)$_2$ thin films in the wavelength region of 300 -1100 nm. The linear nature of the optical absorption plot confirms the direct allowed transition and is obtained by using following relation (8) [10].

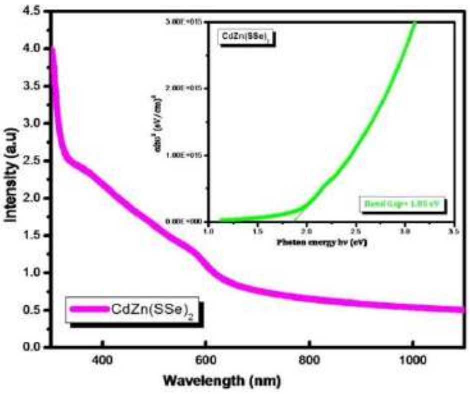

Fig.1: plot of (□ h□)^{2}vs. h□ ofCdZn($S_{0.5}Se_{0.5}$)$_2$ thin film

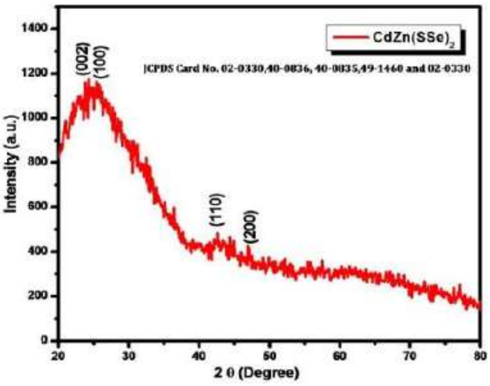

Fig. 2: XRD spectrum

$$\alpha = A(h\nu - Eg)^n / h\nu \qquad (8)$$

The optical absorption data was used to plot a graph of $(\alpha h\nu)^2$ vs. hν as shown in Fig. 1. The plot of $(\alpha h\nu)^2$ vs. hν yielded straight line at higher energies indicating direct allowed type of transition. The intercept of extrapolation to zero absorption with photon energy axis are taken as the value of E_g. The band gap determined from $(\alpha h\nu)^2$ vs. hν plots is 1.84 eV.

X-ray diffraction study:

Fig. 2 shows XRD pattern of the air annealed CdZn($S_{0.5}Se_{0.5}$)$_2$ thin film in the range of angle 2θ between 20^0 to 80^0. The major diffraction peaks centered at 2θ = 25.28, 25.52, 43.07 and 48.76 can be index to (002), (100), (110) and (200) crystal plane respectively, corresponding to observed 'd' values 3.520, 3.490, 2.100 and 1.866 Å. The observed diffraction peak pattern were compared with standard JCPDS data (card No.02-0330,40-0836, 40-0835,49-1460 and 02-0330) confirming the formation of CdZn($S_{0.5}Se_{0.5}$)$_2$ thin films with nanocrystalline nature and pure hexagonal (wurtzite) crystal structure. The average crystallite size (D) was calculated according to well known Scherrer formula [11].

$$D = \frac{k\lambda}{\beta cos\theta} \qquad \text{---(8)}$$

SEM/EDAX Studies:

The SEM micrograph shows well adherent, smooth and uniform film surface without cracks. Figure 2 shows surface morphology of CdZn($S_{0.5}Se_{0.5}$)$_2$ thin film prepared under optimized condition which exhibits spherical grain nature all over the surface. The average grain size obtained from the SEM image is consistent with the results obtained from XRD. The EDAX for CdZn($S_{0.5}Se_{0.5}$)$_2$ film is shown in figure 3. The spectrum peak reveals the presence of Cd, Zn, S and Se in the deposited thin films.

CONCLUSIONS:

APT is a facile, low cost and reliable way to synthesize mixed CdZn $(S_{0.5}Se_{0.5})_2$ thin films. Optical band gap energy value was found to be 1.84 eV. The XRD study revealed the nanocrystalline nature with pure hexagonal crystal structure of the $CdZn(S_{0.5}Se_{0.5})_2$ thin film. The SEM micrograph shows that the surface has layered structure containing dense layer without any pinholes covered by uniform distribution of spherical grains. EDS results confirm the presence of Cd, Zn, S and Se elements in synthesized and annealed thin film. Studies on effect of reaction time and annealing on photoelectrochemical performance of $CdZn(S_{0.5}Se_{0.5})_2$ thin films is in progress in our laboratory.

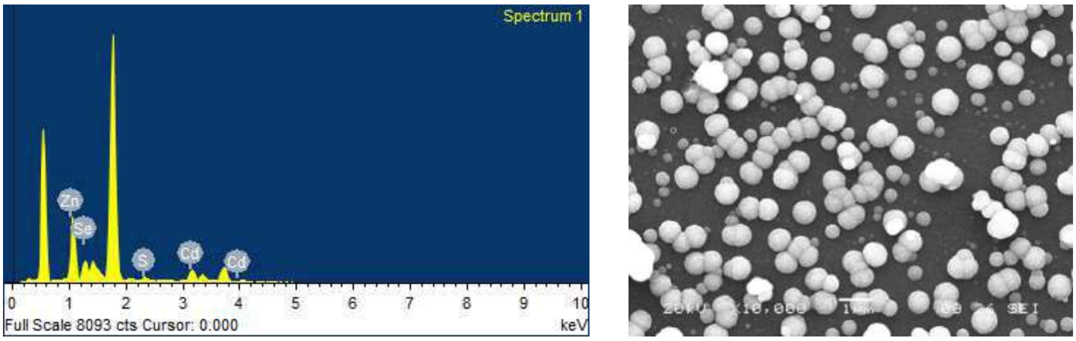

Fig.3: EDAX and SEM of $CdZn(S_{0.5}Se_{0.5})_2$ thin film

REFERENCES:

1. K.V. Khot, S.S. Mali, N.B. Pawar, R. R. Kharade, R. M. Mane, P. B. Patil, P. S. Patil, C. K. Hong, J. H. Kim, J. Heoe and P.N. Bhosale, RSC Adv., 5, 40283 (2015).
2. N. B. Pawar, S. S. Mali b, M. M. Salunkhe, R. M. Mane, P. S. Patil and P. N. Bhosale, New J. Chem., 36, 1807-1812 (2012) .
3. M. Behringer, K. Ohkawa, V. GroDmanna, H. Heinke, K. Leonardi, M. Fehrer, D. Hornmel, M. Kuttler, M. Strassburg, D. Bimberg, J. Crystal Growth, 184/ 185, 580-584 (1998).
4. S.B. Patil, A.K. Singh, Appl. Surface Sci., 256, 2884–2889 (2010).
5. S. K. Jagadale, K. V. Khot, C.S. Bagade, R.M. Mane, V.B. Ghanwat, R.K. Mane, S. S. Mali, C. K. Hong and P. N. Bhosale, J. Mater. Sci: Mater Electron, 28 (3), 2984-2995 (2016).
6. T. Premkumar, S.Saravanakumar, K. Shankaranarayanan, App. Surf. Sci., 257, 1923-1927 (2011).
7. S.M. Thahab, Adel H. Omran Alkhayat, Salah M. Saleh, Optik , 125, 5112–5115 (2014).
8. S. K. Jagadale, D. B. Shinde, R. M. Mane, K.V. Khot, V. B. Ghanwat, P. N. Bhosale and R. K. Mane, Nanosystems : Physics, Chemistry and Mathematics, 7(3), 523 – 527 (2016).
9. W. Ostwald, Lehrbuch der Allgemeinen Chemie, Leipzig, Germany, vol. 2(1) (1896).
10. N.B. Pawar, S.S. Mali, M.M. Salunkhe, R.M. Mane, P.S. Patil and P.N. Bhosale, New J. Chem., 36, 1807–1812 (2012).
11. C. S. Bagade, S. S. Mali, V. B. Ghanwat, K. V. Khot, P. B. Patil, S. D. Kharade, R. M. Mane, N. D. Desai, C. K. Hong, P. S. Patil ,P. N. Bhosale, RSC Adv., 5, 55658 (2015).

STRUCTURAL AND OPTICAL STUDY OF HYDROTHERMALLY SYNTHESIZED COPPER ZINC TIN SULFIDE FOR PHOTOVOLTAIC APPLICATION

S. A. Phaltane[1*], D. L. Kamble[2], P.S. Patil[2] and L. D. Kadam[1]**

[1]Solid State Physics Laboratory, Department of Physics,
Yashvantrao Chavan Institute of Science, Satara, Maharashtra 415001, India
[2]Thin Film Materials Laboratory, Department of Physics,
Shivaji University, Kolhapur, M.S. 416 004, India
Corresponding author E-mail: *shilpa.phaltane@gmail.com, **kdlaxman_222@yahoo.co.in

ABSTRACT:

Copper zinc tin sulfide (CZTS) is a quaternary semiconductor has attracted much more attention as a good absorber material in photovoltaic applications. For the synthesis of CZTS green approach of hydrothermal method has been used. Synthesised powder has been characterized for structural analysis, morphological analysis and UV-Vis spectroscopy. Synthesized sample shows kesterite phase with tetragonal crystal structure and a band gap of 1.47 eV with agglomeration morphology.

Key words: CZTS, hydrothermal

INTRODUCTION:

In photovoltaic applications direct band gap materials plays vital role. Among different solar radiation absorbing materials, a direct band gap material has attracted much more attention. One of the good absorbing materials is Copper zinc tin sulfide (Cu_2ZnSnS_4). CZTS is a p type semiconductor with direct band gap (1.4-1.5 eV) and high absorption coefficient of 10^4 /cm [1, 2]. It is used in energy harvesting, thermoelectric as well as photocatalytic applications [3-6]. CZTS was reported by Katagiri for the first time [7]. Thereafter different methods were used for the synthesis of CZTS such as microwave [8], Sol-Gel [9], solvothermal [10], SILAR [11], Hot injection [12], Electro deposition [13], Sputtering [14], Pulse laser deposition [15], Hydrothermal [16]. Among these methods, hydrothermal has simpler procedure, economical nature and eco friendly. In present work we synthesis CZTS powder by hydrothermal method.

EXPERIMENTAL METHOD:

For synthesis of CZTS, Copper (I) chloride (CuCl), Zinc(II) chloride ($ZnCl_2$), tin (IV) chloride pentahydrate ($SnCl_4.5H_2O$) and thiourea $SC(NH_2)_2$ were used as a precursors in the molar ratio (2:1:1:8). They were dissolved in 40 ml double distilled water under magnetic stirring at room temperature. Obtained solution was transferred into 50 ml Teflon-lined stainless steel autoclave, kept in muffle furnace at 180°C for 48 hours. After cooling to room temperature final product was centrifuged and washed with double distilled water several times for removal of water soluble impurities. It finally dried at 60^{o}C for 6 hours.

CHARACTERIZATIONS:

The XRD patterns of the films were recorded using X-ray powder diffractometer (Bruker AXS Analytical Instruments Pvt. Ltd., Germany, Model: D2 phaser) with Cu Kα radiation. The surface morphology of the CZTS powder was recorded by a scanning electron microscope (SEM; S-4700, Hitachi). The room temperature optical absorption measurements were performed in the wavelength range over 100–1000 nm by using a UV–Vis spectrophotometer (UV1800, Shimadzu, Japan).

RESULT AND DISCUSSION:

Structural analysis (XRD):

The XRD pattern of annealed sample is shown in Fig. 1. It shows three major peaks at 2θ = 28.79, 47.72 and 56.65^0 can be attributed to the diffraction from (112), (220) and (312) planes respectively and some minor peaks at 33.03, 76.65 attributed to the (110) (200), (008) and (332) [16, 19]. These diffraction peaks matches well with the JCPDS data card 26-0575 reveals that the synthesized power has kesterite CZTS phase [16]. The lattice parameters for the tetragonal structure can be calculated by the expression:

$$\frac{1}{d^2} = \frac{h^2+k^2}{a^2} + \frac{l^2}{c^2} \qquad \text{-----Eq. (1)}$$

The observed mean values of the lattice parameters are (a=5.42 Å, c=10.79 Å) which matches well with the JCPDS card 26-0575 (a= b=5.43 Å, c = 10.84 Å).

The standard and observed ‘$d_{h\,k\,l}$’ values with their respective planes of the annealed sample were calculated by using Bragg’s law: $2d_{hkl}\sin\theta = n\,\lambda$ are summarized in following table:

Table 1: ‘d_{hkl}’ spacing of synthesised sample

Sr. No.	Plane (h k l)	‘d’ spacing (in Å)	
		Standard	Observed
1	(112)	3.1260	3.0983
2	(200)	2.7130	2.7096
3	(220)	1.9190	1.9042
4	(312)	1.6360	1.6234
5	(008)	1.3560	1.3488
6	(332)	1.2450	1.2440

Using Scherer’s formula $d = \frac{0.9\,\lambda}{\beta\,Cos\,\theta}$, average grain size can be calculated, where β is full width half maxima (FWHM), λ is the X-ray wavelength. The average grain size of sample using the (112) planes reflection is 25 nm. Some secondary phase such as SnS_2 is detected in XRD pattern.

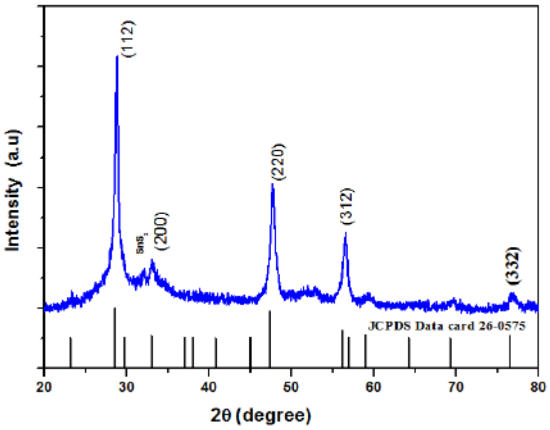

Fig. 1: XRD pattern of CZTS powder.

The fine line shows the simulated pattern of kesterite CZTS (JCPDS no. 26-0575)

SEM analysis:

Surface morphology and microstructure plays very important role for photocatalytic applications. Fig.2 shows SEM image which reveals that CZTS powder is agglomeration of particles.

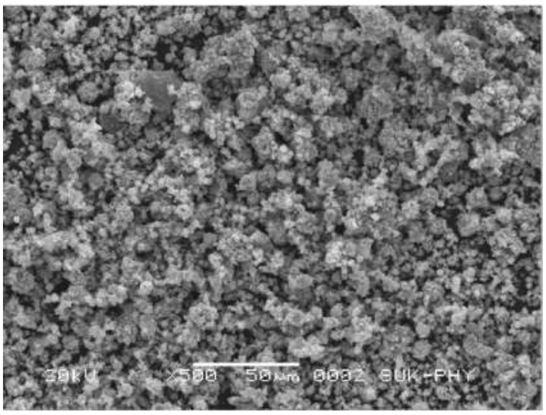

Fig. 2: SEM image of CZTS powder

UV Visible spectroscopy:

Optical absorbance measurement was used to determine the band gap of CZTS sample. Liquid phase method was used to determine the band gap. CZTS powder exhibit broad absorption in visible region whereas the tail of graph extends to the longer wavelength.

Tauc and Davise Mott model was used to obtain optical band gap by using equation:

$$(\alpha h\gamma)^n = A\ (h\gamma - E_g) \qquad \text{-----Eq. (2)}$$

Where A is absorbance, E_g is band gap, hγ is the incident photon energy, α is absorption coefficient and n is index characterizing the type of optical transition. n = 2 for direct band gap. **Fig.3** shows the UV-vis spectra powder sample. By extrapolating the linear part of the graph of $(Ah\gamma)^2$ versus the photon energy gives the direct band gap of 1.47 eV .This value matches well with the literature values [17-19] and indicates that material is efficient for photovoltaic application.

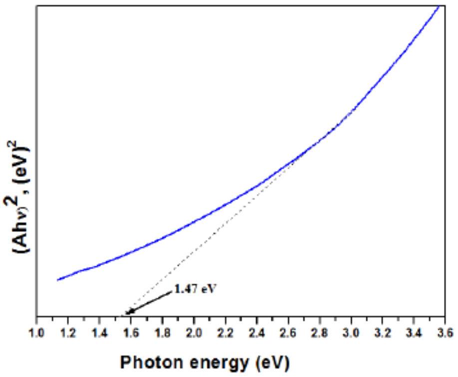

Fig. 3: Tauc plot for measurement of band gap

CONCLUSION:

Copper zinc tin sulfide (CZTS) powder has been synthesised using eco friendly and non toxic hydrothermal method at the temperature of 180^{o}C. XRD of the sample reveals kesterite phase with tetragonal crystal structure. SEM image shows agglomeration of the particle with direct band gap of 1.47eV.

REFERENCES:

1. K.V. Gurav, Appl. Surface Sci., 283, 74– 80 (2013).
2. U. Ghorpade, Chem. Commun., 50, 11258 (2014).
3. P. Kush, J. Mater. Chem. A, 3, 8098 (2015).
4. X. Yu , J. Am.Chem. Soc., 136, 9236 (2014)..
5. J. Wang, RSC Adv., 4, 27805 (2014).
6. L. Rovelli, ACS Appl. Mater. Interfaces, 5, 8018 (2013).
7. K. Ito, Jpn. J. Appl. Phys., 27, 2094 (1988).
8. V. A. Madiraju, J Mater Sci: Mater Electron., 27, 3152 (2016).
9. G. L. Agawane, J Mater Sci: Mater Electron, 26, 1900 (2015).
10. S. S. Mali, Phys. Status Solidi RRL, 7, 12, 1050 (2013).
11. M. Suryawanshi, RSC, Adv. 4, 18537 (2014).
12. D. Xia, J Mater Sci: Mater Electron, 26, 5426 (2015).
13. E. M. Mkawi , J Mater Sci: Mater Electron, 26, 222 (2015).
14. B.T. Jheng , Solar Energy Materials & Solar Cells, 128, (2014) 275
15. S.A. Vanalakar, J. Ceram. Int., 6, 121, (2014).
16. W. C. Liu, J. Mater. Chem. A, 1, 3182 (2013).
17. G. Rajesh, Superlattices and Microstructures, 77, 305 (2015).
18. Y. Zhao, J Mater Sci: Mater Electron , 26, 5645 (2015).
19. P. Kush, Materials Chemistry and Physics, 162, 608e616 (2015).

DABCO ENTRAPPED IN AGAR AGAR: A HETEROGENEOUS GELLY CATALYST FOR MULTI-COMPONENT SYNTHESIS OF 2-AMINO-4H-CHROMENES

Shital Shinde, Gajanan Rashinkar, Popat Pawar, and Rajashri Salunkhe*

ABSTRACT:

An efficient method for the Multicomponent synthesis of 2-amino-4*H* Chromenes by reaction of malanonitrile with various aldehydes and phenols in the presence of Gel entrapped DABCO as catalyst is reported. Mild reaction conditions, reusability of catalyst, easy isolation of product along with excellent yield has made the process more advantageous than conventional method.

INTRODUCTION:

The rapid assembly of molecular diversity utilizing multicomponent reactions (MCRs) has received a great deal of attention, most notably for the speedy synthesis of novel molecular libraries [1]. These methodologies are of particularly great utility when they lead to the formation of privileged medicinal and industrial scaffolds. 2-Amino-4*H*-chromene scaffolds are of significant medical relevance since they have widespread applications including antiviral[2], antimicrobial[3], antiproliferative[4], mutagenicity[5], antitumor[6], sex pheromone[7] and central nervous system activity[8]. Looking at their importance from pharmacological and industrial point of view, several methods for the multi-component reaction for the synthesis of 2-amino-4*H* chromene have been reported. These method include both homogeneous as well as heterogeneous conditions, catalyzed by piperidine[9], aqueous K_2CO_3[10] have been also employed. Although the literature on synthesis of 2-amino-4*H* chromene enjoys a rich array of versatile methodologies, new efficient approaches can be valuable additions to the contemporary arsenal of synthetic strategies.

The concept of gel entrapped base catalysts (GEBCs) combines the advantages of alkali and organic bases with those of heterogeneous supports. These catalysts are prepared by immobilization of alkali or organic bases by entrapping them in an aqueous gel matrix of agar-agar which is a polymer. This method reduces the amount of bases used and affords easy and efficient separation of products from the catalyst. Besides this, bases like alkalis when exposed to air, absorb moisture and are spoiled. On the contrary, the GEBCs do not absorb moisture on exposure to air and remain intact. The use of GEBCs in organic synthesis also provides excellent opportunity of recyclability and reusability which is seldom possible using bases alone as catalysts. In our continued interest in the applications of novel catalysts in organic synthesis, we report herein the synthesis of 2-Amino-4*H* chromenes from MCR of phenols, aldehydes and malanonitrile in the presence of Gel entrapped DABCO as a catalyst.

RESULTS AND DISCUSSION:

Initially, we focused our attention towards the synthesis of Gel entrapped DABCO. A series of experiments were under taken in which different concentrations of DABCO (5-25 %) were dissolved in a varying amount of agar-agar in water. After a considerable experimentation, we found that 20 % *w*/*w* of agar-agar aqua gel containing 10 % DABCO resulted in the formation of soft gel that served as GEBC in the present work. Gel entrapped DABCO was white jelly like substance that could be cut into pieces**.**

Thermal behaviour of Gel entrapped DABCO was studied by thermogravimetric analysis (TGA) and differential scanning calorimetry (DSC) (**Fig. 1**). The TGA/DSC curve revealed that the loss of water occurs initially upto ~150 ^{0}C and is accompanied with endothermic peak in DSC curve. The thermal decomposition of DABCO embedded polymer matrix occurs in two distinct steps giving approximately weight loss 11 % in each step. It is also revealed from the DSC curve that these processes are exothermic. The decomposition is completed at the temperature 510 ^{0}C.

Our next task was to demonstrate the catalytic activity of Gel entrapped DABCO in the synthesis of 2-amino-4*H* Chromenes. As a trial case, equimolar mixture of phenol, benzaldehyde and malanonitrile (5 mmol each) was stirred in the presence of 1 gm of various GEBCs in ethanol at ambient temperature till the completion of reaction as monitored by thin layer chromatography.

The recovery and reuse of catalysts is highly preferable for the large scale operations and industrial point of view. To check the possibility of GEC recycling, the reaction of phenol, benzaldehyde and malanonitrile using Gel entrapped DABCO in ethanol was studied. After completion of the reaction, the catalyst was separated from reaction mixture, washed with ethanol and reused in another reaction with identical substrates. The catalyst showed a remarkable recyclability.

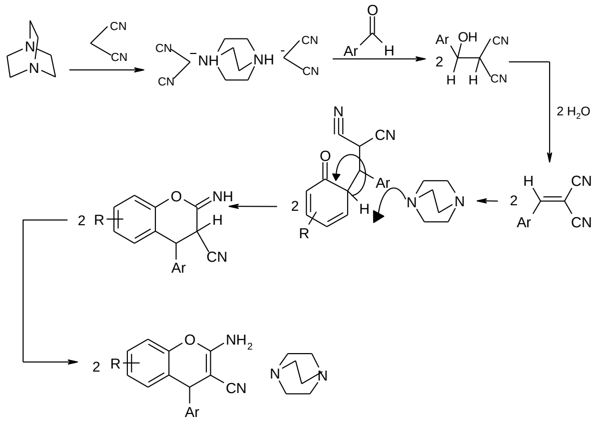

Scheme: **Proposed mechanism for the synthesis of napthopyranes catalysed by DABCO-GEC**

Preparation of DABCO-GECs:

GEBCs was prepared according to literature [accepted] with some modification.

To a boiling mixture of agar-agar (5 gm) in water (35 mL) was added a mixture of base (2.5 gm) in water (2.5 mL). The resultant solution was boiled with stirring for five minutes and cooled in ice bath to yield the desired GEBC.

General procedure for multicamponant reaction of phenol, dimedone and malanonitrile:

A mixture of phenol (5 mmol), aldehyde (5 mmol) and malanonitrile (5 mmol) was stirred in the presence of GEBC (1 gm) in 5 mL of ethanol at ambient temperature till the completion of the reaction as monitored by TLC. The resulting crude product was filtered off, washed with water and recrystallized from ethanol to afford pure products.

CONCLUSION

In conclusion, a novel and highly efficient methodology for multicamponant reaction of phenol, aldehyde and malanonitrile has been developed using recyclable DABCO-GEC. The method offers several significant advantages, such as high conversions, easy handling, clean reaction profile and short reaction time, which make it a useful and an attractive addition to the existing methodologies for the synthesis of multicampoanent ie. 2-amino-4*H* Chromene products.

REFERENCE:

1. For a monograph, see J. Zhu, H. Bienaymé (Eds.), Multicomponent Reactions, 1st ed, Wiley-VCH, Weinheim (2005).
2. Khafagy, M. M.; El-Wahas, A. H. F. A.; Eid, F. A.; El-Agrody, A. M. II Fármaco, 57, 9, 715-722 (2002).
3. Dell, C. P.; Smith, C. W. Euro. Patent Appl. EP 537949; Chem. Abstr., 119, 139102d (1993).
4. Hiramoto, K.; Nasuhara, A.; Michiloshi, K.; Kato, T.; Kikugawa, K. Mutat. Res., 47, 395 (1997).
5. Mohr, S. J.; Chirigos, M. A.; Fuhrman, F. S.; Pryor, J. W. Cancer Res., 35, 3750–3754 (1975).
6. Bianchi, G.; Tava, A. Agric. Biol. Chem., 51, 2001–2002 (1987).
7. (a) Anderson, D. R.; Hegde, S.; Reinhard, E.; Gomez, L.; Vernier, W. F.; Lee, L.; Liu, S.; Sambandam, A.; Snider, P. A.; Masih, L. Bioorg. Med. Chem. Lett., 15, 1587–1590 (2005).
8. (a) Al-Matar, H. M.; Khalil, K. D.; Meter, H.; Kolshorn, H.; Elnagdi, M. H., ARKIVOC, 16, 288-301 (2008).
9. (a) Poddar, R.; Kidwai, M. Cat. Lett. 2008. 124, 311-317. (b) Kidwai, M.; Saxena, S.; Khalilur, R. K. M.; Thukral, S. Bioorganic & Medicinal Chemistry Letter, 15, 4295–429 (2005).
10. Shestopalov, A. M.; Emelianova, Yu. M.; Nesterovb, V. N. Russ. Chem. Bulletin, 51, 12, 2238-2243 (2002).

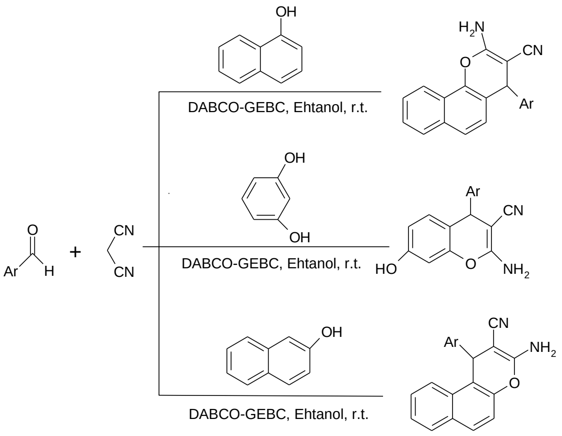

Scheme : Multicomponent reaction of phenol, aldehyde and malanonitrile

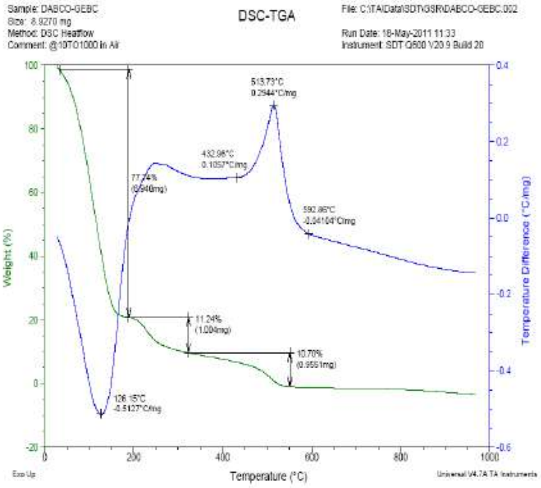

(Fig. 3)

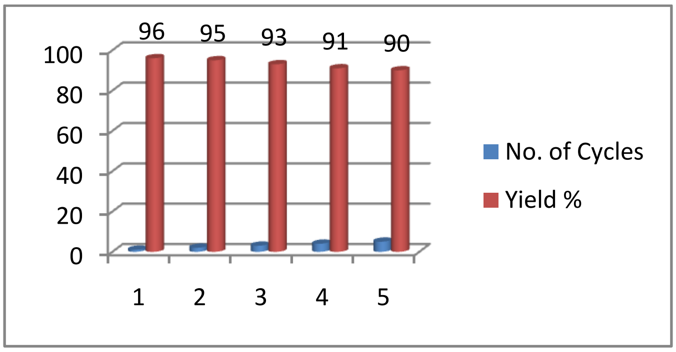

(Fig. 4)

EFFECT OF ECR PLASMA TREATMENT ON SELF-CLEANING BEHAVIOUR OF ZnO THIN FILMS

Shivaji V Bhosale[1*], Pratik Bhagwat[1] and Supriya More[2]

[1]Department of Physics, Sir Parashurambhau College, Pune-411030

[2]Department of Physics, Savitribai Phule Pune University, Pune, 411007

*Corresponding author E-mail: bhosale3399@gmail.com

ABSTRACT:

ZnO nanoparticles were synthesized by sol-gel method. Zinc acetate dehydrate and monoethanolamine (MEA) were used as the precursor materials. The Zinc Oxide (ZnO) thin films were prepared by spin coating technique. The obtained films were further calcined at 500°C. The X-ray diffraction (XRD) technique was used to characterize the thin films. The XRD spectra indicate that the ZnO crystal has a hexagonal wurtzite structure. The grain size of 16nm was obtained from the analysis of XRD pattern. The wettability of thin film was determined by measuring the contact angle. A home-made electron cyclotron resonance (ECR) plasma was used to study its effect on the surface modification of ZnO thin film. The ZnO thin film was treated with Ar-plasma for 20 min. The plasma treatment resulted in the surface modification of ZnO thin films which was observed from the changes in the contact angle measurement.

INTRODUCTION:

Surface engineering is carried out in order to attain superior performance and durability of a substrate. Wetting phenomenon is one such property which deals with the identification of the surface modification [1]. Wettability is strongly affected by the chemical composition and geometrical structure of the solid surface. Wettability has potential application in self- cleaning materials, drag reduction coating, anti-fogging and so on [2,3].

Zinc oxide (ZnO) is a wide-band gap semiconductor which has several favourable properties like high electron mobility, good transparency, and strong room temperature luminescence. ZnO basically crystallizes into two main forms, cubic zinc blende and hexagonal wurtzite [4]. The stable structure which is most common is wurtzite. ZnO can be synthesized in variety of ways with different particle structures and finds potential applications in various fields of technology.

There are various ways to synthesize ZnO thin films ranging from the sol-gel method to pulsed laser deposition. The sol-gel process offers other advantages such as high surface morphology, easy grip over the chemical components and good optical properties of ZnO thin film. Sol-gel method is widely used for the synthesis of oxide materials due to its simplicity and cost effectiveness [5].

In the present work nano-crystalline ZnO thin films were prepared by sol-gel spin coating technique using zinc acetate precursor. These films were further treated with ECR Plasma to induce surface modification. The surface morphologies and optical properties of the as synthesized ZnO film were studied.

EXPERIMENTAL:

ZnO Sol-Gel Preparation:

ZnO thin films were coated on glass substrates by sol-gel method. Zinc acetate de-hydrate, 2-methoxyethanol and monoethanolamine (MEA) were used as precursor, solvent and stabilizer respectively. Zinc acetate de-hydrate and 2-methoxyethanol were mixed together and stirred magnetically for 50 min at 80°C. Further, MEA was added under constant stirring and stirred for 90 minutes to yield a colorless, homogeneous and transparent solution. The solution was aged for 72 hours at room temperature in order to make it more glutinous.

Deposition of Thin Films:

The glass substrates were sonicated for 30 min and then cleaned in acetone. Afterwards, substrates were rinsed with distilled water. The aged ZnO solution was dropped on glass substrates which were rotated at 2000 rpm for 30 seconds. The deposited films were then pre-heated at 150°C for 5 minutes into an oven. This spinning to pre-heating procedure was repeated for fifteen times (layers). Finally, the films were annealed at 500°C for 3 hrs to remove all the unwanted organic species.

Ar-ECR Plasma Treatment:

The ECR system was pre-evacuated and feed with respective gases till operating pressure is obtained. The plasma is generated in the reaction chamber when the resonance conditions are satisfied for the input electric frequency of 2.45 GHz to the magnetic field of 875 G. The Ar-ECR plasma was generated was exposed it onto a ZnO film for 20 min. The samples were placed at a distance of 15 cm from the ECR zone.

The structural properties of ZnO films were characterized by XRD using Bruker advance diffractometer with Cu-Kα radiation. The contact angle measurements of water were obtained for the ZnO films to determine whether the films are hydrophilic or hydrophobic in nature.

RESULT AND DISCUSSION:

Fig 1. shows the XRD pattern of ZnO thin films. The different peak orientations were observed along the (100), (002), (110), (103), and (112) planes. The obtained peaks confirm the formation of ZnO particles with hexagonal wurtzite structure. The crystallite size (D) of the synthesized ZnO nanocrystals was calculated using the Debye-Scherrer formula. The calculated average value of crystallite size is found to be 22.9nm.

Fig.2 shows the contact angle measurement of water drop on glass, ZnO film and plasma treated ZnO film. Contact Angle of DI water on Plain Glass Substrate is found to be 26.20° and on

ZnO Thin Film is found to be 100.27°. Thus it can be observed that the ZnO thin films have considerable effect of Ar-ECR plasma on its surface.

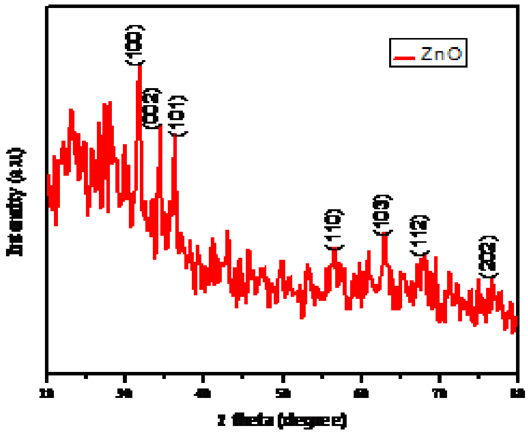

Fig.1: XRD of ZnO thin Film calcined at 500°C

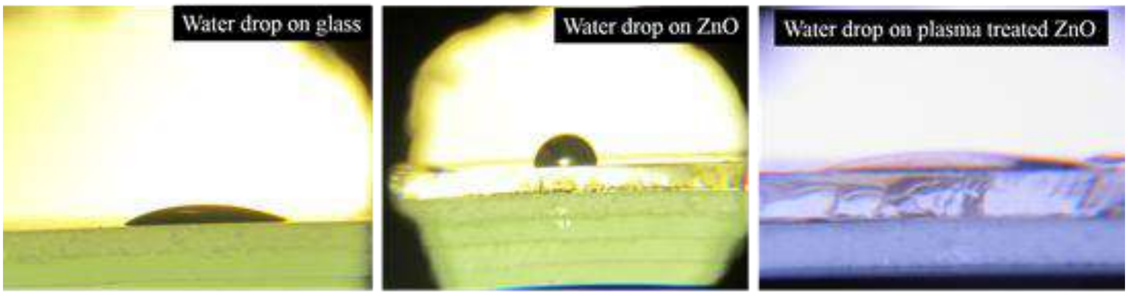

Fig. 2: Contact angle measurement of water onto glass, ZnO film and plasma treated ZnO film

CONCLUSION:

The Ar-ECR plasma has sufficient energy to cause surface modifications in ZnO thin Films. It can be concluded that due to plasma treatment the ZnO thin films surface is modified form hydrophilic to hydrophobic which is desirable for self-cleaning application.

REFERENCES:

1. S. Wang, X. Feng, J. Yao, L. Jiang, Angew. Chemie - Int. Ed. 45, 1264–1267 (2006).
2. T. Kamegawa, Y. Shimizu, H. Yamashita, Adv. Mater. 24, 3697–3700 (2012).
3. Y. Liu, W. Yao, X. Yin, H. Wang, Z. Han, L. Ren, Adv. Mater. Interface, 3, 1500723 (2016).
4. R. Wang, L. Cong, M. Kido, Appl. Surf. Sci., 191, 74–84 (2002).
5. R. Lundy, C. Byrne, J. Bogan, K. Nolan, M.N. Collins, E. Dalton, R. Enright, Appl. Mater. Interfaces. 9, 13751–13760 (2016).

GRAPHENE SUPPORTED IONIC LIQUID PHASE CATALYST FOR ORGANIC TRANSFORMATION

Shivanand Gajare, Altafhusen Naikwade, Prakash Bansode,
Rajashri Salunkhe and Gajanan Rashinkar[*]
Department of Chemistry, Shivaji University, Kolhapur, 416004
*Corresponding author E-mail: gsr_chem@unishivaji.ac.in

Developments in the field of catalysis are being reported continuously, in the form of novel catalysts, new catalytic reactions and alternative methodologies. Much of the attraction for this is driven by the economic demands to develop systems in which easy separation of products and reuse of catalysts is possible along with high reactivity and selectivity. As a part of this effort, an ever increasing degree has been focused on the ionic liquids (ILs) as an alternative reaction media in synthetic chemistry.The tempting properties of ILs such as negligible vapour pressure, large liquidus range, high thermal stability have made them an environmentally attractive alternative to organic solvents. Their properties can be altered by fine tuning of parameters such as the choice of organic cation, inorganic/organic anion and the length of alkyl chain attached to an organic cation. These structural variations offer flexibility to design the plethora of diverse ILs, catering to the needs of any particular process.Immobilization of ILs on porous support material can be achieved in two different ways, either by covalent bonding of ionic liquid fragments to the support or by physisorption*via* van der Waals and dipole forces

Graphene, whose discovery won the 2010 Nobel Prize in physics, has been a shining star in the material science in the past few years. It is one of the most promising materials in nanotechnology. It belongs to sp^2¬carbon nanomaterials that include zero-dimensional (0D) fullerene, 1D carbon nanotubes and 2D graphene Owing to its interesting electrical, optical, mechanical and chemical properties, graphene has found potential applications in a wide range of areas, including biomedicine. From a catalysis point of view, it provides the ultimate two-dimensional model of a catalytic support. Its unique physical, chemical and mechanical properties are outstanding, and allow the preparation of composite-materials with unprecedented characteristics. Even though the use of a single graphene sheet as a catalytic support has not yet been reported, some promising results have already been obtained with few-layer graphene.This has allowed researchers to design and develop countless combinations of graphene-based materials, some rather simple while others considerably more sophisticated. Despite of the promising results obtained in graphene based catalysis; there is a still huge scope to develop new molecules based on functionalized graphene as catalytic materials for achieving efficient organic transformations.The aforementioned facts spurred us to undertake Functionalized graphene and magnetic nanoparticles for catalytic and medicinal applications as a topic of research.

Several catalyst have been using for organic transformation reaction. Graphene, the amazing two-dimensional carbon nanomaterial, has attracted extensive interest in recent years. Graphene based materials hold great promise for facilitating a wide range of transformations and offer extraordinary potential in the design of novel catalytic systems. The surface decorated myriad oxygenated functions in GO allow the functionalization of graphene by covalent or non-covalent methods which as a consequence, can improve its solubility, dispersibility and chemical stability. Furthermore, the high surface area of graphene, reaching up to 2600 m2 g−1, represents a desirable characteristic as two-dimensional support. Moreover, the influence of chemical and physical properties of graphene can assist in obtaining more selective and active heterogeneous catalyst system as seen in the generation of ammonia, hydrogenation of carbon oxides and hydrotreating reaction.

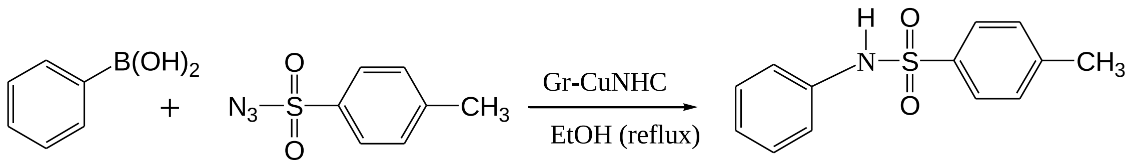

Phenyl boronic acid **TosylAzide** **N-aryl sulfonamides**

Scheme – I

Considering amazing properties of graphene, we have synthesized novel graphene supported ionic liquid phase Gr-CuNHC catalyst. The synthesis involves initial modified graphene oxide (GO) reduces to grapheme-OH which is modified with 3 chloropropyltrimethoxysilane which is subsequently treated with ferrocenyl imidazole salt and CuI to desired an efficient graphene supported Gr-CuNHC catalyst obtained. Thus, in the present work, we have synthesized N-aryl sulfonamides from phenyl boronic acid and aryl azides using graphene supported ionic liquid phase CuNHC catalyst acronymed as Gr-CuNHC (Scheme I).

Catalyst is fullely characterized by the techniques used IR,TGA,BET,EDX, Raman,Solid state C13-NMR & TEM which gives confirmation of the structure.

REFERENCES:

1. (a) T. Welton, Chem. Rev. 1999,99, 2071; (b) C. C. Tzschucke, C. Markert, W. Bannwarth, S. Roller, A. Hebel, R. Haag, Angew. Chem., Int. Ed. 2002,41, 3964; (c) J. Dupont, R. F. de Souza, P. A. Z. Suarez, Chem. Rev.,102, 3667 (2002).
2. P. Wasserscheid, Angew. Chem. Int. Ed., 39, 3772 (2000).
3. (a) M. T. Garcia, N. Gathergood, P. J. Scammells, Green Chem. 2005, 7, 9; (b) K. M. Docherty, C. F. Kulpa, Green Chem. 2005, 7, 185; (c) C. Pretti, C. Chiappe, D. Pieraccini, M. Gregori, F. Abramo, G. Monni, L. Intorre, Green Chem., 8, 238 (2006).
4. Riisager, A., R. Fehrmann, M. Haumann, P. Wasserscheid, Top. Catal., 40, 91 (2006).

5. H. (a) H. Hagiwara, Y. Sugawara, K. Isobe, T. Hoshi, T. Suzuki, Org. Lett. 2004, 6, 2325; (b) J. Huang, T. Jiang, H. Gao, B. Han, Z. Liu, W. Wu, Y. Chang, G. Zhao, Angew. Chem. 2004, 43, 1397; (c) C. P. Mehnert, R. A. Cook, N. C. Dispenziere, M. Afeworki, J. Am. Chem. Soc., 124, 12932 (2002).
6. T. Selvam, A. MacHoke, W. Schwieger, Applied Catalysis A: General, 445-446, 92 (2012).
7. L. Rodríguez-Pérez, E. Teuma, A. Falqui, M. Gómez, P. Serp, Chem. Commun.,4201 (2008).
8. J. Mikkola, P. Virtanen, H. Karhu, T. Salmia, D. Y. Murzin, Green. Chem., 8, 197 (2006).
9. N. Clousier, R. Moucel, P. Naik, P. J. Madec, A. C. Gaumont, I. Dez, C. R. Chimie, 14, 680 (2011).
10. S. Shylesh, V.Schunemann, W.R.Thiel, Angew. Chem. Int. Ed., 49, 3428 (2010).
11. Y. Wang, Z. Li, J. Wang, J. Li, Y. Lin, Trends. Biotechnol., 29, 205 (2011).
12. V. Georgakilas, J. N. Tiwari, K. C. Kemp, J. A. Perman, A. B. Bourlinos, K. S. Kim, R. ZBoril, Chem. Rev., 116, 5464 (2016).
13. A. Hirsch, J. M. Englert, F. Hauke, Acc. Chem. Res., 46, 87 (2013).
14. N. Julkapli, S. Bagheri, Int. J. Hydro. Ene., 40 ,948 (2015).
15. S. Navalon, A. Dhakshinamoorthy, M. Alvaro, H. Garcia,Chem.Rev.,114, 6179 (2014).
16. W. Miao, T. Chan, Acc. Chem. Res., 39, 897 (2006).
17. A. G. Panda, S. R. Jagtap, N. S. Nandurkar, B. M. Bhanage, Ind. Eng. Chem. Res., 47, 969 (2008).
18. A. Sharma, C.Lebigue, R. Deshpande, A. Kelkar,H. DelmasInd. Eng. Chem. Res., 49, 10698 (2010).
19. A. Bordoi, S. Sahoo, F. Lefebvre, S. Halligudi,J. Cat., 259(2), 232 (2008).

JET NEBULIZER SPRAY COATED CZTS PHOTOCATALYTIC FILMS FOR ORGANIC DYE POLLUTANT DEGRADATION

D. David Kirubakaran[1], C. Ravidhas[1]* and Sudhagar Pitchaimuthu[2]**

[1]PG & Research Department of physics, Bishop Heber College (Autonomous),
Tiruchirappalli 620017, Tamilnadu, India
[2]Multifunctional Photocatalyst and SPECIFIC, College of Engineering,
Swansea University (Bay Campus), Fabian Way, Swansea SA1 8EN, Wales, UK
Correponding author E-mail: *cravidhas@gmail.com, **S.Pitchaimuthu@swansea.ac.uk

ABSTRACT:

$Cu_2ZnSn\ S_4$ (CZTS) films were deposited onto glass substrate using jet nebulizer spray pyrolysis technique (j-Ns) at two different substrate temperatures (523K, and 573K).The crystalline structure of as-synthesised films were investigated. The crystalline structure of the as deposited CZTS films has been improved with increase in substrate temperature.The surface of the films was analyzed using scanning electron microscopy (SEM). The photocatalytic dye degradation activity of CZTS films was performed in an annular type reactor by employing methylene blue (MB) dye as model effluent. The maximum degradation efficiency of 88% was achieved for CZTS film prepared at 523K due to its nanocrystalline nature with high surface area.

INTRODUCTION:

The growth of Industrial revolution has produced large amount of waste water due to release of organic dye pollutants in water resources. Water scarcity is one of the major issues faced by the human society. It is immensely important to identify appropriate remedial measures to resolve this problem. Semiconductor photocatalytic dye degradation or advanced oxidation process (AOP) is one of the more favorable and effective approaches for the conversion of organic pollutants into carbon dioxide and water [1]. Recently, broad research has been progressed towards designing narrow band semiconductors which can be work under nature sunlight. CZTS is a p-type chalcopyrite semiconducting material which is more promising candidate for cost effective and eco-friendly absorber layer in tandem solar cells. The optical absorbance of CZTS thin film covers a wide range of visible region in electromagnetic spectrum and has narrow band gap of 1.3 – 1.5 eV [2]. Few reports were available for utilizing CZTS as nanoparticles for photodegradation of organic pollutants. CZTS in thin film form will definitely be more advantageous compared to nanoparticles. Nebulizer spray technique is found to be more convincing technique compared to other vacuum based and chemical solution techniques owing to its simple engineering design and ease of fabrication [3]. Hence in this present work we have investigated the role of substrate temperature on structural, morphological and photocatalytic activity of CZTS thin films prepared by nebulizer spray technique.

EXPERIMENTAL:

CZTS films were deposited by simple jet-nebulizer Spray (j-NS) technique. The principle and working of j-NS technique was described in our previous report [3] . The precursor solution containing cupric chloride (0.02M), zinc chloride (0.01M), tin chloride (0.01M), and thiourea (0.08M) were sprayed on to preheated and ultrasonically cleaned glass substrates at 523K & 573K temperatures to form CZTS films. The structural property of CZTS thin films were studied by x-ray diffraction (XRD) using CuKa(λ = 0.154nm) radiation source (X'Pert Pro PANanalytical).The surface morphology of the films was analyzed by scanning electron microscopy (Quanta 250FEG).The photocatalytic behaviors of the films were carried out by "Heber visible annular type photo reactor". The photocatalytic instrument setup and the procedure has been reported earlier [4].

RESULT AND DISCUSSION:

The structural evaluation of the CZTS thin films (523K & 573K) were determined from X – ray diffraction patterns shown in Fig.1.The diffraction peaks appear at $2\theta = 28.5^\circ$, 47.3° and 56.2° are indexed with (112), (220), and (312) crystallographic planes of CZTS confirming the kesterite nature with tetragonal structure (JCPDS – 26-0575). The X-ray diffraction pattern of CZTS film deposited at 523K exhibits broader and less intense peaks compared to the sample deposited at 573K temperature due to the low thermal energy available for the formation of well crystalline CZTS film.As the substrate temperature increases the crystallinity quality of the CZTS films improves as indicated by the fact that the diffraction peaks narrows in the (112) orientation. The substrate temperature plays a vital role in determining the morphology of the prepared CZTS films (Fig.2). The surface of the CZTS coated at 523K consists of small needle shaped particles. When the temperature is increased to 573K, densely populated, larger spherical grains were observed. This leads to the formation of more compact films, with improved crystallinity as evidenced by the XRD pattern which is one of the uniqueness of the j-NS technique. **Figure 2** shows the pseudo first order kinetics transformation of absorption spectra fitted using Langmuir-Hinshelwood (L-H) model and the rate constant (k_{app}) as well as the correlation coefficient (R^2) values obtained from the relation $\ln (C/C_0) = - k_{app}t$,where 'C_0' is the initial concentration of MB dye and 'C' refers to the concentration of MB dye at a particular time interval 't'. The high apparent reaction rate of 523K (0.017 min^{-1}) might be due to the high surface area which possesses greater number of catalytic active sites available for adsorption of dye molecules compared to CZTS 573K (0.014 min^{-1}).

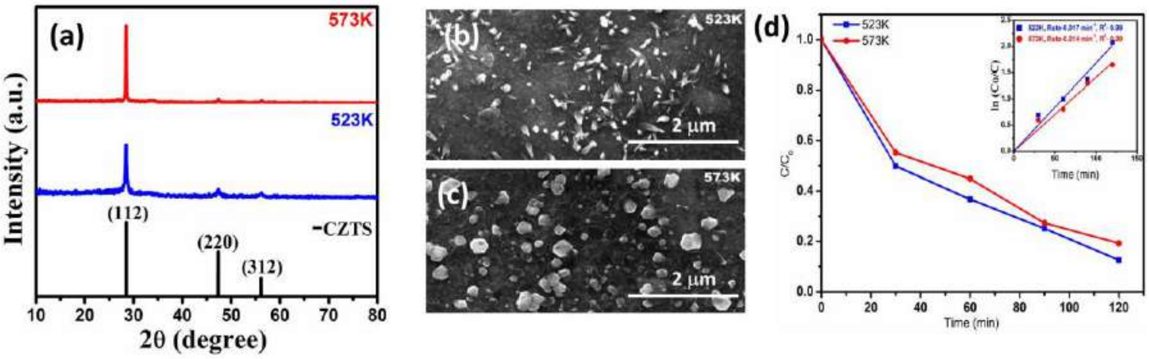

Figure 1. (a) XRD patternof j-NScoated CZTS films at 523K and 573K; (b) SEM images of j-NS coated CZTS samples at (b) 523K and (c) 573K; (d) C/C_0 versus irradiation time curves of photo-degradation of MB by CZTS catalyst (523K and 573K) and inset shows the corresponding linear regression plot

CONCLUSION:

The influence of substrate temperature (523K and 573K) on structural, morphological, photocatalyticproperty of jet-nebulizer spray (j-NS) coatedCu_2ZnSnS_4 thin films was demonstrated. The optimized CZTS film (523K) has the capacity to degrade the MB dye (88%) efficiently and this might be due to high surface area and crystalline property. The less expensive j-Ns spray coated CZTS films shows effective photocatalytic property under visible light which can be applied in solar light driven water treatment applications.

ACKNOWLEDGEMENT:

The authors would like to record their sincere thanks to the University Grants Commission, New Delhi for providing financial support through Major Research Project Scheme (MRP) [F.no. 42-903/2013(SR)].S.P. acknowledges Welsh Government and European Regional Development Fund for supporting Rising Star Fellowship (80761-SU-102 (West).

REFERENCES:

1. Journal of Materials Science: Materials in Electronics, 28, 8186-8191 (2017).
2. Materials Research Bulletin, 60, 628-633 (2014).
3. CrystEngComm, 17, 2624-2628 (2015).
4. Journal of Materials Science: Materials in Electronics, 27, 5020-5032 (2016).

HYDROPHOBIC COATINGS USING LAMP BLACK

Sunetra Dhere[1], Vinayak Ganbavale[2] and Anil Hiragond[3]

[1]Shri S. H. Kelkar College, Devgad

[2]Dattajirao Kadam ASC College, Ichalkaranji

[3]Khare-Dhere-Bhosale College, Guhagar

ABSTRACT:

There is need of protective coatings for industry as well as domestic purpose. A wide range of coating materials are being researched for variety of applications such as corrosion resistance, scratch resistance, hydrophobic coating etc. As carbon black is hydrophobic in nature, an attempt was made to produce hydrophobic coating on metals using lamp black. The water contact angle and sliding angle measured on the lamp black coatings were 142 ° and 9 °, respectively.

INTRODUCTION:

Increasing needs of modern technology have attracted the attention of researchers and scientists from diverse disciplines towards the studies on the properties and applications of surfaces synthesized by various methods. The surface behavior of materials is crucial inour day-to-day lives. The obvious problems such as corrosion, alkali/acid attacks etc. are overcome by special surface treatments which modify the chemical composition and/or the surface morphology [1]. Superhydrophobic coatings are one of the widely applicable types of protective coatings. Hydrophobicity is a key aspect to be considered when the surfaces are bare with high tendency of corrosion. Corrosion of surface lowers down the original inherent function of the surface and decreases its life span. To protect the underlying surface and its properties for intended applications hydrophobic coatings need to be applied. Wetting refers to the study of how a liquid on a solid (or liquid) substrate spreads out [2]. Carbon black has inherent hydrophobic character, therefore it was coated on metal surface by simple method to produce hydrophobic surface to protect the metal surface from water and moisture [3].

EXPERIMENTAL:

Facile way to get carbon black is to burn oil. We used groundnut oil lamp to coat copper and steel surface. The metal substrates were grazed to remove dust, dirt and oxides and thoroughly cleaned. Prior to deposition, a layer of castor oil is applied to the metal substrates for better adhesion of lamp black. A thin layer of the lamb black was deposited at very low deposition rate, manually. Once the layer was deposited, the coating was cold treated at low temperature (~5 °C). The obtained coatings were characterized and tested for hydrophobic character.

CHARACTERIZATIONS:

The thickness of coating (t) was measured mechanically using the following formula

$$t = \frac{m_2 - m_1}{\rho A} \qquad \ldots(1)$$

where m_2 = mass of substrate after deposition, m_1 = mass of substrate before deposition, ρ = bulk density of lamp black, A = area of deposition. Scanning electron microscopy images were obtained to understand the surface morphology and role of surface microstructures in exhibiting hydrophobic character. To obtain contact angle values lab-produced measurement set up consisting of adjustable tripod, glass surface, level tube and travelling microscope was used.

RESULTS:

The photograph in the fig. 1 shows uniformly coated steel and copper substrates by lamp black.

Fig. 1: Uniformly coated steel and copper substrates

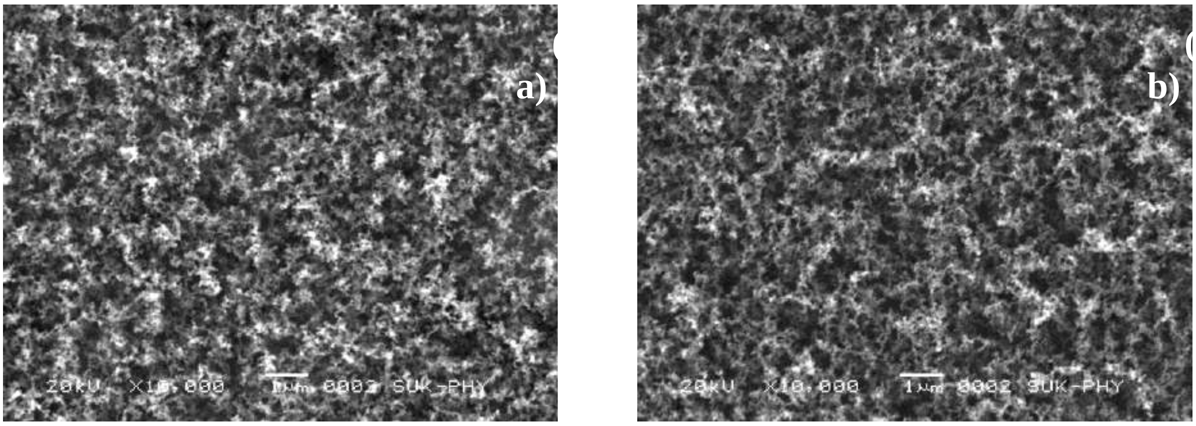

Fig. 2: SEM images of lamp black coated (a) steel and (b) copper substrate

Also from the scanning electron micrographs (SEM) (fig. 2) the uniformity and continuity of coating was revealed. The porous surface morphology seen in SEM is the key factor facilitating the hydrophobic character. The effect of surface roughness on wetting behavior is accounted by Wenzel model. It is assumed that the space between the protrusions on the surface is filled by the liquid. Wenzel had modified the Young's equation as in the following [4].

$$\cos\theta' = \frac{r\,(\gamma_{sv} - \gamma_{sl})}{\gamma_{lv}} = r\cos\theta \qquad \ldots(2)$$

where, γ_{sv}, γ_{sl} and γ_{lv} are solid–vapor, solid–liquid and liquid–vapor interfacial energies, respectively and θ is the contact angle, where r is the ratio between the true surface area and its horizontal projection. The static water contact angle and sliding angle was measured and tabulated in table 1.

The photographs of contact angle measurement with water drops (~ 0.1 ml) on the coated substrates are pictured in the fig. 3.

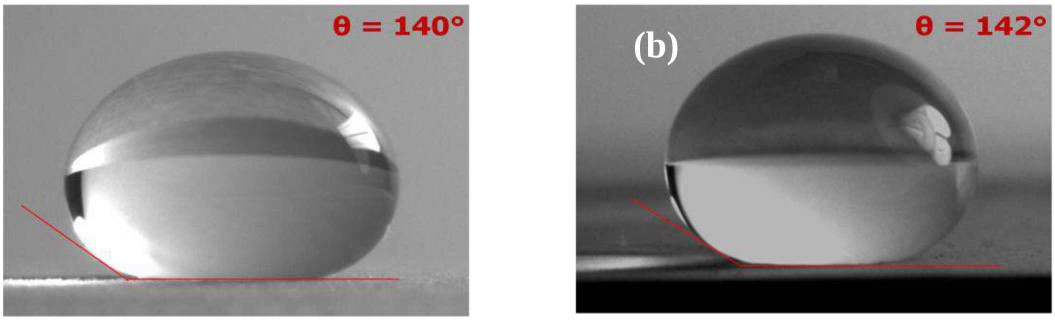

Fig. 3: Water contact angle measuerd for coating on (a) steel (b) copper

Substrate	Contact angle	Sliding angle
Steel	140°	9°
Copper	142°	15°

CONCLUSION:

A facile method to prepare a hydrophobic surface was followed to synthesize lamb black coating. Lamp black being environment friendly and simple to produce possesses great potential for its application in surface coatings. Further attempts are required to increase the coatings adherence to the substrates. High water contact angle (140°) and low sliding angle (9°) was exhibited by the lamp black coating on steel substrate.

REFERENCES:

1. Paint and coatings, Philip A. Schweitzer, Taylor & Francis, pp 31.
2. De-gennes, Capillarity and wetting phenomenon, page 15.
3. Pigment Blacks in Waterborne Coatings, paint & coatings industry, **PCI** Magazine, BNP Media, January 1 (2002).
4. R.N. Wenzel, Ind. Eng. Chem. 28, 988 (1936).

MAGNETIC BEHAVIOUR OF COPPER FERRITE ON ALUMINUM SUBSTITUTION

T. R. Mane[1] and D. H. Bobade[2]

[1]Sangola College, Sangola

[2]C.T.Bora College, Shirur

ABSTRACT:

Copper ferrite samples have been prepared by conventional oxide ceramic method. The effect of aluminum substitution on structural and magnetic properties was studied. Cation distribution was estimated on the basis of magnetic moment per unit cell in Bohr magneton. All aluminum substituted copper ferrite samples exhibits the single domain to supper paramagnetic transition near Curie temperature.

Key words: Copper ferrite, prolate type distortions, , single domain to super-paramagnetic transition aluminum substitution.

INTRODUCTION:-

Copper ferrite exhibits inverse spinel tetragonal structure (1-3). Huheey (4) reported that copper ion is the John-Teller ion. Degree of inversion in copper ferrite depends upon heat treatment during the preparation(5).When the concentration of Cu^{2+} ion is larger on octahedral (B) site than tetrahedral (A) site, it produces the square bond SP^2 orbital (6), that would give rise the macroscopic tetrahedral observable crystal structure. Tetragonality ratio for slow cooled copper ferrite is reported (7-9) in the range of 1.03 to 1.07 when Cu^{2+}, Mn^{3+}, Cr^{3+} occupies (B) site and produces prolate distortion (c/a) >1 and when Cr^{3+}, Mn^{4+}, Ni^{2+} occupied on (A) site produces oblate distortions (c/a) < 1, (10, 11).Seventy percent of copper occupies on (B) site (12). Ten to forty percent occupancy of Cu^{2+} at (A) site in copper is reported (13). It is interesting to study the nature of distorted inverse spinel tetragonal structure of copper ferrite by substituting Al^{3+} ion in the lattice of copper ferrite.

EXPERIMENTAL PROCEDURE:

The compositions of $CuFe2_{-2y}Al_{2y}O_4$ (where y=0.0,0.05,0.15 & 0.25) nano-particle ferrites were prepared by standard ceramic technique. For this, AR grade Fe_2O_3, Al_2O_3 and CuO were used. The sintering process was carried out at 1000^0C for 48 hours. The solid state reaction was confirmed by using X-ray powder diffractometry method. High field hysteresis loop tracer was used for the study of Saturation magnetization. Helmholtz's double coil set-up was used for the study of AC susceptibility of slowly cooled samples. It was carried out in the temperature range 300-800 ^0K.

Table 1: Magnetization data of ferrite $CuFe_{2-2y}Al_{2y}O_4$ system

Sample Id	Y	Curie Temp. in ^0k		Saturation Magnetization (σ_s) in emu/gm	Magnetic moment per unit cell (n_B) in Bohr magnetron
		From Loria Sinha method	From magnetic susceptibility Expt.		
TRM000	0.00	748	768	30.35	1.300
TRM110	0.05	690	730	24.75	1.026
TRM310	0.15	651	700.5	14.17	0.5852
TRM510	0.25	631	668.5	11.21	0.4514

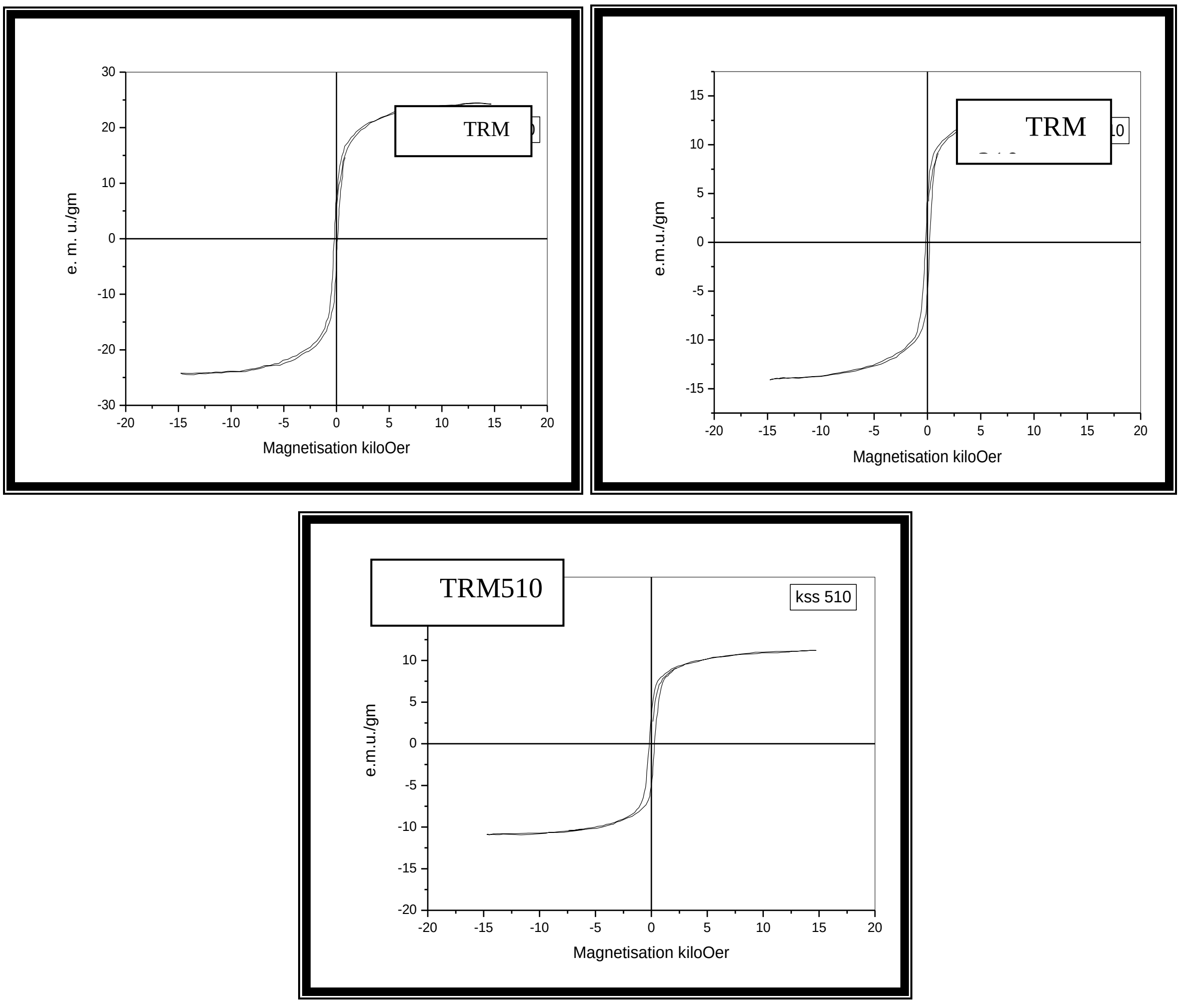

Fig. 1: Hysteresis loop of mixed ferrites $CuFe_{2-2y}Al_{2y}O_4$ system for y = 0.05, 0.15 and 0.25

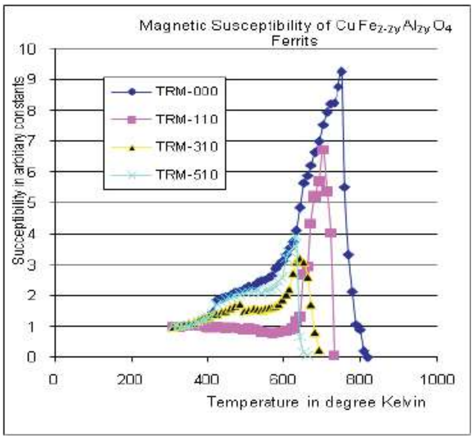

Fig. 2: Magnetic Susceptibility of mixed ferrites aluminum substituted copper ferrite system

RESULT AND DISCUSSION:

For all prepared ferrite samples; normalized AC susceptibility slowly increases with increasing temperature up to certain point, beyond which it drops off sharply but goes on decreasing slowly with increase in temperature. Increase of normalized AC susceptibility up to crystallographic phase transition temperature (T_p) suggests that the prepared ferrite samples exhibit single domain structure, while the exponential decrease in the normalized AC susceptibility (paramagnetic tail) beyond (T_p) indicates the single domain to super paramagnetic transition. The sharp drop in normalized susceptibility near phase transition suggests that impurity phases are not formed in the present ferrite samples. The paramagnetic tail indicates the existence of super paramagnetic cluster in the sample by addition of Al^{3+} in the host lattice of copper ferrite. Similar type behavior is observed by Karche et.al,(17) in $Cd_xMg_{1-x}Fe_2O_4$ ferrite sample for x = 0.4.The Curie temperatures estimated from normalized AC susceptibility variation with temperature experiment are in excellent agreement with their values measured by Loria Sinha method.

CONCLUSION:

Addition of Al^{3+} content in the host lattice of the tetragonal copper spinel ferrite suppresses the tetragonal prolate type distortions and hence crystal structure turned into cubic spinel. All prepared ferrite samples exhibits single domain to super paramagnetic transition. Super paramagnetic cluster is increased due to addition of aluminum in the host lattice of copper ferrite. Al^{3+} affects the structural properties and magnetic properties. Particle size of all prepared samples is found within the nano range.

It is fond that the saturation magnetization and magnetic moment per unit cell decreases with increase in aluminum concentration

REFERENCES:

1. Bertant E.F., J. Phy. Radium 12, 252 (1951).
2. Gorter E.W., Philips Res.Repts. 9, 295 (1954).
3. Ohnishi H and Teranishi T., J. Phy. Soc.Japan 16, 35 (1961).
4. Huheey J E "Inorganic chem." 2nd Ed. Harper and Row publicating co. N. Y. (1978).
5. Xu Zuo, Aria Yang, Carmine Vittoria and Vincent G. Harris, J. Appl. phy. 99, (08) M 909 (2006).
6. Cartmell E; Fowles G.W.A.,Valency and Molecular structure 2nd Ed. Butterworths, London (1961).
7. Prince E., Treuting R.G; Acta Crystallographica 9, 1025 (1956).
8. Sagal K., Tabellen F. Rontegenstrukturanalyse, Springer, Berlin (1958).
9. Borisenko A., Toropov N. A; Z. Prikl Chem 23, 1165 (1950).
10. John H. A and Teller E. Proc . Roy. Soc. A 161, 220 (1937).
11. John H.A. Proc.Roy. Soc. A 164, 117 (1938).
12. Goodenough J.B and Loeb A. L ,Phys. Rev.98, 391 (1955).
13. Mastui T and Wagner J.B (Jr.),J.Ele.Chem.Soc.124, 1141 (1977).
14. A.B. Gadkari, T. J. Shinde and P.N. Vasambekar, J. Mater Electron (2010) 21:96-103.
15. Waldron R.D, Phy.Rev; 99(6), 1727 (1955).
16. K. V. S. Badarinath, Phys. Stat. Solidi (a) 9,1K-19-23 (1985).
17. B. R. Karche, B.V. Khasbardar and A. S. Vaingankar, J. magn. and mag. mater .168, 292-298 (1997).

A SENSITIVE AND RELIABLE RUTIN ELECTROCHEMICAL SENSOR BASED ON PALLADIUM PHTHALOCYANINE-MWCNTS-NAFION NANOCOMPOSITE

Ruimin Xing, Haitang Yang, Shengnan Li, Xiuhua Liu and Shanhu Liu *
Henan Joint International Research Laboratory of Environmental Pollution Control Materials,
College of Chemistry and Chemical Engineering, Henan University, Kaifeng,
Henan, 475004, People’s Republic of Chin

Rutin (rutoside or quercetin-3-o-rutoside) as a kind of flavonoid glycoside compound is widely distributed in fruits and vegetables [1]. From a pharmacological and biochemical point of view, rutin has many properties and functions such as antihypertensive, anti-inflammatory, antibacterial, anticancer, anti-ageing and antioxidant [2-6]. Therefore, it has been used clinically as a therapeutical drug worldwide [7]. To date, various analytical methods have been developed for the determination of rutin, such as spectrophotometric analysis[8], capillary electrophoresis analysis [9], high-speed counter-current chromatography, high performance liquid chromatography [10] and so on. However, some of these methods often require complicated pre-concentration procedures, expensive instruments with mass use of organic solvents, which hamper their "in-situ" application and make them inconvenient in practice. Consider that rutin is an electroactive flavonoid glycoside compound which can be easily subject to redox reaction on some kinds of working electrodes [11,12,1], the electrochemical method seems like a promising alternative due to its simplicity, sensitivity, low cost and the possibility to construct portable devices for on-site determination of rutin [13-15].

In the electrochemical procedure, the crucial step is to fabricate suitable modified electrodes using excellent sensing materials to improve the electrochemical behaviors of analytes, such as sensitivity, stability and antifouling ability. Different kinds of nanomaterials including carbon nanotubes, metal nanoparticles, graphene have been proven to be excellent carriers to enhance response signals. Recently, phthalocyanine-based compounds [16], especially, metallophthalocyanines (MPcs) have gradually cause concern due to their excellent thermal stability, chemical inertness, and conductivity [17]. It is a kind of 2-dimensional 18-electron aromatic porphyrin synthetic analogues with a metal atom located at the central cavity. Several MPc-based molecular materials have been exploited for the detection of some analytes based on the electrochemcial method due to the presence of outstanding electrocatalytic metal centers [18,19,17]. However, MPcs have an obvious disadvantage of easily blocking the transfer of electrons between phthalocyanines and the electrode when being applied as electrocatalysts. One of effective methods to solve this problem is designing the conjugation of non-substituted MPc complexes with carbon materials via π–π interactions [19,20]. For example, Wang fabricated cobalt phthalocyanine nanorods on graphene for the electrochemical detection of hydrogen peroxide and glucose sensing [20]. Except grapheme, MWCNTs could also promote the direct electrochemistry of biomolecules, leading to the improved catalytic and sensing activity of MPc-CNTs [21-23].

Considering that palladium and its complexes are known to be excellent catalysts due to its nontoxic properties and superior catalytic activities towards many electrochemical reactions[24], it could be expected that the catalytic and sensing activity of the electrode modified with palladium (II) phthalocyanine complexes (PdPc) integrated with MWCNTs will be greatly enhanced. In addition, it is well known that Nafion can be used as a binder to stabilize the modified species on electrodes and as a permselective film to alleviate the interferences of anions, in this work, Nafion was used to disperse PdPc-CNTs and a novel electrochemical sensor was constructed based on PdPc-CNTs-Nafion film [25,26]. A pair of well-defined quasi-reversible redox peaks of rutin were obtained with higher sensitivity, compared with those obtained based on only PdPc-Nafion or MWCNTs-Nafion modified electrode. To the best of our knowledge, this is the first time that the self-assembly of PdPc-MWCNTs nanocomposite have been used as an electrode-modified materials for electrochemical sensor. It might be an effective candidate for the detection of Chinese medical analysis or quality monitoring in real samples.

REFERENCES:

1. H. Yang, D. Liu, X. Zhao, J.-H. Yang, H. Chang, R. Xing and S. Liu, Anal. Methods, 9, 3191-3199 (2017).
2. H. Yang, X. Zhao, H. Chang, R. Xing, J.-H. Yang, S. Liu and d. X. Liu, J. Nanosci. Nanotechnol., 18, 500-509 (2018).
3. R. Xing, X. Zhao, Y. Xu, H. Yang, Z. Chang, J. Qu, X. Liu, J.-H. Yang and S. Liu, J. Nanosci. Nanotechnol., 18, 62-67 (2018).
4. H. Yang, B. Li, R. Cui, R. Xing and S. Liu, J. Nanopart. Res., 19, 354 (2017).
5. R. Xing, H. Yang, S. Li, J. Yang, X. Zhao, Q. Wang, S. Liu and X. Liu, J Solid State Electrochem., 21, 1219-1228 (2017).
6. R. Xing, R. Li, Y. Xu, B. Li, J. Liu, S. Liu, D. Luo and L. Mao, Ceramics International, 43, 14426-14430 (2017).
7. S. Liu, Z. Zhang, S. Zhou, L.-P. Jiang and J.-J. Zhu, Analyst, 141, 567-569 (2016).
8. J.-H. Yang, H. Yang, S. Liu and L. Mao, Sensors and Actuators B: Chemical, 220, 652-658 (2015).

BIOSYNTHESIS OF INORGANIC NANOPARTICLES BY USING *DODONAEA VISCOSA* PLANT AND ITS APPLICATIONS

Vishal Vasant Chavan, Pratap Ashok Chougale and Arpita Pandey Tiwari *
Department of School of nanoscience & Technology,
Shivaji University, Kolhapur, 416004, Maharashtra, India

ABSTRACT:

Green synthesis of inorganic nanoparticles is more stable, safe and easily scaled up. There is a growing need of introduce to eco-friendly and sustainable procedures for the synthesis of inorganic nanoparticles. The formation of inorganic nanoparticles is achieved using in *dodonaea viscosa* plant extract. The generated nanoparticles are characterized with UV-visible spectroscopy (UV-vis), Dynamic light scattering (DLS), Atomic force microscopy (AFM), Transmission electron microscopy (TEM), Scanning electron microscopy (SEM), Energy dispersive spectroscopy (EDS), X-ray diffraction (XRD), Fourier transform infrared spectroscopy (FT-IR). The nanoparticles which is found in a spherical in size and shape. The synthesized average nanoparticles which is size in nm. Synthesis of Inorganic nanoparticles include a mild reaction condition's, single reaction setup, use of nontoxic chemicals medium cost effectiveness as well as greater efficiency for biomedical and antimicrobial activity application.

Keywords: Biological synthesis, Green chemistry, Inorganic nanoparticles,Antimicrobial applications

INTRODUCTION:

The nanotechnology has started in 1959 with Richard Feynmans lecture "THERE IS PLENTY OF ROOM AT THE BOTTOM". It was in this lecture that the Feynman alerted the consciousness of the scientific community about the unused potential of nanomaterial.

Nanotechnology is manipulation of matter on atomic, molecular and supramolecular scale .[1, 2] This is science, engineering and technology conducted of nanoscale which is about 1 to 100nm.[3] In the general sense material with at least one dimension in nanometric scale.

Nanoparticles have great scientific interest because of their physical, chemical, and biological properties. In nanoscale, the properties of the material change in comparison to bulk. The various properties that changes in nanoscale material are electronic, thermal, optical, mechanical, conductive, reactivity, and strength etc. The change in properties of the material is due to the decrease in particle size. Generally the surface area to volume ratio is increased and other properties for example colours (In a gold nanoparticle has red colour whereas gold metal has yellow colour) and also the nanoparticle shows huge differences than that of bulk.

The nanoparticle is of great interest for researchers from wide range of application including biotechnology/biomedicine, magnetic fluids, catalysis, electronics, data storage, energy and environmental remediation. This is not only limited with the use of nanoparticle but also utilizes carbon nanotube, fullerene, graphene, nanowire, nanorod, and quantumn dot medicines, electronics, food, fuel cell, solar cell, batteries, fuel, air quality, water cleaning, chemical sensors, fabric, etc. have greater physical, chemical, and biological properties.[4,5]

The nanotechnology represents the connection of biotechnology which is an emerging field showing creation, improvement and value of nanoscale structure. [6] The nanobiotechnology is branch of science which deals with the study of biological concepts in conjugation with nanotechnology. The biogenic synthesis of monodispersed nanoparticles with specific size and shape have been a challenge in biomaterial science. It has created remarkable advantages in the field of medicines, food packaging, agriculture, water purification.

Recently one of the most useful techniques coming up is synthesis of nanoparticles by using plant extract. The structure, shape and properties of nanoparticles by using plant extract have major edge on to method in terms of its interaction and effect on environment. It is fully environmentally friendly and non toxic and has potential for application in medicines, food, agriculture and industries.

REVIEW OF LITERATURE:

"Biosynthesis is the production of complex molecules within living organisms or cells ." [7] The great efforts have been made for the incorporation of biomolecules in to the synthesis of nanoparticles to increase their colloidal stability in biological media and to enable specific targeting.[8] Plants are the chemical factories contains various therapeutic compounds and which are used as traditional medicines from an ancient era. Plant synthesized metal nanoparticles are more stables, safe and easily scaled up. [9]

The Green synthesis of nanoparticles are less time taking, almost negligible in industrial waste and not rely on use of the toxic chemicals and uses in inherent biological methods for nono particles fabrication. It is safe and hold various applications that are not possible with physical and chemical synthesis methodologies. Development of improved bimetallic nanoparticles will surely prove to be a boon to a society. [10] The use of plant biomasss for metal removal of aqueous solutions attraction because it has shown to be very promising for the removal of contaminates from effueints in an eco-friendly approach. Genetic modification of plants with improved metal tolerance and accumulation capacities is the future approach to in increase the productivity of these organisms in nanoparticles synthesis. [11]

The Green synthesis is advantageous over physical and chemical method as the materials synthesized through this way are environment friendly, non toxic and easily scaled up for large scale synthesis. [12] The synthesis of nano and micro length scaled inorganic materials have contributed to the development of relatively new and largely unexplored area of research based on the biosynthesis of nanoparticles. Phytomining is the use of hyper accumulating plants extracts for obtaining metal from the biomass to return on economic profit. The biosynthesis of nanoparticles mechanism in plants may be associated with the phyto remediation of concept in plants. [13]

The huge plant diversity with much more plants species are in way to be exploited and reported in future era towards rapid and single step protocol with green principle. The current scenario nanotechnologies motivates progress in all the sphere of life and biosynthetic route of nanoparticles synthesis will emerge as safer and best alternative to conventional methods. [14] Plants contain abundant natural compounds such as alkaloid, flavonoids, saponino, steroids, taminino and other nutritional compounds. In many study the plants extracts acts as a potential precursor for the synthesis of nano materials in non hazardous ways. [15]

In green synthesis , phyto chemicals are likely responsible for nanoparticles size control through surface activity. [16] The pH value of a plant extracts greatly influence the formation of nanoparticles. The synthesis of metal nanoparticles in plant extract despite obvious limitations has a significant potential and number of substantial advantages relatively to traditional methods of nanoparticles synthesis.[17] The industrial relevance can be attributed to the synthesis of nanoparticles by plants. There are many more examples to be identified and especially in the case of whole plant synthesis, they risks must be thoroughly assessed. [18]

The synthesis process starts by process of “nucleation”. This is immediately followed by a period of the growth when a smaller neighboring particles agglomerate to form a larger nanoparticles that are thermodynamically more stable while further biological reduction of a metal ions takes place.[19] As growth progresses nanoparticles aggregate to form a variety of morphologies such as cubes, spheres, triangles, hexagons, pentagons, rods, and wires. In the final stage of synthesis, the plant extracts ability to stabilize the nanoparticle ultimately determines it’s most energetically favourable and stable morphology. Properties of the plants extract such as its concentration, metal salt concentration, reaction time, reaction solution pH, and temperature significantly influence the quality, size, and morphology of the synthesized nanoparticle. [20]

Biosynthesized inorganic nanoparticles can have applications in diverse fields.Biosynthesized Ceo_2 nanoparticles and CuO Nanoparticles have reported to act as a good photocatalyst and having better antibacterial properties. [21,22] The Pd nanoparticles which can show the properties of antioxidant and catalyst in the green synthesis of nanoparticles. [23] The volume ratio of green ZnO nanoparticle which are the responsible for significant higher antimicrobial activity. [24]

FUTURE ASPECTS:

Biologial synthesized nanoparticles have unprecedented application in various sectors. The Origin of the new technology in the era and improved scientific knowledge have the proved to be the route towards employing the biological entities in the synthesis of nanoparticles . Employing plants for the synthesis of nanoparticles can overcome the time consuming process of employing microbes and maintaining their culture which can loss their potential towards synthesis of nanoparticles during the prospects.[17] Additionally presence of bio-active phyto-chemicals on the surface of biologically synthesized nanoparticles makes them potential candidate for use in biomedical application.

METHODOLOGY:

Preparation of Plant extracts:

1. The samples will be collected from the Shivaji University campus and it is used for our research project. We have searched this plant and this plant has large abundus in our university campus

and also possible envioronment sources. The plant sample will be rinsed thoroughly under running tap water followed by chopping into thin slices and shade drying for the few days at the room temperature. After complete drying, the slices will be pound in the electric blender. Amount of sample finely ground powder will be taken in a quantitative volume and will be boiled and filtered. The filtrate will be collected and stored at °C for further use.

2. Samples will be processed for nanoparticle synthesis by different methods viz., plants extract method and other biological synthesis methods such as by the inorganic chemicals used (Au, Ag, Pt, Zn, Cu, Co, Ce, Pd.,etc).
3. During biological synthesis of metallic nanoparticles, a number of controlling factors are involved in the nucleation and sub sequent formation of stabilized nanoparticles. These factors include pH, reactant concentrations, reaction time, and temperature. Hence, Optimization of various parameters like pH, temperature, reaction time and concentration will be done .

1) pH:

To check the effect of pH, different set of experiments each with different pH will be designed. The formed nanoparticles will be checked further for their structure and size to see the effect of pH on biological synthesis.

2) Reaction concentration:

The concentration of biomolecules found in plants extracts cans significantly influence the formation of metallic nanoparticles. Different set of experiments with different concentration of precursor and different concentration of plant extract will be designed.

3) Temperature:

The effect of temperature of biological synthesis of nanoparticles will be observed by planning different set of experiments with varying temperature and keeping other parameters constant.While it is generally known that reaction temperature is a crucial factor in any synthesis it has been found that temperature is also an important factor in determining the size, shape, and yield of nanoparticles synthesized via plant extracts.

4) Reaction of time:

The effect of incubation time will be also checked for the synthesis of nanoparticles. This is the time duration required for completion of all steps of the reaction.

Chracterization Techniques:

After the reaction, nanoparticles will be separated from the colloid by high speed centrifugation and then using the advanced nano characterization techniques.

Some of the spectroscopy and microscopy techniques routinely used include UV-visible spectroscopy (UV-vis), Dynamic light scattering (DLS), Atomic force microscopy (AFM), Transmission electron microscopy (TEM), Scanning electron microscopy (SEM), Energy dispersive spectroscopy (EDS), X-ray diffraction (XRD), Fourier transform infrared spectroscopy (FT-IR). Microscopy based techniques such as AFM, SEM and TEM are considered direct methods of obtaining data from images taken of the nanoparticles. In particular, both SEM and TEM have been extensively used to determine size and morphological features of nanoparticles.

Spectroscopy based techniques such as UV-vis, DLS, XRD, EDS, FT-IR are considered the indirect methods of the determining data related to the composition, structure, crystal phase, and properties of nanoparticles.

1) UV-visible spectroscopy (UV-vis)-

   The UV-visible spectroscopy covers the UV range between 190 and 380 nm and the visible range between 380 and 800 nm. Wavelengths between 300 and 800 nm are generally used for characterizing metallic nanoparticles ranging in size from 2 nm up to around 100 nm.

2) Scanning electron microscopy (SEM):-

   A scanning electron microscope (SEM) is a type of electron microscope that produces images of a sample by scanning the surface with a focused beam of electrons. SEM will be done for knowing the morphology of of biologically synthesized nanoparticles.

3) Transmission electron microscopy (TEM):-

   The size of nanoparticles will be observed by TEM analysis. Transmission electron microscopy is a microscopy technique in which a beam of electrons is transmitted through a specimen to form an image. The specimen is most often an ultra thin section less than 100 nm thick or a suspension on a grid. An image is formed from the interaction of the electrons with the sample as the beam is transmitted through the specimen. The image is then magnified and focused onto an imaging device, such as a fluorescent screen, a layer of photographic film or a sensor such as a charge-coupled device.

4) Dynamic light scattering (DLS):-

   DLS spectroscopy will be used to determine size distribution and quantity of the surface charge of nanoparticles suspended in a liquid.

5) Energy dispersive spectroscopy (EDS):-

   The elemental composition of nanoparticles will be determined via EDS mapping.

6) X-ray diffraction (XRD):-

   The XRD examination produces a diffraction pattern that is subsequently compared with data contained in a standard crystallographic database to determine structural information. Analysis of the XRD data identifies crystallite size, structure, preferred crystal orientation, and phases present.

7) Fourier transform infrared spectroscopy (FT-IR):-

   FT-IR spectroscopy will be used to investigate surface chemistry and identify surface residues such as functional groups like carbonyls and hydroxyls moieties that attach to the surface during nanoparticle synthesis. It is useful in detecting vibrational modes of molecules and can be used to identify vibrational signals of a variety of chemical species that are attached to the surface of nanoparticles during the synthesis.

RESEARCH OUTCOME EXPECTED FROM PROJECT :-

Synthesized bio nanoparticle are expected to be more efficient and bio compatible than other biological synthesized nano particles which shows vast bio medical application (wound healing) as well as anti microbial activity (food packaging).

REFERENCES:

1. Drexler, K. Eric, Doubleday (1986).
2. Jump up Drexler, K. Eric, John Wiley & Sons (1992).
3. American Elements Archived from the original on 26 December 2014. Retrieved 13 May 2011.
4. Nano in medicine Archived 2011-11-14 (2011).
5. Nano in transport Archived 2011-10-29 (2011).
6. Weiss, R., Archived 2011-06-29 at the Wayback Machine (2008).
7. Goodshell, D. S. John Wiley & Sons, Inc.: Hoboken, NJ (2004).
8. Nair, R., Varghese, S. H., Nair, B. G., Maekawa, T., Yoshida, Y., & Kumar, D. S. Plant science, 179(3), 154-163 (2010).
9. Kuppusamy, P., Yusoff, M. M., Maniam, G. P., & Govindan, N. Saudi Pharmaceutical Journal, 24(4), 473-484 (2016).
10. Thakkar, K. N., Mhatre, S. S., & Parikh, R. Y. Nanomedicine: Nanotechnology, Biology and Medicine, 6(2), 257-262 (2010).
11. Hussain, I., Singh, N. B., Singh, A., Singh, H., & Singh, S. C. Biotech. Lett., 38(4), 545-560 (2016).
12. Metz, K. M., Sanders, S. E., Pender, J. P., Dix, M. R., Hinds, D. T., Quinn, S. J. and Colavita, P. E. ACS Sustainable Chemistry & Engineering, 3(7), 1610-1617 (2015).
13. Makarov, V. V., Love, A. J., Sinitsyna, O. V., Makarova, S. S., Yaminsky, I. V., Taliansky, M. E., & Kalinina, N. O. Acta Naturae, 6, 1(20) (2014).
14. Pantidos, N., & Horsfall, L. E. J. of Nanomed. & Nanotech, 5 (5), 1 (2014).
15. Iravani, S. Green Chemistry, 13(10), 2638-2650 (2011).
16. Mishra, V., Sharma, R., Jasuja, N. D., & Gupta, D. K. Int J Green Herbal Chem, 3, 081-094 (2014).
17. Kavitha, K. S., Baker, S., Rakshith, D., Kavitha, H. U., Yashwantha Rao, H. C., Harini, B. P., & Satish, S. Int Res J Biol Sci, 2(6), 66-76 (2013).
18. Blanco-Andujar, C., & Thanh, N. T. Annual Reports A (In. Chem.), 106, 553-568 (2010)..
19. Akhtar, M. S., Panwar, J., & Yun, Y. S. ACS Sust. Chem. & Eng., 1(6), 591-602 (2013).
20. Shah, M., Fawcett, D., Sharma, S., Tripathy, S. K., & Poinern, G. E. J. Materials, 8(11), 7278-7308 (2015).
21. Surendra, T. V., & Roopan, S. M. J. of Photochem. & Photobiol., 161, 122-128 (2016).
22. Nazar, N., Bibi, I., Kamal, S., Iqbal, M., Nouren, S., Jalani, K., & Atta, S. Int. J. Biol. Macromolecules (2017).
23. Kora, A. J., & Rastogi, L. Arabian J. Chem. (2015).
24. Gunalan, S., Sivaraj, R. and Rajendran, V., Materials Int., 22(6), pp.693-700 (2012).

TEMPERATURE DEPENDENT PROPERTIES OF SPRAY DEPOSITED SnO_2 THIN FILMS

V. L. Patil[1], N. S. Harale[1], N. L. Tarwal[1], S.S. Shendage[1,2] ,
S. A. Vanalakar[3], P. M. Kadam[4], M. M. Karanjkar[5], P. S. Patil [1]* and J. H. Kim[6]**
[1]Thin Film Materials laboratory, Department of Physics,
Shivaji University, Kolhapur-416004, M. S., India
[2]P. V. P. Mahavidyalaya Kavathemahankal, Sangli -416405, M. S. India.
[3]Department of Physics, Karmaveer Hire Arts, Commerce, Science and Education College
Gargoti, Dist: Kolhapur, 416 209, India
[4]KWC College, Sangli, 416416 M. S., India
[5]Vivekanand College, Kolhapur-416 004 Maharashtra, India
[6]Department of Materials Science, Chonnam National University,
Gwangju, Republic of Korea
***Corresponding author E-mail**: *psp_phy@unishivaji.ac.in ; Fax: +91-321-691533, 692333(O)

ABSTRACT:

In the present work we report highly uniform pure SnO_2 thin films have been prepared by simple chemical spray pyrolysis technique. The effect of substrate temperature onto the structural, morphological, optical, electrical and thermal properties has been investigated. XRD analysis reveals that the films are nanocrystalline in nature with orthorhombic crystal structure. SEM images shows that the films surface covered with a smooth, uniform, compact and grain size nanoparticles. The size of grain like morphology is about in the range of 10 -20 nm. The film deposited at optimized substrate temperature exhibits optical band gap energy of 3.7 eV, which lies in the visible region of the solar spectrum. Further, the electrical performance of as grown SnO_2 thin films was presented.

Keywords: SnO_2 thin films; Spray pyrolysis technique; SEM; XRD;

INTRODUCTIONS

Recently, metal oxide semiconductors have drawn good attention because of their low-cost, promising miniaturization and capability of various applications [1]. Among them tin oxide (SnO_2) is a promising candidate due to its a wide band gap (3.6 eV) n type semiconductor, has been the most premeditated material used in applications, gas sensing, transparent electrodes, dye sensitized solar cells, and liquid crystal displays etc. [2]. In the last few years various method to synthesized the SnO_2 thin films such as thermal evaporation [3], sputtering[4] and spray pyrolysis techniques [5] etc. have been employed to prepare nanostructured SnO_2 thin films. Among these methods, spray pyrolysis technique (SPT) is a simple, inexpensive, safe, and allows easy control over the deposition parameters and high reproducibility. The SPT technique offers a most attractive way to synthesize thin films, as reported by Patil [6].

The present work consists of the synthesis of SnO_2 thin films using SPT and its structural characterization. SnO_2 thin films were prepared from different substrate temperature. Characterization of these prepared films using X-ray diffraction (XRD), photoluminescence (PL), UV-visible spectroscopy technique is presented and discussed. Finally, electrical measurements of as synthesized SnO2 thin films are presented.

EXPERIMENTAL DETAILS:

For depositing SnO_2 thin films for various temperatures (350-450^{0}C) were deposited on glass substrate. We have taken 35 gm stannic chloride ($SnCl_4$) was dissolved 50 ml double distilled water to obtain 2M solution concentration which is called the stock solution. SnO_2 films were prepared by adding the 8 ml isopropanol and 2 ml methanol in the 10 ml stock solution. The total prepared solution about 20 ml was sprayed onto the preheated glass substrates maintained at 350^{0}C to deposit SnO_2 films. The SnO_2 thin films were deposited at different substrate temperatures in the range of 350^0 C to 450^0 C in a step of 50^0 C for different concentration. By keeping different substrate temperature, quantity of solution 30c.c, substrate to nozzle distance 28cm and spraying rate 2ml/minute as constant and varied the substrate temperature. These samples were labelled as S1, S2 and S3 respectively. It is found that all the samples were adherent and well developed. As prepared nanostructure SnO_2 thin films were annealed for half an hour with temperature of 450^{0}C.

The X-ray diffraction analysis was carried out using D2 PHASER X-ray diffractometer with CuKα radiation of wavelength 1.54 Å. The morphology of the films was recorded with the help of scanning electron microscope (JEOL-JSM-6360, Japan) operated at 20 kV. The room temperature optical absorption spectra of SnO_2 thin films were recorded over the range of 350–850 nm by using UV- VIS spectrophotometer (UV1800, Shimadzu, Japan) using 1000W Xenon lamp. The electrical resistivity measurements were taken by conventional two probe method. Also Thermoelectric power (TEP) was recorded by using lab made TEP set up.

RESULTS AND DISCUSSION:

X-ray diffraction (XRD):

To investigate the crystalline quality of the films with fixed temperature of 450^{0}C by using XRD analysis and the resulted spectrum is shown in fig. 1 The experimental results indicate that at 450^{0}C these films are polycrystalline in nature showing growth along (113), (023) and (024) directions and belong to the orthorhombic crystal structure (JCPDS- 78-1063) [7]. The grain sizes of the films are calculated from the highly textured (1 1 3) peaks by using Debye Scherrer formula [8]

$$D = \frac{0.9\lambda}{\beta \cos\theta} ---------(1)$$

Where λ: wavelength of the X-ray source (i.e. λ=0.15418nm)

β: full- width at half-maximum (FWHM) in radians

θ: diffraction angle

The grain size values for (1 1 3) peaks, the calculated D value is about 4.73 nm which is possible due to polycrystalline in nature. It is observed that with an increase in substrate temperature, the D value decreases up to 400 °C. Because towards the higher substrate temperature, the rate of evaporation of spray droplets is higher, which results into the formation of porous, uniform and thinner, easily detachable films, hence the good decomposition of precursor solution take place and results into smaller crystallite size [9].

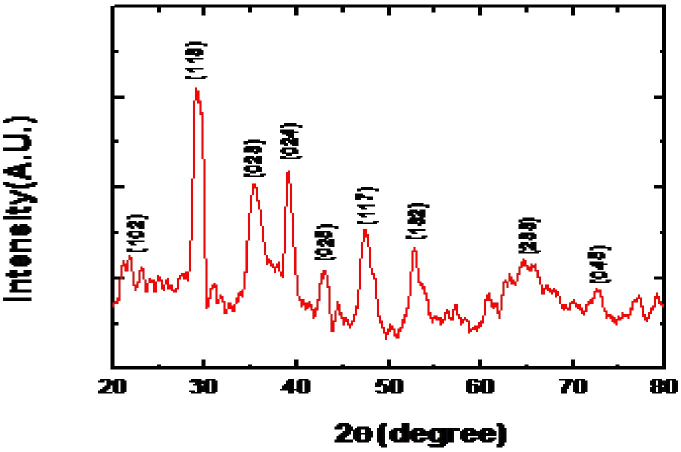

Fig. 1: XRD spectrum of optimized S3 sample

Scanning electron microscopy (SEM):

Fig.2 shows the Scanning electron microscopy (SEM) images of SnO_2 thin films deposited at various substrate temperatures are shown in the fig. All the deposited films are, compact, pin-hole-free and adherent to the substrate. The morphology of the SnO_2 thin film at different temperature is found to be uniform and grain like structure. The size of grain like morphology was calculated forms the SEM images. The size of grain like morphology is about in the range of 10 -20 nm which is very close to the crystallize size, which are well agreements with the rasheed paloly et.al. [10] As temperature increases the thickness of the thin film goes on decreasing because of fast reaction rate and evaporation of the spraying solution before reaching to the substrate. Also the surface of SnO_2 thin film is rougher so this is useful for various applications like photocatalytic degradation; gas sensor etc. due to enlarged the surface area.

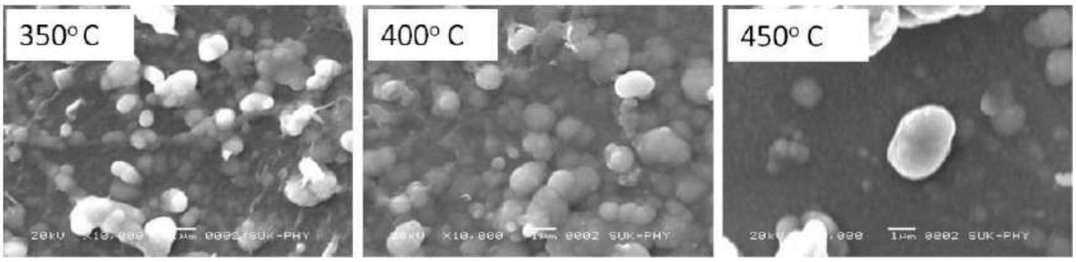

Fig. 2: SEM micrographs of SnO_2 thin films at varing substrate temperature

Electrical study:

Electrical properties of the films measured using two probe resistivity method as shown in fig.3 a) It gives some thermal energy or activation energy required to hop the charges (electrons or holes) from valence band to conduction band of the semiconductor. To determine the activation energy, the variation of electrical resistivity (ρ) as a function of inverse of temperature in the temperature range of 323–473K is studied in inert atmosphere and shown in Fig. From Fig. it is clear that the electrical resistivity decreases with an increase in temperature indicating the semiconducting behaviour of SnO_2 thin films The thermal activation energies were calculated by using the Arrhenius law [11] as given below,

$$\rho = \rho 0 \exp(-Ea/KT) \qquad (2)$$

Here symbols have their usual meaning. The slope of the log (ρ) versus 1/T leads to the estimation of activation energy.

Where, ρ_o is the pre-exponential factor, K is the Boltzmann constant, and T is the temperature. The calculated values of thermal activation energies were vary from 0.00120 eV to 0.00130 for the sample S1 to S3 respectively.

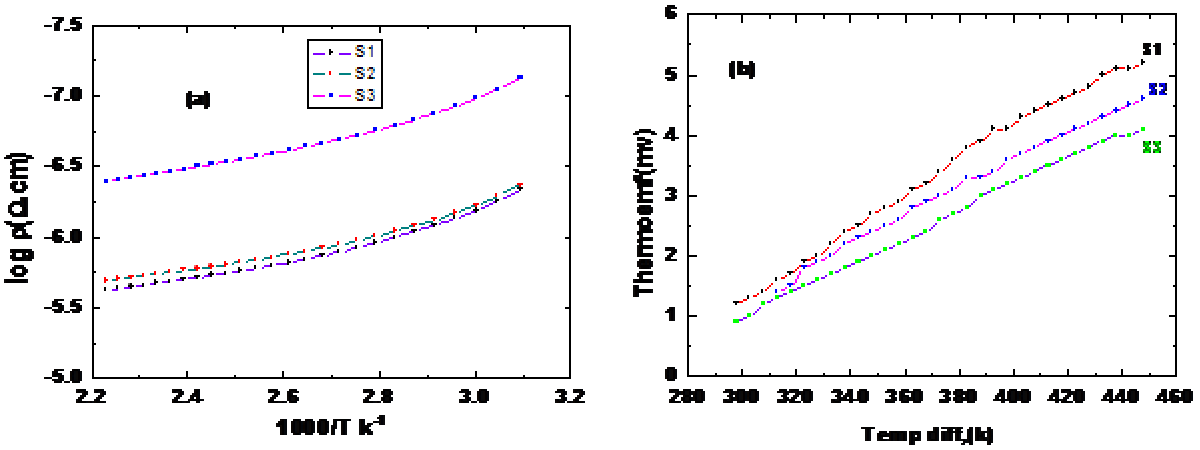

Fig.3 a) Electrical conductivity plot of SnO_2 thin films deposited by varing substrate temperature b) Thermoelectric power plot of SnO_2 thin films deposited by varing substrate temperature

Fig.3 b) shows the thermoelectric power with temperature in the temperature range 300–450K respectively. The graph of thermo-emf Vs temp difference gives us thermoelectric power of given material as well as nature of material i.e. p- type or n-type. The SnO_2 thin film has thermoelectric power at about 0.02mV/K. The slope of graph is positive so SnO_2 is n-type material [12]

Optical properties:

Optical properties of SnO_2 thin films were investigated by UV–Vis spectrophotometer at room temperature. The optical absorption and transmission study was carried out in range of 350-750nm for SnO_2 thin film. Fig. 4 a) shows optical absorption of SnO_2 thin film, it appears that SnO_2 thin film has low absorbance in the visible region. The optical band gap (Eg) for SnO_2 thin film is calculated on the basis of optical absorption using the following equation

$$\boldsymbol{\alpha = \alpha_o (h\nu - E_g)^n / h\nu} \qquad (3)$$

Where, Eg is separation between bottom of conduction band and top of valance band, hv is the photon energy, n is constant. The plot of $(\alpha hv)^2$ versus hv of SnO_2 thin film is shown in Fig below. From the linear nature of the plot the band gap energy (Eg) is obtained by extrapolating the linear portion at $\alpha=0$. From the graph for SnO_2 thin film band gap value 3.7 is observed. It is well agreements with the reported value of SnO_2 thin films deposited by spray pyrolysis techniques [13].

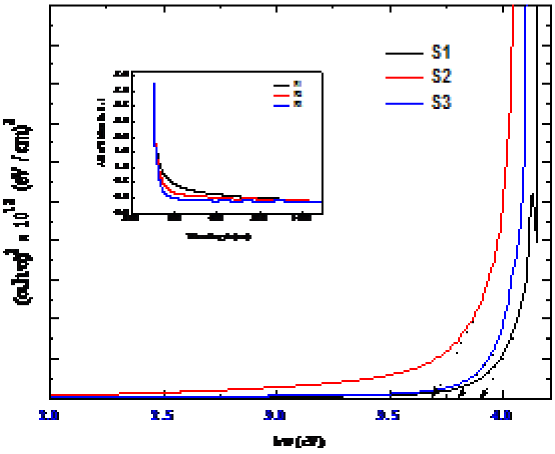

Fig. 4a) Band gap plot of SnO_2 thin films by varing substrate temperature and inset of this the Absorbance graph

Fig. 4 b) shows the optical transmittance curves as a function of wavelength for the SnO_2 thin films. It is clearly noticed that they have an average transmittance greater than 50% in the visible region and high absorption (near 100%) in ultraviolet regions. As the temperature increases, the average transmittance of the films increases slightly due to the decrease in the film thickness. Further, the absorption edge shifts towards the longer wavelength region with increasing temperature. The transmittance value at 350, 400 and 450^0C temperature has increases from 35 %, 40 % and 45 % respectively.

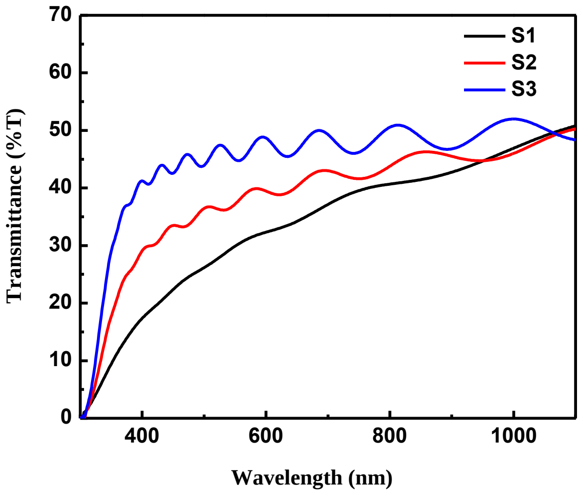

Fig. 4b) Transmittance plot of SnO_2 thin films by varing substrate temperature

CONCLUSIONS:

In summary, SnO2 thin films have been successfully synthesized by a simple spray pyrolysis method. X-ray diffraction analysis shows that SnO2 thin films are polycrystalline in nature with tetragonal structure. SEM study shows the grain like morphology which is in used in various application. The optical band gap of as-deposited film was found to be 3.7 eV. Also study the electrical properties of SnO2 thin films deposited by SPT.

ACKNOWLEDGEMENTS:

This work was supported by the DST-SERB, New Delhi (SR/FTP/PS-083/2012). Authors are grateful to Human Resources Development of the Korea Institute of Energy Technology Evaluation and Planning (KETEP) grant funded by the Korea government Ministry of Knowledge Economy (No.: 20124010203180)

REFERENCES:

1. S.S. Shendage , V.L. Patil , S.P. Patil , S.A. Vanalakar , J.L. Bhosale, J.H. Kim, P.S. Patil J. Anal. and Appl. Pyro. 125, 9–16 (2017).
2. N. G. Deshpande, J. C. Vyas and R. Sharma, Thin Solid Films 516, 8587–8593 (2008).
3. M. Di. Giulio, G. Micocci, A. Serra, A. Tepore, R. Rella, P. Siciliano, Sens. Actuators, B 24, 465 (1995).
4. M.C. Horrillo, P. Serrini, J. Santos, J. Manes, Sens. Actuators B 45 (197) 193 (2016).
5. Dilip L. Kamble, Namdev S. Harale , Vithoba L. Patil , Pramod S. Patil , Laxman D. Kadam, J. Anal. and Appl. Pyro., 127, 38–46 (2017).
6. P.S. Patil, Mater. Chem. Phys. 59, 185 (1999).
7. Sumanta Sain, Arik Kar, Amitava Patra and Swapan K. Pradhan, Cryst. Eng.Comm, 16, 1079 2014.
8. V. L. Patil, S. A. Vanalakar, A. S. Kamble, S. S. Shendage, J. H. Kim and P. S. Patil, RSC Adv., 6, 90916 (2016).
9. Y.M. Hunge, M.A. Mahadik, S.S. Kumbhar, V.S. Mohite, K.Y. Rajpure, N.G. Deshpande, A.V. Moholkar, C.H. Bhosale, Ceram. Int.,08, 178 (2015).
10. Abdul Rasheed Paloly, M. Satheesh, M. Carmen Martínez-Tomás , Vicente Munoz-Sanjosé, Sreekumar Rajappan Achary, M. Junaid Bushiri, Appl. Sur. Sci., 357, 915–921 (2015).
11. S.S. Shendage, V.L. Patil , S.A. Vanalakar , S.P. Patil , N.S. Harale, J.L. Bhosale , J.H. Kim, P.S. Patil, Sensors and Actuators B 240, 426–433 (2017).
12. G. E. Patil, D. D. Kajale, D. N. Chavan, N.K. Pawar, P. T. Ahire, S. D. Shinde, V. B. Gaikwad, G. H. Jain, Bull. Mater. Sci., 34, 1–9 (2011).
13. T. Indira Gandhi, R. Ramesh Babu, K. Ramamurthi, M. Arivanandhan, Thin Solid Films 598, 195–203 (2016).

HIGHLY SENSITIVE AND SELECTIVE SOLID STATE SYNTHESIZED CuO NANOPARTICLES FOR DETECTION OF TOXIC NO_2 GAS

Y. H. Navale[1], S. T. Navale[2], S. M. Ingole[1], I. A. Dhole[1],
R. N. Mulik[1], M. A. Chougule[1] and V. B. Patil[1]*
[1]Functional Materials Research Laboratory, School of Physical Sciences,
Solapur University, Solapur, M.S. 413255, India
[2]College of Materials Science and Engineering, Shenzhen Key Laboratory of Polymer Science and Technology, Guangdong Research Center for Interfacial Engineering of Functional Materials, Nanshan District Key Lab for Biopolymers and Safety Evaluation, Shenzhen University, Shenzhen 518060, P.R. China
*Corresponding author E-mail: drvbpatil@gmail.com

ABSTRACT:

In present study, we report a NO_2 gas sensing spirit of CuO nanoparticles; prepared fruitfully on a quartz substrate by a catalyst free thermal evaporation method. Structural investigation exploded the monoclinic crystal structure of CuO NPs. The morphological analysis revealed that the formation homogeneous nanoparticles on the top of substrate surface. As- prepared CuO NPs was employed to construct sensor for detection of noxious NO_2 gas. The CuO NPs sensor exhibits a elevated response of 70% with hasty response and recovery time at 150°C optimal temperature; also achieve excellent response at very low exposure (1 ppm) of NO_2 gas. Beside, CuO NPs sensor attains a fabulous selectivity, reproducibility and stability.

Keywords: CuO NPs; Quartz substrate; Thermal evaporation; XRD; NO_2 sensor;

INTRODUCTION:

In last few decades, the environmental air contamination is notably increased due to the contemporary industrialization, which is tremendously harmful to environmental issue and all living organisms. NO_2 gas is one of the most regular toxic contaminants often emitted from in various fields, including the combustion of automobile engines, home heaters, furnaces and plants [1]. Thus, gas finding gadgets are desirable to control toxic gases levels, particularly at minor ppm concentrations.

A lot of physical and chemical routes are employ to prepare CuO nanostructures including a hydrothermal reaction, seed-mediated solution growth, thermal oxidation and electro spinning [2-5].

In the present study, we used simple thermal evaporation (TE) technique, for the synthesis of CuO nanoparticles on quartz substrate, which utilize for NO_2 gas sensing application.

EXPERIMENTAL DETAILS:

Preparation of CuO nanoparticles (NPs):

The CuO NPs were synthesised by thermal evaporation of Cu metal on a pre-cleaned quartz substrate followed by annealing in argon atmosphere at 1000°C temperature. The deposition route was carried out in vacuum at of pressure $5x10^{-5}$ mbar. Initially, copper metal was embed into high power attached molybdenum boat and cleaned quartz substrate clutch on substrate holder. The Cu was evaporate on gradually increasing current and set down on quartz substrate. For the preparation of uniform CuO NPs, Cu layered films were annealed in argon atmosphere at 1000^{o}C temperature for 1 hour in tubular zone furnace after cooling at room temperature, the films uses for further analysis.

Gas sensing properties of CuO NPs:

To measure the gas sensing properties of CuO NPs, custom fabricated two probe gas sensor system was used [6-7]. In array to study the response to various toxic gases, the electrical resistance value of CuO NPs changed which was measured by programmable electrometer (Model: Keithley 6514 System) coupled with gas sensor system. The gas response S (%) [8] of the CuO NPs was calculated eq^n as,

$$\text{Response S (\%)} = \frac{|Rg - Ra|}{Ra} * 100 \qquad \ldots\ldots (1)$$

Where, R_g is the electrical resistance values in the existence of target gas, while R_a is in presence of atmospheric air (without gas).

RESULT AND DISCUSSION:

Structural and Morphological revelation:

A characteristic XRD pattern of CuO on quartz substrate is shown in fig.1 (a). The quartz peaks are illustrates in fig also (standard pattern number 46-1045) [9].CuO, with a monoclinic crystal structure which unanimous with standard JCPDS data (card no.72-0629). Moreover, no other peaks observed exploded that as-prepared samples are highly pure. The peak intensity of (111) reflection is higher as compare with other reflection peaks, which indicates the CuO was oriented along the (111) direction.

Scanning electron micrographs of the CuO NPs formed on the quartz substrate are exposed in fig.1 (b). The SEM images clearly show that the formation of uniform CuO NPs with homogeneous porous surface morphology.

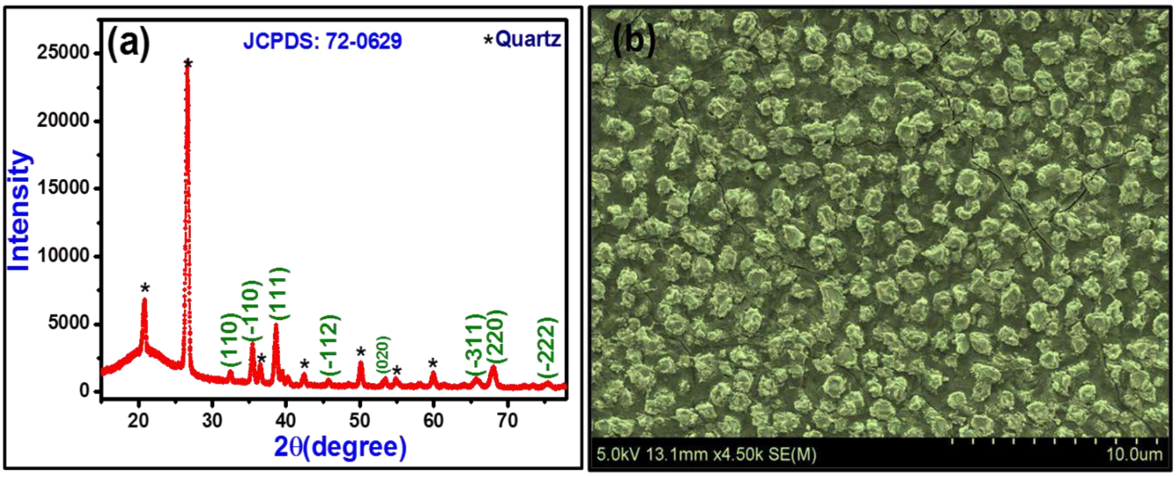

Fig. 1 (a) XRD pattern and (b) SEM image of CuO NPs

Gas sensing study:

In gas sensing investigating the operating temperature is vital factor, which influences the adsorption / desorption process of oxygen ions on the top surface of the sensor, which plays a crucial role in fabrication of the gas sensor. The effected gas response with 100 ppm NO_2 on altering the operating temperature as shown in fig. 2(a).The surface of metal oxide sensor adsorbs oxygen from air and form O^-, O^{2-} and O_2^-. It is well known that the response of metal oxide gas sensor is moderately high in the temperature range of 100°C –300°C, this is due to adsorbed O^- ions. The upmost response for CuO NPs sensor is obtained at an operating temperature of 150°C towards NO_2 gas. At lower temperature (>150°C), the response of CuO nanocube sensor is controlled by speed of chemical reaction and at higher temperature (<150°C) response of sensor is restricted due to rate of diffusion of gas molecules. However, at an arbiter temperature (150°C), the cadence of these two reactions become equivalent and at that temperature, the CuO NPs sensor gives its maximum response.

Selectivity of sensor is a very significant task in view of their gas sensing applications. The selectivity study of CuO NPs sensor of various toxic gases at 100 ppm concentration was studied and illustrate in fig.2 (b). Selectivity graph clearly indicate that the CuO sensor was more sensitive towards NO_2 gas as contrast with other test gases such as LPG, H_2S, methanol and Cl_2 this is due to the rate of reaction between CuO NPs surface and NO_2 gas molecules is much faster.

Fig.2 (c) shows dynamic gas response curve of CuO NPs sensor to diverse concentration of NO_2 gas at optimal operating temperature of 150ºC. The response values of sensor are calculate by using equation (1).From the response curve it is clearly observed that the sensor response linearly increases, as the concentration of NO_2 gas increases. The CuO NPs sensor shows maximum response of 70% at concentration of 100 ppm NO_2 gas, while sensor shows response of 4% on exposure of at very low concentration (1 ppm) of NO_2 gas. It is well known that, at low concentration of NO_2 gas covers lesser surface of sensor and sensor exhibits lower response while on exposure of high concentration of NO_2 gas due to larger coverage, surface reactions increases and sensor exhibits its maximum response [10].

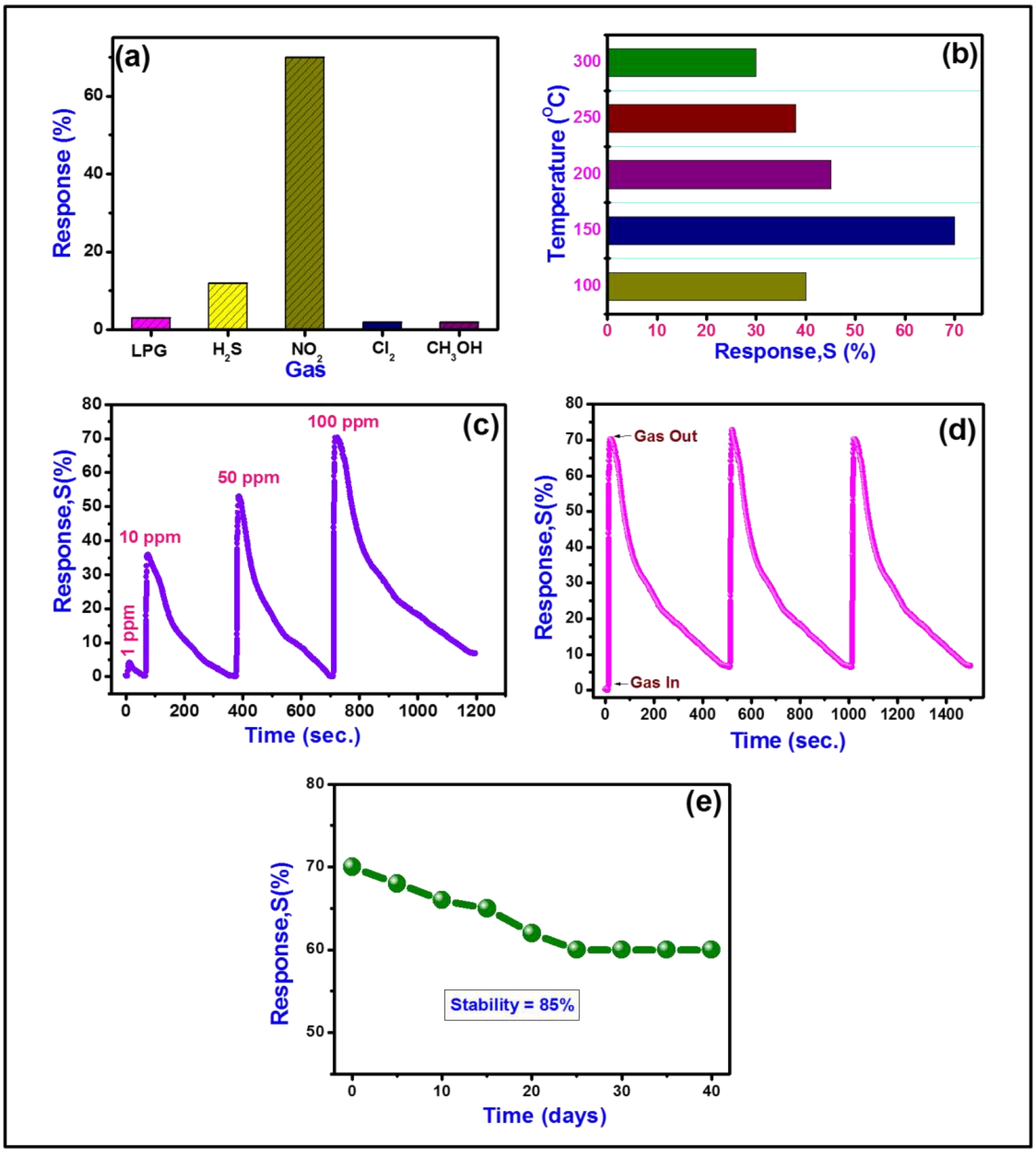

Fig.2 (a) Selectivity study, (b) temperature dependant, (c) Response curve, (d) reproducibility and (e) stability study of CuO NPs

The reproducibility and stability of sensor are considered as imperative parameter in view of their gas sensing applications, also consistency of sensor is mostly reliant on these parameters. The reproducibility study of CuO NPs sensor was investigated by measuring response for three times at 100 ppm concentration of NO_2 gas and obtained results are shown in fig.2(d),which revealed that CuO NPs sensor have excellent response reproducibility. The stability study of CuO NPs sensor was measured for 50 days on exposure of concentration of 100ppm NO_2 gas at 150ºC. The results obtained from stability study are depicted in fig.2(e).Initially, the CuO NPs sensor exhibit highest response of

70%, while after 25 days trivial decreases in response and almost steady with achieving 85% stability. The slightly decrease in response value is primarily due to effect of aging [11]. Such type of stability is admirable for gas sensor applications.

4. Conclusion

A simple catalyst free thermal evaporation technique was competently applied for synthesis of CuO nanoparticle sensor on quartz substrate that intellectual to sense lethal NO_2 gas at very minor concentration (1 ppm). CuO NPs sensor gives really high response with very fast response and recovery time, admirable selectivity, outstanding reproducibility and stability as well in response at 150ºC working temprature. The CuO NPs sensor show highest response of 70% on coverage of 100 ppm NO_2 gas. From the obtained gas sensing results we trust that, as-prepared CuO NPs sensors are proficient for gas sensing applications in industrialized vicinity.

ACKNOWLEDGMENTS:

Prof. VBP would like to thank DAE-BRNS (scheme no. 34/14/21/2015-BRNS) for the financial support.

REFERENCES:

1. S. T. Shishiyanu, T. S. Shishiyanu, O. I. Lupan, Sens. Actua. B, 113, 468–476 (2006).
2. H.M. Xiao, S.-Y. Fu, L.-P. Zhu, Y.-Q. Li, G. Yang, Eur. J. Inorg. Chem., 1966–1971 (2007).
3. A.A. Umar, M. Oyama, Cryst. Growth Design, 2, 453–458 (2007).
4. Y. Liu, L. Liao, J. Li, C. Pan, J. Phys. Chem., C 111, 5050-5056 (2007).
5. H. Wu, D. Lin, W. Pan, Appl. Phys. Lett. 89, 133125 (2006).
6. D. K. Bandgar, S. T. Navale, S. R. Nalage, R. S. Mane, F. J. Stadler, D. K. Aswal, S. K. Gupta and V. B. Patil, J. Mat. Chem. C, 3, 9461 (2015).
7. G.D. Khuspe, D.K. Bandgar, Shashwati Sen, V.B. Patil, Synthetic Metals, 162, 1822– 1827 (2012).
8. A.T. Mane, S.B.Kulkarni, S.T.Navale, A.A.Ghanwat, N.M.Shinde, Jun Ho Kim, V.B.Patil, Cera. Int., 40, 16495–16502 (2014).
9. K. Kihara, Euro. J. Mineral. 2, 63-77 (1990).
10. A.T. Mane, S.T.Navale, S.Sen, D. K. Aswal, S.K.Gupta, V.B. Patil, Organic Electronics, 16, 195–204 (2015).
11. S.T. Navale, D.K. Bandgar, S.R. Nalage, G.D. Khuspe, M.A. Chougule, Y.D.Kolekar, S. Sen, V.B. Patil, Ceram. Int. 39, 6453–6460 (2013).

DIVERSITY OF FLESHY MUSHROOM IN SANGOLA TALUKA, DISTRICT SOLAPUR, MAHARASHTRA (INDIA)

R. R .Tembhurne[1]* and S. P. Nanir[2]

[1]Sangola College, Sangola, Dist. - Solapur (M. S.) 413307

[2]Former Director, Govt. Institute of Science Aurangabad (M. S.) 431004

*Corresponding author E-mail: ramesh_tembhurne@rediffmail.com

ABSTRACT:

During the floristic study of the mushroom of this region author come across a number of mushroom species. In this study five species of mushroom are being discussed. 1. *Stropharia semiglobata* (Batsch) Redhead, Moncalvo & Vilgays (2013)., 2. *Coprinus micaceous* (Bull.:Fr.) Vilgalys, Hopple & Jacq. Johnson., 3. *Mycena capillaripes* (Pers.) P. Kumm. (1871). 4. *Inocybe jurana* (Pat.) Saccardo. and 5. *Cystoderam amianthinum* (Scop.) Fayod (1889) are being discussed with different five genus and species. All the different genus and species are being reported for the first time from this region.

Keywords: Mushroom, Sangola

INTRODUCTION:

Sangola taluka goes under the Western piece of the zone has a place with Solapur locale, Maharashtra. Ordering as dry season inclined regions, shallow and poor kind of soil, not retentive of dampness denotes this part, alongside the inadequate and unverifiable precipitation, because of sparse and non uniform downpours shortage condition win in the talukas. For the most part rainstorm period is from the second fortnight to June to the finish of September bringing downpours from South-West storm. Indeed, even in the shortage of water, we chose this area for the investigation of beefy mushroom. Sangola taluka has number of rustic regions which are extremely rich in vegetation and has land dissemination. We went by various areas all through year, gathered number of tests of mushrooms. All these gathering was from some rustic and urban of said region. Soil is the most essential regular hotspot for advancement of different kind of small scale life forms including consumable and non eatable meaty mushroom. All the saprophytic beefy mushroom are created on soggy rotting logs, soil and excrement. An examining of the decent variety of sporulating growths observed more than one wet seasons i.e. blustery season in Sangola taluka Solapur District. Likewise the dirt is a standout amongst the most imperative and intriguing element and is the most qualities highlight of earthly condition in which investigation of soil increment information and accommodating by and by of Agriculture, Horticulture and Forestry. The dirt is the gritty material in which plants develop. Exhibit think about decent variety of beefy mushroom from Sangola taluka Solapur District is a place with hot and halfway damp climatic condition embraced.

Fleshy mushroom are parasitic, saprophytic, poisonous, non-poisonous, edible and non-edible. Main aspects of this study to find out the poisonous and edible mushrooms from this region. Present study is the floristic study and to collect maximum number of sample from this region and identified and classified. Fleshy mushroom and other plants are directly used as medicines by a majority of cultures around the world. Many food crops and fleshy mushroom have medicinal effects. Fleshy mushrooms and several other plants are resources of new drugs. Studying fleshy mushrooms helps to understand plant toxicity and protect human and animal from natural poisons. Cultivation and preservation of mushroom protect biological diversity. Whole the things there is a poison and there is nothing without a poison. It depends on only upon the those weather a poison is a poison or not. Many of the modern medicines are produced indirectly from mushrooms and medicinal plants. Mushrooms and medicinal plants have played an essential role in the development of human culture. Plants have always been the main forms of medicine in India and now they are becoming popular throughout the world.

In the present work an attempt is made to present some interesting fleshy mushrooms observations recorded in Sangola division, Solapur district, Maharashtra, India. While carrying out the field work, help was taken from the traditional healers in the plants of mushrooms and information, as they are familiar with the plants around them. The findings of this study can provide useful leads for pharmacological and food conformation of these reported uses which might in time become useful for mankind. Many workers reported fungi from decaying log, humus, dung, rhizosphere (Alexopoulos and Mims 1979, Alexopoulos 1962, Lincoff G. and Mitchel D.H. 1977, Lincoff Garry H. 1981, Ainsworth G.G.,Sparrow F.K.and Sussman 1973, Miller O.K.1975,1977, Smith A.H. 1947, 1968, 1971, 1973, 1979, Snail 1970, 1971 Peter Jordan1995, 1996 and 2000, Augusto Rinaldi Vassali Tyndalo 1985, Jacob E.Lange and Morten Lange 1961). Sangola taluka is the region under investigation is very rich in biodiversity-constitute the districts Solapur. The study of fleshy mushrooms was practically neglected from this region. Hence, it was felt to undertake the study.

MATERIAL AND METHOD:

All the sample were collected from different areas of Sangola Taluka. The different region were taken into consideration. From each region sample were collected from different localities. There are more number of sample were collected of fleshy mushroom. All the fleshy mushroom sample were grow on natural media. The source of natural media on which fleshy mushroom grown on humus, deadwood debris, decaying logs, wood decomposing fungi, dung, dying tree roots, roots of living plants, exterior and interior humus contain soil, lawn and garden, health forest and landscape, dead plant material, living plant material, bark of trees, living and non-living host of plants biomass, topsoil.

All the fleshy mushroom collected from wild as well as domestic area of Sangola Taluka during month of August 2017 from the different localities and material deposited in the formalin and photographs it, listed it according to index of preservation and studied. Identification of all mushroom is carried out with the help of movable suiting, stopper photographs, preserve material and following mushroom to taking a refrecnes of Simon and Schusters Guide to mushroom by Giovanni Pacioni, U.S. editor: Gary Lincoff., The mushroom guide and identifier by Peter Jordan, Augusto Rinaldi, Vassili Tyndalo-The complete book of mushrooms, Mushroom of the great lakes region by Verne ovid Graham, Collins Guide to mushrooms and Toadstools by morten lange and F. Bayard Hora. This is the important method are use for the identification of fleshy mushroom.

RESULT AND DISCUSSIONS:

1. *Stropharia semiglobata* (Batsch) Redhead, Moncalvo & Vilgays (2013).

COLLECTION EXAMINED: RRT/151, August-2017, Watambare, Sangola Dist.-Solapur. On moist dung.

DISTIRBUTION: INDIA: M. S. (Tem, 2017), North America, Britain and Ireland, Australia and Mainland Europe.

Cap 0.9 to 1.3 cm in length, 1.1 to 1.5 in width, total height 2 to 6.5 cm, globose to sub-globose, hemispherical, convex, smooth, fleshy, rough, ash or brown in color, periphery fragile or crack, viscid when wet, shiny when dry, thin cap flesh is very pale. **Gills** are many at lower surface of cap, blackish or gray, crowded, dense, free, some gills long and short arises in between the two gill, smooth, fleshy, thick, rigid, adnate, darken to cinnamon with pale edges as the spores mature, bears spores. **Stipe** long, cylindrical, smooth, fleshy, packed, fibrous, concolorous, slender, white to brown color, wart, slightly broad at the base, bent, narrow at the apex, pale at the apex and pale ochre below the transient ring, flesh is solid and pale ochre, length of stipe 1.8 to 6 cm, width of stipe 0.3 to 0.5 cm. **Spores** brown, smooth, ellipsoidal or oval, ovoid, globose, thick, globose spores 2.7 to 4.1 um in diameter, and oval spores 4.1 to 5.5 um in diameter, conspicuous, distinct, not transparent. **Odor** not distinctive. **Habitat** saprobic on animal dung and freshly manured grassland. **Season** rainy, June India and June to November in Britain and Ireland. **Edibility** poisonous, inedible.

2. *Coprinus micaceous* (Bull.:Fr.) Vilgalys, Hopple & Jacq. Johnson.

COLLECTIION EXAMINED: RRT/152, August-2017, Najara, Sangola, Solapur. On moist dung.

DISTRIBUTION: INDIA: M. S. (Tem, 2017), Europe, North America, Britain and Ireland, Asia and in South America and Australia.

Cap 0.5 to 1.2 cm in length, 0.6 to 1.7 cm in width, total height of fruiting 5 to 5.5 cm in length, cap dark brown to irony brown, chocolaty in color, cup like, smooth, fleshy, line arises on the cap form apex to peripheral region, non-fragile, scattered, convex, granular, egg and bell shape, russet central eye. **Gills** are many, white, crowded, dense, free, smooth, fleshy, thick, thin, adnate, Glistening, bears spores. **Stipe** long, cylindrical, smooth, fleshy, packed, fibrous, concolorous, slender, white to brown color, slightly broad at the base, bent, narrow at the apex, length of stipe 4.9 to 5.2 cm, width of stipe 0.2 to 0.3 cm. **Spores** blackish brown in color, globose, 2.7 to 4.1 um in diameter, almond spores length 8.3, width 4.1 um in diameter. **Odor** not distinctive. **Habitat** Saprobic, found growing on or beside broad-leaved tree stumps, dead roots and moist dung. **Season** rainy in India, May to November in Britain and Ireland. **Edibility** poisonous.

3. *Mycena capillaripes* (Pers.) P. Kumm. (1871).

COLLECTION EXAMINED: RRT/153, August-2017, Sangola, Solapur. On moist soil with decaying plant debris.

DISTIRBUTION: INDIA: M. S. (Tem, 2017), Mainland of Europe, Britain, Ireland and North America. the United States, the Pacific Coast from Washington to California, Tennessee, North Carolina, its northern distribution extends to Canada (Nova Scotia), Germany,and Norway.

Cap 1.2 to 1.3 cm in length, 3.9 to 4 cm in width, total height 8 to 9.5 cm, rounded, globose, irony patra like, in between the two gills hallow arrangement, hallow lines with dongi or canal of water flow type arrangement take place, whitish tint brown to creamy, shiny, rough at periphery, at middle part smooth, deposited white shiny granules, conical, companulate to convex, striate, umbonate at maturity, centrally dark brown knot like body, pruinose, peripheral not fragile. **Gills** are many, whitish dark brwon, crowded, dense, free, smooth, fleshy, thick, adnate, slightly sinuate with short decurant teeth, long and short, elastic, arise at the apex part of the stipe, bears spores. **Stipe** long, cylindrical, smooth, fleshy, packed or hallow, pruinose, fibrous, concolorous, slender, whitish to brown in color, broad at the base, bent, narrow at the apex, releasing a milky white fluid (not bitter), length of stipe 8 to 8.2 cm, width of stipe 0.4 to 0.5 cm. **Spores** golden brown in color, globose, almond shape, 4.1 to 5 um in diameter, almond spores length 6.9, width 4.1 um in diameter. Odour taste mild but not distinctive**.** **Habitat** on moist soil and decaying plant debris, Saprobic; among leaf litter in woodlands, on the grassy woodland edges and beside. **Season** rainy, July to late November in Britain and Ireland. **Edibility** unknown, poisonous.

4. *Inocybe jurana* (Pat.) Saccardo.

COLLECTION EXAMINED: RRT /154, August–2017, Sangola College, Solapur. On moist soil.

DISTRIBUTION: INDIA: M. S. (Tem. 2017), Hafod faith, france metropolitaine.

Cap 0.5 to 0.6 cm in length, 0.9 to 1.8 cm in width, total height of fruiting body is 1.5 to 3.5 cm, scattered to gregarious, grouped in to two or many, globose, in immature stage cap like botton or knot like, after mature periphery corymbose, folded, chapatti like surface, smooth, rough, wrinkled, broad, fleshy, elastic, flexible, conic, convex, pallid, whitish brown, brown spots are arise on the surface of cap, gills curling form at ventral side after folding a cap towards the periphery, umbo, margin incurved, then decurved, wavy, sometime rimose, at maturity occasionally upturned, surface radially appressed-fribrilose to minutely squamulose, odor and taste to faintly farinaceous. **Gills** are many at lower surface, brownish pink, crowded, dense, free, smooth, fleshy, thick, adnate, subdecurrent, slightly sinuate, wavy, long and short, elastic, arise at the apex part of the stipe, bears spores. **Stipe**

long, cylindrical, smooth, fleshy, packed or hallow, solid, fibrous, slender, bright white to blackish white, broad at the base, bent, narrow at the apex, thick, sometime basal and apex bent, occasionally compressed, furfuraceous to fibrillose, lower portion striate, scattered, loose, length of stipe 3.5 to 8 cm, width of stipe 0.2 to 0.4 cm. **Spores** brown in color, smooth, thick wall, not conspicuous, distinct, transparent, globose, oval shape, globose 2.7 to 4.1 um in diameter, almond spores length 4.1, width 2.7 um in diameter. **Odour** taste mild but not distinctive. **Habitat** on moist soil and decaying plant debris, Saprobic; among leaf. Season rainy. **Edibility** avoided, poisonous, toxin muscarine.

5. *Cystoderam amianthinum* (Scop.) Fayod (1889).

COLLECTION EXAMINED: RRT/155, August–2017, Sangola, Solapur. On moist soil.

DISTRIBUTION: INDIA: M. S. (Tem. 2017)., Grassland and some woodland habitats in Britain and Ireland, mainland Europe, being most widespread and abundant in cooler northern countries and North America.

Cap 0.4 to 0.5 cm in length, 1 tp 2 cm in width, total heitht 2.9 to 3 cm, globose, hemispheric, singly, scattered, rough, many lines are arise on cap, fleshy, smooth, whitish to brown in color, at the periphery inside outgrowth are formed, bread like appearance at above side of cap, convex, flat, surface finely granular and wrinkled. **Gills** are many at lower surface, whitish to cream in color, crowded, dense, smooth, fleshy, thick, adnate, slightly sinuate, wavy, long and short, elastic, arise at the apex part of the stipe, bears spores. **Stipe** long, cylindrical, smooth, fleshy, packed, solid, fibrous, slender, bright white to above greenish, broad at the base, bent, narrow at the apex, thick, smooth, granular deposition, length of stipe 2 to 2.5 cm, width of stipe 0.3 to 0.4 cm. **Spores** brown in color, smooth, thick wall, not conspicuous, distinct, transparent, globose 4.1 to 8.3 um in diameter. **Odour** taste not significant. **Habitat** on moist soil and decaying plant debris. **Edibility** poisonous.

REFRENCES:

1. P.D.Sharma, The fungi, 279 (1991,1987).
2. Bressa G.L.,L. Cima ,and P. Costa, 16(2): 85-89 (1988).
3. Fox,F.M., The Hague (1983).
4. Stijve, T. J. Wilds Mushrooming 38(1): 9-14 (1992).
5. Stijve,T. R. Funbaux and B. Philippossian, Deutche Leben. Rundschau 82:243-248 (1986).
6. Stijve,T. and R. Roschnik, Trav.chim.alimen.Hyg.,65: 209-220 (1974).
7. Augusto Rinaldi, Vassili Tyndalo, Variaa Grandi Opere (1972).
8. Verne Ovid Grahan, “Mushroom of the Great lakes mushroom.Plate-I to Plate-49
9. Morten Lange, F.Bayard Hora. Collins, Guide to Mushrooms and Toadstools (1963).
10. Peter Jordan, The mushroom guide and Identifier, Anness publishing ltd. (1995,1996,2000).
11. Simon and Schuster’s, Simon and Schuster Inc.New York,.
12. David Arrora’s Mushrooms Demystified (1986).
13. M.Catherina Aime 2,3,4,Rytas Vilgalys 4 and Orson K. Miller Jrs (2004).

14. Maria Drumeva- Dimcheva and Melania Gyosheva-Bogoeva Section The macromyctes fungui of Bulgaria.
15. Michael Kuo. Mushroom Expert (2006).
16. Paul Stamets. Agroforestry.
17. Alexopoulos C.J. and C.W. Mims. Introduction mycology. P.N.359-387,429-445,446-469.
18. Lincoff, Gary H. and Parioni Giovannied, Simon and Schuster's Guide to mushroom, (1981).
19. Breithenbach, J. and Kranzlin, F., Fungi of Switzerland, 368 p (1955).
20. Little, B., Masters Thesis. Humboldt State University: Arcata, CA. 114 p (1991).
21. Noordeloos, M. E. Strophariaceae s. l. Edizioni Candusso: Alassio, Italy. 648 p (2011).
22. Smith KN. A Field Guide to the Fungi of Australia. Sydney, Australia, p. 181 (2005).
23. Redhead SA, Vilgalys R, Moncalvo J-M, Johnson J, Hopple JS Jr.; Vilgalys, Rytas; Moncalvo, Jean-Marc; Johnson, Jacqui; Hopple, Jr. John S. IAPT, 50 (1): 203–41 (2001).
24. Giovanni Robich, Fondazione Centro Studi Micologici (2003).
25. Stangl, J. NuAge Print and Copy: Burnley, UK. 344 p (2011).
26. Paul M. Kirk, Paul F. Cannon, David W. Minter and J. A. Stalpers, Dictionary of the Fungi, CABI, (2008).

Plate 1: ***Stropharia semiglobata*** **(Batsch) Redhead, Moncalvo & Vilgays (2013)**

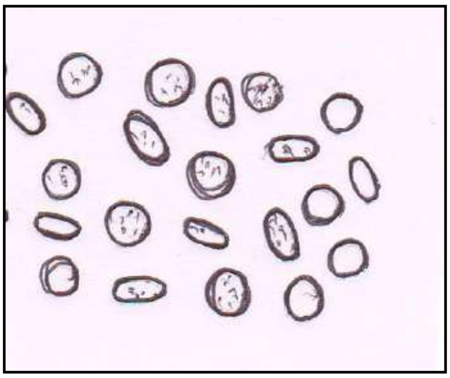

Spores: Globose and Oval

Plate 2: ***Coprinus micaceous*** **(Bull.:Fr.) Vilgalys, Hopple & Jacq. Johnson**

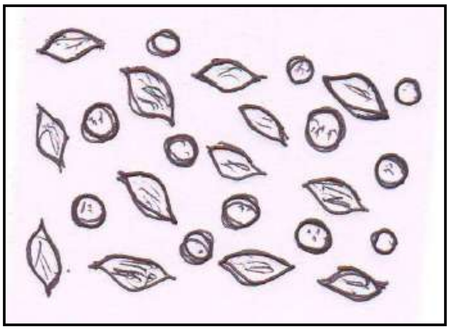

Spores: Globose and Almond

Plate 3: ***Mycena capillaripes*** **(Pers.) P. Kumm. (1871)**

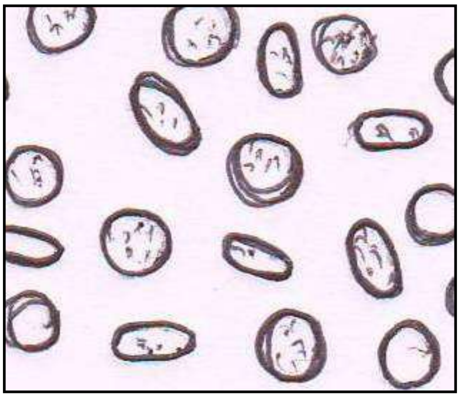

Spores: Globose and Oval

Plate 4: ***Inocybe jurana*** **(Pat.) Saccardo**

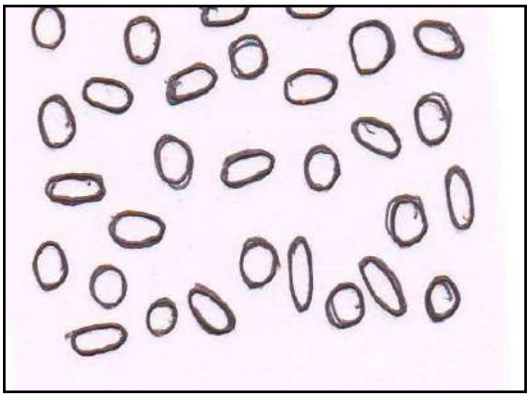

Spores: Globose and Oval

Plate 5: ***Cystoderam amianthinum*** **(Scop.) Fayod (1889)**

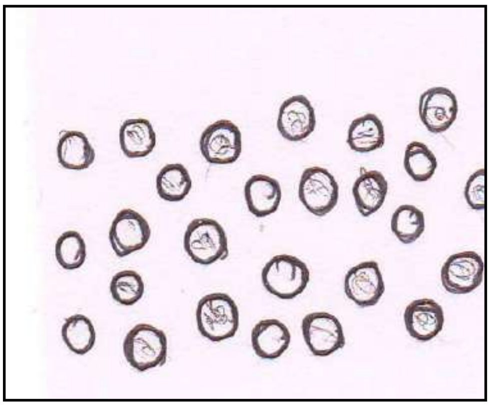

Spores: Globose

REVIEW ARTICLE ON CERIA (CeO_2) THIN FILMS DEPOSITED BY VARIOUS TECHNIQUES

A. K. Bhosale

Department of Physics, Raje Ramrao College, Jath 416 404, Maharashtra, India

Corresponding author E-mail: akbhosale1@gmail.com

ABSTRACT:

Nowadays, there has been considerably increasing demand and interest for the preparation of thin films for their wide range of potential applicability in the various fields of science and technology leading to dramatic reduction of prices of many day-to-day devices. Lot of efforts are being taken to obtain films of various required properties such as thickness, texture, uniformity, adhesivity, orientation etc. suitable for particular application. During the last few years thin films of different materials have been prepared by employing various preparation techniques. It has become fascinating to study the changing behavior of materials in thin film form owing to various conditions imposed during the preparation of films. Depending on the enhanced properties in thin films, they can be utilized in various superconducting microwave devices, electrochromic devices, polymer electrolytes for solid state batteries, optical filters, sensors, electrical shieldings, protective coating solar cells, humidity sensitizers etc. Therefore, one can find hardly any field where thin films are not utilized.

INTRODUCTION:

Ceria (CeO_2) has attracted its attention for its properties in automotive exhausts. Cerium oxide, CeO_2 is an insulator with the fluorite CaF_2 structure with lattice parameter of 5.41 A. The **Fig. 1** representing the structure of Ceria is as shown below. Ceria films have so for been prepared by number of physical and chemical techniques such as sputtering [1-14], evaporation [15-22], pulsed laser deposition [23-27], sol-gel[8,28-36], Chemical Vapour Deposition (CVD) [37-40], Spray Pyrolysis [41-44], Thermal decomposition [45], Electrodeposition [46-48], Epitaxy [49] and other [50-53]. The average survey of papers published over the past few years revels that researchers have employed mostly the technique of sputtering and sol-gel for the preparation of Ceria thin films.

The pure CeO_2 films find applications in number of appliances such as solid oxide fuel cell electrolyte [53], a counter electrode in smart windows [14,32], high temperature oxygen sensor [2,28,29], a substrate for silicon-on-insulator [41,42,43], stable buffer layer between high temperature superconducting materials and silicon substrates [3,42], in stable capacitor devices for large scale integration [42], an automotive exhaust catalysts[15,17] etc. Cerium oxide (CeO_2) is a good candidate as a dielectric material [23] due to its simple cubic structure, stable chemical properties, and good lattice match with silicon and YBCO. Thus, there are potential applications in silicon on insulator

(SOI), dynamic random access memory (DRAM), and the Si-based devices of superconducting, colossal-magnetoresistance, as well as feroo-electrics[65-69].

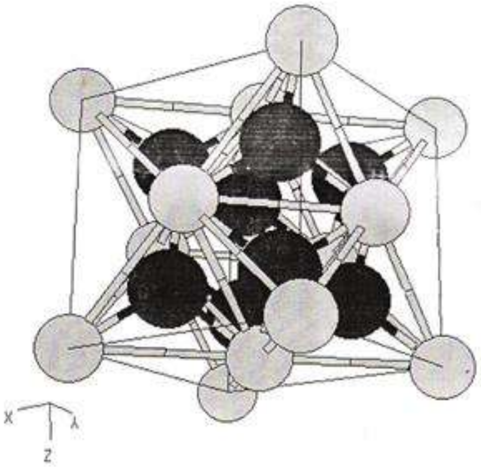

Fig.1: **Structure of CeO_2 (Fluorite)**

Thin films of CeO_2 doped with impurities such as TiO_2, Y_2O_3, BaO_3, ZrO_2, SnO_2 etc. have led to utilize the as corrosion inhabitor [48], buffers for growing high current YBCO superconductor [31], oxygen semipermeable membranes for gas seperation [31,39], both electrolyte and optically passive counter electrode material in the electrochemistry processes [11,12,21,30,34,41]. Again CeO_2 is also used as a buffer layer on Ni-based and hasstelloy metal tapes for the manifacture of YBCO-coated conductors [54-59]. In addition, CeO_2 films doped with Y, Zr, or a lanthanide element show promise as oxygen storage componenets in catalytic converters and as composite electrodes in solid oxide fuel cells [60-64].

N. Savvides et al. have investigated the epitaxial grouth of sputtered CeO_2 thin films as a function of deposition temperature and film thickness on three different single crystal substrate in order to deteremine the deposition conditions to allow synthesis of high quality CeO_2 thin film buffer layers which are suitable for the growth of YBCO thin films[1]. H. Meixner has reported high diffusion coefficient [2] of about 10^{-5} cm^2/s at 970C for oxygen vacancies in sputter deposited CeO_2 thin films. C.C. Chin [3] reported that RF sputtered Ceria flims had offstoichiometry of CeOy with y greater than 2.0 J.P. Holgado has studied oxidation processes of CeO_x defective layers in order to have fast diffusion process of ions [5]. Takehiko Uno [6] has presented a method for the growth of thin films of cerium substituted YIG (Ce:YIG) on an amorphous substrate in two steps. K. Von Rottkay [7] has investigated the influence of total pressure and oxygen partial pressure on the optical constants of TiO_2 in TiO_2 doped CeO_2 thin films produced by d.c. sputtering in wide range of composition. J. Purans et al. [8] have done the x-ray absorption measurements at the CeL_3, L_1 and Ti k-edges to study local structure and electronic properties of CeO_2-TiO_2 thin films produced by reactive d.c. sputtering.

Pure CeO_2 is at best not suitable for electrochromism. However CeO_2 doped with oxides such as ZrO_2, SnO_2, TiO_2 etc. has shown to use these films as passive counter electrodes for electrochromic windows [9, 34]. E. Masetti has investigated the effect of oxygen in the sputtering chamber on the optical and electrochromic properties of RF sputtered Ce-V mixed oxide films [10]. F. Varsano et al. have employed three electroanalyatical technique i.e. potentiostatic intermittent titration technique, galvanostaticinterttent titration technique and electrochemical impedance spectroscopy to study the solid-state ionic diffusion of lithium into Ce-V mixed oxide thin films [11]. A. Azens et al. have studied sputtered W-Ce oxide and Ti-Ce oxide thin films for their use in optically passive counter electrodes for electrochromic devices [12]. Similar attempts have have made by N. Janke et al. [14] for the same applications. M. Hadano et al. have studdied the reaction kinetics of cerium thin films with H_2, O_2 and H_2O systems at 298 K [15]. Cerium (IV) oxide ultrafine particles were prepared by thermal relaxation technique known as the reaxative auto-dispersion (RAD) process [16]. D.R. Mullins et al. [17] have grown ordered cerium oxide thin films of thickness 1-10 ML (monolayer) in situ on the Ru (0001) and Ni (111) surface to study the stability of films in terms of structure and composition at temperature upto 1000 K. A. Ramiez-Duverger et al. have presented a methodology for obtaing CeO_2 films by flash evaporation to sudy ionic conductivity [18]. I. Porqueras [19] has assessed the feasibility of using pure CeO_2 thin films as ion-storage layers in all-solid inorganic electrochromic device. He also studied their dielectric characteristics and DC conductivity [20] Guglielmo and Poli have reported the process conditions and materials performances of optically passive thin films of mixed Ce/Ti and Ce/Zr oxide prepared by electron beam reactive evaporation [21]. A. Pfau has studied influence of Rh surface doping on the electronic structure of stoichiometric CeO_2 surfaces [22]. Jinfeng Kang et al. have studied the impact of process conditions on structural and electrical characteristics of CeO_2 thin films on Si (100) substrate [23]. PiotrJasinski et al. have presented a study of the structure and electrical properties of nanocrystalline CeO_2sensor and investigated its response time and cross-sensitivity to nitrogen dioxide and sulfur dioxide [28].

A. Trinchi et al. have also ivestigated the oxygen gas sensing performance of semiconducting CeO_2-TiO_2 thin films. Different composition in the range of pure TiO_2 to pure CeO_2 have been studied by D. Deroo et al. [32] in order to examine the influnce of film structure on the kinetics and efficincy of lithium electrochemical insertion. J. Gomilsek [33] and Z. Orel [35] have studied electrochromic properties of CeO_2 and Ce/V thin films. M. Berton et al. [36] have studied the influence of SiO_2 addition on electrochemistry of CeO_2 oxide coatings. Z. Lu et al. have studied the crystalline quality and surface morphology of (100) CeO_2 thin films grown on sapphire substrate by solid source MOCVD process [37]. Using the same process, M, Pan et al. [38] have studied pure CeO_2 and yttria doped CeO_2 thin films for electrochromic applications. M. Inaba et al. has applied the modified electrochemical vapour deposition (EVD) method to the preparation of CeO_2 thin films in the form of microtube [39]. B. Elidrissi et al. have reported the structural, surface morphology and optical properties of CeO_2 thin films prepared by spray pyrolysis method [41]. S. Wang also obtained CeO_2 films by SPT and studied the relationship of ratio of pulse time (tp) to the interval time (t_1) with the crystal phase and morphology of the films [42]. He also observed the change of Raman spectrum with crystalline size of nanometer sized CeO_2 [43]. He also carried out XPS study the behaviour of CeO_2 thin films with exposure to the x-ray source [44]. Galembeck et al. obtained cerium oxide coating by metalloorganic decomposition on glass substrate for pyrrole oxidation [45]. Y. Zhou and Switzer have reported, for the first time, the synthesis of CeO_2 films using the electro generation of base method and presented the microstructural features of the CeO_2 films [46]. P. Stefanov et al. have applied a new electrochemical method with new electrolyte composition and electrolysis regime for the preparation of CeO_2 films [47]. M. Balasubramanian et al. have studied the oxidation state and structure of the cerium in electrochemically deposited CeO_2 thin films using XAFS technique [48]. S. Ikegawa [49] has obtaned epitaxial thin films grown on single crystalline substrates by metal-organic molecular beam epitaxy.

CONCLUSION:

In this review article, an extensive survey of both pure and doped cerium oxide thin films prepared by various deposition techniques is made.

REFERENCES:

1. N. Savvides, A. Thorly, S. Gnanarajan, A. Katsaros, Thin Solid Films, 388, 177 (2001).
2. J. Gerblinger, W. Lohwasser, U. Lampe, H. Meixner, Sensors & Actuators B, 26-27, 93(1995).
3. C. C. Chin, R. J. Lin, Y. C. Yu, C. W. Wang, E. K Lin, W. C. Tsai, T. Y. Tseng, Physica C, 260, 86 (1996).
4. Bjorn Skarman, L. R. Wallenberge, P. O. Larsson, A. Andersson, J-O. Bovin, S. N. Jacobsen, U. Helmersson, J. Catalysis, 181, 6 (1999).
5. J. P. Holgado, G. Munuera, J.P. Espinos, A. R. Gonzalez-Elipe, Appl. Surf. Sci., 158, 164(2001).
6. Takehiko Uno, Satoru Noge, J. of European Cer. Soci., 21, 1957 (2001).
7. K. Von Rottkay, T. Richardson, M. Rubin, Slack, L. Kullaman, Solid State Ionics, 113-115, 425 (1998).
8. J. Puans, A. Azens, C.G. Granqvist, Electrochim. Acta, 46, 2055 (2001).
9. F. Varsano, F. Decker, E. Masetti, F. Cardellini, A. Licciulli, Electro. Acta, 44, 3149 (1999).
10. E. Masetti, F. Varsano, F. Decker, A. Krasilnikova, Electrochim. Acta, 46, 2085(2001).
11. F. Varsano, F. Decker, E. Masetti, F. Croce, Electrochim. Acta,46, 2069 (2001).
12. A. Azens, L. Kullman, D. D. Ragan, C. G. Granqvist, Solar Cells, 54, 85 (1998).
13. W. Scoenfeld, M. Puga-Lambers, B. Pathangey, D. Schoenfeld, P. H. Holloway, Appl. Surf. Surf. Sci., 140, 204 (1999).
14. N. Janke, A. Bieberle, R. WeiBmann, Thin Solid Films, 392, 134 (2001).
15. M. Hadano, N. Urushihara, S. Terada, D. Katsuya, H. Uchida, J. of alloys and Comp., 330-332, 498 (2002).
16. T. Masui, K. Machida, T. Sakata, H. Mori, G. Adachi, J. of alloys and Comp, 256, 97 (1997).
17. D. R. Mullins, P. V. Radulovic, S. H. overbury, Surf. Sci., 429, 186 (1999).

18. A. Ramirez-Duverger, A. R.R-Salvador, M.P. H-Sannchez, G.R. Gattorno, Solid State Ionics, 96, 89 (1997).
19. I. Porqueras, C. Person, C. Corbella, m. Vives, A. Pinyol, E. Bertran, Solid State Ionics, 165, 131 (2003).
20. I. Poequeras, C. Person, E. Bertan, Thin Solid Films, 447-448, 119 (2004).
21. GuglielmoMacrelli, ElisabettaPoli, ElectrochemicaActa, 44, 3137 (1999).
22. A. Pfau, K.D. Schierbaum, W. Gopel, Surf.Sci., 331-333, 1479 (1995).
23. Jinfeng Kang, X. Liv, G. Lian, Z. Zhang, G. Xiong, X. Guan, R. Han, Y. Wang, Microelectronic Engineering, 56, 191 (2001).
24. R. Aguiar, F. Sanchez, C. Ferrater, M. Varela, Thin Solid Films, 306, 74 (1997).
25. A. N. Khodan, J. P. Contour, D. Michel, O. Durand, R. Lyonnet, M. Michet, J. Crystal Growth 209, 828 (2000).
26. E. Maiser, P. Fournier, J.L. Peng, F. M. Araujo-Moreira, T. Venkatesan, R. L. Greene, G. Czjzek, Physica C, 297, 15 (1998).
27. C. Mitro, P.Raychaudhuri, S.K. Dhar, A.K. Nigam, R. Pinto, J. of Mag. And Mag. Mater., 226-230, 809 (2001).
28. PiotrJasinski, Toshio Suzuki, H. U. Anderson, Sensor and Actuators B., 95, 73(2003).
29. A. Trinchi, Y. X. Li, W. Wlodarski, S. Kaciulis, L. Pandolfi, S. Viticoli, E. Comini, G. Sberveglieri, Sensors and Actuators B., 95, 145 (2003).
30. F. E. Ghodsi, F. Z. Tepehan, G.G. Tepehan, Sol. Ener. Mater. And Sol Cells, 68, 355, (2001).
31. G.N. Glavee, R.D. Hunt, M. Paranthaman, Mat. Research Bulletin, 34-5, 817 (1999).
32. D. Keomany, J.P. Petit, D. Deroo, Sol. Energy Mater. Sol. Cells, 31, 171 (1993).
33. J.P. Gomilsek, K. Skofic, et al. Thin Solid Films, 446, 117 (2004).
34. Z. Crnjak Orel, I. Musevic, Nanostructured Materials, 12, 186 (1999).
35. Z. Crnjak Orel, Solid State Ionics, 116, 105 (1999).
36. Macros A. C. Berton, Cesar O. Avellaneda, Luis O. S. Bulhoes, Sol. Enet. Mater and Sol Cells, 80, 443 (2003).
37. Z. Lu, R. Hiskes, S.A. Dicarolis, A. Nel, R. K. Route, R.S. Feigelson, J. Crystal growth, 156, 227 (1995).
38. M. Pan, G. Y. Meng, H. W. Xin, C.S. Chen, D.K. Peng, Y.S.Lin, Thin Solid Films, 324, 89 (1998).
39. Minoru Inaba, A. Mineshige, S. Nakanishi, I. Nishimura, A Tasaka, K. Kikuchi, Z. Ogumi, Thin Solid Films, 323, 18 (1998).
40. John McAleese, John C. Plakatouras, Brian C. H. Steele, Thin Solid Films, 280, 152 (1996).
41. B. Eldrissi, M. Addou, M. Regragui, C. Monty, A. Bougrine, A. Kachouane, Thin Solid Films, 379, 23 (2000).
42. Shengyue Wang, Wei Wang, Q. Liu, M. Zhang, Y. Qian, Solid State Ionics, 133, 211 (2000).
43. Shengyue Wang, W. Wang, J. Zuo, Y. Qian, Mater Chem And Phys., 68, 246 (2001).
44. Shengyue Wang, Z. Qiao, W. Wang, Y. Qian, J. Alloys and Comp., 305, 121 (2000).

45. Andre Galembeck, Oswaldo L. Alves, Synthetic Metals, 84, 151 (1997).
46. Yanchun Zhou, Jay A. Switzer, J. of Alloys and Comp., 237, 1 (1996).
47. P. Stefanov, G. Atanasova, D. Stoyenev, T. Marinova, Surf. & Coat.Tech. 180-181, 446 (2004).
48. M. Balsubramanian, C. A. Melenders, A.N. Mansour, Thin Solid Films, 347, 178 (1999).
49. SumioIkegawa, Yuichi Motoi, Thin Solid Films, 281-282, 60 (1996).
50. D.R. Mullins, K.Z. Zhang, Surf. Sci., 513, 163 (2002).
51. D. R. Mullins, S.H.Overbury, Surf. Sci. Lett., 511, L293 (2002).
52. B. Jenewein, M.Fuchs, K. Hayek.Surf.Sci., 532-535, 364 (2003).
53. D.C. Sayle, T.X.T. Sayle, S.C. Parker, J.H.Harding, C.R.A.Catlow, Surf Sci, 334, 170 (1995).
54. Y. Jijima, M. Hosaka, N. Tanabe, N. Sadakata, T. Saitoh, O. Kohono, K. Takeda, J. Mater. Res., 12, 2913 (1997).
55. D.P. Norton, et al., Science, 274, 755 (1996).
56. N. Savvides, S.Gnanarajan, A.Katsaros, in, D.Dew-Hughes, R.G.ScurLock,J.H.P.Watson (Eds), ICEC 17, Institute Of Physics, Bristol, , p411 (1998).
57. X. Chui, F. A. List, D. M. Kroeger, A. Goyal, D. F. Lee, J. E. Mathis, E.D. Specht, P.M. Martin, R. Feenstra, D.T. Verebelyi, D.K. Christen, M. Paranthaman, Physica C, 316, 27 (1999).
58. N. Savvides, S. Gnanarajan, J. Herrmann, A. Thorley, A. Katsaros, A. Molodyk, Mater. Res. Soc. Symp. Proc., 616, 199 (2000).
59. S. Gnanarajan, A. Katsatos, N. Savvides, Appl. Phys. Lett, 70, 2816 (1997).
60. B.C. H. Steele, Nature, 400, 619 (1999).
61. J.vanHerle, D. Seneviratne, A.J. McEvoy, J. Eur. Ceram. Soc., 19, 837 (1999).
62. Y. Gao, G.S. Herman, S. Thevuthasan, W. Jing, D.e. McCready, S.A. Chambers, J. Vac. Sci. Technol. A, 17, 961 (1999).
63. Y. J. Kim, Y. Gao, G. S. Herman, S. Thevuthasan, W. Jiang, D.E. McCready, S.A.Chambers, J. Vac. Sci. Technol. A, 17, 926 (1999).
64. R. Wordensweber, J. Einfield, R. Kutzner, A.G. Zaitsev, M.A.Hein, T. Kaiser, G. Muller, IEEE Trans. Appl. Supercon., 9, 2486 (1999).
65. T. Inoue, T. Ohsuna, L.Luo, X.D.Wu, C.T. Maggiore, Y.Yamamoto, Y. Sakurai, J.H.Chang, Appl. Phys.Lett., 59, 3604 (1991).
66. L.Luo, X.D.Wu, R.C. Dye, R.E.Muenchausen, S.R.Folton, Y. Coulter, C.J.Maggiore, T. Inoue, Appl.Phys.Lett., 59, 3643 (1991).
67. W. Zhang, X. Wang, M. Elliot, I.W. Boyd, Phys. Rev. B., 58, 14143 (1998).
68. T. Hira, Y. Gujisaki, K. Nagashima, H. Koike, Y. Tarui, Jpn. J. Appl. Phys., 36, 5908 (1997).
69. Y-M. Wu, J-T Lo, Jpn. J. Appl. Phys., 37, 5645 (1998).

SYNTHESIS AND CHARACTERIZATION OF POLYPYRROLE THIN FILMS BY LABORATORY MADE AUTOMATIC SILAR METHOD

Ankita Yadav, Sonali Jamdade, Anjali Kumbhar, Akash Pasale and Shrikant Kokare *

Post-Graduate Department of Physics,

Raje Ramrao Mahavidyalay, Jath, Dist: Sangli 416404

*****Corresponding author E-mail: kshirikant@yahoo.com

ABSTRACT:

SILAR (Successive Ionic Layer Adsorption and Reaction): This method is simple, less expensive and less time consuming method for the deposition of binary semiconducting thin films. This method is a step-wise process of chemical deposition of thin films from aqueous precursors. Manual method is very difficult to handle and time consuming. In manual work some impurities may be added in aqueous solution and considerable amount of human errors are involved. We have designed an stepper motor controlled automatic SILAR method. With the help of control unit we can change dipping time, number of cycles to be repeated and speed of motor will be also controlled. The structural, optical and electrical properties we can studies by means of X-ray Diffraction (XRD), Fourier transforms infrared (FTIR) spectroscopy, Raman spectroscopy and UV-VIS spectrophotometer. Electrical resistivity measurements by four point probe method.

Keywords: Stepper motor controlled SILAR, Polypyrrole, Thin film, SEM, XRD, and FTIR etc.

INTRODUCTION:

In all above method the SILAR method it is simple, inexpensive & convenient for large area deposition. Manual depositions are very hectic job involving many human errors and it needs to be automated. The SILAR method is mainly based on the adsorption and reaction of the ions' from the solution & rinsing between every immersion with doubled distilled water to avoid homogenous perception in the solution. They are easy to prepare in the form of large area thin films and are capable of storing charge throughout good adhesives [1]. The Polypyrrole (ppy) is advantages of low oxidation potential of Pyrrole. Conducting polymers are being most popular due to its Interesting conducting properties, light weight and good environmental stability.[2] Among the conjugated polymers, polypyrrole (PPy) is the most representative one for its easy polymerization and wide application in gas sensors, electrochromic devices and batteries.

Conducting polymers can be prepared by using either chemical or electrochemical polymerization. The PPy thin films were deposited on the different substrate.[1,4]S A variety of applications towards technology of these conducting polymer materials has been proposed and demonstrated, viz. The present paper focuses on the synthesis, applications of Polypyrrole polymerization and characterization of composite thin films by X-ray Diffraction (XRD) Raman spectroscopy and UV-VIS spectrophotometer FT-IR spectroscopy, conductivity measurement. Electrical resistivity measurements by four point probe method

MATERIALS:

The SILAR method consist of two (or more than two) chemical baths one for ionic solution, second for cationic solution and third for rinsing. We have chosen Pyrrole solution of 0.1M dissolved in 50ml of 0.1M H_2SO_4 and it will be used as cationic Solution. 0.1M Ammonium per sulphate will be dissolved in 50ml of 0.1M Pyrrole and will be used as a Anionic solution. This will form the Polypyrrole thin films after various numbers of cycles of dipping. The dipping time and number cycles will be tailored to form the well uniform, thin and adhesive film on the glass substrate.

Polypyrrole (PPy) thin films were deposited by simple successive ionic layer adsorption and reaction (SILAR) method on glass substrate from aqueous solution. The growth of Polypyrrole thin films was carried out by the SILAR method at room temperature. The SILAR method consists of two (or more than two) chemical baths. Polypyrrole film will be prepared from the oxidation of 0.1 M solution of Pyrrole dissolve of 0.1M H_2SO_4 (First chemical bath) and 0.1 M Ammonium per sulphate (APS) dissolve of 0.1M Pyrrole (Second chemical bath). The 0.1M ammonium per sulphate of 0.1 M Pyrrole solution was used as a Anionic solution and 0.1M Pyrrole of 0.1 M H_2SO_4 solution was used as an cationic precursor.

One SILAR cycle consists of two steps: (1) adsorption of Pyrrole cations for 10s, (2) reaction with ammonium per sulphate precursor solution for 10s to form stable Polypyrrole. In order to prepare monomer free deposited film, after complete deposition, the deposited films are rinsing with double distilled water.

Reaction:

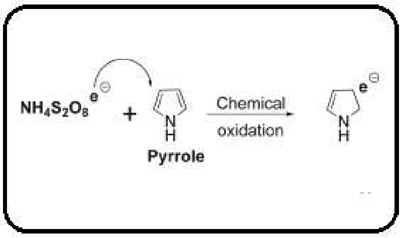

Anionic Reaction

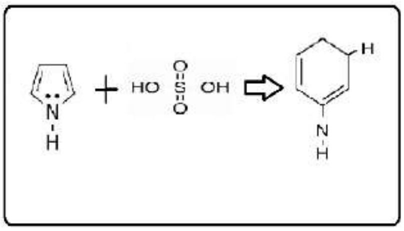

Cationic Reaction

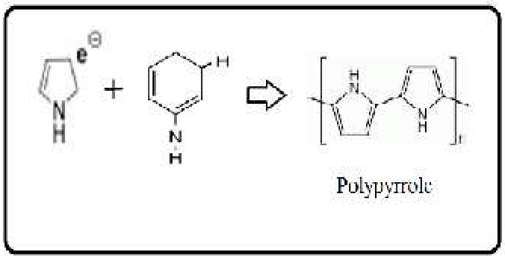

Polypyrrole

Experimental working of SILAR Set-Up:

A stepper motor is connected to axis of horizontally rod which, has fixed with pulley and belt mechanism as shown in figure. A sample holder is attached to the belt and allowed to move horizontally 16cm and move vertically 16cm over the track of beakers.

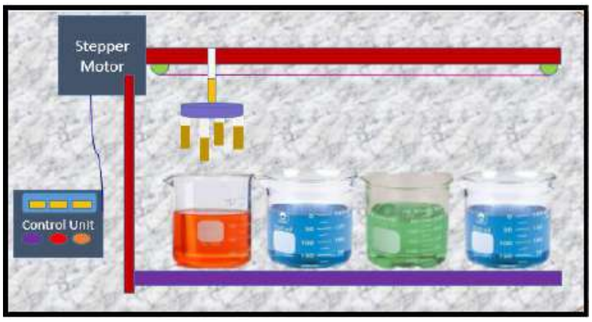

Schematic representation of the SILAR Method

Four stations are made and it has been filled with beakers of various solutions, each solution situated at 16cm distance from each other. After desired number of steps as chosen by the user, motor makes sample holder to move horizontally to reach at every station.

A every station stepper motor also move the sample holder vertically moves to 16cm upward and 16cm downward so that it will be dipped (defined by user), the sample holder will left itself and move further to reach the successive station this cycle of operation will continued till the defined number of cycle is completed. The maximum number of cycle that we can select is 1000 and time of dipping can be varied from few second to an hour. We have designed various types of samples holder which can holds two, four, six and eight substrate.

CONCLUSION:

SILAR Method is relatively simple, low cost and it has highly appropriate for large scale production. It deals with various thin film deposition methods and information about different characterization techniques. The deposition rate and thickness of the film can be easily controlled over range by changing deposition cycle. This instrument is of low cost and machine handling is so easy We can change the number of cycle from minimum to maximum range and also dipping time is varied from few second to an hours. The commercial available instrument in market has very high cost but in our laboratories made instrument is having a very low cost. These method consist of two (or more than two) chemical baths one for anionic solution, second for cationic solution and third for rinsing. The dipping time and number cycles will be tailored to form the uniform, thin and adhesive film on glass substrate.

REFERENCES:

1. S. Sakathivel and A. Boopathi, Synthesis Study of Polypyrrole Thin Films by Silar Method
2. Niwa, O., Tamamura T., J. Chem. Soc. Chem. Commum., 470: pp.817-818 (1934).
3. G.Han, G. Shi, Sensor. Actual. B-Chem.,113, 259 (2006).
4. Gadkari A.B., Bull. Mater. Sci., 29, 5 461-466 (2006).

TAILORING NANOSTRUCTURES OF MANGANESE OXIDE USING SURFACTANT (CTAB) AND ITS ELECTROCHEMICAL PERFORMANCE

A. M. Teli[1], S. Kamble[2], V. Burute[2], P. R. Jadhav[1], N. S. Harale[2],
D. S. Patil[3], S. A. Pawar[3], N. L. Tarwal[1] and P. S. Patil[1,2]
[1]Department of Physics, Shivaji University, Kolhapur
[2]School of nano-science and technology, Shivaji University, Kolhapur
[3]Department of Physics, Yeungnam University, Gyeongsan, Gyeonbuk 38541, South Korea

ABSTRACT:

The CATB assisted manganese oxide thin films were deposited by simple hydrothermal method. The structural and morphological of thin films were studied by different techniques including X-Ray diffraction and (XRD), Field Emission Scanning Electron Microscopy (FE-SEM). Electrochemical measurement was investigated by cyclic voltammetry (CV), galvanostatic charge-discharge (GCD), and electrochemical impedance spectroscopy (EIS). The maximum specific capacitance about 453F/g and energy density 62Wh/kg at 0.5mA/cm^2 current density observed for MnC10 samples.It is important to optimize concentration of surfactant (CTAB) during synthesis of thin films. These nanostructures play an important role for charge storage application.

INTRODUCTION:

The supercapacitors (SC) research has growing attention from both academia andindustry in recent years, with efforts focused on developingsafe, stable, high energy/power density, and low cost materials[1]. SCis a novel energy storage devices, with higher power density (10 kW/kg), shorter charge-discharge time (in seconds), and longer cycling life, as compared to the battery device[2]. Depend upon charge storage mechanism in SCs, the energy stored is either capacitive (non-faradaic)or pseudocapacitive (faradaic) in nature [3]. The electrode materials commonly used for SCs are metal oxides and conducting polymers [4]. Manganese oxide (MnO_2) is a promising semi-conductor material used as a SC application, due to its easy preparation, low cost, low toxicity and environment friendly in neutral aqueouselectrolyte [5]. The electrochemical properties of MnO_2 strongly depend on its particle size,morphology, crystalline structure and bulk density [6]. MnO_2 materials with various nanostructured morphologies were also investigated [7]. It is found that electrochemical performance of MnO_2 is improved by controlling nanostructures or morphologies.In this work, the surfactant (Cetyl trimethylammonium bromide) assisted manganese oxide thin films were prepared by simple hydrothermal method. The effect of change in concentration of surfaceactive molecule with a polar group on nanostructures of MnO_2 investigated and studies their electrochemical performance.

EXPERIMENTAL:

Synthesis:

The typical synthesis of CTAB assisted MnO_2 thin films given as, $KMnO_4$ used as precursor of Mn with concentration about 3mM dissolved in 20 mL double distilled water (DDW) with constant stirring. Initially, CTAB with concentration 2.5mM dissolve in 10mL DDW stirring for 20min.This CTAB solution mixed in Mn^{2+} solution and polished stainless steel (SS) substrate immersed in that solution. The beaker is put in autoclave for hydrothermal reaction at 90°C for 2hr. The blackish layer on SS substrate was observed. The sample is dried at room temperature and assign as MnC2.5.The above procedure repeated by keeping 3mM concentration $KMnO_4$for various concentration of CTAB with 5mM, 10mM and 15mM assigned as MnC5, MnC10 and MnC15 respectively.

RESULT AND DISCUSSION:

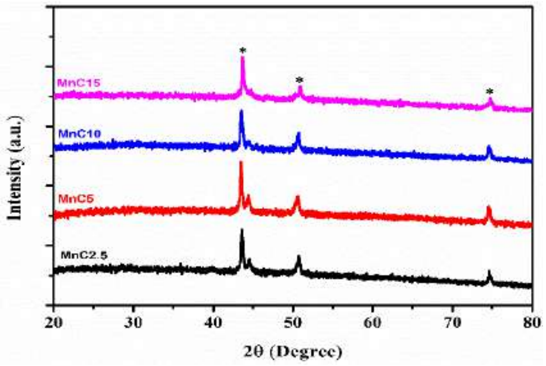

Fig.1: XRD patterns of CTAB assisted MnO_2 thin films

XRD:

Fig.1 shows the XRD patterns of CTAB assisted manganese oxide thin films prepared by hydrothermal method. The peaks at 43.5, 44.48, 50.7 and 74.6° marked with '*' attributed to SS substrate. No any peak, except SS peaks observed, indicates an amorphous nature of thin film. For further confirmation of material FT-IR is used.

Fourier Transform-Infrared spectroscopy:

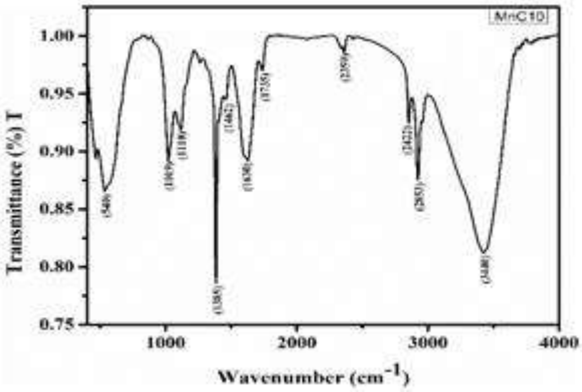

Fig. 2: FT-IR of MnC10 thin film

The FT-IR spectra of MnC10 thin films shown in Figure 2. The region below and above 1400 cm^{-1} contains peaks due to octahedral $MnO_6$and OH vibrations respectively [8]. The absorption peaks from 750–450 cm^{-1} correspond to the Mn–O stretching and bending vibrations. The appeared C–O bonds in various chemical conditions have been shown in between 1300–950 cm^{-1} wavenumber range [9].

The presence of broad band at 3440 cm^{-1} and the weak band at 1630 cm^{-1} indicates, stretching and bending vibration of O–H groupin the adsorbed water molecules. [10][11]. The coordination of Mn by the O–H correspond peaks at 1385 and 1110 cm^{-1}. The peaks at 480 and 540 cm^{-1} are absorption bands corresponding to Mn–O stretching modes of the octahedral layers in the birnessite structure[12]. We concluded that, the prepared amorphous thin films were in good agreement with birnessite MnO_2.

Scaing electron microscopy:

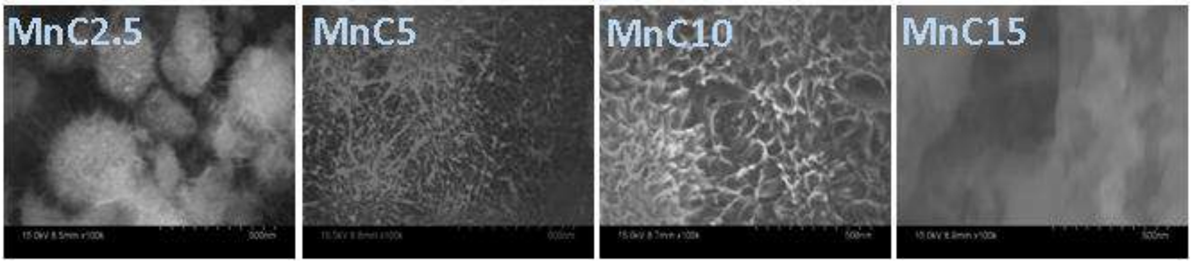

Fig.3. FESEM morphology of all CTAB assisted MnO_2 thin films at 100K

Figure 3 shows surface morphology of CTAB assisted MnO_2 thin films. The FESEM taken at 100K magnification with 15kV applied potential. It is observed that at lower concentration (MnC2.5) the nano-spheres with small thorns like structure were observed. As concentration of CTAB increases (MnC5) the sphere structure disturbs and thrones nanostructures were spreads. At MnC10 the thrones nanostructures modified into sea grass like structure, with high porous structure. If again increase in concentration of CTAB (MnC15) the nanostructures disturbs and agglomerated shown in figure 3D.The MnC10 sample shows sea grass like nanostructures with highly porous nature, and 2D nanostructure which is beneficial for charge storage application.

Cyclic voltammogram (CV):

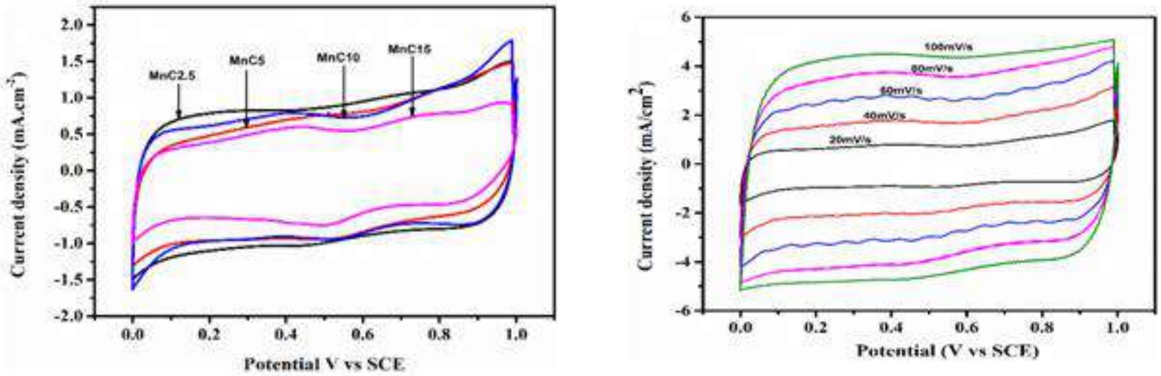

Fig. 4. CV of A) all CTAB assisted MnO_2 samples at 20mV/s

B) MnC10 at 20-100mV/s in 1M aq.Na_2SO_4

Figure 4A shows CV of the CTAB assisted all MnO_2 thin films. All thin films were cycled in an aqueous 1M Na_2SO_4 electrolyte at 20mV/s scan rate over the potential range 0 to 1.0 V. MnO_2 thin films shows the oxidation/reduction of Mn^{3+}/Mn^{4+} ions in the oxide can take place reversibly [13]. The CV curves of all CTAB assisted MnO_2exhibits a rectangular CV curve with no distinct redox peaks, which corresponds to a typical pseudocapacitive behavior, where the current flow is independent of the electrode potential [14].Figure 4B shows, the CV curves of the MnC10 thin film at various scan rates (from 20-100mV/s) to get more information about rate capabilities.The MnC10 sample shows rectangular shapes and mirror-image reveal the ideal pseudocapacitive behavior of the sample.

Galvanstatic charge-discharge (GCD):

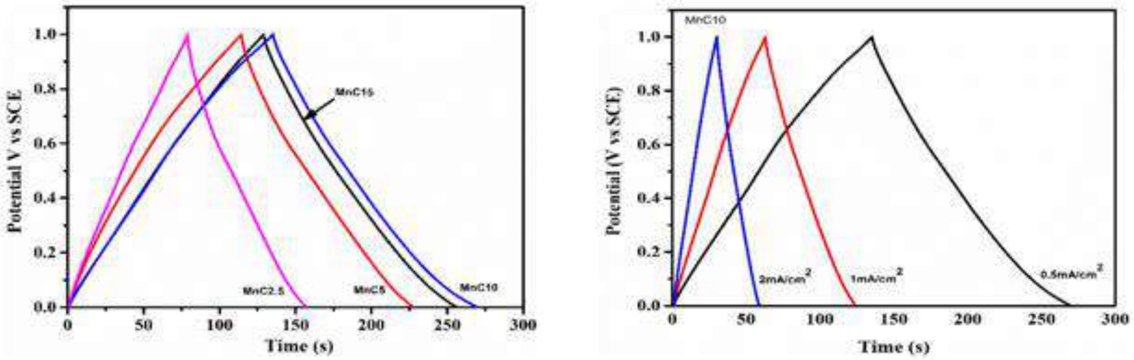

Fig. 5.GCD of A) all CTAB assisted MnO_2 samples at $0.5mA/cm^2$ **B) MnC10 at 0.5,1& $2mA/cm^2$ in 1M aq.Na_2SO_4**

GCD of all CTAB assisted MnO2 samples were recorded between 0-1.0 V vs SCE in 1M aq.Na_2SO_4 at $0.5mA/cm^2$ current density shown in Figure 5A. All curves exhibited an almost triangle shape indicating the good efficiency of the charge-discharge process.The samples shows linear relation between potential and time during charging and discharging cycles, which again confirms capacitive behavior of the materials in addition to exhibiting rectangular voltammograms. The Specific capacitance (Csp), energy density (E.D.) of CTAB assisted MnO_2 thin films were calculated by following equations[15],

$$Csp = \frac{I \times dV}{T_d \times m} \ldots\ldots\ldots\ldots\ldots\ldots (1) \quad E.D. = \frac{1}{2} Csp \times V^2 \ldots\ldots\ldots\ldots\ldots\ldots (2)$$

Where,

I is applied current density, dV is potential range, T_d is time required to discharge the cell, m is deposited weight of the material, Csp specific capacitance, V potential.

The highest specific capacitance about 453F/g and energy density 62.9Wh/kg were obtained. The specific capacitance along with discharge current, discharge time and energy density of all CTAB assisted MnO_2 samples mentioned in table1. To get information about cyclic capability the galvanostatic charge-discharge carried out at various current density (0.5, 1 and $2mA/cm^2$).

Table 1:

Sample code	Current density (mA/cm^2)	Discharge time (T_d)	Potential (dV) (V vs SCE)	Specific capacitance (C_{sp})	ED (Wh/kg)
	0. 5	114	1	285	39.5
MnC5	0. 5	127	1	317.5	44.0
MnC10	**0. 5**	**136**	**1**	**453.3**	**62.9**
MnC15	0. 5	78	1	260	36.1

The sample shows triangular nature of GCD curve for all current densities, which indicates good rate capability of the sample. It is well known that, specific capacitance was decreasedwith increasing the current density (figure 5B) [37].The increase in specific capacitance due to development of sea grass like nanostructure, which gives high surface area and porosity. The ions from electrolyte are easily trapped into the porous structure which increases storage of charges.

Electrochemical impedance spectroscopy (EIS):

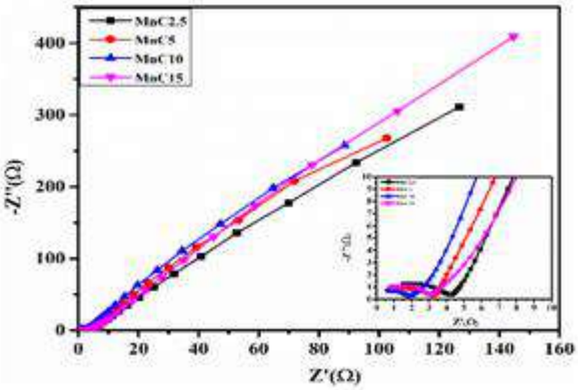

Fig. 6:
EIS of all CTAB assisted MnO_2 samples at 10mV potential

For more investigating, an alternating current (AC) impedance measurements were performed shown in figure 6.The Electrochemical measurement were carried out in three electrode system in 1M aqueous Na_2SO_4 electrolyte at 10mV potential in between frequency range from 1 kHz to 1Hz. The CTAB assisted MnO_2 samples demonstrates a semicircle in high frequency and a linear curve in the low-frequency region inset of figure 6.The semicircle in the high-frequency region is related to reaction kinetics and linear curve at the low-frequency region can be attributed to diffusion controlled process at the electrode-electrolyte interfaces.The table 2 indicates, sample codes along with series (Rs) resistance and charge transfer resistance (Rct)of the CTAB assisted MnO_2 samples. The sample MnC10 have low series resistance (0.5Ω) and charge transfer resistance (1.3Ω).It observed that, the sea grass like nanostructured sample give ease of electron transfer minimizes series and charge transfer resistance, which attribute to improvement in conductivity in sample.

CONCLUSIONS:

The CTAB assisted MnO_2 thin film electrodes were successfully synthesized by simple hydrothermal method and applied to electrochemical measurements. Surface morphology varies from sphere with thrones, separation of thrones and sea grass like nanostructures with concentration of CTAB in MnO_2. The MnC10electrode exhibited good specific capacitance (453 F/g), high energy density (62.9Wh/kg) at 0.5mA/cm^2in 1M aq. Na_2SO_4 electrolyte. The sea grass like structures exhibit high surface with highly porous nano-structures important for charge storage application.

ACKNOWLEDGMENT:

All authors are thankful to PIFC Department of Physics, Shivaji University, Kolhapur for providing the instrumental facility.

REFERENCES:

1. M. Winter and R. J. Brodd, Chem. Rev., vol. 104, no. 10, pp. 4245–4269 (2004).
2. C. Liu, F. Li, L.-P. Ma, and H.-M. Cheng,Adv. Mater., vol. 22, no. 8, pp. E28–E62 (2010).
3. B. E. Conway, Kluwer acadamic/ plenum publisher (1999).
4. G. Yu et al., Nano Lett., vol. 11, no. 10, pp. 4438–4442 (2011).
5. Y. U. Jeong and A. Manthiram, J. Electrochem. Soc., vol. 149, no. 11, p. A1419 (2002).
6. Y. Yang and C. Huang, J. Solid State Electrochem., vol. 14, no. 7, pp. 1293–1301 (2010).
7. D. P. Dubal, D. S. Dhawale, R. R. Salunkhe, and C. D. Lokhande, J. Alloys Compd., vol. 496, no. 1–2, pp. 370–375 (2010).
8. M. Minakshi, P. Singh, T. B. Issa, S. Thurgate, and R. De Marco, J. Power Sources, vol. 138, no. 1–2, pp. 319–322 (2004).
9. C. Luo, R. Wei, D. Guo, S. Zhang, and S. Yan, Chem. Eng. J., vol. 225, pp. 406–415 (2013).
10. X. Xie and L. Gao, Carbon N. Y., vol. 45, no. 12, pp. 2365–2373 (2007).
11. A. Yuan and Q. Zhang, Electrochem. commun., vol. 8, no. 7, pp. 1173–1178 (2006).
12. E. Using, M. O. Diatomite, S. J. Allen, and M. N. M. Ahmad, vol. 76, no. 7, pp. 2655–2663 (2016).
13. M. Toupin, T. Brousse, and D. Belanger, Chem. Mater., vol. 14, no. 9, pp 3946–3952 (2002).
14. M. Nakayama, A. Tanaka, Y. Sato, T. Tonosaki, and K. Ogura, Langmuir, vol. 21, no. 13, pp. 5907–5913 (2005).
15. A. M. Teli et al., Sustain. Energy Fuels, vol. 1, no. 2, pp. 377–386 (2017).

SYNTHESIS, CHARACTERIZATION AND EFFECT OF COBALT SUBSTITUTION ON PROPERTIES OF MG FERRITES

B. N. Kokare[1], M. K. Sakate[1] and S. D. Jadhav[2]*
[1]Smt. Meenalben Mehta College, Panchgani
*[2]Yashawantrao Chavan College of Science, Karad
*Corresponding Author E-mail: sdjchemsuk@gmail.com

ABSTRACT:

Cobalt substituted magnesium ferrites having stoichiometric composition $Mg_{1-x}CO_x\ Fe_2O_4$ with x ranging from 0.0 to 1.0 were prepared by co- precipitation method. X-ray diffraction was used to characterize the structure and phases present respectively. It was found that of all ferrite compositions at 900°C led to cubes of the ferrite grains and there was single phase spinel structure. The X-ray diffraction patterns revealed the presence of (311) peak as the most intense one. The crystallite size was found to be within the range of 21-48 nm. Activation energy of resultant samples decreases from 0.45 ± 0.02 eV ($x = 0.0$) to 0.35 ± 0.02 eV ($x = 1.0$). The saturation magnetization values showed increasing trend with increase cobalt content from 2.37 to 30.70 emu/g.

Keywords: Ferrites, Chemical Synthesis, X-ray Diffraction, Scanning Electron Micrograph, D.C. electrical resistivity and magnetic hysteresis loops.

INTRODUCTION:

Studies of spinel ferrites are highly relevant to modern technologies, so the synthesis and sintering of ferrites have become an important part of modern research [1-3].Polycrystalline spinel ferrites are most important materials due to their interesting electrical properties i.e. low eddy current and dielectric losses. These spinel ferrites find applications in a wide range of frequencies extending from microwave to radio [4]. These are also applicable in many magnetic devices. The order of magnitude of conductivity greatly influences the dielectric and magnetic behavior of the ferrites and depends on the type of preparative method. Structural and magnetic properties of spinel ferrites depend upon the method of preparation, nature of dopant and dopant concentration [6]. The properties of spinel ferrites are strongly dependent on the distribution of the different cations among tetrahedral (A) and octahedral (B) sites [7]. The cation distribution in magnesium ferrite has been studied by various authors and was found to be strongly temperature dependent [8]. Mg-Co ferrite was prepared by the coprecipitation method. In chemical method of preparation particles with desired physical properties, chemical properties and composition flexibility are achieved. Also, it allows a good control on size and shape distribution during synthesis. Due to this co-precipitation method is widely used for preparation of ferrites.

EXPERIMENTAL:

The different compositions of the system have been synthesized by using high purity sulphates of Co^{2+},Mg^{+2} and Fe^{3+} in proper stichometric proportions by a co-precipitation technique using 10 % NaOH at a pH of 9-9.5.The hydroxides were oxidized using 30% H_2O_2 . The precipitates were digested on water bath for 2 hours, filtered and washed with double distilled water to free them from excess alkali and $SO_4^{- -}$ ions. The compounds were oven dried and calcinated at 900oC for 4 hours. [9].

X- ray powders diffraction patterns were recorded on a diffractometer (Philips PW 1730) with microprocessor controller, using nickel filtered CuKα radiation (λ = 1.5428 $\mathring{A}$) [10].

RESULTS AND DISCUSSION:

The XRD data of these ferrite samples agreed very closely with the standard values given in the JCPDS Data Cards, (MgFe2O4-73-2410 and CoFe2O4-22-1086) thus confirming the spinel phase Fig.1.

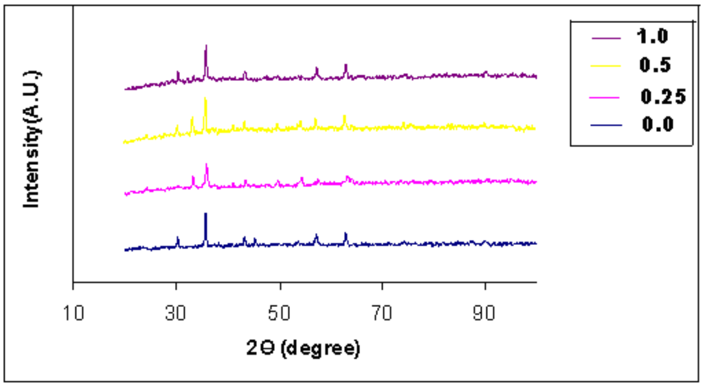

Fig. 1: XRD patterns ofMg$_{1-x}$CO$_x$ Fe$_2$O$_4$ ferrites (0.0 ≥X1.0)

The phase identification of the final products of the various compositions of Mg$_{1-x}$CO$_x$ Fe$_2$O$_4$ oxides were made on Philips PW 1710 with Cu Kα radiation (λ=1.5405A^o) [11]. The X-ray diffraction patterns of the investigated mixed Mg-Co ferrite revealed that all the samples had a single phase cubic structure. Lattice parameters varied between 8.33 and 8.36°A with increasing Co content. This increase may be related to the replacement of Mg^{2+} ion (0.065nm) with larger Co^{2+} ion with ionic radius (0.074 nm). Average particle size was determined from the broadening of X-ray diffraction peaks using the Scherrer equation and found to be in the range 24 to 48nm.(Table no.1)[12]. The morphological features were observed with a scanning electron microscope (SEM: model JEOL-JSM 6360).The scanning electron micrographs of all samples are shown in fig.2. The grain size was calculated from SEM micrographs the average grain size was found to be 50 nm [13]. It appears that increase in the grain size with temperature and because increase in Co content.

Table1: Lattice constant, X-ray density and particle size for $Mg_{1-x}CO_x Fe_2O_4$

Composition constant (x)	Lattice energy (a)	Activation size (eV)	Particle (nm)
0.0	8.332	0.45	24
0.25	8.346	0.25	29
0.50	8.359	0.34	38
0.75	8.364	0.45	41
1.0	8.348	0.35	48

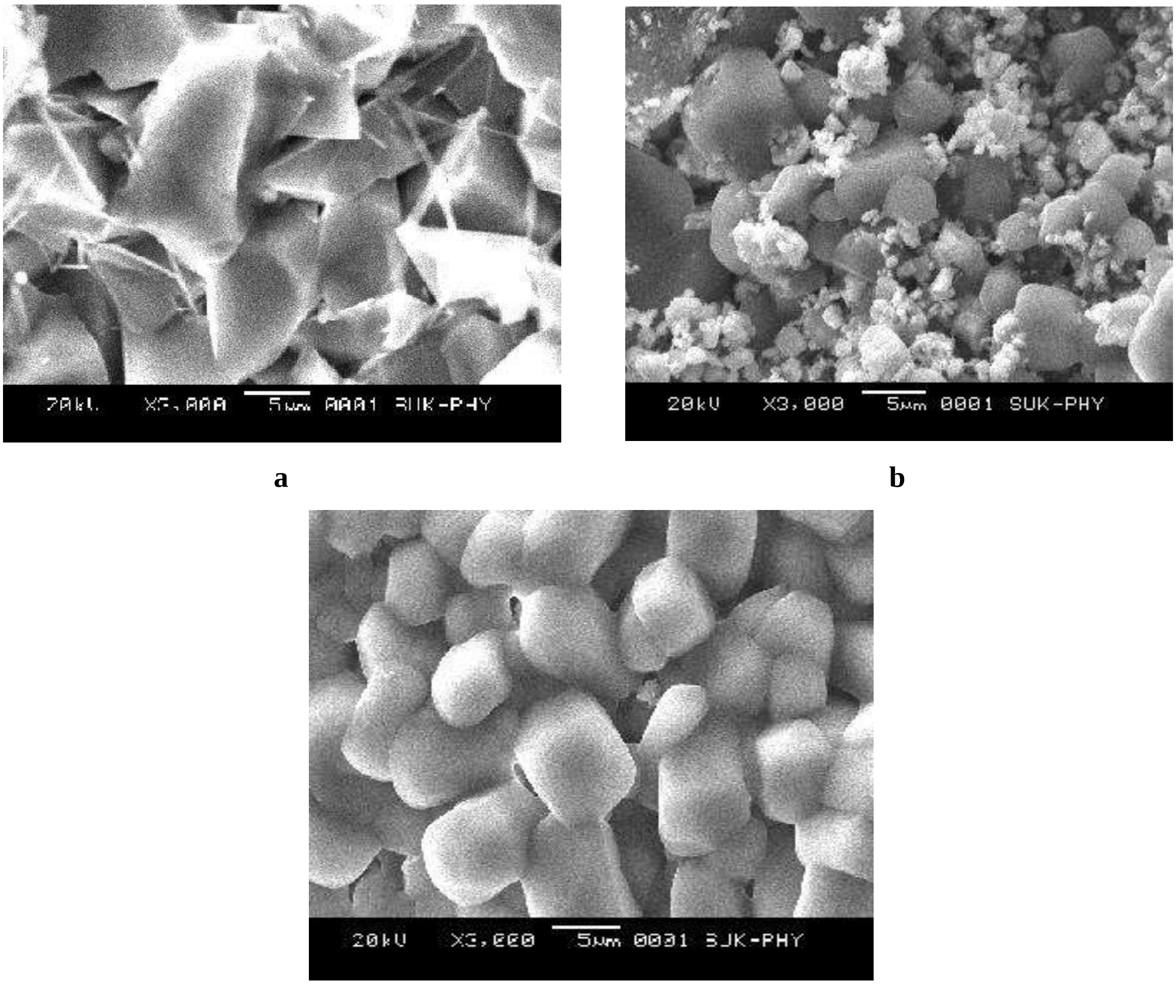

a b

c

Fig.2: SEM micrographs of the $Mg_{-x}CO_x Fe_2O_4$ ferrites (a) 0.0 (b) 0.5 (c) 1.0

The electrical properties indicated that resistivity decreases with increase in temperature obeying Willson's law.

$\rho = \rho o \exp (\Delta E/KT)$ -------------------- (1)

where, ΔE = Activation energy, K = Boltzmann constant & T = Absolute temperature. The variation of resistivity (ρ) as a function of temperature (10^3/T) is shown in Fig.3. [14-15].

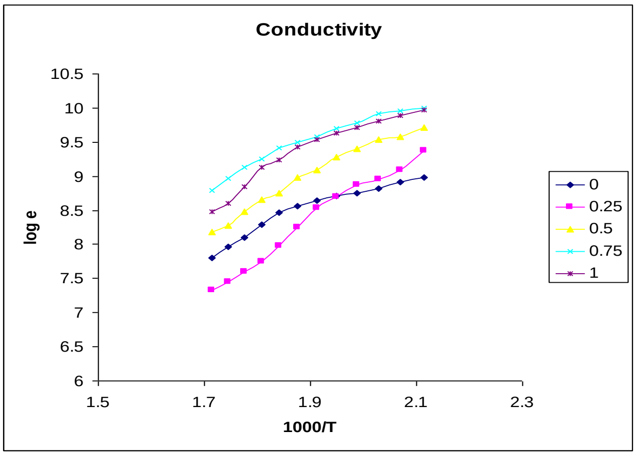

Fig.3: Log ρ versus 1000/T for samples of the $Mg_{1-x}CO_x$ Fe_2O_4 system (0.0 ≥X1.0)

The activation energies are calculated from the slopes, from these values it is evident that the lower activation energy in the ferromagnetic region is attributed to the phase transition or impurity phases, while the change in activation energy is attributed to the change in conduction mechanism [16].The change in activation energy for different compositions is attributed to the hoping of electrons. [17].The addition of cobalt replaces Fe^{3+} ions from B site which intern replaces Mg^{2+} ions in A site. (Table1). An increasing Co content (at A- site) the Mg ion concentration (at B- site) will decrease. This will leads to the migration of Fe^{3+} ions from A to B sites to substitute the reduction in Mg ion concentration at B site (which is responsible for electrical conduction in ferrite) increases. Consequently (ρ) decreases with increase in Co content .Another resion for decreases in (ρ) on increase in Co ion substitution is that Co is less resistive than Mg.The decrease in resistivity with temperature is due to the increase in drift mobility of the charge carriers. Also, conduction in ferrite is attributed to hopping of electrons from Fe^{3+} to Fe^{2+} ions [18]. The number of such ion pairs depends upon the sintering conditions and amount of reduction of Fe^{3+} to Fe^{2+} at elevated temperatures. The resistivity of ferrite is controlled by the Fe^{2+} concentration on the B-site [19].

The hysteresis loops of the system $Mg_{1-x}CO_x$ Fe_2O_4 are shown in Fig.4. It is further observed that all the samples show ferrimagnetic nature. The coericivity of the samples is found to increases from 420 to 1172Oe as the cobalt content increases. The saturation magnetization of the samples increases with increase in cobalt concentration from 2.37 to 30.70 emu/g (Table No.2). The calculated and observed magnetic moments show increasing in trend as cobalt content increases (Table No.1). The variation in calculated and observed magnetic moments is quite predominant. From magnetic moment calculations, it can be said that simple Neel model does not hold good for such compounds [20].

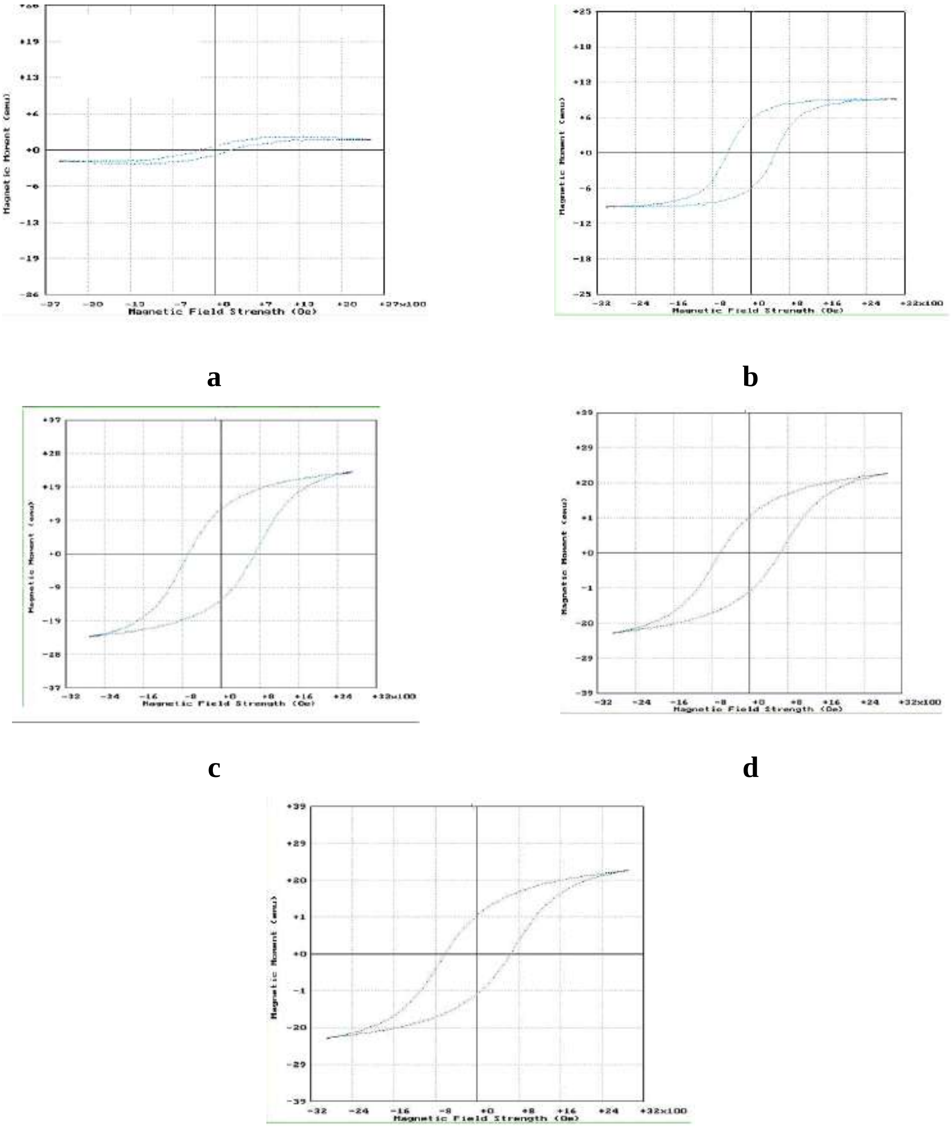

a

b

c

d

e

Fig. 4: Magnetic Hystereses of the $Mg_{1-x}Co_xFe_2O_4$ System $Mg_{1-x}CO_x$ Fe_2O_4

Table 2: Magnetic Hystereses of the $Mg_{1-x}Co_xFe_2O_4$ System

Compound	Saturation Magnetization at 300K (Ms)	Magnetic moment (nB)		Coercive Force (Hc) (Oe)	Remanent magnetization (Mr)
		Cal	obs		
$MgFe_2O_4$	2.37	1.5	0.08	420	0.40
$Mg_{0.75}Co_{0.25}Fe_2O_4$	11.42	-	0.42	1103	0.57
$Mg_{0.5}Co_{0.5}Fe_2O_4$	21.00	-	0.81	1115	0.29
$Mg_{0.25}Co_{0.75}Fe_2O_4$	30.10	-	1.21	1683	0.30
$CoFe_2O_4$	37.70	1.43	1.58	1772	0.42

The lower observed value of M_B are due to different types of magnetic exchange interactions taking place between cations of tetrahedral and octahedral sirtes.Further variation in coercive field and saturation magnetisation may be due to surface spin disorder leading to broken exchange bonds, high anisotropy layer and loss of long range order as particle size increases.

CONCLUSION:

The ferrites $Mg_{1-x}CO_x Fe_2O_4$ have been synthesized by taking components of A. R, quality in appropriate molar proportions. The spinel structure was confirmed by X-ray diffraction. The size of the particles was determined from the broadening of X-ray diffraction peaks. SEM was no very good agreement with each other indicating that there was no agglomeration and that the size distribution of the prepared particles is uniform. The SEM showed that the particles synthesized by co-precipitation technique posses much smaller size as compared to sol-gel or ceramic technique. Magnetic hystersis indicated that all the samples are ferrimagnetic and saturated magnetization increases with increase inCo^{2+} concentration. The mismatch between observed and calculated magnetic moment indicates that Neel's model is not obeyed in Mg-Co ferrites. The conductivity graph shows that resistivity decreases with increasing in temperature, indicating that the samples are semiconducting in nature.

REFERANCES:

1. R. A. McCurrie, Ferromagnetic materials, Academic press, London (1994).
2. Londolt Bornstan, Magnetic oxides and related compounds, Springer, Vol. 314 B (1970).
3. Jan Smit, Magnetic properties of materials, MacGraw Hill, New York, p.20 (1971).
4. S. K. Date, P. A. Joy, P. S. Anil Kumar, B. Sahoo, Keune, Phys. Stat. Sol. (c) 1, 12, 3495–3498 (2004).
5. Virden, A. E. K. O'Grady. J. Magn Mater. 868-870; 290-291 (2005).
6. S. Verma, P. A. Joy, Y. B. Khollam, H. S. Potdar, S. B. Deshpande. Mater Lett. 58, 6, 092-5 (2004).
7. S.K. Pradhan, S. Bidb, M. Gateshki and V. Petkov Materials Chemistry and Physics 93, 224–230 (2005).
8. D. Zhao, X. Wu, H. Guan, E. Han j. Supercritical fluids.42, 226 -233 (2007).
9. P.P. Hankare, V.T. Vader, N.M. Patil, S.D. Jadhav, U.B. Sankpal, M.R. Kadam, B.K. Chougule, N.S. Gajbhiye, Materials Chemistry and Physics, (In Press) (2008).
10. Tsushiokita, F. Saito, S. Sasaki, T. Toyoda, and H. Koinuma, Jpn. J. Appl. Phys., 37, 3441 (1998).
11. V. N. Mulay, K. Bhopal Reddy, V. Devender Reddy, and P. Venugopal Reddy, Phys. Stat. Sol. (a), 130, 397(1992).
12. O. Suwalka, R. K. Sharma, V. Lakshmi, N. Lakshami and K. Venugopalan. J. Mag. and Magnetic Mat. 313, 198-203 (2007).

13. P. P. Hankare, S. D. Jadhav, V.T. Vader, K. J. Waghmare and B. K. Chougule. Alloys and Compounds Article(In Press.)
14. M. A. Ahmed, Phys Stat Sol A. 111, 567-72 (1989).
15. N. Z. Darwish, O.M. Hemeda, Abd El-Ati MI. Appl. Radiat Isot. 45 (4) 45-8.15. JCPDS
16. D. Bahadur, J Giri, B.B Nayak, T. Srihasha, P. Pradhan, N. K .Prasad, K .C. Barick and R. D. Ambasta J. Phys., Vol. 65, 4, (2005).
17. M.H. Khedr, A.A. Omar, S.A. Abdel-Moaty Colloids and Surfaces A: Physicochemical and Engineering Aspects, Vol. 281, Issues 1-3, 15, 8-14 (2006).
18. Hassain, A. A. K. M. Mahmud, S. T.Saki, M. Kawai, H.Tabata, J.of Magnetisum and magnetic Materials 312, 210-219 (2007).
19. Wei-Chih Hsu, S. C. Chen, P. C.Kuo, C.T. Lie and W.S. Tsai, Mat. Sci. and Engg. B111, 142-149 (2004).
20. D. Ravinder, and B. Ravikumar, Mater. Lett. Vol. 57, 4471–4473 (2003).

EQCM STUDY OF ELECTRODEPOSITED MANGANESE OXIDE

N. P. Jadhav[1, 2], P. R. Jadhav[1, 3], P. S. Patil[1] and A. K. Bhosale[2]*
[1]Thin Film Materials Laboratory, Department of Physics,
Shivaji University, Kolhapur, M.S., INDIA 416004
[2]Post-Graduate Department of Physics,
Raje Ramrao Mahavidyalaya, Jath, Dist. Sangali, 416404
[3]Post-Graduate Department of Physics,
Devchand College, Arjunnagar, Via - Nipani, Tal.-Kagal, Dist.Kolhapur, 591269
*Corresponding Author E-mail: akbhosale1@gmail.com

ABSTRACT:

The influence of precursor concentration on the deposition of manganese oxide electrodeposition from a potassium hydroxide contained solution was investigated by electrochemical quartz crystal microbalance (EQCM). The EQCM data were represented as plots Δm versus E, known as massograms. Because massograms are not affected by interference from the hydrogen evolution reaction, they clearly show the manganese reduction and oxidation processes. By comparing the voltammograms with their corresponding massograms, it was possible to differentiate mass changes due to faradaic processes from those due to non-faradaic processes.

INTRODUCTION:

Manganese oxides in various forms have been widely studied for various potential applications [1]. In spite of potential application in various application, less research work has been done on mechanism of electrodeposited manganese oxide [2]. The study of electrodeposition mechanism of manganese oxide is very complicated due to Mn (II) transformation to form Mn(IV)O_2 involving many electrochemical steps [3]. In this study, we used EQCM technique to investigate possible electron transformation and deposited mass.

EXPERIMENTAL:

All chemicals used as received without purification. The EQCM measurements were performed on a gold electrode of area 0.205 cm^2 in a specially designed three electrode electrochemical cell comprising gold electrode as a working electrode, platinum as counter electrode and saturated calomel electrode (SCE) as reference electrode. EQCM study were done at the potential window between -1.0 V to + 1.4V at various concentration of $MnSO_4$ at pH ~ 6.5.

RESULT AND DISCUSSION:

The EQCM experiment relies on the calculation of mass change (Δm) at the quartz crystal using measured frequency change (Δf) (Sauerbrey equation) [4]:

$$\Delta f = \frac{-2 f_0^{\ 2}}{A\sqrt{\mu\rho}} \Delta m \text{--------------(1)}$$

where f_0 is the resonant frequency of the fundamental mode of the crystal, A the area of the gold disk coated onto the crystal 0.205 cm^2 for given crystal), ρ the density of the crystal and μ the shear modulus of quartz. An EQCM study were done in the potential range -1.0 V to + 1.4 V vs SCE at pH 6.5 for all concentration. pH were adjusted using 0.1 M NaOH solution. As a concentration of $MnSO_4$ solution increases from 0.01M to 0.2M the mass loaded on gold working electrode at potential 0.89 V vs. SCE were increases from 3.74 μg to 6.07 μg, which indicate that, at higher concentration of $MnSO_4$ the maximum mass was loaded at potential 0.89 V.

Electrochemical Deposition:

Anodic electrodeposition involves oriented diffusion of charged reactive species through an electrolyte when an electric field is applied, and oxidation of the charged species on the deposition surface that also serves as an electrode. For the anodic electrodeposition of thin film MnO_2, the electro-oxidation of Mn(II) species occurs on the anode surfaces.

The electrochemical deposition of manganese oxide on an inert electrode in an electrolyte containing Mn^{2+} ions occurs following the reaction [5].

$Mn^{2+} + 2H_2O \rightarrow MnO_2 + 4H^+ + 2e^-$ Reaction 1

This reaction occurs in a single step for the following reasons: (i) the oxidation state of manganese increases from 2+ to 4+, and it is improbable that the two electrons are transferred in a single step and (ii) for the formation of MnO_2, oxidation of water molecule must occur concomitantly with the oxidation of Mn^{2+}. It is most probable that the overall Reaction 1 occurs in a sequence of simple reaction steps.

An examination of Reaction1 suggests that Mn^{2+} ions oxidize to Mn^{4+} with simultaneous oxidation of H_2O molecules. The two electron transfer process involving oxidation of Mn^{2+} to Mn^{4+}, accompanied by the oxidation of H_2O cannot occur in a single step. Hence, the following multistep mechanism is envisaged for the anodic deposition of MnO_2.

Step1 $Mn^{2+}_{bulk} \rightarrow Mn^{2+}_{surface}$

The diffusion of Mn^{2+} ion from bulk (electrolyte) to the electrode surface is shown in step1 above.

Step2 $Mn^{2+}_{surface} \rightarrow Mn^{3+}_{ads} + e^-$

Oxidation of Mn^{2+} at the electrode surface to Mn^{3+}_{ads} is the most probable single electron transfer step. Mn^{3+}_{ads} ions formed in the step2 are unstable.

Step3 $H_2O \rightarrow OH_{ads} + H^+ + e^-$

Oxidation of H_2O is considered as another single electron transfer process, producing adsorbed OH radicals

Step4 $2Mn^{3+}_{ads} \rightarrow Mn^{2+}_{ads} + Mn^{4+}_{ads}$

Reformation of the Mn^{2+} at the electrode surface in the adsorbed state.

Step5 $Mn^{2+}_{ads} + 2OH_{ads} \rightarrow MnO_2 + 2H^+$

Step6 $Mn^{4+}_{ads} + 2H_2O \rightarrow MnO_2 + 4H^+$

Which is shown in step 2. In the step 3above, oxidation of H_2O is considered as another single electron transfer process, producing adsorbed OH radicals.

CONCLUSION:

Synthesis of manganese oxide seen successfully at various precursor concentrations. EQCM study confirms that the electrodeposition of manganese oxide occurred at 0.89 V vs SCE. Electrochemical reaction from manganese precursor solution to manganese oxide contains transformation of two electrons and does not occur in a single step. Here, we proposed two electron transfer reaction step by step.

REFERENCES:

1. Sang-Bok Ma, Kyung-Wan Nam, Won-Sub Yoon, Xiao-Qing Yang, Kyun-Young Ahn, Ki-Hwan Oh, Kwang-Bum Kim, J. Power Sources, 178, 483 (2008).
2. Shalini Rodrigues, A. K. Shukla, N. Munichandraiah, J. Appl. Electrochem., 28, 1235 (1998).
3. M.Ghaemi, L.Binder, J. Power Sources, 111, 248 (2002).
4. A.C.Sonavane, A.I.Inamdar, P.S.Shinde, H.P.Deshmukh, R.S.Patil, P.S.Patil, J. Alloys Compd., 489, 667 (2010).
5. P.R. Jadhav, M.P. Suryawanshi, D.S. Dalavi, D.S. Patil, E.A. Jo, S.S. Kolekar, A.A.Wali, M.M. Karanjkar, J.H. Kim, P.S. Patil, Electrochim. Acta, 176, 523 (2015).

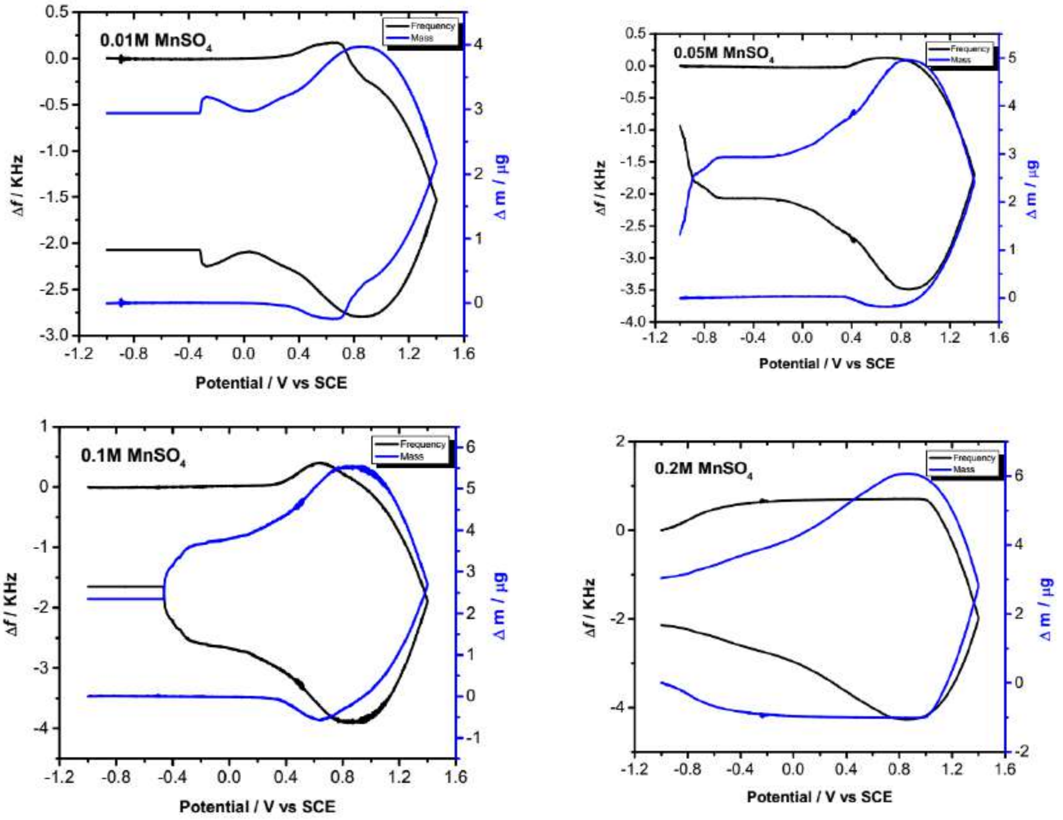

Fig. 1: The EQCM study at (a) 0.01 M (b) 0.05M (c) 0.1M and (d) 0.2 M $MnSO_4$ precursor

SELECTION OF NESTING SITE AND NEST MATERIAL OF *PYCNONOTUS CAFER* (RED VENTED BULBUL) NEAR BIRNAL RESERVIOR, JATH, DIST-SANGLI (M.H.) INDIA

[1]S. B. Deshmukh* and M. Y. Kulkarni

[1]Science Mahavidayalaya, Nanded

[2]N.S.B.College, Nanded

*Corresponding author E-mail: apurvak49@gmail.com

ABSTRACT:

Pycnonotus cafer breeding season is from June to September, around 2-3m (6.6 -9.8 ft) they construct the nest .They build the nest in a hole in mud bank, occasionally inside house ,on tree twigs .The nesting tree twigs and nesting material was identified of various groups such as *citrus limon, Acacia arabica, Azadirachta indica*, smaller shrubs and trees .The material was observed and identified such as feather of birds ,cotton, cloth threads, insect part such as grasshopper body part, larvae part in nest cavity.

Keywords: Nest, Nesting material, Threads, Nest cavity, larvae

INTRODUCTION:

Birds plays important role in ecosystem as pollinators, scavengers and pest-insect controllers. The family Pycnonotidae (bulbul) is a large group of passerienes comprising 138 species and 355 taxa, widespread in southern Asia, Africa, Madagascar and islands of the western Indian Ocean (7). Five species are recorded to occur in Pakistan (3), the red vented bulbul being one.

Birds build variety of nest for protecting themselves from rain ; high or low temperature , from predators ,for egg, the younones (6) Information of pair formation and behaviour of bulbul has been documented (1,2,4).There is great variation in nest building material used by bird species was found (9) .Nests constructed plastic particulates ; rootlets and grasses and metal wires have also observed by (2). In Haryana nests were at a height of 2.0- 3.5 on 12 different plants species (5).

MATERIAL AND METHODS:-

Study Area:

Jath taluka is well developed agricultural area. The landscape of taluka is dotted with many minor and major irrigation reservoirs. These reservoirs are constructed for irrigation Purpose, the perennial reservoir of Birnal is situated in jath taluka 6 km west; its latitude is17^0 3^1 N. & Longitude $75^0 10^1$E . The area is surrounded by agricultural land; the housing is seen surrounded near reservior. The area shows variety of plants and crops such as lemon; jasmine; accacia- grasses; Amla; hibiscus; *Ziziphus mauritiana* [ber] *Azadirachta indica*; hibiscus ; Rosa- sinesis ; *Emblica afficinalis* etc .

Methods:

The survey method was used for the nesting sites of red vented bulbul the survey was conducted during March 2015 to October 2016. To every direction of near reservior the trees are carefully observed at possible site the point count and encounter methods was also used for the nest collection data. The abiotic and biotic ecological factor near the nest was also recorded during the study period.

For nest material:

The survey was conducted to record nest of bulbul. To study the structural aspect of nest; a few nest were collected after completion of breeding. The material used for nest construction was separated and identified

Material:

The Nikon aculon binocular was used for observation of trees and for photography the Nikon p900 zoom camera and Nikon 3200 [55 – 200MM lense camera was used.

RESULT AND DISCUSSION:

During study period about p.caber nest 32 was observed. For nesting material about different 8 sites of unused nest was observed.

Nesting sites:

The bulbul was selected nesting site in the houses near the reservoirs; some nests were observed on the trees twings; shrubs on the branch of the garlic tied on roof of houses near the reservior. some other birds such as baya weaver, parakeet nests was also recorded during study period the nesting was also observed in grasses , smaller trees in the irrigated fields ; road side trees.

Trees selected bulbul for nesting:

It was observed that; the labour of nest building is seen in bulbul. The breeding is seen from early, may to late august .breeding activity including, number of clutches, hatchlings and fledglings was peaked in June and July period. The trees was selected by the bulbul was neem ; hibiscus ; lemon ; jasmine ; accacia- grasses ; Amla ; *Ziziphus mauritiana* [ber] *Azadirachta indica* ; hibiscus ; Rosa-sinesis ; *Emblica afficinalis* etc .

Nest:

During study period (Pycnonotus cafer) red vented bulbul nests observed on the site was small flat swallow cup shaped.

Nesting material:

During study period the nest was observed on site on the trees like shrubs; hibiscus. For the nest material the old or reused nest was selected. The mixed type of material was observed in the nest constructed such as grasses, feathers of birds, cloth, metal wires; cottons. The dried grasses; cottons ; feathers clothes was observed in the nest cavity the primary function to provide soft bed to egg as well as to maintain humidity in the nest (8) the nest material act as insulator to the egg and young one the availability also plays important role in selection of material for nest. The nest material was held together in different ways as, a cup shaped in nest was constructed by the red vented bulbul. Some larvae, grasshopper parts was found in the nest cavity ,The reused nest again planted on the home tree area ,the egg laying ,of bulbul was seen again .

ACKNOWLEDGMENT:

Author are thankful to the principal of K.m college, jath & principal of R.R.College, jath, forest department of jath, irrigation department to providing me the information and support for my research work.

REFERENCES:

1. Dixit, D. Notes on a case of red vented bulbul (*p.cafer)* nesting indoor Pavo, 1:19-31(1963).
2. Lamba B.S. J. Bom. Nat. Hist. Soc., 68:222pp (1968).
3. Lepage D. Bird Life Int., 54:154-157 (2007).
4. Prajapati, S.H., C.D.; parmar, R.V. And patel, MI., Life Sci. Leaflets, 11:298- 3(2011).
5. Rao M.S., Ojha P.R. & Rao R. Int.J. Sci. & Tech., 2(7), 319-322 (2013).
6. Rajesh M.A, Chavan S.P, Patil P.V & Tarte. S.H., Int. J. Curr. Res. & Acad. Review., 4 (6):51-60 (2016).
7. Sibley C.G & Monroe B.L. Yale University press (1990)
8. Sengupta, S. Proce. Zool.Soc.Calcutta. 21:1-27 (1982).
9. Sharma, S. K., J. Bom. Nat. Hist. Soc., 94(3):515-520 (1987).

BISMUTH FERRITE ($BiFeO_3$) THIN FILMS FOR ELECTROCHEMICAL CAPACITOR PERFORMANCE

Shivaji D. Waghmare[1, 2], S. M. Kabbur[1], Rameshwar R. Kothawale[1], M. L. Mane[1], T. N. Lokhande[5] and Rajaram S. Mane[2, 4]*

[1]Department of Physics, Shri Shivaji Mahavidyalaya, Barshi, Solapur, India

[2]Center for Nanomaterials and Energy Devices, School of Physical Sciences Swami Ramanand Teerth Marathwada University, Nanded-431606, M.S., India

[3]Department of Physics, SGRG Shinde Mahavidyalaya, Paranda, Osmanabad, India

[4]School of Materials Science and Engineering, Pusan National University, San 30 Jangjeon-dong, Geumjeong-gu, Busan 609-735, Republic of Korea

[5]Department of Chemistry, Shri. Shivaji Mahavidyalaya, Barshi, Solapur, India

*Corresponding author E-mail: rsmane_2000@yahoo.com Ph.: 919850331971

ABSTRACT:

This paper reports electrodeposited Bismuth Ferrite nanostructures for electrochemical capacitor performance. Further the prepared thin films are used for their structural, morphological, phase confirmation characteristics using X-ray diffraction, field-emission scanning electron microscopy (SEM), and energy dispersive X-ray analysis measurements. Finally, the electrochemical performance has been examined for the prepared thin films.

Keywords: $BiFeO_3$-Nanoparticles; Electrodeposition;Structural-elucidation; Good-stability;

INTRODUCTION:

Electrochemical capacitors are currently called by a number of names: supercapacitor, ultracapacitor, or electrochemical double-layer capacitor. The list of different names is almost as large as the number of manufacturers, and since the technology is only currently beginning to find itself a market a universal term does not seem to have been agreed upon as yet[1-4]. The term 'supercapacitor' finds itself in common usage, being the tradename of the first commercial devices made by Nippon Electric Company (NEC), but 'ultracapacitor' is also commonly used, originating from devices made by the Pinnacle Research Institute (PRI) for the US military [5-6]. Within this thesis the technology will be referred to as much as possible by the term 'electrochemical double-layer capacitor', (EDLC), thus reducing reliance on the use of any commercial names, but sometimes the term 'supercapacitor' will be used for the sole purpose of reducing the tedium of repeated usage of the term 'EDLC'[7]. It should be understood that the two terms are used interchangeably, and that they both refer to a capacitor that stores electrical energy in the interface that lies between a solid electrode and an electrolyte [8-10].While electrostatic capacitors have been used as energy storage elements for nearly a century, low capacitance values have traditionally limited them to low power applications as components in analogue circuits, or at most as short-term memory backup supplies [11]. Recent developments in manufacturing techniques have changed this, however, and with the ability to construct materials of high surface-area and electrodes of low resistance have come the ability to store more energy in the form of electric charge. This has combined with an understanding of the charge transfer processes that occur in the electric double-layer to make high-power electrochemical capacitors possible [8].

EDLCs therefore represent a new breed of technology that occupies a niche amongst other energy storage devices that was previously vacant. They have the ability to store greater amounts of energy than conventional capacitors, and are able to deliver more power than batteries [12-13]. The current position of the EDLC is easily visualized by means of a ragone plot, which graphically represents a device’s energy and power capabilities.Besides bridging the gap between capacitors and batteries, supercapacitors also possess a number of desirable qualities that make them an attractive energy storage option. The mechanisms by which EDLCs store and release charge are completely reversible, so they are extremely efficient and can withstand a large number of charge/discharge cycles. They can store or release energy very quickly, and can operate over a wide range of temperatures [14].

Supercapacitors have only very recently begun to make themselves, known as aviable energy storage alternative, and while most electrical engineers may be aware of the technology it is probable that few possess an understanding of the processes involved and the applications that are possible. Ignorance of the full capabilities of EDLCs will most likely lead to more conventional alternatives being selected instead [15].

It is therefore the aim of this paperto present a complete overview ofelectrochemical double-layer capacitor technology for the purpose of fostering a better understanding within the engineering community [16]. This work will cover various aspects of the technology relevant to the field of electrical engineering, providing an introduction and a firm foundation from which to embark on further endeavors. The content of this thesis is intended for use by practicing electrical engineers or engineering students who wish to become more informed about this new technology.

Bismuth Ferrite (BFO) is one of the few single phase materials that exhibit both ferroelectric and antiferromagnetic properties at room temperature. BFO material was first synthesized by Royen and Swars in 1957. A number of studies have been focused on this compound motivated by its multiferroic properties and the potentially high magnetoelectricproperty.In order to better explore this BFO material, it would be essential to have an understanding of its basic crystal structure.

MATERIALS CHARACTERIZATION:

X-Ray Diffractometer (XRD) Analysis: The XRD pattern was obtained using the PANAlyticalX’Pert Pro MPD advanced powder X-ray diffractometer using Cu-Kα = 1.54056 A° radiation, operating at 40 KV/30 mA.

The diffraction follows the Bragg's law:

$$n\lambda = 2d_{hkl}\sin\theta \qquad (1)$$

where n is an integer, λ is the wavelength of the X-ray, $d_{hkl}$is the lattice spacing between (hkl) planes and θ is the angle between the incident beam and (hkl) plane.

Scanning Electron Microscopy (SEM):

The synthesized BFO nanopowders size and morphology was characterized using the Field Emission Scanning Electron Microscopy (FESEM). Parameters for the SEM are as follows: the voltage setting used was 20 kV and a secondary electron was used. The BFO nanopowders were suspended in the de-Ionised water with 0.1 wt%concentrations and were sonicated with 25 KHz frequency for around 30 minutes before dropping a drop of the suspension on the carbon tape and drying up the water. The specimens to be observed had to be platinum coated at 10 μA current for 100 seconds before the observation was performed.

Fourier Transform Infrared Spectroscopy (FT-IR):

In this work, the spectrometer used in order to obtain the spectra of samples was a FT-IR, Shimadzu FT-IT-8700 using a standard potassium bromide (KBr) pellet technique. Each FT-IR spectrum was collected after 32 scans at a resolution of 2cm^{-1} from 4000 to 1000 cm^{-1}.

Potentiostat:

An Autolab-WPG100 program operating a Potentiostat-galvanostat electrochemical workstation in one compartment and a three-electrode cell at room temperature were used to provide a constant potential in the electrochemical deposition.

Electrolysis cell:

Electrochemical deposition was carried out in a H-shaped cell which can hold 50 mL solution. Working and the counter electrodes were platinum foils with an area of 1.5 cm^2. This cell is a three-compartment one which is divided into two compartments as the catholyte and anolyte with a medium porosity glass disc of 2.0 cm in diameter. Reference electrode was inserted to the working sode of the cell and Ag/AgCl was utilized as the reference electrode.

Sample synthesis details:

In order to investigation of BFO thin films, the precursors such as Bismuth nitrate pentahydrate [Bi $(NO_3)_3\cdot 5H_2O$, Sigma Aldrich], and ferric nitrate pentahydrate [$Fe(NO3)_3\cdot 9H_2O$, Sigma Aldrich], Citric acid ($C_6H_8O_7$, Sigma Aldrich), Sodium tungstate hydrated [$Na_2WO_4\cdot 2H_2O$, Sigma Aldrich] and Ammonia solution, these were obtained from commercial sources and used as received without further purification. Furthermore, synthesis is done into two steps firstly; to synthesized BFO, Bi $(NO_3)_3\cdot 5H_2O$ (0.2M),$Fe(NO_3)_3\cdot 9H_2O$ (0.2M) and $C_6H_8O_7$ (0.2M) are dissolved in doubly distilled water (added nitric acid to dissolve $Bi(NO_3)_3\cdot 5H_2O$ in water) separately with under vigorous stirrer at ambient temperature then pH was adjusted to 8-10 by adding ammonia solution and after 15 min. solution was ready to electrodeposition. After deposition, we further used all sample in Supercapacitor performance testing.

RESULTS AND DISCUSSION:

Structural Analysis:

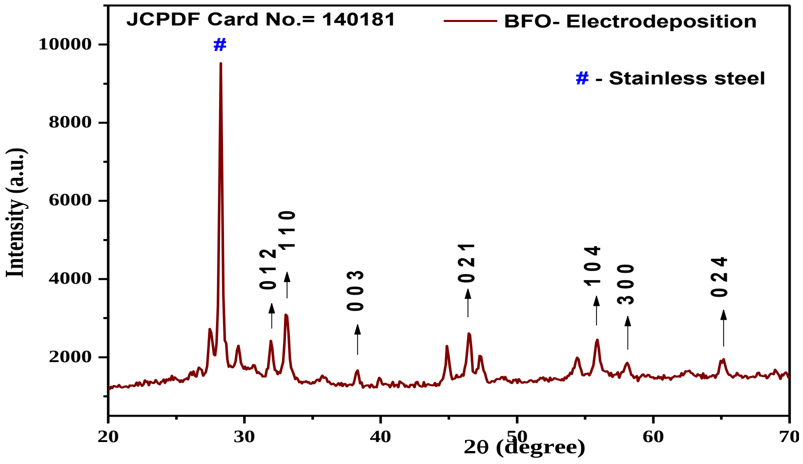

Fig. 1: The XRD pattern of BFO

Above fig. 1.show the XRD pattern of BFO thick nanostructures obtained after 450 °C air-annealing for 4 h. The XRD pattern confirmed $BiFeO_3$phase of BFO with rhombohedralperovskite phase as the reflection planes (120), (110), (003), (021), (104), (300) and (024) belong to the $BiFeO_3$(JCPDF No.14-0181). The BFO film confirmed the presence of a single phase i.e. $BiFeO_3$which was free from other impurities and motile mixed phases such as Bi_2O_2 or Fe_2O_3etc

Energy dispersive analysis (EDX) spectrum:

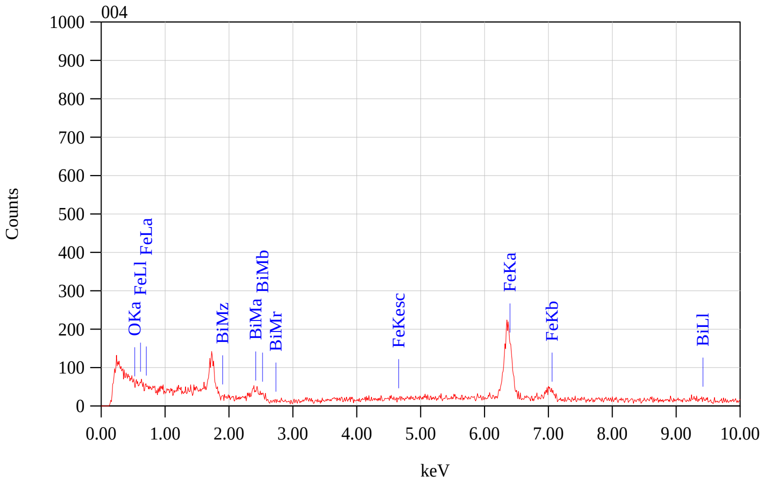

Fig. 2: Energy dispersive analysis (EDX) spectrum

The fig. 2. represents energy dispersive analysis (EDX) spectrum of the BFO film. In consistent to XRD observation, EDX was scanned separately for knowing elemental analysis BFO. However, at both structures there was no change in stoichiometry, confirming that both forms belong to BFO structure the 6:25:69 ratios for Bi, Fe and O, supporting the formation of BFO, consistent to XRD results.

Surface morphology:

In fig. 3., the digital FE-SEM images were confirmed the presence of BFO structures.The lower and higher resolution FE-SEM images, as seen in Fig. 3 (a,b),were well distinguishable for both structures. We presumed that this structure of the high surface area would be advantageous in gas sensors application.

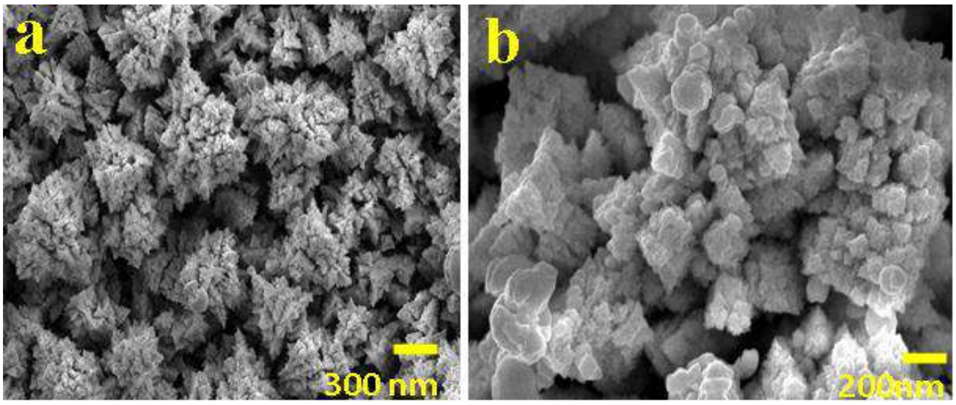

Fig. 3: The FE-SEM images of BFO film at different magnifications

Fourier Transform–Infrared (FT-IR) Analysis:

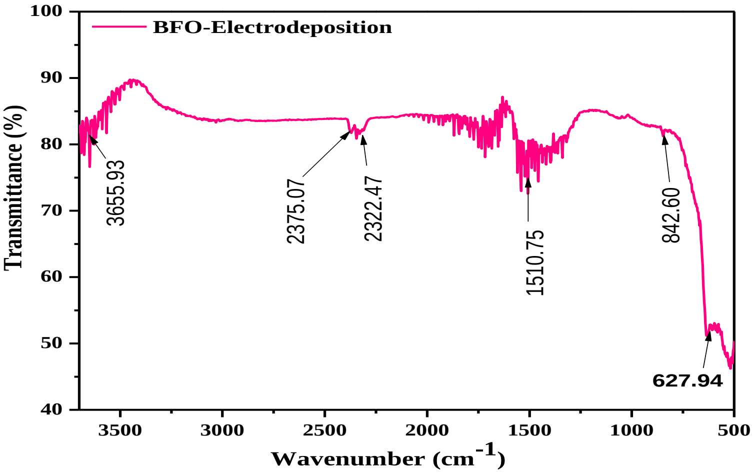

Fig. 4: FT-IR spectrum of pure BFO material

As shown in fig. 4 six strong characteristic infrared (IR) peaks appeared for pure BFO product. In the pure BFO material appeared strong peaks at wavenumbers with transmittance (in cm^{-1}, %) are (3655.93), (2375.07), (2322.47), (1510.75), (842.60) and (627.94) as shown in figure 3.4. The BFO has strong and wide peaks which correspond to stretching vibrations of C=O and –OH.

Supercapacitor properties:

KOH concentration Effect:

In fig. 5 we can see change in C-V with respective concentration of electrolyte (KOH). Thereby, we confirm the best concentration of electrolyte for enhanced performance. It is 0.6 M is best concentration of KOH electrolyte.

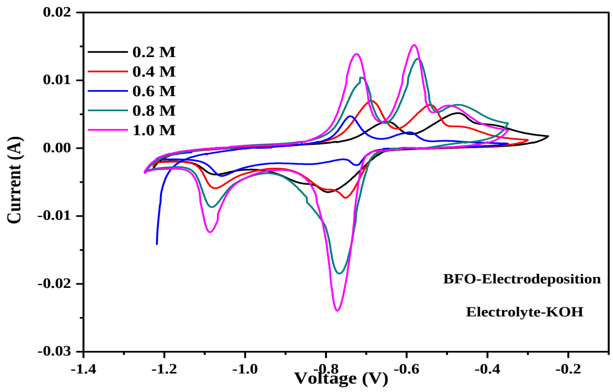

Fig. 5: Concentration Effect of KOH

Effect of Scan rate at fixed 0.6 M KOH:

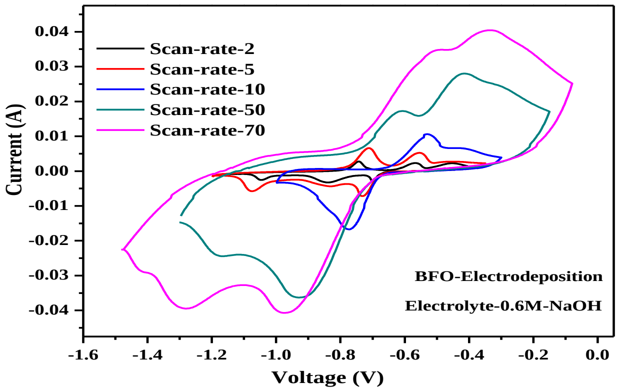

Fig. 6: Scan Rate Effect on C-V

In this case, we have checked scanning effect on the CV at fixed 0.6 M KOH. We carried out CV at various scanning rates such as 2, 5, 10, 20, 50, and 70 mV/s . It is found that window of CV is changing with respect to scanning rate as shown in fig. 6.

Specific Capacitance:

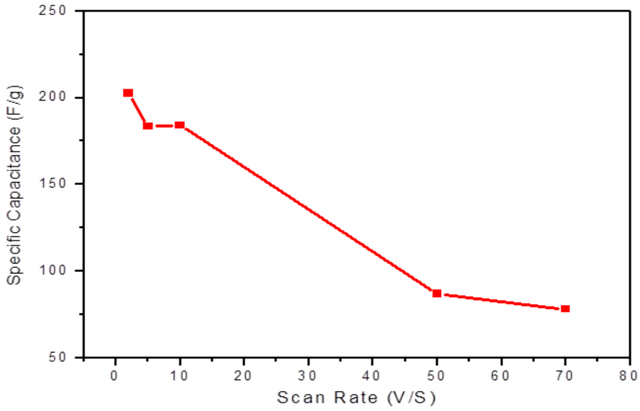

Fig. 7: Shows Calculation of Specific Capacitance

We further calculated the specific capacitance of the material in 0.6 KOH at various scanning rates as demonstrated in fig. 7. As results, Specific Capacitance is decreasing with respect scan rate. The highest specific capacitance about 220 F/g is found at 2 mV/s.

CONCLUSION:

In this work, we have synthesized pure phase Bismuth ferrite by using Electrodeposition routine. The stoichiometry, confirming the formation of BFO, for Bi, Fe and O elements were obtained from the EDX analysis. Phase confirmation was also carried out by X-ray diffraction. Furthermore, The Morphology of the product has been confirmed by using SEM. The thin films of the BFO used to checking of supercapacitive performance. Therein, we have checked the performance with respect to concentration of KOH and scanning rate at fixed 0.6 M KOH effects. Finally, the specific capacitance is calculated and highest capacitance is found to 0.6M KOH at 2 mV/s.

REFERENCES:

1. Bae, S., Kim, H., Lee, Y., Xu, X., Park, J.S., Zheng, Y., Nat. Nanotech. 5(8), 574–578 (2010).
2. Becerril, H. A., Mao, J., Liu, Z., Stoltenberg, R. M., Bao, Z., & Chen, Y., ACS Nano, 2(3), 463–470 (2008).
3. Blake, P., Brimicombe, P., Nair, R., Booth, T., Jiang, D., Schedin, F., Nano Letters, 8, 1704–1708 (2008).
4. Brabec, C., 83, 273–292 (2004).
5. Choi, D., Wang, D., Viswanathan, V. V., Bae, I.-T., Wang, W., Nie, Z., Electrochemistry Communications, 12(3), 378–381 (2010).
6. Eda, G., &Chhowalla, M., Nano Letters, 9(2), 814–818 (2009).
7. Eda, G., Fanchini, G., & Chhowalla, M., Nature Nanotech., 3, 270–274 (2008).
8. Emtsev, K. V., Bostwick, A., Horn, K., Jobst, J., Kellogg, G. L., Ley, L., Nature Materials, 8, 203–207 (2009).
9. Fan, X., Peng, W., Li, Y., Li, X., Wang, S., Zhang, G., Adv. Mat., 20, 4490–4493 (2008).
10. Frackowiak, E., &Beguin, F., Carbon, 39(6), 937–950 (2001).
11. Geim, A. K., &Novoselov, K. S., Nature Materials, 6(3), 183–191 (2007).
12. Gerouki, A., Goldner, M. A., Goldner, R. B., Haas, T. E., Liu, T. Y., &Slaven, S., J. Electrochem. Soc., 143, L262–L263 (1996).
13. Gilje, S., Han, S., Wang, M., Wang, K. L.,&Kaner, R. B., Nano Letters, 7, 3394–3398 (2007).
14. Gratzel, M., Mathe.l, Physical and Eng. Sci., 365(1853), 993–1005 (2007).
15. Ha, M., Xia, Y., Green, A. A., Zhang, W., Renn, M. J., Kim, C.H., ACS Nano, 4(8), 4388–4395 (2010).
16. Han, Y., Ding, B., & Zhang, X. J. New Mate. for Electrochem. Sys. 13, 315–320 (2010).

EFFECT OF Zr DOPING ON STRUCTURAL AND OPTICAL PROPERTIES OF TiO_2 THIN FILM BY SOL-GEL ROUTED SPIN COATING TECHNIQUE

Suresh M. Jadhav, Ravina R. Patil, Tejashri B. Bhutade,
Priyanka B. Mitkal and Shrikant R. Kokare*
Post-Graduate Department of Physics,
Raje Ramrao Mahavidyalaya, Jath, Dist: Sangli 416404
*Corresponding author E-mail: kshirikant@yahoo.com

ABSTRACT:

Thin film of Zirconium (Zr) doped titanium dioxide will be prepared by Sol-gel spin coating technique and further calcinated at 450^0C. The structural and optical properties of Zr doped TiO_2 thin films will be investigated by X-ray diffraction (XRD), Scanning electron microscopy (SEM), ultraviolet-visible spectroscopy (UV-vis) techniques. The XRD results confirm the nanostructured TiO_2 thin films having crystalline nature with anatase phase. The characterization results show that the claimed thin films crystallinity and the effect of Zr substation on crystallinity. The SEM investigation of Zr doped TiO_2 films will give evidence of surface morphology. The optical measurements will show that the films having high transparency in the visible region and the optical band gap energy of Zr doped TiO_2.

Keywords: TiO_2 thin film; Zr doped TiO_2 thin film; Sol-gel method; spin coating.

INTRODUCTION:

In research and development, the TiO_2 will become an important wide band gap semiconductor and photoelectric conversion material. TiO_2 coating has been investigated by many researchers because TiO_2 is stable, nontoxic with band gap of 3.21eV. Making it possible for photovoltaic [1] and photo catalytic [2] applications, well -known TiO_2 nano particle with good physico - chemical properties are mainly dominated by three phases, namely, anatase, rutile and brookite. On a nanometer scale or in a thin layer form,TiO_2 nano particles are transparent and have a wide surface area.[3] To improve the performance of TiO_2 thin film for photovoltaic application such as dye sensitized solar cell, TiO_2 layer has been modified by adding metal ion dopants such as Zr and Zr it is also reported that to improve the crystal size of TiO_2 treatment such as by optimizing dopant concentration of the precursor can be performed. Many application of TiO_2 thin film are at the basis of fundamental properties that relate to surface and interface features of the film. A wide range of metal ions such as iron, Chromium, and cobalt have been used as dopants for TiO_2 with the intention of improving photovoltaic and extending absorption in to the visible light range. Zirconium (Zr) has been the most widely examined among these elements Zr-doped thin films can be prepared by several techniques, including sol-gel, reactive sputtering, pulsed laser deposition, evaporation chemical vapor deposition and spray pyrolysis. The sol-gel technique has emerged as one of the most promising methods as it produces samples by simple synthetic route with good homogeneity, low cost, excellent compositional control and feasibility of producing thin films on large complex shapes with low Crystallization temperature. In this paper, Zr - doped TiO_2 films will be deposited using sol- gel through spin coating technique and investigated for the structural morphological and optical properties as a function of atomic weight percentage (5%, 10%, 15% 20%) of Zr concentration. The novelty of the present work is that the modified preparative conditions of Zr-doped TiO_2 thin films yield better and desirable results useful to photovoltaic applications in solar cell.

EXPERIMENTAL:

The precursors required for the preparation of Zr- doped TiO_2 film by sol- gel spin coating technique were Titanium tetra iso-propoxide Isopropanol (TTIP, 98%), for dopant Zirconium (98%), methanol (97%) and hydrochloric acid (97%).The glass plate will be used as a substrate.

Un-doped TiO_2 and Zr-doped TiO_2 thin films will be deposited on glass substrates using sol- gel spin coating method. The Sol is based on the hydrolysis of alkoxide in alcoholic solution in the presence of an acid catalyst. Titanium isopropoxide (TTIP) ($Ti(OCH\ (CH_3)_2)_4$ is Nanocrystalline un-doped TiO_2 and Zr - doped TiO_2 thin films were deposited on glass used as TiO_2 precursor while isopropanol (CH_3 CH (OH)- CH_3), ethanol (CH_3 OH) and hydrochloric acid (HCl) are used. The procedure of preparation includes the dissolution of ethanol, isopropanol as solvent and hydrochloric acid titanium isopropoxide is also added as precursor after mixing the adequate proportion for 24 h . A schematic flow chart of the Zr - doped TiO_2 thin films prepared by sol - gel spin coating process is shows in fig1 we finally obtain a transparent solution of yellowish color, which is ready for the deposition. The dopant solution for Zr- doped TiO_2 thin film was prepared with different atomic weight percentage of Zr concentration such as 5 wt.% , 10 wt .% , 15 wt .% , 20wt %. After stirring at room temperature for 24 h, the Zr - doped TiO_2 sols were coated on the glass substrate by spin- coating technique. .Glass substrate coated by dropping ~0.2 ml of solution on to glass substrate spun in air for 60s at 4500 rpm. Instantaneous heating at 100 for 30 min.and following by spin coating process.

SYNTHESIS:

In is paper, Zr doped Titanium dioxide films were deposited using sol-gel to trough spin coating technique and investigated for the structural morphological and optical proportions as a function of atomic weight percentages(2%, 5%, 10%, 20%) of Zr concentration.

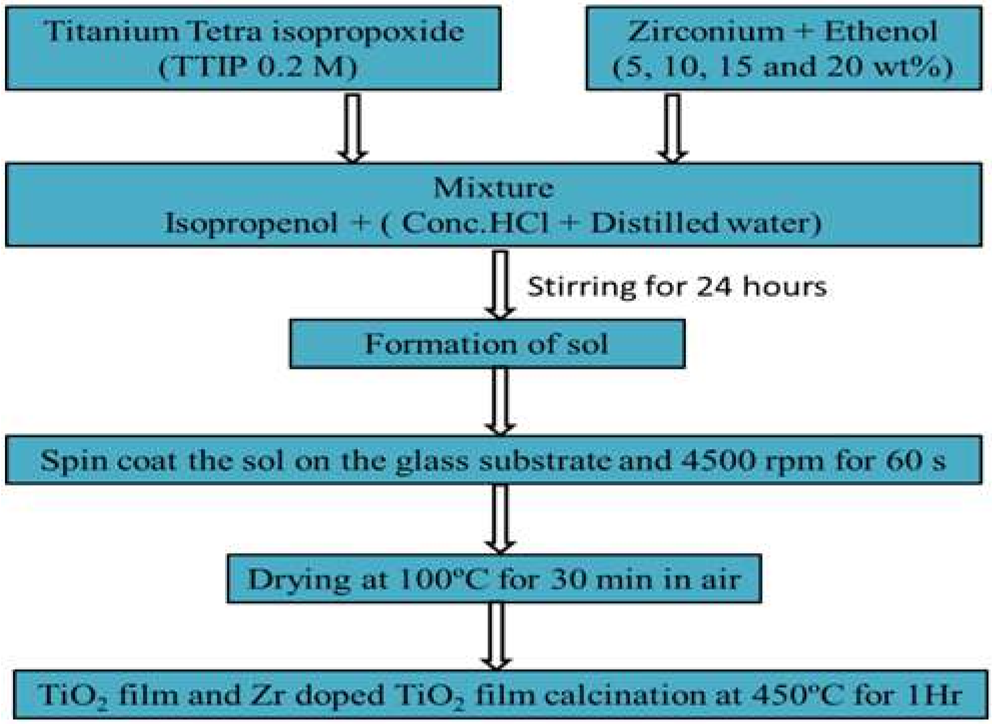

Fig. 1: Flow chart of the Zr-doped TiO_2 thin film prepare by a sol-gel spin coating process

Schematic of Sol-Gel Formation:

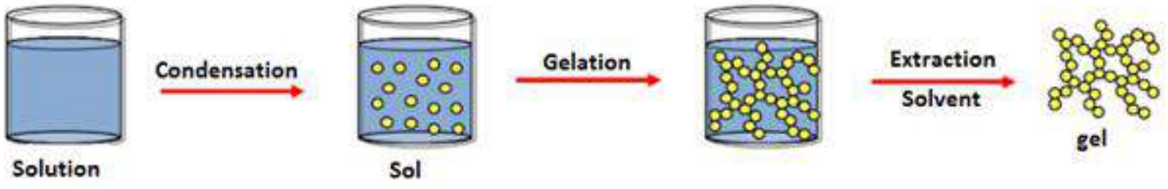

CONCLUSION:

The titanium dioxide and Zr doped Titanium dioxide thin films were prepared using the sol-gel routed spin coating technique. This prepared thin film will be used XRD, SEM and UV analysis for its further characterization.

REFERENCES:

1. G. Liu, J. C. Yu, G. Q. M. Lu an H. M. Cheng, Chem. Commun.,(camb),
2. A. A. Umar, M. Y. A. Rahman, S. K. M. Saad and M. M. Salleh, Int. J. Electrochem. Sci.
3. M. Ouzzine, J. A. Macia-Agullo, M. A. Lillo- Rodenas, C. Quijada and A. Linares – Solano, Appl. Catal. B Environ.

PREPARATION OF SUPERHYDROPHOBIC – SUPEROLEOPHILIC CANDLE SOOT DEPOSITED MEMBRANES FOR OIL – WATER SEPARATION APPLICATIONS

Tejaswini B. Shinde, Smita B. Pawar, Tushar M. Khot,
Dipali R. Gade and Sanjay S. Latthe*
Self-cleaning Research Laboratory, Department of Physics,
Raje Ramrao Mahavidyalaya, Jath 416 404, Maharashtra, India
*Corresponding author E-mail: latthes@gmail.com

ABSTRACT:

We report the fabrication of superhydrophobic – superoleophilic membranes by depositing the candle soot on stainless steel (SS) mesh. The candle soot was deposited on the SS mesh by simply holding the mesh in the middle of the flame. After candle soot deposition on the mesh, the surface turns to black in appearance. On the candle soot modified SS mesh, the water drop achieves the contact angle of 152° (superhydrophobic wettability) and oil drops spreads out with contact angle ~ 0° (superoleophilic wettability). Due to this superhydrophobic – superoleophilic behavior of the membrane, it can be used in oil-water separation applications.

Keywords: Candle Soot, Superhydrophobic, Superoleophilic, Contact angle, Wettability.

INTRODUCTION:

Lotus leaf is the most famous for its self-cleaning behavior. The water contact angle on the lotus leaf is greater than 150° and roll off the leaf surface at very small tilt angle. While rolling, the dust particles are taken off by performing the self-cleaning behavior [1]. Such highly non-wettable surfaces are known as superhydrophobic surfaces. The superhydrophobic surfaces have great industrial applications in self-cleaning industry [2-11]. Such superhydrophobic surfaces show high affinity towards the oil where the oil drop spread completely with oil contact angle nearly equal to 0°. Such superhydrophobic-superoleophilic surfaces are attracting great attention for their use in oil-water separation membranes [12, 13].

Due to remarkable industrialization and oil-spill, the water pollution has become the supreme environmental issue worldwide. Conventional methods are not efficient to separate oil from water as well as it cause secondary pollution, therefore cheap and environmental friendly functional membranes for oil-water separation are seeking great attention of material scientists [14]. Recently, Ju and co-workers [15] have deposited candle soot on copper foam and cloths for oil-water separation. The sample was held on candle flame nearly 1 cm above the wick for deposition of candle soot. The candle soot deposited copper foam showed 20 µm thick porous layer of carbon nanoparticles. Gao and researchers [16] have obtained the carbon soot through open air combustion flame process. The carbon soot was collected by holding silicon wafer on top of the flame. The as-grown carbon soot was introduced into the porous network of melamine sponge by immersing it in the dispersion of carbon soot. An engine oil droplet was immediately absorbed in the modified sponge whereas the water drop maintains the spherical shape. Zhao et al [17] have prepared superhydrophobic and superoleophilic nickel foam for oil – water separation. The nickel foam was held at 3.5 cm on the flame of paraffin candle for about 2 min. Candle soot coated nickel foam was modified by PDMS and cured for 80 ºC. The hexane in water was efficiently separated by the modified nickel foam through gravitational separation. Li et al [18] have prepared superhydrophobic stainless steel mesh with excellent superoleophilicity. A SS mesh was held in the flame of paraffin candle for 3 min for both sides. The hydrophobic silica nanoparticles were sprayed on the candle soot coated SS mesh. A porous morphology was observed on modified mesh which is favorable for superhydrophobicity and superoleophilicity.

In the current research work, the SS mesh was modified with candle soot on which the water drop achieves the contact angle of 152° (superhydrophobic) and oil drops spreads out with contact angle ~ 0° (superoleophilic).

MATERIALS AND METHODS:

Materials:

Paraffin wax candles were purchased from (Shah Patil and Company Interior decoration, Sangli, India). The stainless steel (SS) meshes with pore diameter around 0.8 mm (Shah Patil and Company Interior decoration, Sangli, India) were used for the deposition of candle soot.

Fabrication of Superhydrophobic – Superoleophilic Candle Soot Deposited Membranes:

A simple candle soot deposition process is described here. The pristine stainless steel (SS) meshes (5× 5 cm^2) were cleaned with thorough water and detergent. After drying at room temperature, the SS meshes were held in the middle of the flame for about 1 hour to fully coat the SS mesh. The candle soot deposition process is depicted in **Fig. 1**.

Fig. 1: The optical photograph of candle soot deposition on SS mesh

Characterizations:

The wettability of the membrane was analyzed by water contact angle measurement using contact angle meter (HO-IAD-CAM-01, Holmarch Opto-Mechatronics Pvt. Ltd.). The water drops were placed on the membrane at three different places and average value is reported as final contact angle. The optical images were captured using i-phone camera. The pore size of the membrane was analyzed by capturing the image and using scale.

RESULTS AND DISCUSSION:

Confirmation of Candle Soot on Stainless Steel Mesh:

The deposition of candle soot on SS mesh was confirmed qualitatively. As shown in **Fig.2**, the pristine SS mesh with pore size of 0.8 mm was used. After candle soot deposition, the SS mesh turns into black colour which confirms the deposition of candle soot. The candle soot deposition time was nearly 1 h because it takes time to fill the pores completely.

Fig. 2: The optical photograph of pristine and candle soot modified SS mesh

Wettability of the Candle Soot Deposited Membranes:

The wetting property of the candle soot deposited membranes was studied by water and oil contact angle measurements. At first different colored (green, red and pink) water drops were placed on the modified SS mesh as shown in **Fig. 3**. The water drops achieved spherical shape with contact angle more than 150°. The oil drops placed on the modified SS mesh were quickly absorbed inside the mesh structure confirming its superoleophilicity. The water repellency is due to hydrophobic nature of candle soot which was collected from the middle of the flame [19].

Fig. 3: The optical photograph of colored water drops on candle soot modified SS mesh

However, the durability of the candle soot deposition is one of the measure drawbacks. While performing oil – water separation experiments, the candle soot was washed off by the liquids. After holding under tap water, the candle soot was completely got removed from the SS mesh. Actually, the pore size is very high (nearly 0.8 mm) which could not firmly support the candle soot. We are trying to use low pore size SS meshes to improve the candle soot adhesion on the SS mesh surface. In addition, we are preparing the composite of polymer and candle soot to improve the durability of the membrane.

CONCLUSION:

We have prepared the superhydrophobic – superoleophilic membranes using candle soot for oil – water separation applications. The candle soot was deposited on the membrane from the middle part of the flame. The membranes strongly repelled the water, whereas absorbed the oil. The stability of the candle soot deposited membranes is serious issue and the stability can be increased by enforcing polymers in the structure of candle soot. The experiments are under process in our laboratory.

ACKNOWLEDGEMENT:

This work is financially supported by DST-INSPIRE Faculty Scheme, Department of Science and Technology (DST), Government of India. [DST/INSPIRE/04/2015/000281].

REFERENCES:

1. Barthlott, W. and C. Neinhuis, Planta, 202(1): p. 1-8 (1997).
2. Gurav, A.B., S.S. Latthe, and R.S. Vhatkar, Surface Innovations, 1(3): p. 157-161 (2013).
3. Kim, D.-Y., et al., J. Mat. Chem. A, 3(7): p. 3975-3983 (2015).
4. Latthe, S., et al., Coatings, 4(3): p. 497 (2014).
5. Latthe, S.S. and A.V. Rao, Surface and Coatings Tech., 207(Suppl. C): p. 489-492 (2012).
6. Latthe, S.S., et al., J. Porous Materials, 17(5): p. 565-571 (2010).
7. Madhan Kumar, A., et al., Polymer, 77(Supplement C): p. 79-86 (2015).
8. Xing, R., et al., J.Mole. Liquids, 247(Supplement C): p. 366-373 (2017).
9. Yoon, H., et al., J. Materials Chem. A, 3(21): p. 11403-11410 (2015).
10. Park, J.-J., et al., ACS Applied Materials & Interfaces, 5(13): p. 6155-6160 (2013).
11. Dhere, S.L., et al., J. Phy. and Chem. of Solids, 72(1): p. 45-49 (2011).
12. Beshkar, F., H. Khojasteh, and M. Salavati-Niasari, J. Colloid & Inter. Sci., 497:57-65 (2017).
13. Liu, S., et al., RSC Advances, 5(84): p. 68293-68298 (2015).
14. Dikio, E.D., Int. J. Electrochem. Sci, 6: p. 2214-2222 (2011).
15. Ju, G., et al., Langmuir, 33(10): p. 2664-2670 (2017).
16. Gao, Y., et al., ACS Applied Materials & Interfaces, 6(8): p. 5924-5929 (2014).
17. Zhao, F., et al., RSC Advances, 4(14): p. 7132-7135 (2014).
18. Li, J., et al., Nanoscale, 8(14): p. 7638-7645 (2016).
19. Sahoo, B.N. and B. Kandasubramanian, Mate. Chem. and Phy., 148(1): p. 134-142 (2014).

STUDY OF WORKING PRINCIPLE USED IN NATURAL DYE SENSITIZED SOLAR CELL DYES AND ITS REVIEW

Vidya C. Mali, Krinsha K. Rangar, Rajendra A. Lavate,
Dipak A. Kumbhar and B. N. Kokare*
Raje Ramrao College, Jath, Maharashtra, India
*Minalben Meheta Arts, Commerce and Science College, Panchgani, Maharashtra, India

ABSTRACT:

Looking for greener sources of energy was the subject of research activities for the last decade. For years studies have been using various kinds of energy sources to fulfill energy requirement. In order to reduce further accumulation of greenhouse gases, converter of energy has been designed to replace the conventional (fossil) energy sources. A new technology had been developed that is known as Natural Dye Sensitized Solar Cells (NDSSC) which consists of a group of photovoltaic cells that produces green energy at low cost of sensitization material production since no vacuum systems or low cost equipment are used in fabrication process. In this paper we are reviewing research studies done by different research groups, which includes number of natural dyes used for better result.

Keywords: NDSSC, dye, Photovoltaic.

INTRODUCTION:

The increasing demand in energy supply has accelerated reduction in fossil fuel. It is projected that the reserves of fossil fuels throughout the world could only last 40 years for oil, 60 years for natural gas and 200 years for coal. Their development can be described according to their construction principles[1]. A solar cell is a photonic device that changes photons together with particular wavelengths to electricity[2]. Consequently, low cost alternatives and new varieties of low cost solar cells is surely an instant issue and have absolutely recently been the subject of the research work for the last three decads. The name NDSSC stands for “Natural Dye Sensitized Solar Cell". It is the latest technology of solar cells. It belongs to thin film solar cell that has attracted considerable attention because of their cheap production along with the eco-friendliness.

Natural Dye Sensitized Solar Cell (NDSSC) is a group in the third generation of solar cell that was found by O'Regan and Gratzel in 1991. Although the process is slowly but the potential of renewable energy has been well talked about in the past decade. As a result, the conversion of solar energy into different forms has been the core of the research for the recent past years. Photovoltaic devices have been found to convert the solar energy into electrical energy. The simple assemble of solar cell operates by renovating affordable photon from solar energy to electrical energy according to sensitization of wide band gap semiconductor, dyes and also electrolyte[3]. Natural dyes are well known for their high absorption coefficient, cheap and easy availability, non-toxic and renewable reservoir to materials for many applications. Narayan in his review stated that a number of natural dyes have been extracted as to facilitate dye-sensitized solar cells. Natural dyes compare to semiconductor solar cell are promising alternative sensitizers for Dye Sensitized Solar Cell because they are only available, easy to prepare, cheap and eco-friendly[4].

This review serves the purpose of consolidating all the materials employed for NDSSC fabrication, different electrolytes used and the types of plant pigments and its influencing parameters such as open circuit voltage, short circuit current, fill factor etc. It summarizes the work carried out by different research groups over the years on natural dye based solar cell.

WORKING PRINCIPLE:

The basic operating principle for any solar cell consists of absorption, separation and collection. Different types optimize these parameters accordingly to attain better efficiency. Thus, absorption occurs in the first step of the reactions occurring in NDSSC. Under illumination, sensitizer dye D absorbs a photon which leads to excited sensitizer state D*. Photo excitation of this sensitizer is then followed by the electron injection into the conduction band of the semiconductor. This takes the sensitizer to an oxidized state D^+ with the electron donation from the electrolyte, containing a reduction–oxidation couple, the original state of the dye restored. Iodide/triiodide couple is the preferred and effective reduction–oxidation couple used. Iodide regenerates the sensitizer, and itself gets regenerated by the reduction of triiodide at the counter electrode. This way the circuit gets completed by transfer of electron via the external load. The following reactions summarize the working in a lucid manner: [5,6]

D (absorbed) + hv D*(absorbed) (1)

D*(absorbed) D^+ (absorbed) + e^-(injected) (2)

I^{-3} + 2 . e^- (cathode) 3 I -(cathode) (3)

D^+ (absorbed) + I - D (absorbed) +I^{-3} (4)

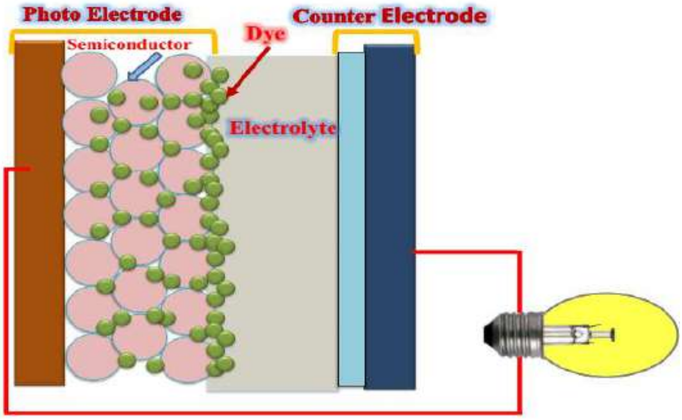

Fig. 1: Schematic diagram of the dye-sensitized solar cell

NATURAL DYES USED IN SOLAR CELL:

Natural dyes provide a viable alternative to expensive organic based Dye Sensitized Solar Cell. Various components of a plant has been tested over the last two decades as suitable sensitizers. Several studies have been reported in the past about the optical properties of dyes such as Anthocyanin and Chlorophyll[7]. Anthocyanin's are brightly colored pigments found in plants and may have different colors depending on the pH. Chlorophyll, on the other hand, refers to a group of closely related green pigments found in green colored vegetables and leaves such as Spinach, Green Cabbage, and Lettuce[8]. Synthetic chlorophyll and anthocyanin have been developed for the production of solar cells. Synthesis of these dyes could be controlled to obtain concentrated and minute dye particles vital for obtaining higher photoelectric conversion efficiency of solar cells[9,]. Since natural dyes are cheaper to obtain, it would be more economical to mass produce Dye Sensitized Solar Cell that could be used in appliances as portable chargers or integrated into building facades[10]. The aim of this work was to investigate and determine the most efficient natural dye and to find a consistent and reliable method for producing the cells.

Now we summarize the photo electro chemical parameters of the NDSSC's sensitized with different natural dyes extracted from leaves, seeds, flowers, vegetables and tree barks which have maximum efficiency[13].

Table 1: Photo electrochemical parameters of the NDSSC's sensitized with different natural dyes extracted from leaves, seeds, flowers, fruits, vegetables and tree barks

Sr. No.	Dyes	λmax (nm)	η (%)
1.	*Hibiscus surattensis*	545	1.14
2.	*Hibiscus rosasinesis*	534	1.02
3.	*Sesbania grandiflora*	544	1.02
4.	*Tagetes erecta*	465	0.80
5.	*Vernonia amygdalin (Bitterleaf)*	400	0.69
6.	*Lawsonia inermis (Henna)*	518	0.66
7.	*Punica granatum (Pomegranate)*	665	0.59
8.	*Nerium olender*	539	0.59
9.	*Rhododendron*	540	0.57
10.	*Perilla*	665	0.50
11.	*Red Bougainvillea spectabilis*	480	0.48
12.	*Broadleaf holy leaf*	-	0.47
13.	*Red Bougainvillea glabra*	535	0.45
14.	*Rosa*	-	0.38

15.	*Grapes*	560	0.38
16.	*Rosella (Hibiscus sabdariffa L.)*	520	0.37
17.	*Bauhinia tree*	665	0.36
18.	*Violet Bougainvillea spectabilis*	535	0.35
19.	*Viola*	546	0.33
20.	*Petunia*	665	0.32

CONCLUSION:

Natural Dye sensitized solar cell (NDSSC), with its advantages of cheap, much to be approved by scientists from all over the world. The sensitizer is the heart of dye solar cell and should not degrade fast which leads in increasing the life of the cell. The Natural Dye contains Antocyanin Pigment which gives maximum efficiency and Chlorophyll Pigment gives minimum efficiency. There should be good electronic binding between sensitizer and semiconductor. Hence, the dye should have a carboxyl and hydroxyl group. Natural dye becomes a hotspot in the research of the dye-sensitized solar cells with low cost, rich diversity, easily and pollution free and ecofriendly. This will help to solve the human energy needs and relief increasingly prominent environmental problems owing to burning fossil fuels.

REFERENCES:

1. Hara K. and Arakawa, H. John Wiley & Sons, 663 -700 (2000).
2. Torchani A., Saaudaoui S., Gharbi R., Fathallah M. Current Applied Physics; Vol. 15, 307 – 312 (2015).
3. Jasim K. E. and Hassan A.M., Int. J. Nano manufacturing, Vol. 4, 1/2/3/4, 242– 247 (2009).
4. Narayan J.K., J. Renew. & Sust. Ener. Reviews, Vol. 16; 208 – 215 (2012).
5. K. Tennakone, G.R.R. Kumara, I.R.M. Kottegoda, V.S.P. Perera, Chem. Commu. 15 (1999).
6. Nazeeruddin Md. K., Baran off E., Gratzel M., Sol. Energy, Vol. 85, 1172-1178 (2011).
7. Hodges, D Mark et al. Planta, 207, 4, 604-611 (1999).
8. Martin A, Green, et al. Progress in photovoltaics: Res. & applic. 20, 1; 12-20 (2012).
9. Repins, Ingrid et al. Progress in photovoltaics: Res. & applic. 16.3; 235-239 (2008).
10. M. Law et al., Nature Materials, 4, 455 (2005).
11. S. Shalini, R. Balasundaraprabhu , S. Prasanna , Tapas K., Renewable and Sustainable Energy Reviews 51, 1306–1325 (2015).

STRUCTURAL AND DC ELECTRICAL RESISTIVITY OF $ZnFe_{1.9}Dy_{0.1}O_4$

V. S. Kodag, P. P. Zambre, A. S. Jagdale, A. N. Todkaree and S. P. Dalawai[*]
Post graduate Department of Physics, Raje Ramrao College, Jath, Dist: Sangli
[*]Corresponding author E-mail: sanjeevdalawai@gmail.com Ph.No. 9890253825

ABSTRACT:

Nano-sized ferrite material with chemical formula of $ZnFe_{1.9}Dy_{0.1}O_4$ was prepared by oxalate co-precipitation method. The prepared ferrite sample was characterized by XRD, FT-IR and SEM technique. The XRD study shows formation of cubic spinel structure and lattice constant of $ZnFe_{1.9}Dy_{0.1}O_4$ is 8.4A^o. The FT-IR spectrum shows two absorption bands near the 400cm^{-1} and 600cm^{-1} corresponding to tetrahedral and octahedral sites respectively. The SEM image shows that the grains are irregular in shape and the average grain size is 0.80nm. The DC resistivity of Dy^{3+} substituted $ZnFe_2O_4$ samples shows semiconductor in nature.

Keywords: XRD, IR, SEM, DC resistivity.

INTRODUCTION:

Nowadays, ferrite materials are promising role in the industrial development and technically important in many recent advanced applications such as microwave [1], magneto optical recording [2], multilayer chip inductors [3], magnetic fluids [4], spintronics [5], etc. In 21st century, utmost of researchers concentrated on their research towards the nanomaterial's and its applications. In spinel ferrite materials, adding with different rare earth ions such as Sm^{3+}, Gd^{3+} and Dy^{3+} in ferrite, improvement of ferrite properties in nano-scale and its study in their electrical [6] and magnetic properties for industrial development and also different valency like Zn^{2+} [7], Nd^{3+} [8], Sn^{4+} [9-11], Ti^{4+} [12] ions to improvement of its structural, magnetic, electrical and gas sensing properties. Recently numerous researcher studies on development of its structural and electrical properties are improved in case of pellet, thin and thick films.

Inbanathan et al. [6] reported that the electrical resistivity was improved due to the structural changes induced by the substitution of R^{3+} (R = Sm, Gd and Dy) ions for Fe^{3+} ions at the B-sites and the formation of small amounts of $RFeO_3$ phase was present. Varshney et al. [7] reported that the Sn^{4+} and Zn^{2+} substituted nickel ferrite was prepared by ceramic method and studied for magnetic properties. Balaji et al. [9] reported that the Sn^{4+} substituted $NiFe_2O_4$ were prepared by novel combustion synthetic method. They also studied the structural and electrical properties of these ferrites and the DC electrical conductivity of the Sn^{4+} substituted Ni ferrite found to be increased with increasing temperature. Dy^{3+} doped Co-Zn ferrites were synthesized by sol-gel auto combustion method and to study of ferrite sample with EDAX technique for the confirmation of elements present in the prepared sample [13].

In this present paper, we report the structural and DC Electrical resistivity of $ZnFe_{1.9}Dy_{0.1}O_4$.

EXPERIMENTAL DETAILS:

The nano-sized $ZnFe_{1.9}Dy_{0.1}O_4$ powders were prepared by oxalate co-precipitation method. The AR grade starting materials, Dysprosium sulfate (Sigma Aldrich), $ZnSO_4.6H_2O$ (Thomas baker) and $FeSO_{4.}7H_2O$ (Thomas baker) were dissolved in the double distal water. The ferrite precipitation reaction is chemically written as

$$ZnSO_4 + 2H_2O + \ C_2O_4^{2-} \rightarrow ZnC_2O_4.2H_2O + SO_4^{2-} \quad (1)$$

$$FeSO_4 + 2H_2O + \ C_2O_4^{2-} \rightarrow FeC_2O_4.2H_2O + SO_4^{2-} \quad (2)$$

$$DySO_4 + 2H_2O + \ C_2O_4^{2-} \rightarrow DyC_2O_4.2H_2O + SO_4^{2-} \quad (3)$$

The P^H of solution is maintained by adding H_2SO_4 simultaneously in the prepared solution. The solutions were put in the hot plate at 80^0C for one hour to optimize the ionization of metal sulphates. This solid solution containing dysprosium oxalate, zinc oxalate, ferrous oxalates were heated for one hour on hot plate to settle down the precipitate at the bottom of the beaker. The precipitate was washed and filtered an average of 20th times with distilled water using Quantitative Filter Paper (HiMedia). The removal of sulphate ions was confirmed by barium chloride test and confirms the solution then precipitate was dried on a hot plate and pre-sintered at 170ºC/1h. The pre-sintered powders were milled in an agate mortar and final sintered at 450ºC/2h.

The X-ray diffraction patterns of $ZnFe_{1.9}Dy_{0.1}O_4$ powders was recorded at step size of 0.02° in angular range 10°-90° (2θ) at 30kV, 10mA with Cu-Kα radiation (λ = 1.54184 A°) on Bruker D2 PHASER desktop X-ray powder diffractometer. The micrograph of the ferrite sample was studied with the help of scanning electron microscope (SEM) Hitachi S-4700 (Japan) with X2000 magnifications. The infrared absorption spectrum of ferrite powders was recorded in the range of 300-800cm^{-1} using Perkin Elmer spectrum one spectrometer.

RESULTS AND DISCUSSION:

Structural properties:

The X-ray diffraction pattern of $ZnFe_{1.9}Dy_{0.1}O_4$ is presented in **Fig.1.** From Figure, It is found that, there is no exists extra peak found in $ZnFe_{1.9}Dy_{0.1}O_4$. The presence of (111), (220), (311), (222), (400), (422), (511) or (333), (440) and (533) planes in the patterns confirms the formation of cubic spinel structure.

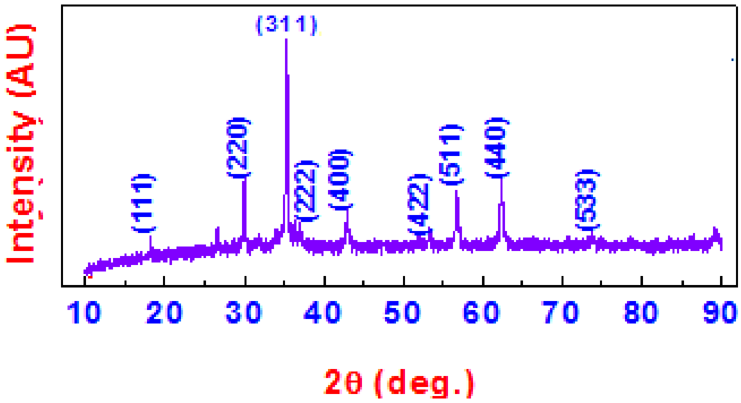

Fig. 1: X-ray diffraction pattern of $ZnFe_{1.9}Dy_{0.1}O_4$

The lattice constant of sample under investigation was calculated by using Bragg's equation [14-15]. The average crystallite size of prepared samples was calculated from the most intense (311) peak of XRD by using a Debye Scherer equation. The average crystallite size of the sample lies in the range 22.54 nm. The calculated value of crystallite size, grain size and lattice constant was presented in the **Table.1**.

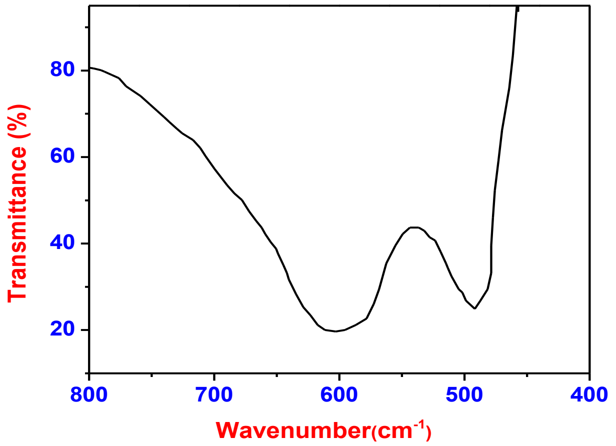

Fig. 2: FT-IR spectra of $ZnFe_{1.9}Dy_{0.1}O_4$

Table 1: The structural parameters of $ZnFe_{1.9}Dy_{0.1}O_4$

Lattice Constant (Å)	Crystallite Size (nm)	Grain Size (nm)	Wavelengths (cm^{-1})	
			υ_1	υ_2
8.3820	22.54	80	574	471

The FT-IR spectrum of $ZnFe_{1.9}Dy_{0.1}O_4$ was presented **Fig. 2.** It can be seen that, there are two bands present in the prepared ferrite system in the range 400–800 cm^{-1}. The values of absorption bands υ_1 and υ_1 are presented in **Table 1.** From figure, it can be seen that two major absorption bands near about 400 cm^{-1} and 600 cm^{-1} of octahedral and tetrahedral sites respectively and FT-IR spectra for several ferrites have been reported by Waldron [16]

The SEM of nanocrystalline $ZnFe_{1.9}Dy_{0.1}O_4$ was presented in **Fig. 3.** From this figure, it is noticed that, the grain are not in regular shape the grain size of the sample was calculated by the linear intercept method [17] and is presented in **Table.1.**

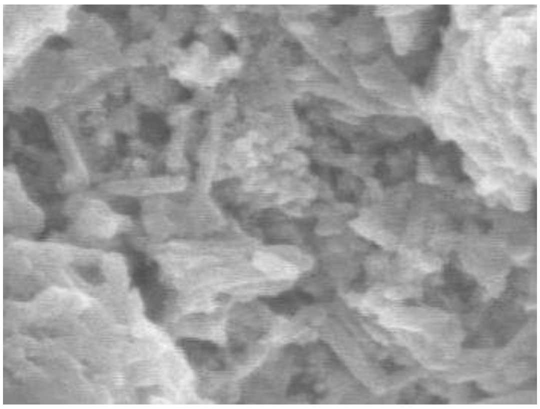

Fig. 3: SEM image of $ZnFe_{1.9}Dy_{0.1}O_4$

DC Electrical resistivity of $ZnFe_{1.9}Dy_{0.1}O_4$:

The DC resistivity of nano-sized of $ZnFe_{1.9}Dy_{0.1}O_4$ was measured by using two probe methods and it is presented in **Fig. 4.** From this figure, it was noticed that the DC resistivity of FTFs was decreasing with increasing in temperature; it shows the semiconductor nature of the ferrite [14]. The room temperature DC resistivity lies in the range of 17.9 to 20.6x10^7 Ω.cm is higher values of bulk sample reported by Shinde et al. [14] in Nd^{3+} substituted Ni-Zn ferrite. Shinde et al. [15] reported that the room temperature DC resistivity of Nd^{3+} substituted zinc ferrite is 10^2 times larger than the pure zinc ferrite. The decrease in resistivity might be understood as due to the formation of grain growth and decrease of grain size.

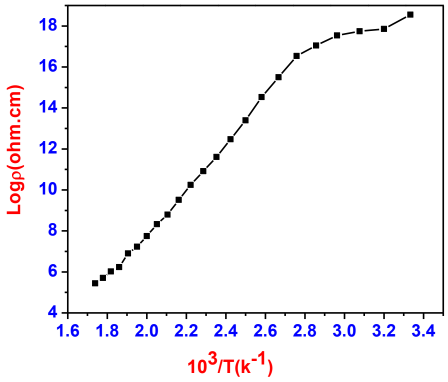

Fig. 4: Variation of logρ with temperature of $ZnFe_{1.9}Dy_{0.1}O_4$

CONCLUSIONS:

A simple useable oxalate co-precipitation method is used to prepare the nano-sized the $ZnFe_{1.9}Dy_{0.1}O_4$ and characterized by XRD, FT-IR and SEM techniques. The X-ray diffraction pattern confirms the formation of cubic spinel structure and its lattice constant is 8.4A^o. The FT-IR spectrum shows two absorption bands near the 400cm^{-1} and 600cm^{-1} corresponding to tetrahedral and octahedral sites respectively. The average grain size of the $ZnFe_{1.9}Dy_{0.1}O_4$ sample calculated by linear intercept method using SEM image, it shows that the grains are irregular in shape. The electrical resistivity of prepared $ZnFe_{1.9}Dy_{0.1}O_4$ samples shows semiconductor in nature.

REFERENCES:

1. Harris VG, et alJ. Magn. Magn. Mater., 321:2035-2047 (2009).
2. Martens J, Voermans A, IEEE Trans., 20: 1007-1012 (1984).
3. Krishnaveni T, Kanth BR, Raju VSR, Murthy SR, J. Alloy. Comp. 414:282–286 (2006).
4. Lin M, Huang J, Sha M., J. Nanosci. Nanotechnol., 14(1) :792-802 (2014).
5. Luders BU, Barthelemy A, Bibes M, Bouzehouane K, Fusil S, Jacquet E, Contour JP, Bobo JF, Fontcuberta J, Fert A, $NiFe_2O_4$: Adv. Mater.18:1733-1736 (2006).
6. Inbanathan SSR, Vaithyanathan V, Chelvane JA, Markandeyulu G, Bharathi KK Mossbauer, J. Magn. Magn. Mater. 353:41-46 (2014).
7. Varshney U, Puri RK. IEEE Tran. Magn. 25:3109-3116 (1989).
8. Shinde TJ, Gadkari AB, Vasambekar PN, J. Magn. Magn. Mater. 322:2777-2781 (2010).
9. Balaji S, Selvan RK, Berchmans LJ, Angappan S, Subramanian K, Augustin CO, Mater. Sci. Eng. B. 119:119-124 (2005).
10. Rao ADP, Ramesh B, Rao PRM, Raju SB, J. Alloy. Comp. 282: 268-273 (1999).
11. Tewari BS, Dhyani A, Joshi SK, Dubey S, Pandey K, Hindawi Pub. Corp. 816970.
12. Vaithyanathan V, Ugendar K, Chelvane JA, Bharathi KK, Inbanathan SSR, J. Magn. Magn. Mater. 382: 88-92 (2015).
13. S.R. Kulal, S.S. Khetre, P.N. Jagdale, V.M. Gurame, D.P. Waghmode, G.B. Kolekar, S.R.Sabale,S.R.Bamane, Mater. Lett. 84: 169-172 (2012).
14. Shinde TJ, Gadkari AB, Vasambekar PN, Mater. Chemi. Phys. 111:87-91 (2008).
15. Shinde TJ, Gadkari AB, Vasambekar PN, J. Magn. Magn. Mater. 322:2777-2781 (2010).
16. R.D. Waldron, Phys,Rev.99,1727-1735 (1955).
17. J.C. Wurst and J.A. Nelson, J. Amer.Ceram.Soc., 55,109-109 (1972).

SYNTHESIS AND ELECTROCHEMICAL CHARACTERIZATIONS OF VANADIUM HYDROXIDE THIN FILMS

Y. S. Kokare* and B. J. Lokhande

School of Physical Sciences, Solapur University, Solapur, INDIA

*Corresponding author E-mail: yogeshrikokare@yahoo.in

ABSTRACT:

Electrochemically synthesized Vanadium hydroxide and oxide thin films were deposited on stainless steel substrate (1.5cm x 5cm) by using 0.15 M aqueous Sodium metavanadate as a precursor solution. Electrodeposited samples were characterized for structural, morphological, elemental and electrochemical analysis using X – ray diffraction, FE-SEM, EDAX, cyclic voltammetry. Both electrodes shows mixed capacitive behavior. The highest specific capacitance of vanadium hydroxide (annealed at 300 K for 1 hr) is 105.66 at 5 mV/sec scan rate in 1 M Na_2SO_4. Charge discharge behavior exhibits specific energy 1.0251 and 297.57 Wh/kg, specific power 7.384 and 24.00 kW/kg and columbic efficiency 99.70 for the vanadium hydroxide electrodes.

INTRODUCTION:

The increasing demand of energy and power, storage device like supercapacitor should be designed [1]. The changing climate and the limited availability of fossil fuels have greatly affected the world economy and ecology [2]. With fast-growing market for portable electronic devices and the development of hybrid electric vehicles, there has been an ever increasing and urgent demand for environmentally friendly high-power energy resources [3]. Supercapacitor, also known as electrochemical capacitors or ultra capacitors, have attracted much attention because of their pulse power supply, long cycle life, simple principle, and high dynamic of charge propagation. Supercapacitor is the capacitor which has high energy density as compared the normal or convention capacitor and high power density as compared to the batteries. In a supercapacitor, the electrical energy is stored in electrolytic double layer capacitors based on Helmholtz's double layer occurs at the surface of electrode and electrolyte interface.

Vanadium is a transition metal oxides which have various forms e.g. $H_2V_3O_8$, V_2O_5, and $V_6O_{13.}$ Vanadium oxide shows amorphous, porous (fig.1), more oxidation state, 3-D network architecture exhibiting very high intercalation reversibility [5], $V_6O_{13,}$ has been widely used as cathode material for lithium ion battery because of their high specific capacitance. It exhibits excellent pseudo-capacitance property with potential window1V in organic and aqueous electrolytes [6]. V_6O_{13} has a blended valence of V (IV) and V (IV) which is favorable for increasing the electronic conductivity and these are promising material in supercapacitorelectrode [7]. Nanostructured

Vanadium nitride (VN) shows specific capacitance (SC) 1340 F/g in 2 mV/sec. and 554 F/g in100 mV/sec [8, 9].

EXPERIMENTAL:

Molar weight concentration of vanadyl sulfate solution is dissolved in distilled water. Initially 0.1M solution of vanadyl sulfate was dissolved in double distilled water. Then thin flexible stainless-steel (SS) substrates (no-304), on which V_2O_5 deposition has to carry were well cleaned. Initially, 20 ml of above prepared vanadyl Sulphate 0.1 M solution was taken in a beaker as a precursor. Then SS substrates were dipped into the precursor solution and set deposition potential at 2.45 V and deposition held for 30 min. The deposited films of vanadium hydroxide thin films were thereafter carried for structural and electrochemical characterizations.

RESULT AND DISCUSSION:

Structural analysis (XRD & SEM):

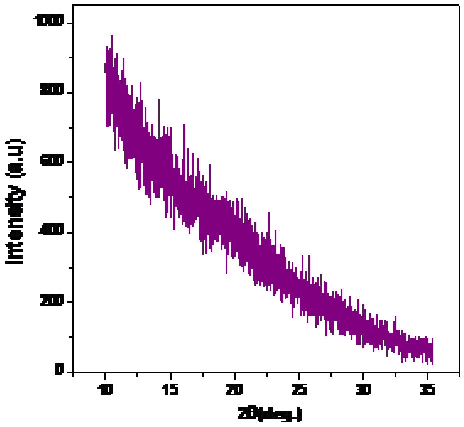

Fig. 1 XRD of vanadium hydroxide

In order to study crystalline nature, type of crystal structure, orientation of planes of the thin films was observed using XRD patterns were recorded in the 2θ range 10–100°. The XRD study was carried out for all samples to be determining the structure of the films, orientation and grain size. Fig. 1 shows the XRD pattern for the sample. The X – ray diffraction pattern shows number of peaks indicating the deposited material is crystalline. The observed 'd' value matches properly with standard'd' values taken from ASTM data card [73-0513]. As deposited samples exhibits triclinic crystal structure

Low and high magnification FE-SEM images of sample prepared are shown in Fig 2. It is clear that the morphology of vanadium oxide material is ring shaped.

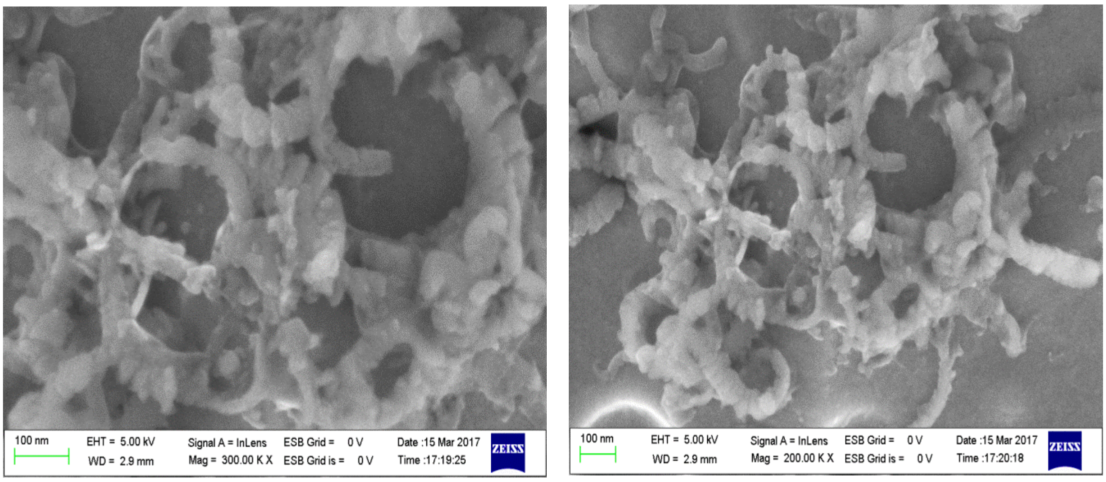

Fig. 2: FESEM image of vanadium hydroxide

2 EDAX:-

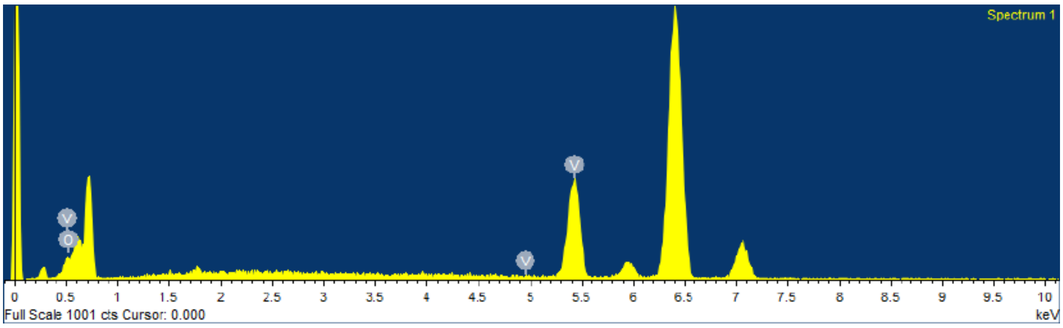

Fig. 3: The elemental analysis of the prepared samples

Elements	Weight %	Atomic %
O	39.77	67.77
V	60.23	32.23
Total	100.00	100.00

The elemental analysis of the prepared sample was carried out using EDAX.Fig.5.3 shows the EDAX spectra for iron hydroxide samples.The EDAX spectra shows the elemental peaks of O this is favorable for super capacitive properties and increase electrical conductivity of electrode ,also may effect on morphology change of Iron oxide electrode which is analogous to FE-SEM result .

Cyclic voltammetry:

In order to study the capacitive performance of vanadium oxide electrodes, cyclic voltammograms were carried out in 1M $NaNo_3$ electrolyte in the voltage range 5 to 100mV. CV behavior and specific capacitance (SC) associated with the electrode was calculated using the relations reported in the literature and detail explanation regarding super capacitor are given in.

$$C = \frac{\int Idt}{dv/dt} \qquad (1)$$

$$SC = \frac{C}{W} \qquad (2)$$

Where, $\int Idt$ = is the area under curve, $\frac{d_v}{d_t}$ = voltage scan rate, C = Capacitance, W = weight of the material dipped in the electrolyte.

CV studies for the capacitive behavior and performance of vanadium hydroxide electrodes, cyclic voltammograms were carried out in 1 M Na_2SO_4 electrolyte in the voltage range –1.4 to 0.2 V. The optimized (0.15 M) aqueous vanadium hydroxide electrode was carried for CVs in 1 M Na_2SO_4. The calculated values of SC for different scan rate are tabulated in table 5.1. It was observed that when scan rate increase area under curve increases SC goes on decrease and at lower scan rate shows highest value of SC 105.66 F/g. It may attribute to scan rate effect at higher scan rate there is improper ionic intercalation.

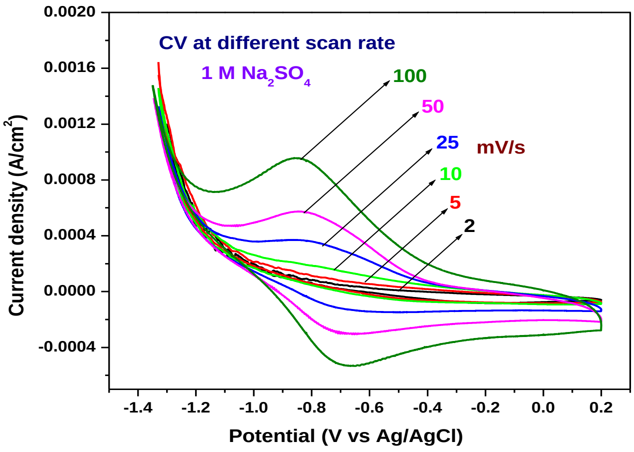

Fig. 4: CVs of vanadium hydroxide

Table 1:Variation of SC with change in scan rate of vanadium hydroxide electrode

Scan rate mV/sec	Capacitance	Specific Capacitance
5	0.013736	105.6615
10	0.01075	82.6923
25	8.964×10^{-3}	68.9538
50	7.402×10^{-3}	56.9384
100	6.552×10^{-3}	50.4

CONCLUSION:

Synthesis of vanadium hydroxide nanocrystalline thin films by Electrodeposition is possible. XRD shows Triclinic crystal structure with crystalline in nature. Sample shows good specific capacitance and charge discharge test.

REFERENCES:

1. NASA Glenn Research Center (NASA-GRC).
2. www.wikipedia.co.in
3. A.K. Geim and K.S. Novoselove , Nat. Mater (2007).
4. www.wikipedia.co.in
5. Chi-Chang Hua, Chao-Ming Huang, Kuo-Hsin Chang, J. Power Sources, 185, 1594–1597 (2008).
6. D.W. Murphy, P.A. Christian, F.J. Disalo, J.N. Carides, J. Electro. Society, 126, 497–499 (1979).
7. H.M. Zeng, Y. Zhao, Y.J. Hao, Q.Y. Lai, J.H. Huang, X.Y. Ji, Journal of Alloys and Compounds, 477, 800–804 (2009).
8. D.W. Choi, G.E. Blomgren, P.N. Kumta, Advanced Materials, 18, 1178 (2006).
9. D.W. Choi, P.N. Kumta, Electrochem. Solid-State Lett., 8, A418 (2005).

HYDROTHERMALLY SYNTHESIZED SnO_2/RGO NANOCOMPOSITE AS NO_2 SENSOR

Bhagyashri Bhangare[1], Nitin R. Linge2, Niranjan Ramgir[2], S. K. Gupta[2], D. K. Aswal[3], K. P. Muthe[2], S. C. Gadakari[2] and Suresh Gosavi[1]*

[1]Centre for Advanced Studies in Material Science and Solid-State Physics,
Department of Physics, Savitribai Phule Pune University, Ganeshkhind, Pune-411007, India
[2]Technical Physics Division, Bhabha Atomic Research Centre (BARC),
Mumbai -400085, India
[3]National Physics Laboratory, Delhi, India
*Corresponding author E-mail: swg@physics.unipune.ac.in

ABSTRACT:

In the present work, the attempt is being made to synthesize SnO_2/RGO nanocomposite by using hydrothermal route. The structural characterization of synthesized nanocomposite was carried out by using XRD and TEM. The synthesized nanocomposite shows excellent response of about4-fold change of magnitude (Rg/Ra) towards threshold limit of 5ppm NO_2 at working temperature of 180^0C.The response and recovery times of the sensor were found to be5 and 20 sec, respectively.

INTRODUCTION:

Nitrogen dioxide (NO_2) gas sensors have attracted considerable interest in research area, because it is harmful to respiratory system of living organisms, plants and ozone layer depletion. So, in order to detect trace amount of NO_2,various detection techniques like chemiluminescence, chromatography, spectrophotometry has been studied. These techniques having main drawback of time line required for analysis. The chemiresistive gas sensors have overcome these drawbacks and are having simple and easy operation. Various nanocomposites like ZnO/RGO,V_2O_5, MoO_3, NiO-CuO [1] have been already reported for NO_2 gas sensing application. Most of metal oxide nanostructures shows good sensor response at higher temperature as it supports more energy to accelerate the charge carriers between the analyte and sensing material[2]. Among these various reported nanomaterials, graphene is the most exciting one, because it has capacity to detect single molecule adsorption and desorption from its surface. In the present work, we have synthesized SnO_2-RGO nanocomposite using hydrothermal route and it is used for NO_2 sensing application.

EXPERIMENTAL:

The synthesis of SnO_2/RGO nanocomposite is being carried out by using hydrothermal route at 180^0C for 7 h. After cooling down to room temperature, the obtained solution was centrifuged by using ethanol and dried in oven at 90^0C to obtain the powder.

RESULT AND DISCUSSION:

The structural characterization of the synthesized SnO_2/RGO nanocomposites was carried out by using XRD and TEM. The XRD results shows that all the diffraction peaks in the XRD pattern (fig.1a) of SnO_2/RGO nanocomposite are indexed to tetragonal structure of SnO_2. The strong intense peak at $2\theta=26.61°$ due to (110) plane of SnO_2 nanoparticles which is overlaps on (002) peak of RGO.

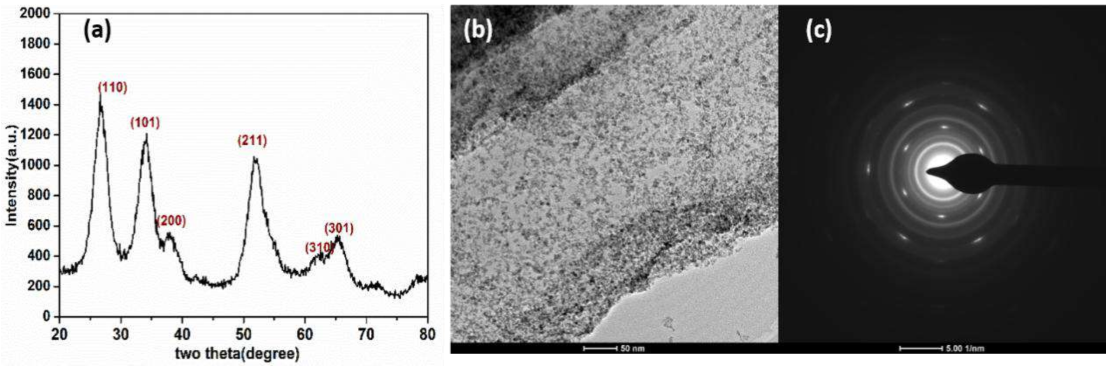

Fig. 2: a) XRD pattern of SnO_2-RGO nanocomposites,b) TEM image of SnO_2-RGO nanocomposite c) SAED pattern of SnO_2/RGO nanocomposites

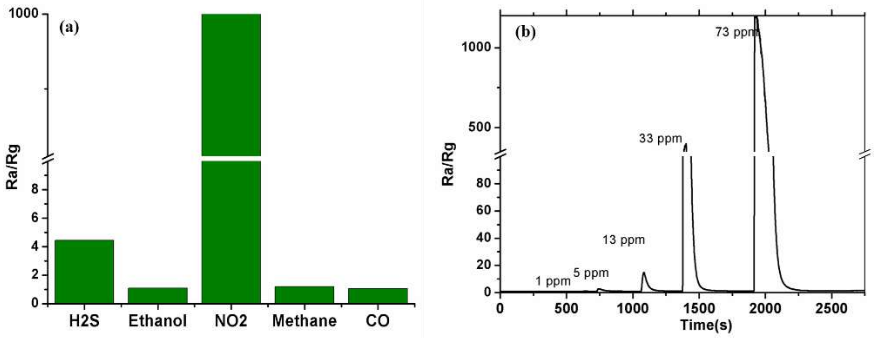

Fig. 2: a) Selectivity of SnO_2-RGO nanocomposite towards different analytes (73 ppm), b) Sensor response toward different gas concentrations of NO_2

The TEM micrographs of the nanocomposites were shown in figure 1b, which clearly shows the decoration of SnO_2 nanoparticles on the RGO nanosheets. The SAED (fig. 1c) shows hexagonal ring pattern along with polycrystalline rings indicates the formation of SnO_2 nanoparticles on RGO sheets. The gas sensing measurement of NO_2 gas were carried out by using well calibrated static gas sensing unit along with data acquisition. The selectivity of the sensor was studied for 73 ppm of hydrogen sulphide, Ethanol, Methane, Carbon monoxide and Nitrogen dioxide, as shown in figure 2a.

The selectivity histogram of the gas sensor shows minimum response to the other analytes and shows best selectivity for NO_2 of about more than 1000 times with response time of about 5 seconds and recovery time of 20 seconds which is effective over some of the reported one[3,4,5].Further the sensor response is also checked for various concentration of NO_2 as shown in figure2b, from which the 4-fold change in resistance was observed at 5 ppm NO_2 concentration. The gas sensing mechanism for the n-type SnO_2 and p-type RGO is mainly attributed to formation of the heterojunctions at the interphase which helps to enhance the NO_2 sensor response.

CONCLUSION:

In conclusion, the synthesis of SnO_2/RGO nanocomposite has been carried out by using hydrothermal route which consists of excellent NO_2 sensing characteristics which may leads to the effective contribution to the NO_2sensing materials.

ACKNOWLEDGMENT:

One of the authors, BB would like to acknowledge BARC-SPPU collaborative program for financial support(GOI-E-177).

REFERENCES:

1. Ziyue Zhang, Mahmood haq, Zhen Wen, Zhizhen Ye, Liping Zhu, J. App. Sur. Sci. (2017).
2. Lei Li, Shuijian He, Minmin Liu, Chunmei Zhang,and Wei Chen, Analytical Chemistry, 87, 1638−1645 (2015).
3. A.A. Mane, M.P. Suryawanshi, J.H. Kim, A.V. Moholkar, J. App. Sur. Sci., 403, 540–550 (2017).
4. S.S. Shendage, V.L. Patil, S.A. Vanalakar, S.P. Patil, N.S. Harale, J.L. Bhosale,J.H. Kim, P.S. Patil, Sensors and Actuators B, 240, 426–433 (2017).
5. Yong Jung Kwon, Ali Mirzaei, Sung Yong Kang, Myung Sik Choi, Jae Hoon Bang, Sang Sub Kim, Hyoun Woo Kim, Applied Surface Science, 413, 242–252 (2017).

POROUS NICKEL OXIDE ARCHITECTURE FOR PSEUDO-CAPACITOR APPLICATION

Ramchandra S. Kalubarme[1], Chiaki Terashima[2] and Suresh Gosavi[1*]

[1]Centre for Advanced Studies in material Science and Solid State Physics, Department of Physics, SavitribaiPhule Pune University (Formerly University of Pune),
Ganeshkhind, Pune- 411007, INDIA

[2]Photocatalysis International Research Center, Research Institute for Science & Technology, Tokyo University of Science, 2641 Yamazaki, Noda, Chiba 278-8510, JAPAN

*Corresponding author E-mail: swg@physics.unipune.ac.in

ABSTRACT:

Nickel oxide (NiO) has been explored as most favourable electrode materials for pseudo-capacitor applications due to its high theoretical specific capacitance. Herein, a porous architecture of NiO-Ni composite prepared using simple glycine-nitrate solution combustion process is explored as electrode for pseudo-capacitor. Well-connected particles sizing 100-150 nm forms the porous network and delivered excellent capacitive performance exhibiting specific capacitance of 662 $F \cdot g^{-1}$. Moreover NiO-Ni electrode also demonstrated superior cycling performance retaining almost the same capacity throughout 1000 cycles. The excellent performance of NiO-Ni architecture is due to the synergetic effect possibly contributed from porous Ni-interconnected NiO structure, which not only provides the channels for electrolyte diffusion but also improve the kinetics as well as utilization of entire material.

INTRODUCTION:

Supercapacitors, also known as ultracapacitors or electrochemical capacitors, warrant broad important applications in electric vehicles and mobile power sources due to the unique combination of their rapid charge–discharge behaviour and higher specific power density. In general to develop a capacitor, having high rate of operation with sufficient energy capacity, it is essential to engineer novel material architectures. For supercapacitor applications, three types of materials are being considered, including carbon based materials, transition metal oxides (TMOs), and conducting polymers.Out of these, TMOs especially NiO have attracted considerable attention as pseudo-capacitive electrode materials due to their outstanding properties, including low cost, high theoretical capacitance value (2,584 $F\ g^{-1}$ within 0.5 V) ,and excellent chemical and thermal stability [1-2]. However, dense morphology and poor electrical conductivity possessed by NiO negatively impact the electrochemical performance of the devices. Therefore, strategies like modification with nanostructured carbon [2], preparation of Ni-NiO nanocomposites [1], and synthesis of nanostructures [3-5], have been proposed to improve the NiO supercapacitor performance.

Hence, in the present work, attempts have been made to prepare porous architecture of an interconnected conductive Ni network on the surface of NiO through partial reduction of NiOusing simple process and explore the material for supercapacitor application.

EXPERIMENTAL SECTION:

A facile solution combustion technique has been employed for the synthesis of NiO. In particular process nitrate precursors of Ni (Sigma Aldrich 99.9%) was used as source of metal ion and glycine (Sigma Aldrich 99.9%) was used as oxidizer. The aqueous solutions of oxidizer was added to solution of metal ions and then mixed thoroughly to obtain homogeneous solution. The final ratio of metal ion to oxidizer was maintained to 1:1. The formed solution was converted into gel by keeping it on magnetic stirrer with heating arrangement. Finally the gel was maintained at 170 ^{o}C for 5 hours to complete the combustion reaction. The obtained ash was further annealed at 450 ^{o}C for 4 hours in inert atmosphere.

The microstructure, surface morphology and chemical composition of synthesized materials were examined by a RIGAKU D/Max Ultima III high-resolution X-ray powder diffractometer (HR-XRD) operated at 40 kV over a 2-theta range of 20-80 ^{o} and a HITACHI S-4700 field-emission scanning electron microscope (FESEM).

The testing electrodes were prepared by screen printing of paste containing active material, conducting carbon and polyvinylidene fluoride binder in the weight ratio of 8:1:1 on conducting substrate. A three electrode cell assembly containing prepared electrode as working, Pt as counter and Hg/HgO as reference electrode, was employed to record cyclic voltammograms for charge storage in the potential range of 0 V to 0.55 V at scan rates of 10 -100 $mV\cdot s^{-1}$.

RESULT AND DISCUSSION:

The powders that were obtained through the glycine assisted solution combustion reaction followed by annealing at 450 ^{o}C showed characteristic well-defined XRD pattern, thereby indicating the polycrystalline nature of the material, as shown in Fig. 1a. The powder sample display 4 peaks at $2\theta = 37.1^{o}$, 43.1^{o}, 62.7^{o} and 75.3^{o}, which are indexed to (111) (200) (220) and (311) peaks from cubic structured NiO (JCPDS No 47-1049).Moreover additional peaks at $2\theta = 44.5^{o}$ and51.8^{o}areindexed to the (111) and (200) peaks of metallic Ni with face-centred-cubic (fcc) structure. These two peaks have relatively low intensities than peaks of NiO confirming the smaller amount of Ni that could interconnect the NiO particle and enhance its electrical conductivity. In XRD pattern, the position and the intensity of the reflection are generally determined by the unitcellsize and the distribution of the atoms in the unit cell, respectively. Therefore, every individual compound has its own XRD-pattern “fingerprint”. The presence of all of the reflection peaks that correspond to the NiO and Ni in the annealed sample confirms that the obtained sample is composed of NiO and Ni.

FE-SEM were performed to investigate the morphology of the prepared sample. The NiO-Ni composite maintained well-connected structure of spherical particles. This interconnection of Ni and NiO particles forms the large number of pores on the surface. Further clear inspection of SEM image (Fig. 1b) reveal that the particle size of the NiO-Ni composite ranges between 100-150 nm. This porous network formed with interconnection of Ni and NiO will be useful for efficient transport of electrons and ions during faradic reaction at elevated rates.

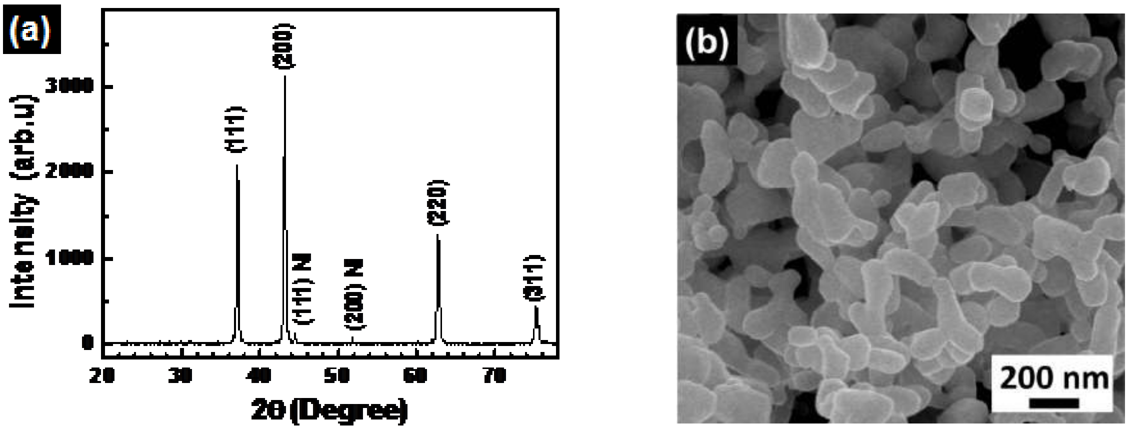

Fig. 1: (a) XRD pattern, (b) FE-SEM image of combustion synthesized Nickel oxide-Ni powder

Electrochemical Performance:

To investigate electrochemical performance of NiO-Ni composite, three electrode cell comprising NiO-Ni electrode as working, Pt as counter and Hg/HgOas reference electrode in 2M KOH electrolyte was used to record cyclic voltammogram (CV) in potential window 0 – 0.55 V. Fig.2a shows CV plot of NiO-Ni at different scan rates of 10, 20, 50, 75 and 100 $mV{\cdot}s^{-1}$. In the CV curve recorded at scan rate of 10 $mV{\cdot}s^{-1}$, a well-defined pair of redox peaksis observed in the potential window of 0.2- 0.45 V arising from the redox reaction shown in equation 1 [6].

$$\mathrm{NiO} + \mathrm{OH^-} \leftrightarrow \mathrm{NiOOH} + \mathrm{e^-} \qquad (1)$$

Further, it is observed that, while increasing the scan rates, redox peak intensities increases with slight peak shift towards higher potential, which was evidence of fast redox reactions occur at the interface between the active material and electrolyte. Generally, the rate capability was mainly dependent on three processes such as (i) the charge transfer in the electrode, (ii) the adsorption of ions on the electrode surface and (iii) the diffusion of electrolyte ions. Any of these processes is relatively slow at higher scan rate which reduces the specific capacitance of the composite. The capacitance of active material was calculated by integrating the area of the CV curve. The NiO-Ni porous material had a specific capacitance of 662 $F{\cdot}g^{-1}$ at scan rate of 10 $mV{\cdot}s^{-1}$. In case of NiO-Ni composite Ni spherical particles provided highly conductive network for NiO particles, due toits uniform dispersion within the powder sample. Moreover the porous structure led to increase the electrochemical surface areas via increasing the internal active sites of NiO. The characteristic shape of the CV curve was not significantly changed, which was an indication that the NiO-Ni composites have an outstanding rate capability.

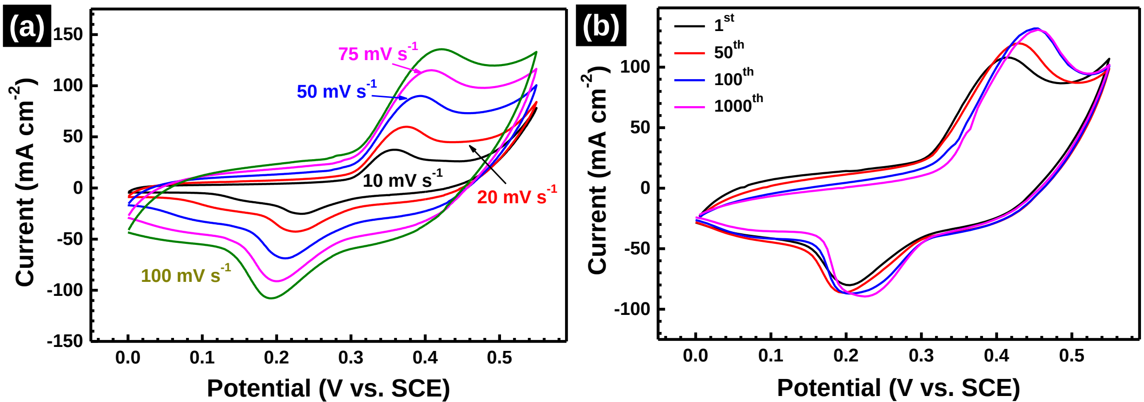

Fig. 2: (a) CV curves at different scan rates 10-100 mV·s^{-1}, (b) CV curves recorded during cycling at scan rate of 50 mV·s^{-1} for NiO-Ni electrode in 2M KOH electrolyte

The electrochemical stability of NiO-Ni composite was evaluated in three electrode cell by recording the cyclic-voltammograms at higher scan rate of 50 mV·s^{-1}, as shown in Fig. 2b. It retained 100% of its initial capacitance after 1000 cycles, demonstrating that the NiO-Ni sample has reasonable electrochemical stability and cycle reversibility.

CONCLUSION:

An interconnected conductive Ni network on the surface of the porous NiO was fabricated successfully using cost effective and simple glycine assisted combustion synthesis, making the material more electrically conductive and considerably improves the electrochemical performance. The composite electrodes exhibited higher specific capacitance of 662 F·g^{-1} and demonstrated highly reversible capacitive nature.

REFERENCES:

1. J.H. Kim, S.H. Kang, K. Zhu, J.Y. Kim, N.R. Neale, A.J. Frank, Chem. Commun., 47, 5214–5216 (2011).
2. B. Zhao, J. Song, P. Liu, W. Xu, T. Fang, Z. Jiao, H. Zhang, Y. Jiang, J. Mater. Chem., 21, 18792–18798 (2011).
3. Q. Lu, J.G. Chen, J.Q. Xiao, Angew. Chem. Int. Ed., 52, 1882–1889 (2013).
4. X. Xia, J. Tu, Y. Zhang, X. Wang, C. Gu, X.B. Zhao, H.J. Fan, ACS Nano, 6, 5531–5538 (2012).
5. S. K. Meher, P. Justin, G.R. Rao, Nanoscale, 3, 683–692 (2011).
6. S. Ci, Z. Wen, Y. Qian, S. Mao, S. Cui, J. Chen, Sci. Rep., 5, 11919 (2015).

SOL-GEL SYNTHESIS OF ZIRCONIA THIN FILMS USING SPIN-COATING TECHNIQUE

Uzma K. H. Bangi[1*], Prashant P. Rupnar[1], Hemant A. Kalel[1] and Hyung-Ho Park[2]

[1]School of Physical Sciences, Solapur University, Solapur - Pune National Highway,
Kegaon, Solapur - 413 255, Maharashtra, India

[2]Department of Materials Science and Engineering,
Yonsei University, Seoul 120-749, Republic of Korea

*Corresponding author E-mail: uzma.phys@gmail.com, Tel.: +91 217 2744771*154

ABSTRACT:

In the present paper, the experimental results on some textural properties of zirconia thin films synthesized using different concentrations of polyvinyl alcohol (PVA) as a polymeric additive are reported. The zirconia thin films were prepared by sol-gel method and spin coating technique. The volume ratio of ZrPr:PrOH:EAA:PVA:Catalyst was fixed at 2:6:1:0.2:0.6 respectively, throughout the experiments, and two different catalyst as well as the weight % of PVA was varied accordingly. The BET surface area and pore size distribution of zirconia thin films were measured using N_2 adsorption-desorption analysis. Field emission scanning electron microscopy (FESEM) was employed to study the influence of various PVA concentrations on the morphology of zirconia thin films.

Keywords: Polyvinyl alcohol; Sol-gel; Spin coating, Zirconia, Thin films

INTRODUCTION:

Sol-gel technology offers efficient and high purity production of nanopwders, fibers, solid structures and thin film coatings [1]. In general for the synthesis of thin films, sol-gel deposition of material on the substrate and drying of these films are the basic steps. So, in the present work also sol-gel process is employed to obtain porous, thin and uniform zirconia films. Zirconia is a unique material of excellent thermal stability, high surface area and chemical inertness [2]. Different precursors like zirconium salts, alkoxides and different deposition techniques such as spin coating, dip coating etc. are used for the synthesis of porous zirconia thin films [3, 4]. Zirconia highly reacts with water and forms precipitate during hydrolysis, therefore the precipitate of zirconia can be postponed by addition of a stabilizer like ethyl acetoacetonate (EAA). The kind and amount of catalyst and the addition of polymeric additive have a strong impact on the properties of thin films. All these parameters influence the hydrolysis-to-condensation ratio and thereby determine the properties of the resulting sol–gel product. Therefore, in the present work attempts have been made to synthesize sol-gel based zirconia thin film by spin coating technique and influence of two different catalyst namely acetic and oxalic acids along with the different concentration of polyvinyl alcohol was studied.

EXPERIMENTAL:

The chemicals used for the synthesis of zirconia thin films were zirconium n-propoxide (70% in n-PrOH, Sigma-Aldrich) as a precursor, n-propanol (n-PrOH) as a solvent, ethyl acetoacetonate (EAA, Fluka) as a stabilizer, acetic acid (CH_3COOH) and oxalic acid ($C_2H_2O_4$) (Sigma-Aldrich) as catalysts, polyvinyl alcohol (PVA) (Sigma-Aldrich) as polymeric additive. Double distilled water was used for the preparation of all the solutions.

The synthesis route for the zirconia thin films is depicted in figure 1. The zirconia depositions were taken on the Si wafers having thickness of 525 μm with 100 orientations. At first, these substrates were cut into the 2x2 cm^2 area. These substrates were subsequently cleaned with acetone, ethanol and D.I. water (in ultrasonic bath for 10 mins.), then subjected to drying at 70°C in oven to remove the water on the substrates.

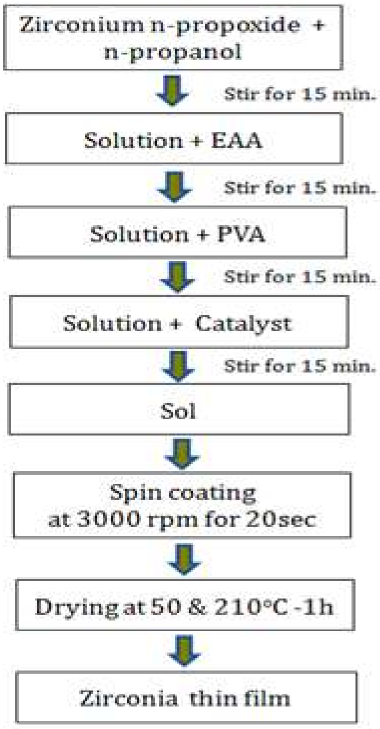

Fig. 1 Flowchart for the synthesis of zirconia thin films

The influence of two different acids such as acetic (2.5 mM), oxalic (10 mM) acids and different concentrations of PVA on the morphology and surface area of zirconia thin films were studied. During the experiments the volume ratio of Zirconium n-propoxide::EAA::polymer::catalyst was fixed at 2::1::0.2::0.6.

The surface area and pore size distribution of the zirconia powder were determined using N_2 adsorption desorption analysis (TriStar 3000 V6.05 A). The morphological investigation of the powder samples was carried out by field emission scanning electron microscopy (FESEM, JEOLJSM-600F).

RESULTS AND DISCUSSION:

It is observed that surface tension and viscosity of the polymeric additive controls the pore sizes and the liquid vapor pressure of the porous network. Therefore, the influence of different concentrations PVA on the morphology and surface area of zirconia thin films have been studied. Fig. 2 exhibited the SEM images of zirconia thin films prepared using PVA (1 wt%) for two different catalyst i.e. acetic acid (2.5mM) and oxalic acid (10mM). From fig. 2 (a), zirconia films synthesized using acetic acid (2.5 mM) have uniform particles without any crack. Therefore, for further study of variation in PVA concentrations, acetic acid (2.5 mM) was used as catalyst.

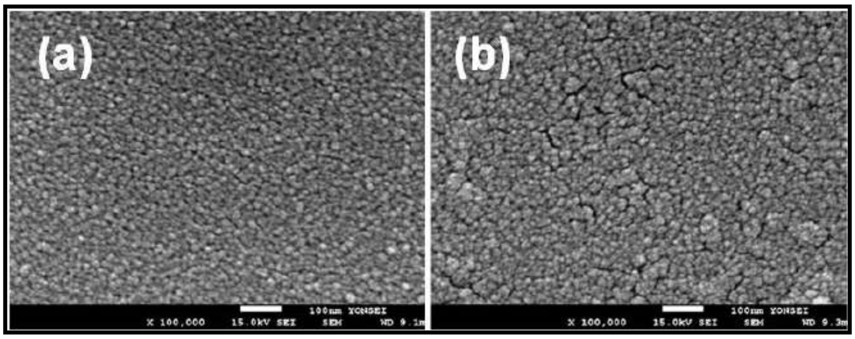

Fig. 2 FESEM images of zirconia thin films prepared using (a) Acetic acid (2.5 mM), (b) Oxalic acid (10 mM)

The FESEM images of pristine zirconia thin film and films prepared using various concentrations of PVA are shown in fig. 3. From fig. 3 (b & c), it seems that films prepared using PVA (0.5 & 1.0 wt%) are crack free with small and uniform particles morphology.

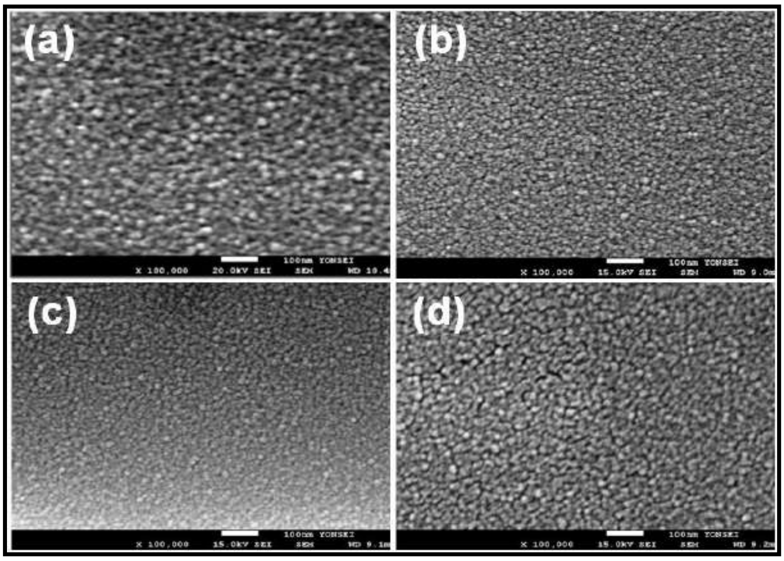

Fig. 3 FESEM images of zirconia thin films (a) pristine, prepared using (b) PVA (0.5 wt%), (c) PVA (1.0 wt%), (d) PVA (2.0 wt%)

Fig. 4 shows the N_2 adsorption-desorption isotherms and pore size distribution of zirconia thin films prepared using various concentrations of PVA. From fig. 4 (a) it is observed that zirconia films prepared using PVA (0.5 & 1 wt%) manifested type-IV isotherm with a narrow pore size distribution with a sharp peak centered at around 38 Å. Zirconia films prepared using PVA (0.5 wt%) have larger surface area (45 m^2/g) than other sample with pore volume of 0.06 cc/g and average pore diameter of nearly 46 Å. The reason behind it may be, the addition of PVA (0.5 wt%) helps to reduce the capillary pressure and sustain the network structure during drying.

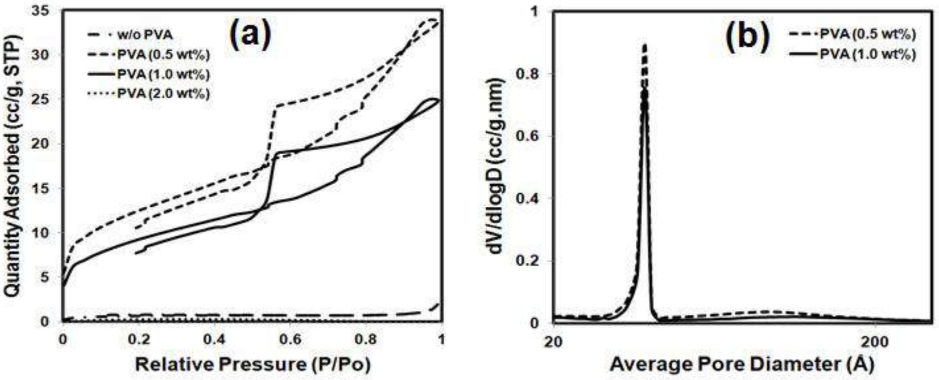

Fig. 4: N_2 adsorption-desorption isotherm and pore size distribution of zirconia thin films prepared using PVA

CONCLUSIONS:

The zirconia films were prepared using sol-gel method and sping coating technique. Addition of polyvinyl alcohol resulted in larger surface area (45 m^2/g) zirconia thin films.

ACKNOWLEDGMENTS:

This study was financially supported by the Department of Science and Technology – Science & Engineering Research Board (DST-SERB), New Delhi, through a major research project on “aerogels” (no. SB/FTP/PS-030/2014). One of the authors, Uzma K. H. Bangi, is very grateful to the DST-SERB for Young Scientist Fellowship under fast-track scheme.

REFERENCES:

1. H. Choi and B. B. Nissan, J. Australian Ceramic Soc. 50(1), 121-136 (2014).
2. S. Chang, R. Doong, Thin Solid Films, 489, 17-22 (2005).
3. L. P. Borilo, L. N. Spivakova, Amrican Journal of Material Science, 2(4), 119-124 (2012)
4. H. Lee, J. Liao, C. Yao et. al. J. Sol-Gel Sci. Technol. DOI. 10.1007/s1097-015-3885-z.

PHYSICAL AND MAGNETIC PROPERTIES OF $Ni_xCo_{1-x}Fe_2O_4$ NANOPARTICLES

M. K. Kokare[1] and S. M. Rathod[2*]

[1]Department of Physics,
Tuljaram Chaturchand College of Arts, Science and Commerce, Baramati, Pune
[2]Department of Physics, Abasaheb Garware College, Pune
[*]Corresponding author E-mail: sopan.rathod@mesac.org

ABSTRACT:

Series of nickel substituted cobalt nanoferrites $Ni_xCo_{1-x}Fe_2O_4$ (x= 0, 0.1, 0.2, 0.3, 0.4, 0.5 and 1.0) were prepared by auto-combustion route. The influence of Ni content on the structural and magnetic properties of $Ni_xCo_{1-x}Fe_2O_4$ powders are studied by XRD, SEM, EDS, TEM and VSM. The SEM images give average particle size 40 nm with a regular morphology and also there is a presence of soft agglomerations. The elemental composition and analysis of as prepared powders is carried out using energy dispersive spectrometer (EDS). The particle size of $Ni_{0.5}Co_{0.5}Fe_2O_4$ is observed from the transmission emission microscopy (TEM) images. Average particle size varies between 30 - 35 nm. The XRD studies confirmed the spinel phase formation of ferrites. The lattice parameter varies with the change in Ni content. Two absorption bands observed in FTIR spectra reveals the characteristic feature of spinel ferrite. It is observer that saturation magnetization values decreases with increase in Nickel content.

Keywords: $Ni_xCo_{1-x}Fe_2O_4$; Ferrites; Auto combustion route; Nanocrystalline; Magnetic properties

INTRODUCTION:

Cobalt ferrite is the hard magnetic material with high coercivity and moderate magnetization, due to which it is widely, used in many applications like audio/video tapes, digital recording disks etc. On the other hand, nickel ferrite is soft magnetic material which is used in the inductors and transformer cores. Nickel substituted cobalt ferrites are highly resistive and magnetostrictive [1-3]. Development in electronic sectors has put pressure on manufacturers to develop smaller and lighter products. Ferrites having spinel type of the structure $M^{2+}M_2^{3+}O_4$, (M^{2+} = Cu^{2+}, Mn^{2+}, Mg^{2+}, Zn^{2+}, Ni^{2+}, Co^{2+}, etc.; M^{3+} = Fe^{3+}) have many unique properties, such as high electrical resistivity, high permeability, high Curie temperature, large magneto crystalline anisotropy, low coercivity, chemical stability and saturation magnetization. Thus, spinel ferrites have been widely used in many fields like high-density information storage, photocatalysts, ferrofluids, drug targeting, magnetic separation, magnetic resonance imaging and gas sensor [4–14]. Cobalt ferrite nano materials are suitable for magneto-optical recording applications i.e high density storage capacity. Low cost, high saturation magnetization and high Curie temperature makes cobalt-nickel ferrites most useful for absorbents and microwave devices. [15-17].The structural, electrical and magnetic properties of materials strongly depend upon stoichiometry, method of preparation, temperature and cation distribution. Most popular methods of bottom–up synthesis approach mentioned are co-precipitation [18], sol-gel method [19], microemulsion method [20], hydrothermal synthesis [21], spray pyrolysis method [22], reverse micelle [23] CBD [24] and wet chemical method [25]. In the present study, the sol-gel auto combustion method is used because it has good chemical homogeneity, high product purity, crystallinity, fine particle size and narrow particle size distribution. It is easy to control stoichiometry; dopant can be easily introduced into the final product, simple instrumentation, preparation process and low processing time. [26, 27]

In this work, Ni substituted cobalt ferrite nanoparticles were prepared by sol-gel auto combustion method and further their structural, morphological and magnetic properties are studied using XRD, SEM, TEM and VSM.

EXPERIMENTAL DETAILS:

Analytical grade Co $(NO_3)_2$, Ni $(NO_3)_2$, $Fe(NO_3)_3$ (99.9% pure) (Fisher Scientific), Citric acid (extra pure, Fisher Scientific) and Ammonia (Loba Chemicals) were used as received without further purification. $Ni_xCo_{1-x}Fe_2O_4$ (x = 0.0, 0.1, 0.2, 0.3, 0.4, 0.5 and 1.0) nanoparticles are prepared by auto-combustion route. Stoichiometric amounts of analytical grade $Co(NO_3)_26H_2O$, $Ni(NO_3)_2$ $6H_2O$ and $Fe(NO_3)_3$ $9H_2O$ (99.9% pure) were dissolved initially in 100 ml double distilled water. Citric acid was used as a complexing agent to get transparent solution with homogenous distribution of metal ions. The above mixture was stirred for 2 hrs to get homogenous clear solution and then heated upto 50 ^{0}C using a hot plate magnetic stirrer. Further the pH of solution was adjusted up to 7 by addition of Ammonia solution. The resulting solution was evaporated by heating on a hot plate with continuous stirring forming a continuous network of gel. On continuous heating of the gel, it gave a fast flameless auto combustion reaction with the evolution of large amount of gases, which gives a burned powder of the resultant product. The burned gel was ground to get a fine ferrite powder by using Agate Mortar and pestle. Finally the ground powders were sintered in air at 560 ^{0}C for 4 hrs and then finally cooled to room temperature.

For the structural determination, powder X-ray diffraction (XRD) patterns were recorded with Rigaku X-ray diffractometer using the Cu (K_α) radiation (λ = 1.5405 A^0). The morphology of synthesized samples is studied using scanning electron microscope JEOL, JEM-2010. Magnetic characterization is done using vibrating sample magnetometer.

RESULTS AND DISCUSSION:

Structural properties:

X-ray diffraction (XRD) patterns of $Ni_xCo_{1-x}Fe_2O_4$ (x = 0.0, 0.1, 0.2, 0.3, 0.4, 0.5, 1.0) are shown in Fig.1. The diffraction patterns provide clear evidence of the formation of a series of solid solutions between $CoFe_2O_4$ and $NiFe_2O_4$. Mixed spinel ferrites were observed with cubic phase for $NiFe_2O_4$ and $CoFe_2O_4$ and it is in confirmation with the JCPDS card no., 00-002-1045 and 01-074-2081, respectively. From JCPDS card it is also confirmed that the prepared material is perfect ferrite material with most intense peak (311) plane and some other planes are observed with low intensity.

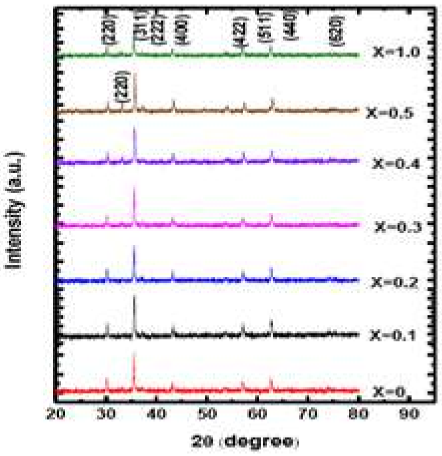

Fig.1: XRD patterns of synthesized $Ni_xCo_{1-x}Fe_2O_4$ (x=0 to 1) nanoparticles

The XRD data are also in good agreement with the other reported data of powdered sample of $Ni_xCo_{1-x}Fe_2O_4$ [15]. The crystallite size of the powdered sample $Ni_xCo_{1-x}Fe_2O_4$ is calculated by using Debye-Scherrer's formula [29],

$$D = \frac{0.9\lambda}{\beta \cos\theta} \qquad (1)$$

where D is the crystallite size, β is the broadening of the diffraction line measured at half of its maximum intensity (FWHM) and λ is the X-ray wavelength of Cu Kα (1.5405A°). The average crystallite size along (311) plane is around 30-35 nm, it is typically in the nano range, which is shown in Table 1. The lattice parameter 'a' is calculated using the relation

$$a = d\,(h^2+ k^2+l^2) \qquad (2)$$

The value of lattice parameter (a) for $CoFe_2O_4$ is 8.38 and for Ni Fe_2O_4 is 8.33. This calculated values of lattice parameters are in also agrees with JCPDS card. The lattice parameter dependence with increase of Ni concentration in the solid solution gives slightly decreasing trend. This decrease could be attributed to the difference in ionic radii of Ni and Co [30].

Fig. 2 (a) shows Scanning Electron Micrograph (SEM) image of the $Ni_{0.5}Co_{0.5}Fe_2O_4$ ferrite powders. The sample reveals average particle size 40 nm with a regular morphology and also there is a presence of soft agglomerations. Particle size calculated from SEM supports the crystallite size determined from Debye-Scherrer's formula earlier. From the SEM images it is also observed that, after sintering, less agglomeration is formed. The typical EDS spectra show the presence of Co, Fe, Ni and O in accordance with the stoichiometric ratio as shown in Fig. 2 (b).

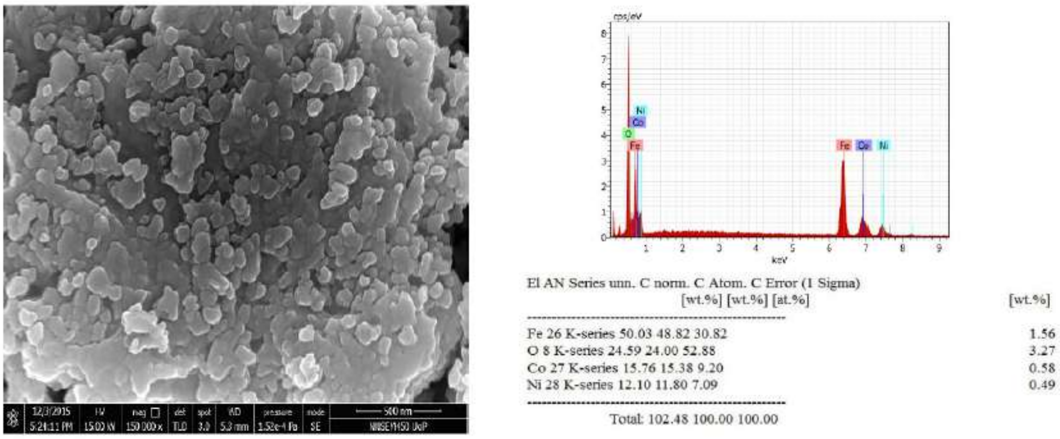

```
El AN Series unn. C norm. C Atom. C Error (1 Sigma)
                 [wt.%] [wt.%] [at.%]                      [wt.%]
-----------------------------------------------
Fe 26 K-series 50.03 48.82 30.82                            1.56
O 8 K-series 24.59 24.00 52.88                              3.27
Co 27 K-series 15.76 15.38 9.20                             0.58
Ni 28 K-series 12.10 11.80 7.09                             0.49
-----------------------------------------------
          Total: 102.48 100.00 100.00
```

Fig. 2: (a) SEM and (b) EDS of $Ni_{0.5}Co_{0.5}Fe_2O_4$ Ni content

Magnetic properties:

The magnetic properties of the synthesized nanoparticles are analyzed using a Vibrating Sample Magnetometer (VSM) at room temperature. Fig. 3 shows typical hysteresis loops of as-prepared Ni substituted Co ferrite samples. The hysteresis curve shows that, the saturation magnetization decreases with increase in Ni concentration. Table 1 also shows the variation in values of saturation magnetization(Ms), coericivity (Hc) and remanence magnetization (M_r) with Ni content. It is observer that saturation magnetization values decreases with increase in Nickel content. This decrease is attributed to the smaller magnetic moment of Ni^{2+} ($2\ \mu_B$) in comparison with that of Co^{2+} ion ($3\ \mu_B$).

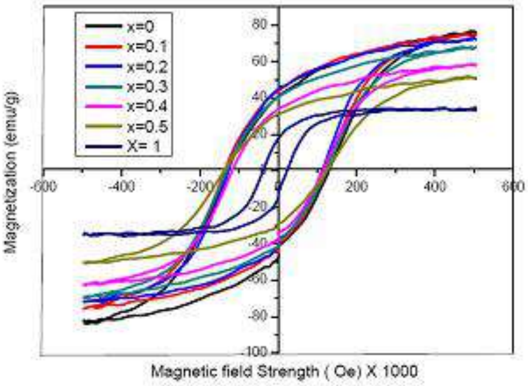

Fig. 3: Hysteresis curve of $Ni_xCo_{1-x}Fe_2O_4$ (x=0 to 1) nanoparticles at room temperature

Table 1: Crystallite size and lattice parameter value 'a' and Magnetic parameters (M_s, H_c and M_r) values with Ni content

Ni content (x)	D (nm)	Lattice parameter 'a'	M_s (emu/gm)	H_c (O e)	M_r (emu/gm)
x=0.0	33.3654	8.385	076.6914	121.48	42.08
x=0.1	33.3975	8.383	075.1098	126.15	43.23
x=0.2	31.1041	8.382	072.7794	115.39	44.32
x=0.3	33.2613	8.378	067.9840	125.49	41.57
x=0.4	34.7629	8.356	058.5563	114.69	34.69
x=0.5	30.9030	8.342	051.8542	**H_c (O e)**	31.74
x=1.0	33.3815	8.337	034.6546	121.48	16.64

CONCLUSION:

We have successfully synthesized nanoparticles of nickel-cobalt ferrites by auto-combustion route. The XRD analysis of prepared samples confirmed nanocrystalline with cubic spinel structure. SEM image reveals random morphology of nickel-cobalt ferrite with interconnected nano-particles. The decrease in Magnetic susceptibility with increasing Ni content is attributed to smaller magnetic moment of Ni^{2+} as compared to magnetic moment of Co^{2+}. This low magnetic susceptibility materials are good candidate for the magnetic gradiometer purpose [32].

ACKNOWLEDGMENT:

We are very much thankful to Tuljaram Chaturchand College, Baramati and Post –Graduate and Research Centre, Abasaheb Garware College, Pune, for providing research facilities.

REFERENCES:

1. Meenakshsundaram A, Gunasekaran N, Srinivasan V, Phys. Status Solidi A, 69, K15 (1982).
2. Pallai V, Shah D O, J. Magn. Magn. Mater., 163, 243 (1996).
3. Skomski R, J. Phys.: Condens. Matter,15, R841 (2003).
4. Maqsood A, Faraz A, J. Supercond. Novel Magn., 25, 1025 (2012) .
5. Msomi J Z, Moyo T, Abdallah H M I, J. Supercond. Novel Magn., 25, 2643 (2012).
6. Abdallah H M I, Moyo T, Msomi J Z, J. Supercond. Novel Magn., 24, 669 (2011).
7. Ronak Eisavi, Seiran Ghadernejad, Behzad Zeynizadeh, Farkhondeh Mohammad Aminzadeh, J. Surf. Chem., 37, 5 (2016).
8. Jinwen Huang, Peng Su, Wenwei Wu, Bang Liu, J. Supercond. Novel Magn., 27, 2317 (2014).

9. Mahmoud Abd El Aleem Ali Ali El-Remaily, Ahmed M. Abu-Dief, Tetrahedron, 71, 2579 (2015).
10. Wang H. B, Wang L, Wang J B., J. Magn. Magn. Mater., 309, 295 (2007).
11. Wu W W, Cai J C, Wu X H, Li Y N, Lia S, Rare Met., 30, 621 (2011).
12. Satyanarayana L, Madhusudan Reddy K, Manorama S V, Mater. Chem. Phys. Mater., 82, 21 (2003).
13. Zhang K, Holloway T, Pradhan A K, J. Magn. Magn. Mater., 323, 1616 (2011).
14. Wenwei Wu, Jinchao Cai, Xuehang Wu, Yongni Li, Sen Liao, Rare Met., 21, 51 (2012).
15. Abo El A M, Attia S M, Meaz T M, Solid State Sci., 6, 61 (2004).
16. Panda R N, Shih J C, Chin T S, J. Magn. Magn. Mater., 257, 79 (2003).
17. Zaki H M, Physica B, 363, 232 (2005).
18. Gul I H, Ahmed W, Maqsood A, J. Magn. Magn. Mater., 320, 270 (2008).
19. Zahi S, Hashim M, Daud A R, J. Magn. Magn. Mater., 308, 177 (2007).
20. Kosak A, Makovec D, Znidarsic A, Drofenik M, J. Eur. Ceram. Soc., 24, 959 (2004).
21. Jiao X, Chen D, Hu Y, Mater. Res. Bull., 37, 1583 (2002).
22. Takayama A, Okuya M, Kaneko S, Solid State Ionics, 172, 257 (2004).
23. Thakur S, Katyal S C, Singh M, J. Magn. Magn. Mater., 321, 1 (2009).
24. Saragi P P, Vadera S R, Patra M K, Ghosh N N, Powder Technol., 203, 348 (2010).
25. Balaji S, Kalai Selvan John Berchmans R, Angappan S, Subramanian K, Augustin C O, Mater. Sci. Eng., B, 119, 119 (2005).
26. Costa A C F M, Morelli M R, Kiminami R, J. Mater. Sci., 42, 779 (2007).
27. Mukasyan A S, Epstein P, Dinka P, Proc. Combust. Inst.,31, 1789 (2007).
28. He H Y, Huang J F, Fei J, Lu J, Liu T T, J. Nanoelectron. Optoelectron., 9, 1 (2014).
29. Rickerby D S, Jones A M, Bellamy B A, Surf. Coat. Technol., 37,111 (1989).
30. Gul I H, Amin F, Abbasi A Z, Anis-ur-Rehmanb M, Maqsood A, Scr. Mater., 56, 497 (2007).
31. Benseba F, Zavaliche F, Eusyer P L, Cochrane R W, Veres T, J. Colloid Inter. Sci., 277, 104 (2004).
32. Andrew Sunderland1, Li Ju, David G Blair, Wayne McRae and Howard Golden, Smart Mater. Struct. 18, 095038 (2009).

HYDROTHERMAL SYNTHESIS OF COBALT DOPED MnO2 NANOCOMPOSITE FOR SUPERCAPACITOR APPLICATION

Sarika Jadhav[1], Ramchandra S. Kalubarme[1], Chiaki Terashima[2] and Suresh Gosavi[1]

[1]Centre of Advanced Studies in Material Science and Solid State Physics,
Department of Physics, Savitribai Phule Pune University (Formerly University of Pune),
Ganeshkhind, Pune- 411007, INDIA

[2]Photocatalysis International Research Center, Research Institute for Science & Technology,
Tokyo University of Science, 2641 Yamazaki, Noda, Chiba 278-8510, JAPAN

*Corresponding author E-mail: swg@physics.unipune.ac.in

ABSTRACT:

Cobalt-doped MnO_2 nacomposite with hierarchically mesoporous structure has been prepared by hydrothermal method and characterized by using X-ray diffraction and transmission electron microscopy analysis. The supercapacitive performance of the material is evaluated using cyclic voltammetry and galvanostatic charge/discharge measurements. A specific capacitance of 350 F g−1 is achieved at a current density of 0.1 A g−1 f with a Co/Mn ratio of 0.5%, much higher than that of the undoped MnO2 nanocomposite which is approximately 168 F g−1.

INTRODUCTION:

Supercapacitors with merits including high power density,superior reversibility, long cycle life, and relatively high energydensity have been regarded as promising energy storage devicesfor hybrid electric vehicles, pulse laser techniques, and energymanagement systems. The energy storage of electrochemical supercapacitors occurs at or near the electrode/electrolyteinterfaces following two mechanisms. The first one is based on quick formation of a double layer of charges or opposite ions atthe electrode/electrolyte interface, called electric double-layercapacitors (EDLCs). Porous active carbons (1) and silicon (2) with large surface areas are generally used electrode materials for EDLCs. The other is based on a charge-transfer Faradaic process, generating pseudocapacitance (3). The most widely used active electrode materials for pseudocapacitors are transition-metal oxides (4) and conducting polymers(5). The electrode materials play a key role in determining theelectrochemical performance of the supercapacitors. It also hasbeen demonstrated that the pseudocapacitance of transition metal oxides is much higher than the electrochemical doublelayeredcapacitance of carbon materials (6). However, ruthenium is a very expensive and toxicelement, and strongly acidic electrolytes such as sulfuric acid are usually involved in supercapacitor fabrication, hindering its general commercial application. Manganese oxide (MnO_2) withadvantages such as low cost, low toxicity, natural abundance, andenvironmental friendliness is considered as one of the mostpromising electrode materials for pseudocapacitors (7). Thecharge storage mechanism of manganese oxide is based onsurface adsorption of electrolyte cations and proton incorporation, accompanied by oxidation/reduction of Mn ions (8).Although the charge-storage mechanism in MnO_2 materials is mainly Faradaic,the particle size and morphology are also efficient in enhancingthe electrode kinetics of these materials.(9) In addition,incorporation of other metal elements into MnO_2 lattices hasalso been proved recently to be feasible in further improving theelectrical conductivity and pseudo-capacitive performance ofMnO_2 materials(10). Metal elements, such as Ni, Cu, Fe, V, Co, Mo, Ru, Au, Ag, and Cu, have been successfully doped into thestructures of MnO2 materials (11). The doping by other metalelements may vary the electronic structure of MnO2,consequently leading to better electronic conductivity andhigher electrochemical performance (12).Thus, it is highly desirableto prepare heteroatom-doped MnO_2 materials with controlledcrystal structure and morphology in one step.

EXPERIMENTAL:

For Cobalt doped MnO_2 nanocomposite synthesis, 0.1 M of Manganese Sulphate ($MnSO_4$) and 0.01M solution of Cobalt nitrate($Co(NO_3)_2$) were added in 100 mL of deionized water . After that 2M urea was added in solution of Co and Mn precursors under constant stirring for 60 min. Subsequently, the suspension was transferred to 200 mL Teflon-lined stainless steel pressure vessel, maintained in the homogeneous reactor at 150 °C and kept for 8h. After completion of reaction the reactor is allowed to cool naturally to room temperature. After cooling precipitate was collected by filtering and washing with distilled water and absolute ethanol for several times then dried overnight in oven at 60°C.

RESULT AND DISCUSSION:

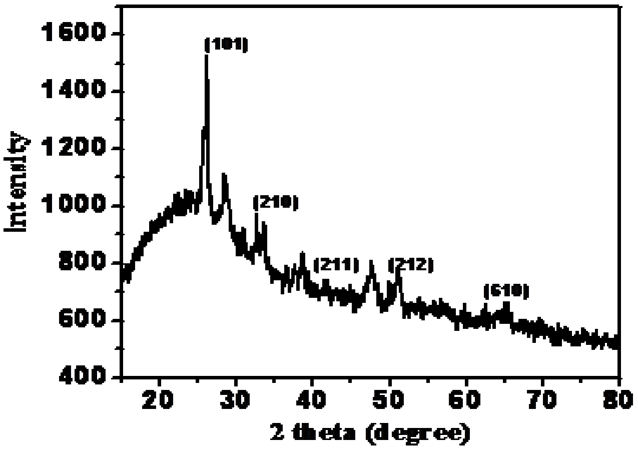

Fig. 1: XRD pattern of Co-MnO2 nanocomposite

XRD patterns of Co−MnO_2 are shown in Figure 1.The diffraction peaks in the XRD patterns of the as-preparedsamples are in good agreement with the MnO_2,crystallized in an othorhombic system with cell parameters of a =9.3720 Å, b = 2.8508 Å, and c = 4.4706 Å (JCPDS No. 44-0142).The peaks located at 25.16°, 35.14°, 42.28°, 53.74°, and 66.74°are ascribed to the typical (101), (210), (211), (212), and (610)diffractions, respectively. The broad nature of the peak profiles suggests the formation of small crystallites with low crystallinity. No diffraction peaks originating from cobalt oxide are observedin the XRD pattern of Co−MnO2, indicating that no crystallizedcobalt oxide is formed.

The morphologies of the samples are revealed by TEMobservation (Fig. 2).The assembly of thesenanoparticles forms a hierarchically mesoporous structure which is facilitatingpenetration of electrolyte. The diameter of nanoparticles is between 20 nm-30 nm.

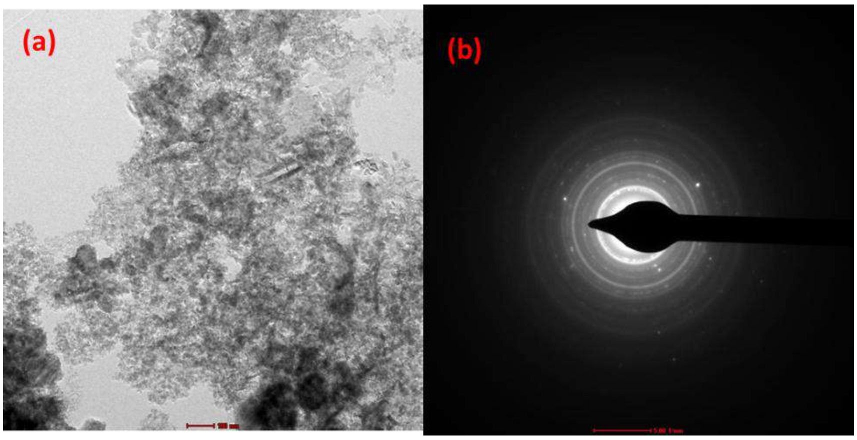

Fig. 2: TEM images of Cobalt doped MnO_2 Nanocomposite

The cyclic voltammograms (CV) of Co-MnO_2 electrodes measured in 1MNa_2SO_4 electrolyte at scan rates of10 mVs-1 are shown in Fig. 3. From the CV curves all the electrodes shows rectangular shapes, revealing the surface Faradaic reaction of the synthesized samples.Specific capacitance of Cobalt doped MnO_2 is 350 F g−1.

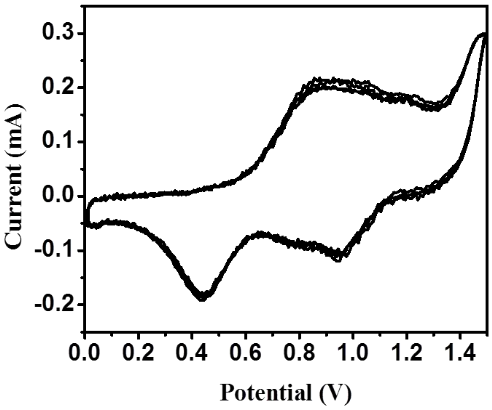

Fig. 3: Electrochemical Performance of Co doped MnO2 nanocomposite

CONCLUSION:

A cost effective and simple hydrothermal method is successfully employed to fabricate Co doped MnO2 nanocomposites as electrode materials for electrochemical supercapcitors. Hierarchically mesoporous like structures of Co-MnO_2 having diameter ranging from 20-30nm is confirmed by TEM analysis. The Co-MnO_2nanocomposite exhibited specific capacitance of 350 F g-1 at 10 mV s-1 scan rate. These composites possess good electrochemical behaviour that are useful as electrode material for supercapacitors. In addition, the prepared materials are expected to have potential applications as catalysts, absorbents, and electrodes for other electronic devices.

REFERENCE:

1. Wang, K. X.; Wang, Y. G.; Wang, Y. R.; Hosono, E.; Zhou, H. S. J. Phys.Chem. C, 113, 1093−1097 (2009).
2. Wang, J. F.; Wang, K. X.; Du, F. H.; Guo, X. X.; Jiang, Y. M.; Chen,J. S. Chem. Commun., 49, 5007−5009 (2013).
3. Lang, X.; Hirata, A.; Fujita, T.; Chen, M. Nat. Nanotechnol., 6, 232−236 (2011).
4. Yuan, C.; Zhang, X.; Su, L.; Gao, B.; Shen, L. J. Mater. Chem., 19, 5772−5777 (2009).
5. Zheng, J. P.; Jow, T. R. A., J. Electrochem. Soc., 142, L6−8 (1995).
6. Conway, B.; Birss, V.; Wojtowicz, J. J. Power Sources, 66, 1−14 (1997).
7. Chun, S. E.; Pyun, S. I.; Lee, G. J. Electrochim.Acta, 51, 6479−6486 (2006).
8. Hu, C. C.; Tsou, T. W. Electrochem.Commun., 4, 105−109 (2002).
9. Sugimoto, W.; Yokoshima, K.; Murakami, Y.; Takasu, Y. Electrochim. Acta, 52, 1742−1748 (2006).
10. Yoo, H. N.; Park, D. H.; Hwang, S. J. J. Power Sources, 185,1374−1379 (2008).
11. Wei, W.; Cui, X.; Chen, W.; Ivey, D. G. Chem.Soc. Rev., 40, 1697−1721 (2011).
12. Hashem, A. M.; Abuzeid, H. M.; Mikhailova, D.; Ehrenberg, H.;Mauger, A.; Julien, C. M., J. Mater. Sci., 47, 2479−2485 (2012).

INFLUENCE OF STRUCTURE, DIELECTRIC AND MAGNETIC PROPERTIES OF $Ni_{(1-x)}Pb_xFe_2O_4$ NANO FERRITE BY SOL-GEL AUTO COMBUSTION METHOD

S. S. Kokare*, A. B. Shinde and S. M. Rathod

Department of Physics, M. E. S Abasaheb Garware College, Pune

* Address for correspondence: kokareshriyog@yahoo.com

ABSTRACT:

Pb doped Nikel Ferrite (where x= 0.2, 0.3, 0.6, 0.7, 0.8) Nanoparticles were synthesized by a simple cost effective method involving sol-gel auto combustion at low temperature. Nickel ferrite is a typical soft as a large number of applications. Nickel- ferrite is obtaining soft ferrite its application such as gas sensor. The present work is to study the structural and magnetic properties of Pb+ doped Nickel Nano ferrite the synthesized samples. The role of Pb^+ (Silver) substituted Ni (Nickel) shows the formation of crystal phase, which was identified by X-ray diffraction method. The lattice constants increase with the increasing in Pb+ contain. We report the synthesis of nanoparticles, soft and spinel with crystalline size is in the range of 34.7791 to 12.498nm. The Vibrating Sample Magnetometer was used to obtain the Hysteresis parameters. The magnetic property of the prepared samples shows remarkable changes with changes Ag percentage.

Keywords: Sol-gel; Ni-Pb Nano ferrite; dielectric properties; UV ; etc

INTRODUCTION:

Ferrites are electrically non-conductive ferrimagnetic ceramic compound materials, consisting of various mixtures of iron oxides such as Hematite (Fe_2O_3) or Magnetite (Fe_3O_4) and the oxides of other metals. The general form of ferrite is MFe_2O_4, where M represents a divalent metal ion; generally transition metal ions like Mn, Fe, Co, Ni, Cu, and Zn. Ferrites are predominantly ionic and have very stable crystal structure. Great majority of ferrites contain iron oxides as major constituents but there are some ferrites based on Cr, Mn and other elements. Ferrite cores are used in electronic inductors, transformers, and electromagnets where the high electrical resistance of the ferrite leads to very low eddy current losses.

METHODS OF SYNTHESIS:

Preparation of nanomaterials can be divided into two broad spectrum top down and bottom up, each of which has two directions physical and wet chemical. The most important criteria for preparation of nanoparticles are: Proper size with narrow size distribution well dispersed particles, equiaxial shape of particles, high purity, and homogeneous composition. Most of the wet chemical methods have common feature that the mixing of components takes place at the atomic or molecular scale. Some of the nonconventional processes are: Sol-gel method, Co-precipitation method, Precursor method, combustion method, Hydrothermal, Spray drying. The most widely used synthetic technique for bulk metal oxides have been ceramic methods which are based of powder mixture. These reactions are completely controlled by the diffusion of the atomic or ionic species through reactants and products. To bring the reaction partners sufficiently close together and to provide high mobility, these solid state processes require high temperature and small particle sizes. Although the harsh reaction conditions only lead to thermodynamically stable phases preventing formation of the metastable solids, these approaches give access to a large number of new solid compounds ; enabling the development of structure properties relationships. However in comparison to organic chemistry where highly sophisticated synthetic pathways are employed to make and break chemical bonds in a controlled way, the ceramic method is a rather crude approach. It is therefore no surprised that for size and shape controlled synthesis of nanoparticles especially liquid phase route represents most promising alternatives. Among the various soft chemistry routes, Sol-Gel procedures were particularly successful in the preparations of bulk metal oxides. (Example: ceramics, glasses, films, and fibers) and therefore they also been used applied for nanoparticle synthesis.

The Sol-Gel process can shortly be defined as the conversation of a precursor solution into an inorganic solid via inorganic polymerization reaction induced by water. In general, the precursor or starting compound is either an inorganic polymerization reaction (no Carbon) metal salts (Chloride, Nitrates, Sulphates etc) or metal organic compound such as an alcoxides. The metal oxides are most widely used precursor because they react readily with water and are known for many metals. In comparison with silicates from silicon alcoxides, the Sol-Gel processing of transition metal oxides has much less been studied mainly due to high reactivity of transition metal alcoxides.

According to wet chemical method using stoichiometric ratio, the raw material is in nitrate form and kept this solution on magnetic stirrer and stirred up to 20 minute for homogeneous solution. pH has been maintained at 7 by adding ammonia drop by drop. Keeping the pH neutral, temperature is increased up to 100^0C with continuous stirring to form the gel. After 3-4 hours the solution becomes gel form. After half an hour it takes place auto combination to get the fine powder. Thus fine powder is sintered at 400^0C. Fine grind for 1 to 2 hours & we get nano powder.

RESULT AND DISCUSSION:

It is seen that with increasing dopant concentration of Pb^{2+} band gap first decreases up to concentration x=0.3 then increases up to x=0.8. As Pb^{2+} replaces Co^{2+}, impurity bands are created due to the formation of the impurity levels inside the gap. At low Pb^{2+} dopant concentration, the distances between the valence band and the lowest impurity band act like effective band gaps. With increasing Pb^{2+} dopant content, the widths of these impurity bands increases and these bands could overlap together leads to decrease in energy band gap.

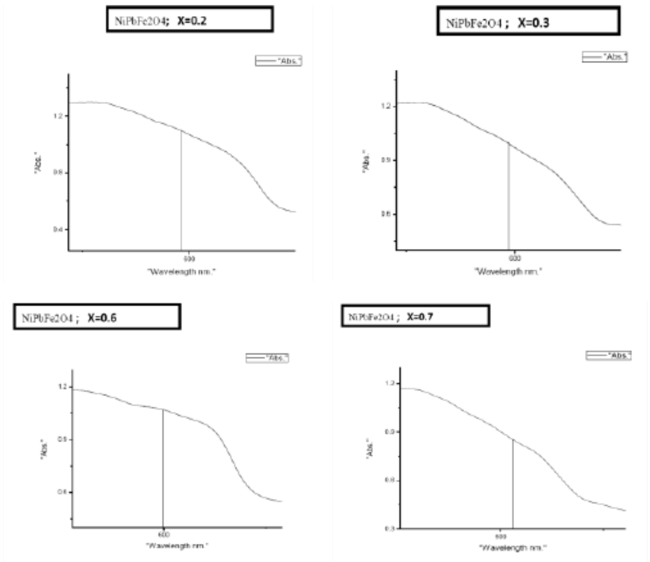

Fig. 1: UV Pattern of $NiPbFe_2O_4$

Table 1: Absorption wavelength and band gap Energy of $NiPbFe_2O_4$

Sr. No.	Name of Material	Concentration (X)	Absorb Wavelength λ (nm)	Band Gap Energy
1	$Ni_{(1-x)}Pb_xFe_2O_4$	0.2	589	2.5833 eV
2		0.3	591	2.8345eV
4		0.6	599	8.4367eV
5		0.7	618	12.986eV
6		0.8	614	20.5306 eV

CONCLUSION:

In the present case, the observed increase in σ_{ac} with increasing frequency can be attributed to the increased hopping rate with increasing frequency. At lower frequencies the grain boundaries are more active and hence the hopping of Ni^{2+} and Ni^{3+} ions is less at lower. It is well known that AC conductivity in disordered solids is directly proportional to frequency. It is also evident that the frequency dependent ac electrical conductivity of $Ni_{1-x}Pb_xFe_2O_4$ is remarkably dependent on the Pb content in the ceramics.

REFERENCES:

1. H. Gul, F. Amin, A.Z. Abbasi, M. Anis-ur-Rehmanb, A. Maqsood, Scripta Materialia, 56, 497 (2007).
2. K. Raj, R. Moskowitz, R. Casciari, J. Magne. & Magne. Mat., 149, 174 (1995).
3. Z. Sun, L. Liu, D.z. Jia, W. Pan, Sens. Actuators, B: Chem. 125, 144–148 (2007).
4. K.-S. Kang, C.-H. Kim, W.-C. Cho, K.-K. Bae, S.-W. Woo, C.-S. Park, Int. J. Hydrogen Energy, 33, 4560–4568 (2008).
5. S. Kameoka, T. Tanabe, A.P. Tsai, Appl. Catal., A: Gen., 375, 163–171 (2010).

SYNTHESIS OF HIERARCHICAL $CdMoO_4$ NANO DISCS FOR SOLAR LIGHT HARVESTING APPLICATION

Sunil R. Kadam[1,2], Suresh Gosavi[1] and Bharat B. Kale[2*]

[1]Centrefor Advanced Studies in Materials Science, Department of Physics,
Savitribai Phule Pune University, (Formerly University of Pune)
Ganeshkhind, Pune -411007, INDIA
[2]Centre for Materials for Electronics Technology (C-MET),
Ministry of Electronics and Information Technology (MeitY),
Government of India, Panchawati, Off. Pashan Road, Pune –411008, INDIA
[*]Corresponding author E-mail: bbkale@cmet.gov.in

ABSTRACT:

Hydrothermal-assisted synthesis is a facile technique used for synthesis of $CdMoO_4$ nano discs in water as a reaction medium. The synthesized $CdMoO_4$ nano discs was characterized by, X-ray diffraction (XRD), Raman spectroscopy, UV–visible spectroscopy and Field emission scanning electron microscopy. The XRD investigations proved formation of tetragonal structured pure $CdMoO_4$ phase and the band gap observed to be 3.6 eV. Microscopic analysis using FESEM confirms formation of nano discs like surface morphology of the sample. The $CdMoO_4$ nano disk-like structure were composed of circular nanoplates orderly packed layer by layer is observed.

INTRODUCTION:

In last decade, researcher focused their work on the synthesis of size, shape, and phase controlled semiconductor materials in various dimensions in order to tailor their chemical and physical properties.[1] The electronic structure, bonding, surface energy, and chemical reactivity are directly related to their unique size and surface morphology and phase purity of the material. Usually, self-assembled superstructures can be formed through the progress of zero or one-dimensional (0-D or 1-D) primary crystals via the oriented growth process, Ostwald ripening process, or both by using surfactants as surface capping reagents or without.[2]

The conservative energy resources have been depleted to a large extent because of continuously rising energy demands.[3] Therefore, it is essential to develop active semiconductor materials, which can harvest the solar energy to fulfil the energy requirements.

However, the binary oxide catalyst such as the TiO_2 and ZnO is reported to be best photocatalyst, but the starting materials used for these materials synthesis is economically not favourable.[3] So, researchers are looking forward to some economically favourable and chemically stable semiconductor photocatalyst for the solar energy harvesting application. Now a day's, among the inorganic materials Molybdenum based semiconductor catalysts have increasing attention because of their potential technological importance in a wide range of applications such as photoluminescent devices, solid-state optical maser, optical fibers, scintillation detector, humidity sensor, photocatalysts, chemical reactors and high density Li ion battery application.[4-7]Among these molybdates, cadmium molybdate ($CdMoO_4$) is a challenging material due to its unique chemical and structure properties, such as electronic excitation with UV-visible spectrum, pressure-induced phase transformations.[8-9]A few attempts have been done to the assessment of efficient approaches for the fabrication of $CdMoO_4$ nanostructures. Zhou et al. reported the synthesis of $CdMoO_4$ microspheres via a simple precipitation reaction without using any templates or additives.[10] Ren et al. synthesized $CdMoO_4$ different morphologies such as sphere, cake, and cubic via a low temperature hydrothermal method.[11]Wang et al. also reported the synthesis of $CdMoO_4$ hollow microspheres via an aqueous solution method.[12]However, considering the research done on metal molybdates, there are only few reports on the synthesis of $CdMoO_4$ hierarchical structures. Therefore, the synthesis of $CdMoO_4$ hierarchical structures with well-defined morphologies and sizes via simple methods is of great importance for potential studies of its physical and chemical properties. In the present study, we report the hydrothermal synthesis of tetragonal phase of $CdMoO_4$having nanodisk-like self-assembled superstructures without any surfactant and template.

EXPERIMENTAL WORK:

Synthesis of $CdMoO_4$ Nano discs:

The chemicals used for the reaction e.g Cadmium nitrate and Ammonium Molybdate all Qualigens make were used without further purification. Solutions of Cadmium nitrate dissolved in water (75 ml) and Ammonium Molybdate were prepared in water (75 ml) separately.

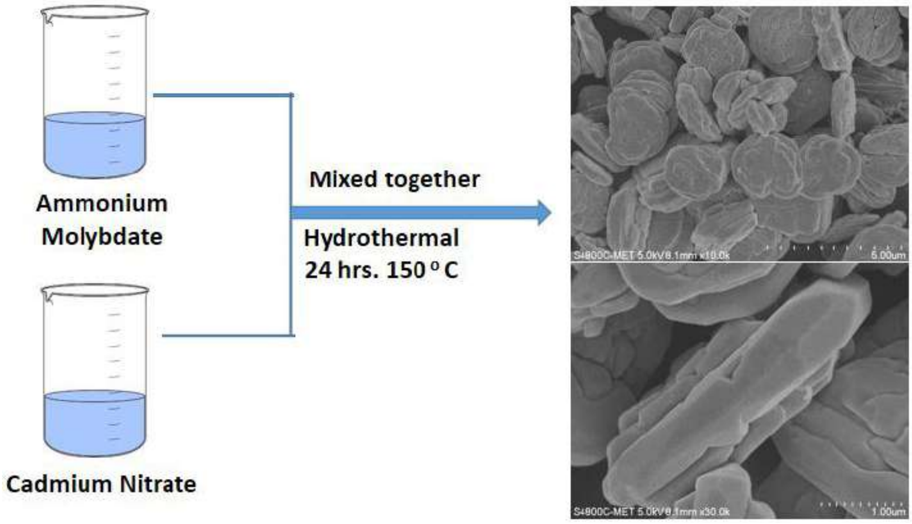

Flow sheet for the synthesis of $CdMoO_4$nanodisc

Ammonium Molybdate solution was added drop wise into Cadmium nitrate solution at room temperature with constant stirring. Followed by allow the solution to 10 more minute. The reaction mixture is then packed in teflon lined reactor, pack it in steel jacket. Then the reactor was kept in oven at 150 ^{o}C for 24 hours. After completion of the reaction, the reactor was allowed to cool naturally. The product is filtered by using whatman filter paper no. 41. The product is dried at 80 ^{o}C for 4 hours in oven. The collected powder sample was further analysed by various characterization techniques. The synthesis of $CdMoO_4$ nano disc sample was explained in above flow chart.

Material Characterisation:

The crystalline phases were investigated using X-ray powder diffraction (XRD) technique (XRD-D8, Advance, Bruker-AXS). The morphologies of the synthesized sample were investigated by Field Emission Scanning Electron Microscopy (FESEM, Hitachi, S-4800). The optical properties of the powder samples were studied using an UV-visible-near infrared spectrometer (UV-VIS-NIR, Perkin Elmer Lambda-950). Room temperature Raman spectroscopy were performed using a Renishaw InVia microscope Raman system with a laser wavelength of 532 nm in the back scattering geometry laser power on the sample was 5 mW with a laser spot size 1 μm.

RESULTS AND DISCUSSION:

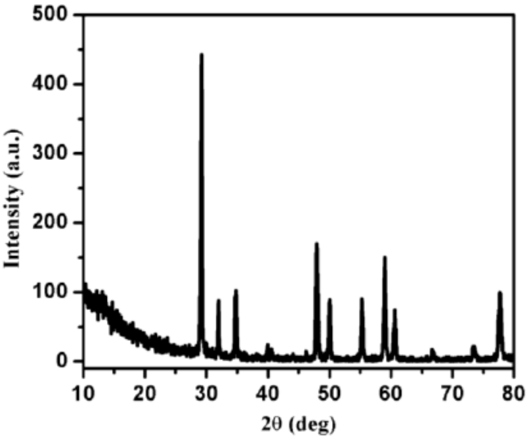

Fig. 1: X-Ray Diffraction pattern of $CdMoO_4$Nano disc sample

The as synthesized $CdMoO_4$ sample is characterized by XRD technique and results was shown in figure 1. The XRD clearly reveals the tetragonal phase formation of the $CdMoO_4$ sample (figure 1). The sharp and intense peak observed in the XRD pattern confirms the presence of highly crystalline material. The XRD patterns of $CdMoO_4$ matches with the previously reported $CdMoO_4$ sample having JCPDS No. 007-0209. The UV- Diffuse reflectance of the synthesized $CdMoO_4$ sample was further characterized by UV-visible spectroscopy and results depicted in the Figure 2. It is observed that $CdMoO_4$ sample show the absorption edge cut off at ~350 nm (3.5 eV).

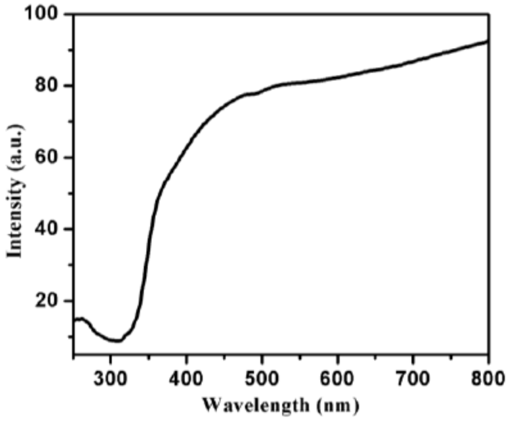

Fig. 2: UV-DRS spectra of $CdMoO_4$ bundles and $CdMoO_4$ burger

The morphological investigations of the as synthesized of $CdMoO_4$sample was investigated by FESEM shown in Figure 3(a-d). From FESEM images, it is clearly observed the formation of the nano disc (1.5 µm) like morphology via solvothermal process. Interestingly, formation of nano discwere composed of circular nanoplates orderly packed layer by layer is observed. The average size of the individual $CdMoO_4$ nano disc is observed to be ~1.5 µm in size (Figure 3a-b). More significantly, the growth of nano particles observed at the surface were circular in shape and the overall thickness of the nano disc is around 500 nm. Overall, FESEM observations depicts that there is uniform distribution of structural morphology.

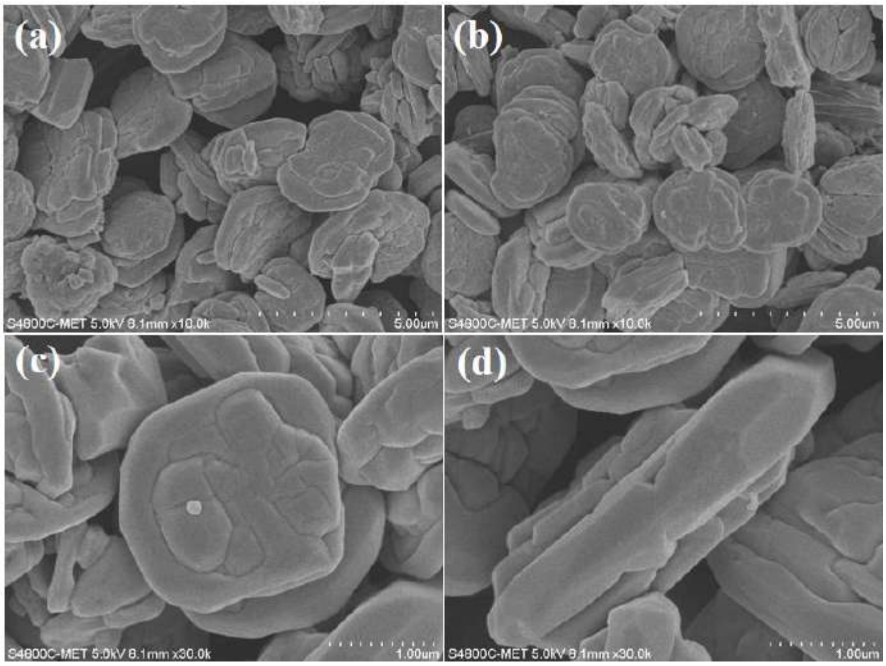

Fig. 3: FESEM images of (a-d) as synthesized $CdMoO_4$nano disc sample

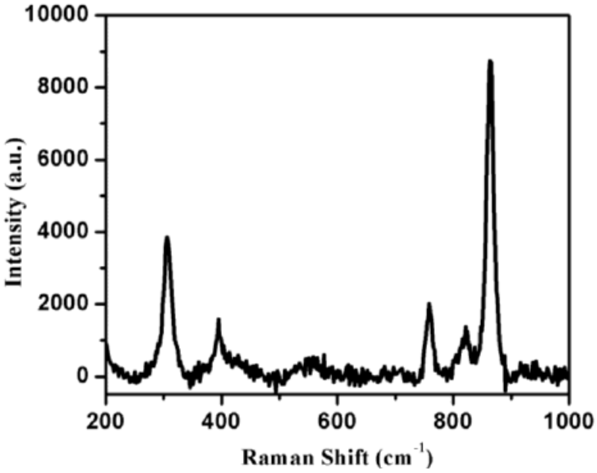

Fig. 4: Raman spectra of as synthesized $CdMoO_4$ nano disc sample

Further, the as synthesized $CdMoO_4$ nano disc sample was characterized by Raman spectroscopy, Raman spectroscopy is a very powerful and non-destructive technique widely used to characterize various materials. It gives very precise and exact information about the change in bond distance and mechanical properties such as strain, stress, phase transition etc. In view of this, as prepared $CdMoO_4$ nano disc sample were characterized by Raman spectroscopy and are shown in Figure 4. The Raman spectra of $CdMoO_4$nano disc sample shows the peak at 866.1 cm^{-1} was assigned as a $\nu_1(A_g)$ symmetric stretching vibration mode of the [MoO_4] cluster in the $CdMoO_4$ structure. The Raman peak at 820 and 760.5 cm^{-1} assigned to significant anti-symmetric stretching $\nu_3(B_g)$ and $\nu_3(E_g)$ vibration modes of $CdMoO_4$ structure, respectively. Further the peak appeared at 397 and 306 cm^{-1} were assigned as a weaker $\nu_4(B_g)$ and stronger $\nu_2(A_g)$ of the [MoO_4] tetrahedrons.

CONCLUSION:

In summary, well crystalline $CdMoO_4$ nano discs were successfully synthesized via one step hydrothermal approach has been demonstrated. The multilayered nano disks were constructed by systematic self-assembly of the circular nanoplates via oriented attachment mechanism. The UV-DRS revealed that, tetragonal $CdMoO_4$ nano disc sample have characteristic optical band gap 3.5 eV. The small sized circular nano plates, edge sites and defects of from catalysts plays an important key role in the enhancement of solar light harvesting.

ACKNOWLEDGEMENTS:

Dr. Sunil Kadam would like to thank University Grants Commission for financial support towards the implementation of the project under D S Kothari Post-doctoral fellowship scheme (grant No. No. F.42/2006 (BSR)/CH/16-17/0066). Author also would like to thank for the C-MET, Pune for allowing access of all Experimental and Characterization facility. All research work is carried out at C-MET, Pune India.

NOTES AND REFERENCES:

1. Q. Xiang, J. Yu and M. Jaroniec, J. Ameri. Chem. Soc., 134, 6575-6578 (2012).
2. F. M. Pesci, M. S. Sokolikova, C. Grotta, P. C. Sherrell, F. Reale, K. Sharda, N. Ni, P. Palczynski and C. Mattevi, ACS Catalysis, 7, 4990-4998 (2017).
3. S. R. Kadam, D. J. Late, R. P. Panmand, M. V. Kulkarni, L. K. Nikam, S. W. Gosavi, C. J. Park and B. B. Kale, J. Mate. Chem. A, 3, 21233-21243 (2015).
4. J.A. Groenink, G. Blasse, J. Solid State Chem., 32, 9–20 (1980).
5. M. Ishii, M. Kobayashi, Prog. Cryst. Growth Charact. Mater., 23, 245–311 (1992).
6. N. Bate, H. Shi, L. Chen, J. Wang, S. Xu, W. Chen, J. Li and E.-B. Wang, Chemistry – An Asian Journal, 10.1002/asia.201700951 (2017).
7. J. Liu, A. Fu, Y. Wang, P. Guo, H. Feng, H. Li and X. S. Zhao, Chem. Electro. Chem., 10.1002/celc.201600769 (2017).
8. V. B. Mikhailik, H. Kraus, D. Wahl, M.S. Mykhaylyk, Phys. Status Solidi B, 242, R17–R19 (2005).
9. A. Jayaraman, S.Y. Wang, S.K. Sharma, Phys. Rev. B 52, 9886–9889 (1995).
10. L. Zhou, W.Z. Wang, H.L. Xu, S.M. Sun, Cryst. Growth Des., 8, 3595–3601 (2008).
11. Y. Ren, J.F. Ma, Y.G. Wang, X.Y. Zhu, B.T. Lin, J. Liu, X.H. Jiang, J.T. Tao, J. Am. Ceram. Soc. 90, 1251–1254 (2007).
12. W.S. Wang, L. Zhen, C.Y. Xu, W.Z. Shao, Cryst. Growth Des., 9 1558–1568 (2009).

PREPARATION OF ZINC FERRITE BY OXALATE CO – PRECIPITATION METHOD

V. S. Kodag, A. S. Jagdale, A. N. Todkaree, P. P. Zambre and S. P. Dalwai*
Post-Graduate Department of Physics, Raje Ramrao Mahavidyalaya, Jath,
Dist: Sangli, 416 404, MH, India
*Corresponding Author E-mail: sanjeevdalawai@gmail.com

ABSTRACT:

Ferrites are ceramic materials generally gray or black in colour containg iron as a main component. The nanocrystalline powder of zinc ferrite (ZnFe2O4) will be prepared by oxalate co–precipitation method using high purity sulphates. The zinc ferrite material have cubic spinel structure. They are among the most widely used materials for a broad category of applications like in electronic ignition system, generators, medical implants, wrist watches, inductor core, transformer circuits, telecommunicatios etc.

INTRODUCTION:

The nanocrystalline zinc ferrite powder was prepared by the oxalate co-precipitation method. Now a days, it is a most interesting and challenging issues of sciences of magnetic nanoparticles are the introduction of new electronic, magnetic and electrical properties and the optimization of magnetic properties. The spinel zinc ferrite ZnFe2O4 have involved more romantic behavior due to its interesting magnetic property[1] and application in the catalysis[2-5]. Ferrite a ceramic similar to material through magnetic properties that be useful in several types of electronic devices. Zinc ferrite is a superior example of the through relation between the nanoparticle structure[6], composition, as well as properties. When prepared as a bulk material, the zinc-iron oxide have a spinel structure AB_2O_4 among a tetrahedral A site unavailable with Zn2+ ions and an octahedral B site by Fe3+ ions. Based taking place the distribution of cations, spinels can be also normal similar to zinc spinel before inverse with half of the trivalent ions in the tetrahedral position and the other half together with the divalent ions in the octahedral sites. several types of methods including ceramic synthesis[7], co-precipitation method[8-10], tartrate precursor method[11], hydrothermal[12], combustion[13], auto-combustion[14], polymeric precursor route[15], solvothermal[16] and sol-gel technique[17-18] etc. have been used to manufacture to the precursor. Co-precipitation method have be intensively investigate to synthesize the precursor. i.e. spinel ZnFe2O4 can be present synthesized by the side of the 650^{o}C for 6 h, which significantly decrease the production rate[19].

Considerable importance have been concerned in current studies appropriate to the large mixture and the practical effectiveness of their physical and chemical properties, as well as humidity sensing, oxygen-sensing, photoelectrical and super-paramagnetic as well as high temperature ceramic properties[20-23]. Therefore, it was consideration of awareness to synthesized zinc ferrite and it's characterization.

EXPERIMENTAL:

The zinc ferrite samples with prepared by oxalate co-precipitation method. The AR grade (Alpha chemika) Zinc sulphate ($ZnSO_4.7H_2O$,99.5% pure), Ferrous Sulphate ($FeSO_4.7H_2O$,99%, pure) , were dissolved in distilled water in the 1:2 proportion. Heat the solution at 80^0c. To check the pH of the solution. The pH of the solution was maintained at 7.5 by adding conc. H2SO4 drop wise[24] . The mixture was heated at 80^0c for 1 hour to optimize the complete ionization of metal sulphates. The precipitating reagent was prepared in distilled water by adding required proportion of AR grade Ammonium oxalate ($C_2H_8N_2O_4.7H_2O$). the precipitating reagent was added dropwise into metal sulphate solution with stirring until the complete precipitation was obtained[25]. The precipitate was filtering by the Whatman filter paper number 41.To removal of the SO_4^{--} to give the Barium chloride test in the filtrate 20-25 times. After removing the SO_4^{--} ions the precipitate was dry. A dried precipitate was pre-sintered at 400^0c for 3 hours. The precipitate sintered at the 650^0c for 4 hours. The prepared nanocrystalline ferrite powder are formed.

Reaction Mechanism:

Reaction mechanism of a chemical reaction is the step by step sequence of events that take place when reactant molecules get converted into products. It is also describes each step known as elementary process when one or more molecule changes geometry by addition or emission of another interacting molecule. A complete reaction mechanism consists of multiple elementary processes, i.e. it accounts for all reactants, the function of a catalyst, stereochemistry, all products formed and the amount of each.

Physical properties of Zinc Sulphate:

- Zinc is a bluish-white with a shiney surface.
- It is neither ductile nor malleable at room temperature.
- Zinc is fairly soft metal.
- Its hardness is 2.5 on the Mohs scale.
- An hydrous Zinc sulphate is colourless crystalline solid.
- Zinc sulphate is also obtained as a heptahydrate $ZnSO_4.7H_2O$
- Molecular formula – $ZnSO_4$
- Molecular weight – 278.02gm/mol.
- Melting point – 212 F.
- Solubility – 57.7 gm.
- Density – 1.96 at 68 F.

Chemical properties of Zinc Sulphate:

- Zinc is a fairly active element.
- It dissolves in both acids and alkalis.
- An alkali is a chemical with properties opposite those of an acid.
- The zinc carbonate forms a thin white crust on the surface which prevents further reaction zinc burn in air with a bluish film.
- Zinc sulphate is a inorganic compound.

Physical properties of Ferrous Sulphate:

- Ferrous sulphate is a greenish or yellow brown crystalline solid.
- Density – 15.0 ib/gal.
- Melts at 64^0c.
- Loses the seven water of hydration at 90^0c.
- The primary hazard is the threat to the environment.
- Used for water or sewage treatment as a fertilizer ingredient.
- Molecular formula – $FeSO_4$.
- Melting point – 64^0c.

Chemical properties of Ferrous Sulphate:

- ferrous sulphate is blue green crystals.
- It is on odourless.
- It is soluble in water.
- Ferrous sulphate is slightly soluble in alcohol.
- It is soluble in anhydrous methanol.

Reaction Mechanism:

$$\begin{array}{c} ZnSO_4.7H_2O+2FeSO_4.7H_2O+H_2SO_4+C_2H_8N_2O_4.7H_2O \\ \downarrow \\ ZnFe2O_4+4SO^{--}_4+C_2H_{10}N_2+28H_2O \end{array}$$

Molecular Weights:

Zn = 65, S= 32, O= 16, H= 1, Fe= 55, C= 12, N= 14

Reactant:

$ZnSO_4.7H_2O+2FeSO_4.7H_2O+H_2SO_4+C_2H_8N_2O_4.7H_2O$ = 287+428+98+250

= 1063gm/mole.

Product:

$ZnFe2O_4+4SO^{--}_4+C_2H_{10}N_2+(7H_2O)_3= 239+384+62+378$

$= 1063$gm/mole.

RESULT AND CONCLUSION:

Nanocrystalline zinc ferrite powder will be prepared by oxalate coprecipitation method. It is easy to synthesize in small scale laboratory. Ferrites are ceramic materials generally gray or black in colour containing iron as a main component. The zinc ferrite material have cubic spinel structure.

REFERENCES

1. C. Yao, Q. Zeng, G. F. Goya, T. Torres, J. Liu, H. Wu, M. Ge and J. Z. Jiang, J. Phys. Chem., 111, 12274 (2007).
2. Y. Chung, Y. Kwon, T. Kim, S. Lee and S. Hoon, Catal. Lett., 131, 579 (2009).
3. J. Wolska, K. Przepiera, H. Grabowska, A. Przepiera, M. Jablonski and R. Klimkiewicz, Res. Chem. Intermed., 34(1), 43 (2008).
4. R. Klimkiewicz, J. Wolska, A. Przepiera, K. Przepiera, M. Jabłonski and S. Lenart, Mater. Res. Bull., 44, 15 (2009).
5. H. Lee, J. Jung, H. Kim, Y. Chung, T. Kim, S. Lee, S. Oh, Y. Kim and I. K. Song, Catal. Lett., 122, 281 (2008).
6. Y. Li, R. Yi, A. Yan, L. Deng, K. Zhou and X. Liu, Solid State Sci., 11, 1319 (2009).
7. C. N. Chinnasamy, A. Narayanasamy and N. Ponpandian, J. Phy. Cond. Matter., 12, 7795 (2000).
8. D. Makovec, A. Kodre, I. Arcon and M. Drofenik, J. Nanopart Res., 13, 1781 (2011).
9. D. Makovec, A. Kodre, I. Arcon and M. Drofenik, J. Nanopart Res., 11, 1145 (2009).
10. M. Maletin, E. G. Moshopoulou, A. G. Kontos, E. Devlin, A. Delimitis, V. T. Zaspalis, L. Nalbandian and V. V. Srdic, J. Eur. Ceram. Soc., 27, 4391 (2007).
11. J. M. Yang and K. L. Yang, J. Nanopart Res., 11, 1739 (2009).
12. L. Nalbandian, A. V. Delimitis, T. Zaspalis, E. A. Deliyanni, D. N. Bakoyannakis and E. N. Peleka, Microporous Mesoporous Mater., 114, 465 (2008).
13. M. Sertkol, Y. Koseoglu, A. Baykal, H. Kavas and M. S. Toprak, J. Magn. Magn. Mater., 322, 866 (2010).
14. M. R. Barati, S. A. S. Ebrahimi and A. Badiei, J. Non-Cryst. Solids, 354, 5184 (2008).
15. M. Gharagozlou, J. Alloys Compd., 486, 660 (2009).
16. S. Yanez-Vilar, M. Sanchez-Andujar, C. Gomez-Aguirre, J. Mira, M. A. SenarisRodriguez and S. Castro-Garcia, J. Solid State Chem., 182, 2685 (2009).

17. G. Aurelija, J. Darius, B. Aldona and K. Aivaras, Mater. Sci., 17(3), 302 (2011). 18. B. Zhang, J. Zhang and F. Chen, Res. Chem. Intermed., 34(4), 375 (2008).
18. H. Lee, J. C. Jung and H. Kim, Catal. Commun., 9, 1137 (2008).
19. W. F. J. Fontijn, P. J. Van der Zaag, L. F. Feiner, R. Metselaar and M. A. C. Devillers, J. Appl. Phys., 85, 5100 (1999).
20. W. Schafer, W. Kockelman, A. Kirfel, W. Potzel, F. J. Burghart, G. M. Kalvius, A. Martin, W. A. Kaczmarek and S. J. Campbell, Mater. Sci. Forum, 321, 802 (2000).
21. H. H. Hamdeh, J. C. Ho, S. A. Oliver, R. J. Willey, G. Oliveri and G. Busca, J. Appl. Phys., 81, 1851 (1997).
22. S. A. Oliver and H. H. Hamdeh, Phys. Rev., B 60, 3400 (1999).
23. T.J. Shinde, A.B. Gadkari, P. N. Vasembekar, Mater chem Phys, 111:87-91 (2008).
24. N Rezlescu, E Rezlescu, C.L Seva, F Tudorache, P.D. Popa, Cryst Res Technol, 36(6):548-57 (2004).

INVESTIGATION OF MAGNETODIELECTRIC PROPERTIES OF SOL-GEL SYNTHESIZED PZT/LSMO THIN FILM HETEROSTRUCTURE

A. N. Tarale[1*], S. R. Jigajeni[2], S. S. Veer[1], V. L. Mathe[3], S. B. Kulkarni[4], S. M. Mane[5]

[1]Arts, Science & Commerce College Indapur, Pune, India - 413106

[2]Department of Physics, Savitribai Phule Pune University Pune - 411007

[3]Govt. Institute of Science, Nagpur - 440001

[4]Institute of Science, Mumbai - 400032

[5]E. S. Andrades College of Science, Vasai Road, Palghar - 401202

*Corresponding author E-mail: tarale.arjun@gmail.com

ABSTRACT:

The PZT/LSMO thin film heterostructure deposited on SiO_2/n-Si(100) substrate using spin coating technique. The solutions of PZT and LSMO required for the spin coating are prepared using citrate gel method (Pechini method). The thin films of PZT/LSMO is characterized for its structural, morphological, dielectric and magnetodielectric properties. The magnetocapacitance (Mc) measured at various frequencies from 100 Hz to 1 MHz and at various magnetic fields H (0 to 0.5T). It is found that the maagnetocapacitance is frequency dependent. It is observed that the maximum value of Mc for PZT/LSMO thin film heterostructure is -20.5% at frequency of 5 kHz.

Key-Words: PZT, LSMO, FESEM,RD, Magnetocapacitance.

INTRODUCTION:

Investigations on magnetodielectric (MD) systems have gained a momentum in recent years, due to their wide applications in the electrically and magnetically tuned devices [1-9]. It is also known as magnetocapacitance Mc, which is a ratio of change in dielectric constant of MD material in presence of magnetic field H and in absence of magnetic field H_o to the dielectric constant in absence of magnetic field. The mathematically Mc is defined as,

$$\mathrm{Mc}\ \% = \frac{\varepsilon(\mathrm{H}) - \varepsilon(0)}{\varepsilon(0)} \times 100\,, \qquad \text{----------}\ (1)$$

Where the ε(H) and ε(0) are the dielectric constants with and without applied magnetic field, respectively [4]. The MD materials simultaneously exhibits ferroelectric and as well as ferromagnetic properties. The MD materials are in the form of single phase, particulate composites, thin/thick film heterostructures of ferroelectric and ferromagnetic materials. It is reported that Mc is maximum for the systems where ferroelectric phase and ferromagnetic/CMR phase possess the transition temperature Tc simultaneously at a particular temperature [3,7]. Therefore, as a basic requirement, one opts to select ferroelectric systems as well as ferromagnetic/CMR systems possessing Tc in the vicinity of room temperature. These systems may exhibit the significant values of Mc at room temperature. The $Ba_{(1-x)}Sr_{(x)}TiO_3$, $BaZr_{(x)}Ti_{(1-x)}O_3$, $PbZr_{(x)}Ti_{(1-x)}O_3$, 0.7Pb $(Mg_{1/3}Nb_{2/3})O_3$-0.3$PbTiO_3$ $Ba_{(1-x)}Ca_xTiO_3$, $BaTi_{(1-x)}Mg_{(x)}O_3$ are the ferroelectric phases of interest, while $La_{(1-x)}Ba_{(x)}MnO_3$, $La_{(1-x)}Sr_{(x)}MnO_3$, $La_{(1-x)}Ca_{(x)}MnO_3$ are the CMR materials used to form magnetodielectric heterostructures or composites [2-9]. It is also observed that the CMR materials like $La_{0.7}Sr_{0.3}MnO_3$ (LSMO0.3) and $La_{0.67}Sr_{0.33}MnO_3$ (LSMO0.33) possess CMR as well as a large magnetostriction at T_c and therefore these are of immense interest view of applications as well as theoretical viewpoints [3-6].

The recent report by Zang et al. explores similar systems and it is observed that for $0.36BiScO_3$–$0.64PbTiO_3/La_{0.7}Sr_{0.3}MnO_3$ (BSPT/LSMO0.33) composite thin films, the Mc is initially negative for (H< 0.3T) and then becomes positive for H up to 7 T[6]. The negative Mc is associated to the stress induced change in dielectric constant ε, while the positive Mc may occur because of variation of magnetoresistance and the interfacial polarization with applied magnetic field H. Here the stress on the ferroelectric phase occurs because of the magnetostriction in the ferromagnetic phase [5,6,8].

It is reported that the laminated composites of ferromagnetic and ferroelectric materials show the larger value of ME effect and simultaneously these materials show MD effect also. Gridnev et al. have reported the magnetodielectric effect in laminated $PbZr_{0.53}Ti_{0.47}O_3/Mn_{0.4}Zn_{0.6}Fe_2O_4$ ME composites [5]. The cause of MD effect in this laminated system is Magnetostriction of ferrite phase, which induces piezoelectric polarization in piezoelectric phase of ME composite [5]. Krupanidhi et al. have reported a magnetocapacitance Mc for $La_{0.6}Sr_{0.4}MnO_3$/0.7Pb $(Mg_{1/3}Nb_{2/3})O_3$-0.3$PbTiO_3$ epitaxial heterostructures [9]. Nature of the Mc as a function of frequency, applied magnetic field, magnetic layer thickness and temperature collectively suggested a combined contribution from strain coupling and MR effect of LSMO layer on the observed MD properties of the heterostructures. The PZT is one of the piezoelectric material with high value of piezoelectric coefficient d_{33}.

Owing to the discussion above we have selected $PbZr_{0.53}Ti_{0.47}O_3$ as a ferroelectric/piezoelectric phase and LSMO as a ferromagnetic phase of the MD heterostructures. The present paper aims at synthesis of PZT/LSMO thin film heterostructure and its characterization for structural, morphological and magnetodielectric properties.

EXPERIMENTAL:

Synthesis of PZT and LSMO citrate gels:

The citrate gel of the $PbZr_{0.52}Ti_{0.48}O_3$ (PZT) was synthesized using modified Pechini method [193]. The precursors used for the synthesis of the gel were $Pb(NO_3)_2$, $ZrO(NO_3)_2$ and $K_2TiO(C_2O_2)_4.2H_2O$ of purity > 99.9%. KOH was used as a precipitating agent. It was observed that $Pb(OH)_2$ was partially soluble in water but insoluble in alkaline medium. Therefore precipitates were washed using dilute solution of NH_3 keeping pH between 9 to 10. Therefore precipitates were washed using dilute solution of NH_3 keeping pH between 9 to 10. The washed precipitates were dissolved in the citric acid using molar ratio of 1 : 6, i.e. PZT: Citric acid. The precipitates were completely soluble in the citric acid [10]. The mixture thus formed was heated at 80-90 ºC to evaporate the excess water molecules. At the point of saturation of the citrate solution, equal moles of ethylene glycol were added to the citrate solution to achieve formation of the gel due to polyesterification [11-14]. The gel contains ions in the polymeric matrix with required viscosity for spin coating. It is customary to use nearly 15 to 20 m.Pas viscous gel for process of spin coating [15]. The required viscosity of the gel was adjusted by varying appropriate quantity of the 2-methoxyethanol [12]. A few drops of HNO_3 were added to the PZT gel to avoid the precipitation. This process ensures that the polymeric solution contains cations of the citrates and no other anion like nitrates or similar. Similarly citrate gel of LSMO was prepared. The details of synthesis of LSMO were given in our earlier published paper [16].

For the deposition of thin films, SiO_2/n-Si (100) was used as a substrate. Here the citrate gels of respective compositions were used for thin film deposition using spin coating technique. The thin films were deposited using the spin coating technique with rpm at 4000 and for 1 minute duration [11]. Thus after deposition of each layer, the films were subjected to heating under IR lamp 10 minutes. Further the films were pyrolized at 400 ºC for 1 hour in a muffle furnace. After the required thickness is achieved, the films were annealed at 900 ^{0}C for 2 hours for formation of required phase of the respective composition. Initially the 10 layers of LSMO were deposited on SiO_2/n-Si(100) substrate. For the MD thin film heterostructures the LSMO0.33 itself used as a conducting bottom layer [6,15]. Initially the LSMO0.33 is deposited on SiO_2/n-Si(100) substrates using spin coating technique. After deposition of conducting bottom layer, 2 layers of the LSMO0.33 and 2 layers of ferroelectric compositions are deposited alternately on each other. Here each layer is pyrolysed at 400 °C and after deposition of 2 layers, thin films of each compositions are annealed at 900 ^{o}C**.** Then the PZT and LSMO are deposited alternatively to form a MD heterostructure. Here the LSMO0.3 works as conducting bottom layer of ferroelectric/paraelectric thin films and silver electrode of 1mm diameter works as top electrode. The structural analysis is carried out using XRD data. The XRD data was recorded using Bruker D8 advance X-ray diffractometer, while FESEM images were recorded using MIRA3 TESCAN FESEM (Hanyang University, South Korea). Dielectric and MD properties were measured usingHP4284A LCR-Q meter (Solapur University Solapur). The parallel capacitance Cp and dielectric loss tangent tan d were determined for frequencies between 100 Hz and 1 MHz with applied magnetic field between 0 and 0.6 T. Magnetic field was varied using electromagnet Model PS-75 by Scientific Equipment Roorkee, India.

RESULT AND DISCUSSION:

Figure 1.(a) shows the X-ray diffractogram of the PZT thin films grown on SiO_2 /n-Si(100) substrates. From the Fig.1.a it is seen that the phase pure and polycrystalline PZT thin films are

obtained. The observed peaks corresponding to the PZT are in good agreement with the JCPDS data card no.330784. It is observed that the PZT exhibit a tetragonal crystal structure. The observed lattice parameters for PZT thin films are ‘a’ = 3.9854 Å, ‘c’ = 4.138 Å and c/a=1.038 [17]. The crystallite size is calculated using Scherer’s formula and it is equal to 35 nm. Figure 1(b) shows the X-ray diffractograms of the PZT/LSMO0.33 thin films. From the Fig. 1(b) it is observed that the PZT thin film grown on the LSMO0.33 is phase pure and polycrystalline in nature. Here, in the Fig. 1. (b) the reflections corrosponiding to SiO_2 are marked as ‘+’, while the reflections corresponding to the LSMO0.3 are marked as ‘*’.

Figure 2 (a) shows the surface FESEM image of the PZT thin film, while the Fig.2(b) shows the cross sectional FESEM image for thickness measurement. From the figure 2 (a) it is observed that the films grown on SiO_2/n-si(100) substrates are fairly uniform. As the PZT forms at lower sintering temperature, the annealing temperature of 900 °C is sufficient for the PZT. It is observed that the grains of the PZT are agglomerated, therefore the particle size is not determined. For the determination of dielectric constant of ferroelectric/dielectric thin films it is customary to know the thickness of the ferroelectric/dielectric thin films.

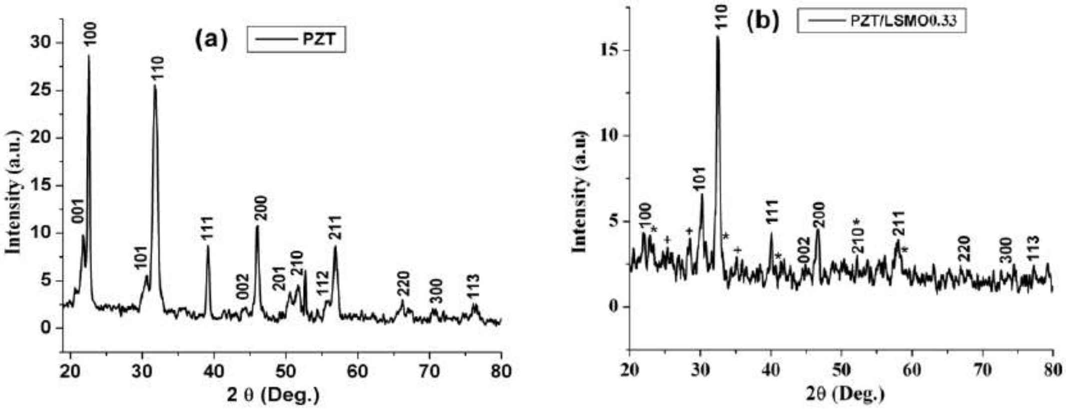

Fig. 1: X-ray diffractogram of the a)PZT, b) PZT/LSMO0.33 thin films on SiO_2/n-Si(100) substrate

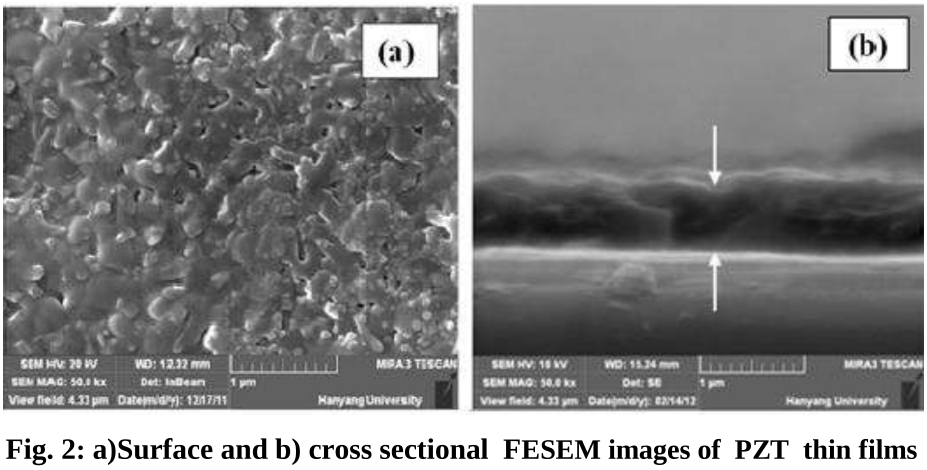

Fig. 2: a)Surface and b) cross sectional FESEM images of PZT thin films

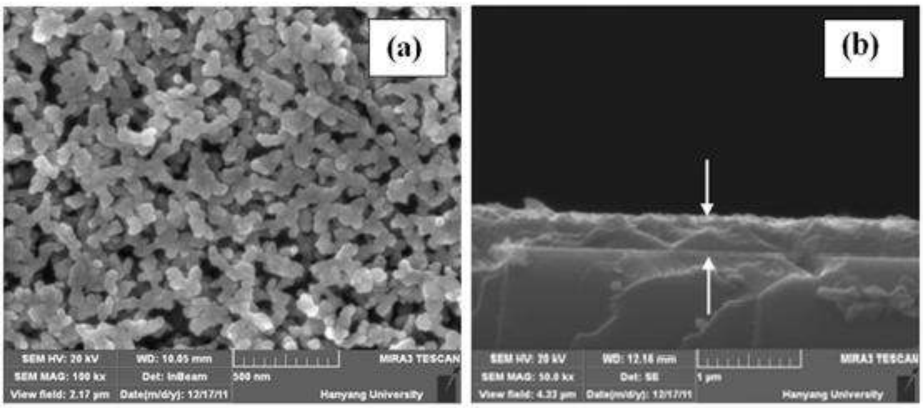

Fig. 3: a)Surface and b) cross sectional FESEM images of LSMO thin films

For the purpose of the thickness measurement of the films, the cross sectional FESEM images of the thin films in present work are determined and are shown in the Figure 2. (b). For the cross sectional FESEM image determination 6 layers of spin coating process are used for the PZT thin films. The observed thickness per unit layer for PZT film is 108 nm.

Figure 3 (a) shows the surface FESEM image of the LSMO0.3 thin film grown on the SiO_2/n-Si(100) substrates. From the Fig.3 (a) it is observed that a fairly uniform microstructure is observed for the LSMO0.3 thin film. The grains of the LSMO0.3 are observed to be elongated and agglomerated. The observed average grain size of the LSMO0.3 is nearly 66 nm. Figure 3(b) shows the cross sectional FESEM image of the LSMO thin films grown on the SiO_2/n-Si(100) substrates. The average thickness of the LSMO thin film per unit layer is 150 nm.

Figure 4(a-b) shows the variation of real part ε' and imaginary part ε'' of the complex permittivity ε^* respectively as a function of frequency f, for various magnetic fields H equal to 0, 0.1, 0.2, 0.3, 0.4 and 0.5 T, for the PZT/LSMO0.33 heterostructures. From figure 4(a) it is seen that the frequency dispersion of ε' is higher at lower frequencies up to 100 kHz and reduces as frequency increases up to 1MHz. Further it is also seen that ε' decreases with increasing applied magnetic field for entire frequency range up to 1 MHz. However the decrease in ε' is more at lower frequencies, while it become almost independent of H for f > 100 kHz. Initially faster decrease in ε' with f could be because of presence of interfacial polarization between the LSMO0.33 and PZT layers. Partially interfacial polarization could be treated as an electrode effect, as the LSMO0.33 is used as a conducting bottom layer.

Now regarding the variation of ε'' with f and H, the observations are similar for the BZT0.15 and PZT. Here it could be noted that the PZT is a strong piezoelectric material as compared to the BZT0.15. From the Fig.4(b) it is seen that the frequency dispersion of ε'' is higher for increasing applied magnetic field at lower frequencies. This feature indicates that the contribution of DC conductivity increases as the applied magnetic field increases. For magnetic field $H< 0.2$ T the contribution of DC conductivity is almost insignificant.

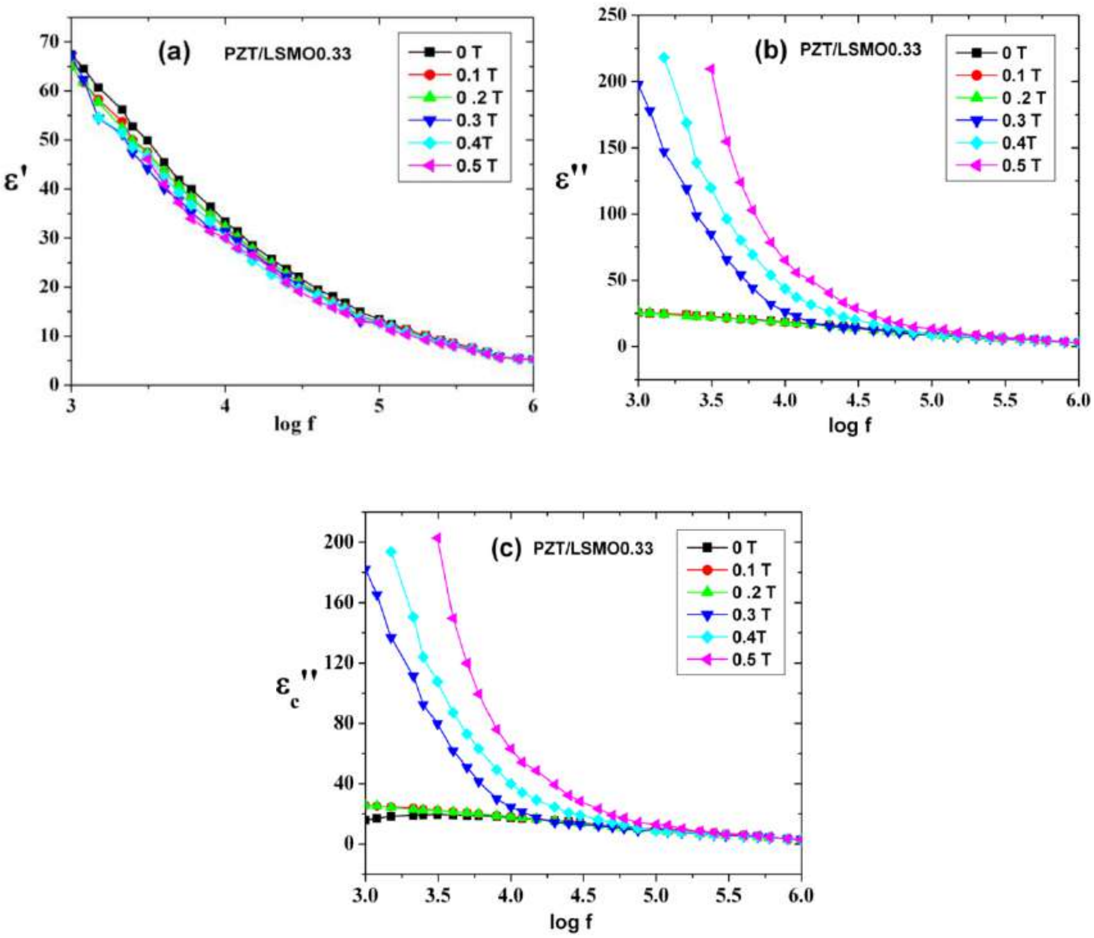

Fig. 4: Variation of (a) ε′ , (b) ε″ and (c) ε_c'' as a function of frequency (log f) for the PZT/LSMO0.33 thin film heterostructure at applied magnetic field H equal to 0, 0.1, 0.1, 0.2, 0.3, 0.4 and 0.5 T

Now the Fig.4(c) shows the variation of ε_c'' after the contribution due to the σ_{dc} is subtracted. From Fig. 4 (c) it is seen that the nature of variation of the ε_c'' is almost same as that of the ε″. Therefore contribution due to the conductivity term is sufficiently small and the extrinsic contribution like interfacial polarization dominates over the DC conductivity term σ_{dc}, especially at lower frequency upto 10 kHz.

Figure 5 shows the variation of loss tangent tan δ as a function of frequency f for various magnetic fields from 0 T to 0.5 T for the PZT/LSMO0.33 thin film heterostructure. From the Fig.5 it is observed that the loss tangent, tan δ, increases as magnetic field increases and this effect is prominent at lower frequencies only. Further the tan δ passes through mild relaxation peak at 500 kHz. Nevertheless the frequency of the peak is almost independent of H. In this case also frequency and magnetic field dependence of ε′ could be understood in terms of contributions due to strain induced effect and the contribution due the CMR effect. At lower frequencies up to 10 kHz the stress induced effect is dominates over the CMR induced effect.

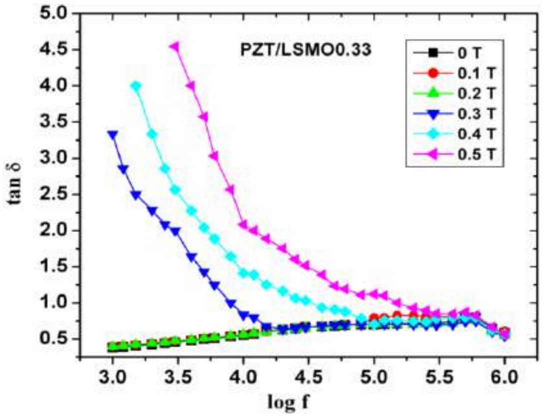

Fig. 5: Variation of tan δ as a function of (log f) for PZT/LSMO0.33 thin film heterostructure at H to equal to 0, 0.1, 0.2, 0.3, 0.4 and 0.5 T

Figure 6 shows the variation of parallel capacitance Cp as a function of applied magnetic field for frequencies 1 kHz, 5 kHz and 10 kHz. Table 1 shows the values of Mc for various frequencies between 1 kHz to 1 MHz. From the Table 1 it is observed that Mc is maximum negative at -20.5% for f equal to 5 kHz and it decreases up to 1.9 % at 1 MHz. Similar behaviour is already reported for the BSPT/LSMO0.33 heterostructure.

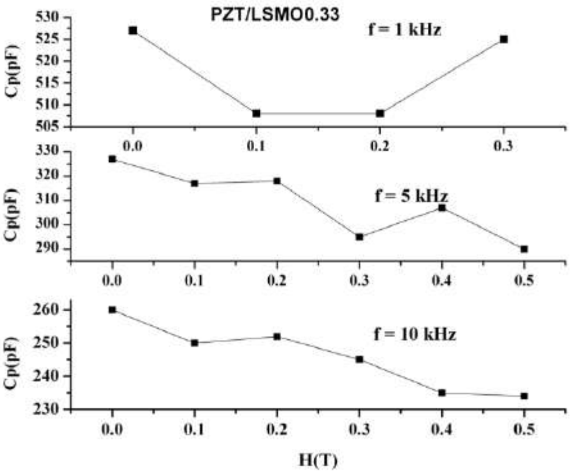

Fig. 6: Variation of Cp as a function of applied magnetic field H for the PZT/LSMO0.33 thin film heterostructure at f equal to 1 kHz, 5 kHz and 10 kHZ

The present observations also could be understood in terms of a theoretical model proposed by Zang et al.[6,8]. The present observation have shown that the Mc is very large i.e. -20.5 % for the PZT/LSMO0.33. The higher value of Mc could be associated to the higher value of piezoelectric coupling coefficient of the PZT as compare to other ferroelectric thin films.

Table 1: Magnetocapacitance (Mc) for the PZT/LSMO0.33 heterostructure

Freq. f (kHz)	Mc %
1	-4.5
5	-20.5
10	-10.0
100	-5.9
500	-5.9
1000	-1.9

CONCLUSION:

The thin film heterostructures of PZT/LSMO are synthesized by citrate gel method followed by spin coating technique. From XRD analysis it is found that the PZT exhibits tetragonal crystal structure with lattice parameter 'a' = 3.9854 Å and 'c' = 4.138 Å . The observed crystallite size of PZT from XRD is 35 nm. From FESEM images it is observed that the PZT grains are agglomerated and the observed thickness of PZT thin film per unit layer is 108 nm, while the observed thickness per unit layer of LSMO film is 150nm. The values of ε', ε'', ε_c'' and tan δ shows the significant variation as a function of frequency f at various magntic field H. The resultant PZT/LSMO MD heterostructure shows significant values of Mc at various frequencies. Comparatively large values of magnetocapacitance Mc for the PZT/LSMO thin film heterostructure are 20.5% and 10 % at 5 and 10 kHz respectively.

ACKNOWLEDGEMENT:

The authors wish to acknowledge the help rendered by Dr. R.C. Pawar for FESEM images, from Hanyang University, South Korea. The authors also acknowledge Solapur University Solapur and UGC-CSR Indore for availing experimental facilities and financial support for this work.

REFERENCES:

1. Y. S. Koo, T. Bonaedy, K. D. Sung, J. H. Jung, J. B. Yoon, Y. H. Jo, M. H. Jung, H. J. Lee, and Y. H. Jeong, Appl.Phys. Lett., 91, 212903 (2007).
2. M. P. Singh, W. Prellier, Ch. Simon and B. Raveau, Appl. Phys. Lett., 87, 22505 (2005).
3. T. Bonaedy, K.M. Song, K.D. Sang , Solid State Commun., 148, 424 (2008).
4. G. Catalan, Appl. Phys. Lett., 88, 102902 (2006).
5. S.A.Gridnev, A.V.Kalgin and V.A. Chernykh, Ferroelectrics, 109, 70 (2009).
6. S. Zhang, X. Dong, Y. Chen, G. Wang, J. Zhu and X. Tang, Solid State Communications, 151, 982 (2011).

7. N. G. Kim, Y. S. Koo, C. J. Won, N. Hur and J. H. Jung, J. Appl. Phys., 102, 014107 (2007).
8. S. Zhang, X. Dong, Y. Chen and F. Cao, J. Appl. Phys., 110, 046103 (2011).
9. A. R. Chaudhuri, P. Mandal, A. Sundaresanand and S.B. Krupanidhi, Materials Research Centre, Indian Institute of Science, Bangalore 560 012, India.
10. S.S. Veer, D.J. Salunkhe, S.V. Kulkarni, S.B. Kulkarni and P. B. Joshi, Material Science Research India, 5(1), 173 (2008).
11. W.D. Yang, S.H. Huang and Y.H. Chang, Thin Solid Films, 478, 42 (2005).
12. J. Zhai, Xi Yao and Hyden Chen, Ceram. International., 30, 1237 (2004).
13. F. M.Pontes, E. R. Leite and J. A. Varela, J. Mater. Scie., 35, 4783 (2000).
14. F. Xinghua, S. Lianwei, D. Biyan, H. Wenping, F. Zhou and F. Zhengyi. Bull. Mater. Sci., 27, 433 (2004).
15. F.M. Pontes, M.T. Escote, C.C. Escudeiro, E.R. Leite, E. Longo,A.J. Chiquito, P.S. Pizani and J.A. Varela, J. Appl. Phys., 96, 4386 (2004).
16. A. N. Tarale , S. R. Jigajeni, D. J. Salunkhe , P. B. Joshi , S. B. Kulkarni, D. M. Phase , R. J. Chaudhary , S. K. Deshapande, JMSE,23, 557 (2012).
17. F.M. Pontes, E.R. Leite, M.S.J. Nunes, D.S.L. Pontes, E. Longo and R. Magnania, J. European Ceramic Society, 24, 2969 (2004).

DIELECTRIC PROPERTIES OF (x) $Ni_{0.5}$ $Zn_{0.5}$ Fe_2O_4 + (1-x) Pb $Zr_{0.8}$ $Ti_{0.2}O_3$ MAGNETOELECTRIC COMPOSITES

C. M. Kanamadi[1] and B. K. Bammannavar[2]

[1]Department of Physics, Devchand College, Arjunnagar, Dist: Kolhapur – 591 237

[2]Department of Physics, Karnatak University, Dharwad – 580 003

ABSTRACT:

Magneto electric composites with composition (x) $Ni_{0.5}$ $Zn_{0.5}$ Fe_2O_4 + (1-x) Pb $Zr_{0.8}$ $Ti_{0.2}O_3$ (PZT- Lead Zirconate Titanate) in which x varies as 0.0, 0.15, 0.30, 0.45 and 1.0 mol % was prepared by the conventional double sintering ceramic technique. The phase analysis was carried out using X-ray diffraction technique, which confirms the absence of any intermediate phases present in the composites. The variation in dielectric constant (ε') and dielectric loss ($\tan\delta$)as a function of temperature in the frequency range 20 Hz to 1 MHz was studied.

INTRODUCTION:

In recent years, much interest has been created in magneto electric materials that generate electrical response (ME output) by application of external magnetic field (called ME_H effect) or magnetization by external electric field (called ME_E effect)[1]. In 1894, Curie pointed out the possibility of the polarization of the asymmetric molecular body under an external magnetic field. Subsequently in 1957, Landu and Lifshitz argued that the ME effect could principally exist in some magnetically ordered crystals[2]. The ME effect was observed for the first time in antiferromagnetic Cr_2O_3 in 1961 and later some single phase crystal families were discovered to have ME effect. However, these single phase materials show weak ME effect that they have not yet found any technological applications. Alternatively, ferrite/ferroelectric (e.g. $NiFe_2O_4/BaTiO_3$) composite ceramics have been found to exhibit a larger ME effect than that of single phase materials which results from the coupling of magnetic-mechanical-electric interactions[3].

In the present case zinc doped nickel ferrite having high resistivity, high magnetostriction coefficient and low eddy current losses is selected as ferrite phase and PZT having high piezoelectric constant, high dielectric permittivity and superior coupling factor as a ferroelectric phase.

EXPERIMENTAL PROCEDURE:

A conventional double sintering ceramic method was used to prepare (x) $Ni_{0.5}$ $Zn_{0.5}$ Fe_2O_4 + (1-x) PZT ME composites consisting of two individual phases, ferrite and ferroelectric. Ferrite is prepared through normal solid state reaction by taking analytical reagent grade (AR) NiO, CoO and Fe_2O_3 powders in Stochiometric proportions. The ferrite was presintered at 800 ^oC for 8 h. Similarly the ferroelectric phase was prepared with PbO, TiO_2 and ZrO_2 as starting materials in molar ratio and was presintered at 1000 °C for 10 h. After presintering, the constituent phases were thoroughly mixed and ground to fine powder. The ME composites were prepared by mixing 15, 30 and 45 mole % of ferrite phase with 85, 70 and 55 mole % of ferroelectric phase respectively. They were presintered again at 1000 °C for 10 h. The disc shaped pellets of the composites with thickness 2-3 mm and diameter 10 -15 mm were prepared using the hydraulic press. The pellets of the composites were finally sintered at 1200 °C for 12 h at the rate of 100 °C /h and furnace cooled to room temperature at the same rate.

The crystal structure of the composites was characterized by X-ray diffraction (XRD) method using CuK_α radiation (λ=1.5554 Å, XRD model, Philips PW 1710). The dielectric constant was measured in the frequency range from 20 Hz to 1 MHz at room temperature by using LCR meter bridge(Model HP 4248 A). Variation of dielectric constant and loss tangent with temperature at four fixed frequencies (1 KHz, 10 KHz, and 100 KHz and 1 MHz) was studied to understand the temperature dependence of composites.

RESULTS AND DISCUSSION:

The typical X-ray diffraction pattern of composites is shown in Fig. 1. All the peaks could be easily identified and no intermediate phase formed in the composites. The occurrence of peaks with specific indices characteristics of spinel and perovskite structure confirms the formation of cubic spinel structure in the ferrite phase and tetragonal perovskite structure in ferroelectric phase of the composites. The intensity of (101) perovskite peak decreases while intensity of (311) ferrite peak increases with increase in ferrite content in the composites. It may due to small percentage of ferrite in the composite and the probable dispersal of tiny particles in the composites[5,6].

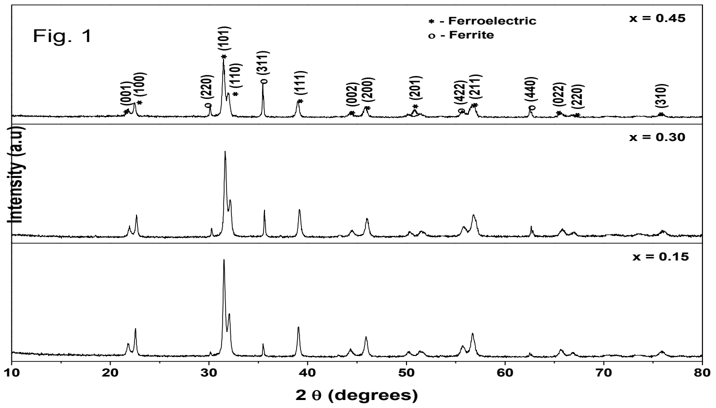

Dielectric properties:

The variation of dielectric constant and loss tangent with frequency are shown in Fig. 2 and 3 respectively. The dielectric constant and loss tangent decreases rapidly at lower frequencies and remain constant at higher frequencies. Because of the different permittivities and conductivities of two media, the dielectric dispersion observed at lower frequencies is attributed to the interfacial polarization. The high dielectric constant observed at lower frequencies is not usually intrinsic but rather associated with a heterogeneous conduction in the multiphase structure of composites. From the Figure, it is also observed that the dielectric constant is decreased with increase in ferrite content. This is because the dielectric constant of ferrite is less as compared to the ferroelectric phase.

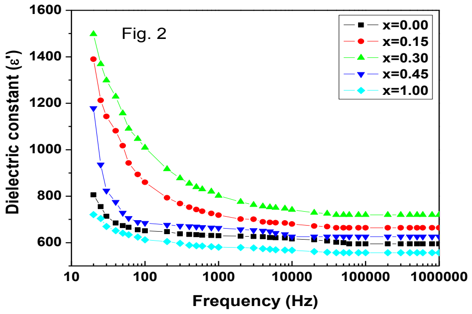

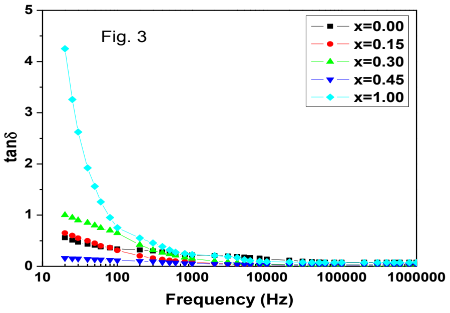

Figure 4 and 5 shows the variation of dielectric constant of the composites with temperature at four different frequencies (Viz. 1 KHz, 10 KHz, 100 KHz and 1 MHz) for x = 0.15 and 0.45 composition respectively. For both the composites, dielectric constant is found to increase with increase in temperature, reaches a maximum value at Curie temperature and follows a decreasing trend indicating the phase transition.

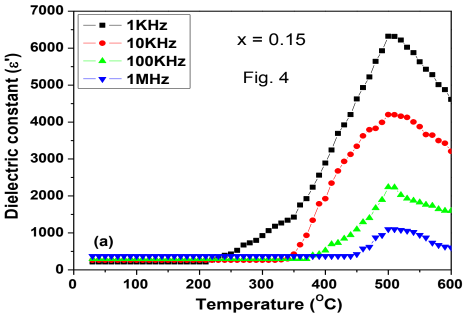

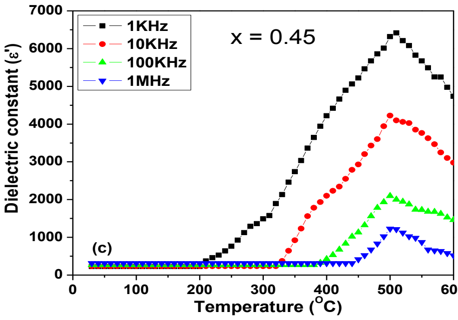

As the temperature increases, AC electric conductivity increases due to increase in drift mobility of thermally activated electrons as a result dielectric polarization increases causing an increase in dielectric constant and loss tangent with temperature. The huge increase in dielectric constant near transition temperature (T_C) can be explained on the basis of temperature dependent characteristics of domain wall motion. At temperatures above T_C the ferroelectric phase has been translated to the paraelectric phase wherein all the domains disappear causing decrease in dielectric constant. The Curie temperature is found to decrease with increase in ferrite content. This is because the electric field induced magnetic phase transition depends on the strength of interaction between electric and magnetic ordering, which is in turn depends on the molar ratio of the phases[7-10]. The decrease in dielectric constant also attributed to the doping effect of ferrite addition in these composites. Also the increase of ferrite content as a result of decrease in polarization efficiency leading to increased conductivity[11].

CONCLUSION:

The ME composites containing ferrite and ferroelectric phases were prepared by standard double sintering ceramic technique. The X-ray diffraction study of these materials reveals the presence of ferrite and ferroelectric phases. The samples show negative temperature coefficient of resistivity indicating semiconducting nature. The decrease in dielectric constant and loss tangent with frequency shows the dielectric dispersion at low frequency regions. The dielectric constant increases with increasing temperature and starts decreasing after passing through the transition temperature indicating phase transitions from ferroelectric to paraelectric state.

REFERENCES:

1. S.V. Suryanarayana, Bull. Mater. Sci., 17(7), 1259 – 1270 (1994).
2. K.K. Patankar,S.L. Kadam, V.L. Mathe, C.M. Kanamadi,V.P. Kothavale and B.K. Chougule, Brit. Ceram. Trans., 102, 19 – 22 (2003).
3. S.L. Kadam, C.M. Kanamadi, K.K. Patankar and B.K. Chougule, Mater. Lett., 59, (2/3), 215 – 219 (2005).
4. C.M. Kanamadi,L.B. Pujeri and B.K. Chougule, J. Magn. Magn. Mater., 295, 139 – 144 (2005).
5. C.W. Nan, Phys. Rev. B., 50, 6082 – 6088 (1994).
6. Hong-Cai He, JingWang, Jian – Ping Zhou, Ce-Wen Nan, Adv. Funct. Mater., 17, 1333 – 1338 (2007).
7. M.A. Jing, Shi Zhan, C.W. Nan, Adv. Mater., 19, 2571 – 2573 (2007).
8. N.A. Spaldin and M. Fiebig, Science, 309, 391 – 392 (2005).
9. S. X. Dong, J. F. Li, and D. Viehland, Appl. Phys. Lett., 83, 2265 - 2267 (2003).
10. T. Kanai, S.I. Ohkoshi, A. Nakajima, T. Watanabe, K. Hashimoto, Adv.Mater, 13, 487 – 490 (2001).
11. M.M. Kumar, A. Srinivas, G.S. Kumar, S.V. Suryanarayana, J.Phys.:Condens. Matter, 11, 8131 – 8139 (1999).

ADVANCES IN MATERIALS SCIENCE

(A SPECIAL ISSUE FOR ICAMS - 2017)

Dr. Shrikant Kokare

Dr. Shrikant Kokare completed his graduation from Bharati Vidyappeth's Dr. Patangrao Kadam Mahavidyalaya, Sangli and post graduation from Shivaji University, Kolhapur. He obtained Ph. D. from Shivaji University, Kolhapur. He has 20 years of teaching and research experience. He has published 25 research papers in various national and international journals. There are twelve books on his credit. He has completed four research projects funded by Department of Consumer Affairs, Govt. of India, UGC, Shivaji University and BAMU, Aurangabad. Apart from his research publications, he also wrote and published more than thousand news articles in various newspapers on social, economical, educational and political issues.

Dr. Kokare has presented research papers in Third International Symposium on Heat Transfer Enhancement and Energy Conservation, (Jan. 2016) at South China University of Technology, Gaoungazou (China). Further he has delivered series of lectures at Beijing University of Technology, Beijing (China) and Hong Kong Polytechnic University, Hong Kong. He is recipient of Summer Research Fellowship by IAS, Bangalore. He was honored by best paper presenter at national level twice. He also completed founadation training programme for scientists and technologists conducted by DST, New Delhi.

Dr. Sanjay S. Latthe

Dr. Sanjay S. Latthe is currently an Assistant Professor in Physics at Raje Ramrao Mahavidyalaya, Jath, Maharashtra, India (June 2016 till date). He received his B. Sc. degree (2005), M. S. degree (2007) and Ph. D. degree (2010) from Shivaji University, Kolhapur, India. He then worked as post doctoral fellow in Prof. A. Levent Demirel's research group in Koc University, Istanbul, Turkey (2010 12) and Prof. Sam S. Yoon's research group in Korea University, Seoul, South Korea (2012 13). He is recipient of prestigious *Japan Society for the Promotion of Science (JSPS)* Post Doctoral fellowship and worked under Prof. Akira Fujishima, President, Tokyo University of Science, Japan (2013 15). In 2015 16, he worked as *DST-INSPIRE Faculty* in Department of Technology, Savitribai Phule Pune University, Pune. He has attended the prestigious *66th Lindau Nobel Laureate Meeting* in Lindau, Germany (June July 2016) and *2nd BRICS Young Scientist Forum* at Zhejiang University, Hangzhou, China (July 2017). He has joined the invitation program carried out under the framework of Japan-Asia Youth Exchange Program in Science (*Sakura Exchange Program in Science*) supported by Japan Science and Technology Agency (JST), Japan for consecutive three years (2016 2018). He authored 01 Chinese Patent, 03 books and over 50 peer reviewed international journal papers, which attracted over 2, 000 citations with an h-index of 29. His scientific interest is focused on bio-inspired surfaces and interfacial materials.

ISBN : 978-84-931247-6-5

Published By :
Bhumi Publishing, India

Shri Shivshambho Tarale